

AUV HYDRODYNAMICS AND MODELLING FOR IMPROVED CONTROL

by

PETER MICHAEL OSTAFICHUK B.Sc., The University of British Columbia, 1997

A THESIS SUBMITTED IN PARTIAL FULFILMENT OF
THE REQUIREMENTS FOR THE DEGREE OF

DOCTOR OF PHILOSOPHY in THE FACULTY OF GRADUATE STUDIES

(Department of Mechanical Engineering)

We accept this thesis as conforming to
the required standard

THE UNIVERSITY OF BRITISH COLUMBIA

April 2004

© Peter Michael Ostafichuk, 2004

ABSTRACT

The performance and management of control surfaces on a near-surface autonomous underwater vehicle (AUV) were examined in terms of hydrodynamics, modelling, and control. Experiments were conducted using a one-quarter scale physical model of the International Submarine Engineering (ISE) Mark II DOLPHIN AUV. The experiments involved extensive tests in wind tunnels and a tow tank and included both force measurement and flow visualization studies. The experiment results were used to mathematically describe the performance of AUV control surfaces for use in simulation. Additionally, based on the new control surface hydrodynamics information, enhancements were made to the vehicle controller. For the various vehicle and controller configurations, the overall vehicle performance was evaluated through simulation using representative manoeuvres and operating conditions.

In straight and level flight, the performance of the forward control surfaces (bowplanes) was well described through existing semi-empirical predictions. Trailing vortices shed by the forward control surfaces significantly affected the performance of the aft control surfaces (sternplanes). This interaction was a strong function of vehicle orientation and was accurately predicted by a simple potential flow model. Significant changes were noted to bowplane performance when the vehicle was oriented with trim or yaw. The influence of waves on the planes, including the dependence on vehicle speed and depth, agreed well with analytical predictions.

In simulation, the effect on vehicle performance of changes in the control surface modelling, control surface configuration, and the controller design were studied. Although significantly different mathematical models of control surface performance were developed, they were found to have similar effects on the overall vehicle performance. Changes to the control surface configuration had a very significant effect on performance. In particular, increasing the bowplane span and adding dihedral to the bowplanes or sternplanes were both found to improve manoeuvring and minimize the effect of waves on the vehicle. Only minor differences in performance were noted between different PD controller implementations. The PD controllers were sensitive to modeling errors and exhibited unstable behavior in one instance. A linear quadratic gaussian controller with loop transfer recovery (LQG/LTR) was more robust and was further improved with the incorporation of sliding mode control.

TABLE OF CONTENTS

Abstract.....	ii
List of Figures.....	viii
List of Tables	xvi
List of Symbols	xviii
Preface.....	xxx
Acknowledgements	xxxi
Chapter 1 Introduction.....	1
1.1 Background	2
1.1.1 Applications for AUVs.	2
1.1.2 AUV Operation	3
1.1.3 The Dolphin AUV	5
1.2 Motivation	7
1.3 Survey of Previous Work.....	8
1.4 Objectives.....	10
1.5 Approach and Rationale	11
1.5.1 Hydrodynamics.	11
1.5.2 Modelling and Simulation	11
1.5.3 Control	12
Chapter 2 Control Surface Hydrodynamics - Theory.....	13
2.1 Conventions.....	14
2.2 Control Surface Geometry.....	18
2.2.1 Chord	18
2.2.2 Span	19
2.2.3 Foil Section.	19
2.2.4 Planform.	20
2.2.5 Aspect Ratio	20
2.2.6 Endplates	21
2.3 AUV Control Surface Layout.....	23
2.3.1 Anhedral and Dihedral	23
2.3.2 Tail Control Surface Configurations	24
2.3.3 Dolphin-Specific Control Surfaces.	24
2.4 Control Surface Performance Prediction.....	27
2.4.1 Isolated Control Surface.	27
2.4.2 Hull Influence on Bowplanes	29
2.4.3 Hull Influence on Sternplanes	31
2.5 Control Surface Interaction	35
2.5.1 Downwash to Aircraft Elevators	35
2.5.2 Interaction Between Warship Stabilizer Fins	35
2.5.3 Control Surface Interaction Predictions on Dolphin-like Vehicles	36

2.6	Free Surface Influence.....	38
2.6.1	Calm Water Free Surface Considerations for AUVs	38
2.6.2	Wave Theory	38
2.6.3	Sea State and Wave Spectra	38
2.6.4	Wave Considerations for AUVs.....	39
Chapter 3	Control Surface Hydrodynamics - Experiments.....	41
3.1	Model and Facilities	42
3.1.1	Similarity and Scaling	42
3.1.2	Scale Model	43
3.1.3	Load Cells and Signal Conditioning	48
3.1.4	Data Collection Protocol	53
3.1.5	Testing Facilities.....	53
3.2	Plane Performance.....	54
3.2.1	Isolated Plane	54
3.2.2	Straight and Level Flight	55
3.2.3	Non-zero Trim	62
3.2.4	Non-Zero Yaw	68
3.3	Control Surface Interaction	73
3.3.1	Straight and Level Flight	73
3.3.2	Non-Zero Trim	81
3.3.3	Non-Zero Yaw	87
3.4	Free Surface Interaction	89
3.4.1	Wave Geometries Tested	89
3.4.2	Wave and Control Surface Force Spectra.....	89
3.4.3	Wave Geometry Influence	90
3.4.4	Depth Influence	93
3.4.5	Speed Influence	95
3.4.6	Bowplane Position Influence	97
3.5	Summary	99
Chapter 4	Control Surface Hydrodynamics - Modelling.....	100
4.1	Background	101
4.2	Reynolds Number Effect Modelling	102
4.2.1	Change in stall angle with Reynolds number	102
4.2.2	Scaling experimental data.....	103
4.3	Control Surface Performance Modelling	107
4.3.1	Hydrodynamic Derivatives.....	107
4.3.2	Bowplane Performance Prediction.....	107
4.4	Trim Effect Modelling.....	110
4.4.1	Experimental Results	110
4.4.2	Analytical Prediction of Trim Influence.....	111
4.5	Yaw Effect Modelling	113
4.5.1	Semi-Empirical Relations for Bowplane Performance in Yaw	113
4.5.2	Analytical Prediction of Yaw Influence on Bowplanes	115
4.6	Control Surface Interaction Modelling.....	119
4.6.1	Potential Flow Model of Control Surface Interaction	119
4.6.2	Modelling Bowplane-Sternplane Interaction in Trim and Yaw	127

4.7	Free Surface Interaction Modelling.....	129
4.7.1	Variation of Wave-Induced Plane Force with Depth	129
4.7.2	Variation of Wave-Induced Plane Force with Forward Speed	131
4.8	Implementation.....	133
4.9	Summary	136
Chapter 5	Control System Design	137
5.1	Control Background	138
5.1.1	Feedback Control	138
5.1.2	PID Control	138
5.1.3	Linear Quadratic Control with Loop Transfer Recovery	139
5.1.4	Adaptive Control Techniques	140
5.1.5	Fuzzy Logic	141
5.2	Control System Implementation.....	143
5.2.1	State Space Representation	143
5.2.2	Feed-forward Compensation	144
5.2.3	Series compensation	145
5.3	PD Controllers.....	146
5.3.1	Basic PD	146
5.3.2	PD Control With Gain Scheduling	147
5.3.3	PD Control With Fuzzy-Tuned Series Compensation	151
5.4	LQG/LTR Controller.....	159
5.4.1	Basic LQG/LTR	159
5.4.2	Sliding Mode LQG/LTR Controller	164
5.4.3	LQG/LTR Controller with Fuzzy-Tuned Series Compensation	169
5.5	Summary	170
Chapter 6	Simulation.....	171
6.1	Simulation Background.....	172
6.2	Simulation Environment and Design	173
6.2.1	Simulation Procedure	173
6.2.2	Simulator Layout	173
6.2.3	Simulation Programming	176
6.3	Simulation Test Cases and Evaluation	177
6.3.1	Evaluation Manoeuvres	177
6.3.2	Evaluation Criteria	178
6.3.3	Simulated Cases	182
6.4	Results: Influence of Modelling Improvements.....	184
6.4.1	Changes to the Plant Model	184
6.4.2	Changes to the Controller Model	185
6.5	Results: Evaluation of Plane Configuration.....	188
6.5.1	Plane Geometry	188
6.5.2	Plane Location	190
6.6	Results: Evaluation of Control System	196
6.6.1	PD Controller Performance	196
6.6.2	LQG/LTR Controller Performance	198
6.6.3	Comparison of PD and LQG/LTR Control Strategies	200

6.7	Summary	206
Chapter 7	Conclusion	208
7.1	Summary	209
7.1.1	Overview	209
7.1.2	Influence of Control Surface Performance Model	210
7.1.3	Influence of Control Surface Configuration	210
7.1.4	Influence of Controller Design	211
7.2	Recommendations	213
7.2.1	Hydrodynamics and Modelling	213
7.2.2	Control and Evaluation	213
7.3	Conclusions	214
Appendices	215
A -	Supplementary Calculations	216
A.1	Bowplane Upwash Calculations	217
A.2	Change in Stall Angle With Aspect Ratio	221
A.3	Change in Maximum Lift Coefficient with Reynolds Number	222
A.4	Analytical Prediction of Yaw Influence on Bowplanes	224
A.5	Control Surface Interaction Potential Flow Model	227
	Bowplane Tip Vortex Model	227
	Bowplane Vortex Interaction with Sternplanes	230
B -	Dolphin Scale Model Details.....	232
B.1	Scale Model Engineering Drawings	233
B.2	Load Cell Design	270
B.3	Boundary Layer Tripping	274
C -	Numerical Calculations.....	277
C.1	Slope Error Estimation	278
C.2	Radius of Curvature Calculation	279
D -	Controller development	281
D.1	State Space Equations	282
D.2	LQG/LTR Controller Design	285
	Determination of Win	285
	Tuning of LQG/LTR Parameters	285
E -	Matlab / Simulink Program.....	288
E.1	MATLAB Simulation m.file® Summary	289
	Overview	289
	Batchfile.m	290
	Calcu0	292
	flqdesign.m	293
	fuzrepid	295
	gsrepid	296
	Jmat	297
	Linearize	298
	Loadparam	304
	Siminit (PID)	307
	rid.m	308
	ridrow.m	308

	smlqgdesign	309
	smlqggainset	312
	SPMA	314
	SPMB	316
	SPMB_S	319
	swnoise.m	322
E.2	Simulink® Block Diagrams	325
F -	Simulation Results	332
F.1	Simulations Conducted	333
F.2	Evaluation of Modelling Influence	336
	Influence of Plant Model Improvements	336
	Influence of Controller Model Improvements	337
F.3	Evaluation of Vehicle Geometry	338
	Plane Geometry	338
	Plane Location	344
F.4	Evaluation of Control System	350
	PD Controller Augmentations	350
	LQG/LTR Controller Augmentations	356
	References	362
	Index of Authors	374
	Subject Index	377

LIST OF FIGURES

Figure 1-1	Typical geometry of an AUV	4
Figure 1-2	AUV degrees of freedom.....	4
Figure 1-3	ISER DOLPHIN Mark II AUV	5
Figure 2-1	Typical geometry of an autonomous underwater vehicle	14
Figure 2-2	Sign conventions.....	15
Figure 2-3	Control surface coordinate system (shown on starboard side plane)	18
Figure 2-4	Control surface parameters (shown on port side plane)	19
Figure 2-5	Variation lift coefficient with aspect ratio	21
Figure 2-6	Inboard and outboard endplates.....	22
Figure 2-7	Span-wise bowplane inclination angle: (a) dihedral, (b) anhedral	23
Figure 2-8	Tail configurations: (a) cruciform; (b) Y-tail; (c) inverted Y-tail; (d) X-tail	25
Figure 2-9	Dolphin-specific control surface locations: (a) keel planes; (b) articulated mast	26
Figure 2-10	Incident flow angle to planes.....	28
Figure 2-11	Flow angle near inclined hull	30
Figure 2-12	Vortex pattern on the leeward side of the hull in yaw	32
Figure 2-13	Fin area used in Lyons and Bisgood's tail efficiency correction factor.....	33
Figure 2-14	Fin area used in Dempsey's tail efficiency correction factor	34
Figure 2-15	Fin vortex model of Lloyd.....	36
Figure 3-1	Quarter-scale model exploded view	44
Figure 3-2	Cut-away view of plane showing load cell.....	45
Figure 3-3	Plane Mounting Locations.....	46
Figure 3-4	Region of tail boundary layer influence	48
Figure 3-5	Boundary Layer Trip Mounting Locations.....	49
Figure 3-6	Wind Tunnel Mount Showing Beam and Base Plate.....	50
Figure 3-7	Towing tank mount showing height adjustable structure	51
Figure 3-8	Load cell mounting to hull (the coupling and motor are specific to bowplanes).....	52
Figure 3-9	Load cell arrangement for bowplane showing direct connection to stepper motor.....	52
Figure 3-10	Isolated standard geometry plane 0.916 scale, $Re_c = 280\ 000$ (equivalent $Re_L = 7$ million).54	
Figure 3-11	Oil film sample image - suction side of port bowplane at +16 degrees deflection. The separation line is shown in dashed black and arrows indicate flow direction in attached region.	56
Figure 3-12	Separation lines on suction side of bowplane at level trim; plane deflection is shown left hand side	57
Figure 3-13	Bowplane force to deflection relationship compared with higher Reynolds number isolated plane relationship (standard bowplane geometry).....	58

Figure 3-14	Bowplane aspect ratio influence on bowplane force production: (a) versus bowplane deflection; (b) versus bowplane deflection	58
Figure 3-15	Bowplane geometry influence on bowplane force production for large planes: (a) versus bowplane deflection; (b) versus bowplane deflection	59
Figure 3-16	Endplate influence on short bowplane performance	60
Figure 3-17	Bowplane position effect	61
Figure 3-18	Keelplane compared to standard bowplane and isolated plane	62
Figure 3-20	Bowplane root incident flow angle versus trim angle from yarn tuft visualization	63
Figure 3-19	Sample yarn tuft visualization images: (a) high bowplane installed, trim angle = +6 degrees; (b) no bowplane installed, trim angle = +6 degrees	63
Figure 3-21	Oil film visualization: bowplane suction side, =2.25 million, trim = +6 degrees	64
Figure 3-22	Oil film visualization: bowplane suction side, =2.25 million, trim = -6 degrees	65
Figure 3-23	Trim influence on bowplane force production	66
Figure 3-24	Trim influence on bowplanes when expressed using effective plane deflection.....	66
Figure 3-25	Trim influence on anhedral bowplanes	67
Figure 3-26	Trim influence on anhedral bowplanes using effective plane deflection	68
Figure 3-27	Trim influence on keel plane force production.....	69
Figure 3-28	Trim influence on keel plane force production expressed using effective deflection	69
Figure 3-29	Trim influence on sternplane force.....	70
Figure 3-30	Yarn tuft visualization of body at +20 degrees yaw: (a) leeward (starboard) side; (b) windward (port) side	71
Figure 3-31	Effect of yaw on port bowplane performance (Re = 2.25 million)	72
Figure 3-32	Helium bubble path sample image; trim: +6 degrees, deflection: +25 degrees, Reynolds number: 2.5 million, model inverted	74
Figure 3-33	Oblique stern helium bubble path sample	74
Figure 3-34	Helium bubble path vortex mapping side view: -6 degrees trim, +16 degrees bowplane deflection, 2.5 million Reynolds number.....	75
Figure 3-35	Standard configuration straight and level flight schematic vortex path diagram	75
Figure 3-36	Bowplane and sternplane force for the standard configuration in straight and level flight.....	76
Figure 3-37	Comparison of bowplane and sternplane interaction force	77
Figure 3-39	Sternplane span influence on sternplane force interaction: (a) versus bowplane deflection; (b) versus bowplane deflection	78
Figure 3-38	Sternplane interaction force dependence on bowplane span: (a) versus bowplane deflection; (b) versus bowplane deflection	78
Figure 3-41	Sternplane geometry influence on sternplane force interaction: (a) versus bowplane deflection; (b) versus bowplane deflection.....	79
Figure 3-40	Bowplane geometry influence on sternplane force interaction for large planes: (a) versus bowplane deflection; (b) versus bowplane deflection	79
Figure 3-42	Influence of endplates on the short bowplanes on bowplane-sternplane interaction	80

Figure 3-43	Helium bubble path schematic for anhedral bowplanes in straight and level flight.....	81
Figure 3-44	Bowplane-sternplane interaction dependence on bowplane position.....	82
Figure 3-45	Bowplane-sternplane interaction dependence on sternplane position.....	83
Figure 3-46	Standard configuration vortex path: (a) +6 degrees trim; (b) -6 degrees trim.....	84
Figure 3-47	Anhedral configuration vortex path for (a) +6 degrees trim; (b) -6 degrees trim	85
Figure 3-48	Interaction force on standard sternplane as a function of trim angle.....	86
Figure 3-49	Ratio of bowplane-sternplane interaction curve slope to bowplane lift curve slope.....	86
Figure 3-50	Interaction force from anhedral bowplane on sternplane as a function of trim angle	87
Figure 3-51	Slope ratio of averaged sternplane interaction to bowplane lift curves versus yaw angle	88
Figure 3-52	Dependence of wave orbital velocity on depth and wavelength	90
Figure 3-53	Wave height and bowplane force trend chart	91
Figure 3-54	Wave height and non-dimensional bowplane force FFT spectra.....	92
Figure 3-55	Wave induced plane force dependence on wave amplitude	93
Figure 3-56	Plane performance dependence on hull depth in calm water	94
Figure 3-57	Wave induced force amplitude as a function of hull depth	95
Figure 3-58	Wave induced force on bowplanes versus Froude number	96
Figure 3-59	Influence of bowplane position on wave induced plane forces.....	97
Figure 3-60	Ratio of wave induced force normalized by horizontal planform area on anhedral bowplanes versus standard bowplanes.....	98
Figure 4-1	Control surface stall angle as a function of Reynolds number	103
Figure 4-2	Isolated appendage force data extrapolated from a Reynolds number of 7 million to 35 million.....	104
Figure 4-3	Bowplane force data extrapolated from a Reynolds number of 2.5 million to 35 million....	105
Figure 4-4	Experimental to semi-empirical comparison of isolated control surface performance	108
Figure 4-5	Experimental to semi-empirical comparison of bowplane performance.....	109
Figure 4-6	Effective shift in bowplane deflection as a function of trim angle.....	110
Figure 4-7	Predicted effective shift in bowplane deflection as a function of trim angle	112
Figure 4-8	Bowplane stall angle as a function of yaw	113
Figure 4-9	Port bowplane lift curve slope as a function of yaw.....	114
Figure 4-10	Normalized bowplane lift curve slope dependence on yaw angle.....	115
Figure 4-11	Normalized bowplane lift curve slope dependence on yaw angle.....	116
Figure 4-12	Description of flow velocity components on the bowplane in yaw	117
Figure 4-13	Analytical prediction of port bowplane lift curve slope dependence on yaw angle.....	118
Figure 4-14	Vortex system used in control surface interaction calculations	120
Figure 4-15	Vortex system for potential flow model of control surface interaction	121
Figure 4-16	Starboard side vortex system at aft plane; port side vortices also contribute to induced velocity but are not shown	121

Figure 4-17	Plane geometry effect on fore-aft plane interaction comparison for: (a) standard configuration; (b) short bowplanes; (c) long bowplanes; (d) short sternplanes; (e) long sternplanes; (f) large sternplanes. Measured data with error bounds are shown with points, values from the numerical prediction are shown with solid lines.	122
Figure 4-18	Plane location effect on fore-aft plane interaction comparison for: (a) centreline bowplanes; (b) high bowplanes; (c) dihedral bowplanes; (d) anhedral bowplanes; (e) Y-tail; (f) Inverted Y-tail. Measured data with error bounds are shown with points, values from the numerical prediction are shown with solid lines.	123
Figure 4-19	Reynolds number effect on fore-aft plane interaction comparison for: (a) ReL = 7.5 million; (b) ReL = 4.2 million; (c) ReL = 2 million; (d) ReL = 1.5 million; (e) ReL = 1.0 million; (f) ReL = 0.5 million. Measured data with error bounds are shown with points, values from the numerical prediction are shown with solid lines.:	125
Figure 4-20	Body trim angle effect on fore-aft plane interaction comparison for: (a) -8 degree trim; (b) -4 degree trim; (c) -2 degree trim; (d) +2 degree trim; (e) +4 degree trim; (f) +8 degree trim. Measured data with error bounds are shown with points, values from the numerical prediction are shown with solid lines.:	126
Figure 4-21	Interaction curve fit of sternplane to bowplane lift curve slope ratio in trim	127
Figure 4-22	Interaction curve fit of sternplane to bowplane lift curve slope ratio in yaw	128
Figure 4-23	Modelled flow over plane.....	130
Figure 4-25	Modelled flow over plane.....	131
Figure 4-24	Analytical prediction of force on bowplanes as a function of depth.....	131
Figure 4-26	Analytical prediction of wave-induced bowplane force as a function of speed.....	132
Figure 4-27	Comparison of modelled and actual stall behavior at 3 m/s and 20 degrees yaw	134
Figure 5-1	Basic feedback control system schematic	138
Figure 5-2	Feed forward compensator	145
Figure 5-3	Feedback controller with series compensator.....	145
Figure 5-4	Basic PD controller block diagram.....	147
Figure 5-5	Gain scheduling PD controller schematic	148
Figure 5-6	Tuner schematic used in gain scheduling PD controller	150
Figure 5-7	Fuzzy-tuned series compensator block diagram.....	151
Figure 5-8	Fuzzy-tuner schematic	152
Figure 5-9	Input (yaw) membership function for and	153
Figure 5-10	Output membership function for and	154
Figure 5-11	Fuzzy logic control surface for	154
Figure 5-12	Fuzzy logic control surface for	155
Figure 5-13	Input (yaw) membership function for	156
Figure 5-14	Input (trim) membership function for	157
Figure 5-15	Output membership function for	157
Figure 5-16	Fuzzy logic control surface for	158
Figure 5-17	LQG/LTR controller block diagram	159

Figure 5-18	Singular value plot for the plant	161
Figure 5-19	Singular value plot for the scaled plant	162
Figure 5-20	Filter singular values	163
Figure 5-21	Filter sensitivity and complimentary sensitivity singular values.....	163
Figure 5-22	Open loop singular value plot for plant and controller.....	165
Figure 5-23	System sensitivity and complimentary sensitivity singular values	166
Figure 5-24	Bumpless switching example for one input variable.....	167
Figure 5-25	Bumpless switching with two input variables	167
Figure 5-26	Switching surface representation in two dimensions for the sliding mode controller.....	168
Figure 6-1	Simulation process schematic.....	174
Figure 6-2	Simulator block diagram	175
Figure 6-3	Simulator plant block diagram	175
Figure 6-4	Simulator sensor and filter block diagram.....	176
Figure 6-5	Manoeuvre used for performance evaluation	177
Figure 6-6	Fictitious scanning operation used in performance evaluation	179
Figure 6-7	Influence of the plant model on PD controller performance in pitch.....	186
Figure 6-8	Depth history in calm water for various plane geometry combinations.....	189
Figure 6-9	Roll history in calm water for various plane geometry combinations.....	190
Figure 6-10	Heave response based on bowplane geometry for sea state three (head seas)	191
Figure 6-11	Bowplane deflection based on plane geometry for sea state three (head seas)	192
Figure 6-12	Trajectory in x-y plane for alternate plane locations	193
Figure 6-13	Roll history in calm water for alternate plane locations	193
Figure 6-14	Roll history in calm water for Y-tail with increased roll error sensitivity	194
Figure 6-15	Bowplane deflection spectra based on plane location for sea state three head seas.....	195
Figure 6-16	Pitch history comparison for PD controller with and without fuzzy compensator	197
Figure 6-17	Depth response spectra for PD controller augmentations is sea state three head seas	198
Figure 6-18	Heave response for LQG/LTR augmentations in sea state three, head seas.....	200
Figure 6-19	Depth history for Gain Scheduled PD and Sliding Mode LQG/LTR in calm water	201
Figure 6-20	Pitch history for Gain Scheduled PD and Sliding Mode LQG/LTR in calm water.....	202
Figure 6-21	Roll history for Gain Scheduled PD and Sliding Mode LQG/LTR in calm water	203
Figure 6-22	Keel planes correcting for depth error.....	203
Figure 6-23	Stability in depth for PID and LQG/LTR controllers with keel planes	204
Figure 6-24	Heave response for Sliding Mode LQG/LTR and PD (sea state 3 head seas).....	205
Figure 6-25	Deflection spectra for Sliding Mode LQG/LTR and PD (sea state 3 head seas).....	205
Figure A-1	Vortex system used in upwash calculations	217
Figure A-2	Vortex system for forward planes (freestream flow into page).....	218

Figure A-3	Vortex system for forward planes (freestream flow into page).....	219
Figure A-4	Upwash comparison for isolated and body-mounted planes.....	220
Figure A-5	Change in Stall Angle With Aspect Ratio for Clark Y Airfoil.....	221
Figure A-6	Effect of Reynolds number on (Barlow et al., 1999).....	222
Figure A-7	Effect of Reynolds number on for NACA 0025 airfoil.....	223
Figure A-8	Normalized bowplane lift curve slope dependence on yaw angle.....	224
Figure A-9	Description of flow velocity components on the bowplane in yaw.....	226
Figure A-10	Vortex system for forward planes (freestream flow into page).....	227
Figure A-11	Vortex system for forward planes (freestream flow into page).....	229
Figure A-12	Starboard side vortex system at aft plane (freestream flow into page).....	231
Figure B-1	Model assembly (ISE98-0011).....	235
Figure B-2	Fore hull section (ISE98-0001).....	236
Figure B-3	Hull nose (ISE98-0002).....	237
Figure B-4	Mid-hull section (ISE98-0003 sheet 1 of 2).....	238
Figure B-5	Mid-hull section (ISE98-0003 sheet 2 of 2).....	239
Figure B-6	Aft hull section (ISE98-0007).....	240
Figure B-7	Tail section (ISE98-0005).....	241
Figure B-8	Mast connection (dorsal) (ISE98-0004).....	242
Figure B-9	Mast tube (ISE98-0010).....	243
Figure B-10	Mast assembly (ISE98-0012).....	244
Figure B-11	Strain gauge assembly to mast (ISE98-0021).....	245
Figure B-12	Mast fairing assembly (ISE98-0023).....	246
Figure B-13	Keel assembly (ISE98-0026).....	247
Figure B-14	Sternplane deflection control assembly (ISE98-0018).....	248
Figure B-15	Sternplane deflection control lead screw nut (ISE98-0015).....	249
Figure B-16	Sternplane deflection control arm components (ISE98-0013).....	250
Figure B-17	Sternplane deflection control motor casing (ISE98-0019).....	251
Figure B-18	Bowplane stepper motor connector (ISE98-0014).....	252
Figure B-19	Bowplane load cell shaft (ISE98-LC-1).....	253
Figure B-20	Sternplane load cell shaft (ISE98-LC-2).....	254
Figure B-21	Load cell sleeve (ISE98-LC-3).....	255
Figure B-22	Load cell sub-assembly (ISE98-LC-5).....	256
Figure B-23	Bowplane load cell strain gauge installation (ISE98-LC-7).....	257
Figure B-24	Sternplane load cell shaft (ISE98-LC-8).....	258
Figure B-25	Bowplane load cell assembly (ISE98-LC-10).....	259
Figure B-26	Sternplane hull insert (ISE98-LC-6).....	260

Figure B-27	Force balance setup in wind tunnel (ISE98-B-1)	261
Figure B-28	Force balance assembly (ISE98-B-2)	262
Figure B-29	Force balance beam (ISE98-B-3)	263
Figure B-30	Balance pitch mechanism load bearing pin (ISE98-B-4)	264
Figure B-31	Balance pitch mechanism adjustment rod (ISE98-B-7)	265
Figure B-32	Main balance beam assembly (ISE98-B-12)	266
Figure B-33	Balance beam clamp for mast (ISE98-B-13).....	267
Figure B-34	Force balance beam strain gauge installation (ISE98-B-14).....	268
Figure B-35	Power and instrumentation wiring diagram (ISE98-E-1).....	269
Figure B-36	Load cell deflection for maximum design load	270
Figure B-37	Load cell microstrain for maximum design load.....	271
Figure B-38	Sample load cell calibration data.....	272
Figure B-39	Boundary Layer Trip Mounting Locations.....	274
Figure B-40	Boundary Layer Trip Terminology	275
Figure D-1	Depth response spectra for various LQG/LTR parameters (sea state three head seas).....	286
Figure D-2	Pitch response spectra for various LQG/LTR parameters (sea state three head seas)	287
Figure D-3	Bowplane spectra for various LQG/LTR parameters (sea state three head seas)	287
Figure E-1	Generic controller layout.....	325
Figure E-2	Navigation Module	326
Figure E-3	Heading correction	326
Figure E-4	Compass Correction	327
Figure E-5	Write data	327
Figure E-6	Noise.....	328
Figure E-7	Anti-aliasing filter.....	329
Figure E-8	Gain scheduling PD controller	330
Figure E-9	Controller tuner.....	330
Figure E-10	Controller with series compensation	331
Figure F-1	Sway response based on control surface geometry in sea state three head seas	340
Figure F-2	Heave response based on control surface geometry in sea state three head seas	340
Figure F-3	Roll response based on control surface geometry in sea state three head seas	341
Figure F-4	Pitch response based on control surface geometry in sea state three head seas	341
Figure F-5	Yaw response based on control surface geometry in sea state three head seas.....	342
Figure F-6	Bowplane deflection based on control surface geometry in sea state three head seas	342
Figure F-7	Sternplane deflection based on control surface geometry in sea state three head seas	343
Figure F-8	Sway response based on control surface position in sea state three head seas.....	346
Figure F-9	Heave response based on control surface position in sea state three head seas	346

Figure F-10	Roll response based on control surface position in sea state three head seas.....	347
Figure F-11	Pitch response based on control surface position in sea state three head seas	347
Figure F-12	Yaw response based on control surface position in sea state three head seas	348
Figure F-13	Bowplane deflection based on control surface position in sea state three head seas	348
Figure F-14	Sternplane deflection based on control surface position in sea state three head seas	349
Figure F-15	Sway response for PD augmentations in sea state three head seas	352
Figure F-16	Depth response spectra for PD augmentations in sea state three head seas	352
Figure F-17	Roll response spectra for PD augmentations in sea state three head seas	353
Figure F-18	Pitch response spectra for PD augmentations in sea state three head seas.....	353
Figure F-19	Yaw deflection spectra for PD augmentations in sea state three head seas	354
Figure F-20	Bowplane deflection spectra for PD augmentations in sea state three head seas.....	354
Figure F-21	Sternplane deflection spectra for PD augmentations in sea state three head seas.....	355
Figure F-22	Sway response spectra for LQG augmentations in sea state three head seas	358
Figure F-23	Depth response spectra for LQG augmentations in sea state three head seas	358
Figure F-24	Roll response spectra for LQG augmentations in sea state three head seas	359
Figure F-25	Pitch response spectra for LQG augmentations in sea state three head seas.....	359
Figure F-26	Yaw response spectra for LQG augmentations in sea state three head seas	360
Figure F-27	Bowplane deflection spectra for LQG augmentations in sea state three head seas.....	360
Figure F-28	Sternplane deflection spectra for LQG augmentations in sea state three head seas.....	361

LIST OF TABLES

Table 1-1	Dolphin specifications	6
Table 1-2	Summary of research into AUV modelling, simulation and control.....	8
Table 2-1	Variable conventions for translation.....	15
Table 2-2	Variable conventions for rotation	15
Table 2-3	Variable conventions for translation.....	16
Table 2-4	Location of Hull Vortices in Yaw	32
Table 2-5	Open ocean sea state occurrences of North Atlantic and North Pacific.....	39
Table 3-1	Key Dimensionless Parameters	42
Table 3-2	Plane Geometries.....	45
Table 3-3	Plane positions.....	46
Table 3-4	Test facility specifications	53
Table 3-5	ANOVA for wave force to wave geometry	93
Table 4-1	Comparison of hydrodynamic derivatives.....	108
Table 5-1	Fuzzy logic calculation methods	153
Table 5-2	Fuzzy rule-base for	153
Table 5-3	Fuzzy rule-base for	155
Table 5-4	Fuzzy rule-base for	156
Table 5-5	Sliding mode controller	166
Table 6-1	Sensor noise characteristics	176
Table 6-2	Body position and orientation corresponding to one sonar segment error.....	180
Table 6-3	Cases considered in simulation.....	183
Table 6-5	Effect of model improvements on performance in calm water with PD control.....	185
Table 6-4	Effect of model improvements on performance in calm water with LQG/LTR control	185
Table 6-6	Effect of controller model on performance in calm water with LQG/LTR control.....	186
Table 6-7	Effect of plane geometry on performance in calm water	188
Table 6-8	Effect of plane geometry on performance in sea state three.....	190
Table 6-9	Effect of plane location on performance in calm water.....	192
Table 6-10	Effect of plane location on performance in sea state three.....	194
Table 6-11	Effect of PD control structure on performance in calm water.....	196
Table 6-12	Effect of PD control structure on performance in sea state three	198
Table 6-13	Effect of LQG/LTR control structure on performance in calm water	199
Table 6-14	Effect of LQG/LTR control structure on performance in sea state three.....	200
Table 6-15	Gain scheduled PD to Sliding Mode LQG/LTR comparison for calm water.....	201

Table 6-16	Gain scheduled PD to Sliding Mode LQG/LTR comparison for sea state three	204
Table A-1	Stall Types for Selected Airfoils	222
Table B-1	Scale model component list.....	233
Table D-1	LQG/LTR tuning parameter combinations.....	286
Table E-1	Summary of simulation m.file®	289
Table E-2	Simulink® Block Diagrams	325
Table F-1	Cases considered in simulation.....	334
Table F-2	Effect of hydrodynamic effects modelled in plant on performance in calm water	336
Table F-3	Effect of hydrodynamic effects included in controller on performance in calm water	337
Table F-4	Effect of plane geometry on performance in calm water	338
Table F-5	Effect of plane geometry on performance in sea state 3.....	339
Table F-6	Spectral analysis for plane geometry effect on performance in sea state 3.....	339
Table F-7	Effect of plane location on performance in calm water.....	344
Table F-8	Effect of plane location on performance in sea state 3.....	345
Table F-9	Spectral analysis for plane location effect on performance in sea state 3	345
Table F-10	Effect of PD controller augmentation on performance in calm water.....	350
Table F-11	Effect of PD controller augmentation on performance in sea state 3	351
Table F-12	Spectral analysis for PD controller performance in sea state 3	351
Table F-13	Effect of LQG/LTR augmentation on performance in calm water	356
Table F-14	Effect of LQG/LTR augmentation on performance in sea state 3.....	357
Table F-15	Spectral analysis for LQG/LTR controller performance in sea state 3	357

LIST OF SYMBOLS

Symbol	Description	Application
A	plant matrix	control
a	wave amplitude of surface wave	hydrodynamics
a_e	aspect ratio $a_e = \frac{b^2}{S}$	hydrodynamics
A_{in}	A matrix in LQG/LTR integrator implementation	control
B	state space input matrix	control
b	plane span	hydrodynamics
b'	spanwise location of plane tip vortex nondimensionalized by b	hydrodynamics
b_{ep}	spanwise location of inboard endplate	hydrodynamics
b_{exp}	exposed plane span	hydrodynamics
B_{in}	B matrix in LQG/LTR integrator implementation	control
C	state space state-to-output matrix	control
\bar{C}	control surface mean chord	hydrodynamics
C_A	Coriolis added mass matrix	all
C_D	coefficient of drag $C_D = \frac{D}{\frac{1}{2}\rho U^2 l^2}$	hydrodynamics
C_{Dc}	crossflow drag coefficient	hydrodynamics
C_{D0}	minimum coefficient of drag value	hydrodynamics
C_{in}	C matrix in LQG/LTR integrator implementation	control
C_L	coefficient of lift $C_L = \frac{L}{\frac{1}{2}\rho U^2 l^2}$	hydrodynamics
$C_{L bp}$	coefficient of lift of general bowplane	hydrodynamics
$C_{L sp}$	coefficient of lift of general sternplane	hydrodynamics
C_{Lsp}^*	coefficient of lift of sternplane nondimensionalized by bowplane area $C_{Lsp}^* = \frac{L_{sp}}{\frac{1}{2}\rho U^2 S_{bp}}$	hydrodynamics
$C_{L\alpha}$	coefficient of lift curve slope $C_{L\alpha} = \frac{\partial C_L}{\partial \alpha}$	hydrodynamics

Symbol	Description	Application
C_0	constant value from curve fitting	hydrodynamics
C_r	control surface root chord	hydrodynamics
C_{rb}	Coriolis matrix	all
C_t	control surface tip chord	hydrodynamics
C_x	coefficient of force in x -direction $C_x = -C_D \cos \alpha + C_L \sin \alpha$	hydrodynamics
C_z	coefficient of force in z -direction $C_z = -C_L \cos \alpha - C_D \sin \alpha$	hydrodynamics
D	state space control output to output matrix	control
D	hull diameter	all
D	drag	hydrodynamics
d	depth	all
D_d	damping matrix	all
D_{dist}	disturbance input vector to plant	control
e	error vector $e = y _{measured} - r$	control
F	statistical value determined in ANOVA procedure	modelling
$F_{critical}$	critical F value determined in ANOVA procedure	modelling
Fr	Froude number $Fr = \frac{U}{\sqrt{gl}}$	all
Fr_c	Froude number based on chord $Fr_c = \frac{U}{\sqrt{gC}}$	hydrodynamics
g	gravitational acceleration	all
H	shape factor in Thwaite's method	hydrodynamics
h	endplate height	hydrodynamics
h'	exposed endplate height $h' = h - t$	hydrodynamics
I	Identity matrix	control
J	LQG controller performance index	control
J_{ct}	simulation performance index for complete trajectory	simulation
j_n	scanning error at time-step n	simulation
	$j_n = \left \frac{y_n - y_r}{s_y} \right + \left \frac{z_n - z_r}{s_z} \right + \left \frac{\phi_n - \phi_r}{s_\phi} \right + \left \frac{\theta_n - \theta_r}{s_\theta} \right + \left \frac{\psi_n - \psi_r}{s_\psi} \right $	
J_{sa}	simulation performance index for response significant amplitude	simulation

Symbol	Description	Application
J_{sl}	simulation performance index for straight and level segments	simulation
\mathbf{K}	controller gain matrix	control
K	moment about x -axis	all
K'	non-dimensional K moment $K' = \frac{K}{\frac{1}{2}\rho U^2 l^3}$	all
\mathbf{K}_{++}	sliding mode LQG/LTR controller (positive trim and positive yaw)	control
\mathbf{K}_{+-}	sliding mode LQG/LTR controller (positive trim and negative yaw)	control
\mathbf{K}_{+0}	sliding mode LQG/LTR controller (positive trim and zero yaw)	control
\mathbf{K}_{-+}	sliding mode LQG/LTR controller (negative trim and positive yaw)	control
\mathbf{K}_{--}	sliding mode LQG/LTR controller (negative trim and negative yaw)	control
\mathbf{K}_{-0}	sliding mode LQG/LTR controller (negative trim and zero yaw)	control
\mathbf{K}_{0+}	sliding mode LQG/LTR controller (zero trim and positive yaw)	control
\mathbf{K}_{0-}	sliding mode LQG/LTR controller (zero trim and negative yaw)	control
\mathbf{K}_{00}	sliding mode LQG/LTR controller (zero trim and zero yaw)	control
$\mathbf{K}_{(a)}$	matrix relating desired to actual plane deflections in gain scheduling	control
k_a	\mathbf{K}_{fc} matrix element for bowplane-sternplane interaction	control
\mathbf{K}_d	PID controller derivative gain matrix	control
k_{ep}	endplate aspect ratio correction factor	hydrodynamics
\mathbf{K}_{fc}	Fuzzy tuned compensator matrix	control
k_{fp}	\mathbf{K}_{fc} matrix element for change in port bowplane force with yaw	control
k_{fs}	\mathbf{K}_{fc} matrix element for change in starboard bowplane force with yaw	control
\mathbf{K}_{gs}	controller gain matrix used in gain scheduling	control
\mathbf{K}_i	PID controller integral gain matrix	control
K_i	inboard K -moment on a plane	hydrodynamics
\mathbf{K}_{in}	LQG/LTR controller with integration controller gain matrix	control
K_o	outboard K -moment on a plane	hydrodynamics
\mathbf{K}_p	PID controller proportional gain matrix	control

Symbol	Description	Application
k_{ss}	hull curvature correction factor	hydrodynamics
K_w	control error weighting matrix used in LQG/LTR control	control
$k_{\eta t}$	tail efficiency correction factor	hydrodynamics
L	LQG/LTR controller filter gain matrix	control
L	lift force	hydrodynamics
l	vehicle length	all
L_{in}	LQG/LTR controller with integration filter gain matrix	hydrodynamics
M	State-space process noise level matrix	control
M	moment about y -axis	all
M'	non-dimensional M moment $M' = \frac{M}{\frac{1}{2}\rho U^2 l^3}$	all
m	mass	all
M_A	added mass matrix	all
M_{in}	M matrix for LQG/LTR integrator implementation	control
M_{rb}	rigid body mass matrix	all
N	noise input vector	control
N	moment about z -axis	all
N	total number of time-steps in simulation	modelling
N'	non-dimensional N moment $N' = \frac{N}{\frac{1}{2}\rho U^2 l^3}$	all
n	state space noise vector	control
n	current time-step in simulation	modelling
n	propeller rotation rate	all
N_{in}	N matrix for LQG/LTR integrator implementation	control
P	matrix determined in solution of Riccati equation for LQG	control
p	angular velocity about x -axis	all
Q	rotational transformation matrix	all
Q	LQG control state error weighting matrix	control
q	angular velocity about y -axis	all

Symbol	Description	Application
R	LQG control control effort weighting matrix	control
R	hull radius	all
r	reference trajectory vector	control
r	angular velocity about z -axis	all
$r_{1/3}$	hull radius at 1/3 chord position of plane	hydrodynamics
Re	Reynolds number $Re = \frac{Ul}{\nu}$	all
Re_t	Reynolds number at transition point	hydrodynamics
S	control surface planform area	hydrodynamics
s	generalized coordinate in boundary layer trip calculations	hydrodynamics
$S(\lambda)$	shear stress correlation factor in Thwaite's method	hydrodynamics
S_{bp}	bowplane planform area	hydrodynamics
S_{exp}	exposed control surface area	hydrodynamics
S_f	response spectrum of scanning error	simulation
S_{sp}	sternplane planform area	hydrodynamics
s_y	sensitivity of sonar scanning error to error in sway in simulation	simulation
s_z	sensitivity of sonar scanning error to error in heave in simulation	simulation
s_θ	sensitivity of sonar scanning error to error in pitch in simulation	simulation
s_ϕ	sensitivity of sonar scanning error to error in roll in simulation	simulation
s_ψ	sensitivity of sonar scanning error to error in yaw in simulation	simulation
T	load cell calibration matrix, force from voltage	hydrodynamics
T^*	load cell calibration matrix, voltage from force	hydrodynamics
t	control surface thickness	hydrodynamics
t	time	all
t_{trip}	boundary layer trip thickness	hydrodynamics
t_{xx}	load cell calibration slope v_x versus X	hydrodynamics
t_{xz}	load cell calibration slope v_x versus Z	hydrodynamics
t_{zx}	load cell calibration slope v_z versus X	hydrodynamics
t_{zz}	load cell calibration slope v_z versus Z	hydrodynamics

Symbol	Description	Application
U	total velocity $U = \sqrt{u^2 + v^2 + w^2}$	all
u	controller output	control
u	velocity in x -direction	all
U'	convective acceleration	hydrodynamics
u_1	controller output in series compensation implementation	control
u_2	compensator output in series compensation implementation	control
u_c	LQG/LTR controller output before integration	control
u_{ff}	feed-forward control signal	control
U_w	wave orbital velocity	hydrodynamics
u_w	wave velocity in x -direction	all
v	velocity in y -direction	all
v_x	load cell voltage for x -axis (drag direction)	hydrodynamics
v_z	load cell voltage for z -axis (lift direction)	hydrodynamics
W	covariance of process noise in state space	control
w	white noise vector with covariance W for process in state space	control
w	velocity in z -direction	all
W_{in}	W matrix for LQG/LTR integrator implementation	control
w_w	wave velocity in z -direction	all
X	force in x -direction	all
X'	non-dimensional X force $X' = \frac{X}{\frac{1}{2}\rho U^2 l^2}$	all
\mathbf{x}	state vector	control
x	forward direction	all
X'_{ap}	X' force of port aft plane (sternplane)	all
x_{ap}	x -position of port aft plane (sternplane) from centre of gravity	all
X'_{as}	X' force of starboard aft plane (sternplane)	all
x_{as}	x -position of starboard aft plane (sternplane) from centre of gravity	all
X'_{bp}	X' force of general bowplane	all

Symbol	Description	Application
X'_{fp}	X' force of starboard fore plane (bowplane)	all
x_{fp}	x -position of port fore plane (bowplane) from centre of gravity	all
X'_{fs}	X' force of starboard fore plane (bowplane)	all
x_{fs}	x -position of starboard fore plane (bowplane) from centre of gravity	all
\mathbf{x}_{in}	state vector for LQG/LTR integrator implementation $\mathbf{x}_{in} = \begin{bmatrix} \mathbf{u} \\ \mathbf{x} \end{bmatrix}$	control
x_{plane}	x -position of general plane	all
X'_r	X' force of rudder	all
x_r	x -position of rudder from centre of gravity	all
X'_{sp}	X' force of general sternplane	all
$X'_{\delta_{ap}}$	first derivative of X' non-dimensional force with δ_{ap} deflection	all
$X'_{\delta_{ap}\delta_{ap}}$	second derivative of X' non-dimensional force with δ_{ap} deflection	all
$X'_{\delta_{as}}$	first derivative of X' non-dimensional force with δ_{as} deflection	all
$X'_{\delta_{as}\delta_{as}}$	second derivative of X' non-dimensional force with δ_{as} deflection	all
$X'_{\delta_{fp}}$	first derivative of X' non-dimensional force with δ_{fp} deflection	all
$X'_{\delta_{fp}\delta_{fp}}$	second derivative of X' non-dimensional force with δ_{fp} deflection	all
$X'_{\delta_{fs}}$	first derivative of X' non-dimensional force with δ_{fs} deflection	all
$X'_{\delta_{fs}\delta_{fs}}$	second derivative of X' non-dimensional force with δ_{fs} deflection	all
X'_{δ_r}	first derivative of X' non-dimensional force with δ_r deflection	all
$X'_{\delta_r\delta_r}$	second derivative of X' non-dimensional force with δ_r deflection	all
Y	force in y -direction	all
Y'	non-dimensional Y force $Y' = \frac{Y}{\frac{1}{2}\rho U^2 l^2}$	all
\mathbf{y}	control system output vector	control
y	lateral direction	all
Y'_{ap}	Y' force of port aft plane (sternplane)	all
y_{ap}	y -position of port aft plane (sternplane) from centre of gravity	all

Symbol	Description	Application
Y_{as}	Y force of starboard aft plane (sternplane)	all
y_{as}	y -position of starboard aft plane (sternplane) from centre of gravity	all
Y_{bp}	Y force of general bowplane	all
y_{cp}	spanwise centre of pressure for a horizontal plane	all
Y_{fp}	Y force of starboard fore plane (bowplane)	all
Y_{fs}	Y force of starboard fore plane (bowplane)	all
y_{fp}	y -position of port fore plane (bowplane) from centre of gravity	all
y_{fs}	y -position of starboard fore plane (bowplane) from centre of gravity	all
y_{in}	plant output vector for LQG/LTR integrator implementation $y_{in} = C_{in}x_{in}$	control
y_n	y -position for time-step n	simulation
y_{plane}	y -position of general plane	all
Y_r	Y force of rudder	all
y_r	y -position of rudder from centre of gravity	all
y_r	commanded (reference) y -position from navigation module	simulation
Y_{sp}	Y force of general sternplane	all
y_v	y -position of hull vortex in yaw measured from hull centreline	all
$Y_{\delta_{ap}}$	first derivative of Y non-dimensional force with δ_{ap} deflection	all
$Y_{\delta_{ap}\delta_{ap}}$	second derivative of Y non-dimensional force with δ_{ap} deflection	all
$Y_{\delta_{as}}$	first derivative of Y non-dimensional force with δ_{as} deflection	all
$Y_{\delta_{as}\delta_{as}}$	second derivative of Y non-dimensional force with δ_{as} deflection	all
$Y_{\delta_{fp}}$	first derivative of Y non-dimensional force with δ_{fp} deflection	all
$Y_{\delta_{fp}\delta_{fp}}$	second derivative of Y non-dimensional force with δ_{fp} deflection	all
$Y_{\delta_{fs}}$	first derivative of Y non-dimensional force with δ_{fs} deflection	all
$Y_{\delta_{fs}\delta_{fs}}$	second derivative of Y non-dimensional force with δ_{fs} deflection	all
Y_{δ_r}	first derivative of Y non-dimensional force with δ_r deflection	all
$Y_{\delta_r\delta_r}$	second derivative of Y non-dimensional force with δ_r deflection	all

Symbol	Description	Application
Z	force in z -direction	all
Z'	non-dimensional Z force $Z' = \frac{Z}{\frac{1}{2}\rho U^2 l^2}$	all
z	vertical direction; depth	all
Z_{ap}	Z' force of port aft plane (sternplane)	all
z_{ap}	z -position of port aft plane (sternplane) from centre of gravity	all
Z_{as}	Z' force of starboard aft plane (sternplane)	all
z_{as}	z -position of starboard aft plane (sternplane) from centre of gravity	all
Z_{bp}	Z' force of general bowplane	all
Z_{fp}	Z' force of starboard fore plane (bowplane)	all
z_{fp}	z -position of port fore plane (bowplane) from centre of gravity	all
Z_{fs}	Z' force of starboard fore plane (bowplane)	all
z_{fs}	z -position of starboard fore plane (bowplane) from centre of gravity	all
Z'_g	Z_{wave} nondimensionalized using gravity $Z'_g = \frac{Z_{wave}}{\frac{1}{2}\rho g l^3}$	all
z_n	z -position at time-step n	simulation
z_{plane}	z -position of general plane	all
Z_r	Z' force of rudder	all
z_r	z -position of rudder from centre of gravity	all
z_r	commanded (reference) z -position from navigation model	simulation
Z_{sp}	Z' force of general sternplane	all
z_t	boundary layer parameter in Thwaite's method $z_t = 0.25 - \lambda_t$	hydrodynamics
z_v	z -position of hull vortex in yaw measured from hull centreline	all
Z_{wave}	Z force due to waves	all
$Z_{\delta ap}$	first derivative of Z' non-dimensional force with δ_{ap} deflection	all
$Z_{\delta ap \delta ap}$	second derivative of Z' non-dimensional force with δ_{ap} deflection	all
$Z_{\delta as}$	first derivative of Z' non-dimensional force with δ_{as} deflection	all

Symbol	Description	Application
$Z_{\delta_{as}\delta_{as}}$	second derivative of Z non-dimensional force with δ_{as} deflection	all
$Z_{\delta_{fp}}$	first derivative of Z non-dimensional force with δ_{fp} deflection	all
$Z_{\delta_{fp}\delta_{fp}}$	second derivative of Z non-dimensional force with δ_{fp} deflection	all
$Z_{\delta_{fs}}$	first derivative of Z non-dimensional force with δ_{fs} deflection	all
$Z_{\delta_{fs}\delta_{fs}}$	second derivative of Z non-dimensional force with δ_{fs} deflection	all
Z_{δ_r}	first derivative of Z non-dimensional force with δ_r deflection	all
$Z_{\delta_r\delta_r}$	second derivative of Z non-dimensional force with δ_r deflection	all
α	incidence angle to plane	all
α_{bp}	incidence angle to bowplane	all
α_{local}	local change in the incidence angle to the planes	hydrodynamics
α_{sp}	incidence angle to sternplanes	all
α_w	local incidence angle due to waves	hydrodynamics
β	dihedral angle	all
Γ	circulation	hydrodynamics
γ	angle of tip vortex to freestream	hydrodynamics
ΔC_z	increase in C_z due to hull curvature	hydrodynamics
δ	plane deflection	all
δ_0	boundary layer thickness	hydrodynamics
δ_1	boundary layer displacement thickness	hydrodynamics
δ_2	boundary layer momentum thickness	hydrodynamics
δ_{ap}	port aft plane (port sternplane) deflection	all
δ_{as}	starboard aft plane (starboard sternplane) deflection	all
δ_{eff}	effective (bow)plane deflection	all
$\delta_{eff,sp}$	effective sternplane deflection	all
$\delta_{eff,keel}$	effective keelplane deflection	all
δ_{fp}	port fore plane (port bowplane) deflection	all
δ_{fc}	commanded plane deflections in fuzzy-compensated implementation	control

Symbol	Description	Application
δ_{fs}	starboard fore plane (starboard bowplane) deflection	all
δ_r	rudder deflection	all
ε	downwash angle	hydrodynamics
ζ	vertical displacement of trailing vortex from longitudinal horizontal axis through fin/fin outreach	hydrodynamics
η	non-dimensional spanwise location on plane from root	hydrodynamics
θ	angular displacement about y -axis	all
θ_n	angular displacement about y -axis at time-step n	simulation
θ_r	commanded angular displacement about y -axis from navigation	simulation
θ_{local}	local trim angle $\theta_{local} = \frac{w - w_w - qx}{U}$	all
Λ	Karman-Pohlhausen parameter used in Thwaite's method	hydrodynamics
λ	control surface taper ratio	hydrodynamics
λ	wavelength of surface wave	hydrodynamics
λ^*	parameter used in determining hull influence $\lambda^* = \frac{b}{c} \left(1 - \left(\frac{R}{b} \right)^2 \right)$	hydrodynamics
λ_t	boundary layer parameter used in Thwaite's method	hydrodynamics
μ	fluid dynamic viscosity	hydrodynamics
μ	LQG/LTR tuning parameter	control
ν	fluid kinematic viscosity	hydrodynamics
ρ	fluid density	all
ρ	recovery factor in LQG/LTR controller	control
τ_w	wall shear stress	hydrodynamics
ϕ	angular displacement about x -axis	all
ϕ_n	angular displacement about x -axis at time-step n	simulation
ϕ_r	commanded angular displacement about x -axis from navigation	simulation
χ	non-dimensional position behind plane non-dimensionalized by span	hydrodynamics
ψ	angular displacement about z -axis	all
ψ_n	angular displacement about z -axis at time-step n	simulation
ψ_r	commanded angular displacement about z -axis from navigation	simulation

Symbol	Description	Application
Ω	control surface quarter-chord sweep angle	hydrodynamics
ω	angular frequency	simulation

PREFACE

Westheimer's Rule states that to predict the time it takes to do a task, estimate the time you think it should take, multiply that by two, and change to the next highest unit of measure; thus, two weeks should be allocated for a one day task. My experiences though this project lead me to believe that, if anything, Westheimer's Rule is too conservative in its prognostication.

The original description of this project was to simply measure and describe forces on an underwater vehicle through scale model testing. Unfortunately, a working, instrumented model was not provided as initially planned and by rough estimates over 2500 person hours were required to produce one. Additionally, a two week period of preliminary wind tunnel testing intended to validate model performance was greatly expanded to over one year to include system debugging, a full force measurement study, three different forms of flow visualization, and research by a second graduate student (namely, the study of yaw by Rodolfo Dominguez). Before experimentation began in the tow tank, many additional months were needed to design and construct mounting hardware and to seal and reconfigure the model for water.

Midway through this work, a transfer was made from the Master of Applied Science program to a doctoral program. Along with the transfer came an expansion of the project scope to include work in modelling and control. Several months of unplanned modification to a simulator originally developed by Adrian Field was required in order to perform the added work and, even then, unexpected results required even more time to confirm and validate.

Still, with each delay and each additional task something was learned and the resulting quality of the project was improved. Throughout all the hardships and countless hours invested in this project, it remains one of the most educational and rewarding experiences of my life.

- December 11, 2003

In the time between when this thesis was sent for review and when it was defended there was a very sad good-bye. Dr. Dale Cherchas passed away after a courageous battle with cancer. Dr. Cherchas co-supervised this thesis and he worked extremely hard to see its completion, all the while fighting his illness. I cannot say enough about how much Dale's contribution means to me and I am left wishing that Dale were still here so I could express my gratitude in person.

Thank you Dale.

- April 22, 2004

ACKNOWLEDGEMENTS

The author would like to thank all the people that have contributed to this project, either through engineering insight and technical assistance, financing, or emotional support.

In no particular order, much deserved thanks are owed to Josephine Lee, Olga and Joe Ostafichuk, Dr. Sander Calisal, Dr. Dale Cherchas, Dr. Mae Seto, Adrian Field, Gord Wright, Shu Oshika, Dr. Gary Schajer, Dr. Ian Gartshore, Dr. Sheldon Green, Doug Yuen, Dave Camp, Dr. George Watt, Matthais Borstad, Ayhan Akinturk, Rodolfo Dominguez, Ben Kaplan, Kevin Lam, Tom Takahashi, Kevin Kondra, Ben Triplett, and Dr. Raphael Cohen.

The author would also like to thank the Science Council of BC, the Advanced Systems Institute (ASI), the Center for Integrated Computer Systems Research (CICSR), the University of British Columbia Graduate Student Society, and ISE for generous financial contributions.

Portions of this work were performed under UBC Project Grant Number PG11R56901.

To Josephine,
for your unlimited love and support

and

To Dale,
for working so hard to see this through while facing your own challenges

1

INTRODUCTION

*Ocean: A body of water occupying about two-thirds of a world
made for man – who has no gills.*

- Ambrose Bierce

The origins of underwater vehicles can be traced back over two millennia. Alexander the Great is said to have descended into the ocean in 332 BCE using a primitive diving bell and Leonardo da Vinci is credited with creating a wooden-frame submersible covered in goatskins with oars for propulsion (Clancy, 1993). Beginning in the early 1900s, submarines evolved into one of the most feared weapons in naval warfare. At times, these vessels ruled the sea in *wolf packs*; now their nuclear-powered descendants lurk undetected in the oceans, surfacing only to restock food and supplies. Recent advancements in electronics and automatic control have resulted in an explosion in the development of small, unmanned vehicles for more benevolent uses.

Even with the long history of underwater vehicles, there is much to learn. In particular, the design and usage of control surfaces—the topic that forms the basis for this research effort—has great potential for advancement. The remainder of this chapter provides an introduction to relevant background information on autonomous underwater vehicles and control surfaces, a brief outline of previous research, and a summary of the motivation and approach used in this thesis. Subsequent chapters contain information relating to the hydrodynamics (Chapter 2), experimental studies (Chapter 3), and modelling (Chapter 4) of typical control surfaces on a near-surface underwater vehicle. The development of control strategies that make use of improved control surface hydrodynamic information is outlined in Chapter 5 and an analysis of vehicle performance through control and dynamics simulation is detailed in Chapter 6. The final chapter includes a summary and discussion of results including recommendations for future research efforts.

1.1 BACKGROUND

Autonomous underwater vehicles, or AUVs, are unmanned, self-contained systems designed to carry out tasks in the marine environment. AUVs typically have one axial propulsor providing thrust with a complement of movable wing-like appendages, called control surfaces, which provide manoeuvring forces. Unlike remotely operated vehicles (ROVs), which are teleoperated using a power and communications umbilical cable, AUVs are almost completely self-sufficient. Operating with on-board power and sensors, command decisions are made with a minimum of human intervention. The lack of an umbilical allows AUVs to operate at ranges unattainable by ROVs; missions of over 1000 kilometres are possible even in areas fully covered by ice (see Ferguson and Pope, 1995, and Ferguson et al., 1999, for example). The purchase and maintenance costs for even elaborate AUVs are far below those associated with a manned launch (Shupe and McGeer, 1987). Likewise, the absence of an on-board human operator permits development of simpler, smaller, and more cost effective vehicles suitable for use in even the most remote and hostile environments.

1.1.1 Applications for AUVs

The possible applications for AUVs are virtually limitless. The traditional role of an AUV is in track-line surveys of static oceanographic features such as bathymetry (An et al. 2001), sea floor magnetism (Willcox et al. 2001), and offshore petroleum deposits (Lorentz and Yuh 1996) for example. An AUV also provides a covert platform for remote minehunting tasks, virtually eliminating risk to both personnel and equipment (Watt et al. 1997; Gilbert 1990). Currently in the development of mine countermeasure systems, multiple coordinated AUV are being developed to detect both proud and buried targets over very large coverage areas (LePage and Schmidt 2002; Edwards et al. 2001).

Although well suited to track-line survey missions, the true potential of AUVs is realized in the study of dynamic oceanographic phenomena. The wide range of temporal and spatial variability found in many oceanographic processes makes surveying by conventional means problematic or impossible (Willcox 2001). AUVs on the other hand are ideal for the study of phenomena such as oceanic circulation as it relates to climate change (Craven et al. 1999) as well as heat and greenhouse gas transport mechanisms (Huggins and Packwood 1995). Similarly, for predictive models of tides, hydrodynamics and bio-optical properties affecting the visibility and buoyancy of coastal waters, AUVs provide a means by which to effectively collect the necessary initial and boundary data (Carder et al. 2001). Numerous other applications are equally well suited to study by AUVs: cable inspection (Asakawa et al. 2002); temperature and salinity profiling (Levine et al. 1997); vertical turbulent velocity and flux measurement (Hayes and Morrison 2002); and oceanic convection measurement (Zhang et al. 2001a; Zhang et al. 2001b), are but a few.

The low-cost, portability, and self-sufficiency of AUVs permits operation in environments unsuited to ROVs and manned vessels. As an example, in 1996 the International Submarine Engineering (ISE) *Theseus* AUV successfully completed a 320 km under ice transit during a fibre-optic cable laying mission (Ferguson et al. 1999). This feat would not have been possible with an ROV and a human crew would have been at risk had the mission been carried out using a manned vessel. Through cost and portability considerations, Laval et al. (2000) selected AUVs for temperature profiling in small lakes. The AUVs offered additional benefits over conventional temperature profiling techniques as they allowed data collection along arbitrary paths and the characterization of

larger phenomena. In a similar fashion, Kumagai et al. (2002) developed a small AUV for the study of plankton distribution and water quality in lakes. From safety and size considerations, AUVs have also demonstrated great potential for use in coastal environments where very shallow water and significant wave effects makes other vessels impractical or unsafe (see Carder et al., 2001, Peterson et al., 1994, and Reidel and Healey, 1998, for example).

Perhaps the most exciting example in the potential future of AUVs lies some 600 billion kilometers away on the Jovian moon, Europa. This satellite, roughly the same diameter as the Earth's moon, is believed to have an ocean of liquid water covered by vast sheets of ice. Akiyama et al. (1999), in addition to many others, suggest sending a probe capable of drilling through the ice to release an AUV to search for signs of life in Europa's waters. It is believed that life may be present surrounding thermal vents on the sea floor, at depths un-reachable by ROVs. It will be many years before manned space travel to even Mars is attempted, let alone through the oceans of a moon in the outer solar system; however, the technology is within reach to send an AUV to Europa. The cost and remoteness of such a mission—signals would take close to an hour to travel from Europa to Earth—reinforces the need for AUVs that are very well designed, intelligent, and completely self-sufficient.

1.1.2 AUV Operation

AUVs fall under the category of *flight vehicles* as they require forward motion to manoeuvre. The typical geometry for an AUV is a streamlined shape with an axially-mounted propeller, as shown in Figure 1-1. ROVs, in contrast, are generally box-like and manoeuvre with thrusters, which allow those vehicles to hover but restrict speeds to about 3 knots (1.5 m/s). It is worth noting that several hybrid AUV/ROV concepts are currently being considered (see Underwater, 2000, Cancelliere, 2001, and McFarlane et al., 2001, for example) so the distinctions between AUV and ROV are not entirely rigid. However, these hybrid vehicles are generally designed for very specific environments or tasks; as such the inherent complexity generally makes them impractical for widespread use.

Manoeuvring of an AUV is achieved through adjustment of the control devices shown in Figure 1-1; specifically these include the propeller, bowplanes, sternplanes, and rudder. Except in very special circumstances, an AUV is a six degree-of-freedom (DOF) system capable of three translational motions and three rotational motions (as shown in Figure 1-2). In general, these different motions are non-linear and strongly coupled. Various strategies have been devised for distributing the responsibility for control of each motion between the various control devices. Typically, surge control is restricted to the propeller and no attempt is made to control sway directly. The rudder is generally used for heading (yaw) control but in the process introduces an unwanted roll moment due to the rudder distance from the hull longitudinal axis. The bowplanes and sternplanes are used for control of pitch and depth (heave), as well as for compensation of the roll effects introduced by the rudder. In some instances, authority for pitch and depth control is assigned separately to the sternplanes and bowplanes respectively (see Watt, 1997, or Shupe and McGeer, 1987). This strategy is well suited to vehicles that have bowplanes positioned close to the longitudinal centre of mass as in this position they do not impart a large pitch moment.

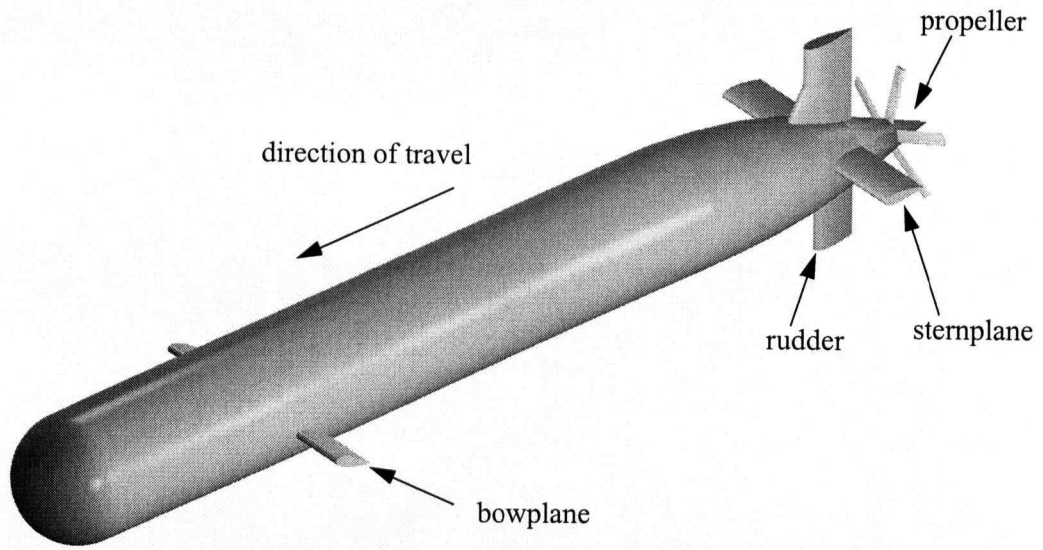


Figure 1-1 Typical geometry of an AUV

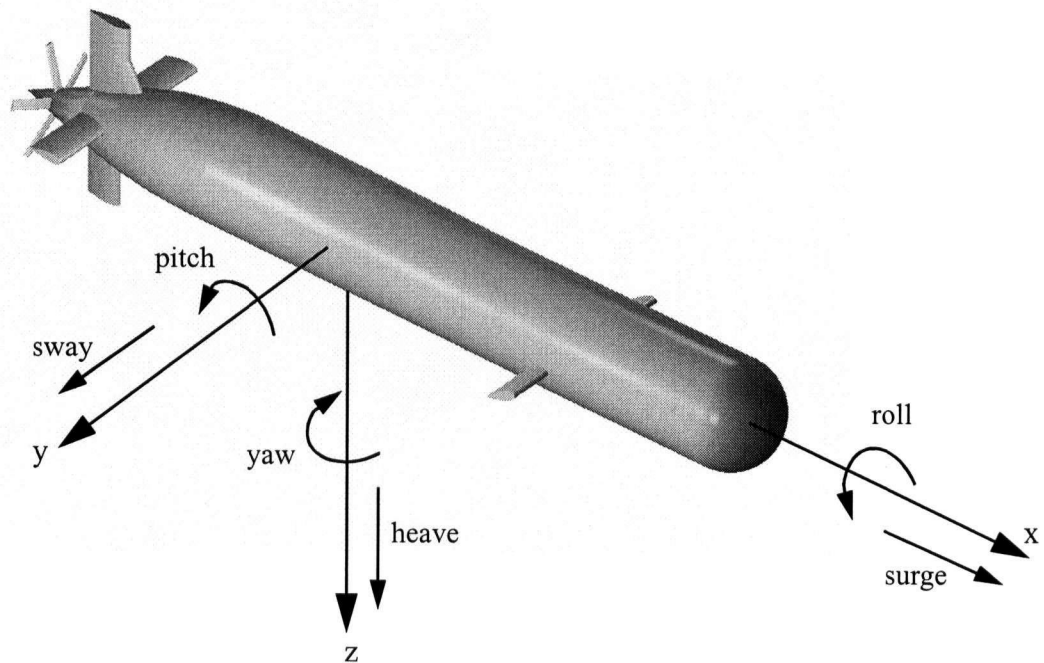


Figure 1-2 AUV degrees of freedom

1.1.3 The DOLPHIN AUV

The DOLPHIN is a near-surface AUV developed by International Submarine Engineering Research (ISER). The initial development of DOLPHIN began in 1981 in conjunction with the Canadian Hydrographic Service. Since that time, a number of different variants have been produced (including the Mark I, Mark II, and Dorado). The work in this thesis is based on the Mark II DOLPHIN shown in Figure 1-3; key features are identified in the figure.

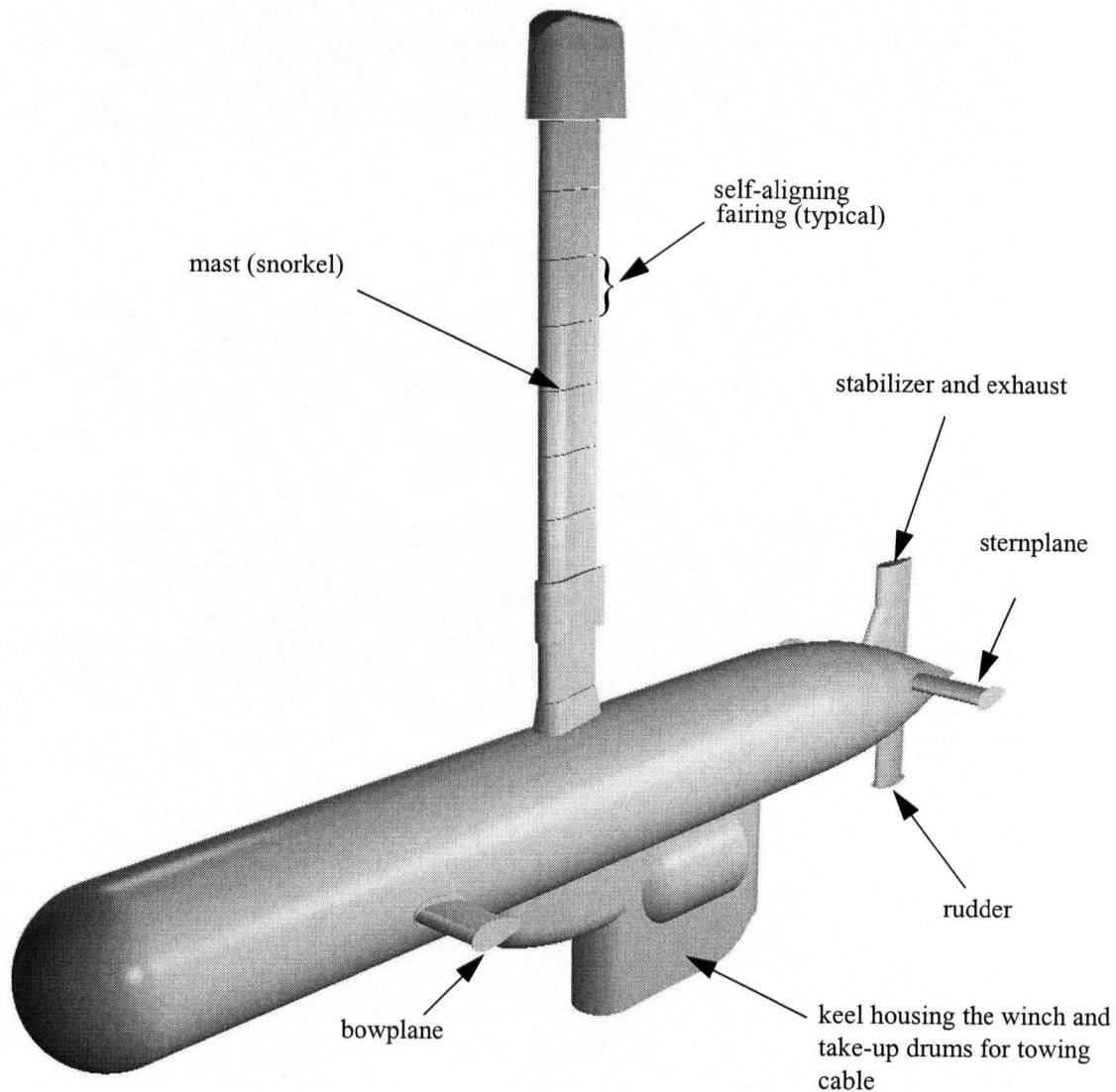


Figure 1-3 ISER DOLPHIN Mark II AUV

The unique characteristic of DOLPHIN is the semi-submersible design. The vehicle operates with the hull centreline at depths of 3 to 4.5 hull diameters (Williams et al., 2000) in conditions up to sea state 5 (Seto and Watt, 1998). Throughout operation, the top of the mast remains above the waterline and is used to provide air to the diesel powerplant and facilitate data communication. This vehicle design allows the stability and covertness of a submarine vehicle with the endurance and communications benefits of a surface ship. In particular, although the DOLPHIN is less than

8.5 m in length, in waves it behaves similarly to a much larger surface vessel. The greatly reduced above-water profile also makes the DOLPHIN much more covert than even similarly sized surface craft. DOLPHIN operates with a diesel engine which provides both increased power and endurance in comparison to typical submarines. Similarly, the surface piercing snorkel provides a mounting point for global positioning system and real-time communications hardware, a feature not found on conventional underwater vehicles. The snorkel is fitted with self-aligning fairings to minimize the effects of cross flow on vehicle roll. The specifications of the Mark II DOLPHIN (obtained from Watt et al. (1997) and Seto and Watt (1998)) are given in Table 1-1.

Table 1-1 DOLPHIN specifications

Parameter	Value
Overall length	8.534 m
Hull diameter	1 m
Dry mass	4500 kg
Variable ballast	907 kg
Power	350 horsepower
Top speed ^a	18 knots / 9.3 m/s
Endurance ^b	16 hours

a. with towfish housed at the keel

b. while towing

The DOLPHIN was developed as a platform for instrumentation with typical applications including oceanographic surveys, seafloor mapping, and mine reconnaissance, for example. The common requirement in these operations is the ability to maintain heading and orientation while travelling through potentially adverse seas. In comparison to other underwater vehicles, the disturbances that DOLPHIN is subjected to are particularly large due to the proximity to the surface. Likewise, the permissible range of operating depths and roll angles is comparatively small for DOLPHIN as the vehicle cannot continue to operate if the mast should become fully submerged. These conditions and restrictions make the DOLPHIN an ideal candidate vehicle for examining the control surface effectiveness and improved control strategies for underwater vehicles in general.

1.2 MOTIVATION

The performance of autonomous underwater vehicles is governed by the effectiveness of the vehicle control system. The control system is comprised of the controller (which is responsible for low-level command decisions) and the plant (the AUV). Control actions are administered by the propulsor and control surfaces. The command decisions made by the controller are based on knowledge or estimates of the position and orientation of the vehicle. In order to compensate for errors in position or pose, the controller determines required hydrodynamic forces on the control surfaces necessary for corrective action. Estimates of control surface performance are used to determine the required positions of each of the control surfaces in order to generate the desired forces.

The effectiveness of such a system is dependent not only on the performance of the controller and the control surfaces but also on their inter-relationship. It is essential that the control surfaces be capable of generating forces that are sufficient in magnitude and oriented in suitable directions. Likewise, the control surface forces—hence the control surfaces themselves—must be positioned at appropriate locations on a vehicle. The behavior of the control surfaces is a function of the control surface configuration, the vehicle orientation, and the operating conditions and can be complicated, non-linear, and highly coupled. Furthermore, the controller must make appropriate decisions regarding the management of control surfaces in the presence of environmental disturbances based on measurements that may be contaminated by noise. Without a sound understanding of the hydrodynamic performance of the control surfaces under all conditions, controller decisions will likely be sub-optimal and, in some cases, may threaten vehicle stability. Additionally, with improved knowledge of control surface behavior, more intelligent choices can be made regarding the control methodologies and strategies employed.

As the development of an AUV is both costly and time consuming, the use of modelling and simulation are essential to the design process. There is a need for mathematical descriptions of control surface performance that are accurate and complete while at the same time not overly complex so as to be difficult to implement. Existing control surface models used in AUV development and simulation are based on simple, linear representations (see, for example, Triantafyllou and Hover, 2002, Presterio, 2001a, or Doucy et al., 2000) or second order representations (see Oh et al., 2002, or Field, 2000); these models do not account for changes in control surface performance due to vehicle orientation, flow field interactions, or viscous effects such as flow separation. It is important to fully understand the hydrodynamic behavior of the vehicle control surfaces but it is also important to know how much detail is required in mathematical models used for simulation and control. Models of control surface performance should be as simple as possible while retaining key performance characteristics.

Specifically for the DOLPHIN AUV, ISER identified the need to conduct a detailed investigation of the performance of the bowplanes and sternplanes. During the development of the first DOLPHIN, past experience, field tuning, and “good guesses” were used for determining the vehicle geometry (den Hertog 1997). ISER speculated that the arrangement of control surfaces on the Mark II DOLPHIN was not ideal based on both geometric and operational considerations (Seto, 1997). Furthermore, small scale preliminary testing by university student groups (Han et al. 1998) and simple analytical models (Watt et al. 1997) suggested flow based interactions between fore and aft control surfaces (unaccounted for in the controller strategy) may significantly compromise depth and roll control as well as stability.

1.3 SURVEY OF PREVIOUS WORK

A summary of work by others on underwater vehicle modelling, control, and simulation is provided below in Table 1-2 (based in part on work by Lea et al. (1999)). None of the previous work focussed specifically on the performance of control surfaces, either in terms of hydrodynamics or controller design. The research vehicle studied in each is noted along with the variables controlled and the control methodology. The predominant method of research is indicated as either experimental (Exp) or simulation (Sim). (Bibliographic references are provided for each entry in the table.)

Table 1-2 Summary of research into AUV modelling, simulation and control

Researchers	Year	Variables			Vehicle
		Controlled ^a	Type	Control ^b	
Byström	1988	z, θ	Sim	LQ	Submarine
Rodriguez & Dobeck	1989	y, z, θ, ψ	Exp	GS	<i>LSV</i>
Cristi, Papoulios & Healey	1990	z	Sim	A-SM	<i>NPS AUV II</i>
Dougherty & Woolweaver	1990	z, ϕ, θ, ψ, u	Exp	SM	<i>MUST</i>
Healey & Marco	1992	x, y, z, ψ, u	Exp	SM	<i>NPS AUV II</i>
Venugopal, Sudhakar & Pandya	1992	z, θ, ψ	Sim	NN	<i>Ocean Voyager</i>
Healey & Lienard	1993	x, y, z, ψ, u	Sim	SM	<i>NPS AUV II</i>
Fryxell et al.	1994	x, y, z	Sim	GS- H_∞	<i>MARIUS</i>
Hills & Yoerger	1994	z, θ, ψ	Exp	SM	<i>LDUUV</i>
Jalving	1994	z, θ, ψ, u	Exp	PID	<i>NDRE-AUV</i>
Smith, Rae, Anderson & Shein	1994	z, θ, ψ	Sim	FL	Torpedo
Peterson, Nguyen & Rodriguez	1994	z, θ	Sim	LQR	<i>CSS</i>
Xu & Smith	1994	z	Sim	FL	Torpedo
DiBittero	1995	z	Sim	FL	<i>ARPA UUV</i>
Liceaga-Castro & van der Molen	1995a	z	Sim	GS	Submarine
Liceaga-Castro & van der Molen	1995b	z	Sim	H_∞	Submarine
Lorentz & Yuh	1996	z	Sim & Exp	NN	<i>ODIN</i>
Perrier & Canudas-de-Wit	1996	-	Sim & Exp	PID, PID-NL	<i>VORTEX</i>
Lea	1997	ψ, u	Sim & Exp	PID	<i>Subzero II</i>
Lea, Allen & Merry	1997	u	Sim	GS, FL, SM	<i>Autosub</i>

Table 1-2 Summary of research into AUV modelling, simulation and control (Continued)

Researchers	Year	Variables		Control ^b	Vehicle
		Controlled ^a	Type		
Silvestre, Pascoal & Healey	1997	z, u	Sim	H_{∞}	<i>NPS AUV II</i>
Suto & Ura	1997	z	Exp	NN	<i>Manta-Ceresia</i>
Riedel & Healey	1998	z, ϕ, θ, ψ, u	Sim	SM	<i>NPS PHOENIX</i>
An & Smith	1998	z, θ	Exp	SM-FL	<i>Ocean Explorer</i>
Barlow, Harris & Ranzenbach	1998	z, θ	Sim & Exp	PID	Generic AUV
Field, Cherchas & Calisal	2001a	z, ϕ, θ, ψ, u	Sim	LQG/LTR	<i>DOLPHIN</i>
Field et al.	2001b	z, ϕ, θ, ψ, u	Sim	A-LQG/LTR	<i>DOLPHIN</i>
Song, An & Smith	2002	θ, ψ	Sim & Exp	SM-FL	<i>Ocean Explorer</i>

a. see Section 2.1 on page 14 for a definition of the variables used

b. Control Methodology Legend: A - adaptive, FL - fuzzy logic; GS - gain scheduling; H_{∞} - H-infinity; LQG/LTR - linear quadratic gaussian with loop transfer recovery; LQR - linear quadratic regulator; NN - neural network; PID-PID or three-term; NL - non-linear; SM - sliding mode. Two traditional control strategies combined to form a hybrid are separated by a hyphen; multiple control schemes examined independently are separated by a comma.

In the survey of previous work, sixteen of the twenty-eight cases were based solely on simulation. Without physical measurement of control surface performance or validation of simulation results, the complicated and non-linear behavior of the control surfaces is unlikely to manifest itself in the results. Of the remaining twelve cases, seven relied exclusively on experimentation which is not only costly and impractical for typical AUV development, but is difficult to generalize and not well suited to the study of control surface modelling. With the five cases that use both simulation and control, in each case motion is restricted to two degrees of freedom. As the performance of the control surfaces is known to depend on body orientation, restricting the permissible vehicle motions results in flow conditions and control surface performance that are not representative of a typical AUV.

The work of this thesis is intended to address the shortcomings in the previous research in regard to hydrodynamic, modelling, and control aspects of AUV control surface performance. Experimentation is used to accurately determine control surface hydrodynamic characteristics; modelling is used to represent the experimental results in a compact mathematical form; and simulation is used to study the effect of control surface modelling and control on overall vehicle performance.

1.4 OBJECTIVES

The primary objective of this research was to improve AUV performance through improvements to vehicle control surface effectiveness. The factors affecting the performance of control surfaces are interdisciplinary in nature—spanning hydrodynamics, modelling, and control—and this was reflected in the primary objective. To improve control surface effectiveness, it was necessary to fully describe the hydrodynamic performance of control surfaces for the test vehicle, improving the accuracy and completeness of existing performance predictions where possible. The control surface hydrodynamic behavior was required to be modelled in a practical mathematical form that retained all key performance characteristics. It was also necessary to determine the significance of including or ignoring various aspects of control surface performance in performance models. Finally, understanding the consequence of incorporating new control surface hydrodynamic effects in control system design, as well as the investigation of enhanced control methodologies to account for any new hydrodynamic effects, was needed.

A secondary objective of this research was to provide ISER with guidelines and strategies for use in development of control surfaces for their AUVs. In particular, an assessment of the current control surface configuration on the Mark II DOLPHIN was needed in addition to recommendations for improvements to the control surface layout. Additionally, it was important to establish the validity of previous simulations conducted for ISER on controller development that were conducted with less complete control surface hydrodynamic models (Field, 2000). Lastly, DOLPHIN-specific improvements to the control strategy based on the new control surface hydrodynamic information were sought.

1.5 APPROACH AND RATIONALE

Improvements to control surface effectiveness on near-surface underwater vehicles was considered from three main approaches: hydrodynamics, modelling and simulation, and control. The understanding of the physics regarding control surface performance is furthered through a systematic series of hydrodynamic experiments on several scale models. The resulting information of control surface behavior can be directly applied to underwater vehicle control surface designs and layouts. However, with the enhanced understanding of control surface hydrodynamics, improved control schemes are also developed through modelling and simulation.

1.5.1 Hydrodynamics

Two main aspects of the physics of control surface performance were studied in multiple testing facilities. The first area of study was the influence of operating factors (such as the body orientation and the free surface) on the performance of control surfaces. The second was the effect of control surface geometry and mounting location on the control surface effectiveness.

Both wind tunnels and towing tank facilities were used for experimental testing with findings presented in Chapter 3. The wind tunnels provided a means by which to quickly investigate the behavior over a wide range of operating conditions and were also conducive to a wide variety of flow visualization techniques. Generally, the time required per test is much lower in a wind tunnel compared to a towing tank (Watt et al. 1993) or other water based facility (such as a flume or water tunnel for example). However, wind tunnels are incapable of fully duplicating the operating environment for near-surface underwater vehicles and the wind speeds required exceed the capabilities of most facilities. For these reasons, preliminary control surface force measurement tests were conducted in the wind tunnels covering a wide range of conditions. Several flow visualization techniques were also employed to complement the wind tunnel force measurement work. Based on the findings from the wind tunnel, additional testing was conducted in a towing tank for the most important cases to improve the modelling realism.

1.5.2 Modelling and Simulation

The hydrodynamic information obtained through testing was modelled numerically. The numerical modelling (detailed in Chapter 4) was used to describe the control surface behavior in as concise and simple a representation as possible without loss of realism. The influence of operating parameters such as Reynolds number, body orientation, and the free surface condition, for example, were treated separately and then linearly combined.

The numerical representation of control surface performance was incorporated into a simulation package (outlined in Chapter 6). Simulations were conducted to examine the importance of the various improvements in control surface modelling. By comparing simulation results with changes to only specific aspects of the control surface modelling, the importance of those changes could be quantified. The influence of modifications to control surface geometry and layout were examined in the same manner as were improvements to the control methodology (Chapter 5). A single performance parameter criterion, based on sonar image smearing in a representative case, was developed for comparison between simulations.

1.5.3 Control

The performance of the existing LQG/LTR control scheme was examined using the control and dynamics simulation package mentioned above. Augmented control methodologies (as discussed in Chapter 5) were studied by incorporating additional modules into the simulation package. A base-line PD controller was also developed to represent the existing controller in the DOLPHIN.

Due to the scope of this work, limited time and resources were available for the study of vehicle control. Accordingly, the intention of the work in controller augmentation was only a "proof-of-concept". Extensive validation and further development would be required prior to implementation of the control strategies on a vehicle; in particular, a rigorous analysis of stability would be required.

2

CONTROL SURFACE HYDRODYNAMICS - THEORY

Diving [a submarine] is a carefully controlled and balanced procedure that resembles a ballet danced by an elephant.

-Tom Clancy on the USS Miami Naval Submarine

The manoeuvrability and stability of a submarine, as well as the ability to compensate for disturbances, are dependent on the hydrodynamic forces generated by the control surfaces. Underwater vehicles are frequently unstable (Barlow et al., 1999) and would be unusable without active operation of the control surfaces. Accurate knowledge of the control surface performance is essential in all stages of underwater vehicle development including initial design and specification, modelling, simulation, and control system development.

Within this chapter, the background information relating to control surface hydrodynamics is presented. Following a description of conventions and terminology, a brief summary of semi-empirical findings is presented for both isolated control surfaces and control surfaces mounted on a hull. (In the literature on underwater vehicle technology, the term “semi-empirical” is used to describe analytical relationships derived from experimental data.) The chapter concludes with a discussion of the interaction between fore and aft control surfaces as well as with the free surface.

2.1 CONVENTIONS

The components of an AUV (or any underwater flight vehicle) that are central to this research were highlighted in Figure 1-1 and are reproduced in Figure 2-1 below.

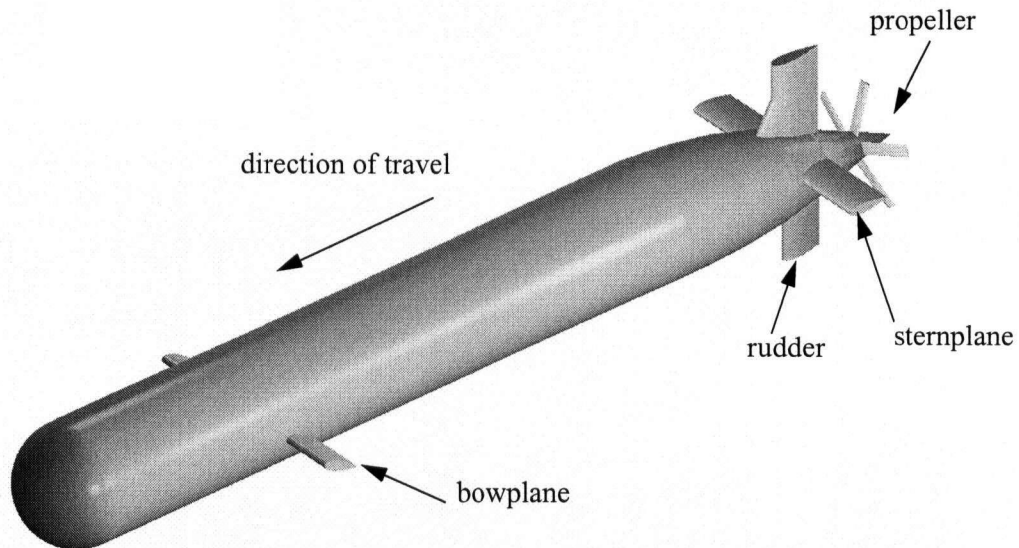


Figure 2-1 Typical geometry of an autonomous underwater vehicle

Of particular importance are the horizontal control surfaces identified as the *bowplanes* and *sternplanes*. These wing-like appendages are also referred to as *fore planes* and *aft planes* respectively, or in general as simply *planes*. Typically the planes and the rudder are all-moveable, but in some cases they may be fixed to the body with a moveable flap on the trailing edge. Other concepts are possible, such as rotating cylinders on fixed fins (den Hertog and Modi, 2001), but the all-movable design is by far the most studied and most commonly employed.

The conventions in this thesis for describing position, pose, motion and forces relevant to an AUV are the same as those proposed by Feldman (1979). The sign conventions are shown in Figure 2-2 and the symbols used are summarized in Table 2-1 and Table 2-2 for translation and rotation respectively.

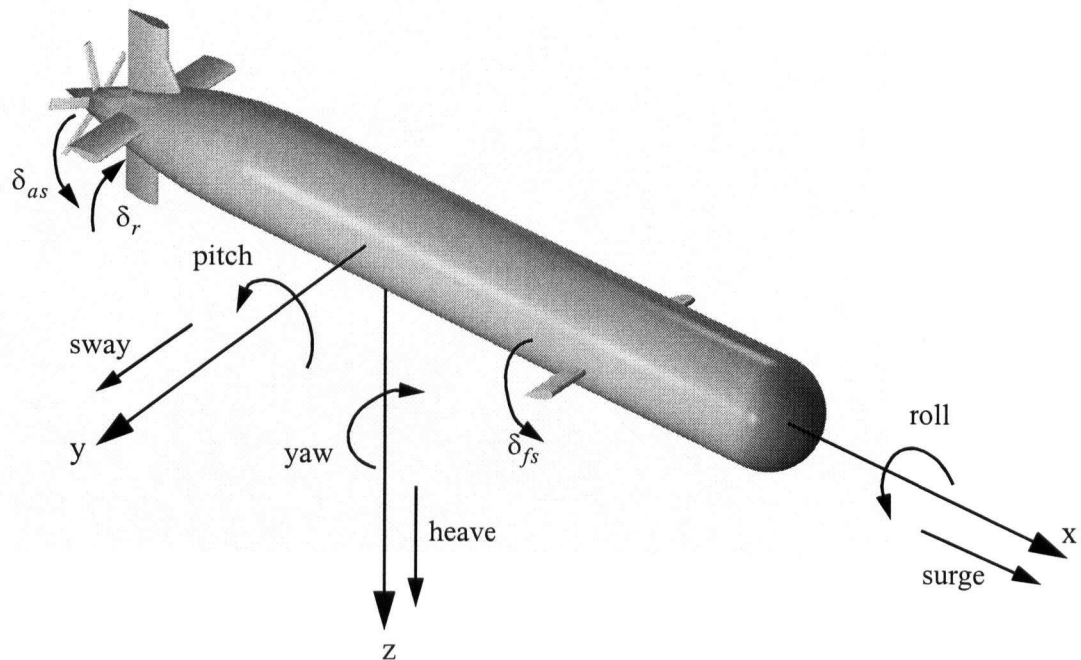


Figure 2-2 Sign conventions

Table 2-1 Variable conventions for translation

Quantity	Symbol used			
	Displacement	Velocity	Force (dimensional)	Force (non-dimensional)
surge	x	u	X	X'
sway	y	v	Y	Y'
heave	z	w	Z	Z'

Table 2-2 Variable conventions for rotation

Quantity	Symbol used			
	Angular Displacement	Angular Velocity	Moment (dimensional)	Moment (non-dimensional)
roll	ϕ	p	K	K'
pitch	θ	q	M	M'
yaw	ψ	r	N	N'

Where practical, forces are non-dimensionalized using the dynamic pressure and the vehicle length squared. For example, in the x -direction, the force is non-dimensionalized according to

$$X' = \frac{X}{\frac{1}{2}\rho U^2 l^2} \quad (1)$$

where ρ is the fluid density, U is the speed of the freestream flow, and l is the vehicle length. The dynamic pressure specifically is the combination $\frac{1}{2}\rho U^2$. Moments are non-dimensionalized by dynamic pressure and vehicle length cubed. For example, the moment about the x -axis, K , is non-dimensionalized as

$$K' = \frac{K}{\frac{1}{2}\rho U^2 l^3} \quad (2)$$

In some instances, such as with isolated control surfaces, the forces are non-dimensionalized by a reference area, S , and expressed as a force coefficient. For example, the lift force, L , on an isolated plane with exposed planform area, S_{exp} , is described by the coefficient of lift, C_L by

$$C_L = \frac{L}{\frac{1}{2}\rho U^2 S_{\text{exp}}} \quad (3)$$

The variables describing the actuator deflections (and propeller speed) are summarized in Table 2-3 and use the sign conventions of Figure 2-2.

Table 2-3 Variable conventions for translation

Control Surface		Deflection
Name	Alternate Name	Symbol
port bowplane	port fore plane	δ_{fp}
starboard bowplane	starboard fore plane	δ_{fs}
port sternplane	port aft plane	δ_{ap}
starboard sternplane	starboard aft plane	δ_{as}
rudder	-	δ_r
propeller	-	n

Derivatives of force and moment with respect to control surface deflections—referred to as hydrodynamic derivatives—are expressed using subscript notation. For example, the first derivative of the X' force with respect to the port bowplane is

$$\frac{\partial}{\partial \delta_{fp}} X' \equiv X'_{\delta fp} \quad (4)$$

while the second derivative of the X' force with respect to port bowplane deflection is

$$\frac{\partial^2}{\partial \delta_{fp}^2} X' \equiv X'_{\delta fp \delta fp} \quad (5)$$

2.2 CONTROL SURFACE GEOMETRY

The geometric and sign conventions used with isolated control surfaces in this work are shown in Figure 2-3. Note that the coordinate system for the isolated appendage is fixed to the appendage while the coordinate system for a plane on a body is fixed to the body (see Figure 2-2). In both cases, the angle of incidence, α , of the flow onto the plane is defined by the angle between the incoming flow vector, U , and the chord line as shown. The main parameters that define control surface geometry are summarized in Figure 2-4. Details regarding each of these parameters are discussed in turn below.

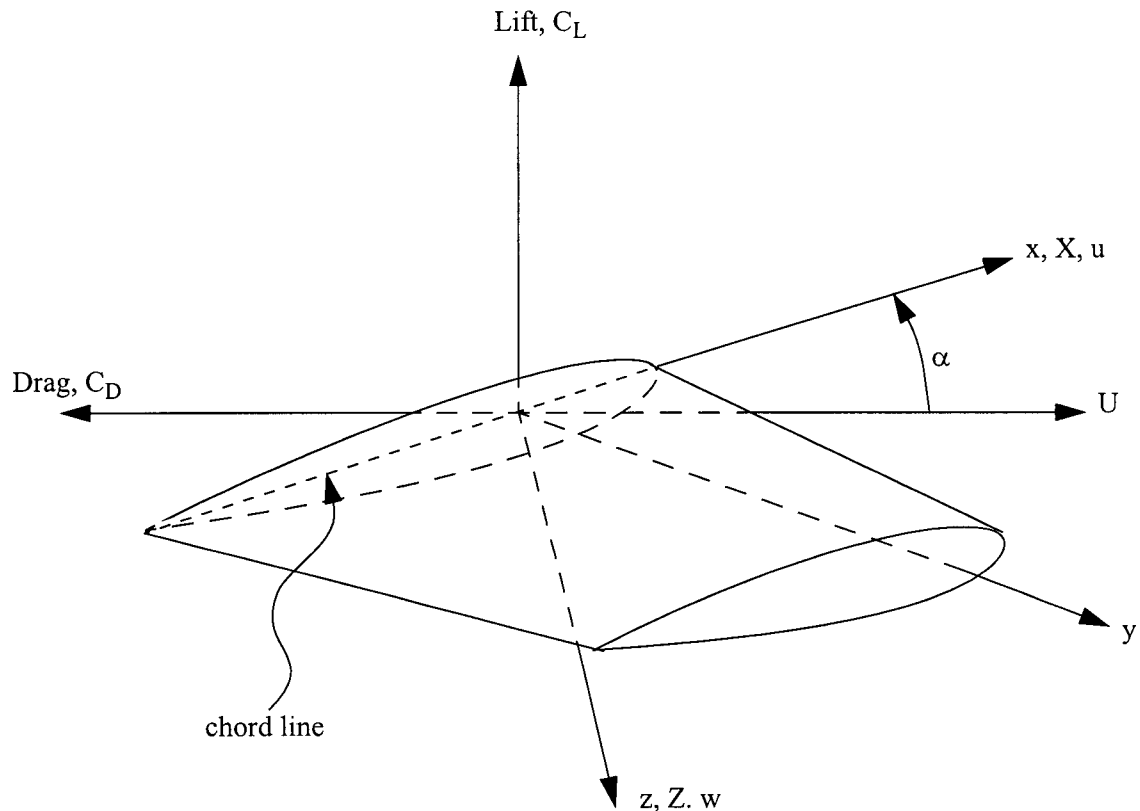


Figure 2-3 Control surface coordinate system (shown on starboard side plane)

2.2.1 Chord

The *chord* is denoted by C and, for a given two-dimensional section, it is defined as the distance from the leading edge to trailing edge. The chord is measured parallel to the section at the root, or inboard portion, of the control surface. In general, the chord can vary along the span (defined below), in which case the geometric mean chord, \bar{C} , is used in computations unless noted. For this work, trapezoidal shaped control surfaces are used and \bar{C} is defined based on Figure 2-4, as

$$\bar{C} = \frac{C_r + C_t}{2} \quad (6)$$

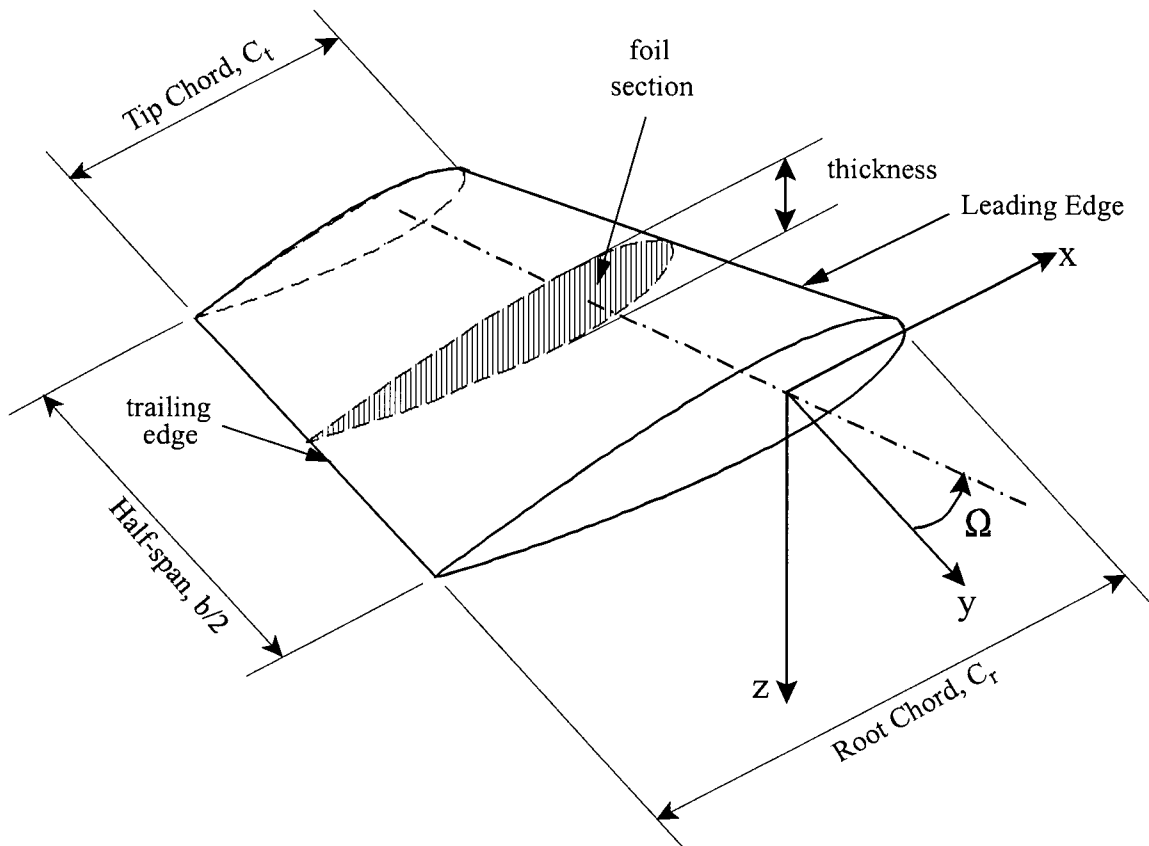


Figure 2-4 Control surface parameters (shown on port side plane)

2.2.2 Span

The *span*, denoted by b , is a measure of the distance from the control surface root to tip along the line perpendicular to the root section. Mathematically, there are several ways in which the span is commonly defined: the root-to-tip distance for an isolated plane; the distance from the body centreline to the plane tip; the tip-to-tip distance for two planes mounted on opposite sides of a body; or twice the root-to-tip distance for a plane mounted on a large body. For the first two cases, the measurement indicated is sometimes also referred to as the semi-span. For this work, unless noted otherwise, the “twice root-to-tip distance” method (as shown in Figure 2-4) is used.

2.2.3 Foil Section

The geometry of a control surface is mainly defined by the two-dimensional *foil section(s)* used and the *planform*. The foil section is identified by the shaded region in Figure 2-4; it can take almost any geometry although virtually all forms have a rounded leading edge and a sharp trailing edge. Symmetric, four-digit National Advisory Committee for Aeronautics (NACA) sections are most often used with underwater vehicles. For symmetric foils, the four-digit NACA designation is “NACA 00XX” where the “XX” represents the thickness expressed as a percentage of the foil chord. In practice, the same section is generally used throughout a plane although a transition between sections is possible along the control surface span. In this work, a NACA 0025 section,

corresponding to a thickness-to-chord ratio of 0.25, was used except where noted otherwise; the planes and rudder on the Dolphin vehicle all use the NACA 0025 section.

2.2.4 Planform

While the section describes a two-dimensional slice through a control surface, the planform identifies the layout of sections that form the three-dimensional plane. Essentially, the planform describes the chord as a function of the position along the span. In most cases, simple trapezoidal planforms are used that can be defined by four main parameters: chord, span, taper ratio, and sweep. The *taper ratio*, λ , is defined for a trapezoidal planform as the ratio of tip chord to root chord. The *sweep* can be defined in several ways; for this work the quarter-chord sweep angle, Ω , as given in Figure 2-4 is used. A *rectangular* planform has a taper ratio of unity and sweep angle of zero. Complicated planforms, such as the elliptical one made famous on the *RAF Spitfire*, can offer slight performance benefits but are not often used due to added difficulty in manufacture. Further information about low aspect ratio swept wings can be found in Aronson and Lekander (1986) and van den Berg et al. (1977).

The planform area, S , is often used in reference to control surfaces. The definition of S can be based on either the exposed area of a single control surface, as with Aucher (1981), or on two control surfaces, as with Whicker and Fehlner (1958). In either case, the mathematical definition is

$$S = b\bar{C} \quad (7)$$

where the difference in interpretation of S is included within the definition of b .

2.2.5 Aspect Ratio

The aspect ratio is based on the planform and represents one of the main parameters determining control surface performance. Denoted by a_e in this work, and sometimes denoted by AR by others, aspect ratio is a dimensionless value that describes the planform slenderness. As with the other parameters, various definitions of aspect ratio exist but typically for underwater vehicles it is defined as

$$a_e = \frac{b^2}{S} \quad (8)$$

For this work with rectangular and trapezoidal control surfaces, this is equivalent to

$$a_e = \frac{b}{\bar{C}} \quad (9)$$

with b and \bar{C} as defined in Figure 2-4 and equation (6). Thus, a large value of a_e corresponds to a slender wing.

Control surfaces are considered to be of *low aspect-ratio* when the span is of the same order as the mean chord, that is for values of a_e less than about 2 or 3 (Aucher 1981). In general, a reduction in aspect ratio results in reduced force generation for a given angle of incidence but is also associated with delayed stall and an increase in the range of operation (see White, 1986, or Talay, 1975). For illustration, Figure 2-5 shows the variation in the lift coefficient with aspect ratio for a Clark-Y airfoil (reproduced from Zimmerman, 1933, and Hoerner and Borst, 1975). Note that from the source, the data were adjusted to zero lift at zero degrees incidence.

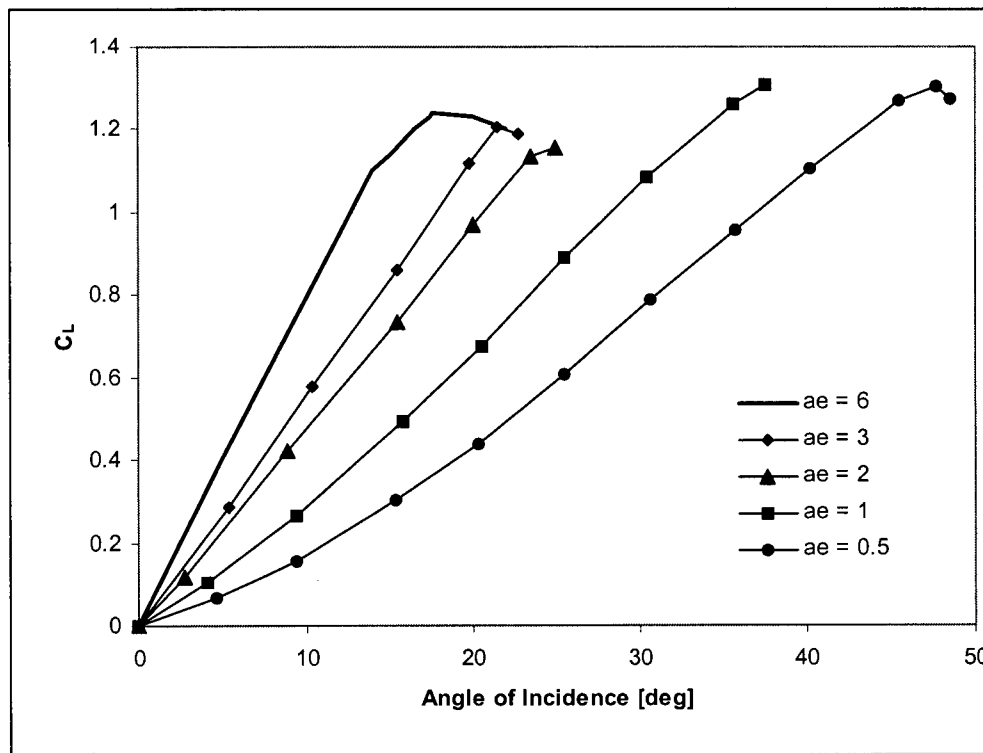


Figure 2-5 Variation lift coefficient with aspect ratio

2.2.6 Endplates

Endplates, sometimes called *fences*, are added to the ends of control surfaces in order to minimize leakage from the suction to pressure side. Typically, endplates are added to the tip of an appendage but may also be added to the root (see Figure 2-6).

Endplates reduce the spanwise flow near ends of the plane and thereby increase the effective aspect ratio. According to Talay (1975) the endplates also reduce the strength of the tip (trailing) vortices shed by a plane.

In terms of performance prediction, Mackay (1998) provides the following endplate factor

$$k_{ep} = 1 + 1.9 \frac{h}{2b} - 0.5 \left(\frac{h}{2b} \right)^2 \quad \text{for } \left(\frac{h}{b} \leq 2.5 \right) \quad (10)$$

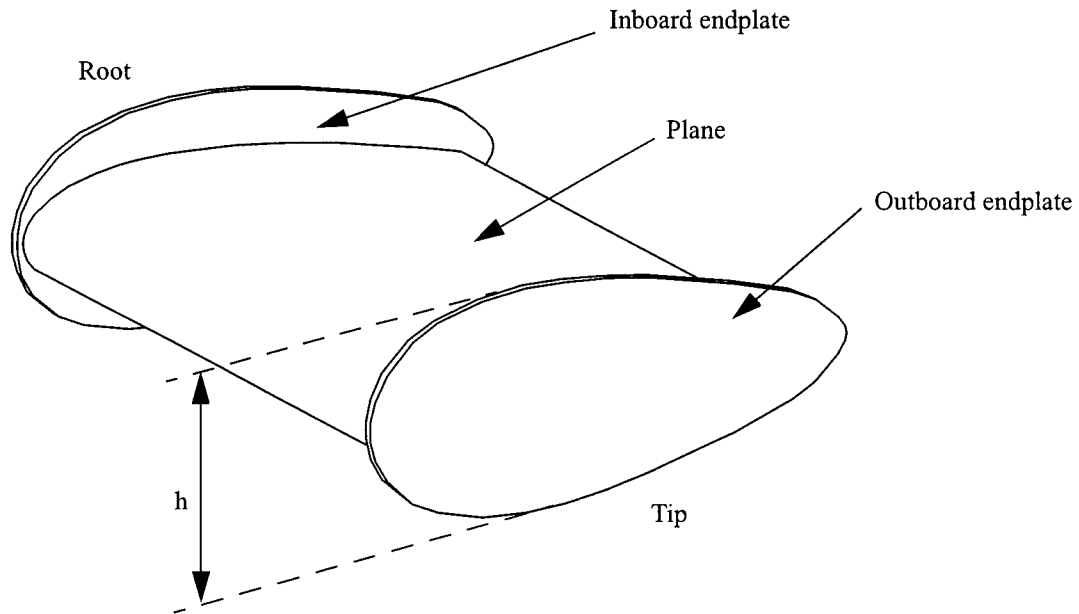


Figure 2-6 Inboard and outboard endplates

The endplate factor is used to adjust the effective aspect ratio of the planes. The endplate height is given by, h , and the plane span, b , is measured to the hull centreline. For outboard (tip) endplates, the effective aspect ratio becomes

$$a_e \Rightarrow k_{ep} a_e \quad (11)$$

while for inboard (root) endplates, the effective aspect ratio is

$$a_e \Rightarrow \left(1 + (k_{ep} - 1) \left(\frac{b_{ep}}{b} \right)^2 \right) a_e \quad (12)$$

where b_{ep} is the spanwise location of the endplate measured to the hull centreline.

2.3 AUV CONTROL SURFACE LAYOUT

The effectiveness of control surfaces is determined in part by the control surface geometry but also by the placement of the control surfaces on a vehicle. Typically, control surfaces are mounted as shown in Figure 2-1 with the rudder in the vertical plane and bowplanes and sternplanes in the horizontal plane. There may be a vertical offset between the bowplanes and sternplanes—the bowplanes on the DOLPHIN Mark II, for example, have a vertical position just over 0.01 body lengths lower than sternplanes. More elaborate options include adding dihedral (anhedral) to the bowplanes, modifying the orientation of control surfaces on the tail, or repositioning planes to locations vehicle-specific locations.

The size and location of control surfaces is often limited by practical considerations. Increased span (width of horizontal control surfaces from the vehicle) may be advantageous in terms of increased force and moment generation but may be undesirable due to increased vulnerability to damage during launch and recovery. Likewise, low appendages may be at risk in shallow water or in towing operations (Watt et al., 1997).

2.3.1 Anhedral and Dihedral

Dihedral refers to the span-wise inclination angle of a wing or control surface from the horizontal plane and about the longitudinal axis of a vehicle. The dihedral angle is measured positive as shown in Figure 2-7 (a); negative dihedral is called *anhedral* as shown in Figure 2-7 (b). In the literature, the symbols Γ or θ are often used for dihedral but for this work, β is chosen as Γ and θ are reserved to denote circulation and pitch angle respectively.

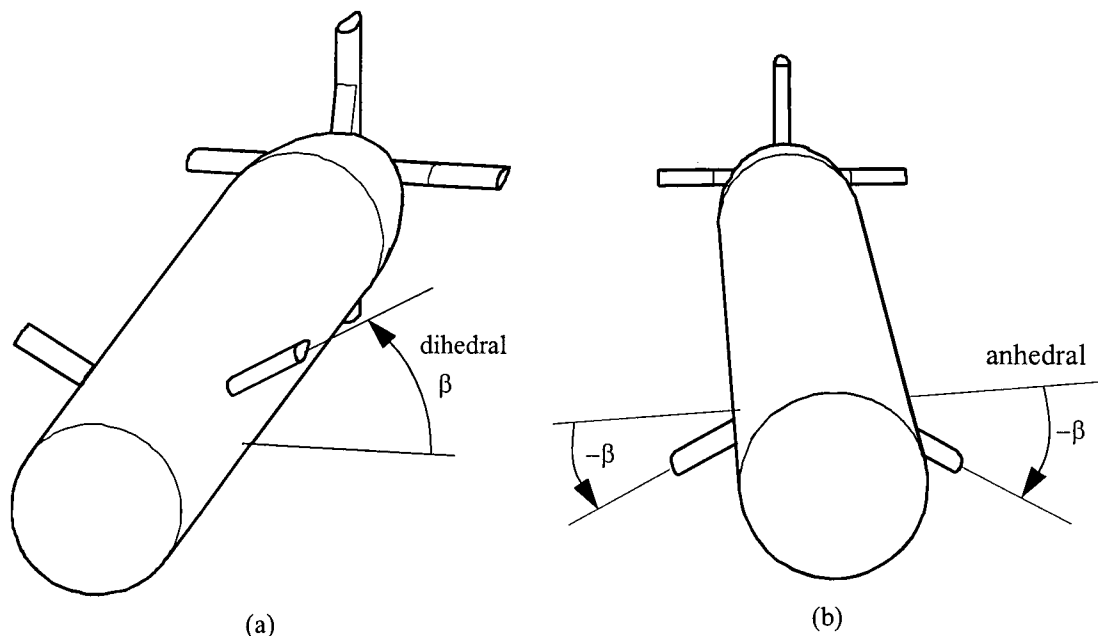


Figure 2-7 Span-wise bowplane inclination angle: (a) dihedral, (b) anhedral

Dihedral is often added to aircraft wings to alter lateral stability characteristics. For underwater vehicles, dihedral has several additional benefits: Firstly, the bowplanes tips generate significant flow disturbances that can have adverse effects on the sternplanes; inclining the bowplanes with

dihedral tends to move the bowplane tips to a position less in-line with the sternplanes, thus potentially reducing the flow interactions. Secondly, a bowplane with non-zero dihedral generates a control force with both horizontal and vertical components. This allows for greater redundancy in the control of yaw (otherwise controlled solely by the rudder) and makes active control of sway possible. Thirdly, the use of anhedral specifically (not dihedral) orients the bowplanes in a position less likely to be influenced by free surface disturbances such as waves.

2.3.2 Tail Control Surface Configurations

The common configurations for the stern control surfaces (the sternplanes and rudder) are shown in Figure 2-8. These include the standard (cruciform) tail and several variations with the sternplanes at non-zero inclination angles. In the case of the Y- and inverted Y-tail there is a vertical rudder with two inclined planes while with the X-tail all four planes are inclined at non-zero dihedral.

The benefits of the alternate tail geometries presented in Figure 2-8 (b) through (d) are similar to those for dihedral bowplanes. Namely, the sternplanes are positioned such that flow from bowplanes is less likely to result in adverse interactions and there is increased redundancy in the control of pitch and yaw. The drawback of these alternate control surface layouts is the increased complexity in relating control actions to vehicle responses.

2.3.3 DOLPHIN-Specific Control Surfaces

Other control surface configurations also possible for this work include options specific to the DOLPHIN AUV. Two such examples are shown in Figure 2-9. Figure 2-9 (a) shows a configuration with the bowplanes relocated to the vehicle keel. The advantage of such a configuration is that the bowplanes are moved away from the hull centre line where considerable flow disturbances are expected in yaw and pitch. Additionally, the control surfaces are moved further below the free surface thus reducing the influence of waves. Lastly, as the keel thickness is less than the hull diameter, it is possible to use planes of greater span and higher aspect ratio—and hence higher efficiency—while maintaining the same tip-to-tip distance. This configuration is considered in this work but has limited opportunity for application to AUVs of more typical geometry.

Figure 2-9 (b) illustrates another concept that has been considered for the DOLPHIN in which a vertical control surface is added to the mast. Such a design would allow for improved effectiveness in roll control although additional roll (and sway) loading on the mast would result from the replacement of the self-aligning fairings. This configuration is presented for completeness and is not considered in the current work; further details regarding the performance of such an articulated mast can be found in Williams et al. (2000).

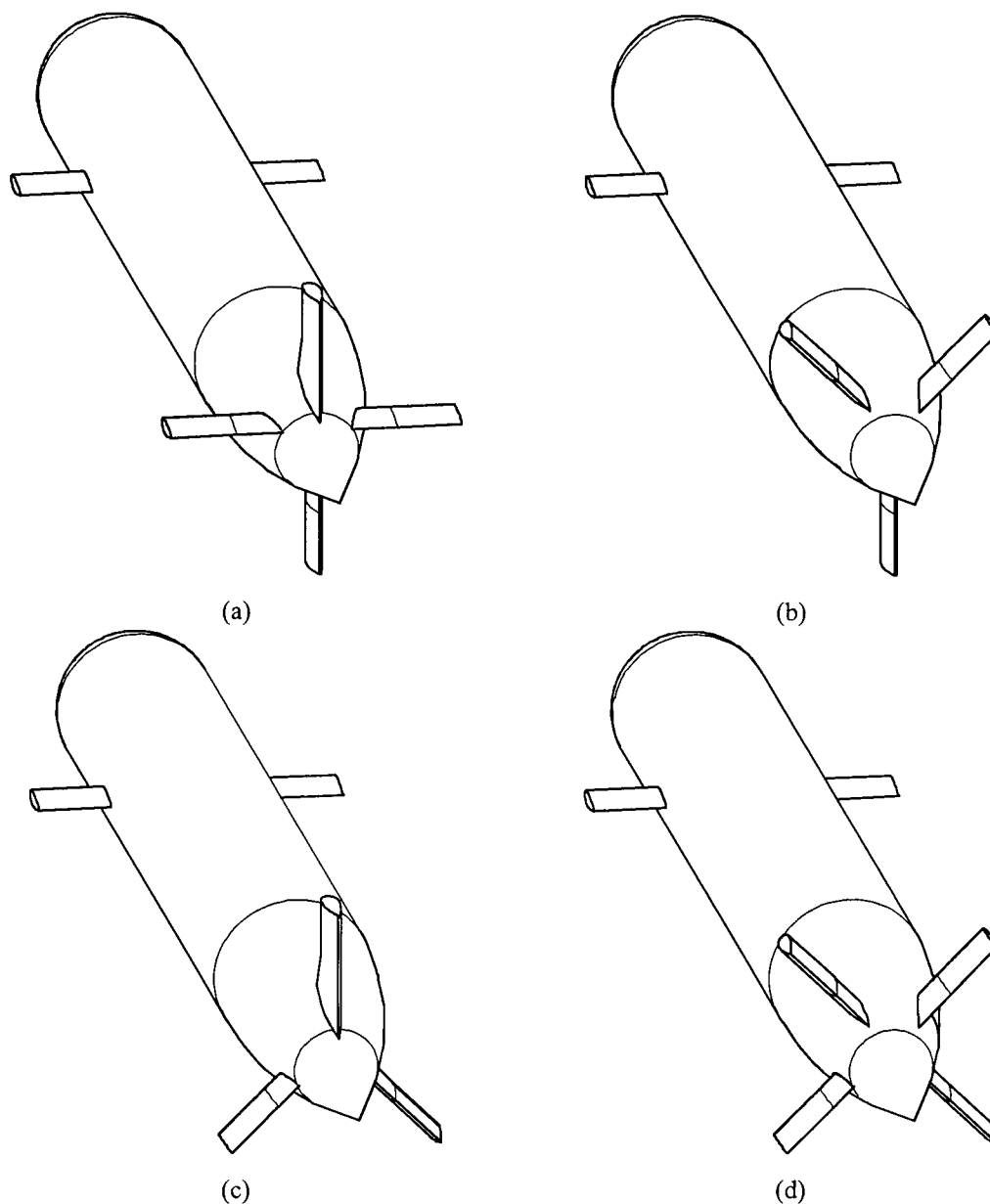


Figure 2-8 Tail configurations: (a) cruciform; (b) Y-tail; (c) inverted Y-tail; (d) X-tail

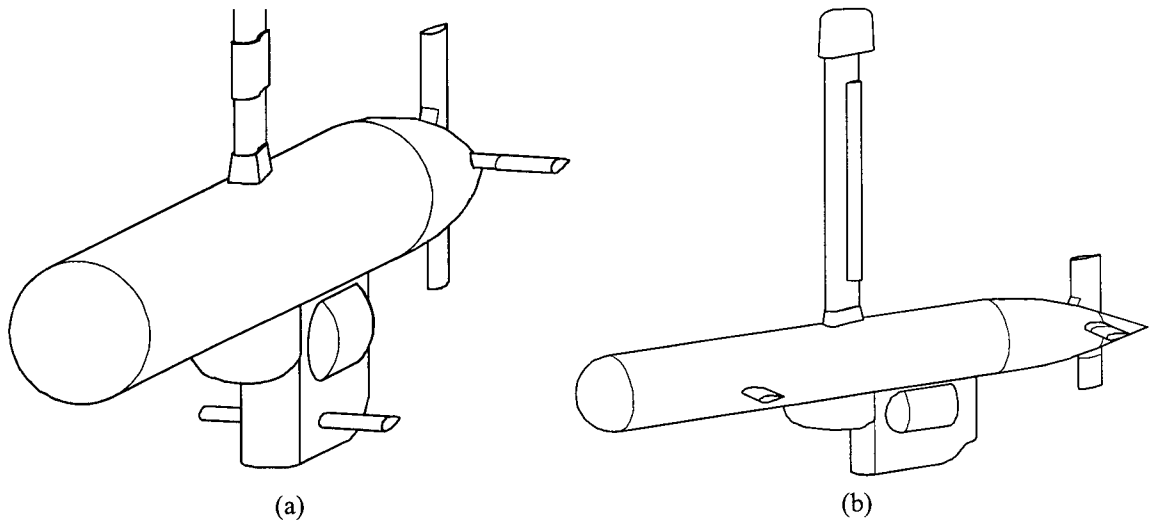


Figure 2-9 DOLPHIN-specific control surface locations: (a) keel planes; (b) articulated mast

2.4 CONTROL SURFACE PERFORMANCE PREDICTION

Control surface performance prediction is discussed below in turn for isolated planes, bowplanes, and sternplanes.

2.4.1 Isolated Control Surface

Method of Whicker and Fehlner

The performance of isolated control surfaces, based mainly on NACA 0015 airfoil sections, was studied by Whicker and Fehlner (1958). This semi-empirical study provided the approximation of the lift-curve slope of an isolated low aspect ratio wing as reproduced in equation (13).

$$C_{L\alpha} = \frac{1.8\pi a_e}{1.8 + \cos\Omega \sqrt{4 + \frac{a_e^2}{\cos^4\Omega}}} \quad (13)$$

Here a_e is the effective aspect ratio and Ω is the angle of the quarter chord. The second-order lift coefficient (that is, C_L as shown in Figure 2-3 on page 18) is then determined from equation (14) by using the localized angle of incidence, α , the lift-curve slope, and the crossflow drag coefficient, C_{Dc} .

$$C_L = C_{L\alpha}\alpha + \frac{C_{Dc}}{a_e}\alpha|\alpha| \quad (14)$$

As noted by Field (2000), the angle of incidence for a plane can be expressed as

$$\alpha = \delta + \frac{w - q_{x_{plane}}}{U} + \alpha_{local} \quad (15)$$

where δ is the deflection of the plane relative to the hull, the middle term gives the angle between the freestream flow and the velocity of the point on the hull where the plane is mounted, and the term α_{local} includes local changes in the flow direction about the hull. The angle of incidence is shown graphically in Figure 2-10 and further information regarding α_{local} provided in Section 2.4.2.)

The crossflow drag is a function of the plane tip geometry only; Whicker and Fehlner (1958) provide the following suggested values based on the taper ratio, λ .

$$C_{Dc} = \begin{cases} 0.1 + 0.7\lambda & \text{for a round tip} \\ 0.1 + 1.6\lambda & \text{for a square tip} \end{cases} \quad (16)$$

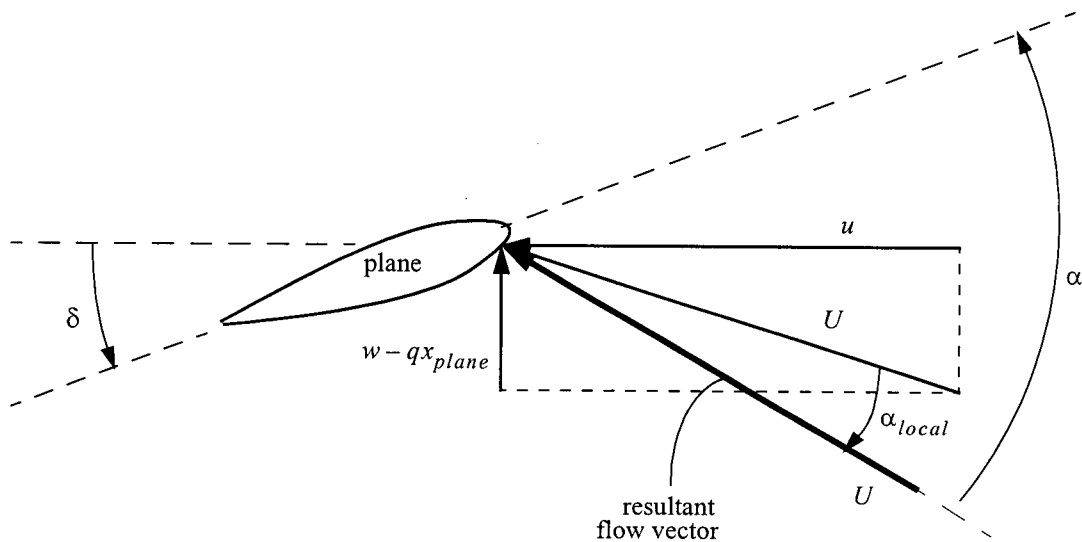


Figure 2-10 Incident flow angle to planes

The drag coefficient is determined as

$$C_D = C_{D0} + \frac{C_L^2}{0.9\pi a_e} \quad (17)$$

For the minimum drag value, C_{D0} , 0.0065 can be used for a NACA 0015 plane.

The force coefficients, C_x and C_z , are related to the lift and drag by a coordinate transformation from the frame of the free stream flow to that of the submarine axes:

$$C_x = -C_D \cos \alpha + C_L \sin \alpha \quad (18)$$

$$C_z = -C_L \cos \alpha - C_D \sin \alpha \quad (19)$$

Method of Aucher

Aucher (1981) provides an alternate estimate of force prediction on low aspect ratio wings based on experience and theoretical calculations.

$$C_z(\alpha) = \frac{Z}{\frac{1}{2}\rho S U^2} = \frac{2\pi a_e \left[1 - 3\left(\frac{t}{C}\right)^2 \right]}{2.6 + \cos \Omega \sqrt{2 + \frac{a_e^2}{\cos^2 \Omega}}} \alpha + 2.1 \alpha^3 \quad (20)$$

where $\frac{t}{C}$ is the thickness ratio and a_e is the aspect ratio, defined for rectangular or trapezoidal wings as:

$$a_e = \frac{2b}{C} \quad (21)$$

Aucher notes that equation (20) is valid only for taper ratios less than about 2 or 3 and angles of incidence not exceeding 25 degrees.

2.4.2 Hull Influence on Bowplanes

The flow field surrounding control surfaces mounted on a body are, at times, substantially different from that of isolated appendages. In the case of the bowplanes, there is a change in lift curve slope due to the cylindrical hull. For non-zero trim angles, there is acceleration and significant redirection to the incoming flow to the planes, particularly near the root.

Hull Curvature Correction (Mackay)

As noted by Mackay (1998), an appendage has a lower effective aspect ratio when mounted on a simple convex surface as compared to a plane surface since the appendage image has reduced span. Mackay modifies the aspect ratio by the factor k_{ss} ,

$$k_{ss} = \frac{1}{2} \left(1 + \frac{R}{R + b_{\text{exp}}} \right) \quad (22)$$

where R is the radius of curvature of the surface (hull) and b_{exp} is the exposed bowplane span. With this formulation, a_e in equation (13), for example, would be replaced by $k_{ss}a_e$.

Hull Curvature Correction (Aucher)

Aucher (1981) also considers the effect of a curved surface to which the plane is mounted. To begin, he suggests that the clearance between a plane and a flat wall does not significantly affect the validity of equation (20) provided that the clearance does not exceed 0.02 times the length of the adjacent chord. In the presence of a curved wall, he recommends augmenting the result of equation (20) by

$$\Delta C_z(\alpha) = \frac{\pi}{2} \left(1 - \frac{R^2}{b^2} \right) \lambda^* \left(1 - \frac{\lambda^*}{11} \right) \left(1 + \sqrt{\frac{R}{b}} \right) \left(1 - 3 \left(\frac{t}{C} \right)^2 \right) \alpha \quad (23)$$

where

$$\lambda^* = \frac{b}{C} \left(1 - \left(\frac{R}{b} \right)^2 \right) \quad (24)$$

and again R is the hull radius and b , C and t are the plane geometric parameters (span, chord, and thickness, respectively).

Influence of Bowplane Location

Mackay (1998), notes that bowplanes may be located in a high, mid, or low position with respect to the hull centreline. Quoting Lawerence and Flax (1954) and Schlichting (1949) as sources, he goes on to say that the plane lift is generally insensitive to this location within a moderate range. Unfortunately, Mackay does not quantify what this range is but does say that location cannot be ignored for bowplanes sufficiently smaller than the hull radius, particularly when mounted in an extremely high or low position.

Flow Angle Correction (Trim)

When the hull trim angle differs from zero with respect to the free stream flow, localized changes in flow velocity along the hull centreline are expected. Aucher (1981) as well as Hoerner and Borst (1975) show that the local flow angle against the hull at the centreline is equal and opposite to the hull trim angle (see Figure 2-11).

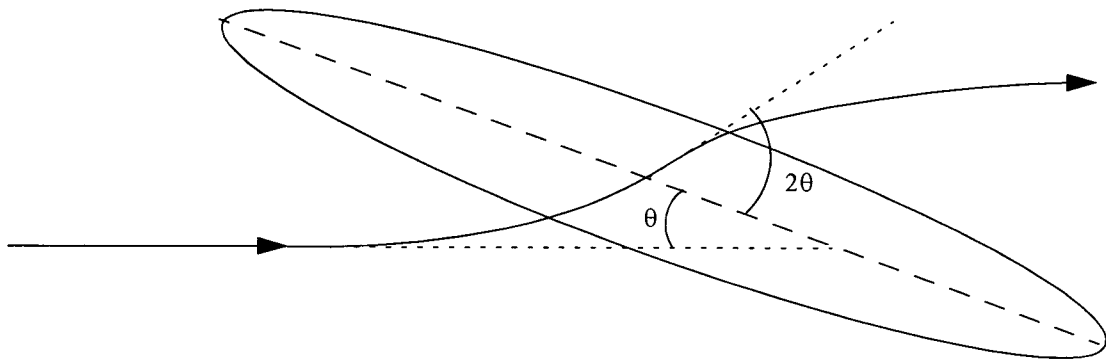


Figure 2-11 Flow angle near inclined hull

The local incident flow angle, α , diminishes with radial distance, y , from the AUV centreline; Aucher gives the relationship

$$\alpha(y) = -\theta \left[1 + \left(\frac{R}{y} \right)^3 \right] \quad (25)$$

where θ is the hull trim angle measured from the incoming flow and α is measured from the hull centreline. In contrast, Mackay (1998) suggests that the incident flow angle relationship is

$$\alpha(y) = -\theta \left[1 + \left(\frac{R}{y} \right)^2 \right] \quad (26)$$

which also agrees with Figure 2-11 but decays more slowly with radial distance. In either case, during a manoeuvre with the hull at a trim angle of θ , there will be a distribution of angle of incidence across the span of a plane. In the limit of $\theta = 90$ degrees, the equation suggested by

Mackay follows the R^2/y^2 behavior expected in the velocity field about a circular cylinder inclined perpendicular to a uniform flow (White, 1986).

Hull Vortices (Yaw)

It is known that two counter rotating vortices form on the lee side of a body of revolution inclined to a freestream flow (Allen and Perkins, 1951). Using flow visualization, Kubota et al. (1992) identified the position of the vortices at various locations along the length of an inclined cylindrical body with length to diameter ratio, $l/D = 6$. In Figure 2-12, a submersible with a cylindrical hull is shown oriented at a yaw angle, ψ . As shown in the figure, the two counter rotating vortices follow the longitudinal axis of the hull rather than the free stream flow. From the flow visualization images of Kawamura and Aihara, the locations of the vortices at 25 degrees yaw were measured and are summarized in Table 2-4. As shown in the table, along the length of the hull there is no appreciable change in the lateral position of the two vortices and only a minimal increase in the vertical separation ($2z_v/R$).

2.4.3 Hull Influence on Sternplanes

Several sources are available for predicting the combined lift effectiveness of low aspect ratio wings located on the aft portion of streamlined bodies. Lyons and Bisgood (1950) examined the lift slope of small aspect ratio wings on aircraft. Dempsey (1977) used a systematic series of stern control surfaces on a representative streamlined body of revolution to determine the forces due to angle of attack.

Lyons and Bisgood

Lyons and Bisgood (1950) suggest treating sternplanes and rudders as carried through to the hull centreline as shown in Figure 2-13. The modified appendages are treated as isolated and performance is computed using one of the methods above. A tail efficiency correction factor is then applied based on a span parameter defined by $r_{1/3}$, the hull radius at the 1/3 chord position of the (actual) appendage root:

$$k_{\eta t} = \begin{cases} 1 - 0.267(r_{1/3}/b) - 0.7455(r_{1/3}/b)^2 & \text{for a bluff tail} \\ 1 - 0.0846(r_{1/3}/b) - 0.843(r_{1/3}/b)^2 & \text{for a tapered tail} \end{cases} \quad (27)$$

In practice, the tail efficiency factor would be applied as follows

$$Z_{sp} \cong k_{\eta t} \cdot Z_{sp}|_{\text{extended}} \quad (28)$$

where $Z_{sp}|_{\text{extended}}$ is the estimated force of the hypothetical sternplane of Figure 2-13, treated as an isolated appendage for the purpose of calculation.

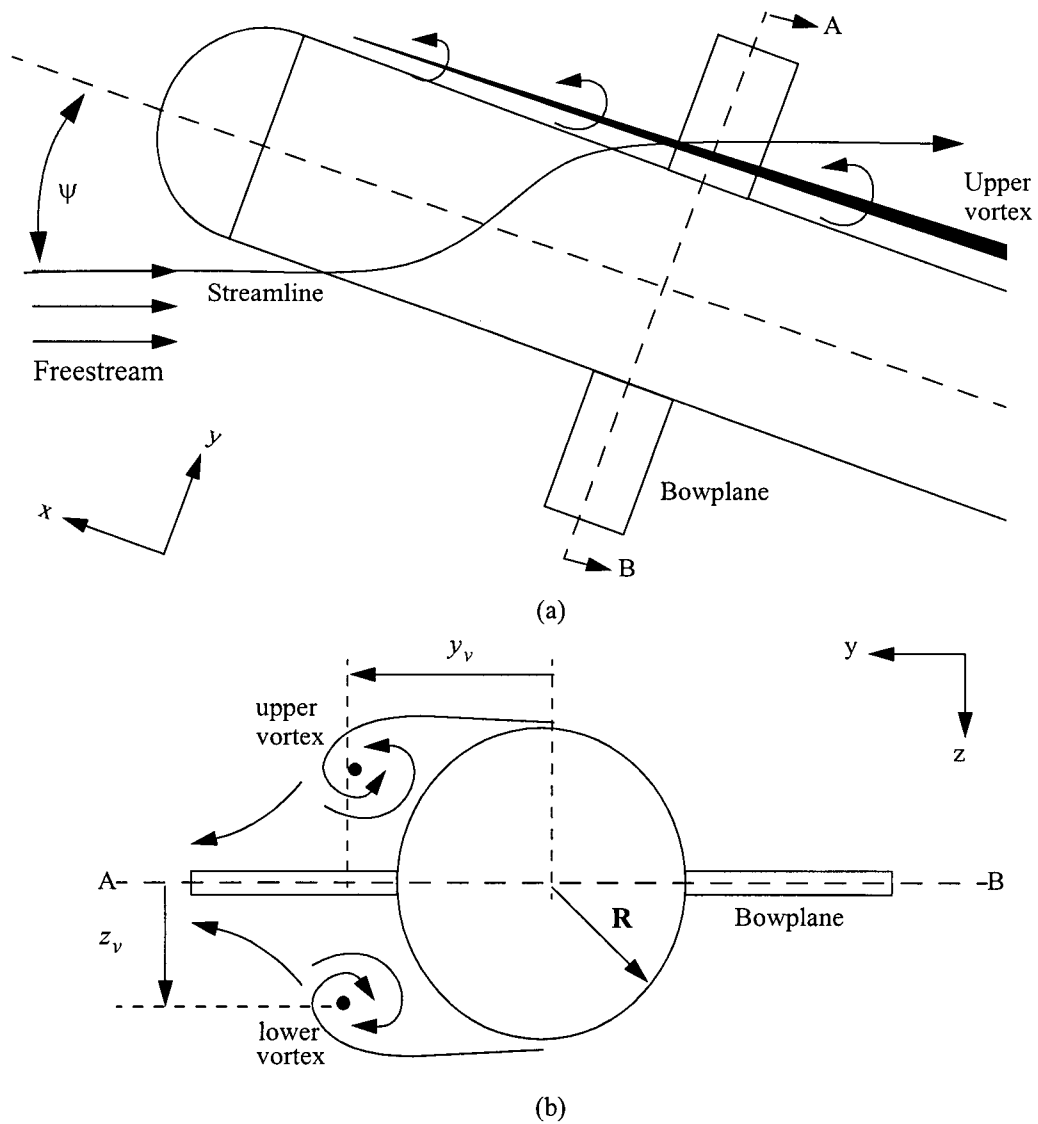


Figure 2-12 Vortex pattern on the leeward side of the hull in yaw

Table 2-4 Location of Hull Vortices in Yaw

Station	Lateral Location	Vertical Location
$-x/L$	y_v/R	z_v/R
0.243	0.88	+/- 0.35
0.388	1.12	+/- 0.37
0.426	0.98	+/- 0.42
Average	0.99	+/- 0.38

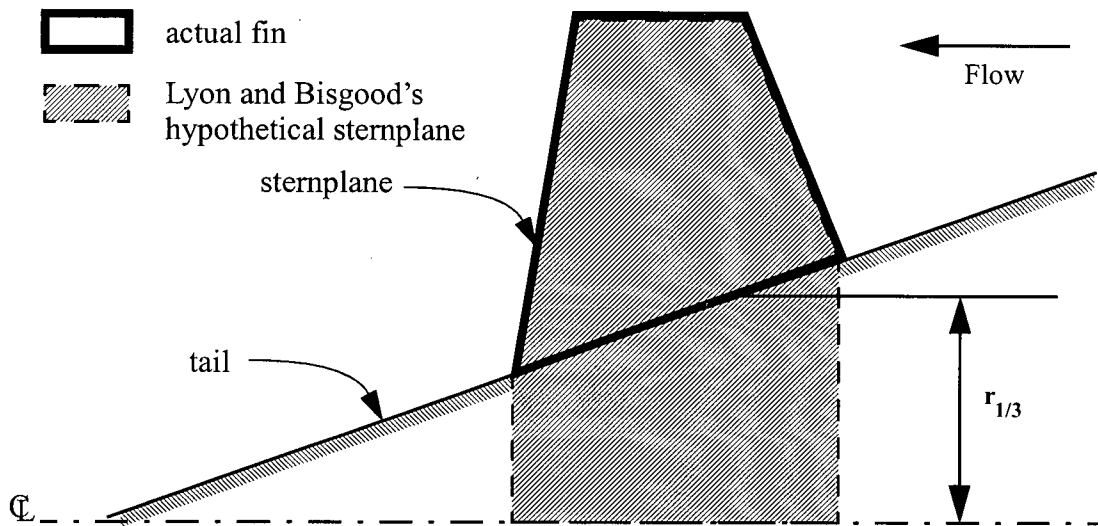


Figure 2-13 Fin area used in Lyons and Bisgood's tail efficiency correction factor

Dempsey

Dempsey proposes that the leading and trailing edges should be extended to the tail centreline as shown in Figure 2-14. Again, an efficiency factor is applied in the same manner, this time using the maximum hull radius, R , in the span parameter. Dempsey suggests the efficiency factor

$$k_{\eta t} = -0.3644 + 1.2380 \frac{b}{R} - 0.3728 \left(\frac{b}{R} \right)^2 \quad (29)$$

$$\text{for } 0.734 \leq \frac{b}{R} \leq 1.426$$

and

$$k_{\eta t} = 1 - \frac{0.2556}{\left(\frac{b}{R} \right)^2} \sqrt{\left(\frac{b}{R} \right)^2 - 0.1612} - 0.6366 \sin^{-1} \left(\frac{0.4015}{\frac{b}{R}} \right) \quad (30)$$

$$\text{for } 0.4015 < \frac{b}{R} < 0.734 \text{ and } 1.426 < \frac{b}{R} < \infty$$

As noted by Mackay (1998), the negative root for $b/R \leq 0.4015$ represents a practical lower limit for submarine and submersible appendages.

The main drawback of the method presented by Dempsey is that the results were obtained using appendage Reynolds numbers based on chord between 0.32 and 1.05 million with no guidance for scaling results to other Reynolds numbers. On the other hand, the use of the local hull radius in the span parameter in the method of Lyons and Bisgood implies very high Reynolds number flow (Mackay 1998). This corresponds to a small hull boundary layer and fully attached flow on the

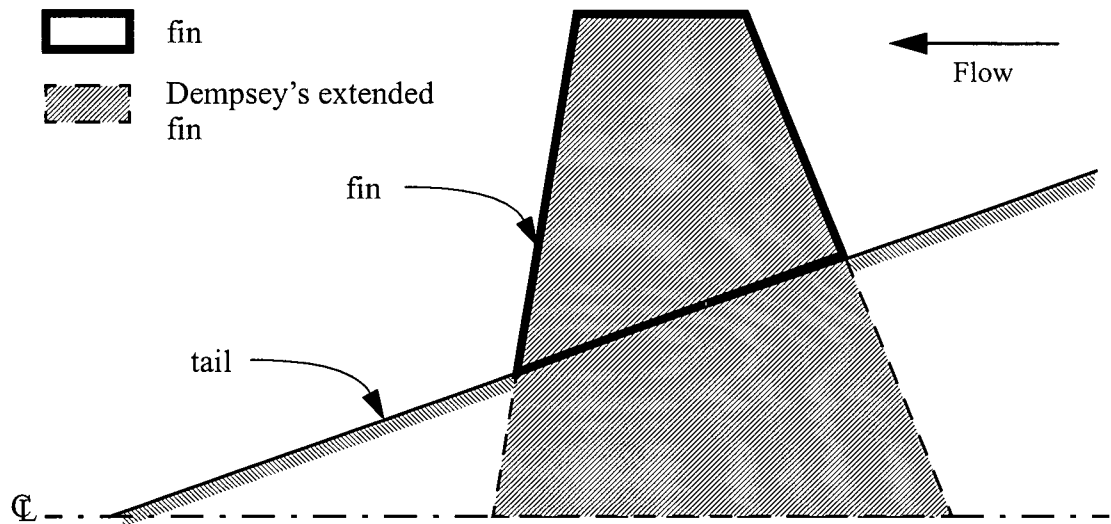


Figure 2-14 Fin area used in Dempsey's tail efficiency correction factor

appendages. For sternplane efficiency prediction in this thesis, the method of Dempsey has been used since the full-scale chord-based Reynolds numbers on the DOLPHIN were only 1.4 million, close to the upper limit of those in the experiments by Dempsey.

2.5 CONTROL SURFACE INTERACTION

Limited information exists regarding the interaction between fore and aft low aspect ratio control surfaces on slender bodies. Given the significant longitudinal separation of typical control surfaces, interaction is essentially limited to flow disturbances generated by the bowplanes and carried aft with the bulk flow to the sternplanes. Previous work includes a study of downwash to elevators on aircraft, the interaction between roll stabilizer fins and bilge keels on warships and a preliminary investigation of induced roll effects from bowplanes to the tail of a DOLPHIN vehicle.

2.5.1 Downwash to Aircraft Elevators

Munk (1923), demonstrated that the angle of downwash at various locations along the span of an aircraft wing was not uniform. Munk related the downwash angle, ε , to various wing parameters by the relationship:

$$\varepsilon = g(y) \frac{C_L S}{b^2 \pi} 57.3^\circ \quad (31)$$

where y , C_L , S and b are used as defined in Section 2.2. The values of the function g are determined by experiment as they varied not only by the arrangement of the wing but also point to point on the wing. For the limited range of conditions considered by Munk, the values of g were varied from 1.2 to 2.2. This range of variation was observed not only between wings, but sometimes at different points on the same wing. Unfortunately, the reliance on wing specific experimental information for the parameter g makes the application of Munk's equation difficult for generalized use.

2.5.2 Interaction Between Warship Stabilizer Fins

The interference between roll stabilizer fins and bilge keels on warships was studied by Lloyd (1974). Lloyd modelled the stabilizer fin trailing vortex as a line vortex with strength determined by the circulation about the fins. The ship hull was modelled as an infinite vertical plane by the use of an image vortex mirrored about the fin root (as shown in Figure 2-15).

The downwash localized at the inception of the trailing vortex (near the fin tip) was computed using the induced flow of the image vortex. The vortex trajectory was assumed linear and oriented at an inclination angle given by ratio of the computed local downwash velocity to freestream velocity. Using the linearly approximated position of the fin trailing vortex in the longitudinal plane of the bilge keel, the downwash due to the trailing vortex and associated image vortex were computed. The incident flow on the bilge keel was thereby determined as the ratio of downwash to freestream velocity. Lloyd gives the downwash angle, ε , at any point aft of a fin by

$$\varepsilon = \frac{C_L}{2\pi a_e b'} \left[\frac{\eta + b'}{\zeta^2 + (\eta + b')^2} - \frac{(\eta - b')}{\zeta^2 + (\eta - b')^2} \right] \quad (32)$$

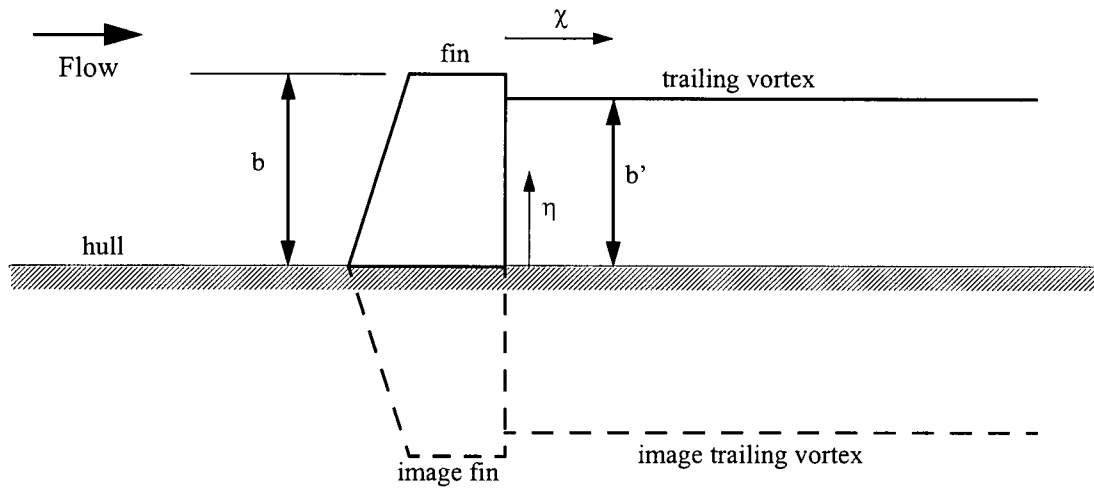


Figure 2-15 Fin vortex model of Lloyd

where a_e is the effective aspect ratio, $2b/\bar{C}$, b' is the spanwise position of the trailing vortex, η is the non-dimensional spanwise position,

$$\eta = \frac{y}{b} \quad (33)$$

and ζ is defined in terms of the point of interest aft of the fin, x , as follows

$$\zeta = \frac{x}{b} \frac{C_L}{4\pi ab'^2} \quad (34)$$

For the system examined by Lloyd, ζ represents the vertical displacement of the trailing vortex from the longitudinal horizontal axis through the fin tip.

Several key features of the system studied by Lloyd are similar to those found on submarine-like vehicles. Most notably, stabilizer fins are of similar aspect ratio to submarine control surfaces and interaction effects are predominantly due to the fin trailing vortices. Nonetheless, the fin to body dimension ratio is essentially zero in Lloyd's analysis which means it is not directly applicable to slender body vehicles (where the fin to body width ratio may approach unity). Likewise, Lloyd's development does not permit the trailing vortex trajectory to have a transverse component (that is, lie outside the x - z plane). This is of concern in any case where the fin tip is vertically offset from the hull image vortices, such as with a dihedral plane or a plane vertically offset from the hull centreline. In such situations, there will be a transverse component to the vortex trajectory.

2.5.3 Control Surface Interaction Predictions on DOLPHIN-like Vehicles

Hopkin et al (1990) used a combination of numerical modelling and experiments to examine downwash effects on a towed underwater vehicle. They were able to show that a single vortex, shed from forward wing tips, was sufficient to predict the loading on the aft wings. Unfortunately,

the geometry studied by Hopkin was somewhat different than that for typical AUVs such as DOLPHIN. As such, the exact findings of Hopkin cannot be directly applied in this research but the general observations about interaction modelling can be used.

Watt et al. (1997) used similar methods to Lloyd to provide a simple demonstration of counter-intuitive flow interaction effects due to bowplane tip vortices on a DOLPHIN vehicle. They examined the effect of differentially deflected bowplanes on the aftward portion of the DOLPHIN Mark I vehicle. A potential flow model consisting of the bowplane tip vortices with appropriate image vortices to represent the cylindrical hull was used. It was suggested that the two equal bowplane tip vortices and a single coalesced hull vortex on the vehicle centreline would generate rolling moments on the keel, rudder, vertical stabilizer, and sternplanes of the vehicle. Specifically, the induced rolling moment was suggested to be opposite in direction and have a strength 1.4 times that generated by the bowplanes. In other words, a roll moment of K generated by the bowplanes would result in a net vehicle roll of $-0.4K$. Considering only the bowplane-sternplane roll interaction, Watt suggested that an interaction level of 30% was present in straight and level flight (for bowplane roll moment of K the induced roll moment on the sternplanes would be $0.3K$).

The analysis of Watt et al. provides some indication of the interaction between the bowplanes and sternplanes. Although the work only considered differentially deflected bowplanes, when the methods are applied to bowplanes deflected in the same direction, the difference in theoretical induced flow on the sternplanes was reduced by only 4.8%. Therefore, this model suggests that the bowplane-sternplane interaction for a DOLPHIN-like vehicle is approximately 25% to 30%. The limitation of the model of Watt et al. for general use includes the condition that bowplanes and sternplanes must be horizontal positioned and on the hull centreline. Furthermore, the model does not account for downwash influencing the trajectory of the trailing vortices; that is, the transverse and vertical position of the bowplane tip vortices does not shift from their inception point.

2.6 FREE SURFACE INFLUENCE

2.6.1 Calm Water Free Surface Considerations for AUVs

In calm water, Wadlin et al. (1955) experimentally determined the lift and drag of various plates over a range of angles of incidence. The depths studied ranged from 0.07 to 0.85 chord lengths and the Froude numbers based on chord ranged from 1.1 to 5.2. The Froude number based on chord is defined as

$$Fr_C = \frac{U}{\sqrt{gC}} \quad (35)$$

With a plate of aspect ratio 1.00 at a 12 degree deflection, Wadlin et al. found that the most significant change in lift occurred for depths of 0.5 chord lengths and less. Ventilation of the plate at 12 degrees deflection was not observed for depths greater than 0.07 chord lengths. Wadlin et al. concluded that for depths greater than 0.85 chord lengths, the surface effect is negligible.

2.6.2 Wave Theory

In deep water, waves travelling along a surface in one direction cause cyclical motion in a plane. With a wave travelling in the x -direction, a particle in the water traces a circular path in the x - z plane. When the wavelength, λ , is small compared to the depth of the body of water, the velocity of a particle is given by the following two equations (see Lamb, 1997, or Newman, 1977):

$$u_w(t) = a \sqrt{\frac{2\pi g}{\lambda}} e^{-\frac{2\pi d}{\lambda}} \sin\left(\frac{2\pi x}{\lambda} - \sqrt{\frac{2\pi g}{\lambda}} t\right) \quad (36)$$

$$w_w(t) = -a \sqrt{\frac{2\pi g}{\lambda}} e^{-\frac{2\pi d}{\lambda}} \cos\left(\frac{2\pi x}{\lambda} - \sqrt{\frac{2\pi g}{\lambda}} t\right) \quad (37)$$

where a is the wave amplitude, d is the depth from the calm water surface, λ is the wavelength, and x is the position in the x -direction. Thus particles trace out circles with a constant speed of

$$U_w = a \sqrt{\frac{2\pi g}{\lambda}} e^{-\frac{2\pi d}{\lambda}} \quad (38)$$

Clearly, the wave influence diminishes with depth. The case where the wavelength was not small compared to the depth of the body of water was not considered for this thesis; however, further information regarding wave behavior in this regime can be found in Lamb (1997).

2.6.3 Sea State and Wave Spectra

The random, irregular wave pattern that can be found in open water is described using statistically derived spectra. The forms of the spectra depend on the seaway being modelled but in general, the wave energy density is determined as a function of wave frequency. Following Field (2000), this

thesis uses the Bretschneider spectrum which can be considered an average spectrum suitable for open sea areas (Journée, 2001). The Bretschneider spectrum is described by

$$S_{\zeta}(\omega) = \frac{172.8 \cdot H_{1/3}^2}{T_1^4 \cdot \omega^5} e^{-\frac{691.2}{T_1^4 \cdot \omega^4}} \quad (39)$$

where S_{ζ} is the energy density in m^2/s , ω is the wave frequency in s^{-1} , $H_{1/3}$ is the significant wave height in m , and T_1 is the average wave period, in s . The relation of sea state to $H_{1/3}$ and T_1 is given in Table 2-5

Table 2-5 Open ocean sea state occurrences of North Atlantic and North Pacific

Sea State Number	$H_{1/3}$		North Atlantic		North Pacific	
	Mean	Range	T_1	Probability	T_1	Probability
0-1	0.05 m	0-0.1 m	-	0 %	-	0%
2	0.3	0.1-0.5	7.5 s	7.2	7.5	4.1
3	0.88	0.5-1.25	7.5	22.4	7.5	16.9
4	1.88	1.25-2.5	8.8	28.7	8.8	27.8
5	3.25	2.5-4	9.7	15.5	9.7	23.5
6	5.0	4-6	12.4	18.7	13.8	16.3
7	7.5	6-9	15.0	6.1	15.8	9.1
8	11.5	9-14	16.4	1.2	18.0	2.2

By the principle of superposition, waves of differing amplitude and frequency (wavelength) are combined to form the overall sea state. The response of a vehicle in irregular waves can similarly be described by the summation of the responses to each of the distinct wave frequencies (Journée, 2001). In other words, to find the general dynamic response of a vessel in irregular seas of a known spectrum, it is sufficient to determine the response at distinct wave frequencies and to scale those responses by the wave spectrum.

2.6.4 Wave Considerations for AUVs

Little work has been conducted on the study of the free surface influence to control surface operation on AUVs although there is a demonstrated need for active wave disturbance compensation. An and Smith (1998) have shown that even at depths of up to three hull diameters, depth following abilities are significantly compromised at sea state 2 and above. Not surprisingly, An and Smith stress the importance of plane and controller design for near-surface depth keeping performance. The influence of waves on control surfaces is often neglected as the magnitudes of wave induced forces on the hull are much greater (see for example (Peterson et al., 1994) and (Ananthakrishnan and Zhang, 1998)).

In examining the effect of wave-induced motion on AUV imaging sensor performance, Peterson et al. (1994) show that active control of bowplanes could eliminate the majority of unwanted pitch

and heave motions. In a related topic, Riedel and Healey (1998) have demonstrated that on-board sensors on a typical low-cost AUV can provide an estimate of wave induced disturbances. Furthermore, through simulation, they demonstrated that it was possible to compensate for the disturbances from shallow water waves resulting in an improvement in position and heading station keeping.

For his work on the DOLPHIN AUV, Field (2000) estimated wave-induced forces using Morrison's equation for the hull and using wave trajectory approximations for the planes. In particular, the wave disturbance force on the planes was computed by augmenting the plane incident flow angle given in equation (15) by a wave angle, α_w , as defined by

$$\alpha_w = -\frac{w_w}{U} \quad (40)$$

where w_w is the vertical component of the wave orbital velocity and U is the vehicle forward speed. Components of the wave orbital velocity in the axial direction of the vehicle (x -direction) were ignored as they were small in comparison to the forward speed of the vehicle. Note that for an AUV capable of large depth excursions or pitch angles, this approximation is no longer valid and the complete wave orbital trajectory must be considered.

The complete angle of incidence on a plane, by incorporating the wave disturbance effects of equation (40) to equation (15), is

$$\alpha = \delta + \sin^{-1} \frac{w - w_w - qx_{plane}}{U} + \alpha_{local} \cong \delta + \frac{w - w_w - qx_{plane}}{U} + \alpha_{local} \quad (41)$$

The local variation in angle of incidence due to the hull, α_{local} , given by equation (26) for example, is computed with the wave induced velocity included. That is, the trim angle, localized at the bowplanes, is determined from

$$\theta_{local} = \sin^{-1} \frac{w - w_w - qx_{plane}}{U} \cong \frac{w - w_w - qx_{plane}}{U} \quad (42)$$

The resulting force is computed using the formulation presented above beginning with equation (13).

3

CONTROL SURFACE HYDRODYNAMICS - EXPERIMENTS

*Measurements are not to provide numbers but insight.
- Ingrid Bucher*

In the design of an underwater vehicle, manoeuvrability and controllability must be examined in advance, preferably with the use of a mathematical model (Kim, 2002). The validity of the model, as well as the findings it yields, depends on how accurately the operational characteristics of the vehicle are represented. There are several techniques commonly employed in determining mathematical models for AUVs, including analytical, computational, system identification, and empirical methods (see Chapter 4 for further information). Each of these techniques has specific benefits and shortcomings, but empirical and semi-empirical methods still form the basis for most modelling of AUVs.

Empirical techniques rely on experiments to characterize vehicle performance. Experiments are most often conducted with a scale model in a research facility but at times may use a full-scale vehicle in open water (Hopkin and den Hertog, 1993). Towing tank tests with captive models or with planar-motion-mechanisms are commonly employed to determine submarine performance characteristics (Feldman, 1995). In some advanced testing facilities, a model can also be made to follow a prescribed path in three dimensions (Perron et al., 1998). Alternatively, with proper treatment of scaling effects, wind tunnels can be used (Barlow et al., 1998, Huggins and Packwood, 1995, and Watt et al., 1993); the benefit of working in the air environment is a ten-fold or more increase in the rate of testing.

This chapter summarizes experiments examining control surface performance that were conducted for this thesis. It begins with a discussion of the equipment and facilities used followed by experimental findings regarding the performance of isolated planes, bowplanes, and sternplanes. The chapter concludes with results from experiments examining the interaction of the free surface (waves) with the control surfaces. In Chapter 4, these experiment results are used to develop the mathematical models describing underwater vehicle performance.

3.1 MODEL AND FACILITIES

3.1.1 Similarity and Scaling

Dimensional analysis provides procedural techniques in which to simplify a physical process in terms of non-dimensional groups. Similarity, a key result of dimensional analysis, guarantees that if all the relevant variables for a process are included, there is a set of dimensionless groups—less than or equal in number to the number of original variables—that completely describes the process. Additionally, similarity states that the number of dimensionless groups is less than or equal to the number of original variables. Further information regarding dimensional analysis and similarity can be found in (White, 1986), (Potter and Wiggert, 1997), or (Avallone and Baumeister, 1996), for example.

In reference to experiments with underwater vehicles, similarity means that model results can be scaled to the actual vehicle as long as the dimensionless groups have been maintained. There are several key dimensionless groups that are used including the Reynolds number, the Froude number, and the force coefficients; a simplified list is summarized in Table 3-1, for a complete list the reader is referred to (Feldman, 1979). The Reynolds number and Froude number are independent parameters controlled by adjusting the model speed in the fluid during testing. The force (and moment) coefficients are dependent parameters measured through the course of the experiments.

Table 3-1 Key Dimensionless Parameters

Parameter	Symbol	Definition	Notes
Reynolds number	Re	$Re = \frac{Ul}{\nu}$	Always relevant
Froude number	Fr	$Fr = \frac{U}{\sqrt{gl}}$	Relevant near the free surface
Isolated control surface force	C_L	$C_L = \frac{L}{\frac{1}{2}\rho U^2 S}$	Force non-dimensionalized by plane area
Control surface (on body) force	Z	$Z = \frac{Z}{\frac{1}{2}\rho U^2 l^2}$	Force non-dimensionalized by body length squared

For model testing in the wind tunnel, the Reynolds number was used as the main scaling parameter. Due to the increased kinematic viscosity of air compared to water, compounded by the reduced scale of the model, it was not possible to match Reynolds number between the model and full-scale vehicle. As such, additional precautions were required to account for the Reynolds number discrepancy (as detailed in Section 3.1.2 on page 47). In the tow tank, ideally both Froude number and Reynolds number similarity should be maintained; however, without complete control of fluid properties (that is, ν), simultaneous Froude and Reynolds number similarity is not possible. As flows near the free surface are dominated by Froude number (White, 1986), Froude number similarity is generally used for vessels with shallow depth in the tow tank. For deeply submerged submarines and for control surfaces on near-surface vehicles, Reynolds number is preferred as the governing parameter (Barlow et al., 1999). For this thesis, testing was conducted

over a range of speeds up to the facility maximum; at maximum speed, Froude number scaling was achieved and coincided with a three-fold increase in Reynolds number compared to the wind tunnel. The same Reynolds number corrections as in the wind tunnel were applied for the tow tank.

3.1.2 Scale Model

A 1/4-scale model of the ISE Mark II DOLPHIN was constructed for both wind tunnel and towing tank testing. In the original project description, ISE was responsible for the construction of a water-tight, self-propelled model complete with mounts and instrumentation (Seto, 1997). ISE was unable to fulfill this obligation and model development was added to the scope of this thesis research. The model development represented a significant portion of the experimental work; over 20 persons (from both the University and ISE) were involved in the process and, by rough estimates, over 2500 person-hours were invested. Details regarding the general model design, the control surfaces geometry and actuation, scaling considerations, and mounting hardware are discussed below.

Model Design

The philosophy adopted for the model design was to maintain a high level of flexibility with a simple, cost-effective construction. The scale of one-to-four was chosen partly because several components from an existing 1/4-scale Mark I DOLPHIN model were available, thus reducing fabrication time and costs. The hull was assembled from five main segments with the addition of a keel and mast, as illustrated in Figure 3-1. The nose and tail from the Mark I model were used and the remaining components were designed and fabricated specifically for this work. Hull segments were machined from aluminum tube, the mast was constructed from stainless steel tube and bar, and the fairings and keel were constructed from syntactic foam. All joints were fitting with o-rings or seals such that the hull was water tight. Based on the one-quarter scale, the model length was approximately 2.13 m and the hull diameter was 0.248 m. Complete engineering drawings for the scale model are provided in Appendix B.1.

For a vehicle with control surfaces located at the tail, Barlow et al. (1999) recommend including in the model a propeller that is operated at the correct advance coefficient. In wind tunnel tests of submarine propulsion, Watt and Fournier (1995) found that it was unnecessary to model propulsion while measuring the overall hydrodynamic forces; however, they suggest that propulsion should be modelled in the study of tailplanes. Unfortunately, through space, cost, and time constraints, it was not possible to incorporate a propulsion system to the DOLPHIN 1/4-scale model. The implications of the absence of propulsion on the current model are believed to be a local reduction in the flow velocity and reduced resistance to boundary layer separation at the tail. These factors would tend to cause deterioration in sternplane performance on the model. The concerns are partially addressed by the model design in that the movable (measuring) portions of the sternplanes were located outside of the maximum hull diameter (discussed further on page 47 in regards to Reynolds number considerations). As a final note, although Barlow et al. (1999) advise against omitting propulsion on the model, Barlow (1998) uses a static model without propulsion for wind tunnel tests of a submarine with sternplanes located completely within the maximum hull diameter.

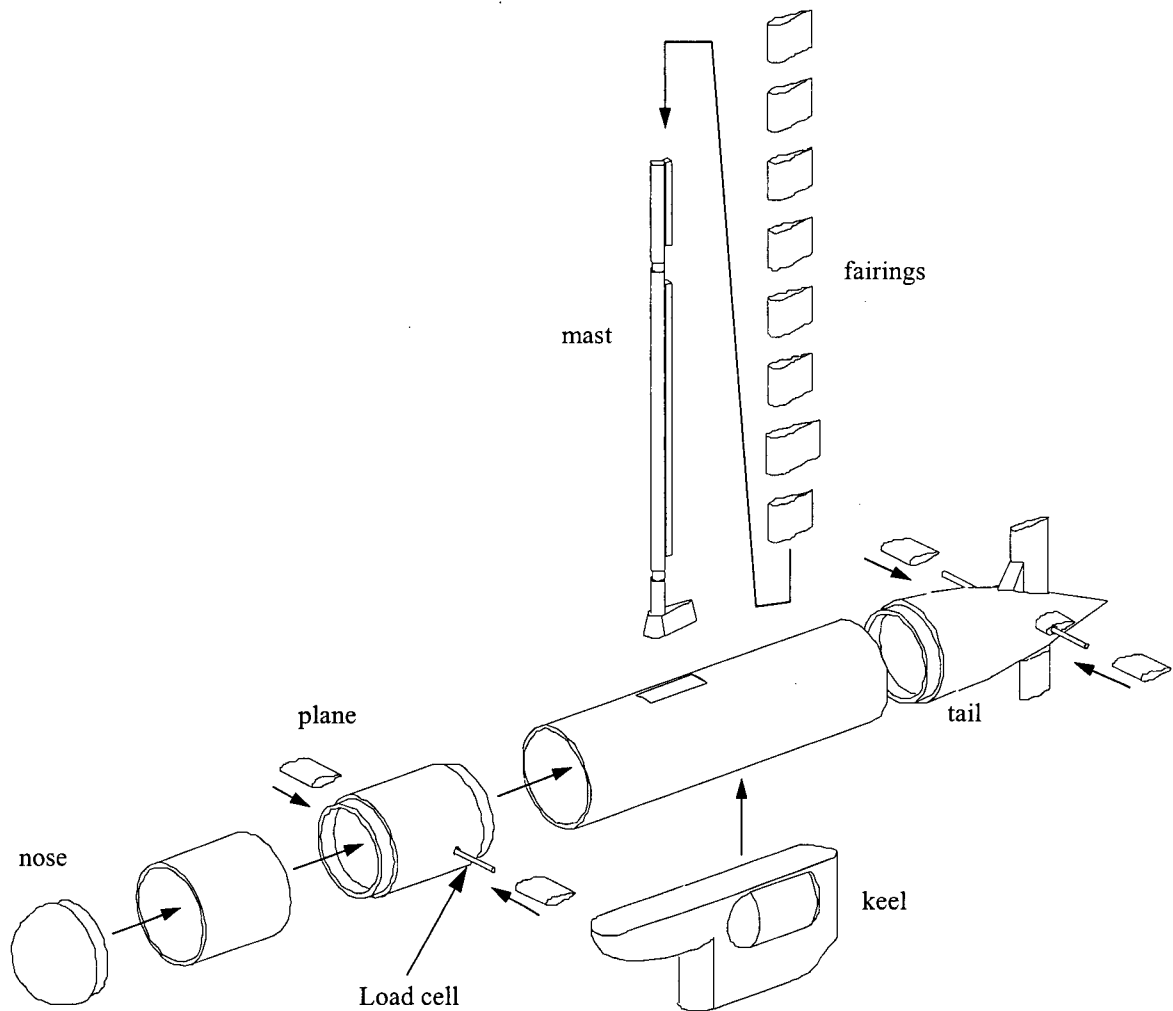


Figure 3-1 Quarter-scale model exploded view

Control Surfaces

Control surfaces of various geometries were constructed from composite materials. Basic plane forms were hot-wire cut from high-density foam insulation using two-dimensional templates. The foam core was coated in layers of carbon fibre and room temperature cure two-part epoxy. Planes were painted and sanded to a smooth finish.

The planes were symmetrical, NACA 0025 sections with no span-wise twist and aspect ratios ranging from about 2.3 to 4.1. The *short* planes were also used with endplates similar to those on the full size vehicle. The endplate height, h , was 3.95 cm (0.35 times the exposed span of the *short* planes) and the shape approximated a NACA 0045 foil. The endplate thickness was approximately 1.6 mm (1.86 chord lengths). The complete range of plane geometries constructed is detailed in Table 3-2.

The planes were attached to the vehicle through load cells (discussed further below) that passed along the quarter chord location. A 0.75" diameter span-wise hole drilled in the foam core was

used to fasten the planes to a sleeve through an interference fit (see Figure 3-2). The sleeve was in turn fastened to the load cell with a sliding fit secured with a cap screw.

Table 3-2 Plane Geometries

Plane Name	Exposed Span ^a	Mean Chord	Aspect Ratio	Exposed Area ^b	Taper Ratio	1/4 chord sweep [deg.]
Short	0.0530	0.0399	2.66	0.00211	1.0	0
Std Bowplane	0.0613	0.0399	3.07	0.00245	1.0	0
Long	0.0810	0.0399	4.06	0.00323	1.0	0
Std Sternplane	0.0483	0.0399	2.42	0.00193	1.0	0
Swept	0.0613	0.0488	2.51	0.00299	0.691	11.4
Large Swept	0.0613	0.0539	2.27	0.00333	0.588	18.7
Large	0.0702	0.0601	2.34	0.00422	1.0	0

a. exposed span and mean chord are non-dimensionalized by vehicle length; exposed span = $b/2$

b. exposed plane area has been non-dimensionalized by vehicle length squared

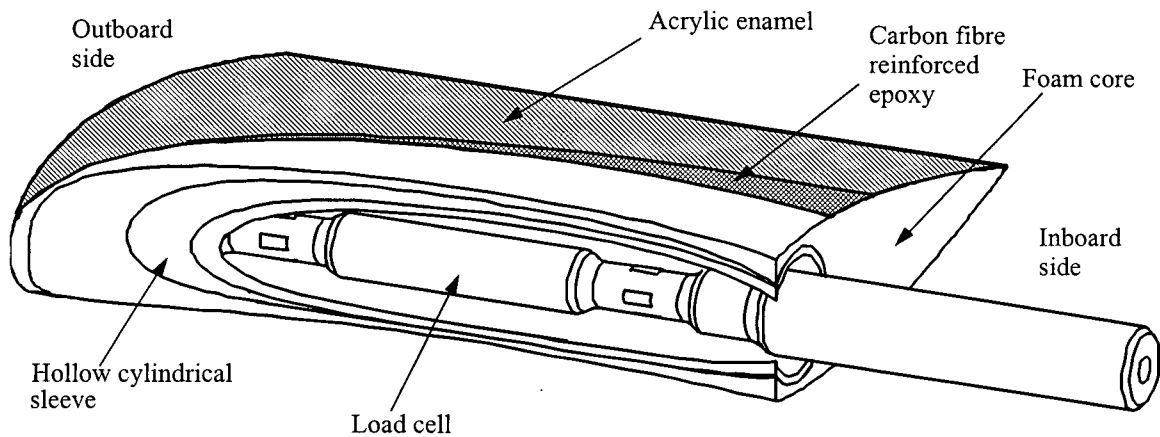


Figure 3-2 Cut-away view of plane showing load cell

In total, fifty different combinations of bowplane and sternplane mounting position were possible with the model; Figure 3-3 shows the various plane positions superimposed on the DOLPHIN body. Details regarding each of the plane locations are provided in Table 3-3. For reference, the vehicle centre of gravity is located at $x/l = 0.489$, $y/l = 0.000$, and $z/l = 0.022$ as measured from the nose and non-dimensionalized by the vehicle length, l .

Control Surface Actuation

Each bowplane and sternplane was outfitted with a stepper motor actuator to control deflection. The bowplanes were connected directly to the motors while the sternplanes were connected through a lead screw. The corresponding bowplane deflection step size was 0.9 degrees and the sternplane step-size was better than 0.05 degrees.

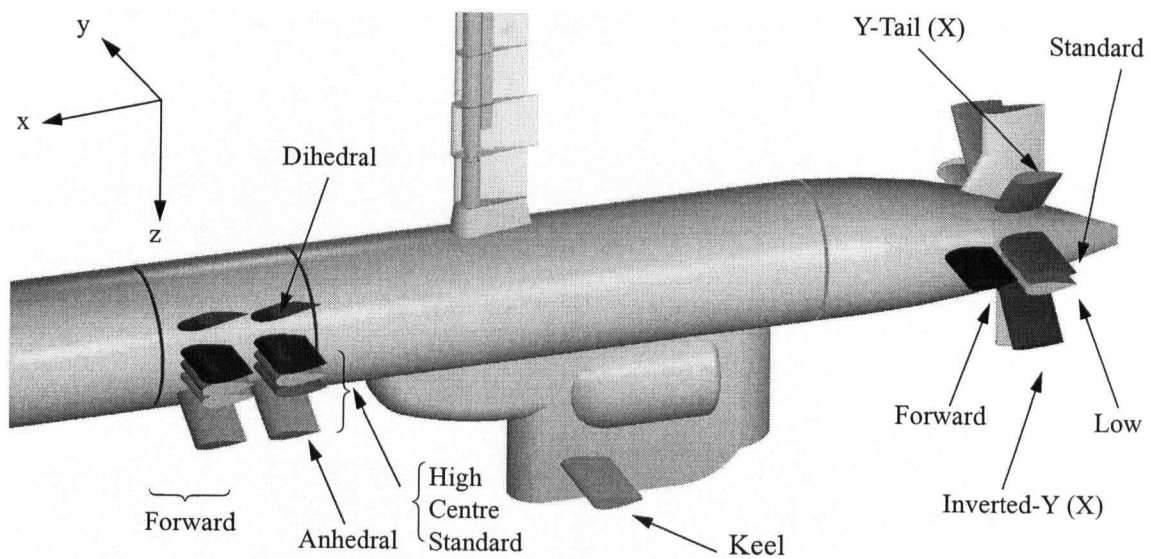


Figure 3-3 Plane Mounting Locations

Table 3-3 Plane positions

Bowplane Location	1/4 Chord Position (non-dimensional)		Dihedral Angle ^c
	x ^a	z ^b	
Standard	0.261	0.010	0 degrees
Centreline	0.261	0	0
High	0.261	-0.010	0
Dihedral	0.261	0	30
Anhedral	0.261	0	-30
Forward Standard	0.216	0.010	0
Forward Centreline	0.216	0	0
Forward High	0.216	-0.010	0
Forward Dihedral	0.216	0	30
Forward Anhedral	0.216	0	-30
Keel	0.557	0.225	0
Sternplane Location	x	z	Dihedral Angle
Standard	0.906	-0.002	0
Forward	0.848	-0.002	0
Low	0.906	0.022	0
Y-tail	0.882	0.008	45
Inverted-Y	0.882	0.008	-45

a. measured from the 1/4 chord line to the nose and non-dimensionalized by the vehicle length

b. determined by the distance to the hull centreline when the 1/4 chord line is extended to the x-z plane

c. measured in the positive roll direction for port planes and negative roll direction for starboard planes

A basic three-axis stepper motor controller was modified and software was written to allow control of the motors via a personal computer. Additional circuitry was constructed to increase the power output of the motors and hence the torque to the control surfaces. The software permitted the control of the motors in a single step (jog) mode or in a pre-programmed sequence. The pre-programmed deflection sequence was used extensively in the wind tunnel due to the absence of restrictions on measurement duration. In particular, for the majority of wind tunnel testing the bowplanes were deflected in 3.6 degree increments from 0 degrees to +28.8 degrees, then to -28.8 degrees, and back to 0 degrees. In the towing tank, the planes were held fixed for each trial due to the limited measurement duration.

Reynolds Number Considerations

The Reynolds number is the governing parameter for the boundary layer on the vehicle and control surfaces. Unless otherwise noted, the Reynolds number based on vehicle length has been used

$$\text{Re} = \frac{Ul}{\nu} \quad (43)$$

In regions with a strong adverse pressure gradient, such as near the tail and trailing edges, flow separation characteristics may be strongly dependent on Reynolds number. In particular, a turbulent boundary layer (associated with large Reynolds number) is known to exhibit greater resistance to separation than a laminar boundary layer (associated with lower Reynolds numbers). Ideally, in wind tunnel and tow tank tests the model would be scaled matching the Reynolds number to the full scale vehicle thus ensuring similar flow characteristics. Using a 1/4 scale model, the maximum Reynolds numbers based on length in the wind tunnel and tow tank were 2.5 million and 7.5 million respectively; the full scale vehicle operates in the Reynolds number range of 30 to 50 million. In terms of control surface performance, separation at lower angles of attack, and consequently lower maximum control forces, could be expected from the reduced Reynolds numbers in the model tests. However, these concerns were mitigated by the positioning of the planes on the model and the use of boundary layer stimulators.

For the experimental work, the model was designed such that forces on the sternplanes were measured on the movable portion of the planes (which extended from radially from roughly the maximum hull diameter outward as shown in Figure 3-4). The influence on the experimental data of premature flow separation behind the tail due to the lower Reynolds numbers was therefore minimized. Hull flow separation near the bowplanes was not of concern; it was expected that the hull boundary layer thickness near the bowplanes would change slightly with Reynolds number but not enough to significantly influence the results.

In order to minimize the Reynolds number dependence of boundary layer transition, boundary layer trips of a style recommended by Torres et al. (1999) were installed in various locations on the model. The function of the trips was to cause a transition from laminar to turbulent flow in the boundary layer by placing an obstruction in the flow. As noted above, the (artificially tripped) turbulent boundary layer would be more resistant to flow separation than the otherwise laminar boundary layer. The regions in which boundary layer trips were located are identified in Figure 3-5. In particular, the trips were positioned on the nose, mast fairings, keel (two positions), rudder, stabilizer, and on all of the control surfaces. Detailed information regarding boundary

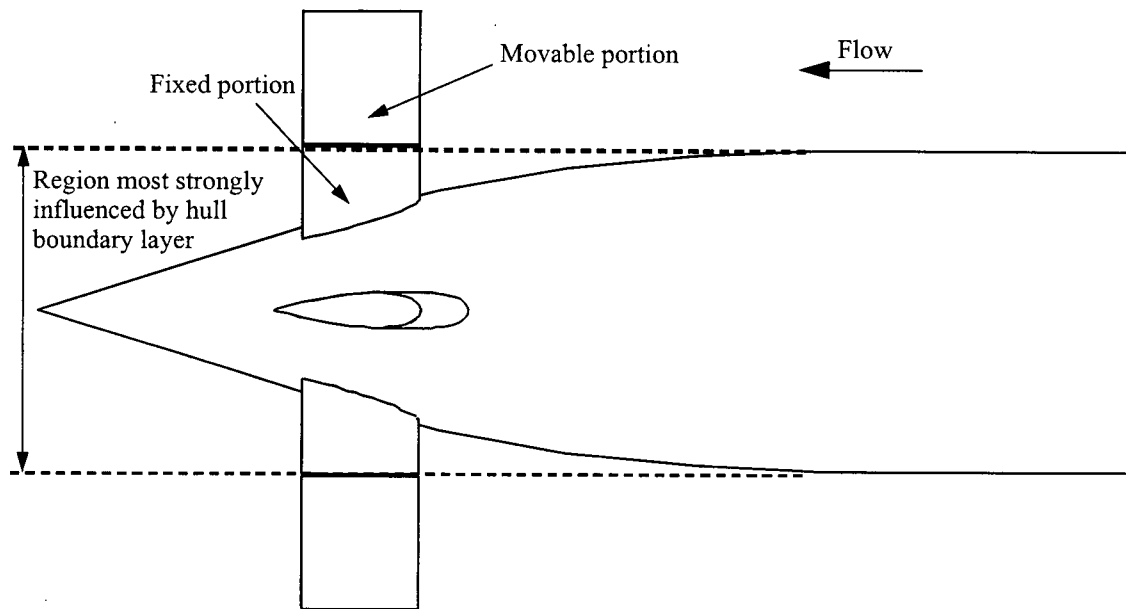


Figure 3-4 Region of tail boundary layer influence

layer transition on wings can be found in (Eppler, 1990, and Eppler, 1999); further details regarding the trip design and associated calculations for this thesis can be found in Appendix B.3.

Mounting Hardware

For both wind tunnel and towing tank tests, specially designed mounting hardware was constructed. In the wind tunnel, the model was mounted upside-down by the mast as shown in Figure 3-6. Underneath the wind tunnel, the mast was connected to a mounting beam which was in turn attached to a heavy steel base. Both the mast and the mounting beam were instrumented with strain gauges to allow measurement of body forces. The trim angle of the submarine was changed using a lead screw mechanism connected to the mounting beam. In research conducted by others, yaw was achieved by rotating the model and base using a low-friction pivot mechanism connected to the base (not shown in the figure). In the towing tank, the same basic mounting hardware was used except in this case the model was mounted right side-up and the steel base was replaced by a height adjustable frame (see Figure 3-7). The mounting hardware was manually rotated and re-fastened in order to adjust the yaw angle in the tow tank.

3.1.3 Load Cells and Signal Conditioning

Each plane was outfitted with a load cell located along the 1/4 chord line. The load cells were mounted to the body as shown in Figure 3-8 and key features are identified in Figure 3-9. In particular, eight strain gauges were affixed to hollow stainless steel cylindrical beams in two longitudinal positions. The diameter was reduced in the regions where the strain gauges were applied in order to locally increase the strain without compromising the overall stiffness. Each half-bridge circuit measured bending moment—two corresponding to lift and two corresponding to drag—and in post-processing the moments were used to estimate lift and drag.

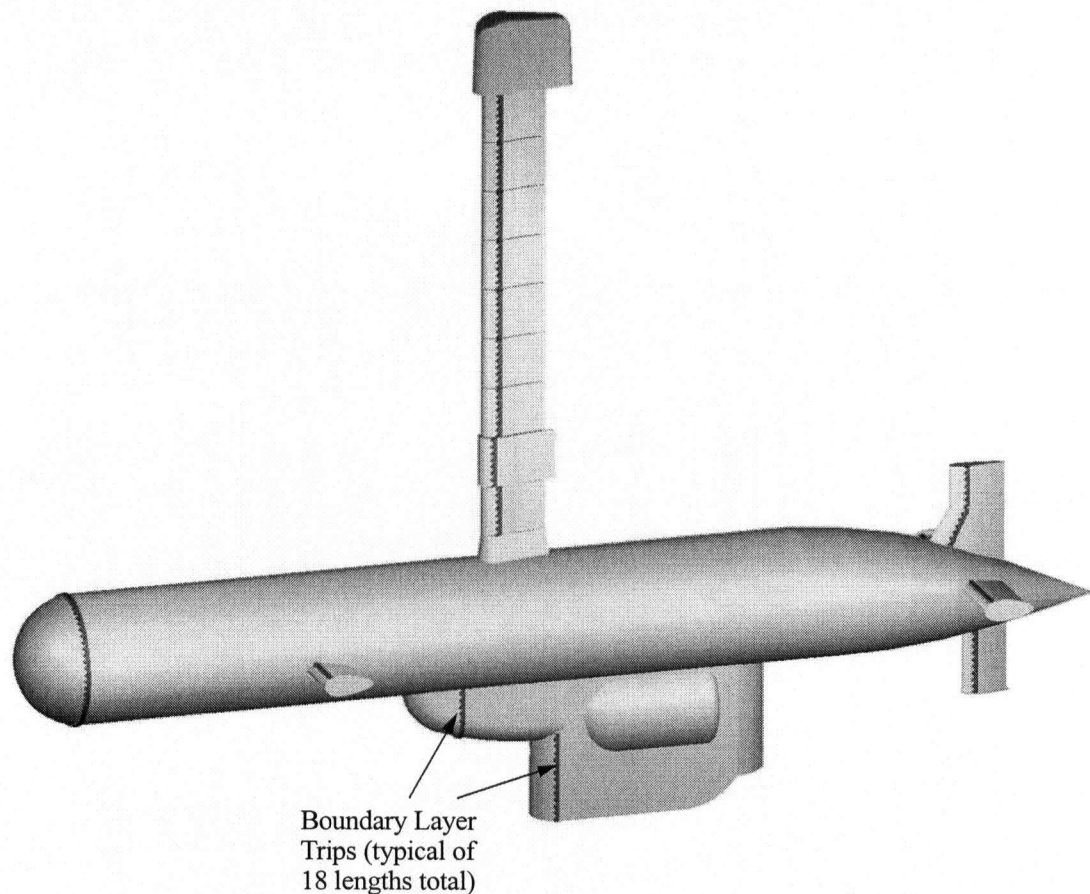


Figure 3-5 Boundary Layer Trip Mounting Locations

Considering either lift or drag, with moments on the inboard and outboard gauges of K_i and K_o respectively, and a longitudinal separation distance of the gauges of Δy , the corresponding force is

$$Z = \frac{K_i - K_o}{\Delta y} \quad (44)$$

This represents a shear-beam style arrangement and is insensitive to the point of force application. The span-wise center of pressure—that is, the location along the plane span at which the force, Z , could be assumed to act—was also computed from the moment measurements by

$$y_{cp} = y_i + \frac{K_i}{K_i - K_o} \Delta y \quad (45)$$

where y_i is the span-wise position of the inboard gauges. Further information regarding the design and calibration of the load cells can be found in Appendix B.2.

The task of measuring, conditioning, and recording the load cell voltage signals was handled by an *IOTech* PC-based data acquisition system. A 12-bit *DAQBoard 100/A* A/D card was used with ten

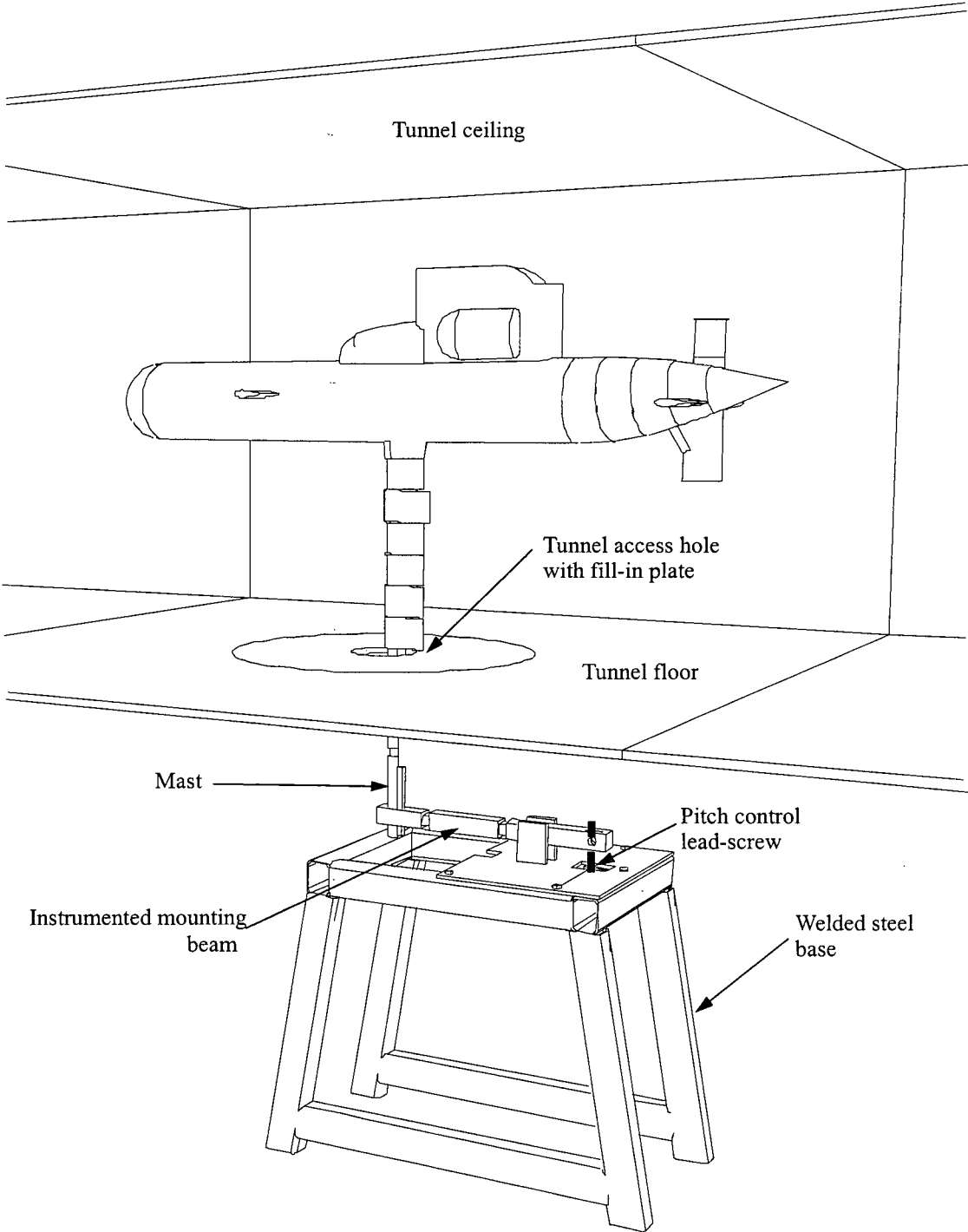


Figure 3-6 Wind Tunnel Mount Showing Beam and Base Plate

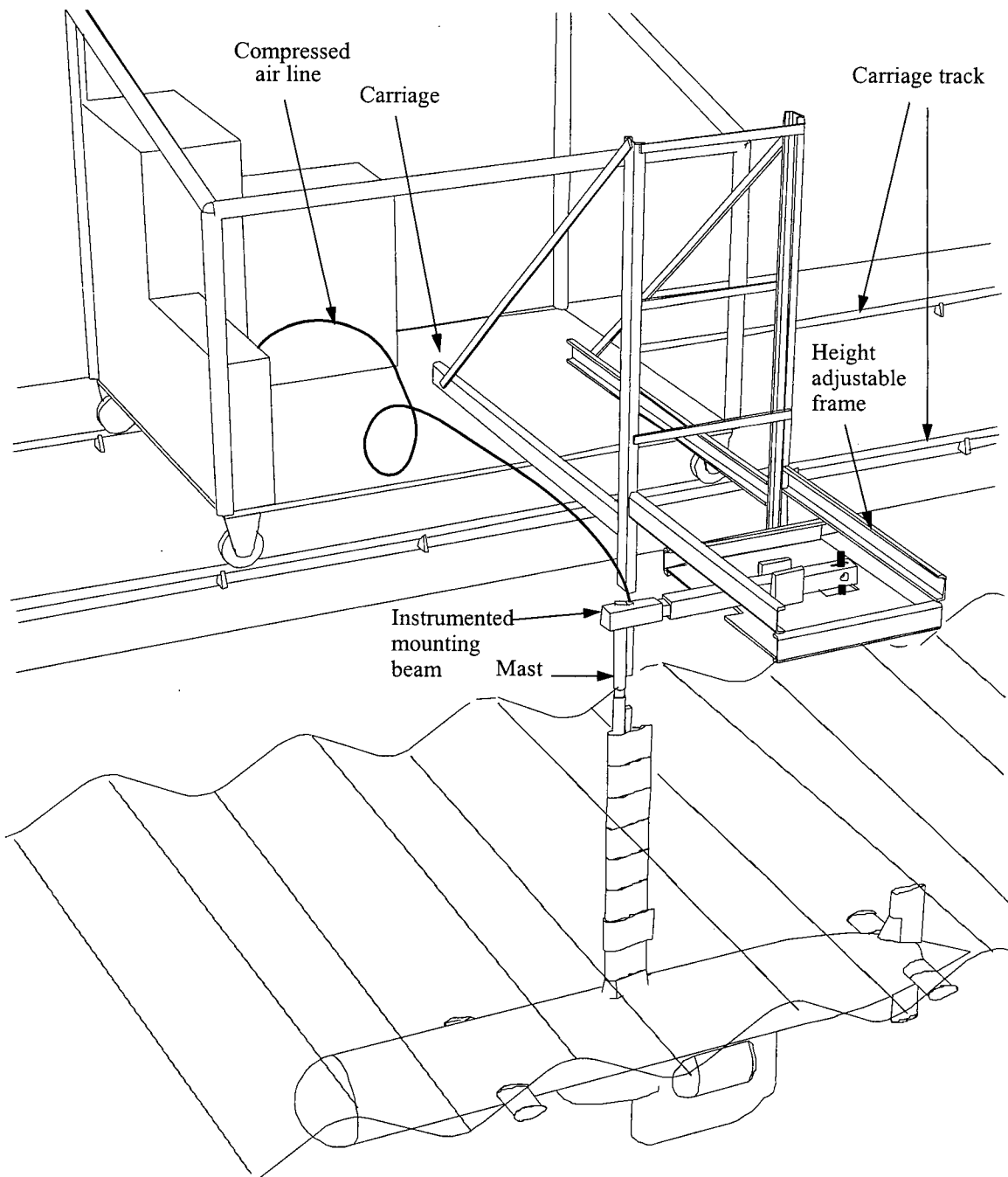


Figure 3-7 Towing tank mount showing height adjustable structure

DBK16 strain gauge signal conditioning cards, two *DBK 8* general purpose voltage cards, and one *DBK32A* auxiliary power card. Eight of the *DBK16* cards, one *DBK8*, and the *DBK32A* were mounted in a specially designed rack and placed inside the model hull. The signal conditioning hardware was located inside the model to minimize the length of cable carrying low-level voltage signals from the load cells. As low-level signals are much more susceptible to noise, the signal-to-noise characteristics of the measurements was greatly improved in this manner. Special precau-

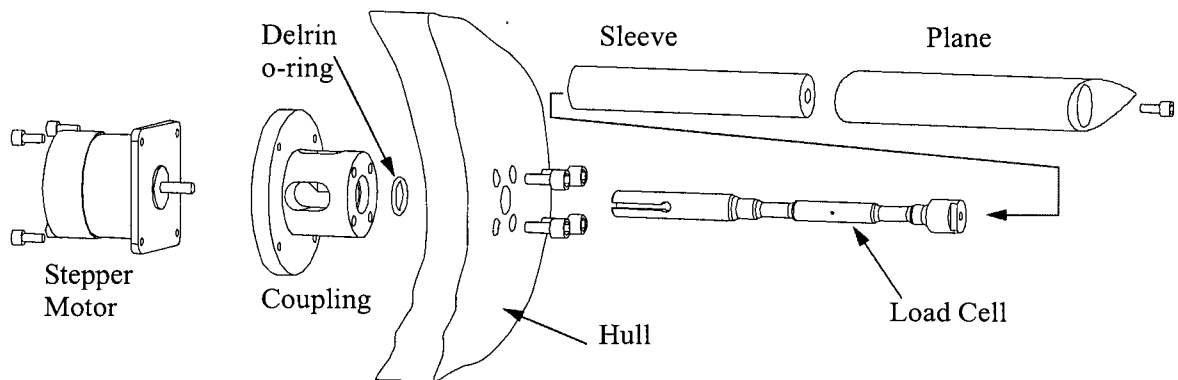


Figure 3-8 Load cell mounting to hull (the coupling and motor are specific to bowplanes)

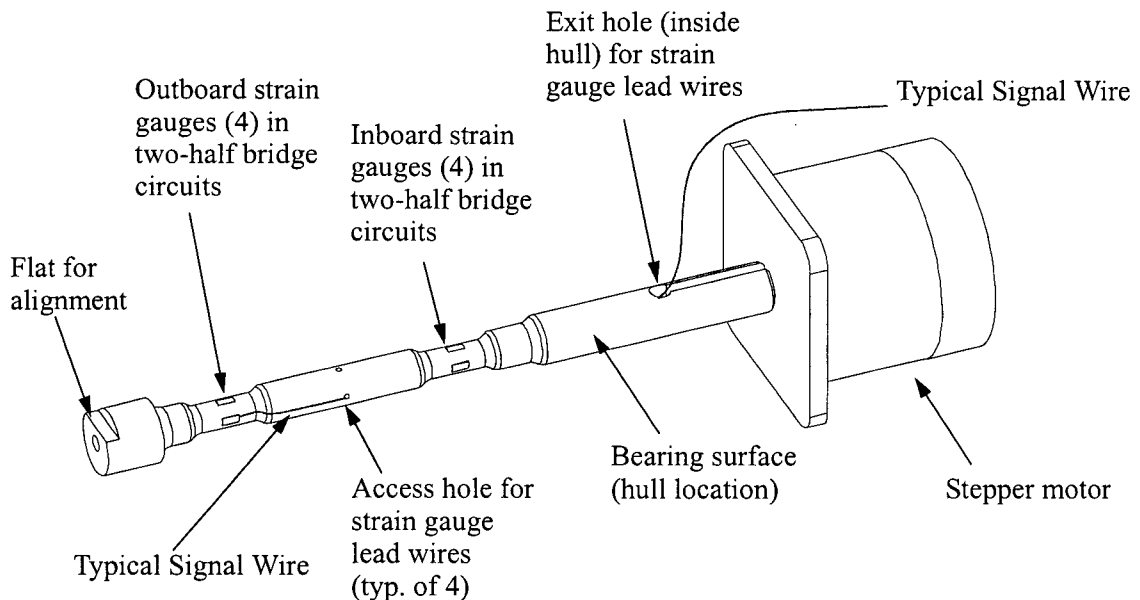


Figure 3-9 Load cell arrangement for bowplane showing direct connection to stepper motor

tions were taken with the model to ensure the electronics housed inside the hull were not damaged by water during tow tank tests: o-rings and other seals were used on joints; numerous small cracks in the hull introduced during manufacture were sealed; and the hull was pressurized to approximately 70 kPa (see Figure 3-7) to both serve as a leak indicator and to prevent inflow of water in the event of a leak. The remaining two *DBK16* and the *DBK8* cards were used for body force measurements and were located in close proximity to the personal computer.

Under static calibration, the load cells demonstrated exceptional overall performance. All load cells were highly linear and showed minimal hysteresis; the typical correlation coefficients were 0.99999 and the largest residuals from a linear best-fit were approximately 0.2% of full scale. Cross-talk between the lift and drag axes on the order of 6.5% was noted with similar linearity in

the coupling as with the primary measurement axis. A 2x2 calibration matrix was used to convert the measured voltages to lift and drag forces while at the same time removing the coupling effects. Overall, the load cell accuracy was approximately 0.5% of full scale when including all sources of error.

3.1.4 Data Collection Protocol

Raw voltage data was recorded in the ASCII text file format during the experiments and was later post-processed to determine hydrodynamic quantities. Initial readings of quiescent loads (zeros) were taken in each case followed by the measurement of interest. The data collection rate for both the wind tunnel and towing tank tests was 50 samples per second and measurement duration varied by experiment.

Specialized data analysis software written in *Visual Basic* was used to extract the relevant data from the ascii text files. In particular, the software coordinated data windowing with measurement initiation and termination, as well as changes in control surface deflection (as outlined on page 45), in order to avoid transient flow effects. Over a minimum window of 15 seconds (750 samples) the analysis software computed the mean voltage for each strain gauge bridge—with quiescent loads removed—and the standard deviation in the measurements.

3.1.5 Testing Facilities

Tests were conducted in two different wind tunnels and a towing tank, all located on the campus of the University of British Columbia. The Boundary Layer Wind Tunnel (BLWT) was used for the majority of tests with the scale model. A smaller, faster wind tunnel (the Parkinson Wind Tunnel) was used for high Reynolds number tests on an isolated control surface. Finally, the BC Research Inc. towing tank was used with the fully instrumented model to study wave and free surface effects. Table 3-4 summarizes the basic specifications for each of the test facilities.

Table 3-4 Test facility specifications

Specification	Boundary Layer Wind Tunnel	Parkinson Wind Tunnel	Towing Tank
Description	Open-circuit wind tunnel with upstream fan	Closed-circuit wind tunnel	Rectangular freshwater basin with cantilever carriage and wavemaker
Dimensions	2.4 x 1.6 m (w x h)	0.91 x 0.69 m (w x h)	3.7 x 2.4 x 60 m (w x h x l)
Maximum Speed	20 m/s	35 m/s	3.5 m/s
Turbulence Intensity	<2%	unknown	negligible

3.2 PLANE PERFORMANCE

In addition to isolated control surfaces, the performance of body-mounted planes was examined using various techniques over a range of orientations. Namely, oil film and yarn tuft visualization were employed along with direct force measurement for different yaw and trim angles; the majority of tests were conducted with yaw and trim angles of zero (straight and level flight) as that represents the most common operating condition.

3.2.1 Isolated Plane

The performance of an isolated control surface was examined in the Parkinson wind tunnel with a 0.916 scale plane fitted with a load cell (as described in Section 3.1.3). The Parkinson tunnel and larger plane were used to achieve higher Reynolds numbers than those possible with the 1/4-scale model in the BLWT. The plane was mounted near the wind tunnel floor with a gap of approximately 5 mm. Tests were conducted at 13.6 m/s for deflections from -32.4 to $+32.4$ degrees in 1.8 degree increments. The corresponding Reynolds number based on chord was 280 000; at this scale, the equivalent Reynolds number based on vehicle length is 7 million. The resulting force to deflection curve is shown in Figure 3-10.

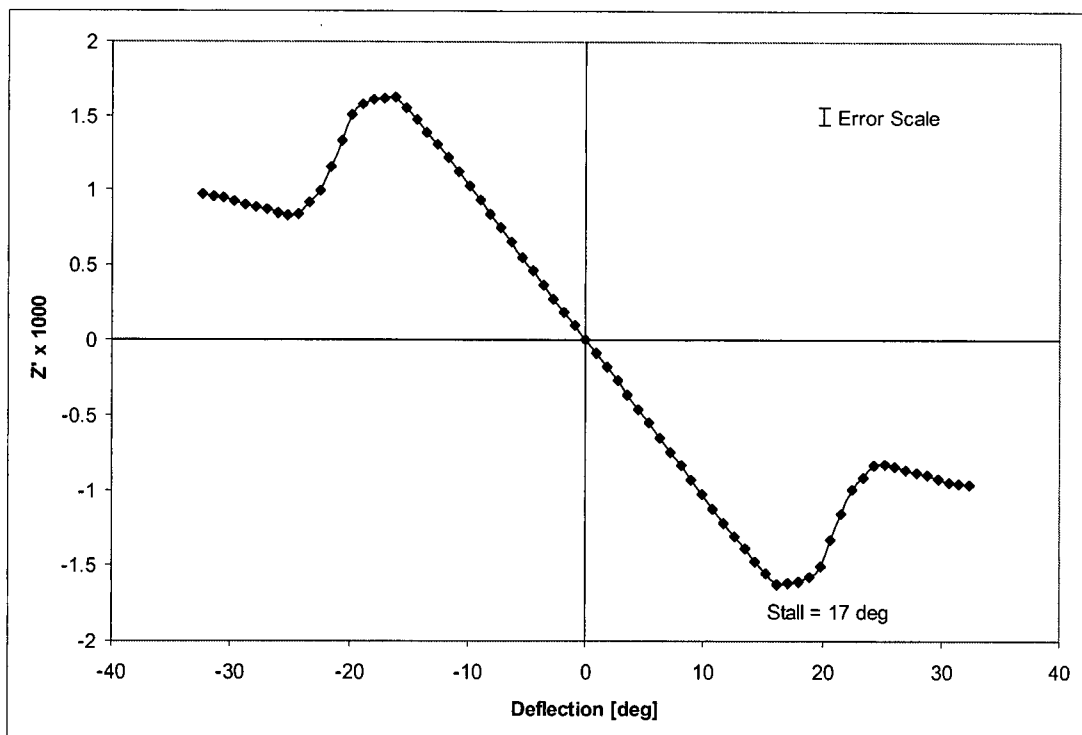


Figure 3-10 Isolated standard geometry plane 0.916 scale, $Re_c = 280\ 000$ (equivalent $Re_L = 7$ million)

The force, Z' , has been non-dimensionalized according to Section 2.1. Namely,

$$Z' = \frac{Z}{\frac{1}{2}\rho U^2 l^2} \quad (46)$$

where ρ is the air density, U is the freestream velocity, and l is the vehicle length.

The stall angle was approximately 17 degrees but is expected to increase with Reynolds number; a detailed examination of the effect of Reynolds number on stall can be found in Section 4.2.

3.2.2 Straight and Level Flight

In testing the bowplanes in straight and level flight conditions, both oil film visualization and direct force measurement were employed. In the force measurement tests, a configuration similar to the Mark II DOLPHIN was used (the standard configuration) as well as configurations with different bowplane geometry and location on the hull.

Oil Film Visualization

Oil film visualization is a common technique used to identify various surface flow phenomena such as separation, boundary layer transition, and unsteadiness. This technique is well documented (the reader is referred to Barlow et al. 1999, Merzkirch 1987, Maltby and Keating 1962, and RWDI 1989 for further information). In this research, oil film was used to detect regions of flow separation on horizontal control surfaces where the influence of gravity was less significant. Merzkirch (1987) has shown that the distance from the leading edge of an airfoil to the line of separation is changed by not more than 2% due to the presence of an oil sheet making the oil film technique ideal for this application.

A variety of different oil mixtures were tested but best results were obtained with the traditional "China clay" mixture. The exact mixture used consisted of 16 parts kerosene, eight parts kaolin, two parts oleic acid and one part artists' black oil paint. The Kerosene was selected due to the low viscosity and relatively fast evaporation under wind-on conditions. This was important as particulate matter was deposited on the model during a test as the oil evaporated thus allowing sufficient time for photography without concern for movement of the oil streaks.

The oil film technique worked best when the oil mixture was evenly applied to the entire control surface by sponge brush. The wind tunnel was then quickly brought to speed to minimize premature drying of the oil mixture. After approximately one minute at speed, the wind was turned off and photos were taken from directly above and below the planes.

A sample image from the oil film technique is provided in Figure 3-11 for the suction side of a bowplane at 16 degrees deflection. The leading edge is at the top of the figure and a boundary layer trip is visible. Arrows have been added to indicate the flow direction in the attached region and the separation line is indicated with a dashed black line. Separation is delayed for the outboard region of the plane, likely due to momentum introduced through leakage from the pressure side of the plane.

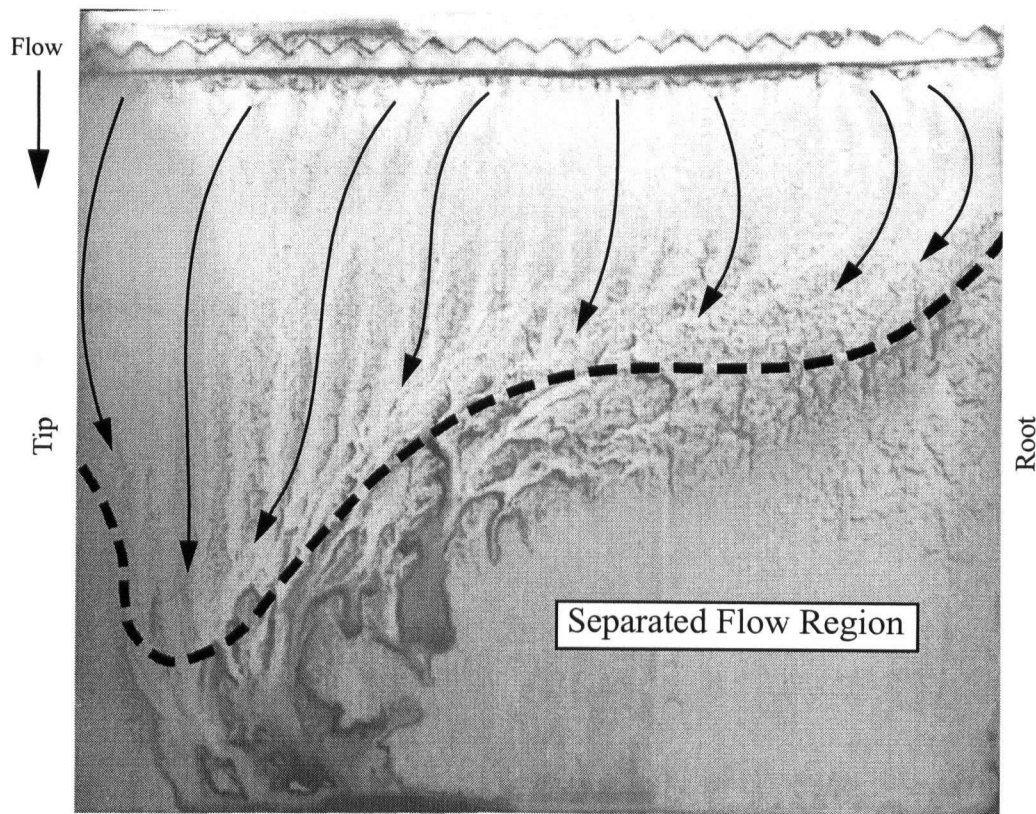


Figure 3-11 Oil film sample image - suction side of port bowplane at +16 degrees deflection. The separation line is shown in dashed black and arrows indicate flow direction in attached region.

A series of images such as Figure 3-11 were used to form a composite image to illustrate the trends in separation. Figure 3-12 shows the composite image for the standard bowplanes in straight and level flight. The approximate size of the separated flow for moderate angles is roughly in agreement with wind tunnel tests of the NACA 0025 airfoil by NACA [Bullivant 1941]. In the NACA tests, a large aspect ratio airfoil was tested and showed a span-wise symmetrical stalling pattern. In the current tests, hull and tip influence are apparent due to the non-symmetrical stalling pattern at larger angles of attack.

Standard Configuration Force Measurement

Force measurement results are shown in Figure 3-13 for the standard configuration in straight and level flight. The experiments were conducted at the maximum sustainable wind speed in the BLWT (16 m/s) which corresponded to a length-based Reynolds number of 2.25 million. For comparison in the figure, the force to deflection curve is also shown for an isolated plane of the same geometry but tested at a Reynolds number of 4.0 million in the Parkinson Wind Tunnel.

In general, the isolated plane showed more linear behavior and delayed stall compared to the bowplane. This can be partially attributed to the difference in Reynolds number (see Section 4.2 for information regarding Reynolds number scaling effects). It was also shown in Section 2.4.2 that the presence of the hull influences the effective geometry of the bowplane as well as the incident

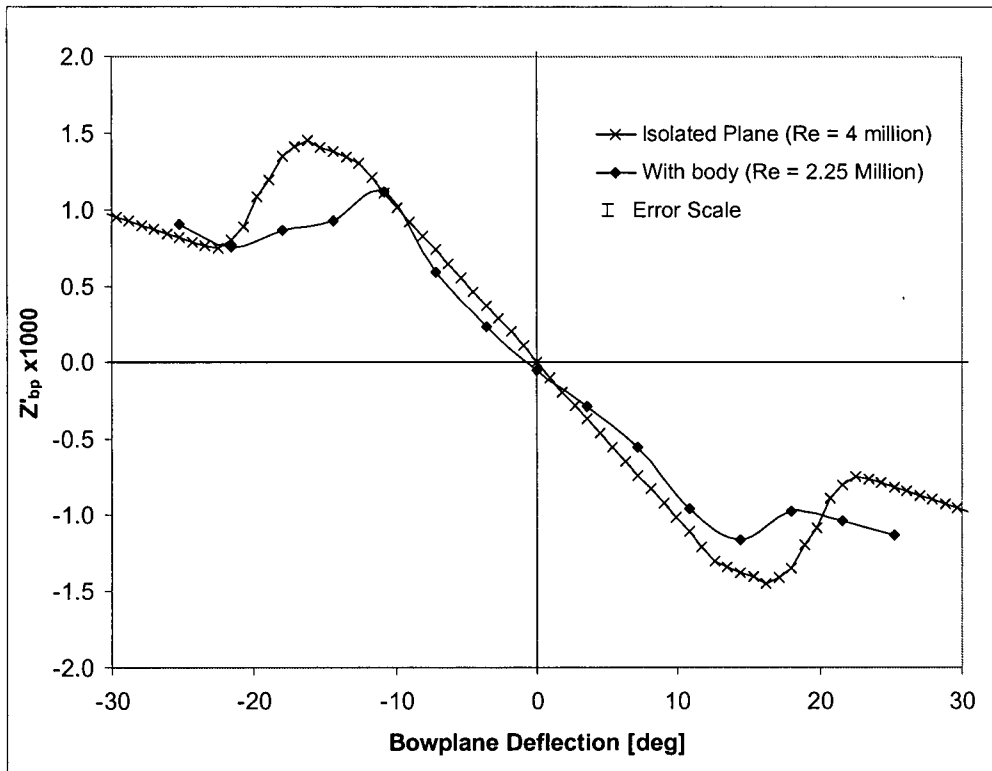
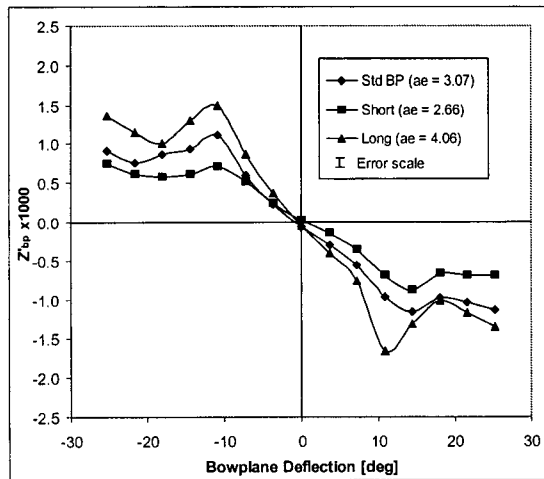
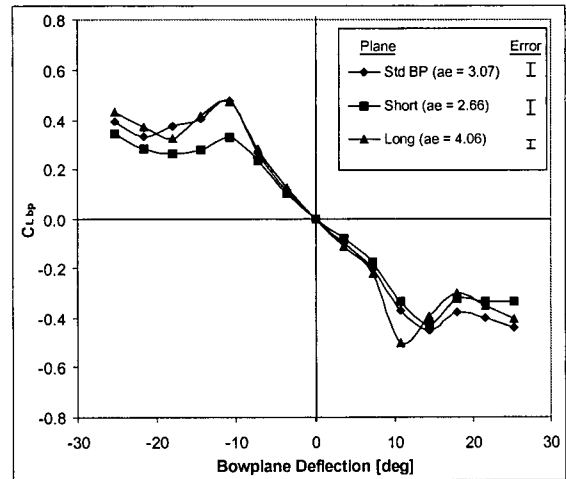


Figure 3-13 Bowplane force to deflection relationship compared with higher Reynolds number isolated plane relationship (standard bowplane geometry)



(a)



(b)

Figure 3-14 Bowplane aspect ratio influence on bowplane force production: (a) Z'_{bp} versus bowplane deflection; (b) $C_{L, bp}$ versus bowplane deflection

performance between the different planes was more similar, particularly for the two planes with larger span. Following typical behavior for finite wings, the lower aspect ratio planes generated marginally less force for a given deflection but also showed less abrupt stall. (Note that the curves in Figure 3-14 (b) have been shifted vertically to pass through the origin in order to more clearly illustrate the differences between the planes.)

In addition to the planes of varying aspect ratio, three other planes were considered: two tapered swept wings and one large-scale plane. As with the other planes, details regarding geometry can be found in Table 3-2 on page 45. Figure 3-15 shows the force to deflection behavior for these additional planes using both nondimensionalization by vehicle length (Figure 3-15 (a)) and by exposed plane area (Figure 3-15 (b)). Considerable differences were noted between the planes in the vehicle length non-dimensionalization, as would be expected. However, when forces were non-dimensionalized by planform area, for deflections prior to stall the resulting curves agreed to within 3% of the force range. Significant differences were still noted beyond stall. Of particular interest was the large plane which demonstrated stall that was both the most gradual and occurred at the highest angle of attack.

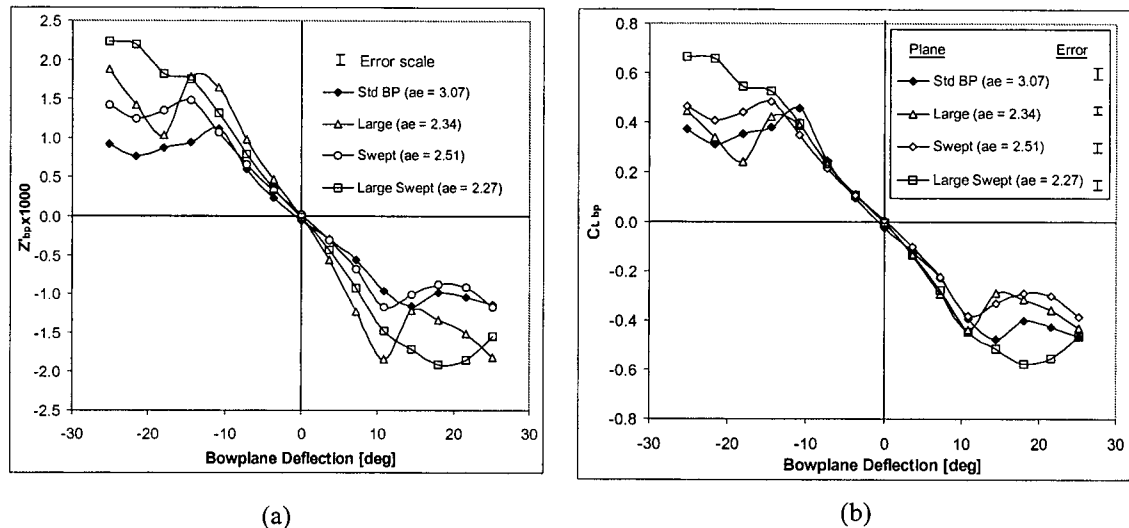


Figure 3-15 Bowplane geometry influence on bowplane force production for large planes: (a) Z'_{bp} versus bowplane deflection; (b) $C_{L, bp}$ versus bowplane deflection

Finally, tests were conducted with endplates installed on the *short* bowplanes and data were compared to the previous tests without endplates (square tips). As shown in Figure 3-16, the planes with the endplates show very similar performance to the square tips although there is a small but consistent increase in force (2.5% on average before stall). The significance of this finding is limited given that the difference is within the measurement error of the system.

For comparison, through the endplate factor (from equation (10) on page 21),

$$k_{ep} = 1 + 1.9 \frac{h}{2b} - 0.5 \left(\frac{h}{2b} \right)^2 \quad \text{for} \quad \left(\frac{h}{b} \leq 2.5 \right) \quad (47)$$

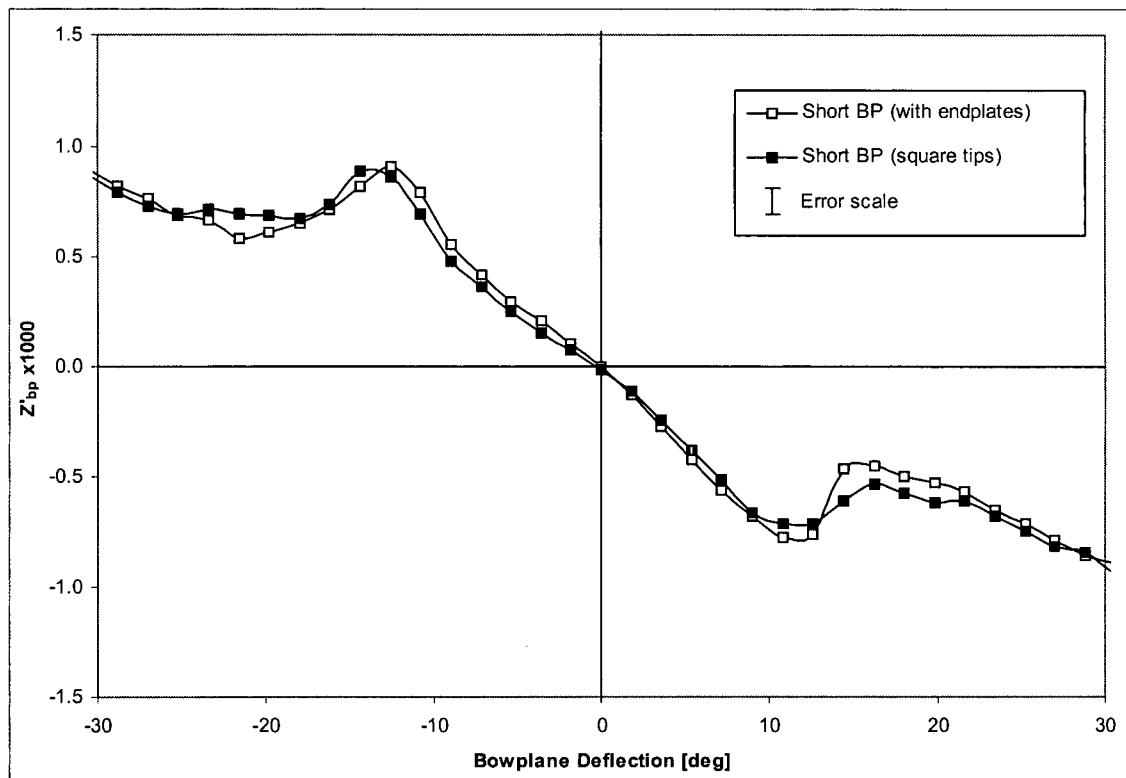


Figure 3-16 Endplate influence on short bowplane performance

it is predicted that there should be an increase of 8.6% in the bowplane force. The significant difference between prediction and measurement may lie in the fact that equation (47) does not take into account the plane thickness. Clearly, there should be no endplate correction as the endplate height approaches the plane thickness (there would however be a minor influence from the increase in plane aspect ratio due to the non-zero endplate thickness). For the configuration tested, the thickness of the NACA 0025 control surface was 0.25 chord lengths while the endplate height was 0.47 chord lengths. If, instead, the exposed endplate height is used in equation (47), a 3.4% increase in force is predicted (the exposed endplate height, h' , is given by $h' = h - t$ where h is the endplate height and t is the plane thickness). This prediction compares more favorably with the measured difference of 2.5% and suggests that h' should be used in place of h in equation (47).

Plane Location Influence

The effect of the bowplane location on the hull was studied using the standard geometry bowplanes in six different locations on the hull. Horizontal planes were used at different elevations for the *standard*, *high* and *centreline* positions. In the *anhedral* and *dihedral* positions, the bowplanes were inclined to the horizontal plane at 30 degrees downward and upward respectively. Finally, *keel* planes were examined but only in a limited number of tests as deflections had to be adjusted manually (due to space constraints in the keel, it was not possible to use the stepper motors required for computer controlled articulation). With the exception of the *keel* planes, all planes were located at the same longitudinal position on the hull. Complete details regarding each of the bowplane positions can be found in Table 3-3 on page 46.

Figure 3-17 shows the resulting force to deflection behavior of the *standard* bowplanes in the five positions on the hull described above (the *keel* planes are considered separately). For moderate deflections (up to stall), the differences between the curves are of similar order to the error scale. Interestingly, both the *high* and *anhedral* planes showed delayed stall for negative deflections but earlier stall for positive deflections. Overall, bowplane position does not appear to be a major factor influencing bowplane performance for straight and level flight.

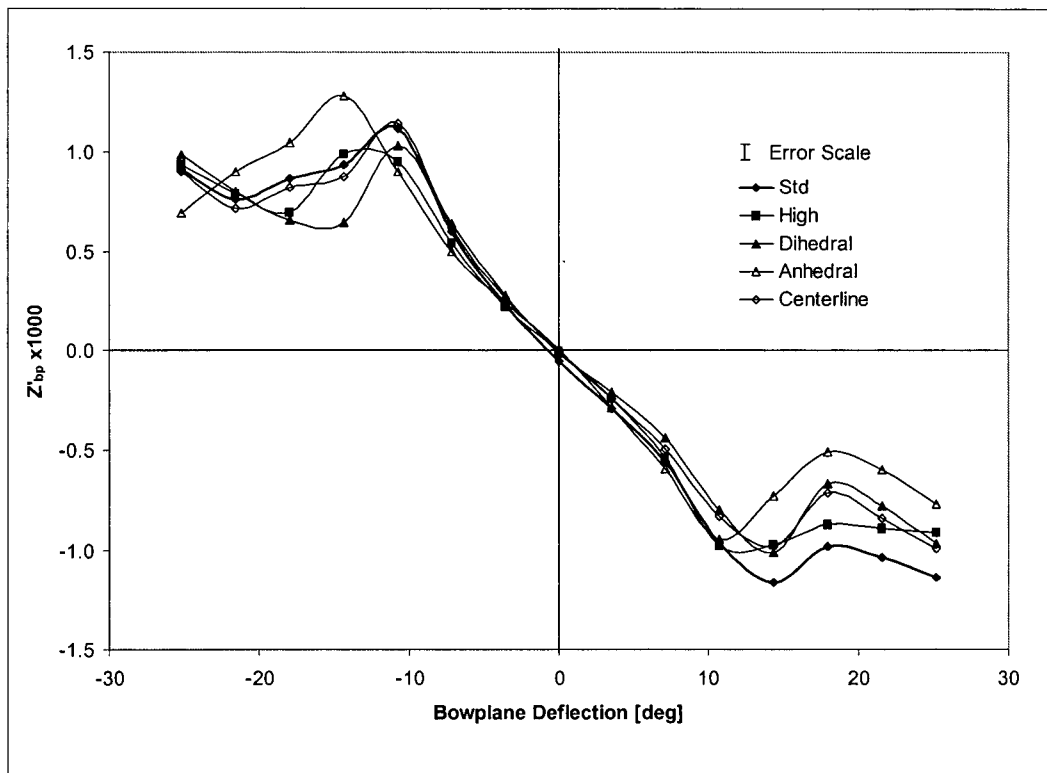


Figure 3-17 Bowplane position effect

The performance of the *keel* planes is compared to the *standard* bowplanes and an isolated plane in Figure 3-18. The data for the isolated plane was taken from Section 3.2.1. The performance of the *keel* planes was more similar to the isolated appendage which is to be expected since the *keel* planes are mounted against a relatively large flat surface (the keel). Between stall angles, the force to deflection behavior of the *keel* plane closely matches that of the isolated plane with all measurements agreeing within experiment error. Differences were noted in the stall behavior of the *keel* plane and isolated plane; however, the Reynolds number from the isolated plane tests was larger than that from the *keel* plane tests making comparison difficult (see Section 4.2 for further information about the effects of Reynolds number). The stall angles were similar on the *keel* planes and *standard* planes.

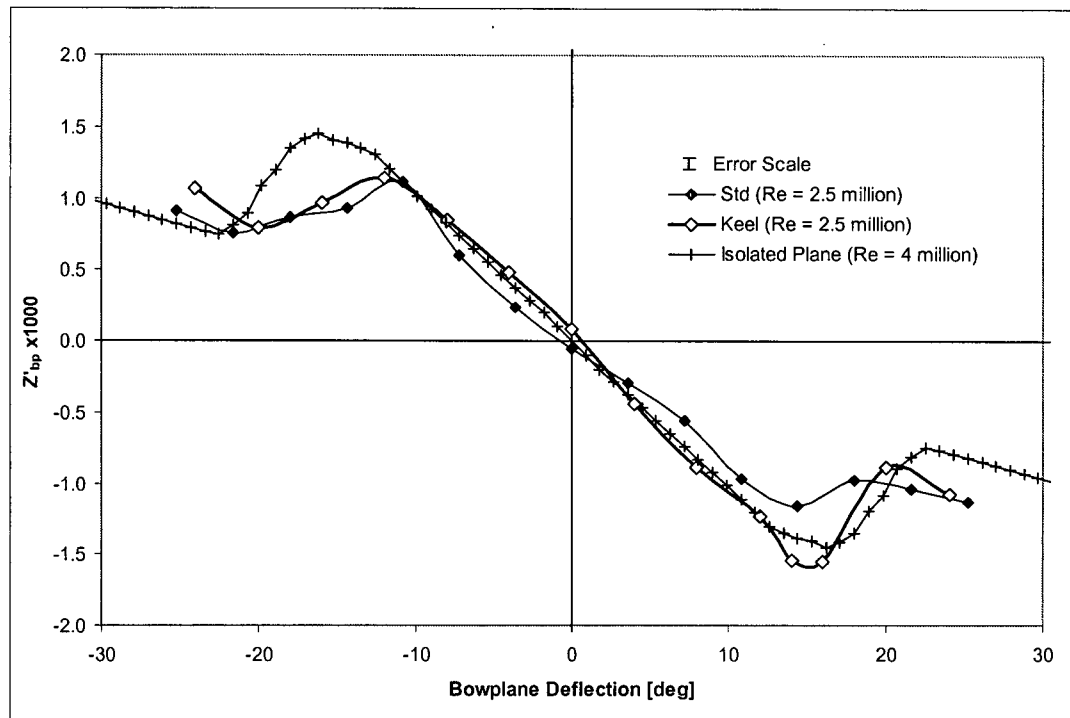


Figure 3-18 Keelplane compared to standard bowplane and isolated plane

3.2.3 Non-zero Trim

Various techniques were used to study how vehicle trim influenced plane performance. Yarn tuft visualization was used to estimate incident flow angles on the body (at the root of the planes), oil film visualization was once again employed to identify stall patterns on the planes, and force measurement was used to quantify performance.

Yarn Tuft Visualization

The yarn tuft technique is an excellent method for quickly obtaining preliminary flow field data. Short lengths of material are attached on one end to the body and align with the flow to indicate flow direction. In unsteady conditions, the tufts exhibit a certain degree of motion and in separated flow they often lift completely off the surface or hang limp. Further information on this techniques can be found in many fluid mechanics texts including (Barlow et al. 1999), (Merzkirch 1987), and (Pope and Harper, 1966), to name a few.

The main use of tufts for this research was to determine flow orientation and condition for various regions about the hull. Specifically, the incident flow angle for the root portion of various potential bowplane mounting locations was examined. Best results were found with a high-quality wool yarn due to the low weight, low stiffness, and large thickness. Figure 3-19 shows sample images from the yarn tuft study both with and without a bowplane installed.

The flow angles for the various regions of interest on the hull were determined through measurements of digitized photographs using a computer. Corrections were applied for parallax, camera

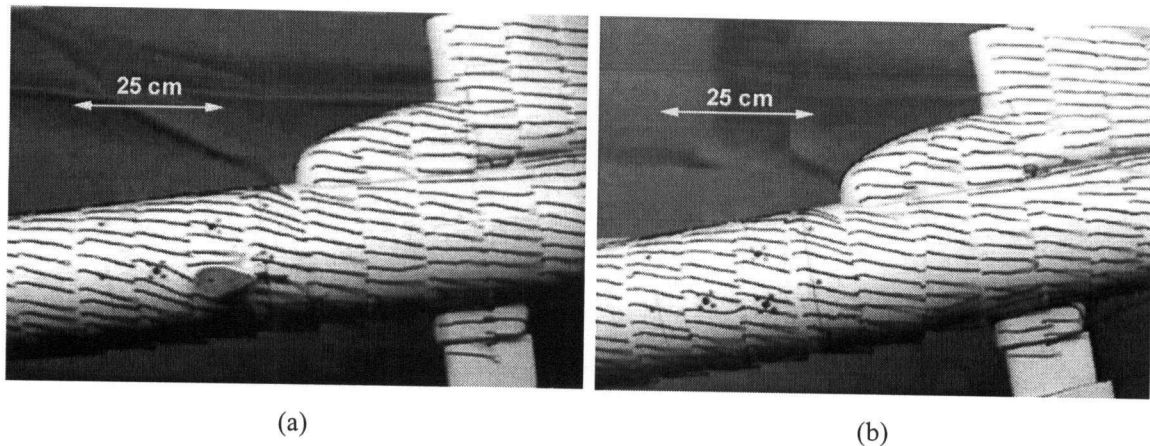


Figure 3-19 Sample yarn tuft visualization images: (a) *high* bowplane installed, trim angle = +6 degrees; (b) no bowplane installed, trim angle = +6 degrees

angle, and the effect of gravity on the tufts (adjusted by location on the hull). The resulting tuft angles as a function of hull trim angle for the *centreline*, *anhedral*, and *keel* bowplane locations (see Table 3-3 on page 46 for details) are shown in Figure 3-20. The tuft angles were measured with respect to the hull. The relationship for the *centreline* location was in agreement with the literature (Aucher, 1981) in that the tuft angles were roughly equal and opposite to the hull trim angle. For both the *anhedral* and *keel* locations the trim influence on the incident flow angle at the plane root was less than for the *centreline* location as noted by the reduced slope; however, the influence of the keel on the *anhedral* plane position, and possibly the *keel* plane position as well, is apparent due to the lack of symmetry across the *y*-axis.

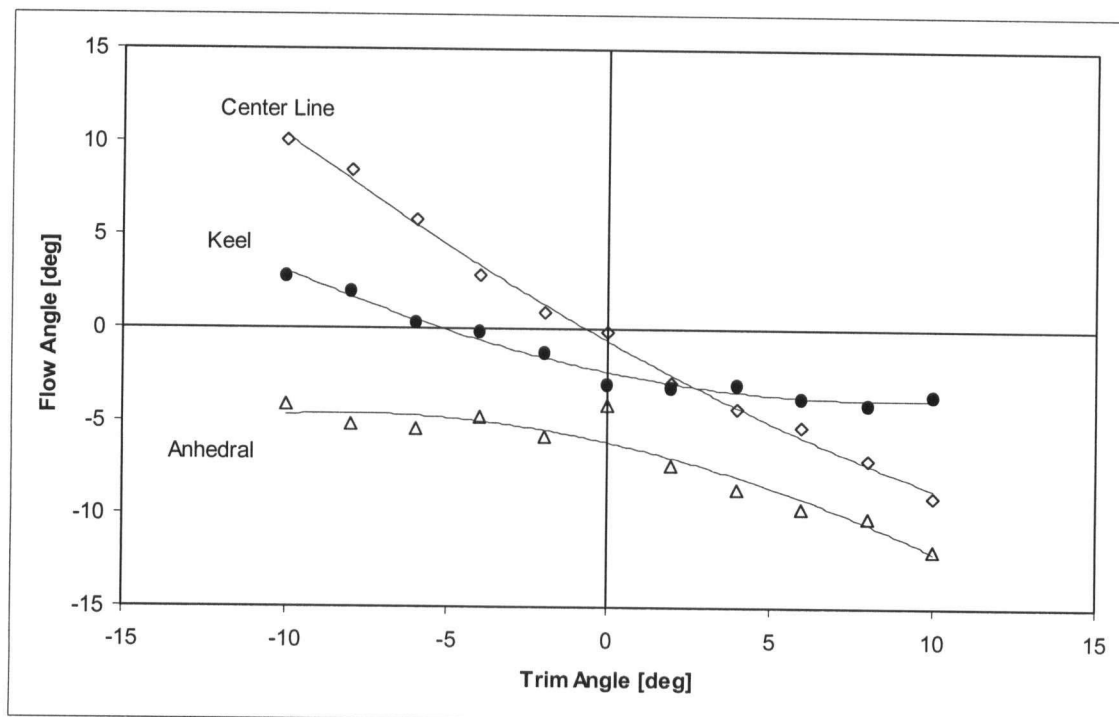


Figure 3-20 Bowplane root incident flow angle versus trim angle from yarn tuft visualization

Oil Film Visualization

The oil film technique was used on the standard bowplanes in the standard position for trim angles of +6 and -6 degrees. The composite separation line images are shown in Figure 3-21 and Figure 3-22 respectively. In this case, two major differences were noted to the separation patterns of Figure 3-12 on page 57: the separation lines were considerably more uniform across the plane span and the angle at which large scale separation was first noted was significantly different. As noted in Section 2.4.2, in trim the hull is responsible for a significant change in the flow angle across the bowplane span. For +6 degree trim (Figure 3-21), the majority of the suction side of the plane showed attached flow at deflections of even 24 degrees. For comparison, approximately 50% of the plane showed signs of flow separation at 16 degrees for straight and level flight. With -6 degrees trim (Figure 3-22), flow on the suction side of the plane was almost fully separated at only 6 degrees deflection.

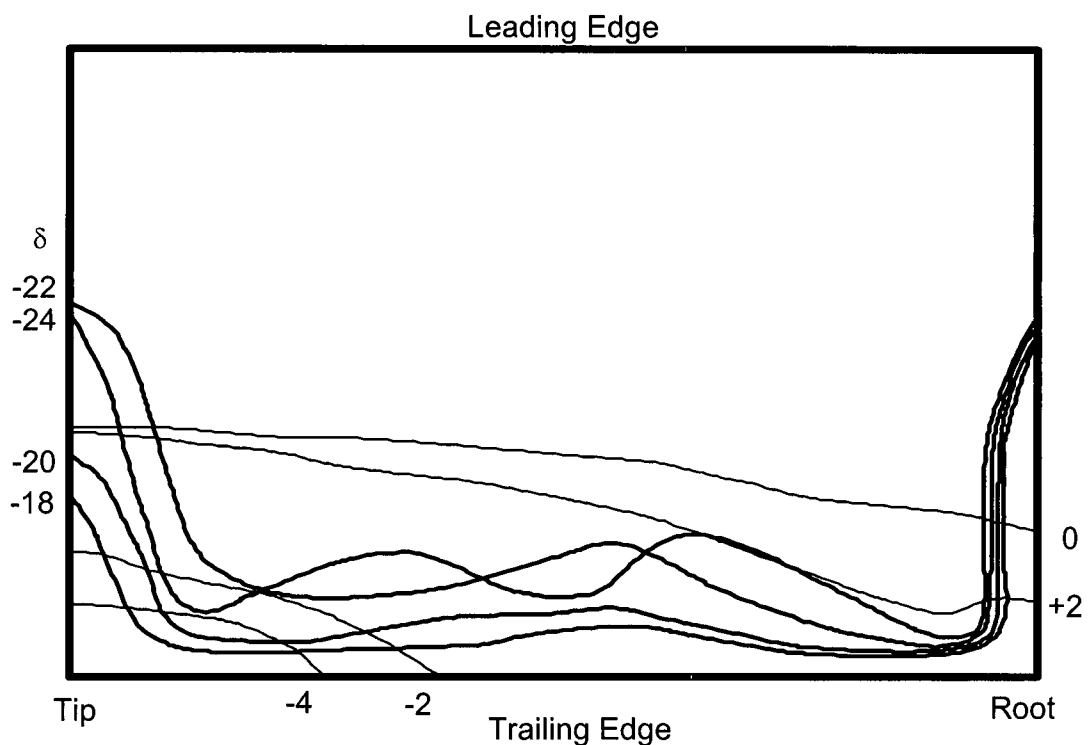


Figure 3-21 Oil film visualization: bowplane suction side, $Re_L = 2.25$ million, trim = +6 degrees

Trim Influence on Bowplane Performance

The measured forces are shown Figure 3-23 for the *standard* bowplanes in the *standard* position as a function of body trim angle. The predominant effect of trim was to introduce a horizontal shift in the bowplane force to deflection curves. Based on a least squares best fit, the curves were shifted horizontally to pass through the origin (for details regarding the shift of the bowplane curves, see Section 4.4). The result was equivalent to defining an effective plane deflection of the form

$$\delta_{\text{eff}} = \delta + 1.5\theta \quad (48)$$

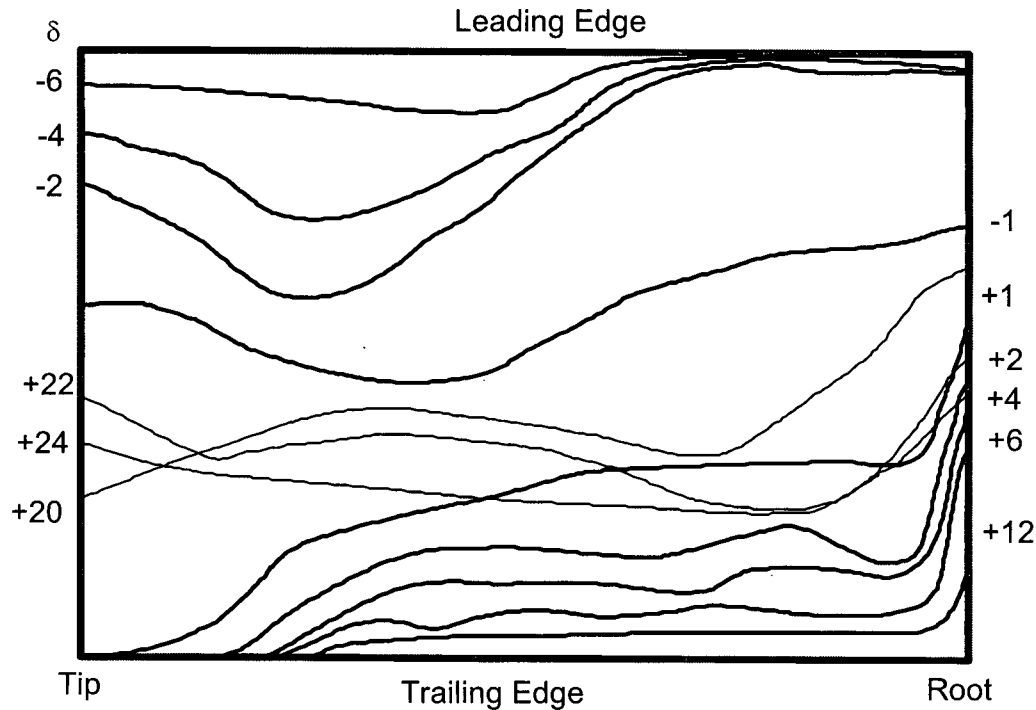


Figure 3-22 Oil film visualization: bowplane suction side, $Re_L = 2.25$ million, trim = -6 degrees

In other words, with non-zero trim the planes behaved as if in straight and level flight but at a deflection augmented by 1.5 times the trim angle. Recall from equation (26) on page 30 that trim induces an incidence angle of 2θ at the root of the planes and θ very far from the body. The bowplane force data in trim expressed using the effective plane deflection is shown in Figure 3-24. As evident in the figure, the eleven individual force to deflection curves essentially collapse to a single curve with reasonable agreement even in the regions beyond stall.

Bowplane Location Effects in Trim

Limited tests were conducted with alternate bowplane configurations in trim. The force on the bowplanes in the *anhedral* and *keel* configuration was measured for trim angles of -6, 0, and +6 degrees. As shown in Figure 3-25, the effect of trim on the *anhedral* bowplanes is similar to that with the *standard* configuration in that a horizontal shift in the curves was observed. When the effective deflection from equation (48) is used, the data again approaches a single curve as shown in Figure 3-25. This result suggests that equation (48) reasonably approximates the effect of trim angle on bowplanes on the hull and that the effect is not highly sensitive to the bowplane location or orientation.

The *keel* planes behaved more like isolated appendages, as was noted in Section 3.2.2. As shown in Figure 3-27, the effect of vehicle trim on the force to deflection behavior was again a lateral shift in the curves; however, the magnitude of the shift in this case was equal to the trim angle.

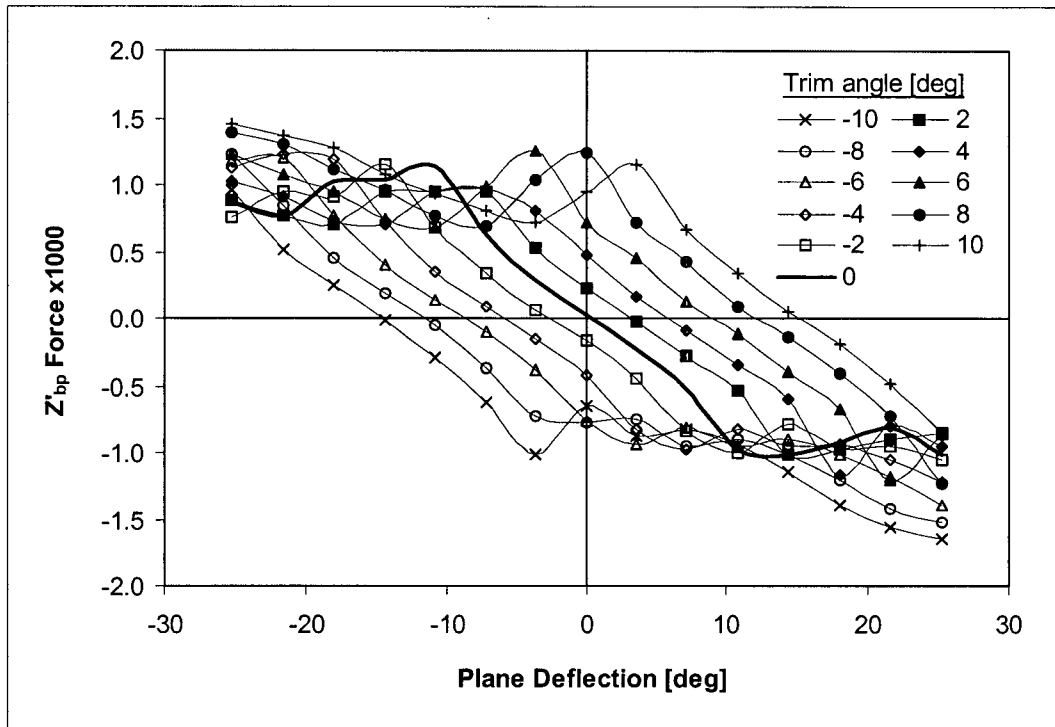


Figure 3-23 Trim influence on bowplane force production

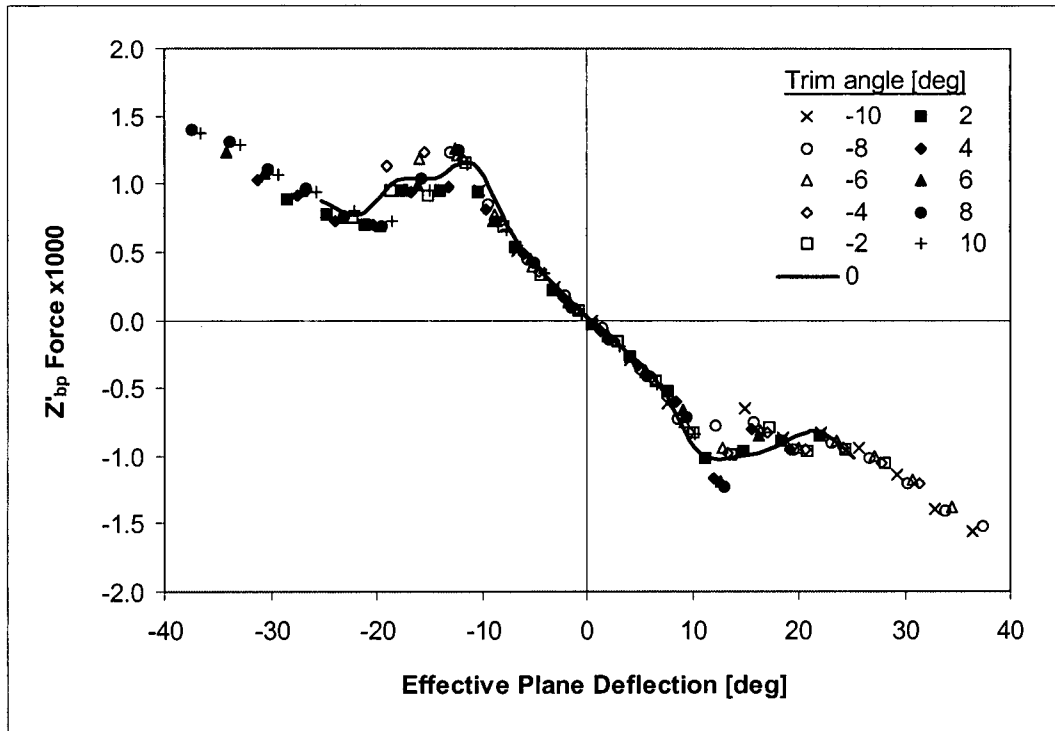


Figure 3-24 Trim influence on bowplanes when expressed using effective plane deflection

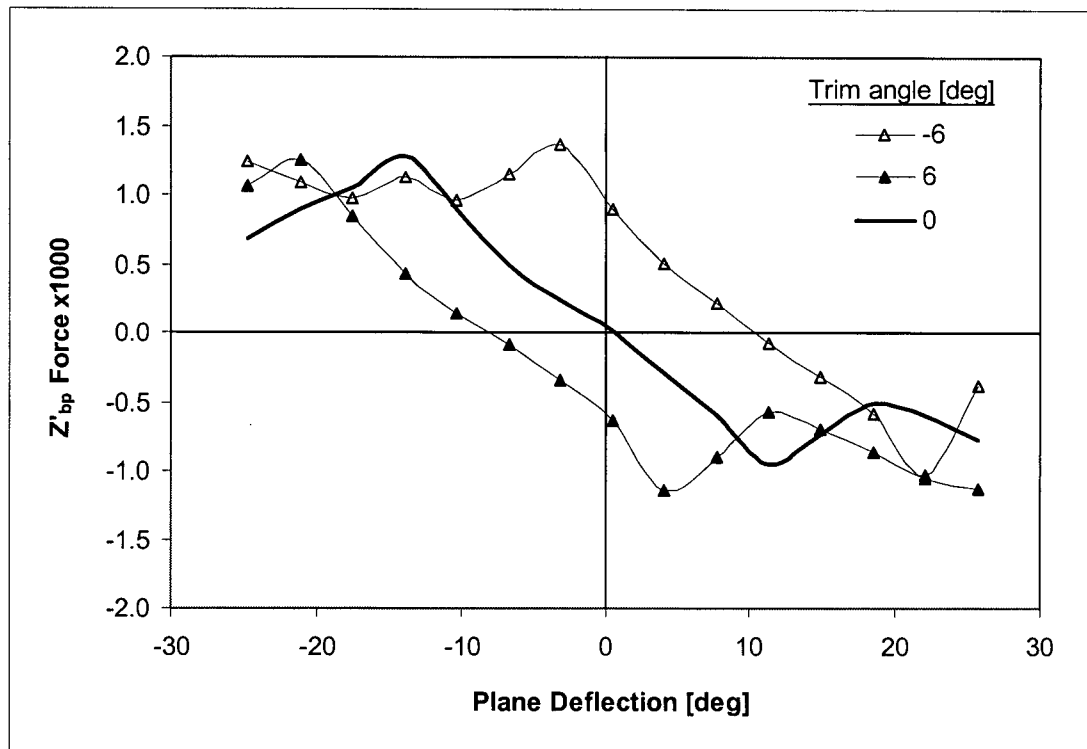


Figure 3-25 Trim influence on anhedral bowplanes

That is, the effective deflection for the *keel* planes was defined not as in equation (48), but rather by

$$\delta_{\text{eff, keel}} = \delta + \theta \quad (49)$$

The shifted *keel* plane data is shown in Figure 3-28. In general, the *keel* plane force curves collapse reasonably well but not with the same agreement as observed with the *standard* planes. This is likely because the body geometry in the proximity of the keel planes is not symmetric for positive and negative trim angles and only about 50% of the *keel* plane span extended beyond the lateral extent of the hull.

Trim Influence on Sternplane Performance

The study of the influence of trim on sternplane performance was limited to force measurements. It was not practical to test over a complete range of sternplane deflections for each trim angle but measurements were conducted at zero degrees sternplane deflection for trim angles between -10 and +10 degrees. The results are shown in Figure 3-29; the measured force on the sternplanes is indicated using points and the estimated force due to a sternplane deflection equal to the trim angle (with the vehicle straight and level) is indicated by the solid line. Unlike the influence of trim on the bowplanes (see equation (48)), the effect of trim on the sternplanes was essentially limited to a change in deflection due to body inclination. That is

$$\delta_{\text{sp,eff}} = \delta + \theta \quad (50)$$

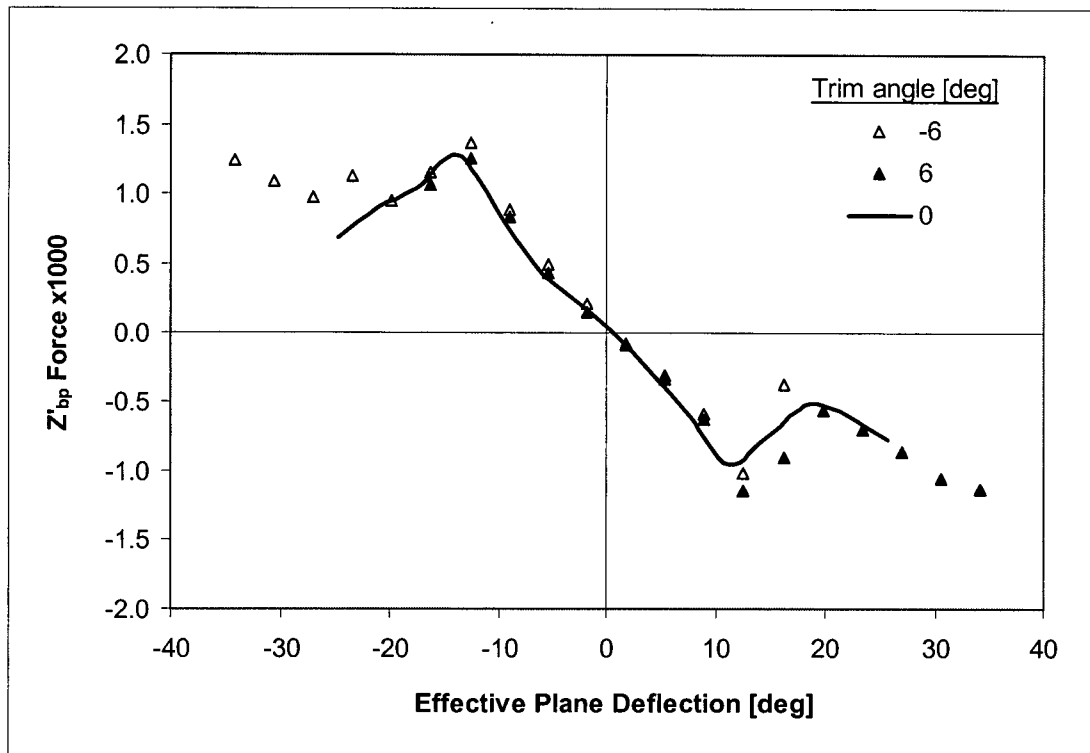


Figure 3-26 Trim influence on anhedral bowplanes using effective plane deflection

3.2.4 Non-Zero Yaw

Yaw can result from a number of conditions such as turning and transverse currents and waves. The effect may be uniform along the hull (as with a current) or it may be localized (as with rotation in the horizontal plane). Under typical conditions, the total yaw angle at the bowplanes can reach as high as 20 degrees (Dominguez 2000). With non-zero yaw, the port and starboard bowplanes are subjected to different flow fields. Experiments examining the effect of yaw on plane performance were conducted by Dominguez (2000) as part of his Master of Engineering degree requirements. Dominguez used yarn tuft visualization and force measurement in the wind tunnel with the one-quarter scale DOLPHIN model; the key findings are reproduced below.

Yarn Tuft Visualization

With yarn tufts positioned uniformly about the hull, the body influence in yaw was observed. In Figure 3-30 (a) the starboard side of the vehicle is pictured for +20 degrees yaw; hereafter, the side of the vehicle in the wake of the hull is referred to as the leeward side. The port side of the vehicle for +20 degrees yaw, or windward side, is shown in Figure 3-30 (b).

It is well documented that two counter rotating vortices form on the leeward side of a finite length inclined cylinder in uniform flow (see, for example, Kawamura and Aihara (1992) or Allen and Perkins (1951)). Considering the yarn tuft images, the flow divides over the windward side of the hull as noted by the chevron pattern in the tufts. However, as the flow reaches the leeward side of the hull it does not appear to fully separate as the yarn tufts also form a relatively uniform chevron

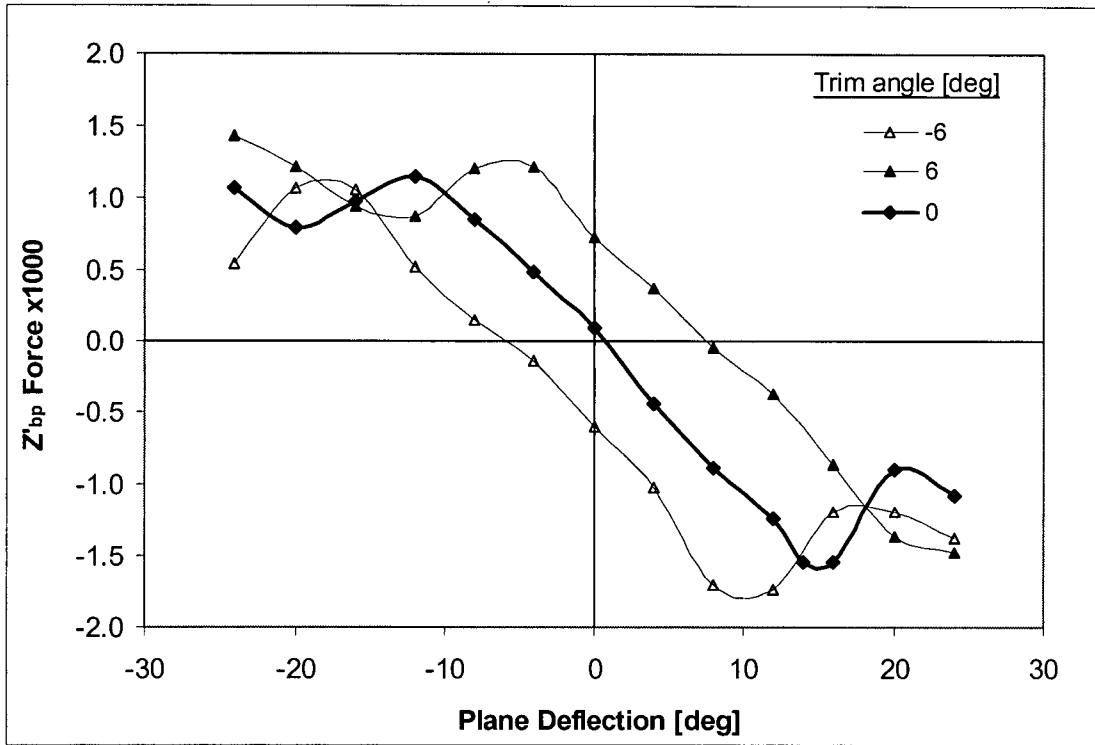


Figure 3-27 Trim influence on keel plane force production

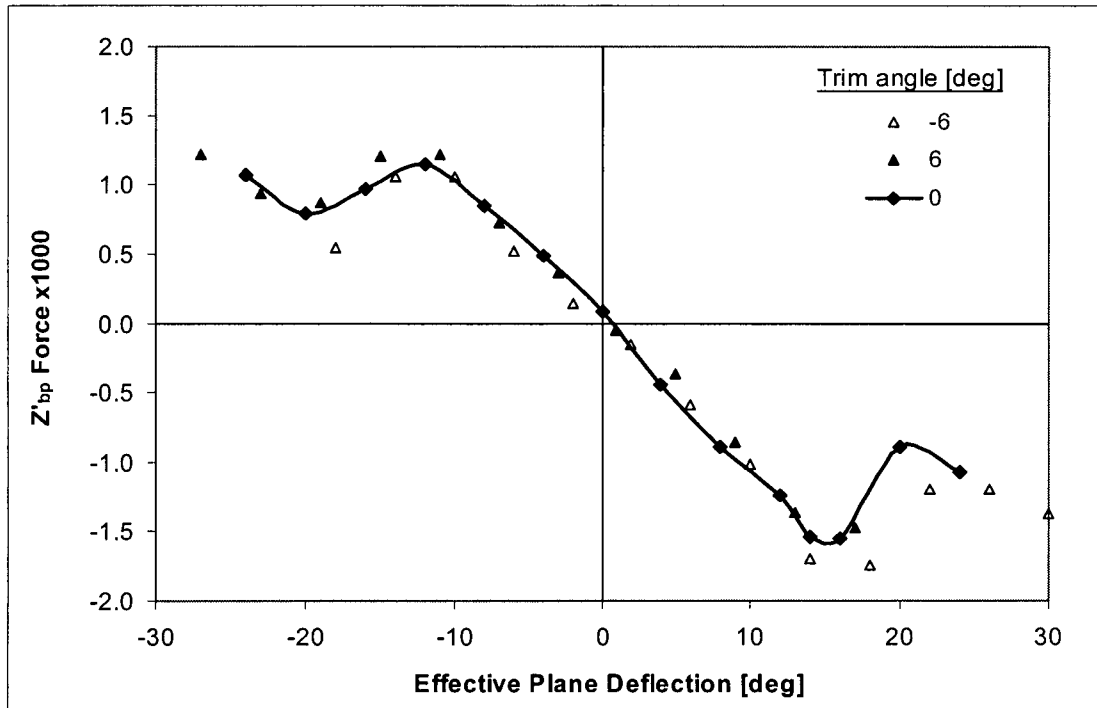


Figure 3-28 Trim influence on keel plane force production expressed using effective deflection

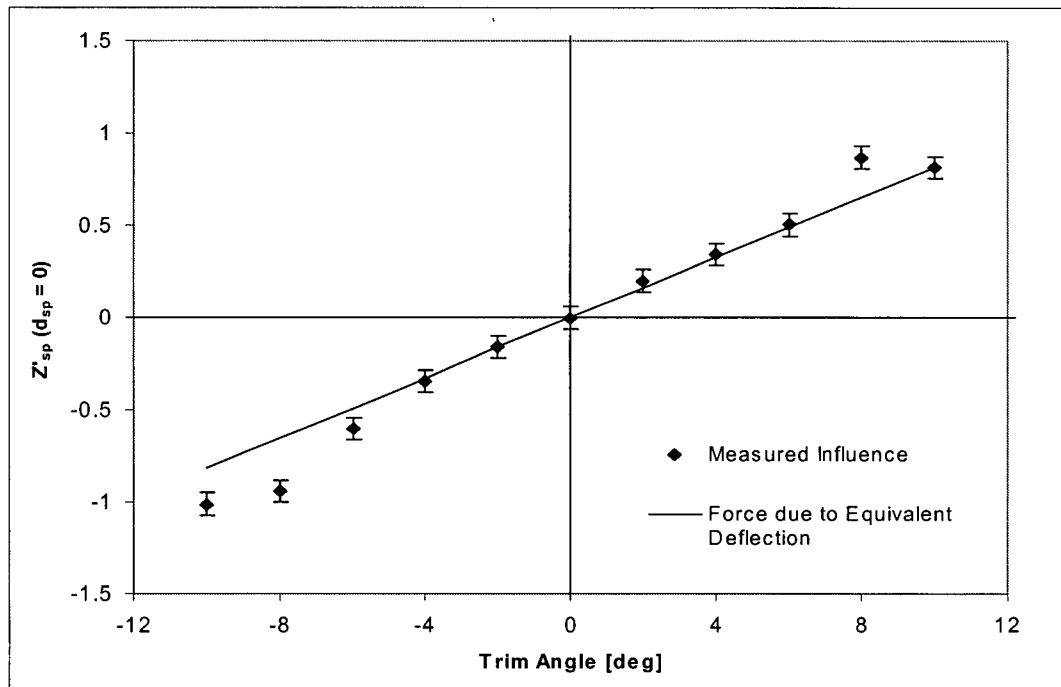


Figure 3-29 Trim influence on sternplane force

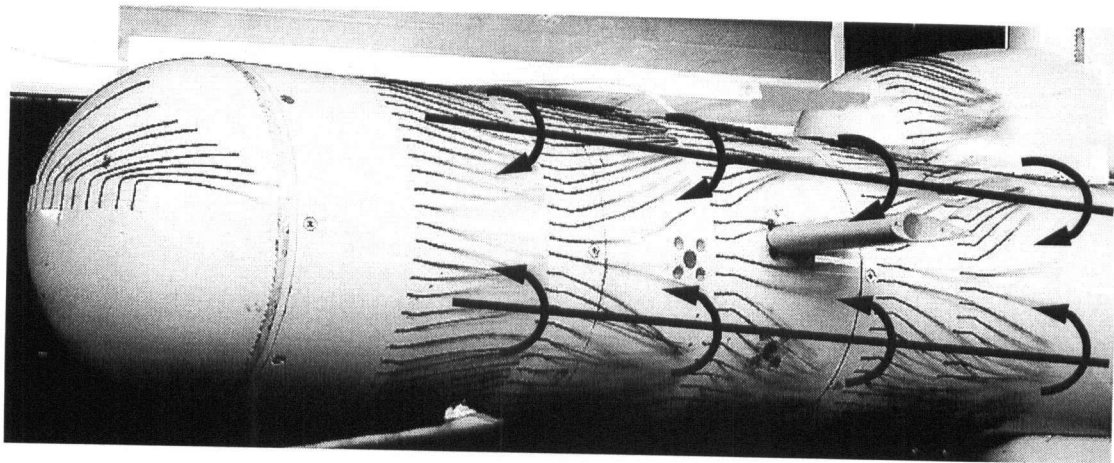
pattern. The flow pattern in Figure 3-30 (a) suggests the presence of two counter rotating vortices (located approximately as shown in the figure). Unfortunately, further attempts to verify the existence and location of such vortices—helium bubble flow visualization and a vortex probe were used—were only partially successful.

Baseline Configuration Force Measurements

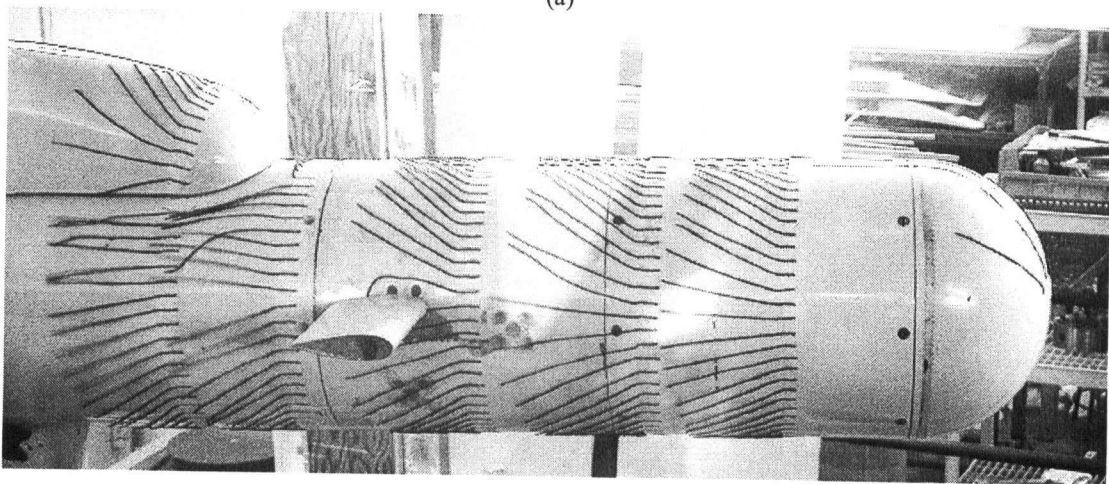
The forces on the bowplanes were measured over a range of deflections and yaw angles. The forces measured on the port bowplane are shown in Figure 3-31. In a more general sense, the curves with positive yaw angle apply to the windward side plane while negative yaw correspond to the leeward plane.

There are significant differences in the bowplane performance for changing yaw angle. Specifically, the magnitude of the force and the stall angle both increased for increasing yaw on the leeward bowplane. Stall was not observed at even 25 degrees deflection for 20 degrees yaw (compared to stall at approximately 14 degrees for straight and level flight). Conversely, for the windward side plane the force magnitude and stall angle decreased with increasing yaw.

The force measurement results are consistent with the suggestion of two counter-rotating vortices located on the leeward side of the body. Such vortices would tend to draw momentum from the freestream and increase the local flow velocity near the planes. As such, the planes would effectively be operating in a higher velocity and higher Reynolds number flow which would increase both the magnitude of forces as well as the stall angle. In contrast, with increasing yaw angle, the windward planes would experience greater span-wise crossflow and obstruction from the body and hence decreased chord-wise flow velocity.



(a)



(b)

Figure 3-30 Yarn tuft visualization of body at +20 degrees yaw: (a) leeward (starboard) side; (b) windward (port) side

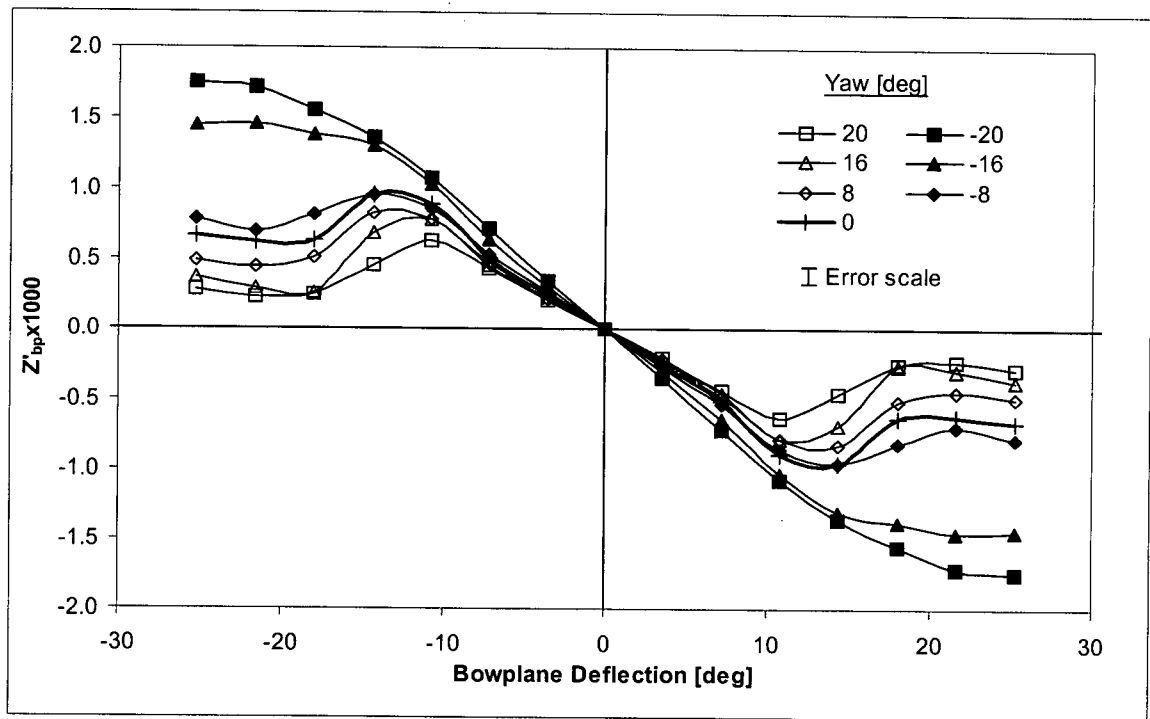


Figure 3-31 Effect of yaw on port bowplane performance (Re = 2.25 million)

3.3 CONTROL SURFACE INTERACTION

Flow induced interaction from the bowplanes to the sternplanes was examined as part of the wind tunnel and towing tank research. Wind tunnel flow visualization was used to identify the location of trailing vortices shed from the bowplanes and their proximity to the sternplanes. In both the wind tunnel and tow tank, the force measurement techniques used previously with the bowplanes were used for the sternplanes to measure the resultant forces due to the interaction.

3.3.1 Straight and Level Flight

Helium Bubble Flow Visualization

For straight and level flight, helium bubble flow visualization was used to identify and map the tip vortices shed from the bowplanes. These vortices are believed to adversely influence the performance of the sternplanes.

With the helium bubble technique, helium-filled soap bubbles of neutral buoyancy are injected into the freestream flow upstream from the model. The bubbles track the flow due to their very low mass and deviations from the fluid pathlines are generally quite small (Merzkirch 1981). The main advantage of bubbles over a smoke streakline technique is that where smoke tends to dissipate in high speed and regions of turbulence, helium bubbles persist. With appropriate lighting, film, and shutter settings on a camera, the bubbles appear as streaks when photographed. For further information regarding the helium bubble path technique, the reader is referred to Barlow et al. (1999), Hale et al. (1971), and Ostafichuk et al. (1999).

A sample image from the helium bubble path technique is shown in Figure 3-32. The photograph shows the starboard bowplane with flow passing from left to right (the model is inverted). The streaks in the image are the trails left from individual bubbles. To the right of the plane the bubbles follow a helical path and quickly migrate to the core of the bowplane tip vortex; the vortex core is identified by the thick horizontal white line. A second sample image for the helium bubble path technique is shown in Figure 3-33. In this case the tail of the vehicle is shown with the helium bubble streaks digitally enhanced. Once again, the vortex core is easily identified by the thick white line running along the length of the hull. The helical motion of the individual bubbles is also evident as they migrate to the vortex core.

For the purpose of mapping the bowplane tip vortex path, a wide angle lens was used with a long exposure time. As shown in the sample image in Figure 3-34, the contrast of individual streaks was reduced in the process but the path of the trailing vortex was maintained. In the image, the model is shown as mounted in the wind tunnel (inverted) and a dashed white outline has been added. For various body orientations and bowplane configurations, the relative proximity of the bowplane tip vortex to the sternplane was measured using similar vortex path images.

For straight and level flight, the strongest bowplane trailing vortices are shown schematically in Figure 3-35. The bowplane deflections associated with the two vortices are +12 and -12 degrees which also coincide with the approximate deflection with maximum force from Figure 3-13. From the schematic it is apparent that the bowplane tip vortex is closer in proximity to the sternplane for +12 degrees deflection compared to -12 degrees deflection.

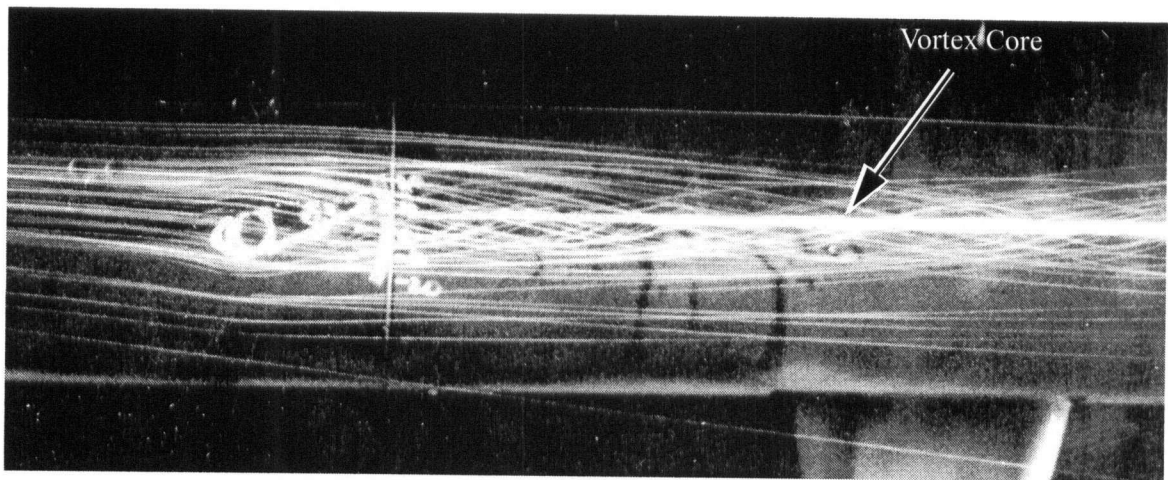


Figure 3-32 Helium bubble path sample image; trim: +6 degrees, deflection: +25 degrees, Reynolds number: 2.5 million, model inverted

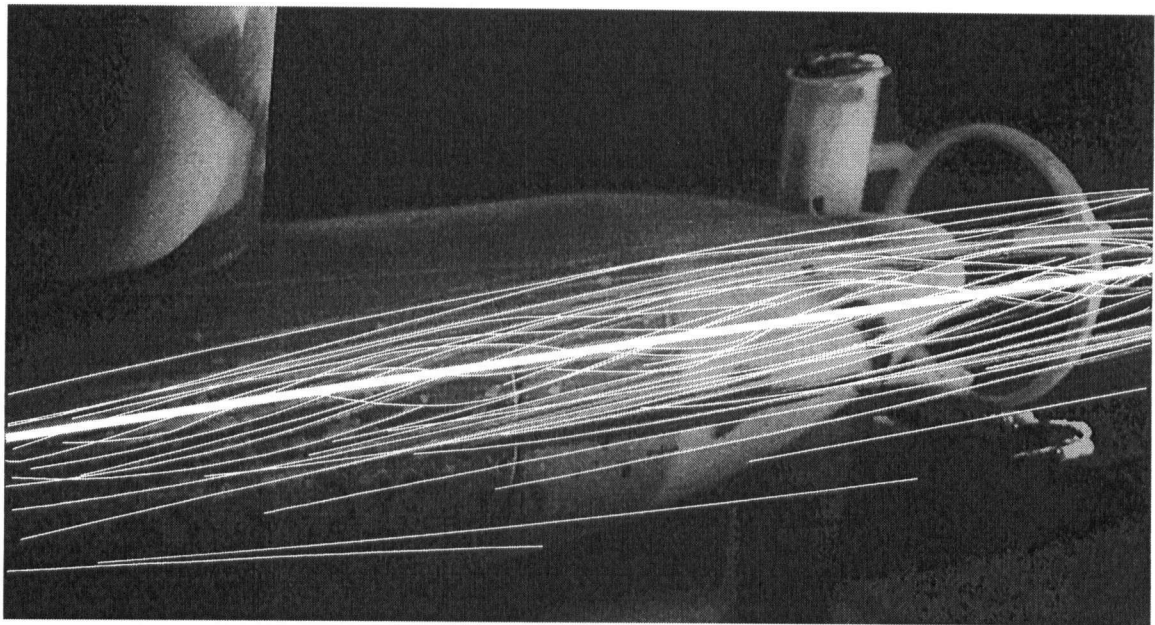


Figure 3-33 Oblique stern helium bubble path sample

Baseline Configuration

The force measured on the bowplanes and sternplanes for the standard configuration in straight and level flight is shown in Figure 3-36. The bowplane deflection is used as the independent variable and the sternplane deflection was fixed at zero degrees. The flow induced interaction between the bowplane and sternplane is apparent given the change in sternplane force with bowplane deflection; without interaction, the sternplane force would be a horizontal line.

For a qualitative comparison, in Figure 3-37 the interaction force measured on the sternplanes from Figure 3-36 was scaled and plotted against the bowplane force. A scale factor of -4.5 was used and, as shown in Figure 3-37, the scaled sternplane force very closely matches the bowplane

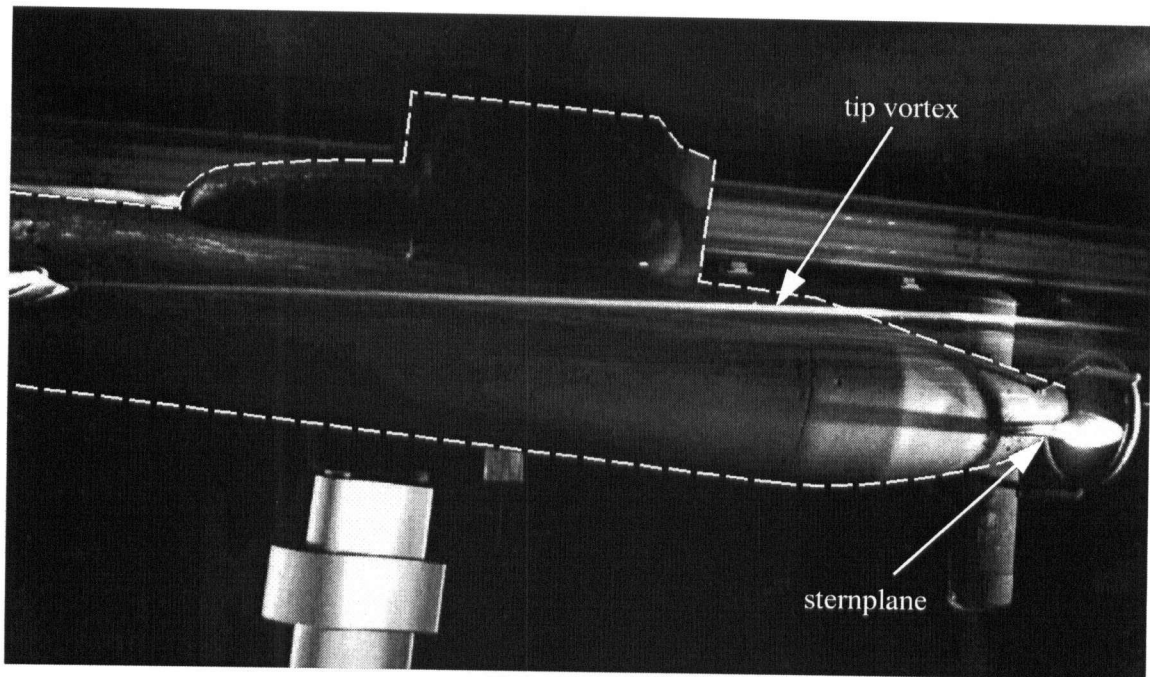


Figure 3-34 Helium bubble path vortex mapping side view: -6 degrees trim, +16 degrees bowplane deflection, 2.5 million Reynolds number

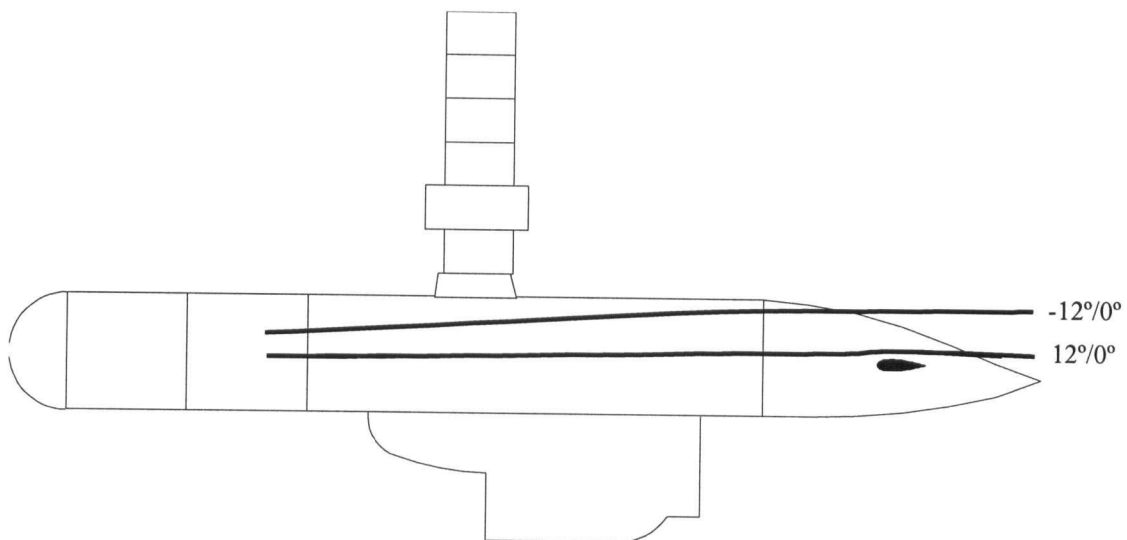


Figure 3-35 Standard configuration straight and level flight schematic vortex path diagram

force over bowplane deflections of approximately -7 to +14 degrees. In other words, over this range of bowplane deflections, there is an interaction force on the sternplanes of approximately 22% ($1/4.5$) of the force generated on the bowplanes. As shown in both Figure 3-36 and Figure 3-37, the interaction force on the sternplanes is smaller for negative bowplane deflections; this is consistent with the closer proximity of the bowplane tip vortex to the sternplane for positive bowplane deflections (noted in Figure 3-35). For deflections beyond stall on the bowplanes, the interaction force measured on the sternplanes is proportionally smaller. This effect would be

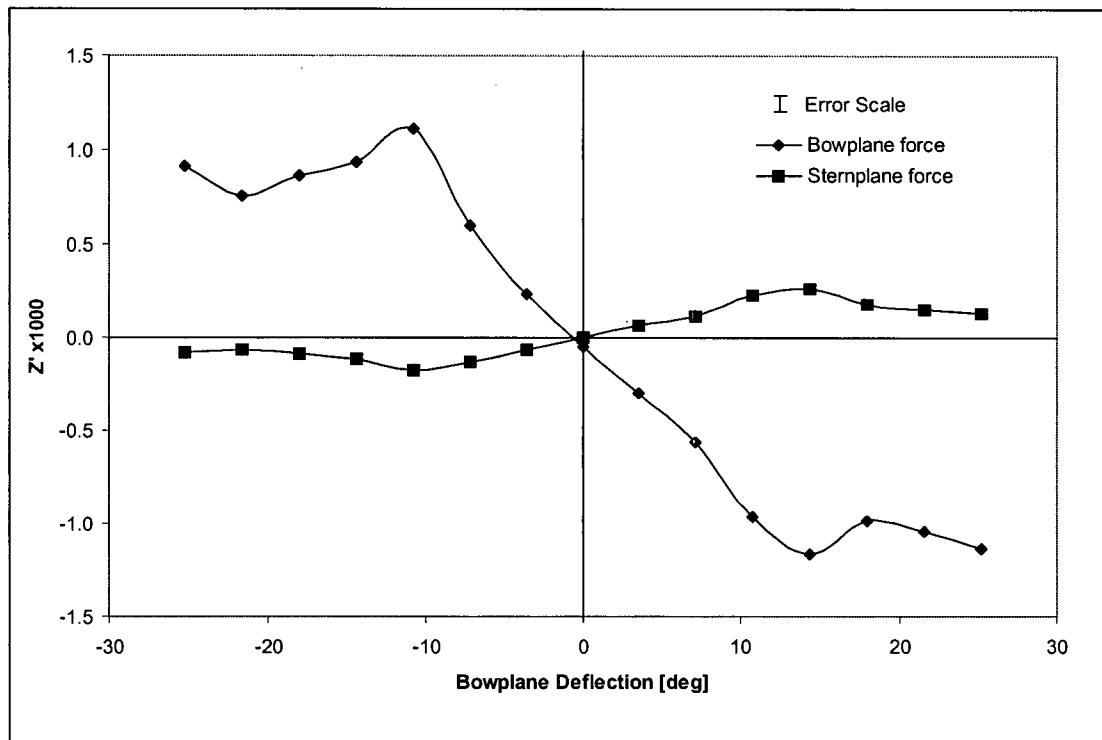


Figure 3-36 Bowplane and sternplane force for the standard configuration in straight and level flight

expected due to the diminished bowplane tip vortex strength and large scale turbulence in the wake of bowplanes as a result of flow separation. The role of the bowplane tip vortex in the interaction with the sternplanes is examined in greater detail in Section 4.6.

Plane Geometry Influence

In addition to the standard configuration, the bowplane-sternplane interaction force was examined for a variety of different plane geometries (both bowplane and sternplane). In Figure 3-38 and Figure 3-39 the effect of plane span is examined for the bowplanes and sternplanes respectively. The influence of other geometric changes (including sweep, taper, and size) to the bowplanes and sternplanes are considered respectively in Figure 3-40 and Figure 3-41. In each figure, the interaction force measured on the sternplanes is plotted as a function of bowplane deflection. Additionally, for each figure, the sternplane force is shown non-dimensionalized in the standard form using vehicle length squared, Z' , well as using the bowplane planform area, $C_{L,sp}^*$

$$C_{L,sp}^* = \frac{Z_{sp}}{\frac{1}{2}\rho U^2 S_{bp,exp}} \quad (51)$$

The intent of the latter normalization is to account for differences in bowplane force associated with changes to bowplane geometry since it was established in Figure 3-37 that there is a strong correlation between the force on the bowplanes and the interaction force on the sternplanes.

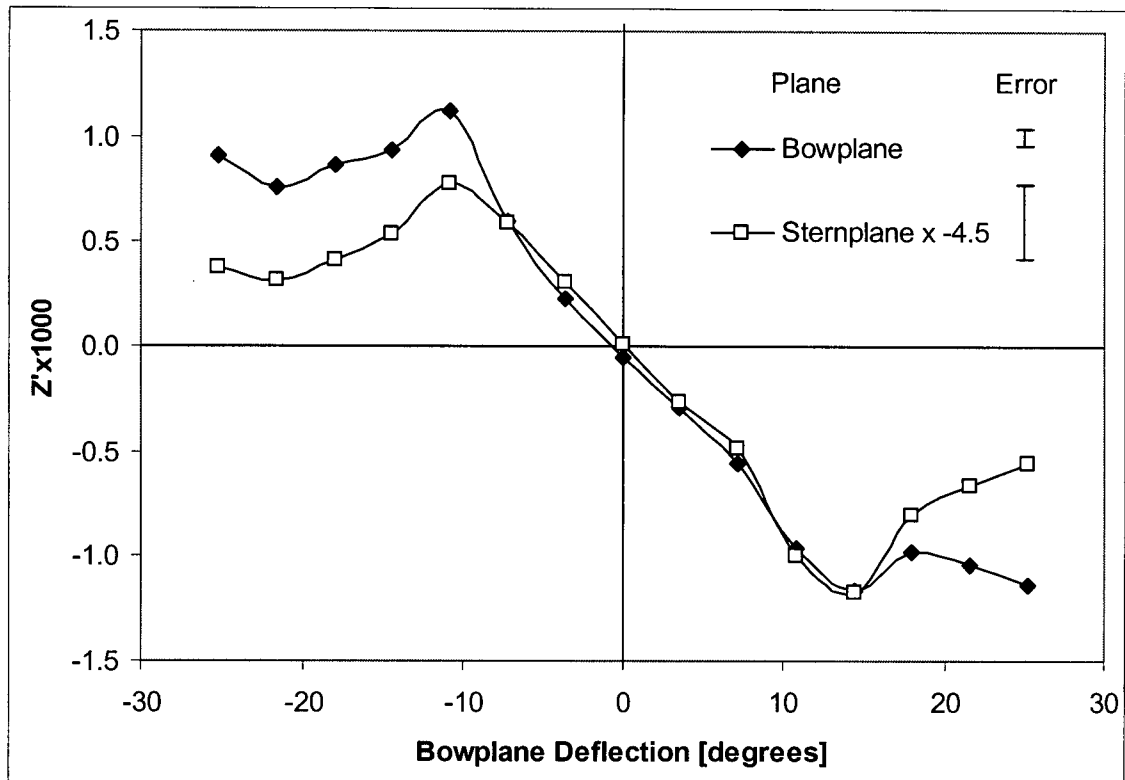


Figure 3-37 Comparison of bowplane and sternplane interaction force

Bowplane span has a moderate effect on the interaction with the sternplanes as shown in Figure 3-38 (a). Surprisingly, the *short* bowplanes (with an exposed span of 0.0530 vehicle lengths) show the largest absolute interaction force for positive deflections and the least interaction for negative deflections. Considering the force normalized by bowplane area in Figure 3-38 (b), over all deflections, the *long* bowplanes have the least effect on the sternplanes. As will be shown in Section 4.6, the reason for the reduced interaction appears to be the relative position of the bowplane tip vortex to the sternplanes.

The effect of sternplane span in the bowplane-sternplane interaction appears to be similar in magnitude to that of bowplane span. Figure 3-39 (a) shows the measured interaction force normalized by vehicle length squared. The standard sternplanes exhibit the greatest force due to interaction with the bowplanes; however, the differences are of the same order as the experimental error. When the interaction force is expressed in non-dimensional form using the sternplane area (Figure 3-39 (b)), the relative difference between the various sternplanes increases (with the standard sternplanes again showing the largest interaction). This second form of representation, $C_{L,sp}$, is not to be confused with $C_{L,sp}^*$ above.

The effects of changes to the bowplane geometry other than aspect ratio (span) are shown in Figure 3-40. The *swept* plane had the same span as the *standard* plane with slightly larger planform area while the *large* and *large swept* planes had considerably larger area (see Table 3-2 on page 45). Not surprisingly, the bowplanes with the largest planform area developed the largest

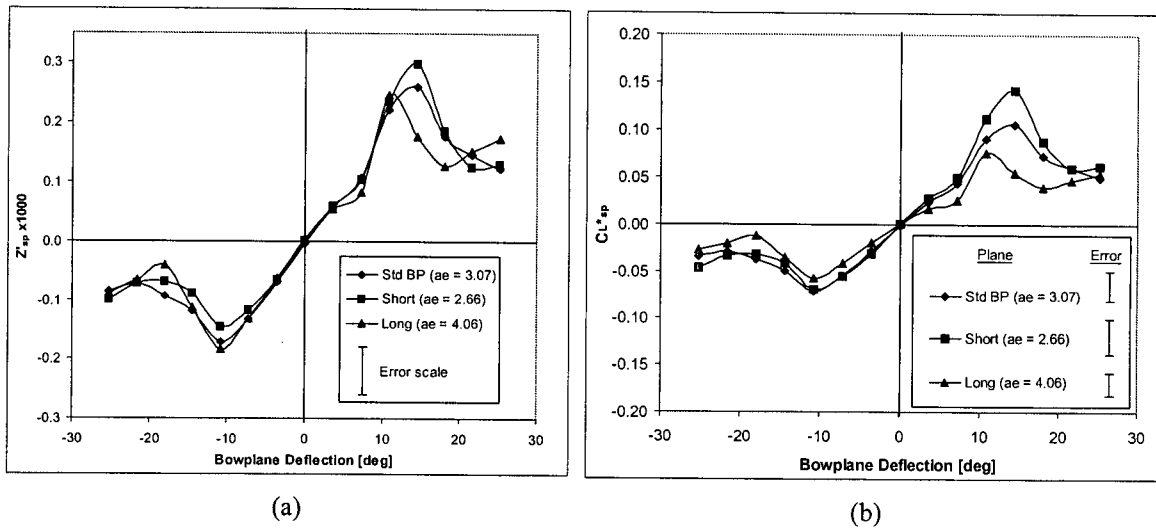


Figure 3-38 Sternplane interaction force dependence on bowplane span: (a) Z_{sp} versus bowplane deflection; (b) C_{L*sp} versus bowplane deflection

force (see Figure 3-15 on page 59) and also showed the greatest interaction force with the sternplanes (Figure 3-40 (a)). When the interaction force was expressed in non-dimensional form in terms of bowplane planform area (Figure 3-40 (b)), the differences in interaction resulting from bowplane geometry were statistically insignificant based on measurement error for deflections between deflections of approximately -7 to 11 degrees. Beyond this range, differences were noted but can be largely attributed to the different performance of the bowplanes near and after stall (Figure 3-15). In short, the bowplane-sternplane interaction does not appear to be strongly dependent on bowplane shape for planes of similar span; however, the size of the bowplanes, as measured by planform area, does have a significant effect due to the associated increase in bowplane force.

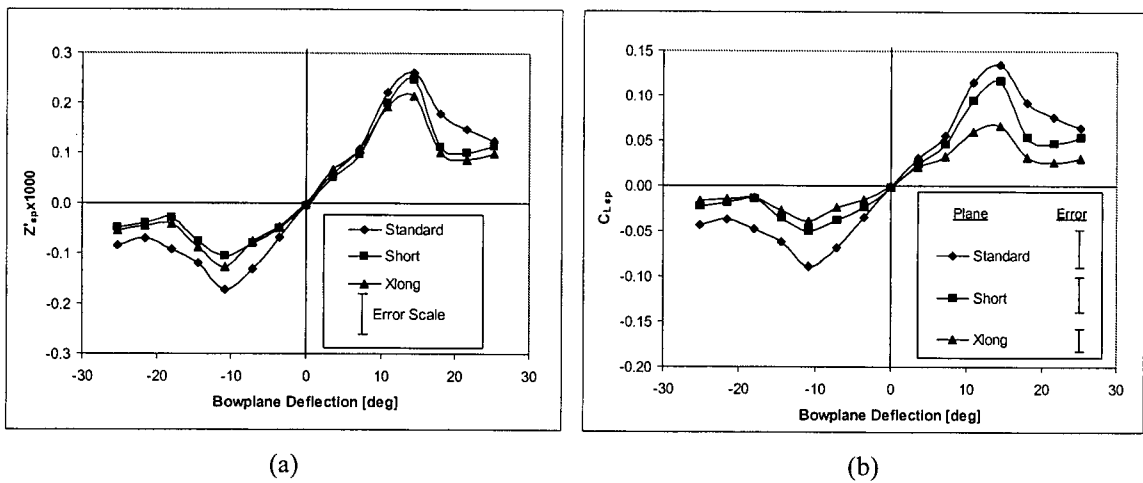


Figure 3-39 Sternplane span influence on sternplane force interaction: (a) Z_{sp} versus bowplane deflection; (b) C_{L*sp} versus bowplane deflection

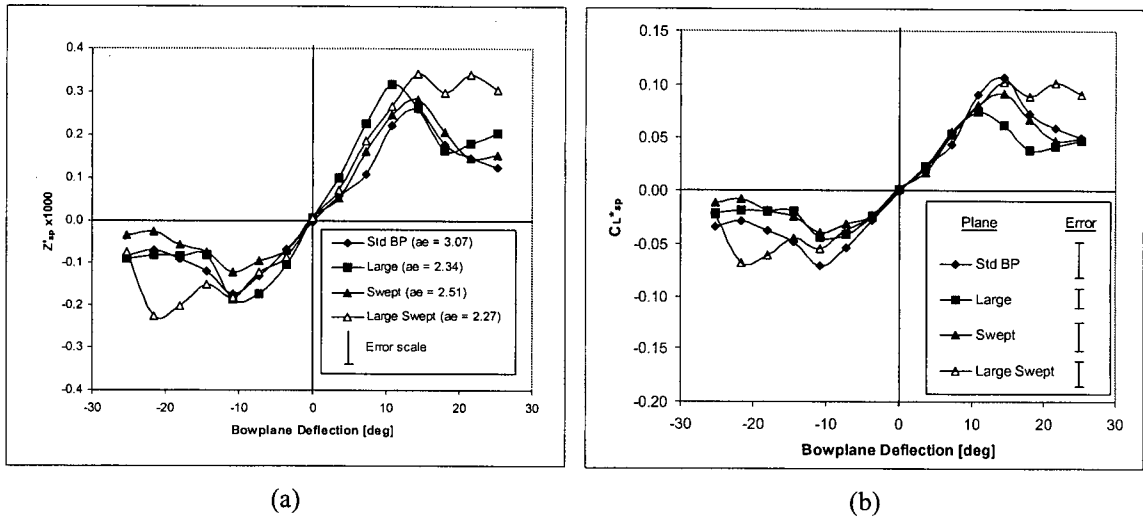


Figure 3-40 Bowplane geometry influence on sternplane force interaction for large planes: (a) Z_{sp}^* versus bowplane deflection; (b) $C_{L^*_{sp}}$ versus bowplane deflection

As with changes to bowplane geometry, the interaction force measured on the sternplanes increased with increased sternplane planform area. As shown in Figure 3-41 (a), the interaction force for the larger planes (*swept*, *large*, and *large swept*) was greater than the *standard* plane; however, when the interaction force was non-dimensionalized by sternplane planform area, the largest interaction was found with the *standard* plane and the smallest interaction with the *large* plane. In other words, although the bowplane-sternplane interaction force increased with sternplane size, the increase was not as large as the near proportional increase noted for the bowplanes.

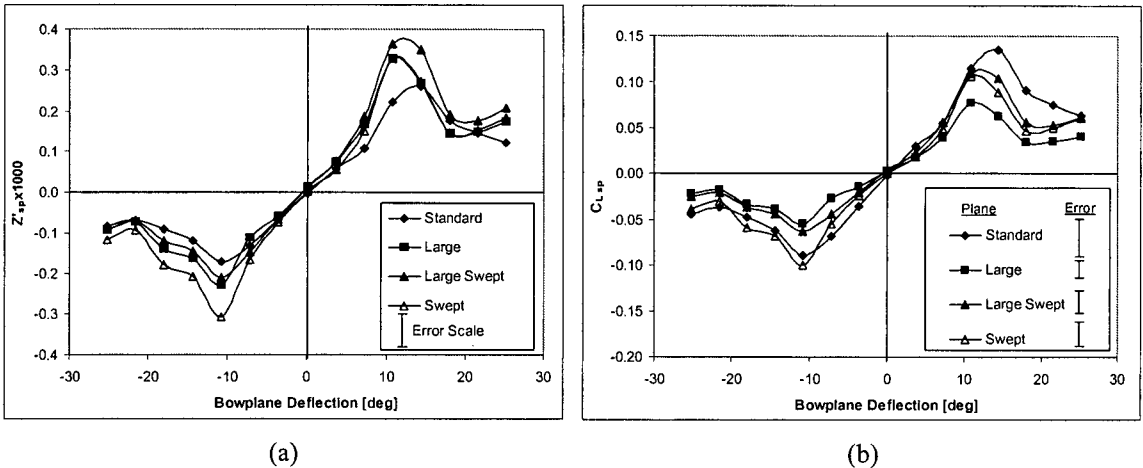


Figure 3-41 Sternplane geometry influence on sternplane force interaction: (a) Z_{sp}^* versus bowplane deflection; (b) $C_{L^*_{sp}}$ versus bowplane deflection

Finally, the effect on bowplane-sternplane interaction of the endplates added to the *short* bowplanes was examined. As was shown in Figure 3-16 on page 60, the endplates had limited effect on the force production by the bowplanes. The interaction force on the sternplanes is shown in

Figure 3-42 to which the bowplane endplates appear to have limited influence other than a localized decrease in interaction near the bowplane stall angle for negative deflection. Thus, the reduction in bowplane tip vortex strength as claimed by Talay (1975) appears to be a local phenomenon.

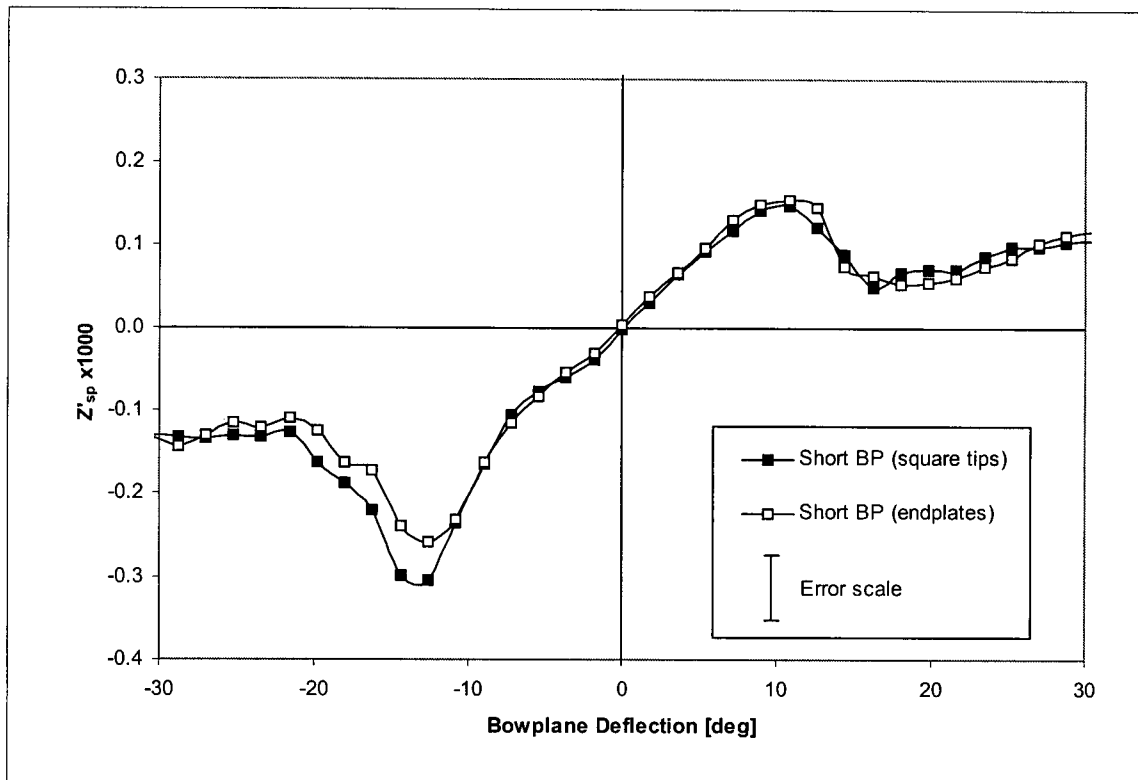


Figure 3-42 Influence of endplates on the *short* bowplanes on bowplane-sternplane interaction

Plane Location Influence

The bowplane-sternplane interaction was more strongly influenced by changes to the location of the planes on the hull than by the geometry of the planes. Limited flow bubble path visualization was used to evaluate alternate bowplane configurations followed by extensive direct force measurement for a wide range of plane arrangements.

The helium bubble path flow visualization technique was used for the anhedral bowplanes in several trim angles. Figure 3-43 shows the path of the bowplane tip vortices for the *anhedral* bowplanes in straight and level flight. In comparison to the *standard* bowplanes (Figure 3-35 on page 75), there is greater separation between the bowplane tip vortices and the sternplane with the *anhedral* configuration. Similarly, while the tip vortex map for the *standard* configuration bowplanes suggests stronger interaction for positive bowplane deflections, Figure 3-43 suggests that the interaction for the *anhedral* planes will be stronger for negative deflections.

The plane locations considered in force measurement testing included bowplanes in the *standard*, *high*, *centreline*, *anhedral*, and *dihedral* positions and sternplanes in the *standard*, *Y-Tail*, and *Inverted-Y* positions (with reference to Table 3-3 on page 46). As indicated previously, with changes to bowplane position the sternplanes were held in the *standard* location and *visa versa*.

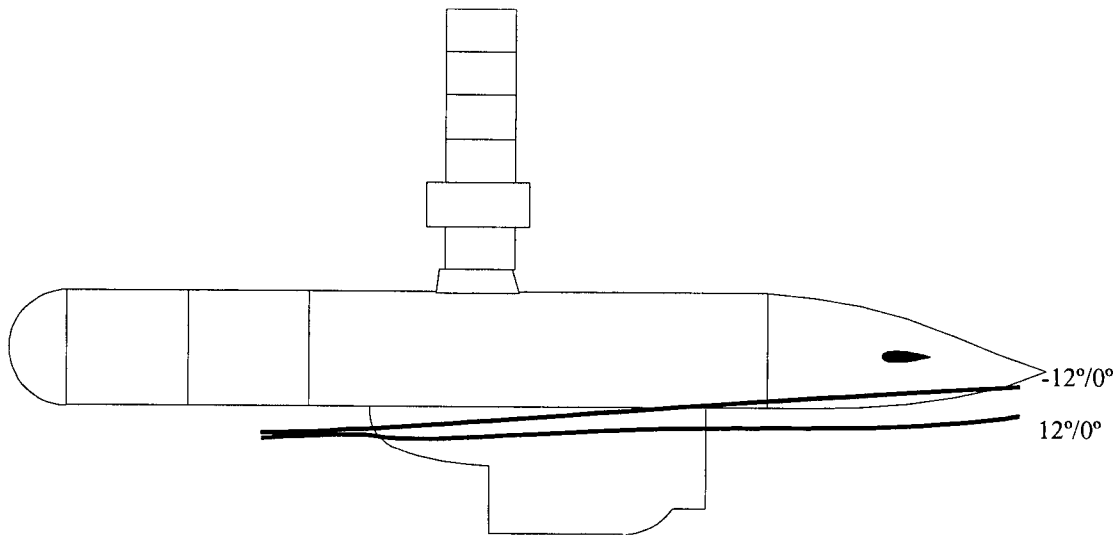


Figure 3-43 Helium bubble path schematic for anhedral bowplanes in straight and level flight

The interaction force plotted against bowplane deflection is shown in Figure 3-44 for the different bowplane configurations. Most notably, the *anhedral* and *dihedral* configurations show significantly reduced interaction compared to the three configurations near the centreline (*standard*, *high*, and *centreline*). As was suggested by the helium bubble path visualization, the *standard* configuration shows greater interaction compared to the *anhedral* configuration and the largest interactions in each case occur for positive and negative deflections respectively. In addition to providing detailed information regarding the performance of specific bowplane locations these results demonstrate the value of the simple tip vortex mapping in qualitatively predicting bowplane-sternplane interaction.

Figure 3-45 shows the bowplane-sternplane interaction for two alternate sternplane locations. The *Y-tail* and *Inverted-Y* were similar to the *anhedral/dihedral* bowplanes in alignment and also resulted in significant reduction in bowplane-sternplane interaction. Although flow visualization was not conducted in either of these cases, the bowplane tip vortex path from Figure 3-35 on page 75 suggests that the reduced interaction is due to increased separation between the sternplane and the vortex.

3.3.2 Non-Zero Trim

Analysis of the bowplane-sternplane interaction for non-zero trim was conducted in the same manner as for straight and level flight. Helium bubble path visualization was again used for several plane configurations while direct force measurements were used for a more comprehensive selection of configurations.

Helium Bubble Path Visualization

Schematic diagrams of the bowplane tip vortex path for the *standard* configuration are shown in Figure 3-46 (a) and (b) for trim angles of +6 and -6 degrees respectively. Through the proximity

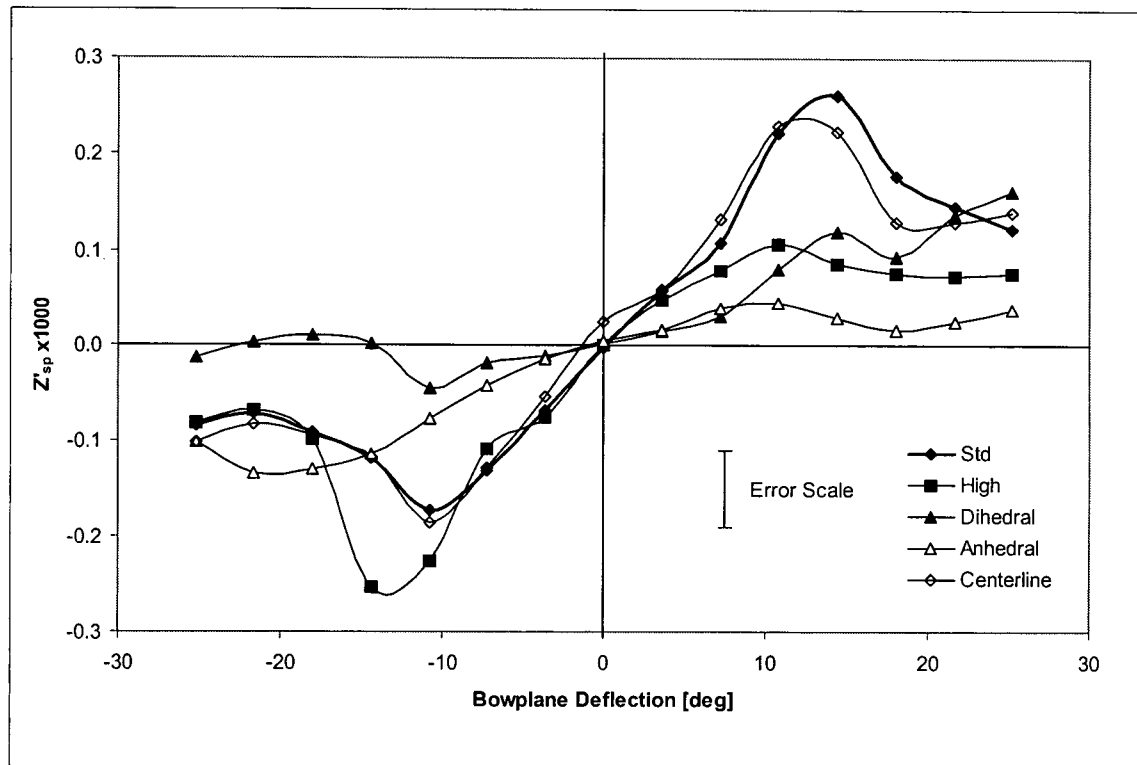


Figure 3-44 Bowplane-sternplane interaction dependence on bowplane position

of the tip vortex to the sternplanes, the flow visualization demonstrates that there is still potential for adverse bowplane-sternplane interaction even at trim angles as large as 6 degrees.

Similar schematic diagrams are shown for the *anchedral* configuration at +6 and -6 degrees in Figure 3-47 (a) and (b) respectively. The flow visualization suggests that interaction will remain small for *anchedral* bowplanes with negative trim angles but the interaction may increase for positive trim angles approaching 6 degrees.

Baseline Configuration Force Measurement

With the planes in the standard location, the bowplane-sternplane interaction was measured for changing vehicle trim angle. Figure 3-48 shows the sternplane force for trim angles ranging from -10 to +10 degrees in 2 degree increments. As the incident flow onto the sternplanes changes with trim, the various curves are shifted vertically; however, since the force is plotted as a function of bowplane angle, the interaction for each curve is characterized by the *change* in force with bowplane deflection. It is apparent that the interaction is less significant for larger trim angles as the variation from the average value of each curve becomes increasingly smaller. This result is more clearly demonstrated in Figure 3-49 where the ratio of the bowplane-sternplane interaction curve slope to the bowplane lift curve slope is plotted versus trim angle. The slopes were computed over the range of bowplane deflections from -7.2 to +7.2 degrees. The largest interaction between the planes is measured for +2 degrees trim (not zero) which can be attributed to the below-centreline position of the bowplanes. As shown in the figure, the interaction quickly diminishes with trim

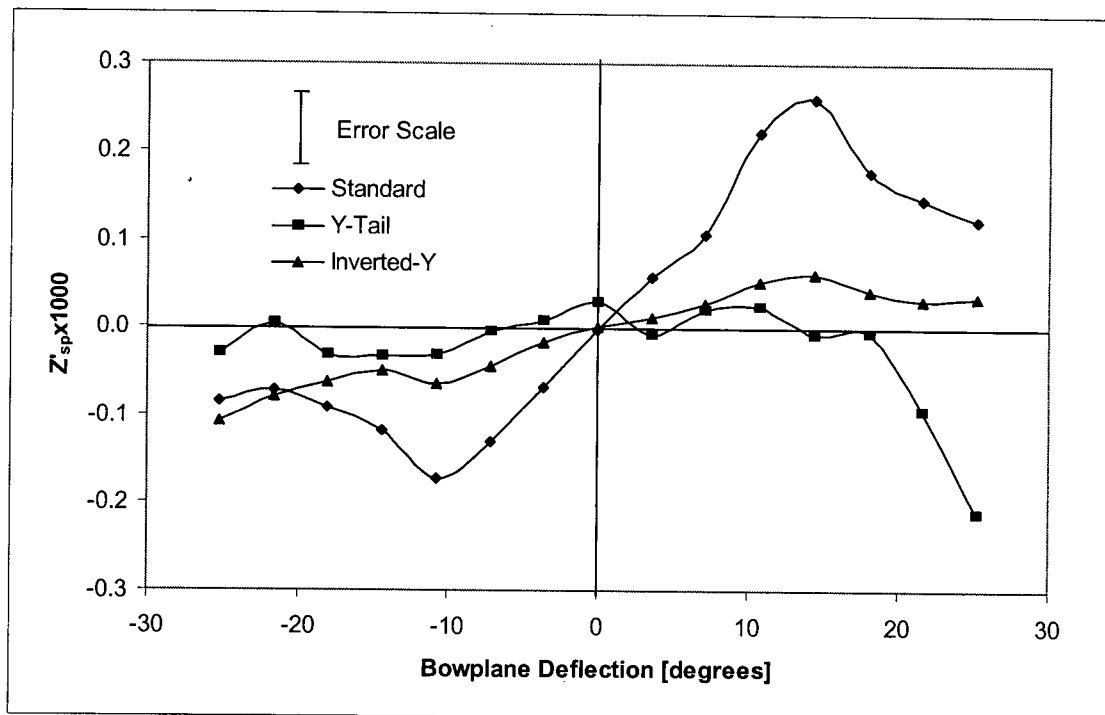
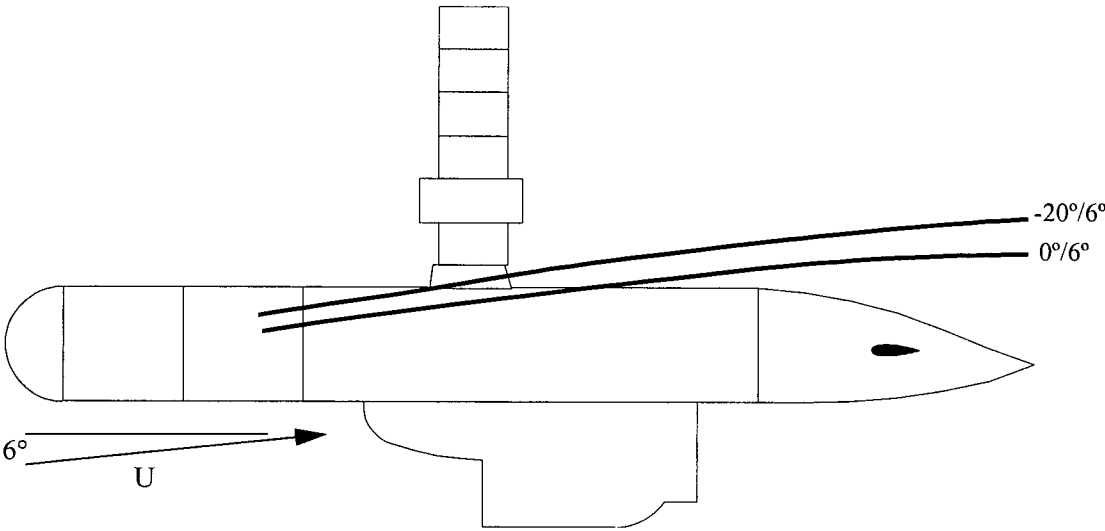
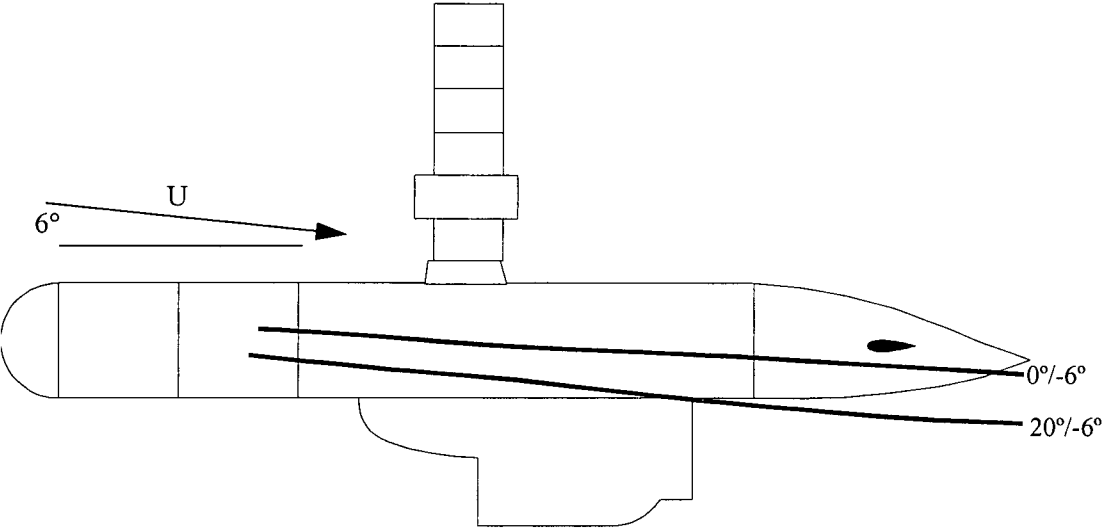


Figure 3-45 Bowplane-sternplane interaction dependence on sternplane position

angle and reaches approximately 5% or less of the bowplane lift curve slope for trim angles of approximately 10 degrees.



(a)



(b)

Figure 3-46 *Standard* configuration vortex path: (a) +6 degrees trim; (b) -6 degrees trim

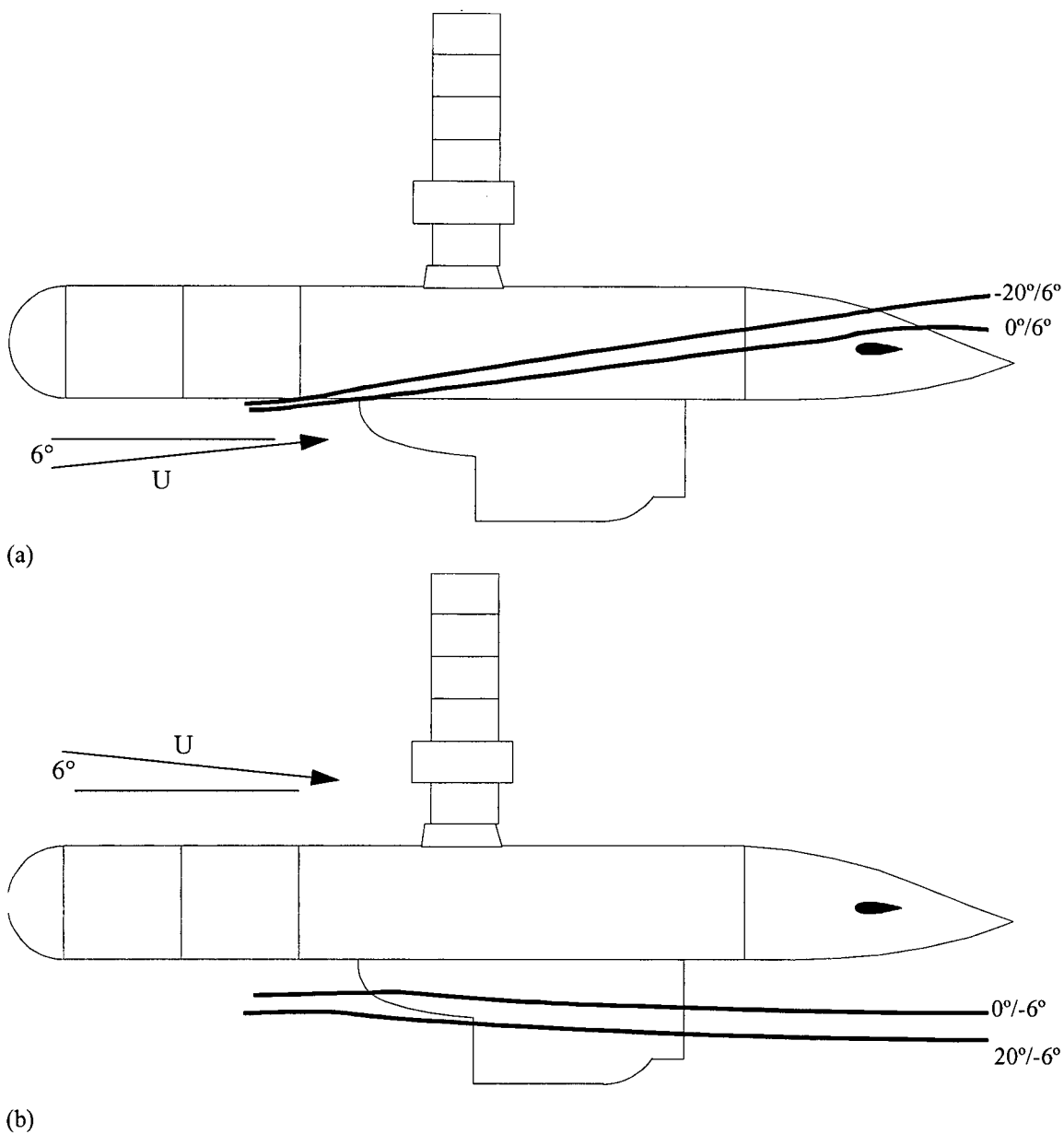


Figure 3-47 Anhedral configuration vortex path for (a) +6 degrees trim; (b) -6 degrees trim

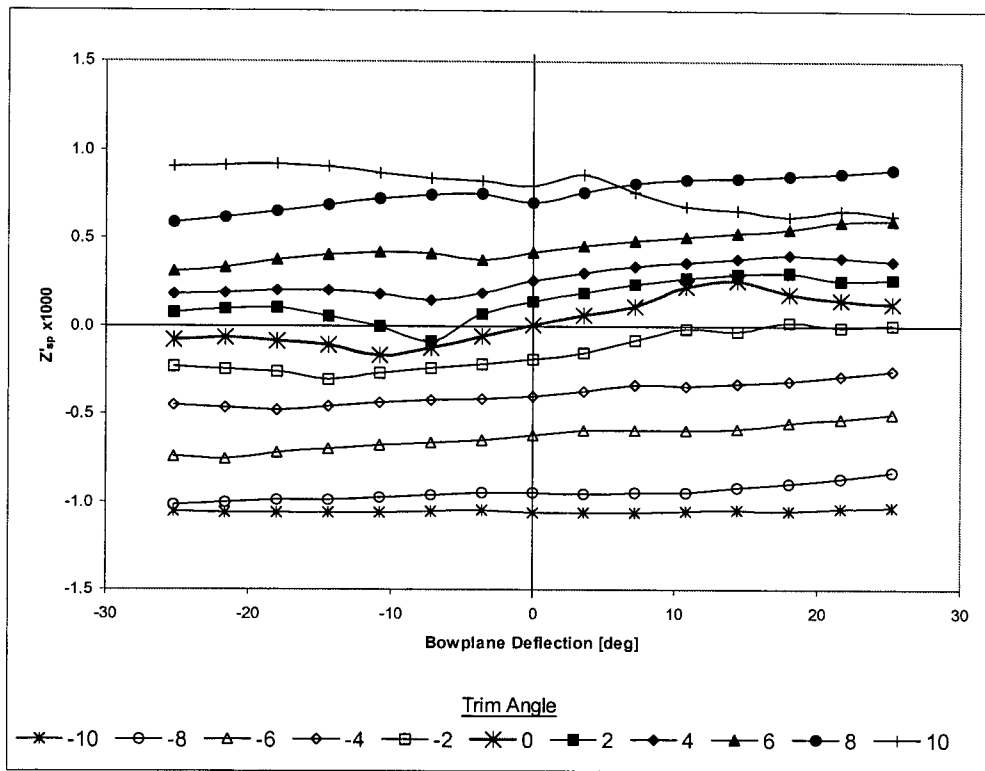


Figure 3-48 Interaction force on *standard* sternplane as a function of trim angle

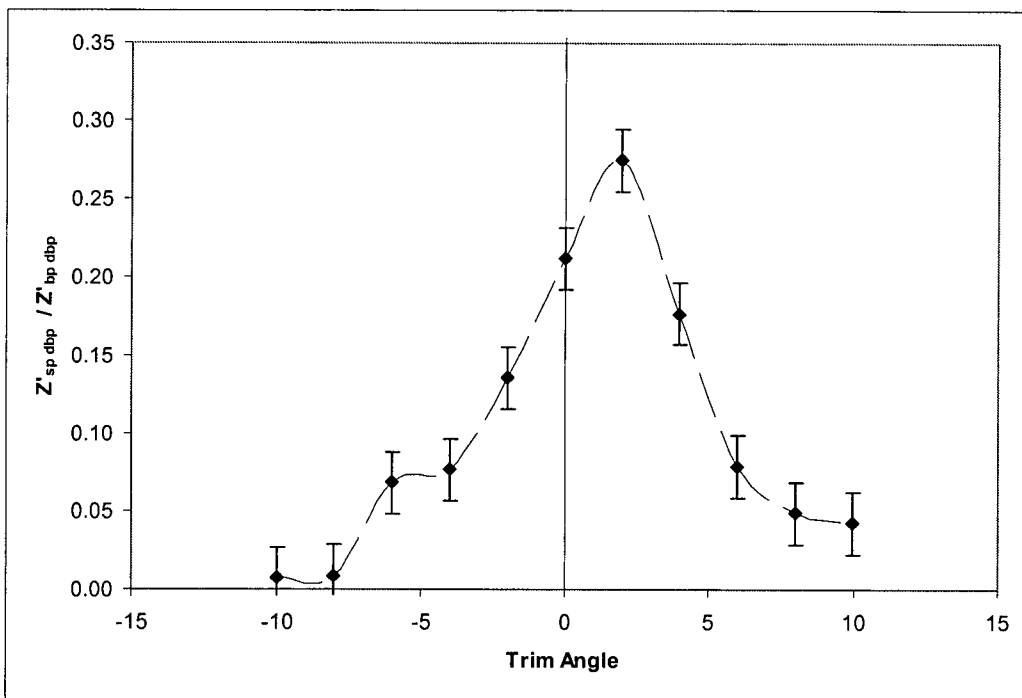


Figure 3-49 Ratio of bowplane-sternplane interaction curve slope to bowplane lift curve slope

Plane Location Influence

With the *anhedral* bowplanes in place of the *standard* bowplanes, the interaction force measured on the sternplanes as a function of trim angle is shown in Figure 3-50. The strongest interaction is noted for +6 degrees trim and there is comparatively little interaction at -6 degrees trim; these findings correspond to the bowplane tip vortex mapping that was shown in Figure 3-47.

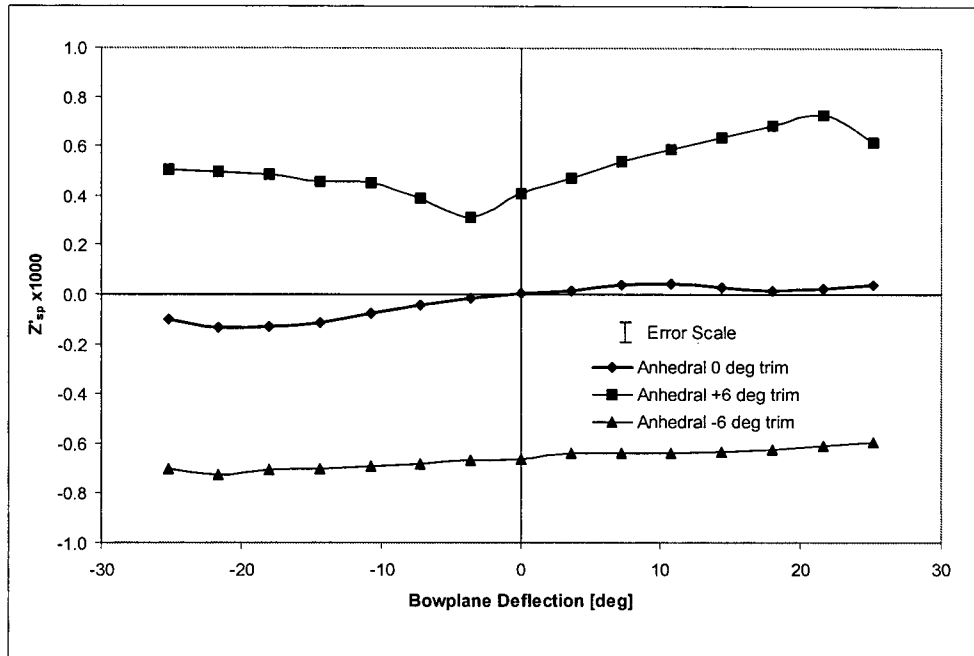


Figure 3-50 Interaction force from *anhedral* bowplane on sternplane as a function of trim angle

3.3.3 Non-Zero Yaw

The final aspect of the bowplane-sternplane interaction that was examined was the influence of vehicle yaw. Experimental data was collected by Dominguez (2000) through wind tunnel testing with the 1/4-scale model. The interaction force to bowplane deflection slope, normalized by the slope for straight and level flight, is shown as a function of yaw angle representative of the port sternplane in Figure 3-51. Data from both sternplanes was used to form the curve; negative yaw angles from the starboard sternplane were averaged with the corresponding positive angles from the port plane. The error bars are based on the standard error in the computation of the slopes.

Similar to the observation with trim, the bowplane-sternplane interaction quickly diminished with increasing yaw. With the *standard* configuration, the strongest interaction was observed for zero degrees yaw. Interestingly, for yaw angles greater than roughly 8 degrees in magnitude, the interaction force and the force on the bowplanes were oriented in the same direction (under normal conditions, the bowplane and interaction force on the sternplanes are oriented in opposite directions).

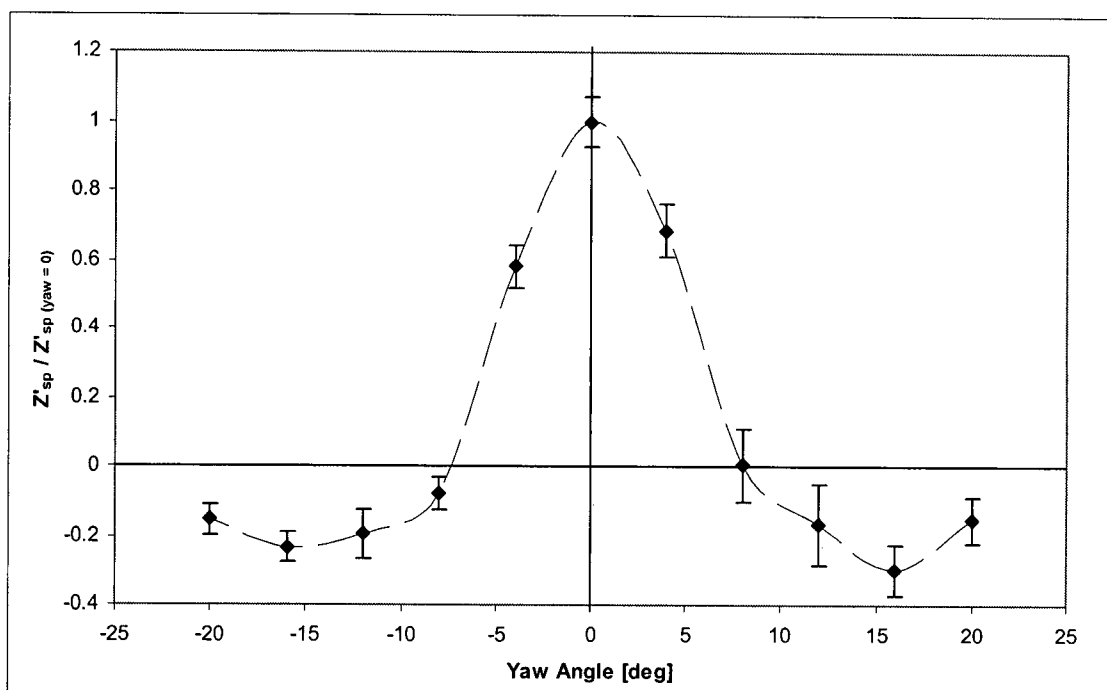


Figure 3-51 Slope ratio of averaged sternplane interaction to bowplane lift curves versus yaw angle

3.4 FREE SURFACE INTERACTION

The wave conditions encountered by an AUV in practice are random in nature and classified by a statistically determined sea state. By the principle of superposition (see, for example, Tipler, 1991, or Journée, 2001), it is possible to replicate the irregular sea conditions by summing a series of regular waves (that is, sinusoidal waves with well defined frequency and amplitude). In order to determine the effect of the free surface and waves on plane performance, tests were conducted in the towing tank using the instrumented quarter-scale model in regular waves. Time series data were examined using fast Fourier Transform (FFT) analysis. The relationship between wave geometry and the force on the control surfaces was examined in terms of vehicle depth, speed, and plane position.

3.4.1 Wave Geometries Tested

Wave frequencies of 0.4, 0.6, 0.8, and 1.0 Hz were used and corresponded to wavelengths of $4.57 l$, $2.00 l$, $1.14 l$, and $0.73 l$ respectively (where the wavelengths have been non-dimensionalized by vehicle length). Nominal wave heights included $0.011 l$, $0.024 l$, $0.0417 l$, and $0.0714 l$ (corresponding to 2.5, 5, 9, and 15 cm respectively). These wavelengths and amplitudes roughly span the range of well formed regular waves obtainable in the tow tank facility. For the maximum wavelength of $4.57 l$, only the $0.011 l$ amplitude waves were used as other amplitudes resulted in non-sinusoidal waves.

The wavelengths tested at the tow tank are substantially below those encountered in sea state 3. (From Section 2.6.3 on page 38, the most probable wave period is 7.5 seconds which corresponds to a wavelength of 88 m in full scale, or 22 m for the 1/4-scale model.) As vehicle depth is determined using pressure sensors (Field, 2000), at wavelengths greater than several vehicle lengths the vehicle will track the wave profile rather than maintain constant depth with respect to the calm water free surface. Therefore, in terms of influence on the control surfaces on DOLPHIN, the most significant waves are those of length of the same order of magnitude or less than the vehicle and with maximum wave orbital velocity at the depth of the control surfaces. The wave orbital velocity is a function of both depth and wavelength (see Section 2.6.2) and is illustrated in Figure 3-52 for $0.011 l$ amplitude waves. In the figure, the range of wavelengths considered for this thesis is indicated and, as shown, roughly covers the maximum expected wave influence over operating depths.

3.4.2 Wave and Control Surface Force Spectra

In the tow tank tests, force data was collected from each of the planes along with carriage speed and wave height (measured using a capacitance-style wave probe). Typical data for the bowplane force and wave amplitude is shown in Figure 3-53 over a seven second window for a forward speed of 1 m/s and a depth of one hull diameter (to the centreline). Note that the force and wave amplitude share the same graph but use different vertical axes. The general agreement between the signals is good—they have similar overall responses with similar dominant frequencies—although the force signal shows more noise and a phase delay of approximately one-quarter cycle. The phase delay can be largely attributed to differences in longitudinal position and time response of the force transducer and wave probe.

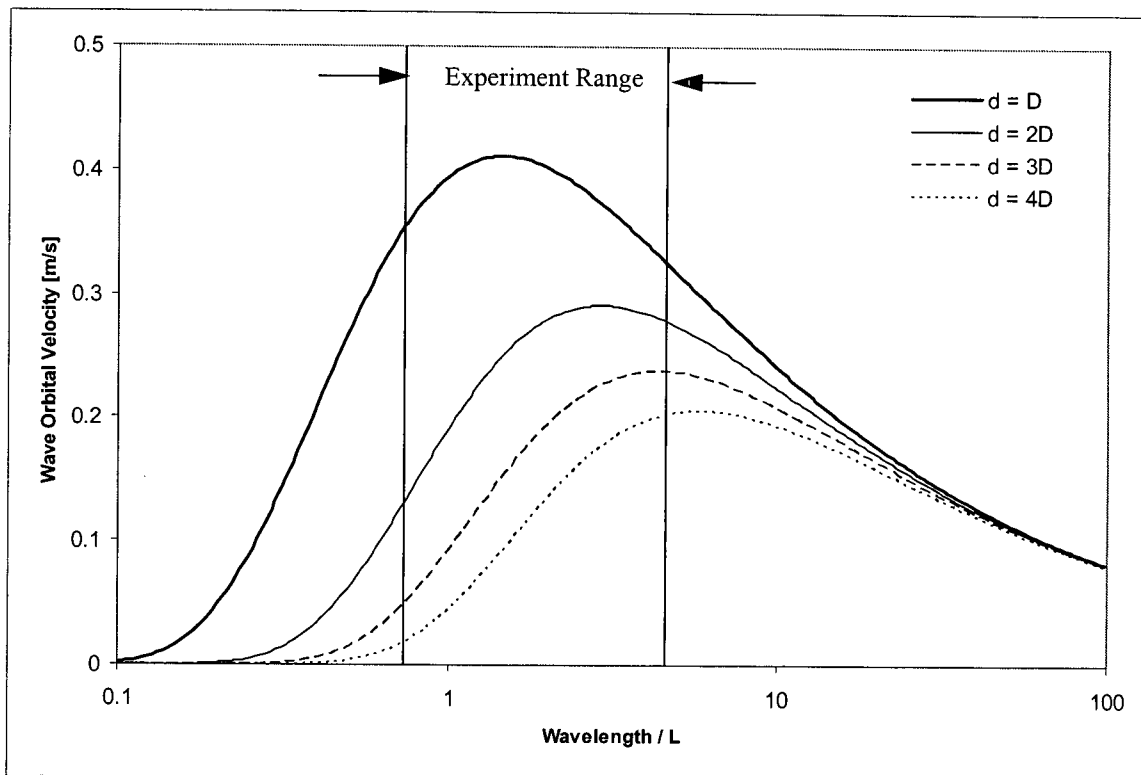


Figure 3-52 Dependence of wave orbital velocity on depth and wavelength

The time series data is shown in spectral form in Figure 3-54 from the FFT analysis (again using different axes for the wave amplitude and plane force). The peaks from the wave amplitude and plane force are sharp, very well defined, and almost indistinguishable (both indicating a dominant frequency of 1.26 Hz). The peak frequency amplitudes of 0.484 for Z_{bp} and 0.0155 for the wave height also agree well with visual observations from Figure 3-53. By using spectral analysis, signals were effectively averaged over a large number of cycles and the complications introduced by phase shift and noise observed in the time series data were avoided. Subsequent findings are based on the peak values obtained from the dominant frequencies found in the FFT analysis.

3.4.3 Wave Geometry Influence

The effect of the wave amplitude and wavelength on the oscillatory forces on the planes was measured using the quarter-scale model held stationary in the tow tank. The vehicle depth during these experiments was 1.5 hull diameters ($0.174 l$) as measured from the calm water line to the hull centreline. A 3×3 test matrix consisting of three wavelengths and three wave amplitudes, plus one additional point, was used. Wavelengths of $0.73 l$, $1.14 l$, and $2.00 l$ with nominal wave heights of $0.024 l$, $0.0417 l$, and $0.0714 l$ were used. An additional test point was added with $4.57 l$ wavelength and $0.011 l$ wave amplitude; again this combination represented the low frequency limit of the wave generation equipment at the tow tank. In all cases, the exact wave amplitudes were measured using a capacitance wave probe with the *FFT* method outlined above.

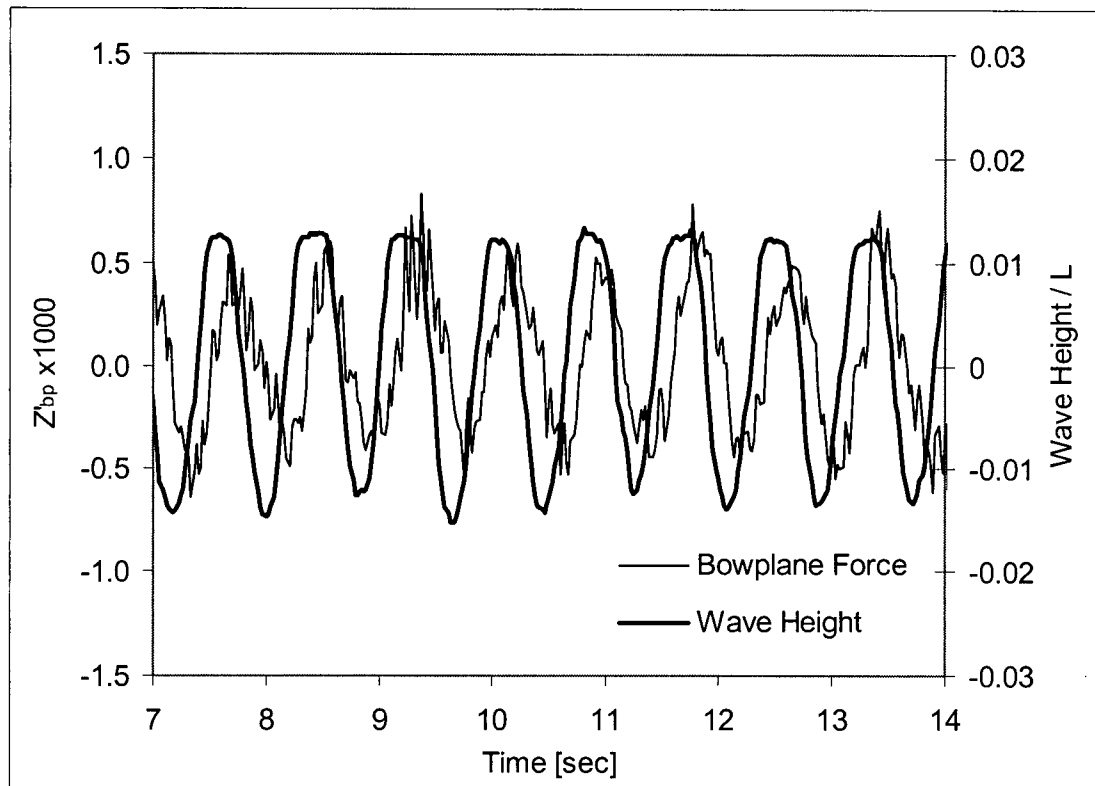


Figure 3-53 Wave height and bowplane force trend chart

The results of the wave geometry tests are shown in Figure 3-55. The wave amplitude, a , has been non-dimensionalized by the vehicle length and the plane forces, Z_{wave} have been non-dimensionalized by density, ρ , gravity, g , and the vehicle length as:

$$Z'_g = \frac{Z_{wave}}{\frac{1}{2}\rho g l^3} \quad (52)$$

Furthermore, so as to compare all data on a single graph, the sternplane forces have been scaled by the bowplane to sternplane planform area ratio. Data is not shown for the bowplanes with the 15 cm nominal wave amplitude test due to a fault that occurred in the instrumentation. A least squares best-fit line has been added to the figure and suggests that the oscillatory force on the planes is primarily a linear function of the wave amplitude with little influence from wavelength for the range of wave slopes considered. For comparison to previous data, the maximum force a bowplane would generate when moving at 1 m/s in water corresponds to $Z'_g \approx 50 \times 10^{-6}$.

The linear dependence of the plane force on wave length and amplitude was examined using a statistical analysis of variance (ANOVA). The key parameter of the ANOVA output is the F -ratio, or simply F , which indicates whether a trend in data is significant enough to be related to a particular variable or if it can simply be attributed to measurement error. Based on the number of samples, a critical F value is computed; if the F of a particular variable is greater than $F_{critical}$, then the

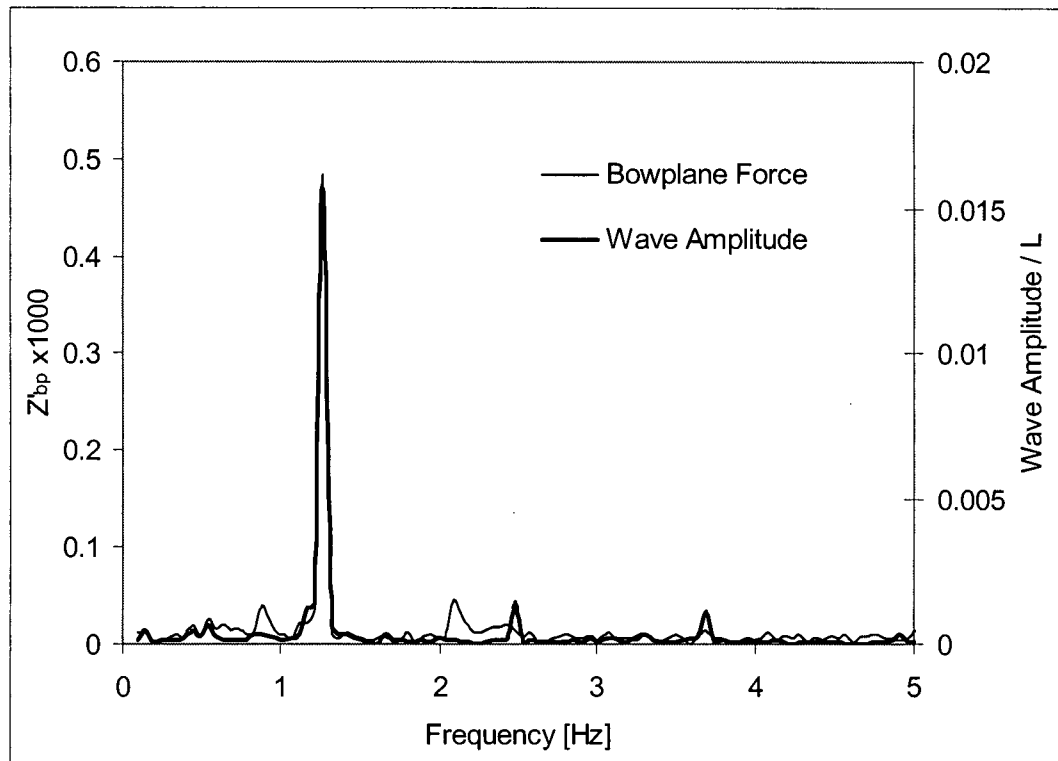


Figure 3-54 Wave height and non-dimensional bowplane force FFT spectra

effects of the variable are considered to be significant, otherwise effects are attributed to noise. Further information regarding the ANOVA technique can be found in any standard statistical analysis text (such as Hogg and Ledolter, 1992, or Spiegel, 1992).

Considering plane force as a function of wave length and wave amplitude, the ANOVA results are given in Table 3-5 as based on a 95% level of confidence. The F -value for the plane force dependence on wavelength is below the critical value ($4.4 < 5.7$) while the F -value for wave amplitude is well above the critical value ($154.9 \gg 5.7$). In other words, there is a very strong relationship between wave amplitude and the force on the planes while the influence of wavelength is statistically insignificant. This is not to suggest that in general wavelength does not affect the force on the planes—there is a clear relationship in Figure 3-52—but rather it indicates that there was little change in performance for the range of wavelengths considered in the experiments. Likewise, the

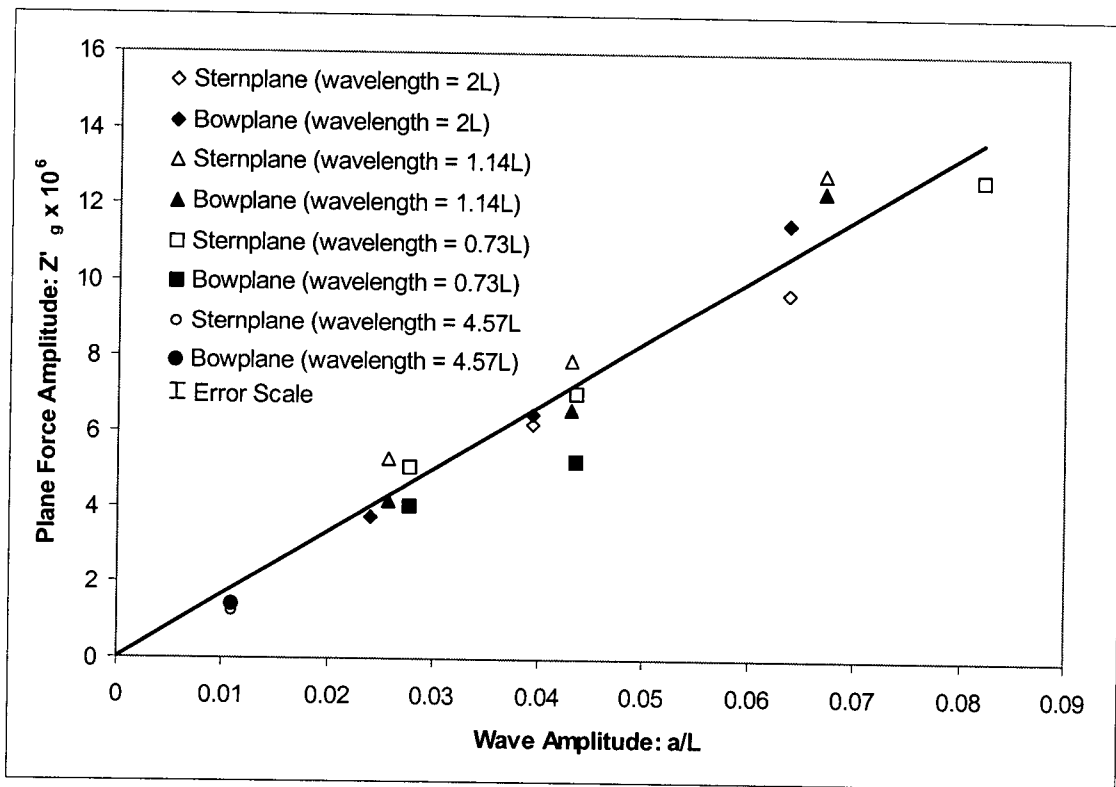


Figure 3-55 Wave induced plane force dependence on wave amplitude

F -value associated with the interaction between wavelength and wave amplitude is well below the associated critical value indicating that the interaction is also statistically insignificant.

Table 3-5 ANOVA for wave force to wave geometry

Source	F	F critical
wavelength	4.4	5.7
wave amplitude	154.9	5.7
interaction	1.2	4.1

3.4.4 Depth Influence

The influence of depth was examined in both calm water and for various wave conditions. The calm water tests were conducted at speed while the tests with waves were conducted with the model held stationary.

Calm Water Tests

Due to the proximity of the hull to the free surface, the flow field about the control surfaces is not necessarily like that for deep water (equivalent to the wind tunnel tests). Tests were conducted in calm water at various depths in order to determine the surface influence at shallow depths. Depths

of 1, 2, and 3 hull diameters measured from the free surface to the hull centreline were considered. The resulting force to deflection curves for the bowplanes are shown in Figure 3-56.

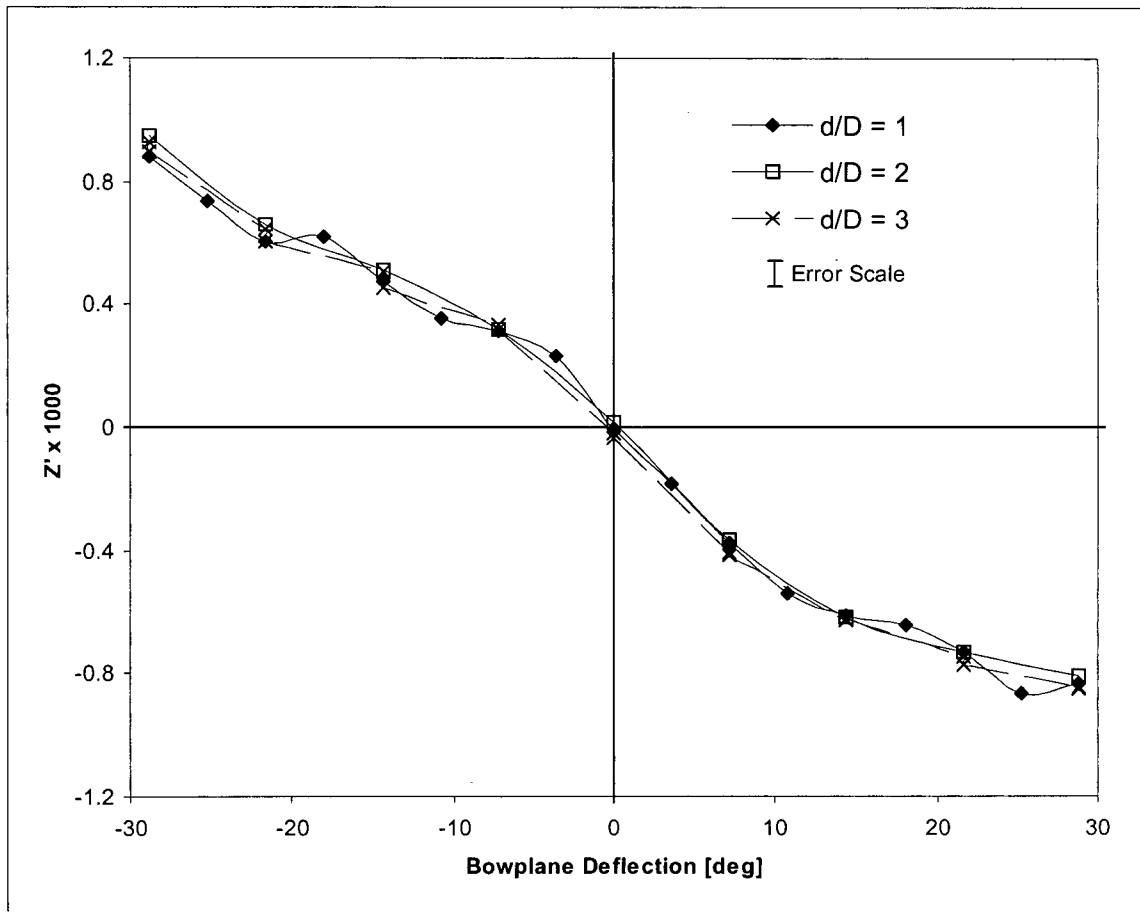


Figure 3-56 Plane performance dependence on hull depth in calm water

Unfortunately, after the tests were conducted, it was discovered that boundary layer trips were not correctly installed on the planes. The result was a much more gradual stall with earlier onset; in short, the force to deflection curves were different from those measured previously in the wind tunnel and subsequently in the tow tank. However, on average, the three curves agree with each other to better than 0.75% of the full-scale range. Furthermore, the maximum difference between any two measurements was only 0.07 units of Z' (3.8% of full-scale) while the measurement accuracy was 0.04 units of Z' . This similarity within the curves from Figure 3-56 strongly suggests that the calm water free surface effect on the planes is negligible over typical operating depths.

These findings agree with results for submerged rectangular flat plates reported by Wadlin et al. (1955) and provided in Section 2.6.1 on page 38. Wadlin et al. concluded that for depths greater than 0.85 chord lengths, the surface effect is negligible. For comparison with the DOLPHIN, a depth of 1 hull diameter corresponds to 2.9 chord lengths.

Wave Influence at Depth

The influence of vehicle depth on the wave-induced force on the planes was examined primarily using a stationary model in the tow tank. The wave amplitude for these tests was approximately $0.042 l$ and the wavelength was approximately $1.14 l$ (corresponding to a frequency of 0.8 Hz). Figure 3-57 shows the dependence of the wave force amplitude on the bowplanes in terms of vehicle depth, d , measured from the hull centreline to the calm water line. The depth has been non-dimensionalized by the hull diameter, D . The best-fit curve shows the expected exponential form:

$$Z = C_0 e^{-\frac{4\pi d}{\lambda}} \quad (53)$$

For the wave geometry considered, there was over a four-fold reduction in the wave force at 3.5 hull diameters depth compared to that at 1.5 hull diameters depth. The data for the depth of $d/D = 0.5$ did not agree well with the exponential fit however significant interference was introduced by waves breaking over the exposed hull at that depth. The comparison between experimentally and analytically derived wave forces is examined in detail in Section 4.7.

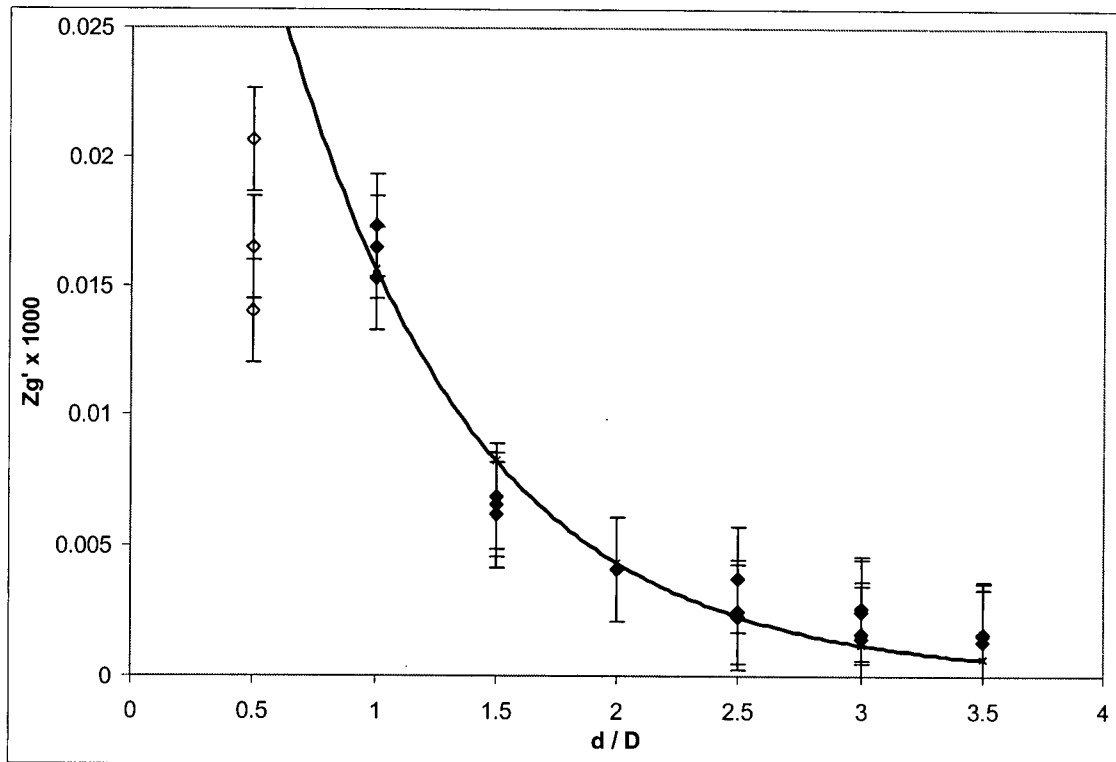


Figure 3-57 Wave induced force amplitude as a function of hull depth

3.4.5 Speed Influence

The influence of forward speed of the vehicle on the wave induced force on the bowplanes was examined for the speed range obtainable in the tow tank. For all tests, waves with $0.016 l$ amplitude and $1.14 l$ wavelength were used. Figure 3-58 shows the force amplitude plotted against

Froude number for depths of 1.5 and 3.5 hull diameters. The wave force amplitude is nondimensionalized in the standard form using forward speed:

$$Z' = \frac{Z}{\frac{1}{2}\rho U^2 l^2} \quad (54)$$

where the Froude number is defined as:

$$Fr = \frac{U}{\sqrt{gl}} \quad (55)$$

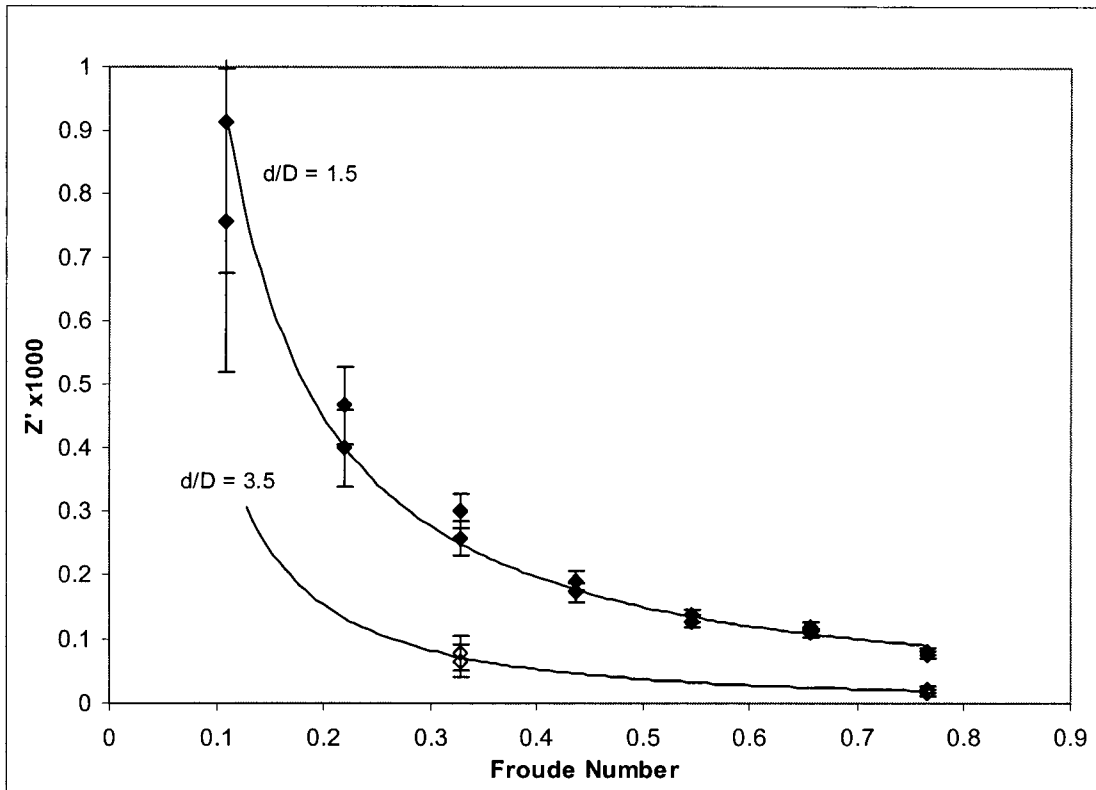


Figure 3-58 Wave induced force on bowplanes versus Froude number

There is a dramatic reduction in the wave influence with speed. This is to be expected since the wave orbital velocity (constant in this case) represents a smaller proportion of the total velocity on the planes at higher forward speeds.

For Froude numbers of 0.33 and 0.77, tests were conducted at both 1.5 and 3.5 hull diameters depth. The wave induced force at the 3.5 hull diameter depth for these two speeds was 26% and 25% respectively of that at the 1.5 hull diameter depth. For the stationary model tests (Section 3.4.4), the ratio of plane force for 3.5 to 1.5 hull diameters depth was 23%. This favorable comparison suggests that the best fit form of wave induced force versus depth from the stationary tests (Figure 3-57) is valid over typical speeds.

3.4.6 Bowplane Position Influence

The effect of relocating the bowplanes was studied using the stationary model with waves of varying wavelength and 9 cm (0.0417 L) nominal amplitude. Tests were conducted using the standard bowplane configuration along with the bowplanes in the anhedral position (angled 30 degrees downward.) Figure 3-59 shows the wave induced force amplitude on the bowplanes as a function of the incoming wavelength. The maximum wavelength examined was extended beyond that of previous experiments; however, the wave amplitude in those cases was necessarily decreased to prevent generation of non-linear waves. The non-dimensionalized plane force was subsequently normalized by the non-dimensional wave amplitude, a/l , to account for wave amplitude variation between trials. The normalization justified by the near-linear behavior of plane force with wave amplitude (as demonstrated in Figure 3-55)

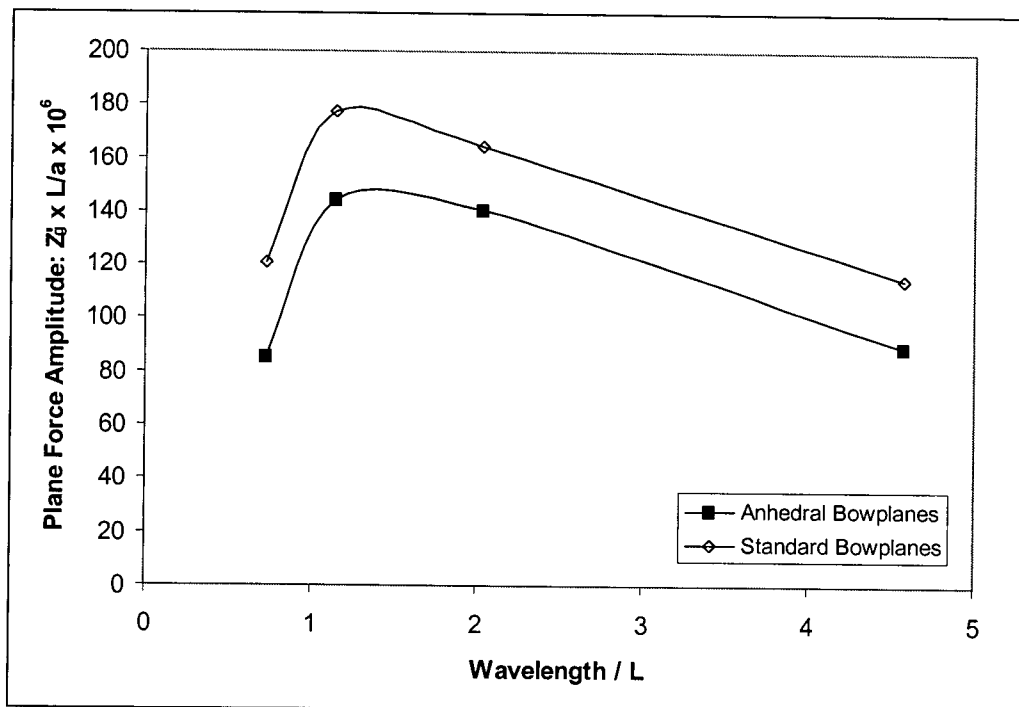


Figure 3-59 Influence of bowplane position on wave induced plane forces

For the range of wavelengths studied, the *anhedral* bowplanes consistently show less wave induced force as compared to the *standard* bowplanes. This can be partially attributed to the downward inclination of the anhedral planes in that the exposed plane area is reduced when viewed from above. Figure 3-60 shows the ratio of wave amplitude force on the *anhedral* planes to that on the *standard* planes with a correction for horizontal planform area. That is, the forces have been non-dimensionalized by the exposed control surface area in the x - y plane such that the wave induced forces on the *anhedral* planes from Figure 3-59 have been increased by $1/(\cos\beta)$ (where β is the anhedral angle). This is approximately equivalent to an increase in the span of the *anhedral* planes by $1/(\cos\beta)$; even for this condition, the wave induced forces remain smaller on the *anhedral* planes than the *standard* planes for all free surface conditions that were used in the experiments.

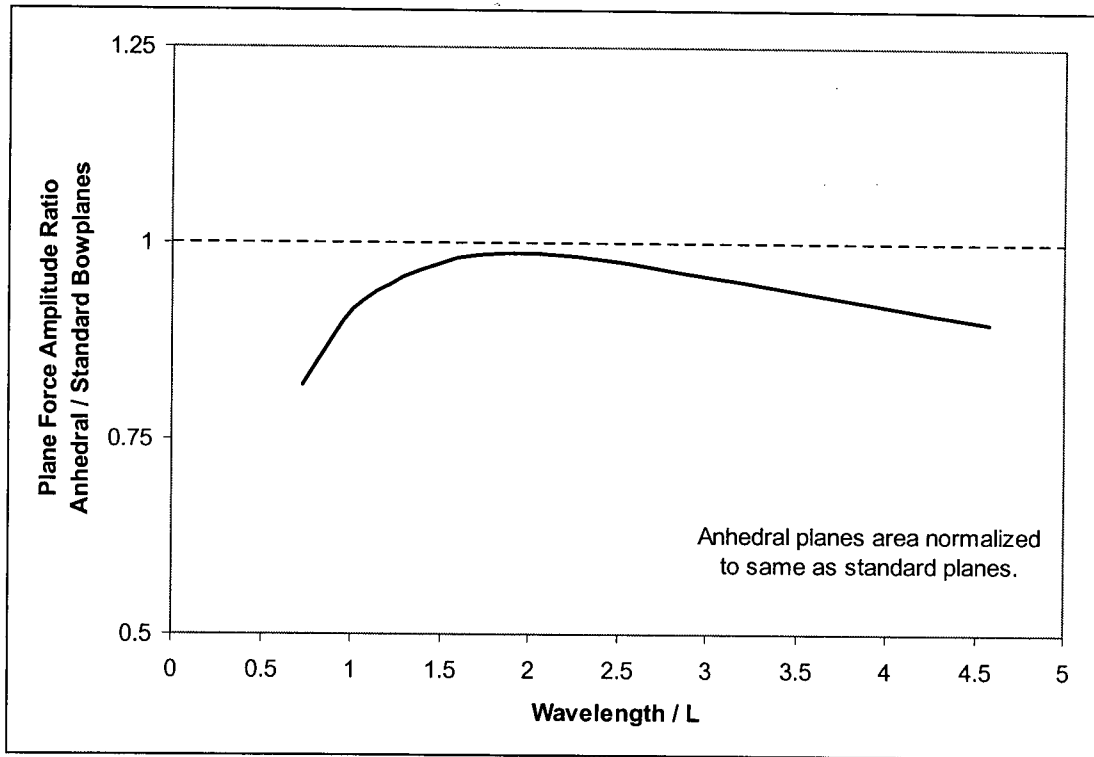


Figure 3-60 Ratio of wave induced force normalized by horizontal planform area on *anhedral* bowplanes versus *standard* bowplanes

3.5 SUMMARY

In this chapter, the experimental findings from both wind tunnel and towing tank tests were discussed. Following a discussion of the experimental hardware and facilities, the following observations were presented:

Straight and Level Flight

- a body mounted plane has similar (though slightly less linear) force versus deflection behavior compared to an isolated appendage
- oil film visualization indicates a gradual increase in the separated flow region on bowplanes for deflections well below stall angle and a sudden increase in separation near the plane root for deflections close to stall
- plane geometry was found to influence force generation but the effect was associated mainly to the change in the control surface planform area
- the mounting location of the bowplanes on the hull was found to have little effect on their performance in straight and level flight in calm water

Bowplane Sternplane Interaction

- bowplane tip vortices were identified through bubble path visualization and found to pass very near sternplanes in some cases
- bowplane tip vortices were found to interact with the sternplanes resulting in a force on the sternplanes of 22% of the force on the bowplanes (for the standard configuration)
- the bowplane-sternplane interaction was somewhat dependent on plane geometry and highly dependent on plane location (both bowplane and sternplane)

Non-Zero Trim and Yaw

- yarn tuft visualization indicated significant changes in flow angle on the hull with trim
- the effect of trim on the bowplanes was to shift the force to deflection curves horizontally
- in yaw, the leeward planes showed improved performance while the performance of the windward planes deteriorated
- with increasing yaw or trim, the bowplane-sternplane interaction quickly diminished

Free Surface Effects

- there was negligible effect from the calm water free surface on the plane force based on tests over a range of depths
- there was a measurable effect from waves on the planes; the wave influence decayed exponentially with depth and increased almost linearly with wave amplitude
- the wave effect was less significant with increasing forward speed as the wave induced force represented a smaller component of the total force

4

CONTROL SURFACE HYDRODYNAMICS - MODELLING

Everything should be made as simple as possible, but not simpler.
- Albert Einstein

The design and development of an AUV is a costly and time consuming process and the use of modelling and simulation to predict and evaluate system performance is essential. The relevance of any such simulations depends on the accuracy and completeness of the models used. In some cases, (as noted by Watt, 1993, for example) small errors in modelling coefficients may significantly affect outcomes depending on how simulations are conducted. Field (2001) suggests that accurate determination of the hydrodynamic values is essential and represents the most demanding area of submarine modelling.

In general, as the closed-loop bandwidth of a control system is increased, greater precision is required in the model (Palm, 1986); conversely, the requirements on model accuracy are relaxed if the closed-loop bandwidth is decreased (Åström and Wittenmark, 1997). The need for mathematical descriptions that are accurate and complete suggests models of ever-increasing complexity; however, extremely complex models are cumbersome and difficult to implement. Thus, one of the goals of modelling is to represent a given system in a way that is as simple as possible while retaining all key performance characteristics. For this thesis, emphasis was placed on modelling the DOLPHIN using vehicle-specific experimental data.

This chapter builds on the experimental results from Chapter 3. It begins with a presentation of background information relevant to AUV modelling. The remaining sections use various analytical and numerical techniques to validate, predict, and mathematically describe the experimental findings from Chapter 3. In particular, attention is given to Reynolds number scaling effects, control surface performance prediction, the influence of trim and yaw on bowplanes, bowplane-sternplane interaction, and the interaction with waves and the free surface. The models developed will be used for closed-loop AUV control (Chapter 5) and simulation (Chapter 6).

4.1 BACKGROUND

There are several techniques commonly employed in AUV modelling including analytical methods, computational methods, system identification, and empirical methods. Perhaps the simplest of these are analytical methods which include development from physical laws and first principles, as given by (Nahon, 1996) or (Solberg, 1992) for example. Computational methods can also be employed, such as strip theory (see, for example, McTaggart et al., 1993), panel methods, (see Conway and Mackay, 1990, or Barlow et al., 1998), and even computational fluid dynamics approaches (McDonald and Whitfield, 1997, and Huyer, 2001). Due to the complexity, nonlinearity, and coupling in actual AUV systems, such approaches are often only useful for rudimentary analysis. Quite often, these techniques are employed initially and then later validated by experiment (such as with Hopkin, 1990.) Others, such as Caccia and Gianmarco (2001) use a combination of modelling and system identification with the general Newton-Euler motion equation for derivation of the dynamic model of an AUV.

System identification involves treating the plant as a black box and attempts are made to correlate the input-output behavior. There are various limitations in using system identification with AUVs including the presence of significant disturbances as well as the coupled, nonlinear plant behavior. As Cellier et al. (1996) note, identification of nonlinear systems in even noise-free environments is difficult to say the least. Recent advances in identification, such as nonlinear observers (Kim, 2002) and neurofuzzy identification (Bossley et al., 1999) show promise for use with AUVs and other nonlinear systems. Nonetheless, input-output information for a given AUV is usually not readily accessible either because it is not possible to consider all aspects of system performance or because the AUV being studied does not yet exist.

As such, empirical and semi-empirical methods form the basis for most modelling on AUVs. As was outlined in Chapter 3, experiments may be conducted in towing tanks, wind tunnels, or in open water. The data from the experiments is most often condensed, simplified, and generalized to some degree for use in simulation and prediction. For example, in the DREA Submarine Simulation Program (DSSP), plane forces and moments are expressed in terms of hydrodynamic coefficients (see Feldman, 1995); for DSSP, these coefficients were evaluated experimentally or derived from other semi-empirical sources (Mackay, 1993). Additionally, it is common practice to simplify modelling by considering the vehicle as a set of decoupled subsystems consisting of forward speed, roll, vertical plane motions, and horizontal plane motions (Lea et al., 1999). The unmodelled coupling effects that remain are assumed to be small and are treated as disturbances in application (see, for example, Healey and Lienard, 1993, or Jalving, 1994).

4.2 REYNOLDS NUMBER EFFECT MODELLING

As mentioned in Section 3.1, it was not possible to conduct experiments with the same Reynolds number for the model as for the full-scale vehicle. The major change in plane performance with Reynolds number was the angle at which stall occurred. Experimental data is examined below followed by the procedure used to scale this data to full-scale.

4.2.1 Change in stall angle with Reynolds number

The stall angle was determined from experimental data for a range of different Reynolds numbers. For this work, the control surface stall angle was defined as the smallest magnitude control surface deflection for which the first derivative of the Z force with respect to deflection became zero. In general, the stall angles for positive and negative deflection were not the same as the influence of the hull was not symmetric (the bowplanes were located below the centreline). The Reynolds numbers considered, based on vehicle length, ranged from 1 to 7 million; these correspond to chord-based Reynolds numbers of approximately 40 000 to 280 000. Measurements were conducted for bowplane deflections ranging from -28.8 to $+28.8$ degrees in increments of 3.6 and 1.8 degrees. The uncertainty in the stall angle was assumed to be one half of the deflection increment angle, that is, 1.8 and 0.9 degrees respectively. All experimental data are based on the standard vehicle configuration in straight and level flight.

Data were compared to published results of wind tunnel tests on standard NACA 0012, 0015, 0018, and 0021 sections (Jacobs and Sherman, 1937, and Stack, 1931); unfortunately, only the 0021 section had finite aspect ratio and the others were two-dimensional sections. Figure 4-1 shows a comparison on the experimental data on the NACA 0025 section as well as the other NACA sections from the literature. For each foil, a logarithmic best-fit is included to indicate the trend of stall angle versus Reynolds number.

As expected, the thicker sections of the same aspect ratio tend to show larger stall angles for a given Reynolds number (see White, 1986, for example). The stall angle to Reynolds number dependence for all three sections agree quite well with the logarithmic trends suggested. The high Reynolds number stall angle performance for the 0025 section has been extrapolated from the experimental data.

The logarithmic curve fit to the NACA 0025 data in Figure 4-1 for the stall angle in degrees and radians respectively are given by:

$$\alpha_{stall}[deg] = 6.221 \ln Re - 78.24 \quad (Re > 1 \times 10^6) \quad (56)$$

and

$$\alpha_{stall}[rad] = 0.109 \ln Re - 1.366 \quad (Re > 1 \times 10^6) \quad (57)$$

To confirm that the logarithmic extrapolation of the NACA 0025 data gave a reasonable prediction of stall behavior, high Reynolds number data from a two-dimensional NACA 0025 section was used. The two-dimensional airfoil data was based on NACA experiments conducted at a Reynolds number of 5 million (Bullivant, 1941). The stall angle of the equivalent low-aspect ratio section was predicted based on a relationship derived from *Clark Y* airfoils of different aspect ratio (pro-

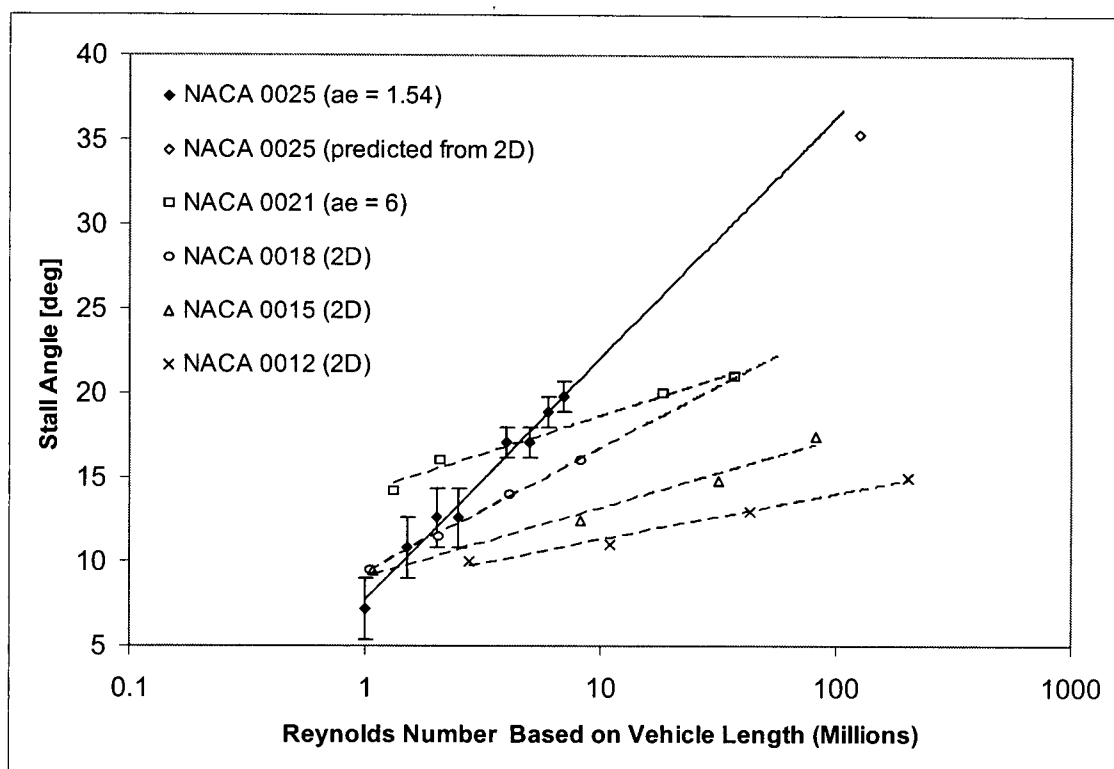


Figure 4-1 Control surface stall angle as a function of Reynolds number

vided in Appendix A.2). The prediction of the NACA 0025 performance at high Reynolds number is shown in Figure 4-1 and agrees to better than 7% with the logarithmic extrapolation.

The lower bound on Reynolds number corresponds to a full-scale vehicle speed of 0.12 m/s, well below typical operating speeds. At a forward speed of 6 m/s ($Re = 51$ million), the predicted stall angle is 32.2 degrees; this is sufficient for the maximum obtainable range of the planes on DOLPHIN used in practice (± 25 degrees). The results from this analysis were used to predict the stall angle as a function of Reynolds number in vehicle simulations.

4.2.2 Scaling experimental data

Reynolds number scaling for the experimental plane force versus deflection data was performed using a method outlined by Barlow et al. (1999). Specifically, the steps of the scaling procedure are:

1. The linear portion of the lift curve from experimental data is extended with the same slope
2. The maximum lift (full scale), $C_{L,max}$ is estimated (detailed below)
3. The curved portion of the experimental lift curve is raised until it has the proper value of $C_{L,max}$ and is shifted laterally until it joins the linear part of the constructed full-scale lift curve

As Barlow notes, this method results in a full-scale lift curve that has the proper lift at zero deflection, slope, and $C_{L,max}$ but likely has an angle of maximum lift that is too great and a stall that is too gentle.

Isolated Planes

Scaled experimental data for an isolated plane are shown in Figure 4-2 using the above method. The experimental data were collected at a vehicle length based Reynolds number of 7 million and scaled to 35 million (Reynolds number of 0.28 to 1.4 million based on chord). The sign conventions and force non-dimensionalization outlined in Section 2.1 on page 14 are used. Specifically, in terms of the dimensional force, Z , the fluid density, ρ , the freestream velocity, U , and the vehicle length, l , the non-dimensional force is:

$$Z = \frac{Z}{\frac{1}{2}\rho U^2 l^2} \quad (58)$$

Two methods were used to predict the maximum full-scale lift (step 2 above). The first method was provided by Barlow et al. (1999) in which the change in section maximum lift coefficient, $\Delta C_{L,max}$, was determined from tabulated semi-empirical data (see Appendix A.3). The second method was to predict the stall at full-scale Reynolds number using an extrapolation from the data in Section 4.2.1 and then to shift the model data along the lift curve to achieve the predicted stall angle. Both methods predict similar performance and are shown with the original experimental data in Figure 4-2.

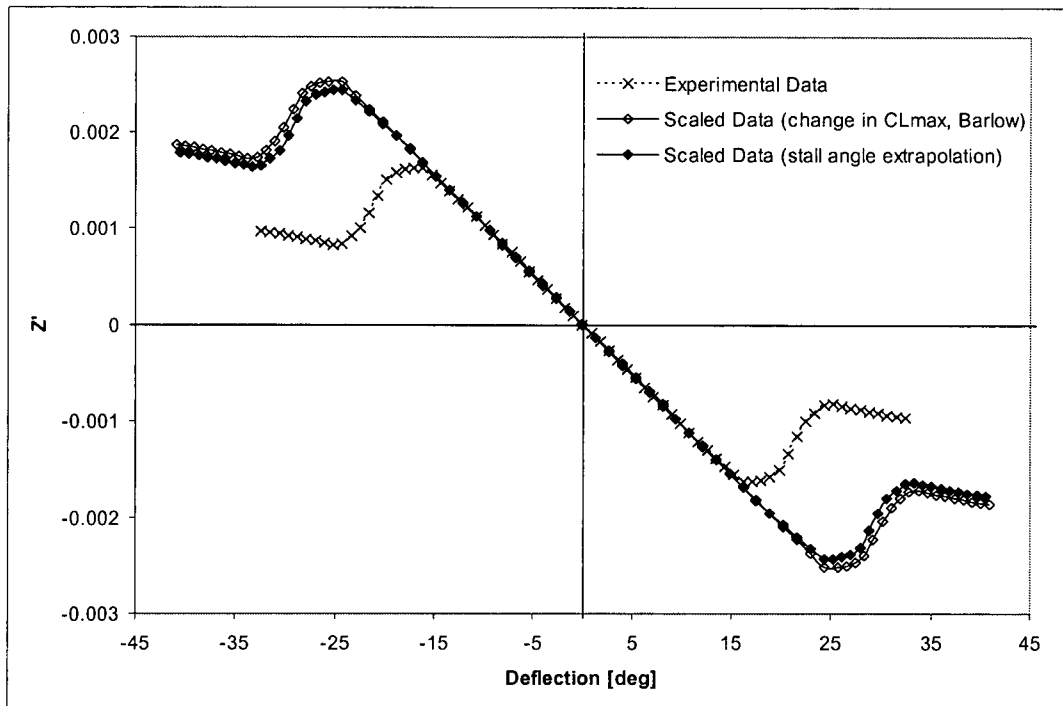


Figure 4-2 Isolated appendage force data extrapolated from a Reynolds number of 7 million to 35 million

Bowplanes

With the bowplanes, the above scaling method was used with maximum lift determined through an extrapolation of the stall angle. As the force to deflection curve of the bowplanes was less linear than that of an isolated appendage (see Figure 3-13 on page 58), the curve was extended based on the best linear curve fit to the data between positive and negative stall angles. Between the stall angles, the curve was scaled uniformly for both force and deflection; beyond stall, the curve was not scaled. The bowplane force curves, both scaled and original, are shown in Figure 4-3.

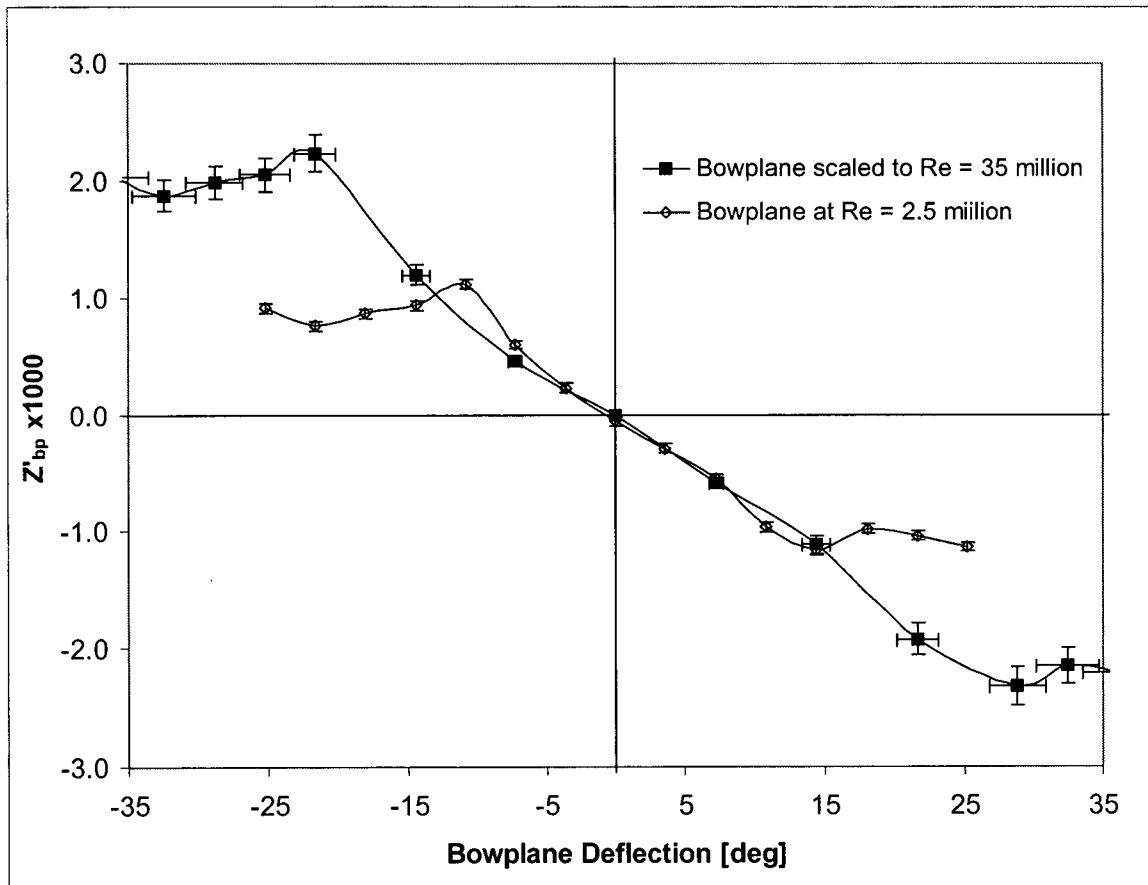


Figure 4-3 Bowplane force data extrapolated from a Reynolds number of 2.5 million to 35 million

As a result of the 'stretching' of the bowplane force to deflection curve, the localized second derivative was less in the scaled curve than in the original. As a result, for similar deviations about a given deflection, the scaled curve had increased linearity. As noted by Jacobs and Sherman (1937), the variation in lift curve slope with Reynolds number is very small; however, as the Reynolds number increases, the lift curve slope does become more linear.

Given the significant difference in Reynolds number between experiment and full-scale, caution must be exercised when using the data for absolute deflections greater than 15 degrees. Recall from Section 4.2.1 on page 102, that a 7% difference was noted between the stall angle determined through the extrapolation procedure (used to generate Figure 4-3) and the stall angle approximated

from two-dimensional tests on a NACA 0025 section. The error bars shown in Figure 4-3 for the scaled curve represent $\pm 7\%$ accuracy. Note that the stall angle comparison in Section 4.2.1 was made at a Reynolds number based on vehicle length of 125 million (significantly larger than the full-scale Reynolds number).

4.3 CONTROL SURFACE PERFORMANCE MODELLING

The performance of both bowplanes and sternplanes in straight and level flight was modelled using experimental data from the wind tunnel and towing tank. The performance of isolated control surfaces was considered first and hull interaction effects were added subsequently. The plane performance was described by a second order polynomial for use in the simulations; the coefficients of the polynomial are the hydrodynamic derivatives. The effects of plane stall were considered separately and were used to establish the maximum permissible plane deflection in operation.

4.3.1 Hydrodynamic Derivatives

The force to deflection curves of the control surfaces was represented using second order hydrodynamic derivatives of the form:

$$Z \cong Z_{\delta}\delta + Z_{\delta\delta}\delta|\delta| \quad (59)$$

Here the coefficients Z_{δ} and $Z_{\delta\delta}$ are first and second derivatives respectively of the force to deflection curve about the origin (see Section 2.1 for further information). For positive deflections, experimental plane data is shown in Figure 4-4. The curve has been scaled to a vehicle length Reynolds number of 35 million and a second order best fit curve was added for the portion of the curve prior to stall. Also shown in the figure are performance predictions from Whicker and Fehlner (1958) and Aucher (1981); detailed information regarding these performance estimates can be found in Section 2.4.

The lift curves from the experimental best fit and the two semi-empirical predictions all show good agreement up to stall although the curve from Whicker and Fehlner slightly over predicts the force on the plane. The RMS errors for the method of Whicker and Fehlner and Aucher, compared against the experimental data, were respectively 1.24×10^{-4} and 8.3×10^{-5} , in units of Z . These RMS errors respectively represent 2.6% and 1.7% of the force range between stall angles.

The resulting second-order hydrodynamic derivatives for each method are shown in Table 4-1. Aucher predicts greater curvature in the lift to deflection behavior compared to the experimental data while Whicker and Fehlner predict a more linear curve. Overall, the method of Aucher appears to more accurately predict the performance of isolated appendages.

4.3.2 Bowplane Performance Prediction

The isolated appendage performance prediction methods above were used as the basis for estimating the performance of the bowplanes. Corrections to account for the presence of the curved hull, as outlined in Section 2.4.2, were applied. For the isolated appendage force prediction of Aucher (1981), the suggested curvature correction was used (reproduced below from equation (23) on page 29):

$$\Delta C_z(\alpha) = \frac{\pi}{2} \left(1 - \frac{R^2}{b^2}\right) \lambda^* \left(1 - \frac{\lambda^*}{11}\right) \left(1 + \sqrt{\frac{R}{b}}\right) \left(1 - 3\left(\frac{t}{C}\right)^2\right) \alpha \quad (60)$$

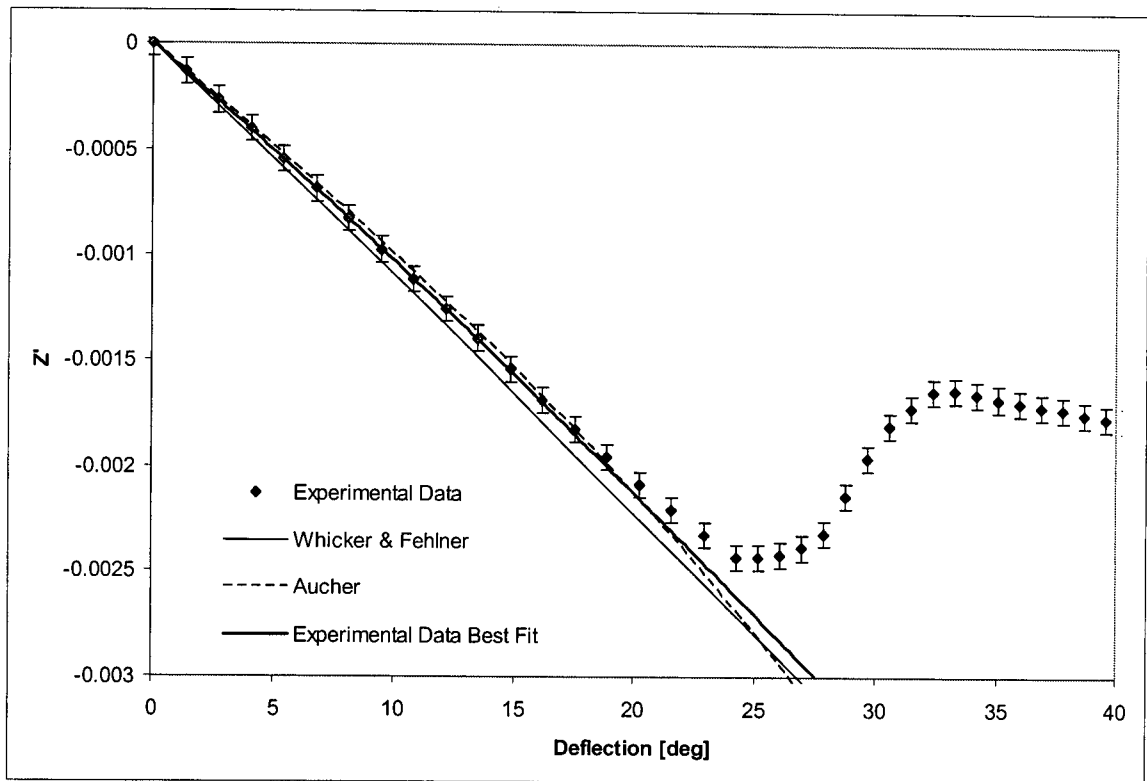


Figure 4-4 Experimental to semi-empirical comparison of isolated control surface performance

Table 4-1 Comparison of hydrodynamic derivatives

Method	Z'_δ	$Z'_{\delta\delta}$
Experiment best fit	-0.0057	-0.0018
Whicker & Fehlner	-0.0063	-0.0003
Aucher ^a	-0.0046	-0.0043

a. a second-order fit was used; the method of Aucher is based on a third-order polynomial

In the case of isolated appendage curve from Whicker and Fehlner, a correction was used to account for the cylindrical hull. The correction, derived from equation (22) on page 29, was applied to the effective aspect ratio, a_e , of bowplanes:

$$a_e = \frac{1}{2} \left(1 + \frac{R}{R + b_{\text{exp}}} \right) \frac{b}{C} \quad (61)$$

Additionally, for the estimate from Whicker and Fehlner, the upwash to the plane was modelled using lifting line theory (see, for example, Ashley and Landahl (1965) or von Mises (1959) for more information). As flow incident to the hull was redirected as discussed in Section 2.4.2, the

incidence angle, $\alpha(y)$, was augmented using the computed upwash at each span-wise location, y , according to:

$$\Delta\alpha(y) = \alpha_{\text{upwash}}(y) \left(\frac{R}{y} \right)^2 \quad (62)$$

Compared to the upwash of a plane mounted against a flat wall (an isolated appendage), it was computed that there was a reduction in upwash due to the hull image vortices (see Appendix A.1 for details). The resulting bowplane force to deflection predictions are shown in Figure 4-5 along with the experimental data (adjusted to full-scale Reynolds number). The agreement between the experimental data and both semi-empirical methods is good. For the deflection range between positive and negative stall, the RMS error in the prediction from Aucher to the experimental data was 0.000 33 (units of Z') while the RMS for the prediction from the modified Whicker and Fehlner method was 0.000 18. When expressed in terms of the force range between stall, these errors are 7.2% and 4.0% respectively. Considering only the range between ± 22 degrees, the RMS errors are 3.8% and 2.9%. In short, both the method given by Aucher and the method of Whicker and Fehlner (modified as described above) provide good estimates of the bowplane force as a function of deflection. Whereas the method of Aucher more accurately predicted the performance of an isolated plane, the modified method of Whicker and Fehlner appears to provide better performance predictions for a bowplane.

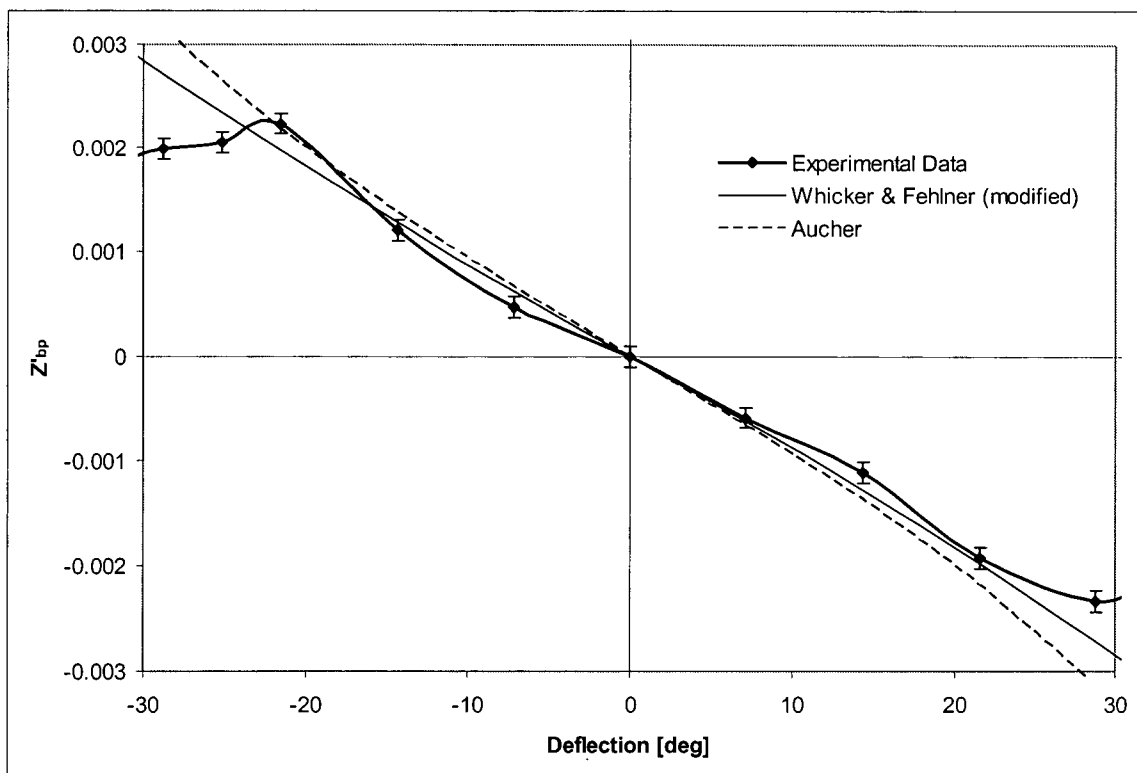


Figure 4-5 Experimental to semi-empirical comparison of bowplane performance

4.4 TRIM EFFECT MODELLING

It is known that there is a distribution of angles of incidence across the span of the bowplanes for non-zero trim angles (see Section 2.4.2). Furthermore, the experimental data showed that the effect of trim on the bowplanes was to cause a horizontal shift in the bowplane force to deflection curves. This horizontal shift in the data is quantified below and then compared with theoretically predicted shift based on an analytical expression of the incidence flow angle.

4.4.1 Experimental Results

In Section 3.2.3, experimental results were provided describing the performance of bowplanes in trim. The effect of trim was to shift the bowplane force to deflection curves horizontally. The amount of shift, measured from the origin, is shown as a function of trim angle, θ , in Figure 4-6.

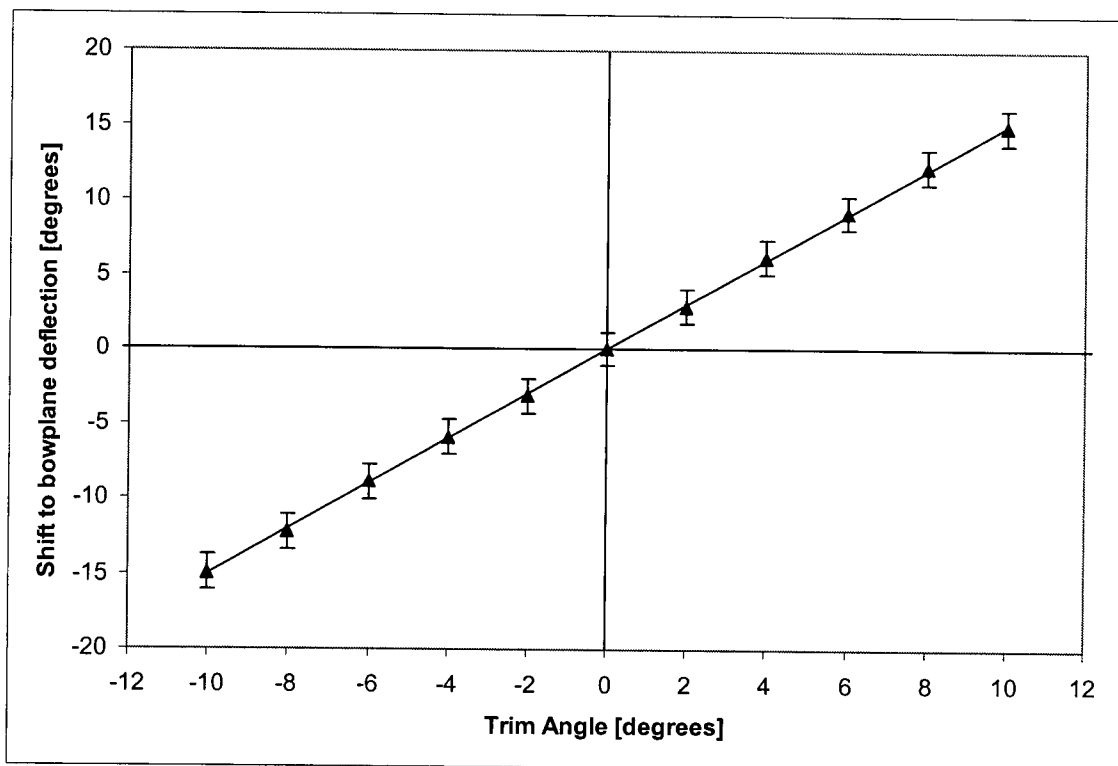


Figure 4-6 Effective shift in bowplane deflection as a function of trim angle

Based on a linear least squares fit in the above figure, the force on the bowplanes was described by the effective plane deflection

$$\delta_{\text{eff}} = \delta + 1.5\theta \quad (63)$$

In regions very far from the body, the influence of the hull is negligible and the effective deflection in that region is

$$\delta_{\text{eff},\infty} = \delta + \theta \quad (64)$$

In other words, very far from the body, the effective angle is simply the sum of the plane angle relative to the body and the body angle relative to the freestream. Close to the body, it is known that there is a change in the flow angle around the hull when the vehicle has non-zero trim (see Section 2.4.2, for example). From the yarn tuft visualization, the incident flow angle at the root with respect to the freestream was equal and opposite to the trim angle. Therefore, the effective deflection for this region is

$$\delta_{\text{eff,root}} = \delta + 2\theta \quad (65)$$

which is in agreement with both equations (25) and (26) on page 30. Coincidentally for the DOLPHIN plane and body geometry considered, the effect of the hull on the entire plane, equation (63), is midway between the effect at the plane root, equation (65), and the effect at very large distances, equation (64). Although equation (63) is directly dependent on the bowplane and hull geometry considered, the same result was found for both the *standard* and *anhedral* bowplane configurations suggesting the effect is not highly sensitive to bowplane location or orientation.

4.4.2 Analytical Prediction of Trim Influence

The influence of trim on the bowplanes was estimated through predicting the change in incidence angle on the planes due to the hull. The incidence was estimated using equation (26) on page 30, reproduced below

$$\alpha(y) = -\theta \left[1 + \left(\frac{R}{y} \right)^2 \right] \quad (66)$$

The effect of the hull-induced change in incidence angle was averaged across the bowplane span, from $y = R$ to $y = b = 2.06R$. The result was equivalent to a net increase in the angle of incidence of 0.49θ ; in addition to the geometric angle to freestream of θ due to the vehicle trim, the resulting effective plane angle is

$$\delta_{\text{eff}} = \delta + 1.49\theta \quad (67)$$

which compares very favorably with the best fit of $\delta_{\text{eff}} = \delta + 1.50\theta$ to the experimental data as given in equation (63). The resulting shift predicted in the bowplane force curves as a function of trim angle is shown in Figure 4-7 (the predicted shift is shown against the measured shift from Figure 4-6).

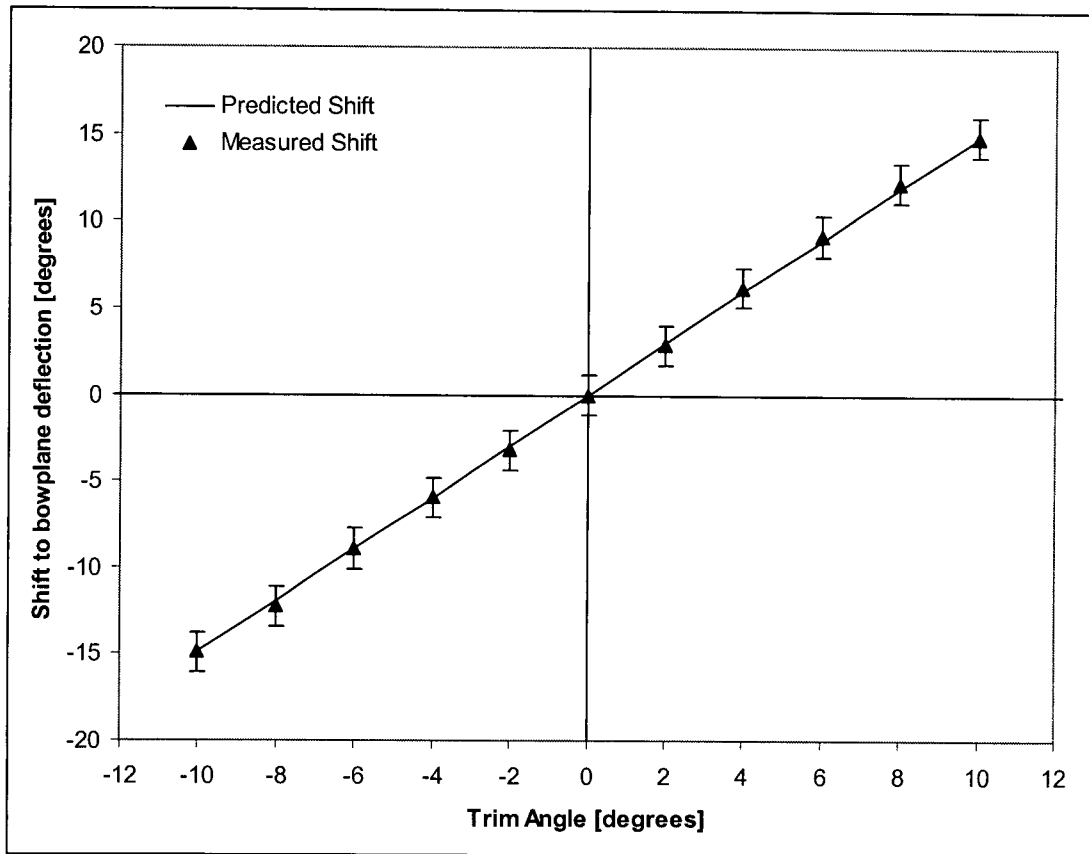


Figure 4-7 Predicted effective shift in bowplane deflection as a function of trim angle

4.5 YAW EFFECT MODELLING

In modelling the influence of yaw on the bowplanes, two aspects were examined. First, empirical relations were developed to mathematically describe the influence of yaw on the bowplanes for the purpose of simulation. Second, simplified analytical models were used to verify whether the presence of two lee-side hull vortices could account for the bowplane behavior described in Section 3.2.4.

4.5.1 Semi-Empirical Relations for Bowplane Performance in Yaw

Based on the data of Section 3.2.4, and in particular Figure 3-31 on page 72, semi-empirical relations were developed to simplify bowplane models for the purpose of simulation. The dependence of stall angle and of lift curve slope with yaw were both considered.

Stall Angle Dependence on Yaw

As noted in Chapter 3, the influence of yaw on the bowplanes was to increase the stall angle on the leeward plane and decrease the stall angle on the windward plane. The stall angle (measured to the nearest 3.6 degree increment) was determined from Figure 3-31 and is shown for the port bowplane in Figure 4-8 as a function of the yaw angle relative to the straight and level conditions. Data are expressed in terms of the ratio of stall angle in yaw to the stall angle for straight flight where the yaw angle is equal to zero. This ratio is hereafter referred to as the 'yaw stall scaling factor' and was modelled using a polynomial curve fit.

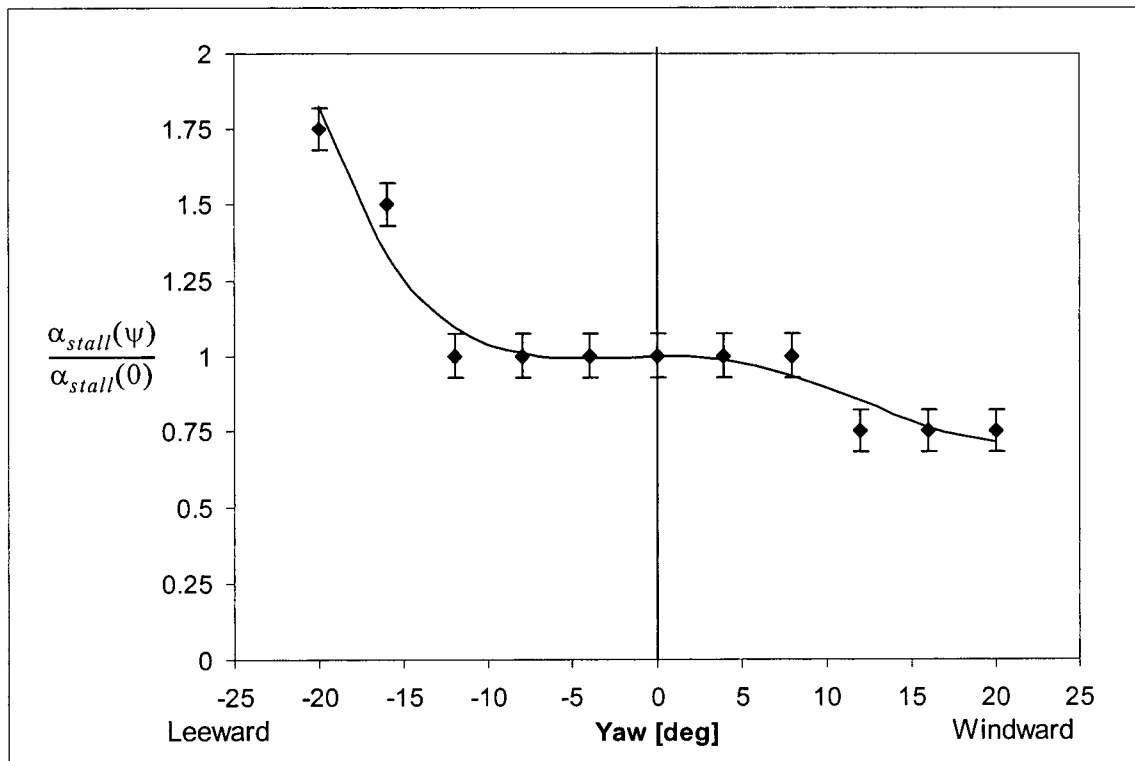


Figure 4-8 Bowplane stall angle as a function of yaw

The yaw stall scaling factor is represented by the polynomial $h(\psi)$ where the equation describing $h(\psi)$ for the port bowplane with yaw measured in degrees is

$$h(\psi) = \frac{\alpha_{stall}(\psi)}{\alpha_{stall}(0)} \approx 1 - 6.86 \times 10^{-4}\psi^2 - 6.944 \times 10^{-5}\psi^3 + 3.403 \times 10^{-6}\psi^4 \quad (68)$$

For the starboard bowplane, ψ is substituted with $-\psi$ in equation (68).

Lift Curve Slope Dependence on Yaw

Again using on the results of Section 3.2.4, the dependence of the lift curve slope on yaw was computed and is shown for the port bowplane in Figure 4-9. As was noted in Chapter 3, for larger yaw angles there is a greater lift curve slope magnitude for the leeward bowplane and a reduced slope magnitude for the windward plane (note that, as shown in the figure, the slope is negative). The computation of the slope was based on a linear regression using measured Z'_{bp} values from -10.8 to +10.8 degrees. The error bars shown in the figure are based on the standard error in the slope (computed as shown in Appendix C.1).

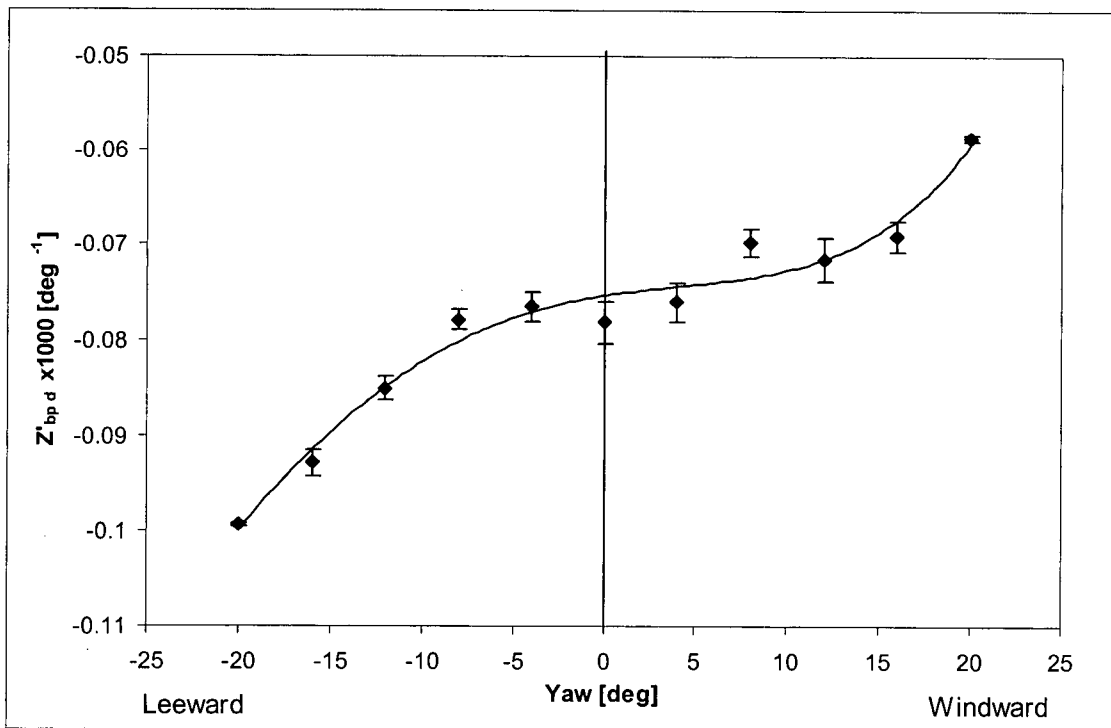


Figure 4-9 Port bowplane lift curve slope as a function of yaw

For the purpose of simplifying the results with the intent of using them in simulation, the influence of yaw was converted to a format where the lift curve slope for a given yaw angle was normalized

by the lift curve slope for zero yaw. In Figure 4-10, this 'yaw scaling factor', $f(\psi)$, is shown in terms of yaw angle. The third-order best fit curve of Figure 4-10, with yaw in degrees, is

$$f(\psi) = \frac{Z_{bp\delta}}{Z_{bp\delta}|_{\psi=0}} \approx 1 - 0.00384\psi - 2.28 \times 10^{-5}\psi^3 \quad (69)$$

The above approach of modelling the lift curve slope dependence on yaw was used in simulation as opposed to attempting to model the curve in Figure 4-9 directly due to the simplicity in resulting expression. (The fifth-order polynomial for the curve in Figure 4-9 requires six coefficients whereas the curve in Figure 4-10 requires three, as given by equation (69).)

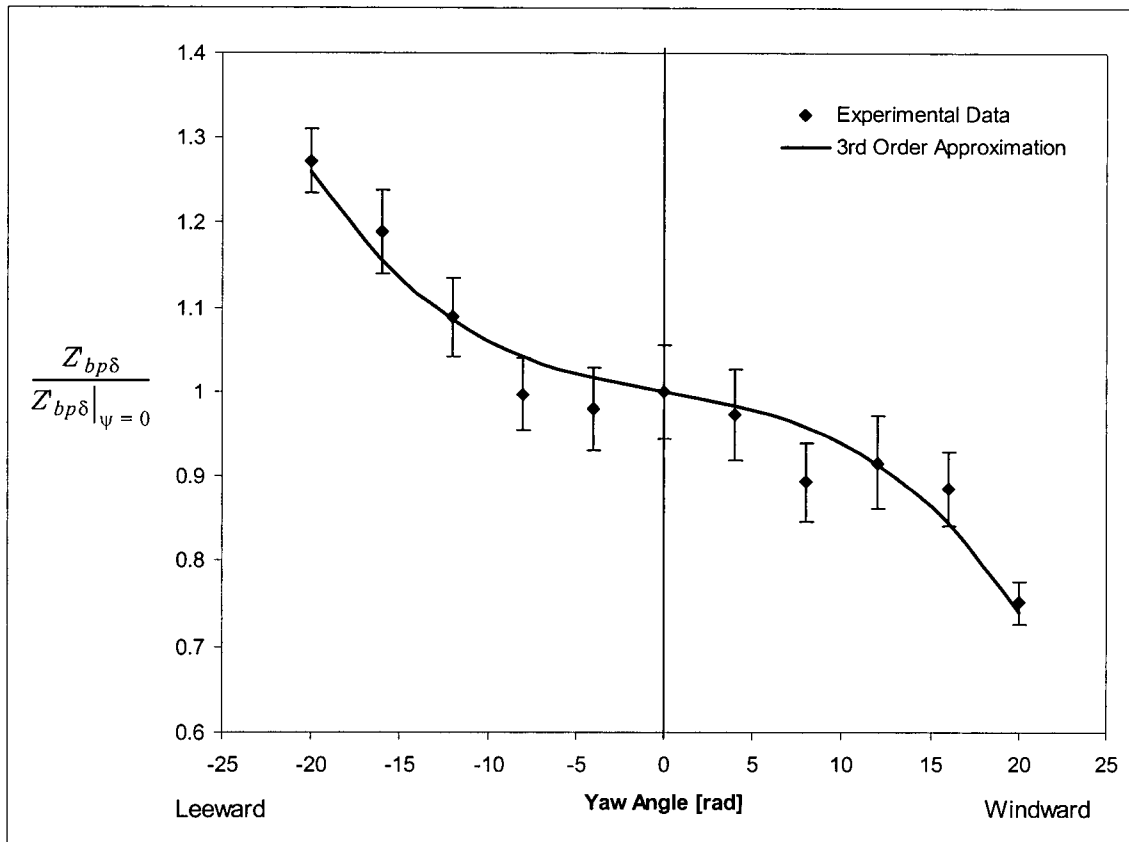


Figure 4-10 Normalized bowplane lift curve slope dependence on yaw angle

4.5.2 Analytical Prediction of Yaw Influence on Bowplanes

An analytical analysis of the effect of the two hull vortices due to yaw on the bowplanes was conducted. The objective of the analysis was not to predict bowplane performance but simply to determine if the increased lift curve slope observed on the leeward planes could be attributed to the hull vortices. The vortex pattern in yaw was presented in Figure 2-12 on page 32 and is shown in Figure 4-11 below in a slightly different form.

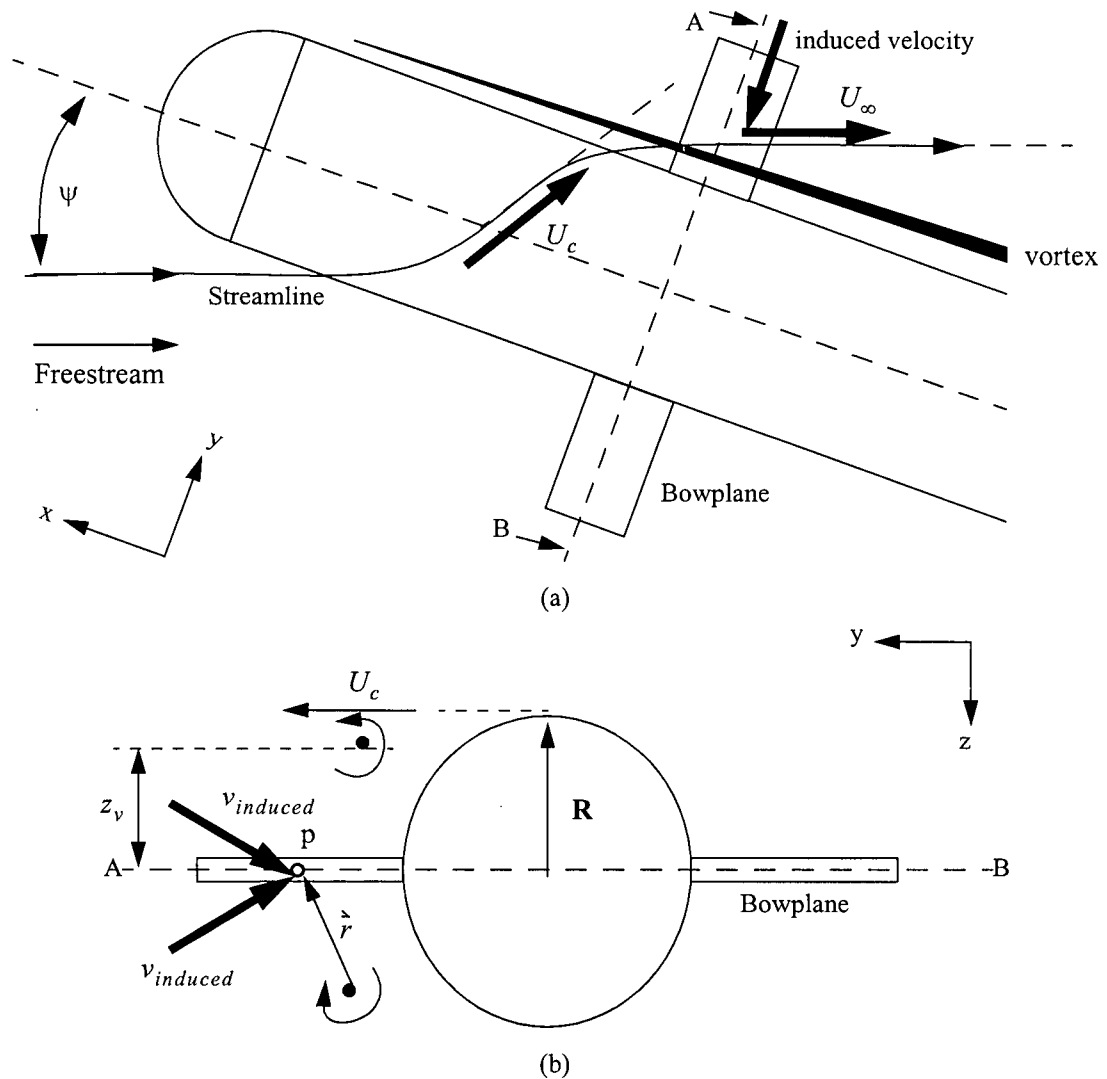


Figure 4-11 Normalized bowplane lift curve slope dependence on yaw angle

In order to predict the effect of yaw on the bowplanes, the two hull vortices were idealized as line vortices as shown in part (b) of Figure 4-11. Each vortex induces a velocity for every point on the bowplane. As the two hull vortices are symmetric about the x - y plane, the vertical components of the induced velocity cancel and the result is a net induced velocity along the plane span, as shown in Figure 4-11 (a).

Using rough estimates of the strength and location of the hull vortices (details are provided in Appendix A.4), the induced velocity across a leeward bowplane was predicted. At each point, p , along the plane span, the net velocity, U_{plane} , and the flow angle with respect to the $-x$ -axis, ψ_{plane} , were computed (see Figure 4-12). As noted by Hoerner (1939), lift force on a rectangular wing of low aspect ratio (that is, $a_e \approx 1$ to 5) decreases roughly in proportion to the cosine of the yaw angle. Therefore, each element along the span was treated as an airfoil at a yaw angle of ψ_{plane} in

a freestream flow with velocity U_{plane} . For a given point, p , described by the vector, \hat{r} , the net induced velocity on the plane span is approximated by

$$v_{\text{induced}}(\psi) \approx 3.2 U_{\infty} \sin \psi (R - z_v) \frac{z_v}{|\hat{r}|^2} \quad (70)$$

where the induced velocity is directed on the y -axis towards the body. Complete details regarding the assumptions and computations of the hull vortex effect on the bowplanes can be found in Appendix A.4.

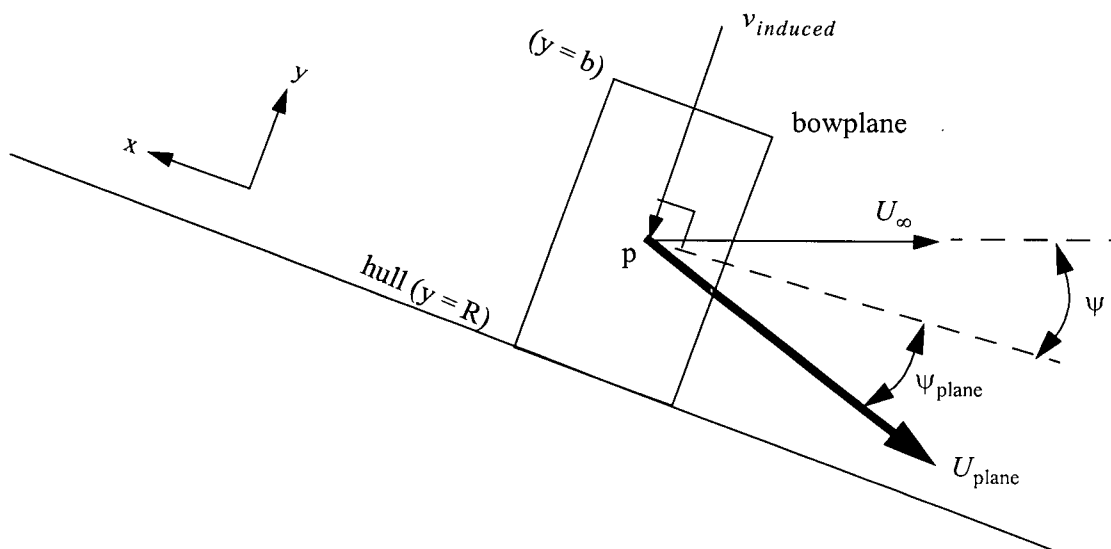


Figure 4-12 Description of flow velocity components on the bowplane in yaw

Using the above model, the ratio of force on the leeward bowplane to a bowplane at zero yaw was computed. Since the two hull vortices were shown not to induce a change in the local angle of attack of the bowplane—the vortices are symmetric about the hull centreline—the change in bowplane force was computed from the local increase in velocity on the plane modified by the yaw correction of Hoerner given above:

$$\frac{Z_{bp}}{Z_{bp}|_{\psi=0}} \approx \text{average} \left(\frac{U_{\text{plane}}^2(\psi) \cos \psi_{\text{plane}}}{U_{\infty}^2} \right) \quad (71)$$

Expressed in terms of the ratio of bowplane lift curve slope for a given yaw angle to that at zero yaw angle, the estimated yaw influence is presented in Figure 4-13. For most yaw angles there is surprisingly good agreement between the estimate developed above and experimental data (reproduced from Figure 4-10). At large yaw angles, the estimate does not fully match the observations; this is to be expected given the assumptions used and the simplicity in the model. Nevertheless, the purpose of the model above was not as a predictive tool but rather to verify whether the vortices from the hull could be responsible for the increase in bowplane lift curve slope. The results strongly suggest that the hull vortices indeed may be responsible for the increased force measured on the leeward bowplanes in yaw.

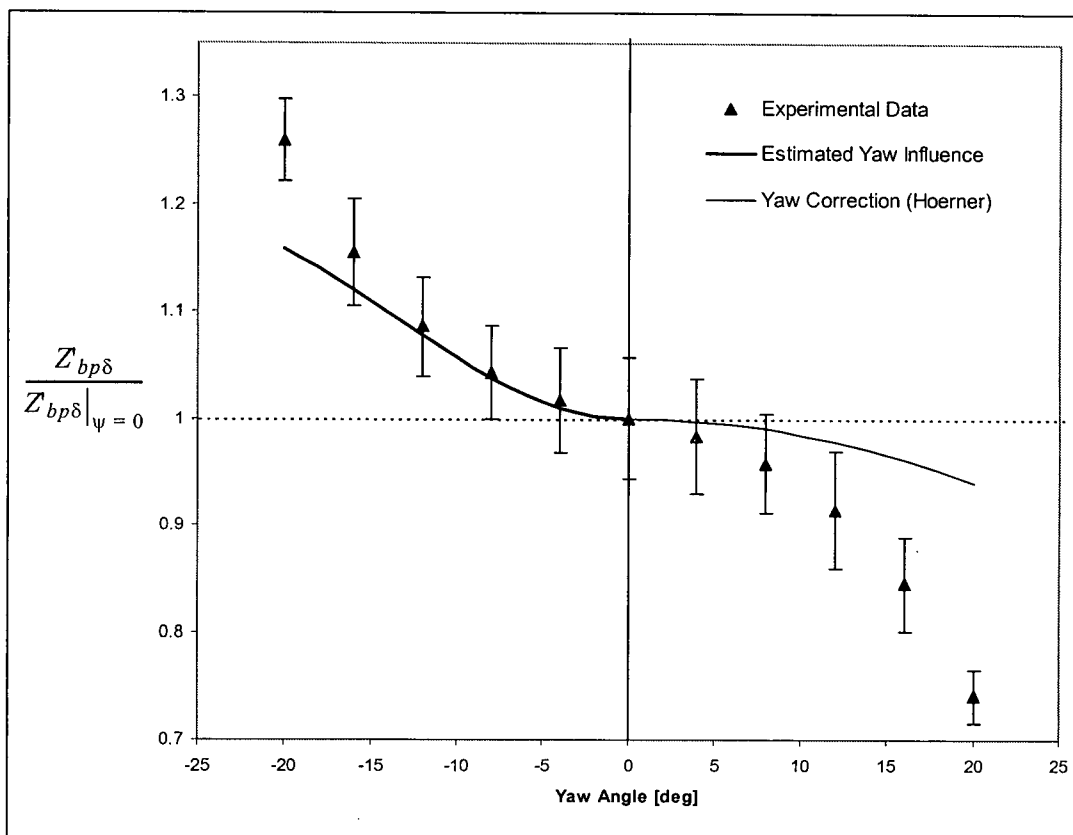


Figure 4-13 Analytical prediction of port bowplane lift curve slope dependence on yaw angle

In terms of the windward bowplanes, the yaw angle correction from Hoerner (1939) was applied and is shown in Figure 4-13 (for positive yaw angles). Given the poor comparison to experimental data, the orientation of the windward planes to the freestream flow alone is not enough to account for the decrease in the performance of those planes.

4.6 CONTROL SURFACE INTERACTION MODELLING

To characterize the interaction between bowplanes and sternplanes, a potential flow model was developed and the results were compared with the experimentally measured interaction. For the purpose of simulation, empirical relations regarding the dependence of the bowplane-sternplane interaction on body orientation were determined from experimental data.

4.6.1 Potential Flow Model of Control Surface Interaction

A simple numerical model was used to predict the interaction between fore and aft planes on a cylindrical body. Planes were modelled with a system of bound and trailing vortices as shown in Figure 4-14. Vortex strength, Γ , was predicted using two-dimensional lifting line theory (see Talay, 1975, or Jacob, 1995, for example). With the experimentally determined bowplane force, C_L , the vortex strength was approximated by

$$\Gamma \cong \frac{C_L U_\infty b_{\text{exp}}}{a_e} \quad (72)$$

As an aside, this method of approximating the tip vortex strength neglects the span-wise variation in circulation predicted on a finite aspect ratio wing. Specifically, Prandtl proposed an elliptical distribution for the circulation (see von Mises, 1959) such that

$$\Gamma(y) = \Gamma_0 \sqrt{1 - \left(\frac{2b}{y}\right)^2} \quad (73)$$

where Γ_0 is the maximum circulation at the wing centreline. Since the circulation is approximated from the measured lift on the planes and since all bound vorticity is assumed to roll-up into the tip vortex, the same prediction of tip vortex strength is obtained regardless of whether constant or distributed circulation is assumed.

Returning to the potential flow model, as shown in Figure 4-15, image vortices were added to satisfy wall boundary conditions of the body (excluding the control surface). To predict the position of a trailing vortex at the longitudinal location of the sternplanes, the velocity components induced by the opposite trailing vortex and the image vortices were added vectorially to the freestream. The trailing vortex was assumed to follow a linear path in the direction of this resultant velocity vector (directed at an angle of γ to the freestream as shown in Figure 4-14). To satisfy the wall boundary conditions of the tail, image vortices were added and the resulting induced flow was computed from the freestream and the trailing and image vortices (see Figure 4-16). The local incident flow velocity to the aft planes, along with the previously measured lift curve slope, was used to compute the interaction force on the aft planes. Complete details in the development of the potential flow model can be found in Appendix A.5.

A comparison of results from the numerical interaction model and experimental data is provided below. A representative set of cases has been chosen including the examination of the influence of plane geometry, plane location, Reynolds number, and trim angle.

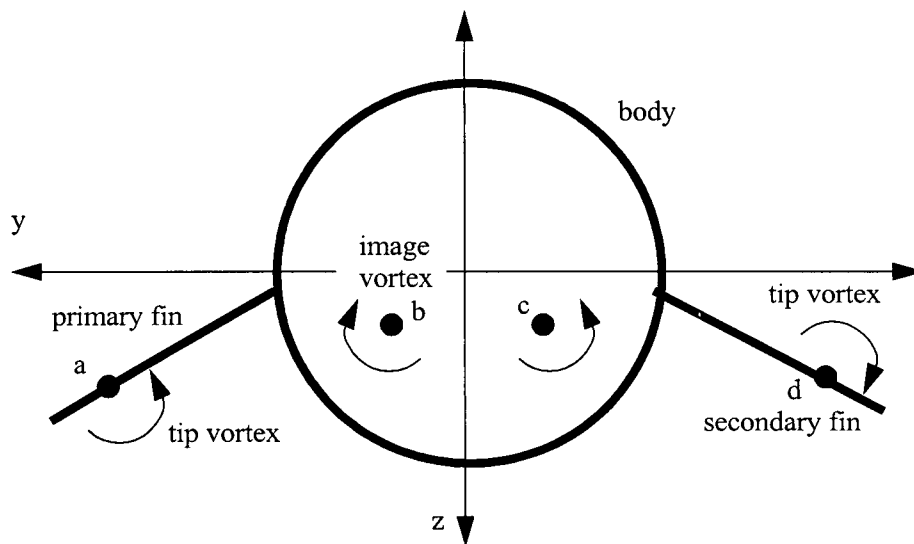


Figure 4-15 Vortex system for potential flow model of control surface interaction

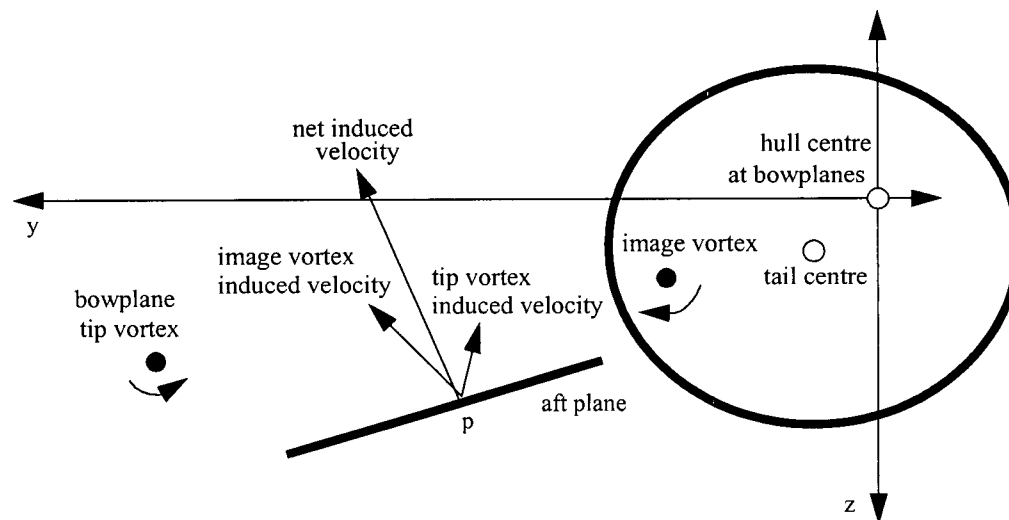
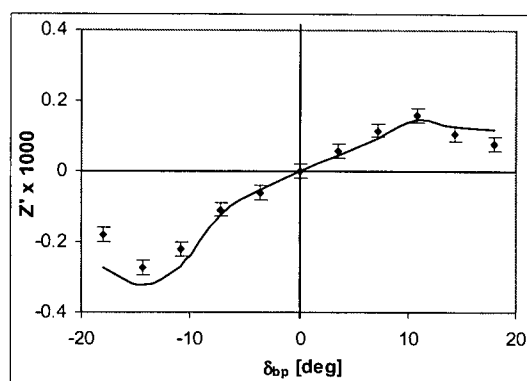


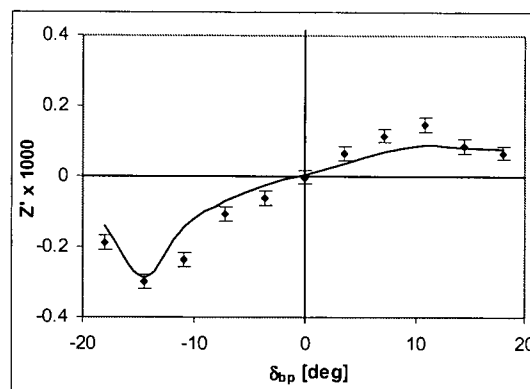
Figure 4-16 Starboard side vortex system at aft plane; port side vortices also contribute to induced velocity but are not shown

Plane Location Effects

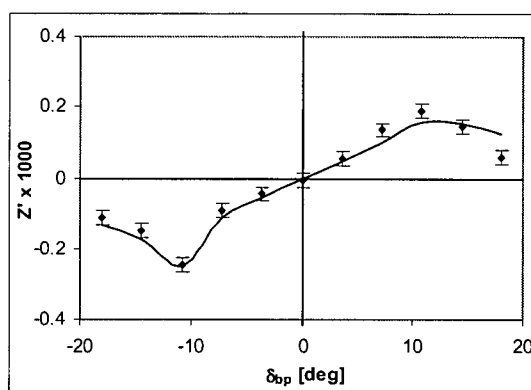
The interaction resulting from various fore and aft plane locations on the body was studied. Figure 4-18 shows results for both the experimental and numerical methods. Included in the figure are bowplanes located along the *centreline* and *high* positions as well as both *anhedral* and *dihedral* bowplanes and sternplanes. Detailed specifications of each of the plane locations were provided in Table 3-3 on page 46. The baseline (*standard*) configuration is shown in Figure 4-18 (a). Note the change in the vertical axis scale for cases (c) to (f) in Figure 4-18. Once again, the agreement between the experimental data and the computational data is exceptionally good.



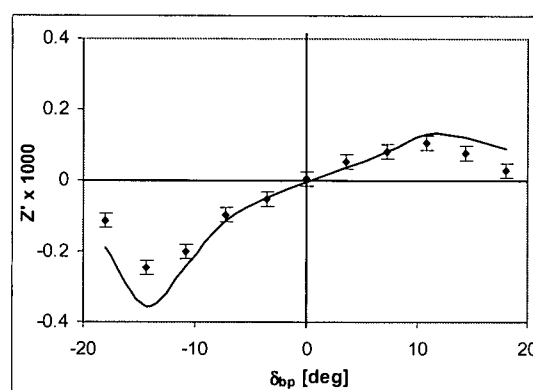
(a)



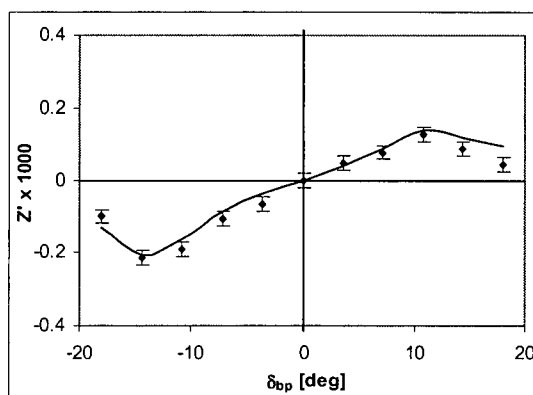
(b)



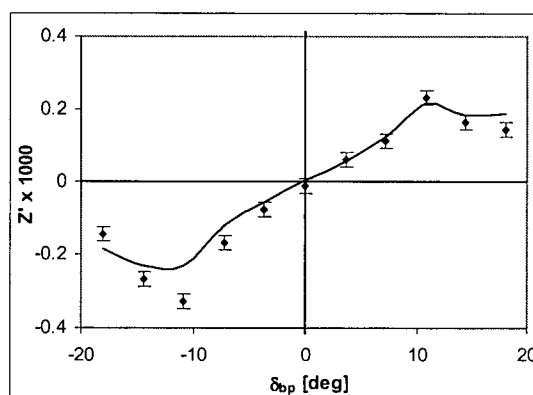
(c)



(d)



(e)



(f)

Figure 4-17 Plane geometry effect on fore-aft plane interaction comparison for: (a) standard configuration; (b) short bowplanes; (c) long bowplanes; (d) short sternplanes; (e) long sternplanes; (f) large sternplanes. Measured data with error bounds are shown with points, values from the numerical prediction are shown with solid lines.

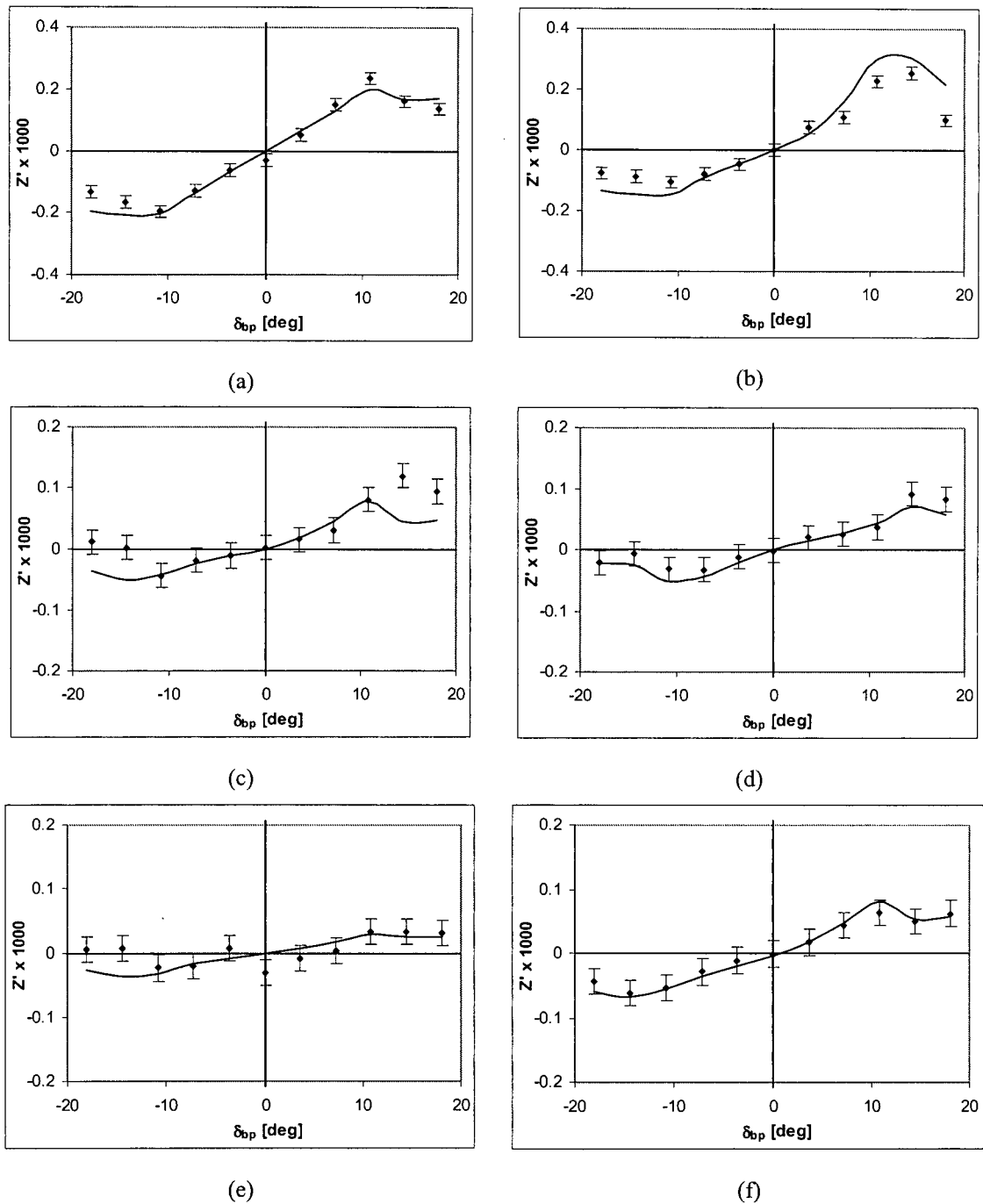


Figure 4-18 Plane location effect on fore-aft plane interaction comparison for: (a) centreline bowplanes; (b) high bowplanes; (c) dihedral bowplanes; (d) anhedral bowplanes; (e) Y-tail; (f) Inverted Y-tail. Measured data with error bounds are shown with points, values from the numerical prediction are shown with solid lines.

Reynolds Number Effects

The influence of Reynolds number on the interaction between fore and aft planes in the baseline configuration is summarized in Figure 4-19. Higher body length-based Reynolds numbers of 7.5 million (Figure 4-19 a) and 4.2 million (Figure 4-19 b) were obtained during towing tank tests at a depth of three hull diameters. The water surface was ignored in the numerical model as justified by the findings of Section 3.4.4 on page 93. Lower Reynolds numbers based on body length, ranging from 2.0 million (Figure 4-19 c) to 0.5 million (Figure 4-19 f) were obtained through wind tunnel testing.

At higher Reynolds numbers, the agreement of the computational result to experimental data is excellent, both in the shape and magnitudes of the curves. As the Reynolds number is reduced, the agreement becomes less favorable. The model under predicts the maximum force at a Reynolds number of 1.0 million and under predicts the maximum and minimum forces at a Reynolds number of 0.5 million. This disagreement at lower Reynolds number can partly be attributed to several factors: the reduced bowplane tip vortex strength and coherence at lower speeds; the reduction in stall angle at low Reynolds number; and the increased non-linearity in the bowplane force to deflection curve (which is used as an input to the potential flow model). From an operational point of view, the low Reynolds number data is the least important for an AUV such as DOLPHIN (that operates in the 35 to 50 million Reynolds number range); the numerical results are included to identify limitations in the modelling technique.

Body Trim Angle Effects

Figure 4-20 shows the change in fore-aft interaction with body trim. Results are shown for trim angles of +8, +4, +2, -2, -4, and -8 degrees for the baseline configuration. The zero trim case can be found in Figure 4-17 (a). Even though the model is very simple and does not take into account the effect of the hull on the freestream flow, the bowplane-sternplane interaction is still well predicted for all trim angles up to +8 and -8 degrees.

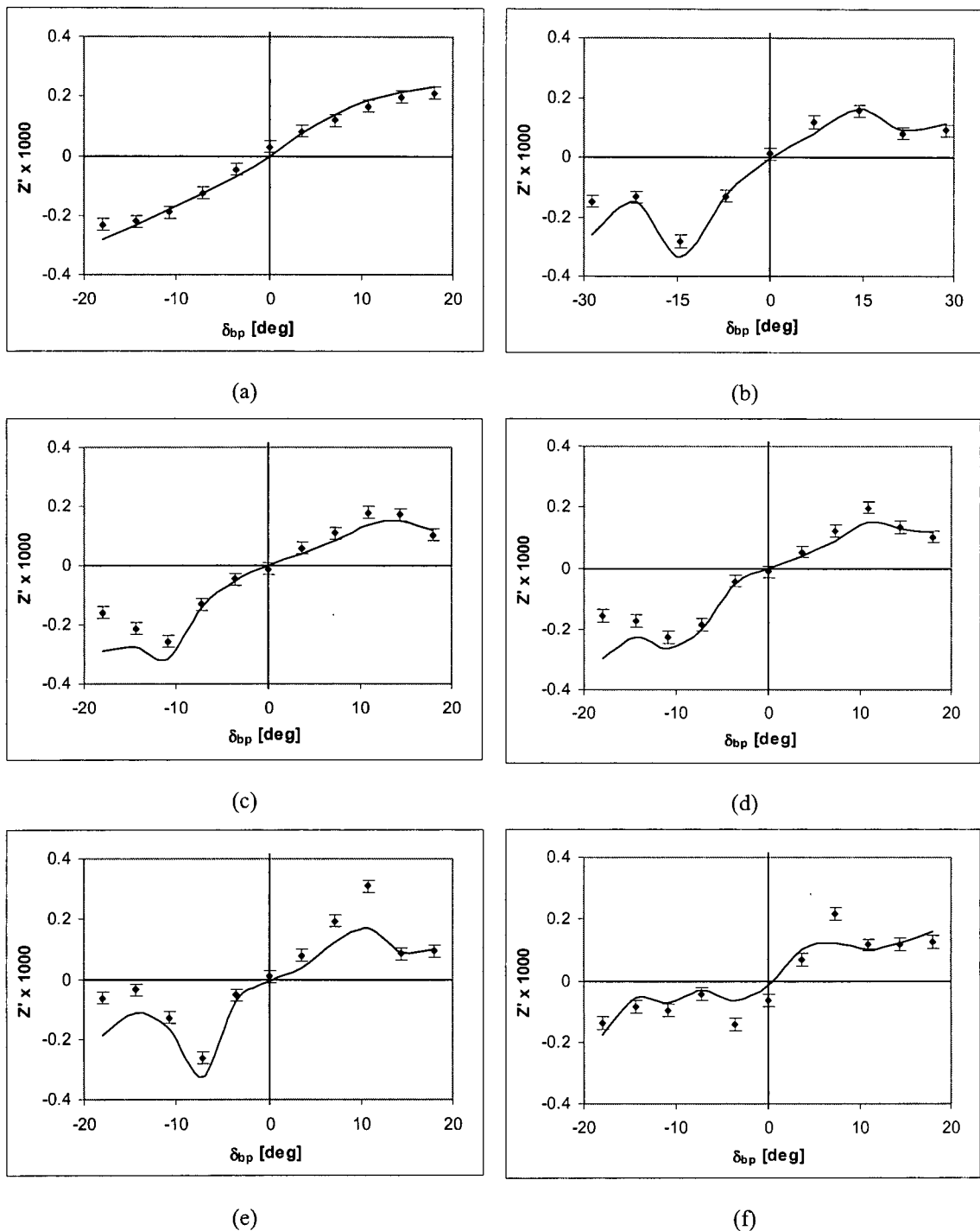


Figure 4-19 Reynolds number effect on fore-aft plane interaction comparison for: (a) $Re_L = 7.5$ million; (b) $Re_L = 4.2$ million; (c) $Re_L = 2$ million; (d) $Re_L = 1.5$ million; (e) $Re_L = 1.0$ million; (f) $Re_L = 0.5$ million. Measured data with error bounds are shown with points, values from the numerical prediction are shown with solid lines.:

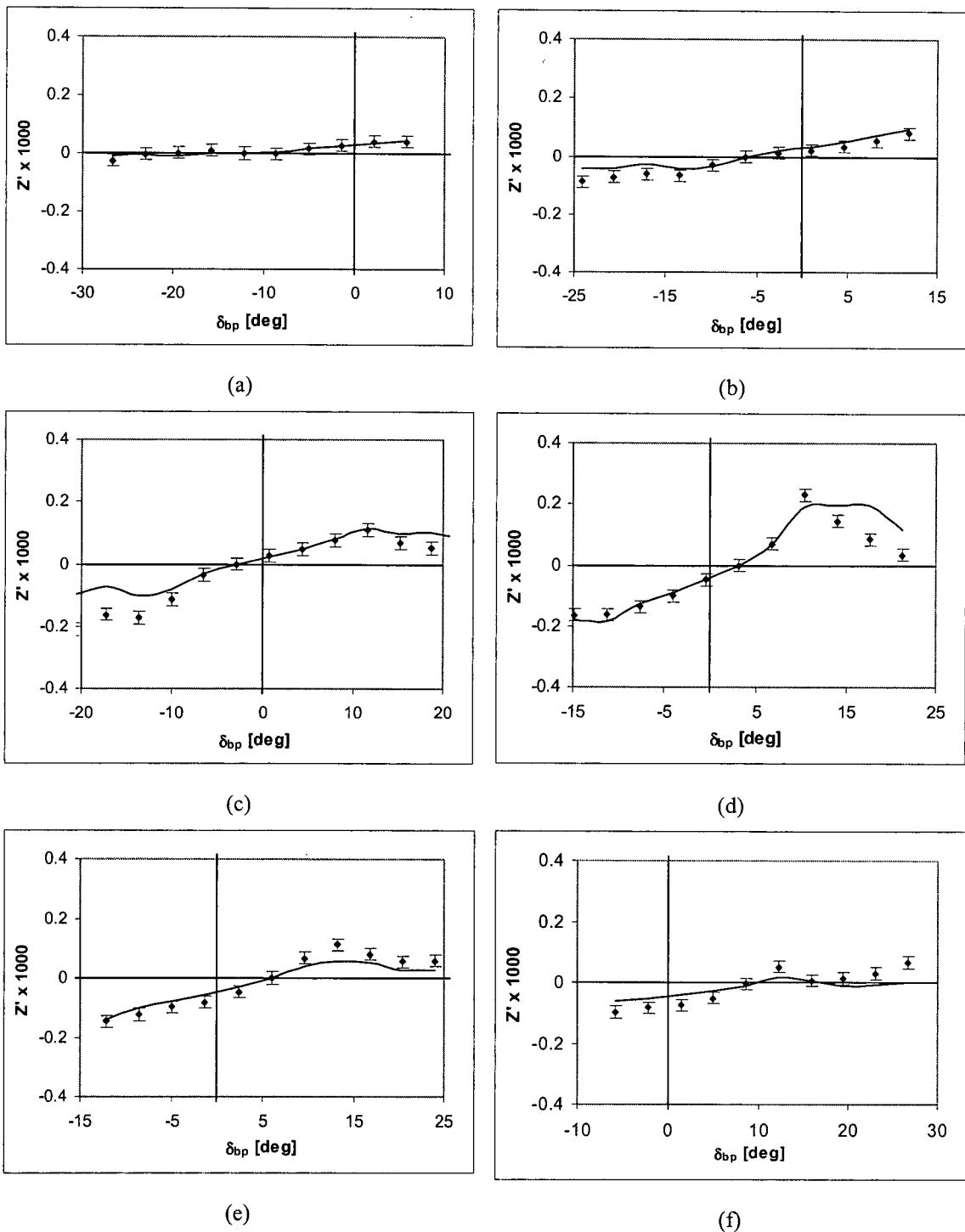


Figure 4-20 Body trim angle effect on fore-aft plane interaction comparison for: (a) -8 degree trim; (b) -4 degree trim; (c) -2 degree trim; (d) +2 degree trim; (e) +4 degree trim; (f) +8 degree trim. Measured data with error bounds are shown with points, values from the numerical prediction are shown with solid lines.:

4.6.2 Modelling Bowplane-Sternplane Interaction in Trim and Yaw

The change in bowplane-sternplane with body orientation was modelled using curve fits to empirical data. In each case, the slope through the origin of the sternplane force to bowplane deflection was used as the dependent variable.

Interaction Dependence on Trim

As a function of trim angle, the slope of the interaction force on the sternplanes was considered in Section 3.3.2. In Figure 4-21, the interaction curve slope is shown non-dimensionalized by the corresponding bowplane force to deflection slope.

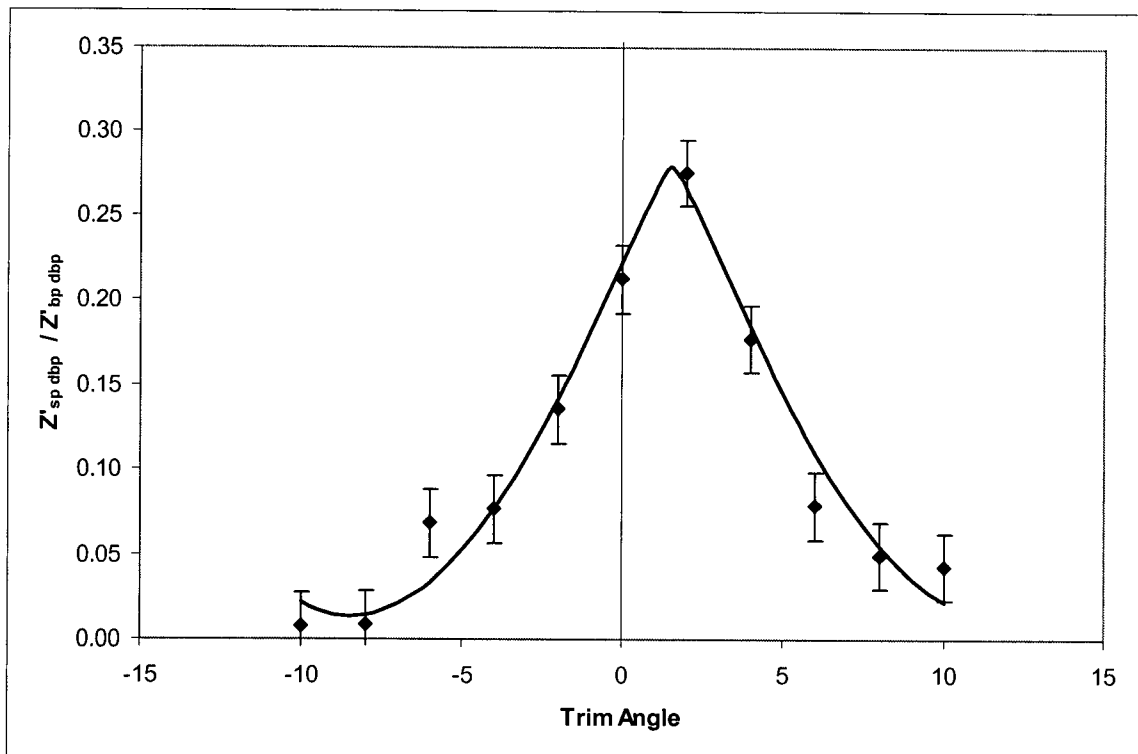


Figure 4-21 Interaction curve fit of sternplane to bowplane lift curve slope ratio in trim

A polynomial best fit to the data was established using the least squares method. The expression defining the curve is

$$\frac{Z'_{sp} \delta_{bp}}{Z'_{bp} \delta_{bp}}(\theta) \approx 0.28 - 0.03606|\theta - 1.55|^{1.5} + 0.008715|\theta - 1.55|^2 \quad (74)$$

where θ is measured in degrees. In general, the polynomial fit shows good agreement with the data; however, the local minima at a trim angle of -9 degrees suggests that the polynomial approximation is only suitable for trim angles between approximately -10 and +11.5 degrees. This range is adequate for the work in this thesis since a practical limit for the range of trim angle in operation for the DOLPHIN vehicle is +/-6 degrees (Seto, 1998).

The 1.55 degrees subtracted from the trim angle in each term in equation (74) is due to the maximum interaction occurring at a trim greater than zero. As was noted previously, this is due to the position of the standard bowplanes below the hull centreline. For comparison, considering only the relative position of the planes in the standard configuration, maximum interaction would be anticipated for a trim angle of 1.1 degrees (in which case the sternplanes are directly downstream of the bowplanes).

Interaction Dependence on Yaw

As above with trim, the dependence of the bowplane-sternplane interaction on the vehicle yaw was examined. In Section 3.3.3, the slope of the sternplane interaction force versus bowplane angle, normalized by the slope at zero yaw, was presented for a range of yaw angles. A polynomial best fit curve was added to the experimental data and is shown in Figure 4-22.

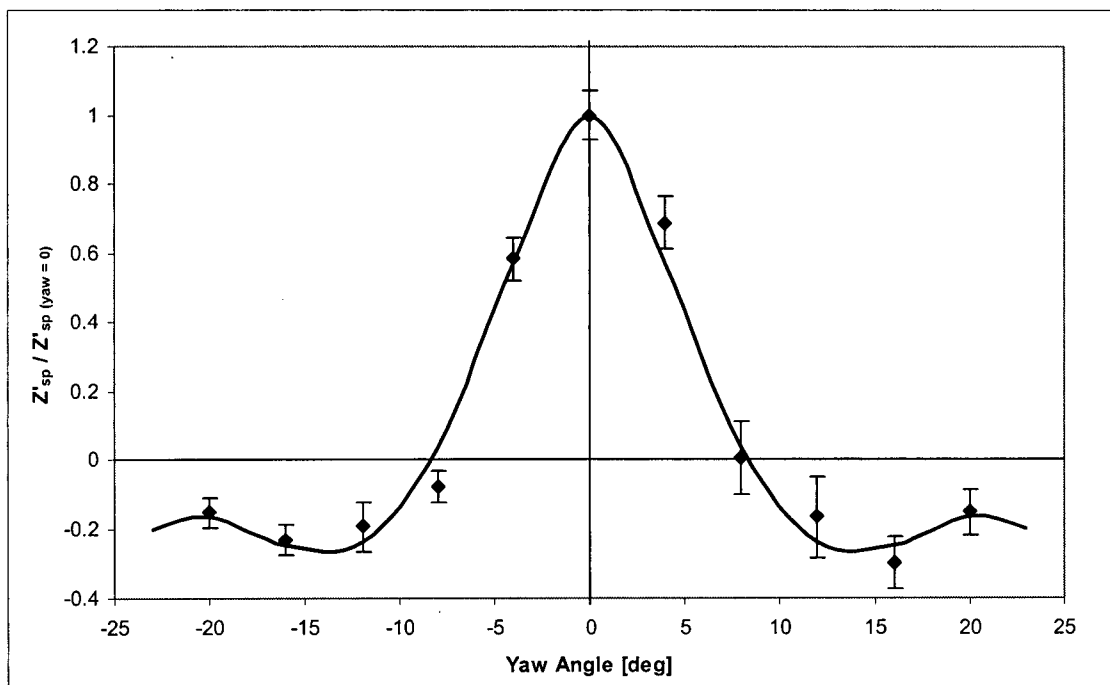


Figure 4-22 Interaction curve fit of sternplane to bowplane lift curve slope ratio in yaw

The curve shown in the figure is defined by

$$\frac{Z'_{sp}(\psi)}{Z'_{sp}|_{\psi=0}} \approx 1 - 0.07063|\psi|^2 + 0.02741|\psi|^{2.5} - 0.00274|\psi|^3 \quad (75)$$

There are local maxima in equation (75) for yaw angles of approximately +/-20 degrees; these values are believed to represent the limit for the local yaw angles to which the bowplanes are subjected (Dominguez, 2000).

4.7 FREE SURFACE INTERACTION MODELLING

In Section 3.4, experimental results were presented regarding the effect of waves on the planes. Using simplified analytical models, the form and magnitude of the wave induced forces on the planes are predicted below for varying vehicle depth and speed. Only sinusoidal waves (with a single, well defined frequency and amplitude) are considered; the principle of superposition (see, for example, Tipler, 1991) can be used to reconstruct the complete wave spectrum.

4.7.1 Variation of Wave-Induced Plane Force with Depth

Surface waves induce rotational velocity components as a function of depth. The magnitude of the wave orbital velocity is given by

$$U_w = a \sqrt{\frac{2\pi g}{\lambda}} e^{-\frac{2\pi d}{\lambda}} \quad (76)$$

where a is the wave amplitude, g is the acceleration due to gravity, λ is the wavelength, and d is the depth (Lamb, 1997).

In order to predict the form of the wave induced force on the planes of the stationary hull, the maximum Z force was assumed to result from flow in the $+z$ or $-z$ direction (that is, straight up or down). This was justified through a comparison of the force coefficient in lift and drag. The maximum measured lift force, expressed in terms of C_L , was approximately 0.6 for the standard bowplanes while a flat plate of the proportions of the bowplane (exposed aspect ratio of 1.5) has a maximum drag coefficient, C_D , of approximately 1.18 (White, 1986). In other words, throughout one wave cycle the largest positive and negative forces on the plane are expected to result from drag when the angle of incidence is ± 90 degrees to the plane. With a wave induced velocity directed vertically, the cylindrical hull experiences cross-flow and the velocity profile across the plane (shown in Figure 4-23) is predicted using experimental results reported by White, (1991).

The maximum wave-induced force on the bowplanes was estimated using the velocity profile described by Figure 4-23 and equation (76) with the force coefficient, C_D , given above. For a given plane element with area dS and position y , the force to depth relationship has the form

$$dZ_{wave}(d) = C_D \frac{1}{2} \rho w^2(y, d) dS \quad (77)$$

Integrating this expression, with reference to equation (76) and Figure 4-23, yields

$$Z_{wave}(d) = C_D \frac{1}{2} \rho S a^2 \frac{2\pi g}{\lambda} e^{-\frac{4\pi d}{\lambda}} \left(\frac{25b^4 - 3R^4 - 30R^2b^2 + 8Rb^3}{25b^3} \right) \quad (78)$$

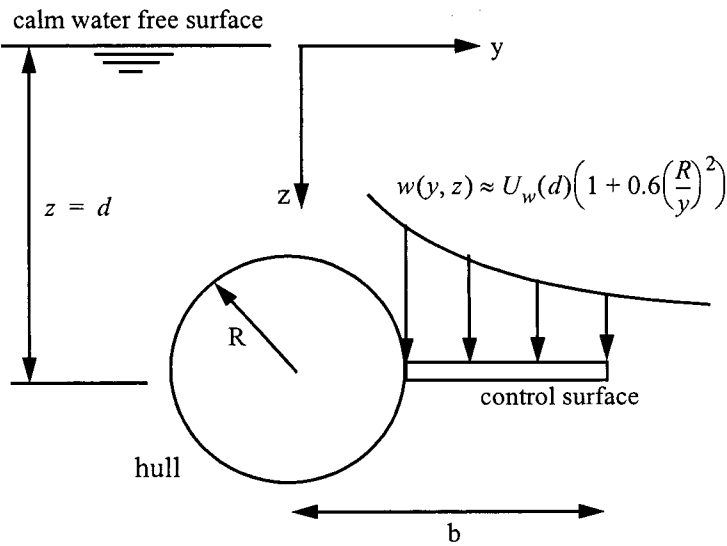


Figure 4-23 Modelled flow over plane

Finally, collecting all the parameters not relating to wave geometry into the variable, C_o , the wave force dependence on wave parameters can be expressed as

$$Z_{wave} = C_o \frac{2\pi g}{\lambda} a^2 e^{-\frac{4\pi d}{\lambda}} \quad (79)$$

In other words, the force is predicted to increase linearly with the square of wave amplitude (contrary to what was observed in Figure 3-55 on page 93) and decay exponentially with d/λ . The difference in the predicted behavior with wave amplitude may be a result of interference with the hull as well as a consequence of the limited range of amplitudes considered in testing.

The amplitude of the wave induced force was computed for conditions corresponding to experiments; specifically, a wave amplitude of $a = 0.043l$ and a wavelength of $\lambda = 1.14l$ were used. The computed wave-induced velocity ranged from approximately 0.5 m/s (at a depth of 0.5 hull diameters) to 0.07 m/s (at 3.5 hull diameters depth). Over this range of depths, the estimated force was computed using equation (78) and was non-dimensionalized according to

$$Z'_g = \frac{Z_{wave}}{\frac{1}{2}\rho g l^3} \quad (80)$$

The resulting predicted wave force on the bowplanes is compared to experimental results in Figure 4-24. Except for the shallowest depth, the predicted wave influence on the bowplanes shows good agreement with the experimental data. For the $d/D = 0.5$ depth, hull immersion was observed and, in general, diffraction forces are very significant for small values of d/D . The general form of the predicted wave force to depth curve closely matches that from experiments. The methods outlined above appear suitable for the prediction of wave induced forces on underwater vehicle control surfaces.

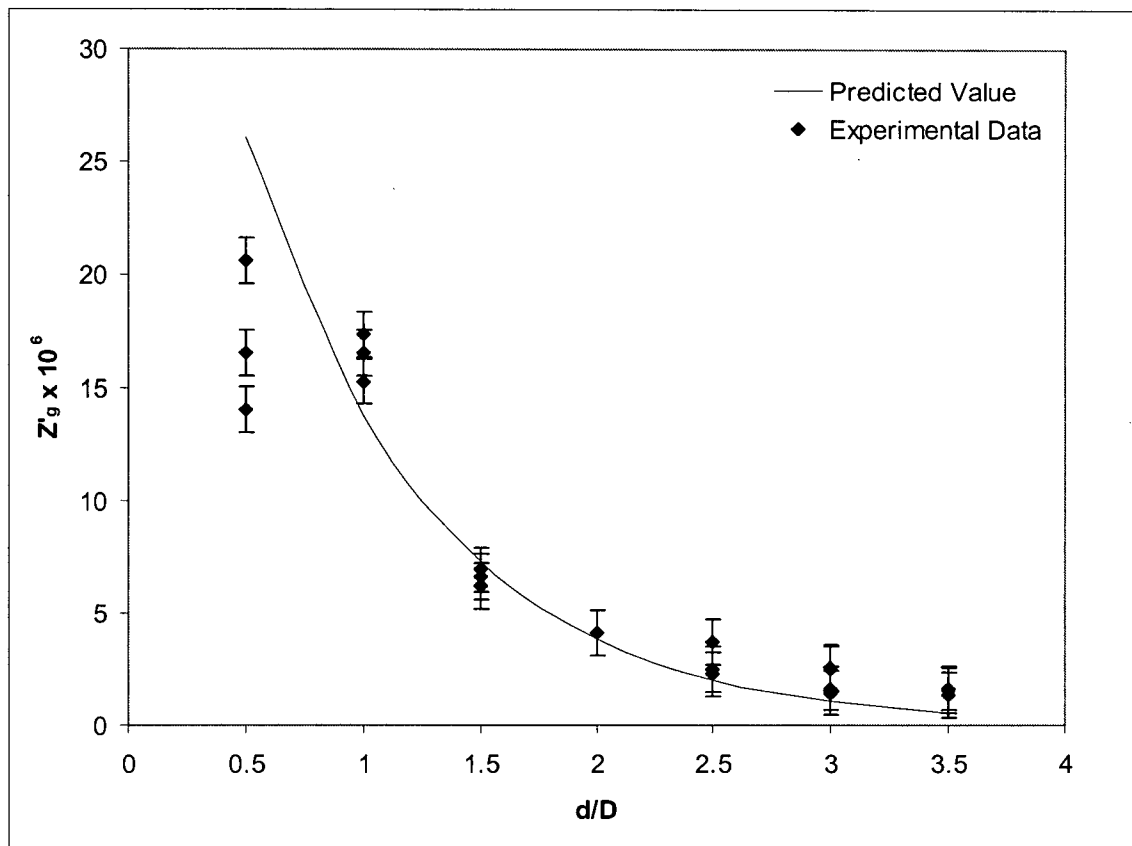


Figure 4-24 Analytical prediction of force on bowplanes as a function of depth

4.7.2 Variation of Wave-Induced Plane Force with Forward Speed

With the same formulation as above, the effect of vehicle forward speed on the wave-induced force was computed. In this case, the largest velocity component was along the vehicle axis due to forward motion. The wave orbital velocity was vectorially combined with the forward speed and the resulting incidence angle was used with the findings of Section 4.3 to estimate the force on the bowplane. The largest force was found when the wave induced velocity was directed orthogonally to the incoming flow, creating the maximum incidence angle (see Figure 4-25).

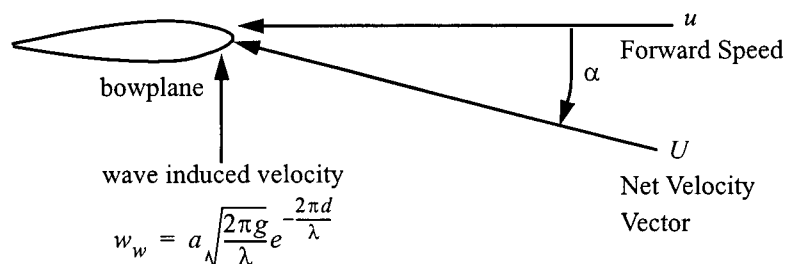


Figure 4-25 Modelled flow over plane

For a wave amplitude of $a = 0.016l$ and a wavelength of $\lambda = 1.14l$, the wave induced velocity ranged from 0.018 m/s to 0.066 m/s for depths of 3.5 and 0.5 hull diameters respectively. Forward speeds of 0.5 to 3.5 m/s were considered in 0.5 m/s increments; these speeds corresponded to Froude numbers based on vehicle length of approximately 0.1 to 0.75. The resulting force on the bowplanes, non-dimensionalized in the standard form to Z , is shown in Figure 4-26 against the experimental data from Section 3.4.5.

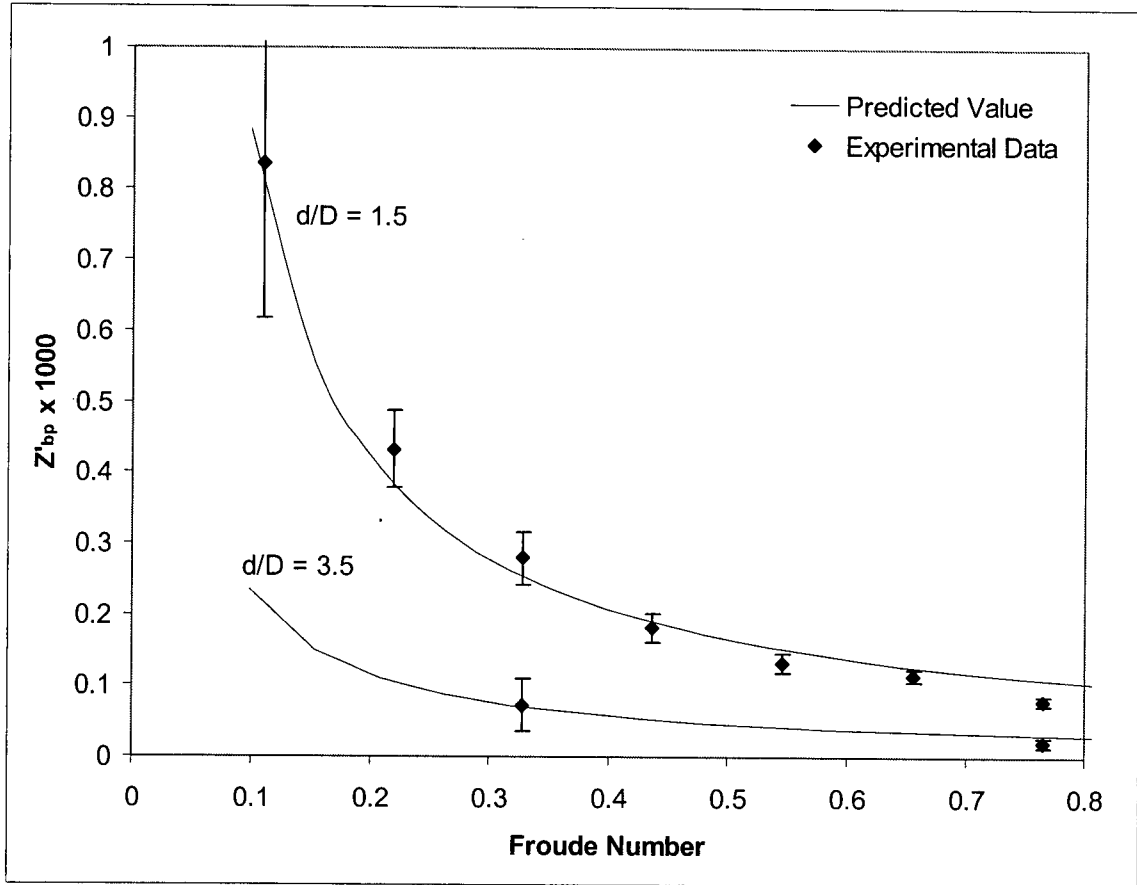


Figure 4-26 Analytical prediction of wave-induced bowplane force as a function of speed

Overall, the agreement between the predicted and measured oscillatory force on the bowplanes is good. With the exception of the point at maximum Froude number and 1.5 hull diameter depth, the predicted force lies within or very close to the error bands of the experimental data. Furthermore, the variation in wave induced force with depth is also accurately predicted as shown by the data at 3.5 hull diameters.

4.8 IMPLEMENTATION

For the purposes of control and simulation, the implementation of the above hydrodynamic modelling is summarized below.

The hydrodynamic forces on the planes were computed from the flow incidence angle and the vehicle speed and orientation. Specifically, the flow incidence angle, α , was used with the second-order hydrodynamic derivatives to establish the force on single control surfaces in straight flight. For example, the force computed for a generic plane is given by

$$Z(\theta, 0) = Z_{\delta}\alpha + Z_{\delta\delta}\alpha|\alpha| \quad (81)$$

where α is the effective incidence angle on the plane due to deflection, vehicle motion, wave induced velocity, and the trim effects (outlined in Section 4.4.1). In reference to equation (41) on page 40, α is given by

$$\alpha \cong \delta + \frac{w - w_w - qx_{plane}}{U} + \alpha_{local} \quad (82)$$

where α_{local} is the local change in flow angle due to the hull. For the bowplanes, α_{local} is the effect of trim described by equation (63) on page 110 and the resulting flow incidence angle is

$$\alpha_{bp} \cong \delta + 1.5 \frac{w - w_w - qx_{bp}}{U} \quad (83)$$

For the sternplanes, local hull effects were not observed (see equation (50) on page 67) thus giving $\alpha_{local} = 0$ and

$$\alpha_{sp} \cong \delta + \frac{w - w_w - qx_{sp}}{U} \quad (84)$$

Based on the vehicle speed, U , the Reynolds number was calculated and the stall angle computed from equation (56) on page 102

$$\alpha_{stall}[deg] = 6.221 \ln Re - 78.24 \quad (Re > 1 \times 10^6) \quad (85)$$

This was compared to the sternplane incidence angle; if the sternplane incidence angle given by equation (84) exceeded the stall angle (in equation (85)) then the sternplane force was computed in equation (81) using the stall angle. The procedure was the same for the bowplanes except the stall angle from equation (85) was scaled by the yaw stall scaling factor ($h(\psi)$ from equation (68)) prior to comparison with the incidence angle of equation (83).

To illustrate the minimal error introduced in this approximation, the actual and modelled forces are shown for the worst case with a windward bowplane in Figure 4-27. The local yaw angle considered is 20 degrees and the speed is 3 m/s (this represents 50% of the typical operating speed in the simulations). Over the range of maximum physical plane deflections, the error in the modelled force remains less than 5% of the force range. For comparison, in the simulations presented in

Chapter 6, the speed remained above 4.7 m/s and local yaw remained below 4 degrees under all cases; for these conditions, the minimum predicted stall angle is 29 degrees, well above the physical plane deflection limit of 25 degrees.

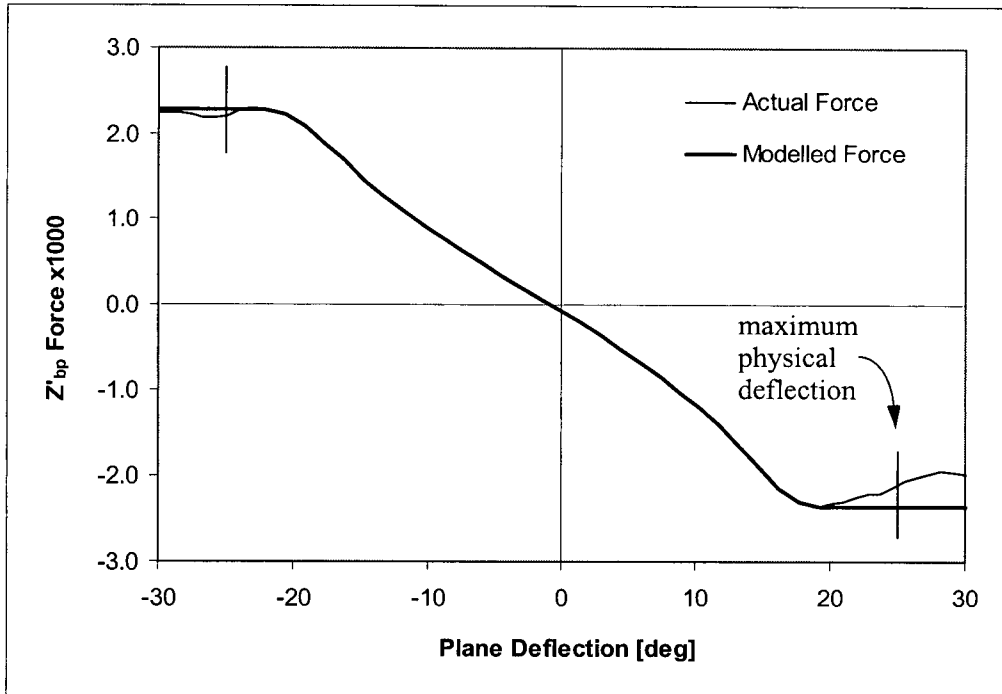


Figure 4-27 Comparison of modelled and actual stall behavior at 3 m/s and 20 degrees yaw

The force from equation (81) was then adjusted to account for the yaw influence the bowplanes and the bowplane influence on the sternplanes. The bowplane force was scaled according to Section 4.5.1; specifically the bowplane force was scaled by the yaw scaling factor, $f(\psi)$, first given in equation (69) on page 115

$$f(\psi) = 1 - 0.220\psi - 4.295\psi^3 \quad (86)$$

The force on the port and starboard bowplanes respectively was

$$Z'_{fp}(\theta, \psi) = f(\psi)Z'_{fp}(\theta, 0) \quad (87)$$

$$Z'_{fs}(\theta, \psi) = f(-\psi)Z'_{fs}(\theta, 0) \quad (88)$$

The force on the sternplanes was augmented by the interaction force due to the bowplanes. The interaction was characterized by the factor, $g(\theta, \psi)$, which was a function of trim and yaw. Specifically, $g(\theta, \psi)$ was the product of equation (74) and equation (75)

$$g(\theta, \psi) = (0.28 - 0.03606|\theta - 1.55|^{1.5} + 0.008715|\theta - 1.55|^2) \times (1 - 0.07063|\psi|^2 + 0.02741|\psi|^{2.5} - 0.00274|\psi|^3) \quad (89)$$

The resulting force on the port and starboard sternplanes respectively was

$$Z_{ap}(\theta, \psi) = Z_{ap}(\theta, 0) \Big|_{\text{no bowplane}} + g(\theta, \psi) Z_{fp}$$

$$Z_{as}(\theta, \psi) = Z_{as}(\theta, 0) \Big|_{\text{no bowplane}} + g(\theta, \psi) Z_{fs}$$

Finally, the force for each plane was re-dimensionalized by multiplying by the dynamic pressure, $\frac{1}{2}\rho U^2$, and the vehicle length, l , squared, to give

$$Z = Z \frac{1}{2} \rho U^2 l^2$$

4.9 SUMMARY

In this chapter, various analytical and numerical techniques were used to validate, predict, and mathematically describe the experimental findings from Chapter 3. The topics considered included: Reynolds number scaling effects, control surface performance prediction, the influence of trim and yaw on bowplanes, bowplane-sternplane interaction, and the interaction from the free surface. The key outcomes of the control surface modelling are outlined below.

Reynolds Number Scaling Effects

- the stall angle was found to increase with the logarithm of Reynolds number
- several methods for scaling plane force to deflection curves with Reynolds number were found to give similar results

Control Surface Performance Prediction

- the semi-empirical control surface performance prediction techniques of Aucher were found to agree closely with experimental data for an isolated appendage. Similar methods of Whicker and Fehlner showed a slight over prediction but generally reasonable agreement with the measured force
- when the hull corrections were applied to the isolated appendage predictions, both Aucher and Whicker and Fehlner yielded estimates that closely matched experimental data for bowplanes

Trim and Yaw Influence

- for both trim and yaw, simple analytical models were able to predict the change in bowplane performance with changing vehicle orientation
- in yaw, polynomial curve fitting was used to describe the change in stall angle and lift curve slope of the bowplanes

Bowplane-Sternplane Interaction

- the interaction between the bowplanes and sternplanes was accurately described using a simple potential flow model
- the agreement between the potential flow model and experimental data was exceptional for changing plane geometry and location as well as changing Reynolds number and trim angle

Free surface Interaction

- the influence of depth and forward speed on the wave induced force on the planes was examined with a simple analytical model
- the magnitude and form of the wave influence predicted from the model matched data from experiments

5

CONTROL SYSTEM DESIGN

A good scientist is a person with original ideas. A good engineer is a person who makes a design that works with as few original ideas as possible.

- Freeman Dyson

Active control is required to operate the DOLPHIN as it has been shown to be unstable in pitch and heave (Shupe and McGeer, 1987); as noted by Field (2000), this instability is related to the hydrodynamic drag of the vehicle when in motion. In general, the highly nonlinear behavior of autonomous underwater vehicles (AUVs), in addition to the noisy operating environments, places challenges on controller design. Furthermore, with the exception of thrust from the propeller, AUV control forces are only generated when the vehicle is in motion. For these reasons, Song et al. (2002) suggest that from the outset of development, a robust control law must be considered. Recently, through significant effort, advances have been made in the development of controllers suitable for underwater vehicles but only minimal emphasis is placed on the treatment of control surfaces by the controller.

Based on the experimental data from Chapter 3 and the modelling relationships developed in Chapter 4, improvements to the design of control systems for underwater vehicles is considered in this chapter. In total six controllers are considered including three variants on a PD controller and three variants on an LQG/LTR controller. In addition to a conventional design with the PD controller, fuzzy-tuned series compensation and gain scheduling implementations are also developed. Likewise, the basic LQG/LTR controller is augmented with sliding mode control and fuzzy-tuned series compensation.

This chapter begins with background information on various feedback control strategies including PID, LQG/LTR, adaptive control and fuzzy logic. The implementation of the control system is then discussed including information on state space representation and control system block diagrams. Finally, three PD controller variants and three LQG/LTR controller variants are introduced for use in simulation in Chapter 6.

5.1 CONTROL BACKGROUND

Various feedback control strategies were considered in this thesis for use with the DOLPHIN AUV. These included PID control, linear quadratic gaussian control with loop transfer recovery (LQG/LTR), various adaptive control techniques, and fuzzy logic. Background information is provided below for each of these methodologies following a discussion of the fundamentals of feedback control.

5.1.1 Feedback Control

The general feedback control system for use with underwater vehicles is shown in block diagram form in Figure 5-1. The controller acts upon the submarine model (or plant) using feedback that has been measured and filtered from the plant output, y . The difference between the reference trajectory, r , determined by a navigation module and the measured output gives the error, e . The error is used as an input to the controller from which the controller determines the required control action, u . Physically, the control action represents the commanded plane deflections or propulsor speed given to the plant. Disturbances, D_{dist} , (from waves, for example) act upon the plant and the measured plant output is also contaminated by noise, N .

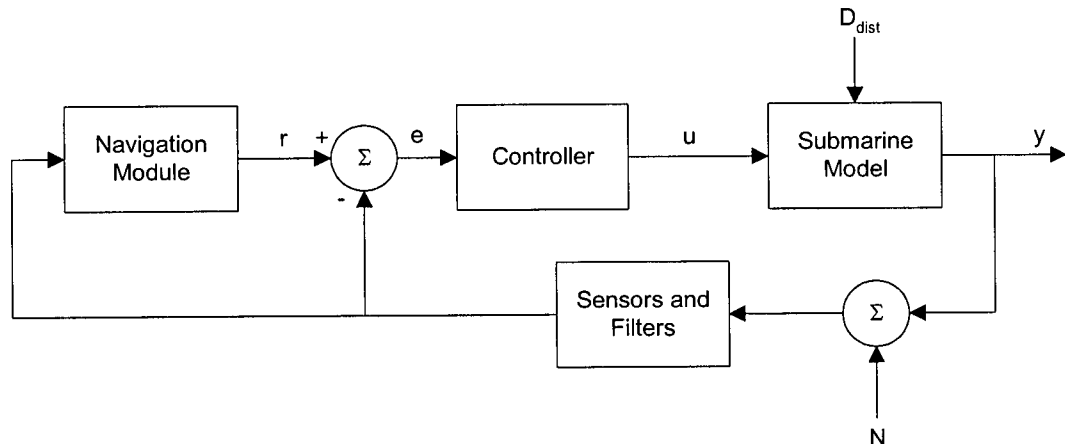


Figure 5-1 Basic feedback control system schematic

Specific details regarding the controller block are described beginning in Section 5.3 following background information on control strategy; details regarding the implementation of the remaining blocks for simulation are outlined beginning in Section 6.2.2 on page 173. Two further augmentations to the basic feedback control structure, including feed-forward compensation and series compensation, were also considered and are described in Section 5.2.

5.1.2 PID Control

PID (proportional-integral-derivative) control and its variants are by far the most commonly used strategy in automatic control. This is largely due to the ease of implementation and intuitive nature of the control methodology. PID control is well described in any elementary control text

(see for example, Dutton et al., 1997, Palm, 1986, or Åström and Wittenmark, 1997). The control action, $u(t)$, is determined from the state error, $e(t)$ according to

$$u(t) = K_p e(t) + K_i \int e(t) + K_d \frac{d}{dt} e(t) \quad (90)$$

where K_p , K_i , and K_d are the gain matrices for the proportional, derivative, and integral components of the control law.

The proportional term produces a control signal that is proportional to the error. Stable response with large steady-state error is associated with low values of K_p . For higher values of K_p , the steady-state performance improves but at the expense of transient performance (overshoot and settling time increase). If K_p is too large, system instability can result.

With the use of integral action, steady state error can be reduced. The integral term acts like an automatic reset to the controller in the presence of disturbances. The integral action does not take effect instantly but continuously corrects for error over time. The drawback of integral action is a reduction in stability as well as increases in oscillation and settling time. In cases where actuators have limited operating range (that is, they can be saturated), special steps must be taken to avoid integrator wind-up which occurs when the commanded control output exceeds the physical limits of an actuator.

Finally, derivative action increases system damping and reduces overshoot and oscillation. Inclusion of a derivative term also allows increases in the proportional and integral gains and has no effect on steady-state behavior. When inputs to the controller are noisy, undesirable behavior can result as the controller inputs may have artificially high rates of change.

PID control has been applied to AUVs in the past and has been used with DOLPHIN (see Shupe and McGeer, 1987, and Butler, 1990); however, it must be implemented with care for several reasons. The highly nonlinear and coupled nature of underwater vehicles results in sub-optimal and potentially unstable behavior with PID controllers. Additionally, tuning of the PID controller gains remains a significant problem and requires extensive knowledge about the vehicle performance characteristics and adequate field testing. Recent efforts, by Pierre and Canudas-de-Wit (1996) for example, have shown success in handling some nonlinear characteristics by adding an outer nonlinear control loop to a standard underwater vehicle PID controller; however, tuning of the original PID controller gains, in addition to the new non-linear components, remains difficult.

5.1.3 Linear Quadratic Control with Loop Transfer Recovery

LQG is a model-based form of optimal control which has been applied to underwater vehicles in the past. In general, linear quadratic (LQ) controllers, operate by minimizing a quadratic performance index, J .

$$J = \int_0^{\infty} (x^T Q x + u^T R u) dt \quad (91)$$

where x is the error in the outputs that are controlled and u is the control effort. An attractive feature of LQ controllers is that as long as the performance index is well formed, the resulting LQ controller will be stable (Dutton et al., 1997). The LQ design process does not produce a unique controller since the matrices Q and R can be adjusted to weight the output error or control effort respectively. The controller is determined by solving the algebraic Riccati equation

$$A^T P + P A - P B R^{-1} B^T P + Q = 0 \quad (92)$$

where, as will be discussed in Section 5.2.1, A and B are matrices that represent the system for which the controller is being designed. In general, the Riccati equation is not solvable except for by numerical means (Dutton et al., 1997). The value of P is determined in the solution of equation (92) and is in turn used to determine the controller

$$K = R^{-1} B^T P \quad (93)$$

The resulting controller, K , is implemented in a feedback control loop according to

$$u = -Kx \quad (94)$$

As opposed to traditional linear quadratic controllers, the LQG control scheme is designed to operate in a noisy environment and as such uses feedback with state estimates in lieu of actual states. The result is a potential loss in robustness over the original LQ design; loop transfer recovery (LTR) provides a means by which to modify the design in order to regain some of the robustness lost from using state estimates (Tay and Moore, 1991). In the LTR approach, the frequency response of the controller is shaped to achieve desired stability and performance properties. The Kalman filter optimization procedure is used for this loop shaping and the combined estimator and controller are designed simultaneously to achieve the desired bandwidth. Further information regarding LQG/LTR, the reader is referred to Stein and Athans (1987) or Kulcsár (2000). LQG/LTR control was employed by Field for his work on the DOLPHIN AUV (Field, 2000); other researcher that has used this control scheme on underwater vehicles includes (Triantafyllou and Grosenbaugh, 1991), (Juul, 1994), and (Naeem et al., 2003).

Although LQG/LTR is known to be robust for linear systems, the application of this methodology to non-linear systems often leads to unnecessary conservatism in the controller; additionally, the control robustness is valid only in the neighborhood of the operating point around which the system was linearized (Ghalia, 1997). In the case of an AUV, several new control surface hydrodynamic features identified in Chapter 3 and Chapter 4 depend on body orientation (such as the trim and yaw effects on the bowplanes and stall angle dependence on Reynolds number). Since the most suitable operating point for the vehicle is straight and level flight, an LQG/LTR controller designed for this case will not take into account effects that only become apparent at non-zero trim and yaw angles.

5.1.4 Adaptive Control Techniques

The control strategies described thus far are based on a stationary (unchanging) submarine plant model. Adaptive control accounts for either changes or uncertainty in plant behavior by adjusting control parameters during operation. In practice, many parameters describing the submarine

dynamics are functions of one or more operating conditions, such as the trim and yaw effects on the bowplanes, as mentioned above. Modelling errors, and hence sub-optimal performance, are introduced by failing to allow changes in control system parameters to account for physical changes in the plant. With adaptive control, it is possible to operate over a wider range of conditions without sacrificing control optimality.

Many forms of adaptive control exist, such as self tuning control, learning control, and model-referenced control, to name a few. Sliding mode control and switching control, in which the controller shifts between different modes depending on operating conditions, is a form of adaptive control. Sliding mode control increases robustness in the presence of nonlinearity, model uncertainty, disturbances, and parameter variation (de Silva, 1995) and has been shown to be effective for the control of AUVs in the dive plane (Cristi et al., 1990). In reference to the transformation of existing Navy platforms, Cancelliere (2001) recommends a system that uses an adaptive nonlinear controller for unmanned underwater vehicles; nonlinear sliding mode control methodology, augmented with real-time model adaptation through neural networks, is used to maintain robust control of a vehicle with a single axial propulsor for velocity control and four small control fins for attitude control.

Gain scheduling techniques are similar to sliding mode control except that the measured changes in operating condition are used to adjust the gain or other parameters in a controller rather than to switch between different controllers. Nonetheless, switching and gain scheduling should produce similar results because the error, controller gains, and controller output should be the same within a given set-point for similar controllers; it is only during sudden transition that the two methods differ (Field et al., 2001). Gain scheduling is widely used in flight control systems and is most applicable to situations where the plant parameters change due to changes in plant load (Dutton et al., 1997).

An attractive feature of gain scheduling is that it allows the application of proven linear design methods to nonlinear problems. In traditional gain scheduling techniques, a series of controllers is designed for the various local equilibrium points and then they are combined. However, this limits operation to the near equilibrium conditions and the dynamic characteristics of a controller with gain-scheduling can be strongly dependent on the manner in which the local (equilibrium) controllers are combined (Leith and Leithead, 1997). Gain scheduling representations based on fuzzy logic and neural network approaches have shown success in addressing this issue (see Leith, 2000, and Lee et al., 2001).

5.1.5 Fuzzy Logic

The roots of fuzzy logic can arguably be traced back as far as to the time of Lao-tze and the Buddha (Kosko, 1993). In conventional or bivalent logic, quantities are represented in a crisp sense with discontinuous boundaries. In contrast, fuzzy logic uses a more continuous form by expressing quantities in matters of degree. Conventional logic is akin to black and white while fuzzy logic is analogous to 'shades of grey'. Moreover, while a quantity is strictly true or false in conventional logic, in fuzzy logic that same quantity can simultaneously be both true and false in differing degrees.

In control applications, fuzzy logic is particularly suitable in situations where the plant is complex or ill-defined (de Silva, 1995). Full fuzzy logic control has been attempted with underwater vehi-

cles in the past; for example, Lea et al. (1999) compared data from the *Subzero II* test AUV operating with fuzzy, sliding mode, and classical control schemes. Performance was satisfactory with all three controllers but each had drawbacks. The fuzzy logic controller in particular required extensive tuning through simulation and even then performance was not as good as with the sliding mode controller. For pitch and heading, automated design of fuzzy logic controllers for AUVs has shown comparable performance to more conventional methodologies (Song and Smith, 2000a).

As noted by de Silva (1995), although fuzzy logic can be implemented independently as a low-level controller, it is better suited to tuning and other high-level tasks. With such a scheme, fuzzy logic operates much like a human supervisor, intelligently adjusting control parameters in the presence of imprecise, general, or uncertain information. For example, Craven et al. (1999) employed a fuzzy inference system for tuning of an AUV autopilot which in turn sends commanded trajectories to a low-level multivariable controller.

Research has developed recently in the application of fuzzy logic to adaptive control; particular areas of research include model reference (Banerjee et al., 2001), gain scheduling (Tzafestas et al., 2001), sliding-mode control (Tzafestas and Rigatos, 1999), and sliding-mode control guidance laws (Lin and Hsu, 2000). By implementing the same controller on different types of vehicles without a significant change in performance, Song and Smith, (2000b) demonstrated robustness benefits of a fuzzy logic sliding mode controller.

5.2 CONTROL SYSTEM IMPLEMENTATION

The state space representation used for modelling and simulation in this thesis is introduced below. Additionally, a description of the basic feedback control system design is provided along with information on feed-forward compensation and series compensation augmentations that were utilized.

5.2.1 State Space Representation

In state space, the submarine model is represented by the following equations

$$\dot{\mathbf{x}} = \mathbf{A}\mathbf{x} + \mathbf{B}\mathbf{u} + \mathbf{M}\mathbf{w} \quad (95)$$

$$\mathbf{y} = \mathbf{C}\mathbf{x} + \mathbf{D}\mathbf{u} + \mathbf{I}\mathbf{n} \quad (96)$$

where \mathbf{x} is the vehicle state vector

$$\mathbf{x} = [u \ v \ w \ p \ q \ r \ x \ y \ z \ \phi \ \theta \ \psi]^T, \quad (97)$$

\mathbf{u} is the controller output vector given by the commanded plane deflections, rudder deflection, and propeller speed

$$\mathbf{u} = [\delta_{fp} \ \delta_{fs} \ \delta_{ap} \ \delta_{as} \ \delta_r \ n]^T \quad (98)$$

and \mathbf{y} is the vehicle output

$$\mathbf{y} = [u \ z \ \phi \ \theta \ \psi]^T \quad (99)$$

The construction of the plant matrix, \mathbf{A} , for a six degree-of-freedom submarine is complicated; it is easiest to visualize the 12×12 matrix as the union of four 6×6 sub-matrices as shown in equation (100).

$$\mathbf{A} = \begin{bmatrix} -(\mathbf{M}_{rb} + \mathbf{M}_A)^{-1}(\mathbf{C}_{rb} + \mathbf{C}_A + \mathbf{D}_d) & -(\mathbf{M}_{rb} + \mathbf{M}_A)^{-1}\mathbf{G} \\ \mathbf{Q} & 0 \end{bmatrix} \quad (100)$$

The terms that combine to form the plant matrix are: the rigid body mass matrix, \mathbf{M}_{rb} ; the Coriolis matrix, \mathbf{C}_{rb} ; the added mass matrix, \mathbf{M}_A ; the Coriolis added mass matrix, \mathbf{C}_A ; the damping matrix, \mathbf{D}_d ; and the rotational transformation matrix, \mathbf{Q} . Further information regarding the components that form the plant matrix is provided in Appendix D.1 and complete details are provided by Field (2000).

The input matrix, \mathbf{B} , is a linear description of the forces generated by the control surfaces and propeller for a given deflection or engine speed. Specifically,

$$\mathbf{B} = \begin{bmatrix} X_{\delta fp} & X_{\delta fs} & X_{\delta ap} & X_{\delta as} & X_{\delta r} & X_n \\ Y_{\delta fp} & Y_{\delta fs} & Y_{\delta ap} & Y_{\delta as} & Y_{\delta r} & Y_n \\ Z_{\delta fp} & Z_{\delta fs} & Z_{\delta ap} & Z_{\delta as} & Z_{\delta r} & Z_n \\ K_{\delta fp} & K_{\delta fs} & K_{\delta ap} & K_{\delta as} & K_{\delta r} & K_n \\ M_{\delta fp} & M_{\delta fs} & M_{\delta ap} & M_{\delta as} & M_{\delta r} & M_n \\ N_{\delta fp} & N_{\delta fs} & N_{\delta ap} & N_{\delta as} & N_{\delta r} & N_n \end{bmatrix} \quad (101)$$

Examining the relationship between vehicle state and the output, the remaining matrices in this implementation are

$$\mathbf{C} = \begin{bmatrix} 1 & 0 & 0 & 0 & 0 & 0 & 0 & 0 & 0 & 0 & 0 \\ 0 & 0 & 0 & 0 & 0 & 0 & 0 & 0 & 1 & 0 & 0 \\ 0 & 0 & 0 & 0 & 0 & 0 & 0 & 0 & 0 & 1 & 0 \\ 0 & 0 & 0 & 0 & 0 & 0 & 0 & 0 & 0 & 0 & 1 \\ 0 & 0 & 0 & 0 & 0 & 0 & 0 & 0 & 0 & 0 & 1 \end{bmatrix} \quad (102)$$

and \mathbf{D} is the zero matrix or

$$\mathbf{D} = 0 \cdot \mathbf{I}$$

The process noise levels are represented by the matrix \mathbf{M} with white noise \mathbf{w} of unit intensity and covariance \mathbf{W} . The sensor noise, \mathbf{n} , is also assumed to be white noise of unit intensity with covariance \mathbf{N} .

5.2.2 Feed-forward Compensation

In some instances, non-zero control output is desirable even when the error signal input to the controller is zero. As an example with DOLPHIN, there is a non-zero pitching moment that changes with speed and depth as a result of the vehicle asymmetry about the horizontal plane; likewise, there is a hydrostatic pitching moment that changes as fuel is consumed and replaced by seawater ballast. Rather than allow these effects to act as unmodelled disturbances, the control signals necessary to maintain level trim can be automatically added to the controller output. These feed-forward control signals, \mathbf{u}_{ff} are determined using a feed-forward compensator as shown in Figure 5-2. For this thesis, the feed-forward control is computed based on the initial conditions and thereafter remains constant; it is included in all further controller augmentations whether stated explicitly or not.

5.2.3 Series compensation

It is not always possible to adjust controller gains in order to satisfy all performance requirements; in such cases, one option is to add a compensator to the system to alter the original controller response. In addition to the feed-forward method discussed above, there are several common forms in which compensation is implemented including series, parallel, and disturbance compensation (see, for example, Palm, 1995). In this thesis, several controllers are augmented with series compensation (shown in Figure 5-3). As an input, the compensator takes the commanded plane deflections from the controller and adjusts these based on operating conditions. The form of the compensator is tuned during operation (discussed in detail in sections Section 5.3.3 and Section 5.4.3).

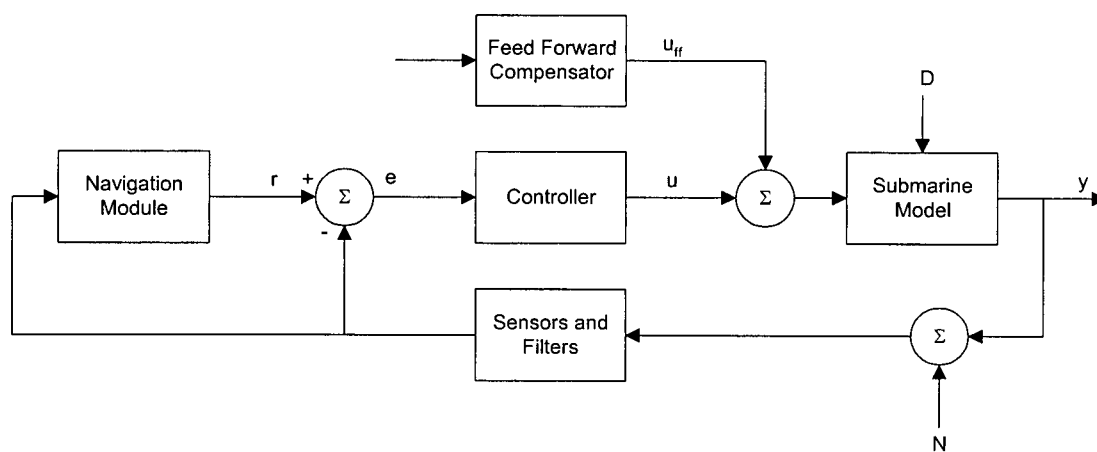


Figure 5-2 Feed forward compensator

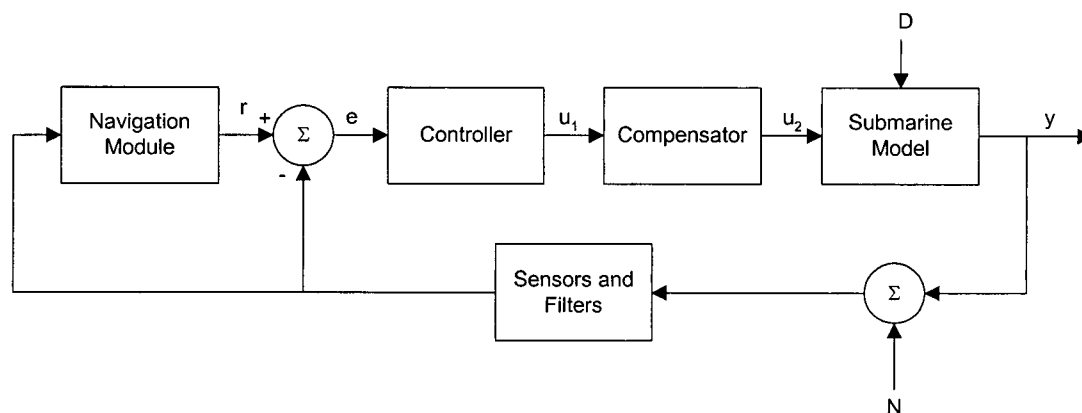


Figure 5-3 Feedback controller with series compensator

5.3 PD CONTROLLERS

A simple PD controller was developed based on previous work on the DOLPHIN. Two augmentations to the basic controller methodology were also considered in an attempt to better compensate for the newly identified control surface hydrodynamic effects outlined in Chapter 3 and Chapter 4. In one instance, gain scheduling is used to change the controller gains during operation based on the predicted control surface performance. In a second augmentation, a series compensator is added to the controller to adjust the controller outputs again based on predicted control surface performance.

5.3.1 Basic PD

A basic PD controller was developed based on a design reported by Shupe and McGeer (1987). The form of the controller is shown in Figure 5-4 where the controller is represented by the 6×12 matrix, K . In state space, the control signals are generated according to

$$\mathbf{u} = -\mathbf{K}\mathbf{e} \quad (103)$$

In expanded form this becomes

$$\begin{bmatrix} \delta_{fp} \\ \delta_{fs} \\ \delta_{ap} \\ \delta_{as} \\ \delta_r \\ n \end{bmatrix} = - \begin{bmatrix} 0 & 0 & 0.25 & 0 & 0 & 0 & 0 & 0 & 0.125 & 0 & 0 & 0 \\ 0 & 0 & 0.25 & 0 & 0 & 0 & 0 & 0 & 0.125 & 0 & 0 & 0 \\ 0 & 0 & 0 & -4 & 4 & 0 & 0 & 0 & 0 & -3.6 & 3.57 & 0 \\ 0 & 0 & 0 & 4 & 4 & 0 & 0 & 0 & 0 & 3.6 & 3.57 & 0 \\ 0 & 0 & 0 & 0 & 0 & 4 & 0 & 0 & 0 & 0 & 0 & 4 \\ 1 & 0 & 0 & 0 & 0 & 0 & 0 & 0 & 0 & 0 & 0 & 0 \end{bmatrix} \begin{bmatrix} e_u \\ e_v \\ e_w \\ e_p \\ e_q \\ e_r \\ e_x \\ e_y \\ e_z \\ e_\phi \\ e_\theta \\ e_\psi \end{bmatrix} \quad (104)$$

Depth control is provided exclusively by the bowplanes; port and starboard planes are coupled (that is, deflected by the same amount in the same direction as opposed to being controlled differentially). Depth control is based on the depth error, e_z , as well as depth rate error, e_w (these represent the proportional and derivative elements of the PD control respectively). Roll and pitch control authority are assigned to the sternplanes. In this case the port and starboard planes are coupled in pitch control and have equal and opposite commanded deflections in roll control. For the roll and pitch errors, the sternplanes operate with a proportional component (based on e_ϕ and e_θ) and a derivative component (based on e_p and e_q). The rudder is solely responsible for heading (yaw) control based on the heading error, e_ψ , and the heading rate error, e_r . Finally, the propeller

speed, n , is controlled proportionally, based on the error in surge, e_u . Evident by the columns in K with only zero entries, there is no control of the error in v , x , or y .

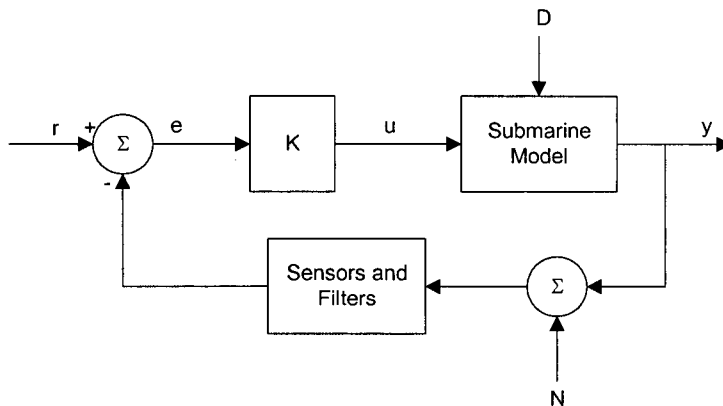


Figure 5-4 Basic PD controller block diagram

The controller gains, K , were tuned through simulation (Chapter 6) using initial values provided by Shupe and McGeer for the Mark I DOLPHIN. In the simulation, controller gains were iteratively modified using an evaluation manoeuvre until the gain matrix with the best performance was determined. This is not unlike the procedure used in the initial development of DOLPHIN where controller parameters were tuned in the field (den Hertog, 1997). More systematic methods of tuning PID controllers exist—the most common of these tuning methods being that of Ziegler-Nichols (1941) (see also, Dutton et al., 1997, Palm, 1986, or Åström and Wittenmark, 1997)—however, due to the strong coupling in the plant equations, it was not possible to implement this type of tuning in this case.

5.3.2 PD Control With Gain Scheduling

Gain scheduling was incorporated in one implementation of the PD controller to account for change in bowplane force with body orientation. In this case, a crisp (that is, non-fuzzy) tuner was used to alter the values of the gain matrix, K_{gs} , during operation. As shown in Figure 5-5, the tuner used the measured vehicle state as input from which it adjusted the controller accordingly.

Adjusted Bowplane Deflection

Based on the commanded port bowplane deflection, δ_{fp} , the approximate commanded port bowplane force (to the first order) is:

$$Z_{fp} \cong Z_{\delta_{fp}} \delta_{fp} \cdot f(0) = Z'_{\delta_{fp}} \delta_{fp} \quad (105)$$

Where $f(0)$ is the yaw scaling factor introduced in Section 4.5; in this case it is applied for the initial conditions with a yaw angle of zero, in which $f(0)$ is equal to unity. However, the first order

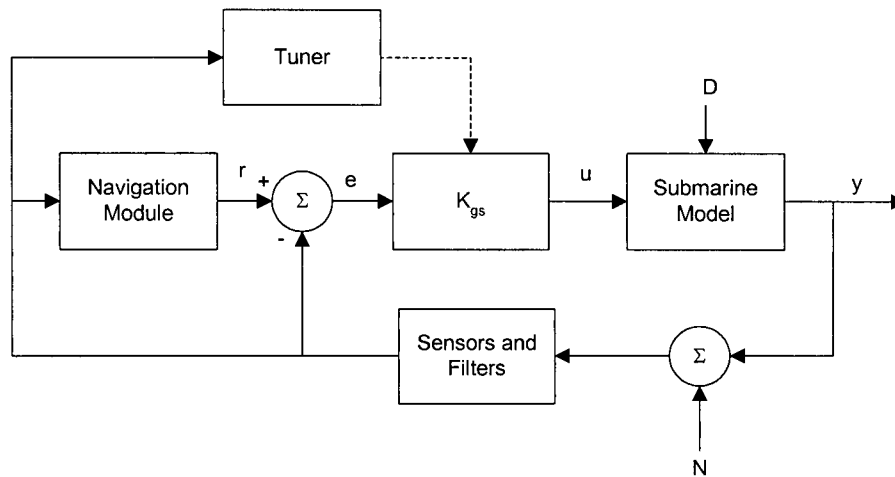


Figure 5-5 Gain scheduling PD controller schematic

approximation of the actual force, $Z_{fp(a)}$ (for which the yaw angle may not be zero) includes the yaw scaling factor, $f(\psi)$, giving:

$$Z_{fp(a)} \cong Z_{\delta fp} \delta_{fp(a)} \cdot f(\psi) \quad (106)$$

As the actual force should be equal to the commanded force, equation (105) and equation (106) can be equated to give the desired plane deflection, $\delta_{fp(a)}$:

$$\delta_{fp(a)} \cong \frac{\delta_{fp}}{f(\psi)} \quad (107)$$

Similarly, for the starboard bowplane, the desired plane deflection is:

$$\delta_{fs(a)} \cong \frac{\delta_{fs}}{f(-\psi)} \quad (108)$$

Adjusted Sternplane Deflection

For the port sternplane, the force based on commanded deflection is:

$$Z_{ap} \cong Z_{\delta ap} \delta_{ap} \quad (109)$$

The actual port sternplane force includes the bowplane-sternplane interaction factor, $g(\theta, \psi)$:

$$Z_{ap(a)} \cong Z_{\delta ap} \delta_{ap(a)} + g(\theta, \psi) \cdot Z_{fp(a)} \quad (110)$$

Substituting the port bowplane force from equation (106) gives

$$Z_{ap(a)} \cong Z_{\delta ap} \delta_{ap(a)} + g(\theta, \psi) \cdot Z_{\delta fp} \delta_{fp(a)} \cdot f(\psi) \quad (111)$$

Again, the actual force should be equal to the commanded force and therefore equation (109) and equation (111) can be equated to give

$$Z_{\delta ap} \delta_{ap} \cong Z_{\delta ap} \delta_{ap(a)} + g(\theta, \psi) \cdot f(\psi) \cdot Z_{\delta fp} \cdot \delta_{fp(a)} \quad (112)$$

and the desired port sternplane deflection is

$$\delta_{ap(a)} \cong \delta_{ap} - g(\theta, \psi) \cdot f(\psi) \cdot \frac{Z_{\delta fp}}{Z_{\delta ap}} \cdot \delta_{fp(a)} \quad (113)$$

Likewise, the desired starboard sternplane deflection is

$$\delta_{as(a)} \cong \delta_{as} - g(\theta, \psi) \cdot f(-\psi) \cdot \frac{Z_{\delta fs}}{Z_{\delta as}} \cdot \delta_{fs(a)} \quad (114)$$

Changes to Controller Gain Matrix

The desired plane deflections can be expressed in a relationship to the commanded deflections as:

$$\mathbf{u}_{(a)} = \mathbf{K}_{(a)} \mathbf{u} \quad (115)$$

where $\mathbf{K}_{(a)}$ is based on the above empirically-derived relationships giving:

$$\mathbf{K}_{(a)} = \begin{bmatrix} \frac{1}{f(\psi)} & 0 & 0 & 0 & 0 & 0 \\ 0 & \frac{1}{f(-\psi)} & 0 & 0 & 0 & 0 \\ -g(\theta, \psi) f(\psi) \frac{Z_{\delta fp}}{Z_{\delta ap}} & 0 & 1 & 0 & 0 & 0 \\ 0 & -g(\theta, \psi) f(-\psi) \frac{Z_{\delta fp}}{Z_{\delta ap}} & 0 & 1 & 0 & 0 \\ 0 & 0 & 0 & 0 & 1 & 0 \\ 0 & 0 & 0 & 0 & 0 & 1 \end{bmatrix} \quad (116)$$

In the Basic PD control implementation, the control output was determined according to $\mathbf{u} = -\mathbf{K}\mathbf{e}$. To determine the desired control action, $\mathbf{u}_{(a)}$, that accounts for the new control surface hydrodynamics, $\hat{\mathbf{u}}$ must be pre-multiplied by $\mathbf{K}_{(a)}$ (as given in equation (115)). The new control law is therefore described by

$$\mathbf{u}_{(a)} = -\mathbf{K}_{(a)} \mathbf{K} \mathbf{e} = -\mathbf{K}_{gs} \mathbf{e} \quad (117)$$

where K_{gs} is the new gain matrix for use with gain scheduling and is given by

$$K_{gs} = \begin{bmatrix} 0 & 0 & \frac{0.25}{f(\psi)} & 0 & 0 & 0 & 0 & 0 & \frac{0.125}{f(\psi)} & 0 & 0 & 0 \\ 0 & 0 & \frac{0.25}{f(-\psi)} & 0 & 0 & 0 & 0 & 0 & \frac{0.125}{f(-\psi)} & 0 & 0 & 0 \\ 0 & 0 & -g(\theta, \psi) f(\psi) \frac{Z_{\delta fs}}{Z_{\delta fs}} 0.25 & -4 & 4 & 0 & 0 & 0 & -g(\theta, \psi) f(\psi) \frac{Z_{\delta fs}}{Z_{\delta fs}} 0.125 & -3.6 & 3.57 & 0 \\ 0 & 0 & -g(\theta, -\psi) f(-\psi) \frac{Z_{\delta fs}}{Z_{\delta fs}} 0.25 & 4 & 4 & 0 & 0 & 0 & -g(\theta, -\psi) f(-\psi) \frac{Z_{\delta fs}}{Z_{\delta fs}} 0.125 & 3.6 & 3.57 & 0 \\ 0 & 0 & 0 & 0 & 0 & 4 & 0 & 0 & 0 & 0 & 0 & 4 \\ 1 & 0 & 0 & 0 & 0 & 0 & 0 & 0 & 0 & 0 & 0 & 0 \end{bmatrix} \quad (118)$$

Implementation

The gain scheduling matrix, K_{gs} , and the tuner are implemented as shown Figure 5-5. The tuner design is shown in Figure 5-6.

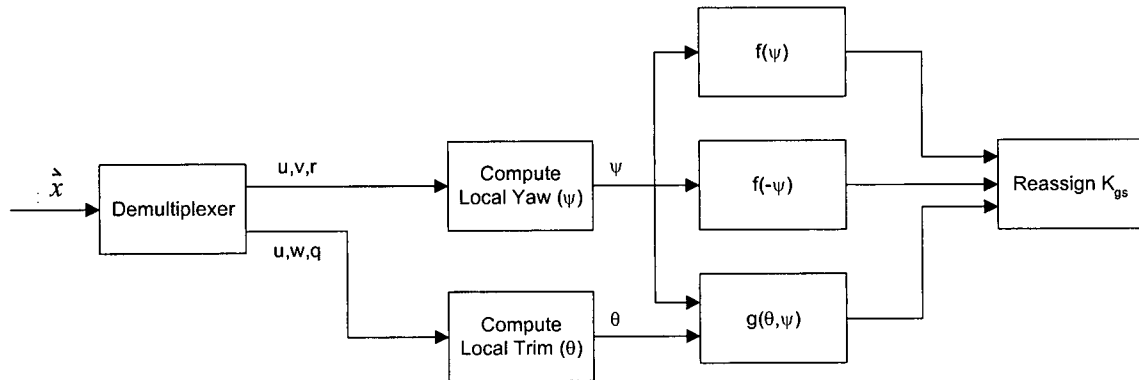


Figure 5-6 Tuner schematic used in gain scheduling PD controller

The measured state, \hat{x} , is separated into the elements of u , v , w , q , and r and then the local trim and yaw at the bowplanes are computed. The trim, θ , is given by

$$\theta = \text{atan}\left(\frac{w - x_{bp}q}{u}\right) \quad (119)$$

where x_{bp} is the x -coordinate of the bowplanes measured from the centre of gravity. Likewise, the local yaw is given by

$$\psi = \text{atan}\left(\frac{v + x_{fp}r}{u}\right) \quad (120)$$

With the local values of θ and ψ , the yaw scaling effect on the bowplanes, $f(\psi)$, and the bowplane-sternplane interaction factor, $g(\theta, \psi)$ are computed. These values are used to recompute the gain matrix, K_{gs} , as given in equation (114); the value of K_{gs} is then updated to the controller.

5.3.3 PD Control With Fuzzy-Tuned Series Compensation

A second method of correcting for the control surface performance characteristics outlined in Chapter 4 was devised using a series compensator and fuzzy logic. In principle, the design of series compensation augmenting was similar to that of the gain scheduling; commanded outputs from the controller were adjusted to account for the known control surface hydrodynamic effects. The block diagram for the control system with the fuzzy-tuned series compensator is shown in Figure 5-7.

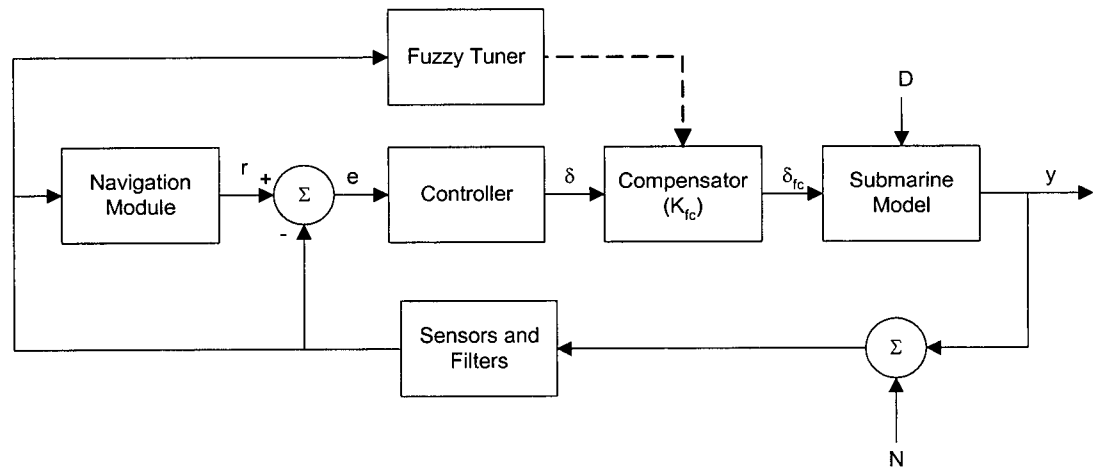


Figure 5-7 Fuzzy-tuned series compensator block diagram

Fuzzy Tuner Layout

The schematic of the fuzzy tuner is shown in Figure 5-8. Similar to the gain scheduling controller of Section 5.3.2, the local yaw and trim is computed based on the measured states. These two values are used as inputs to three fuzzy logic input-output modules. One module accounts for the change in port bowplane force with yaw angle (k_{fp}), a second accounts for the change in starboard bowplane force with yaw angle (k_{fs}), and the final module accounts for the change in bowplane-sternplane interaction as a function of trim and yaw (k_a).

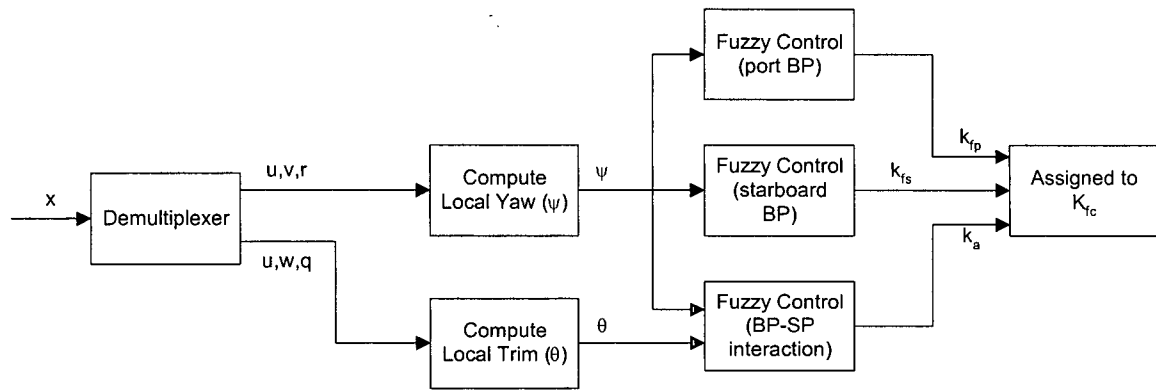


Figure 5-8 Fuzzy-tuner schematic

The output from the fuzzy modules is assigned to the series compensation matrix, K_{fc} shown in Figure 5-7 and given by:

$$K_{fc} = \begin{bmatrix} k_{fp} & 0 & 0 & 0 & 0 & 0 \\ 0 & k_{fs} & 0 & 0 & 0 & 0 \\ k_a & 0 & 1 & 0 & 0 & 0 \\ 0 & k_a & 0 & 1 & 0 & 0 \\ 0 & 0 & 0 & 0 & 1 & 0 \\ 0 & 0 & 0 & 0 & 0 & 1 \end{bmatrix} \quad (121)$$

Determination of Tuning Parameters

The tuning parameters k_{fp} , k_{fs} , and k_a were computed using the local yaw and trim as inputs for functions developed off-line. The functions were developed using fuzzy logic and were based on the control surface behavior determined in Chapter 3 and Chapter 4.

The deflection for the port bowplane is increased by a factor k_{fp} to account for changes in the performance of that plane in yaw. The fuzzy rule-base used in determining the value of k_{fp} is given in Table 5-2. The three conditions of the yaw input refer to positive yaw (PY), zero yaw (ZY), and negative yaw (NY); three conditions of the k_{fp} output refer to negative k_{fp} (NO), zero k_{fp} (ZO), and positive k_{fp} (PO). In short, if the yaw is zero then there is no correction; for positive yaw k_{fp} is increased; and for negative yaw k_{fp} is decreased. The fuzzy logic calculation methods used are summarized in Table 5-1. The membership functions of the yaw input and k_{fp} output are shown in Figure 5-9 and Figure 5-10 respectively.

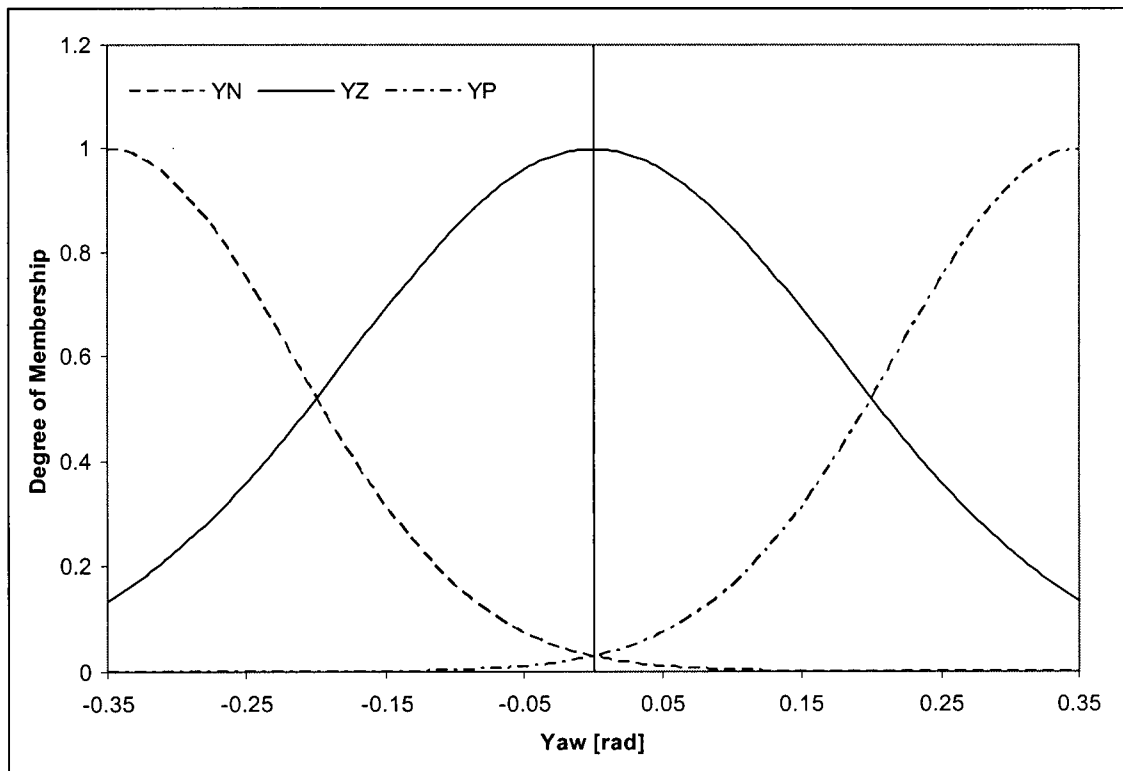
After defuzzification, the resulting fuzzy control surface—as used in the conventions of fuzzy logic and not to be confused with the planes on the vehicle—is given in Figure 5-11.

Table 5-1 Fuzzy logic calculation methods

Method	Type
And method	min
Or method	max
Implication	min
Aggregation	max
Defuzzification	centroid

Table 5-2 Fuzzy rule-base for k_{fp}

Rule	Input	Case	Output	Case
1	if Yaw is PY	then k_{fp} is PO		
2	if Yaw is ZY	then k_{fp} is ZO		
3	if Yaw is NZ	then k_{fp} is NO		

Figure 5-9 Input (yaw) membership function for k_{fp} and k_{fs}

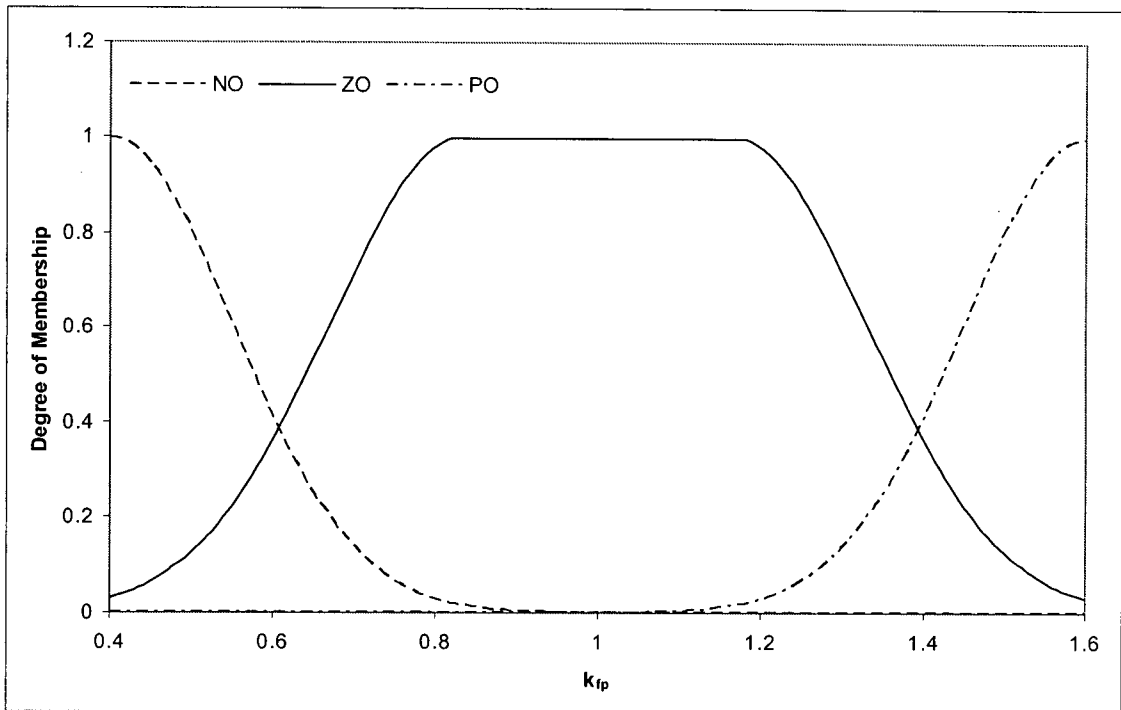


Figure 5-10 Output membership function for k_{fp} and k_{fs}

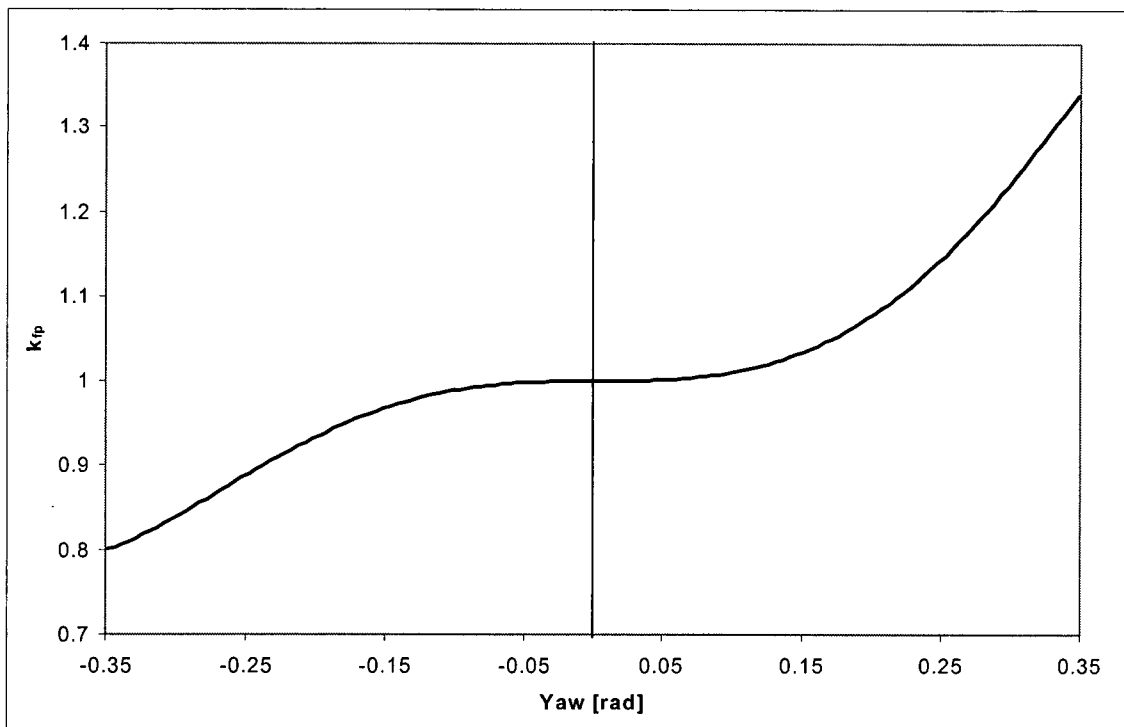


Figure 5-11 Fuzzy logic control surface for k_{fp}

For the starboard bowplane, the membership functions for k_{fs} are the same as those for k_{fp} above. The only difference is in the rule-bases (shown in Table 5-3) which results in a control surface for k_{fs} that is a mirror image of that for k_{fp} (see Figure 5-12).

Table 5-3 Fuzzy rule-base for k_{fs}

Rule	Input	Case	Output	Case
1	if Yaw is YP	then k_{fs} is NO		
2	if Yaw is YZ	then k_{fs} is ZO		
3	if Yaw is YN	then k_{fs} is PO		

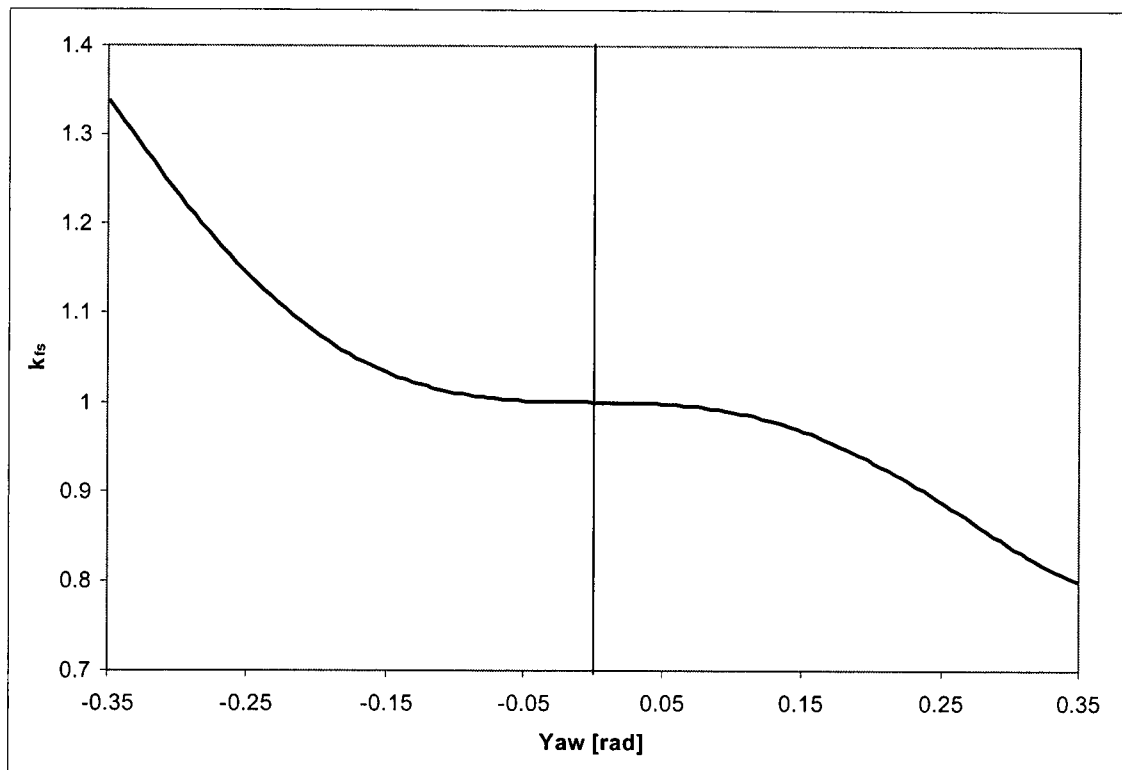


Figure 5-12 Fuzzy logic control surface for k_{fs}

For the bowplane-sternplane interaction (corrected using k_a) both yaw and trim are used as inputs in generating the fuzzy control surface. The rule-base for this case is given in Table 5-4 where the output, k_a , is now either small and positive (SPO), zero (ZO), small and negative (SNO), or large and negative (LNO). The correction factor, k_a , is largest for straight and level flight where trim and yaw are both zero, there is no correction when both trim and yaw are large, and there are small corrections otherwise. The membership functions for the yaw input, trim input, and k_a output are

given in Figure 5-13, Figure 5-14, and Figure 5-15 respectively. The resulting fuzzy logic control surface for k_a is given in Figure 5-16.

Table 5-4 Fuzzy rule-base for k_a

Rule	Input 1			Case	Input 2			Case	Output	Case		
1	if	Yaw	is	YN	and if	Trim	is	TN	then	k_a	is	ZO
2	if	Yaw	is	YN	and if	Trim	is	TZ	then	k_a	is	SPO
3	if	Yaw	is	YN	and if	Trim	is	TP	then	k_a	is	ZO
4	if	Yaw	is	YZ	and if	Trim	is	TN	then	k_a	is	SNO
5	if	Yaw	is	YZ	and if	Trim	is	TZ	then	k_a	is	LNO
6	if	Yaw	is	YZ	and if	Trim	is	TP	then	k_a	is	SNO
7	if	Yaw	is	YP	and if	Trim	is	TN	then	k_a	is	ZO
8	if	Yaw	is	YP	and if	Trim	is	TZ	then	k_a	is	SPO
9	if	Yaw	is	YP	and if	Trim	is	TP	then	k_a	is	ZO

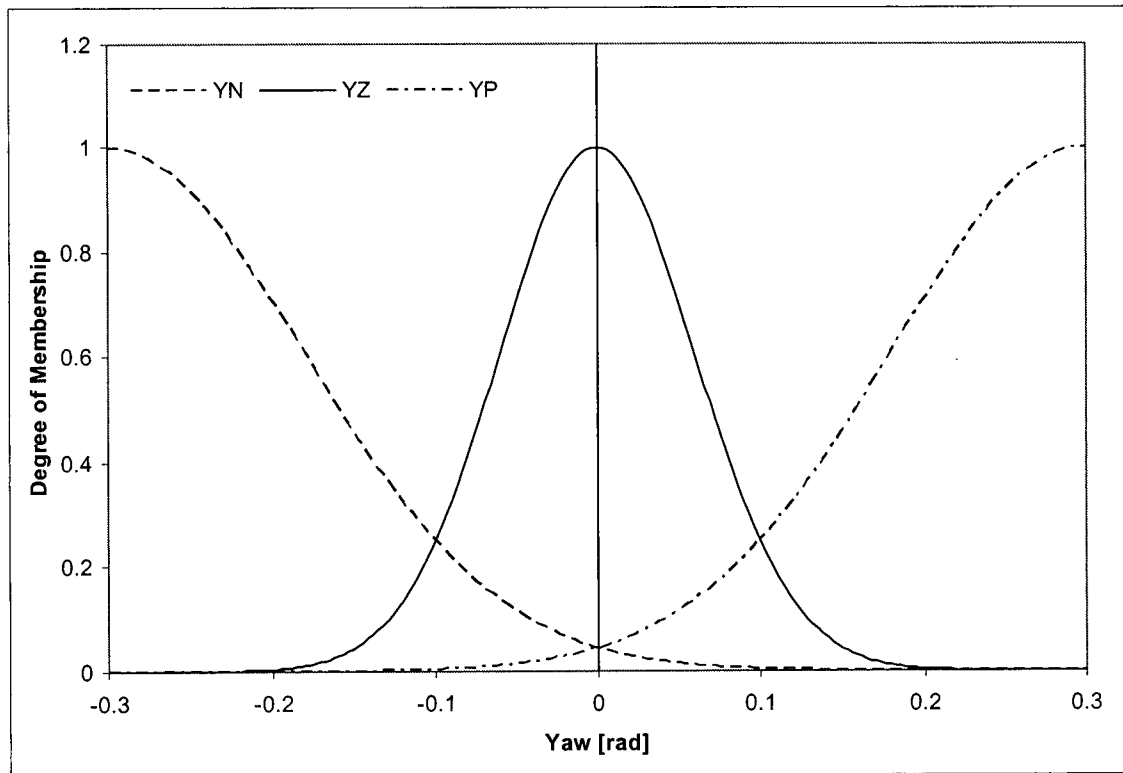


Figure 5-13 Input (yaw) membership function for k_a

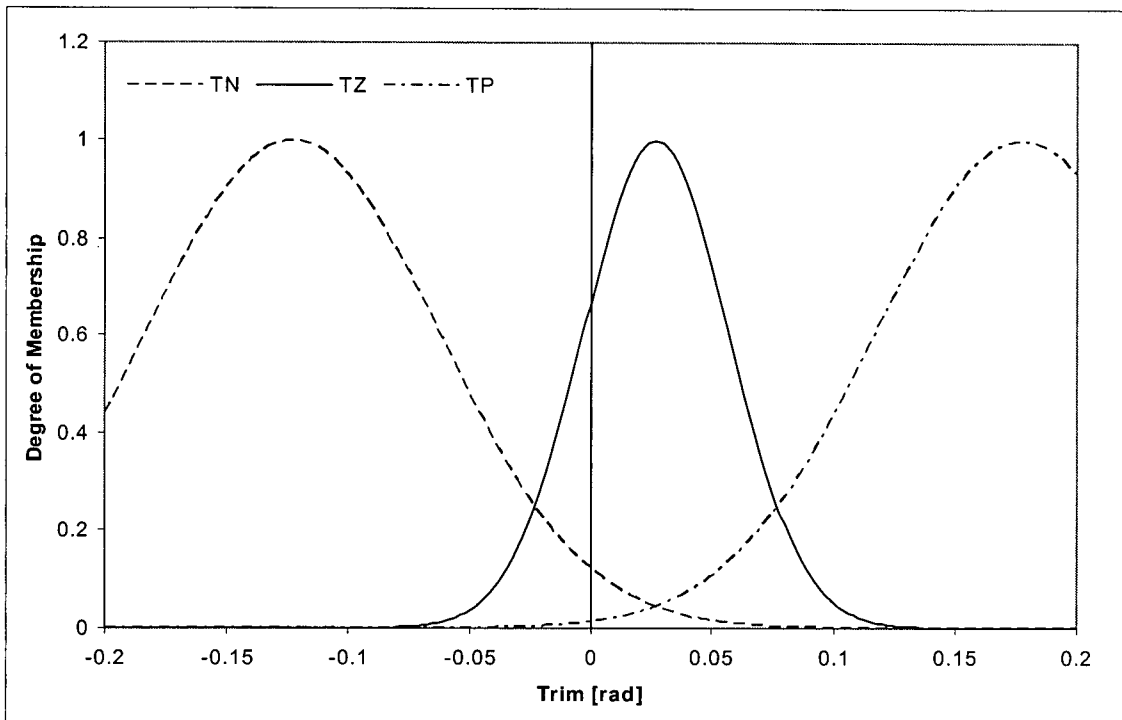


Figure 5-14 Input (trim) membership function for k_a

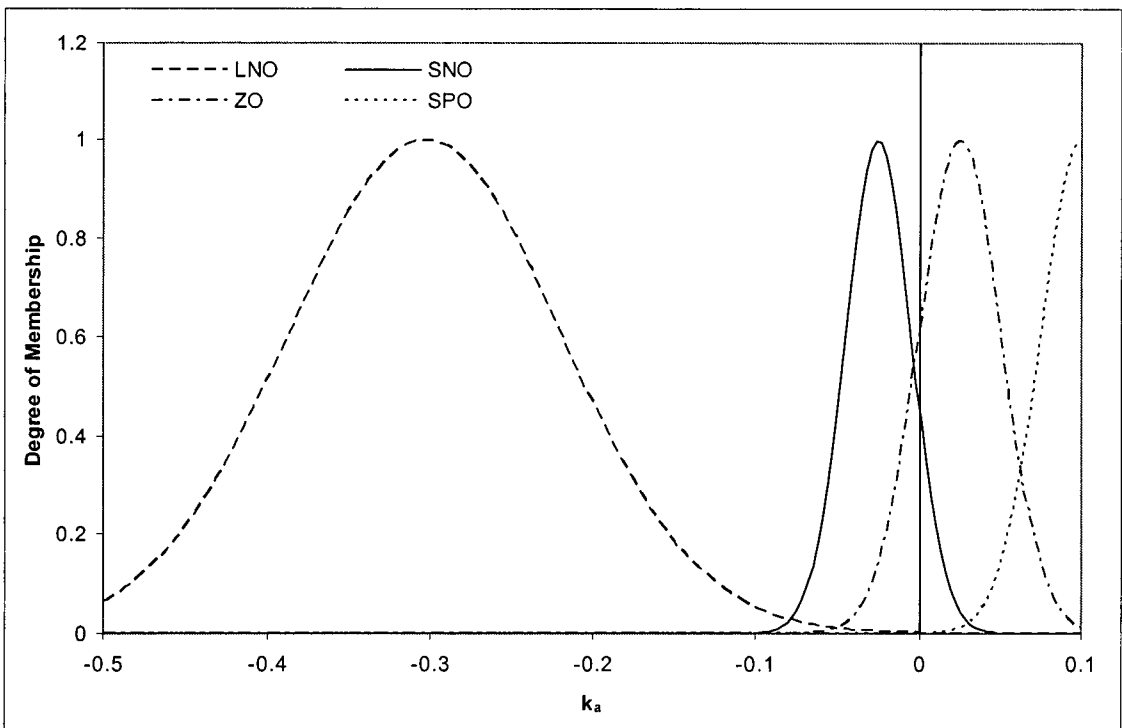


Figure 5-15 Output membership function for k_a

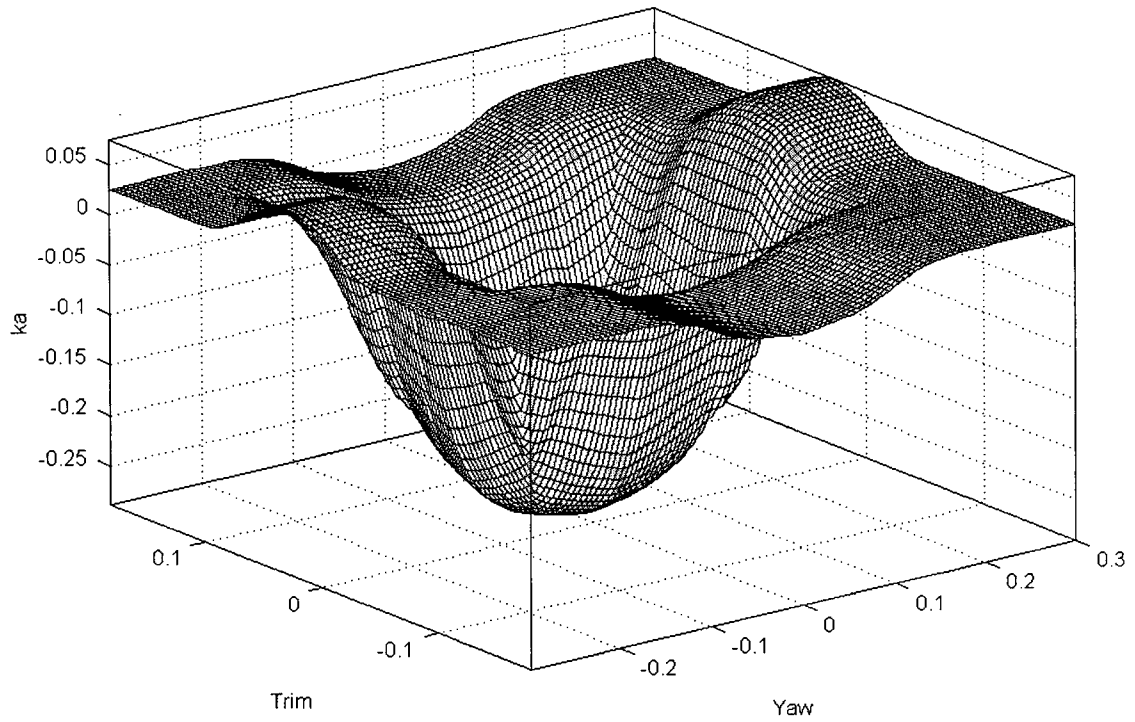


Figure 5-16 Fuzzy logic control surface for k_a

5.4 LQG/LTR CONTROLLER

Three different LQG/LTR controller implementations were developed to examine potential benefits to control surface performance. A basic LQG/LTR controller developed by Field (2000) is presented first, followed by a sliding mode LQG/LTR controller and an LQG/LTR controller with fuzzy-tuned series compensation.

5.4.1 Basic LQG/LTR

Complete details regarding the development of the LQG/LTR controller was provided by Field (2000); the key steps in the controller development are reproduced below.

Controller Layout

The block diagram of the LQG/LTR controller used is shown in Figure 5-17. The Kalman filter (shown in the dashed box) has a gain matrix L_{in} and takes the error, e , scaled by the matrix K_o as input. The errors from the different states have different ranges and different units; by applying the scaling gain K_o , the states are artificially adjusted to have similar range. K_o was a square matrix with diagonal elements $[2.5 \ 8 \ 4 \ 8 \ 5]$. The controller is contained in the gain matrix K_{in} and is applied to the state estimate output of the Kalman filter, \hat{x} . Following the design of Field (2000) the controller output, u_c , is integrated and then multiplied by a second scaling matrix, K_i . This second scaling matrix is used to adjust the output to the propeller and is diagonal with elements $[1 \ 1 \ 1 \ 1 \ 5]$.

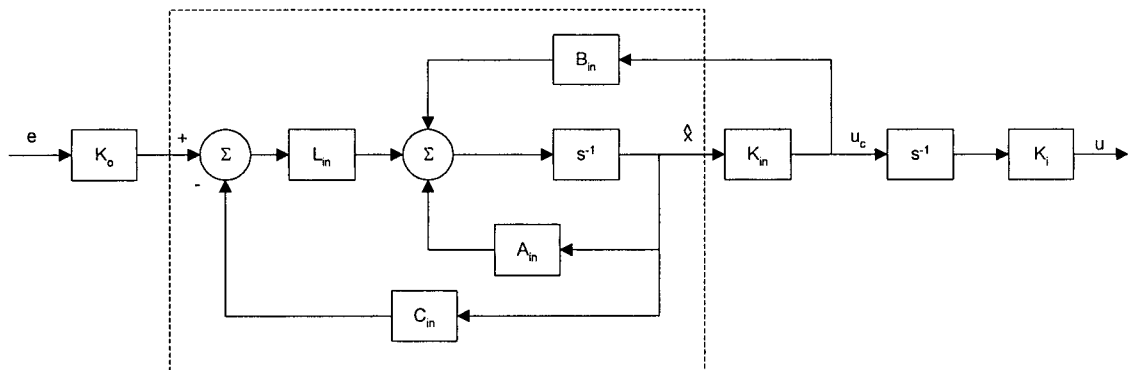


Figure 5-17 LQG/LTR controller block diagram

Both integrators in the controller had saturation limits (that is, they include anti-wind up). In order to facilitate the integrator implementation, a change in the use of state variables was required in the controller design. Specifically, a modified system was considered with revised state equations

$$\begin{bmatrix} \dot{\mathbf{u}} \\ \dot{\mathbf{x}} \end{bmatrix} = \begin{bmatrix} 0 & 0 \\ \mathbf{B} & \mathbf{A} \end{bmatrix} \begin{bmatrix} \mathbf{u} \\ \mathbf{x} \end{bmatrix} + \begin{bmatrix} \mathbf{I} \\ 0 \end{bmatrix} \mathbf{u}_c \quad (122)$$

$$\mathbf{y} = \begin{bmatrix} 0 & \mathbf{C} \end{bmatrix} \begin{bmatrix} \mathbf{u} \\ \mathbf{x} \end{bmatrix} \quad (123)$$

where \mathbf{u}_c is the commanded control signal prior to integration, \mathbf{u} is the integrated control signal, and \mathbf{x} is the state vector as given in equation (97). The benefit of this approach is that steady-state error due to continuous plane deflection can be eliminated. In the notation of Field, this system can be rewritten with noise, \mathbf{n} , and disturbances, \mathbf{w} , (both assumed to be white noise in the design process) as

$$\dot{\mathbf{x}}_{in} = \mathbf{A}_{in}\mathbf{x}_{in} + \mathbf{B}_{in}\mathbf{u} + \mathbf{M}_{in}\mathbf{w} \quad (124)$$

$$\mathbf{y}_{in} = \mathbf{C}_{in}\mathbf{x}_{in} + \mathbf{n} \quad (125)$$

where,

$$\mathbf{x}_{in} = \begin{bmatrix} \mathbf{u} \\ \mathbf{x} \end{bmatrix} \quad (126)$$

and

$$\mathbf{M}_{in} = \begin{bmatrix} \frac{1}{2}\mathbf{K}_i \\ \mathbf{B} \end{bmatrix} \quad (127)$$

Open Loop Plant Behavior

The open loop plant behavior for the five controlled states is described by the singular value plot in Figure 5-18. Of particular concern is the yaw singular value curve that is below unity gain at low frequency; as Field (2000) notes, in operation this would be reflected by large steady state error and poor disturbance rejection properties. Also noted is the differences noted in the magnitudes and crossover frequencies of the curves which is a consequence of the differences in dynamic behavior of the different states.

When the input and output scaling gain matrices, \mathbf{K}_o and \mathbf{K}_i , are included in the computation of the plant singular values, the above concerns are alleviated. As shown in Figure 5-19, the singular values of the scaled plant are much more similar and have similar crossover frequencies.

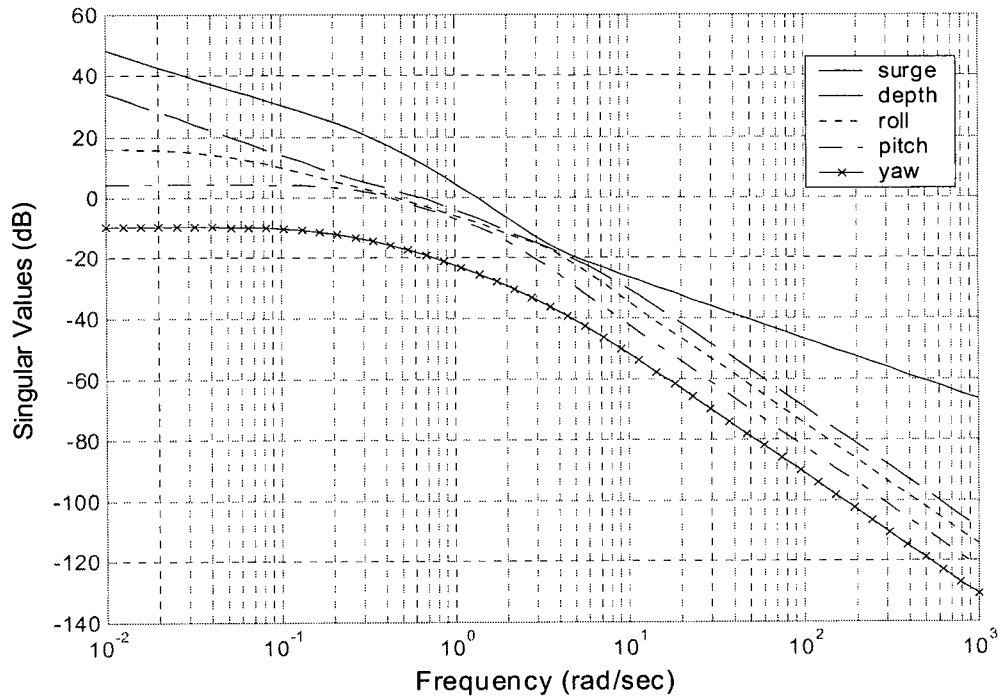


Figure 5-18 Singular value plot for the plant

Filter Design

With the LQG/LTR controller, both the filter, L_{in} , and controller, K_{in} must be designed. Due to the properties of duality in the system, the process is similar for each and either one can be designed first. Following the work of Field (2000), the filter was designed first and the controller design (recovery) was completed once a suitable filter was realized.

The filter was determined by solving the algebraic Riccati equation

$$A_{in}P + PA_{in}^T - PC_{in}^T(\mu N_{in})^{-1}C_{in}P + M_{in}W_{in}M_{in}^T = 0 \quad (128)$$

where μ is a design scaling factor; increasing μ decreases the bandwidth and decreasing μ increases the bandwidth. N_{in} is a 5×5 identity matrix and W_{in} was determined by Field (2000) through singular value decomposition so as to bring the singular value curves together at cross-over. The procedure of determining W_{in} is outlined in Appendix D.2.1.

The filter gains, L_{in} , are determined from equation (128) by

$$L_{in} = PC_{in}^T(\mu N_{in})^{-1} \quad (129)$$

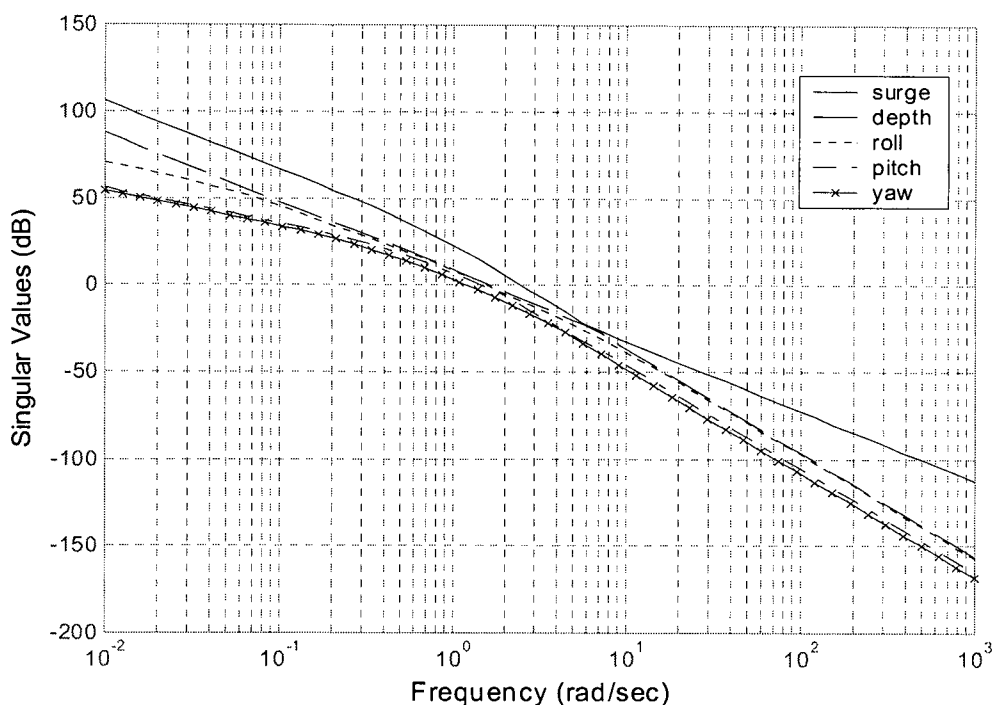


Figure 5-19 Singular value plot for the scaled plant

where \mathbf{P} is solved as part of the Riccati equation. The determination of the filter gains is accomplished with the MATLAB® command

$$\mathbf{L}_{in} = \text{LQE}(\mathbf{A}_{in}, \mathbf{M}_{in}, \mathbf{C}_{in}, \mathbf{W}_{in}, \mu \mathbf{N}_{in})$$

The resulting singular value plot for the filter based on $\mu = 0.0005$ is shown in Figure 5-20. This value of μ was determined through results presented by Field (2000) and through tuning by simulation. (Details regarding the simulation tuning are provided in Appendix D.2.2.)

The sensitivity and complementary sensitivity functions for the filter are shown in Figure 5-21. The sensitivity function dictates disturbance rejection and tracking performance of the system and the complementary sensitivity function governs the noise rejection. Ideally both quantities should be small but this is not possible and a trade-off between the two functions is required. Since noise tends to be a high frequency phenomenon, it is desired that the complementary sensitivity function is small at high frequencies and the sensitivity function is small at low frequencies. The resulting sensitivity functions in Figure 5-21 show a reasonable compromise and are similar to those of Field (2000).

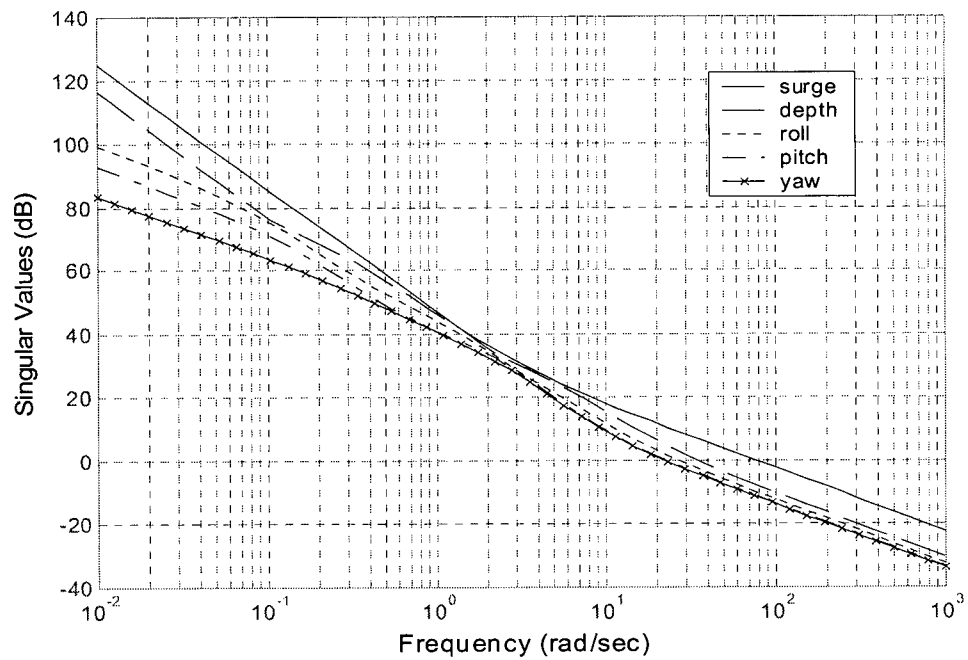


Figure 5-20 Filter singular values

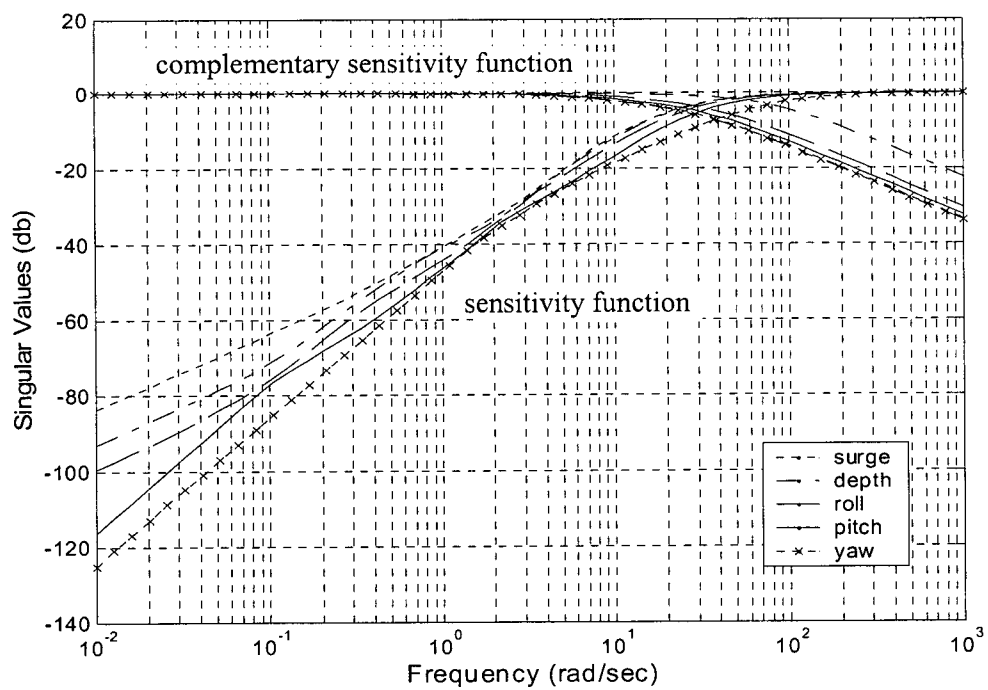


Figure 5-21 Filter sensitivity and complimentary sensitivity singular values

Controller Design

Having determined the filter, it remains to determine the controller gain matrix, K_{in} . A similar procedure was used as for the filter design and is described in detail by Field (2000). The objective was to minimize a cost function of the form:

$$J = \int_{t_0}^{t_f} (\mathbf{x}^T \mathbf{Q} \mathbf{x} + \mathbf{u}^T \rho \mathbf{R} \mathbf{u}) dt \quad (130)$$

where the matrices \mathbf{Q} and \mathbf{R} are used to weight the state error and actuator deflections. The parameter ρ is used to tune the amount of recovery in the control. As ρ approaches zero, the controller approaches full recovery of the Kalman filter; however, small values of ρ are associated with large gains and thereby introduce a risk of increased actuator saturation. The values $\mathbf{Q} = \mathbf{C}_{in}^T \mathbf{K}_w \mathbf{C}_{in}$ and $\mathbf{R} = \mathbf{I}$ were used by Field where \mathbf{K}_w was a 6×6 diagonal matrix with elements $[1 \ 1 \ 1 \ 1 \ 100 \ 1]$. Specifically, \mathbf{K}_w was used to weight pitch error due to significant non-linearities in that state. Like the filter, the controller design was based on solving the Riccati equation and in this case was implemented in MATLAB® using

$$K_{in} = LQR(A_{in}, B_{in}, Q, \mu R)$$

Field found that values for ρ of 0.05 to 0.005 performed adequately. For this thesis, unless stated otherwise, a value of $\rho = 0.05$ was used in the LQG/LTR controller. This value was tuned along with μ through simulation based on actuator performance in conditions with disturbances (see Appendix D.2.2 for further information).

The resulting singular values for the plant with the LQG/LTR controller are shown in Figure 5-22. The four states controlled by the planes (depth, roll, pitch, and yaw) have similar responses and almost identical crossover frequencies. The low frequency limits of the singular value curves all approach infinity suggesting that steady state error and low-frequency disturbance rejection properties of the system are good. The sensitivity and complementary sensitivity functions are shown for the complete system in Figure 5-23.

5.4.2 Sliding Mode LQG/LTR Controller

The second augmentation of the LQG/LTR controller used sliding mode to account for changes in performance of the control surfaces based on body orientation. In short, the LQG/LTR controller is designed based on linearization about a setpoint; by allowing that setpoint to change based on operating condition, the errors due to linearization are reduced. In this implementation, nine controllers in total were designed and spanned a range of trim and yaw angles encountered during typical simulated manoeuvres (see Table 5-5).

For this thesis, the nine controllers were designed by changing only the control surface hydrodynamic effects in each instance. In all other regards, the body was assumed to remain at zero trim

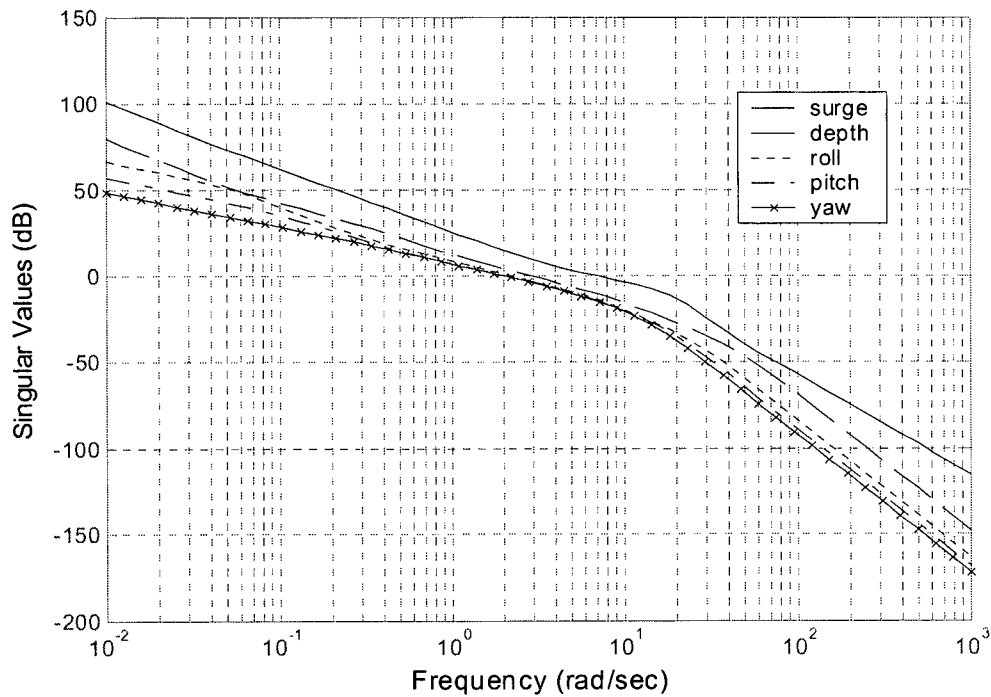


Figure 5-22 Open loop singular value plot for plant and controller

and yaw for the controller design such that any differences in performance observed could be attributed solely to the controller treatment of the control surfaces.

Bumpless switching was used to transition from one controller to another based on operating condition. Similar to the fuzzy membership functions introduced in Section 5.3.3, there was a distribution of conditions over which each controller was applied. As a simplified example considering trim only, Figure 5-24 shows the proportion of three trim controllers applied based on trim angle. At a trim angle of zero, only the \mathbf{K}_0 controller would be applied; as the trim angle is increased, the \mathbf{K}_0 and \mathbf{K}_+ controllers would be averaged with increasing weight given to the \mathbf{K}_+ controller and decreasing weight to the \mathbf{K}_0 controller; and for positive trim angles greater than 2.3 degrees, the \mathbf{K}_+ controller would be used exclusively. For this thesis, the sliding mode controller used both trim and yaw as inputs and therefore the curves of Figure 5-24 were replaced by surfaces as shown in Figure 5-25. For simplicity, only the \mathbf{K}_{00} and \mathbf{K}_- controllers are shown in the figure. The \mathbf{K}_- surface continues indefinitely in the negative trim and yaw directions. The complete set of nine surfaces used in the sliding mode control are shown in two-dimensional form in Figure 5-26. In each case, the base of the surface is identified by the solid line and vertices in the surfaces are indicated with a point (corresponding to 100% implementation of the controller as in Figure 5-24).

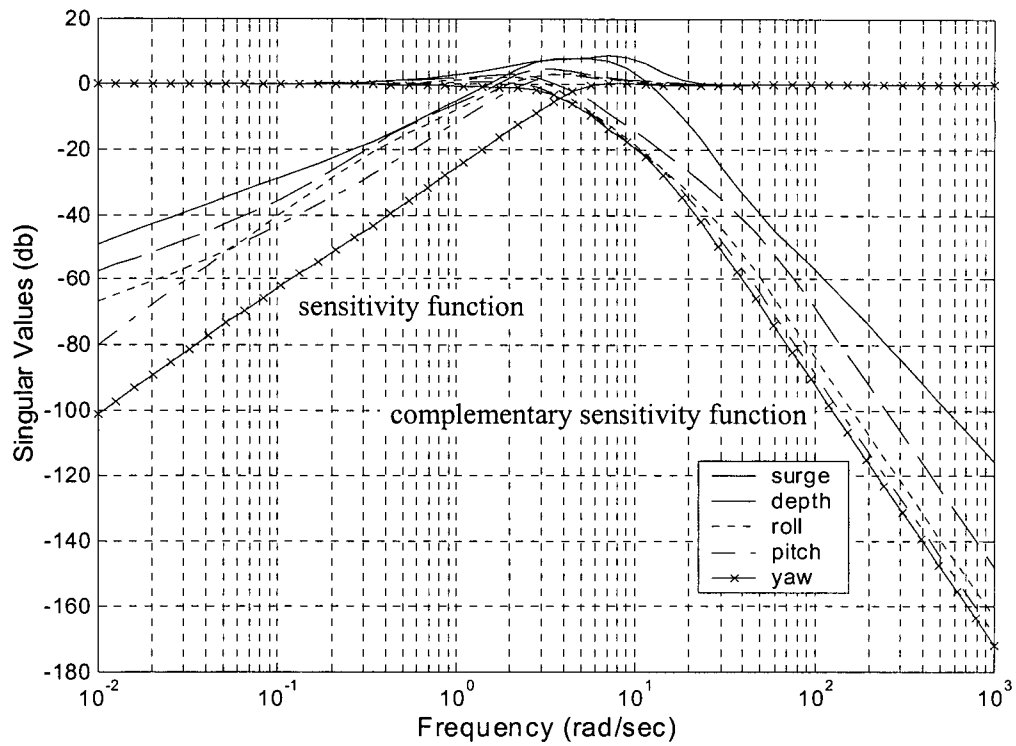


Figure 5-23 System sensitivity and complimentary sensitivity singular values

Table 5-5 Sliding mode controller

Name	Trim	Yaw
K_{00}	0 deg	0 deg
K_{+0}	2.3	0
K_{-0}	-2.3	0
K_{0+}	0	3.4
K_{0-}	0	3.4
K_{++}	2.3	3.4
K_{+-}	2.3	-3.4
K_{-+}	-2.3	3.4
K_{--}	-2.3	-3.4

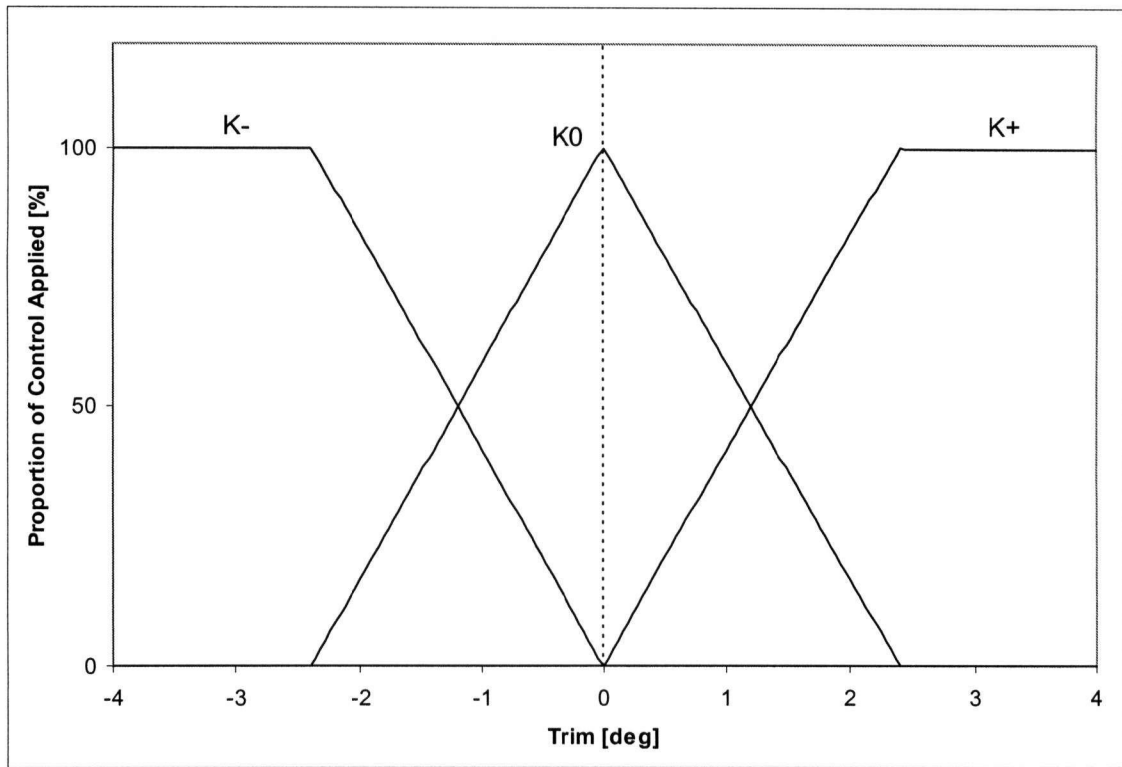


Figure 5-24 Bumpless switching example for one input variable

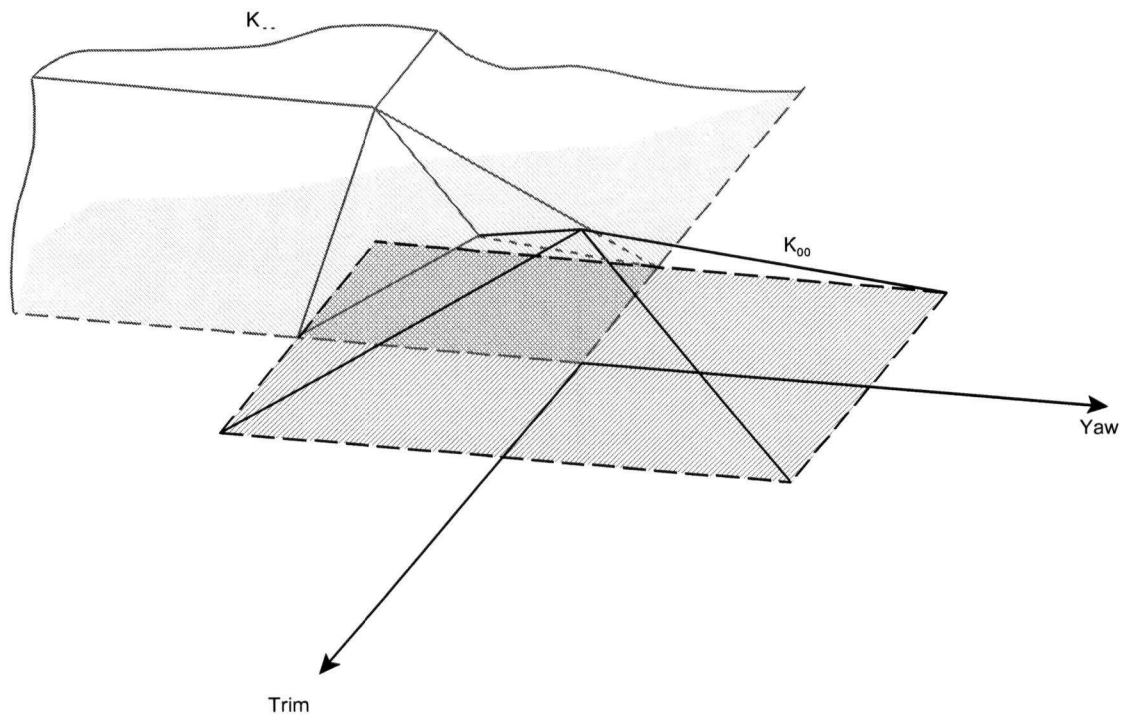


Figure 5-25 Bumpless switching with two input variables

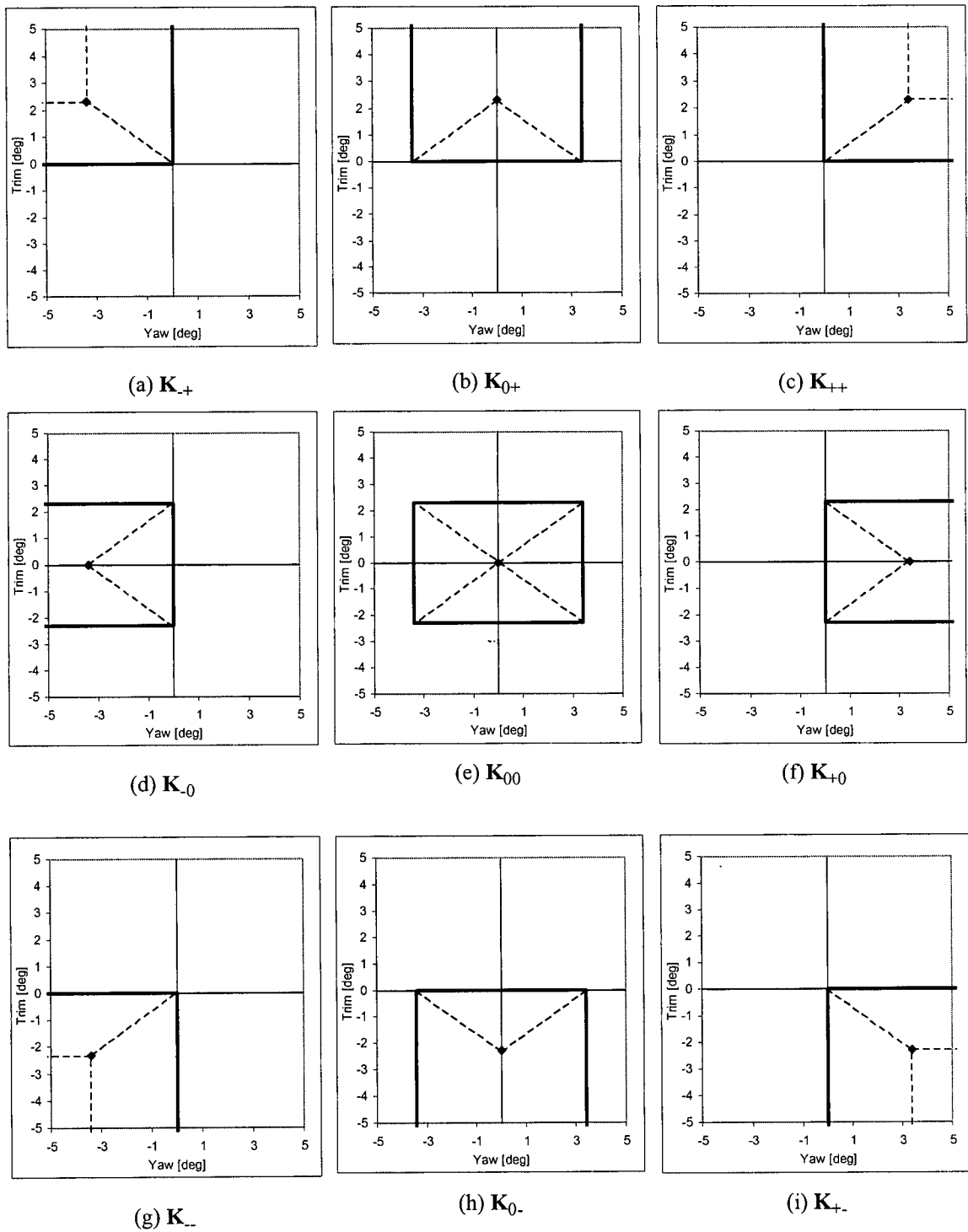


Figure 5-26 Switching surface representation in two dimensions for the sliding mode controller

5.4.3 LQG/LTR Controller with Fuzzy-Tuned Series Compensation

The LQG/LTR controller with series compensation, tuned using fuzzy logic, was developed in the same manner as the equivalent PD controller augmentation described in Section 5.3.3. The only difference was that the controller of Figure 5-7 was replaced with the basic LQG/LTR version detailed above.

5.5 SUMMARY

The development of controllers for use in simulation with the DOLPHIN AUV was discussed in this chapter. Following a discussion of background information on various control methodologies and implementations, six controllers were presented in total.

PD Controller Variants

- A basic PD controller was presented based on a publication regarding the DOLPHIN AUV by Shupe and McGeer (1987).
- The first augmentation of the PD control strategy used gain scheduling in an attempt to account for changes to control surface performance with body orientation. The controller was designed such that the gain matrix was actively modified during operation based on results from Chapter 4.
- The second augmentation of the PD control strategy used a series compensator to adjust the output from the controller based on vehicle orientation. The series compensator consisted of a square 6×6 matrix that modified the 6 controller outputs before they reached the plant. The series compensator was tuned using fuzzy logic with rules and membership functions based on the data of Chapter 3.

LQG/LTR Variants

- Following the work of Field (2000) an LQG/LTR controller was developed. The controller parameters used to tune performance (μ and ρ) were selected based on the findings of Field and the results of simulation (discussed in Chapter 6).
- The first augmentation of the LQG/LTR controller used sliding mode control to switch between different LQG/LTR controllers designed (off-line) for different operating conditions. The changes in the different controllers were restricted to the treatment of control surfaces. Depending on vehicle trim and yaw angle, the various controllers were combined using bumpless switching.
- The second augmentation of the LQG/LTR controller was a fuzzy-tuned series compensator identical in form to that designed for the PD controller.

6

SIMULATION

Physicists like to think that all you have to do is say, these are the conditions, now what happens next?

- Richard Feynman

For complex nonlinear plants, such as AUVs, modelling and simulation are central to the design of the control systems. The validity of such simulations depends on the accuracy and completeness of the model used in simulation. Nahon (1996) suggests that the greatest errors in the simulation of an underwater vehicle arise from uncertainty in the hydrodynamic characteristics. Short of building a dedicated test platform, simulation is often the only way to examine plant and controller behavior.

This chapter uses the experimental results from Chapter 3—modelled according to Chapter 4—to improve the realism of AUV control and dynamics simulations. Following a presentation of background information regarding AUV simulation, the mechanics of the MATLAB®-based simulator are outlined. The remaining sections present simulation results in three main areas: the differences in simulation outcome depending on the accuracy and completeness of control surface hydrodynamic modelling; the effect of the configuration of vehicle control surfaces on performance; and potential control strategies for accounting for the previously unmodelled control surface hydrodynamic characteristics. In terms of control strategy, several possible enhancements to basic PD and LQG/LTR controllers, as outlined in Chapter 5, are considered.

6.1 SIMULATION BACKGROUND

If a model is nonlinear, time-variant, or complex, closed form solutions are almost certainly not available and numerical methods must be used to evaluate system performance. Simulation is the term given to the process of using numerical methods to predict the response of a system (Palm, 1986). Complex, nonlinear models can be used in simulation and are necessary for investigating performance of a control system designed based on a linearized model (such as PD and LQG/LTR controllers). However, simulation results must be used with caution as it is not always possible to investigate all conditions that are unfavorable in terms of stability or observability (Åström and Wittenmark, 1997). Likewise, it is difficult to decide when the nonlinear model is sufficiently accurate and to know when simulations have examined all conceivable modes of plant operation (Dutton et al., 1997).

Development of underwater vehicles, including changes to the geometry or control of existing vehicles, can be an expensive, time-consuming process. Simulation is essential for validation and evaluation of the system design and can minimize unsafe or costly errors in the field. Song et al. (2002), for example, recommend extensive in-lab simulation of the control subroutines and entire control structure long before conducting sea trials.

Of direct relevance to this thesis, Field (2000) developed a six degree-of-freedom simulation package specifically for the DOLPHIN AUV. Field's simulator included several augmentations of a linear submarine model for study and design of control compensators. Field invested considerable effort in formulating the equations of motion for a near-surface AUV. In addition to an extensive analysis of the rigid body dynamics, his model included forces arising from radiation (added mass and damping), restoring forces, incident and diffracted forces (due to the wave field) and control forces. The majority of these quantities are hydrodynamic in origin and Field used several methods to estimate the values. In particular, Field employed semi-empirical methods—such as those of Whicker and Fehlner (1958), Dempsey (1977), and Lyons and Bisgood (1950) outlined in Chapter 2—numerical methods using strip theory (McTaggart, 1996), and aerodynamics software (Nahon, 1993). Simulink®, in conjunction with the MATLAB® programming environment, was used for the development of control and dynamics simulator. Although his work was general in nature, Field's simulator was based on the DOLPHIN AUV making it ideal for the current research. To study control surface effectiveness, the formulation developed by Field is used with modelling improvements as outlined in Chapter 4.

6.2 SIMULATION ENVIRONMENT AND DESIGN

A basic simulator of the control and dynamics of the DOLPHIN AUV was developed by Field (2000) and was modified for this work. Based on the experiments and modelling presented in Chapter 3 and Chapter 4, improvements were made to the simulator in terms of the representation of the control surface hydrodynamics. Simulations were developed in the Simulink® environment of MATLAB® in block diagram form; specialized routines were programmed using native MATLAB® m-file® code. Others (such as Naeem et al., 2003, Prestero, 2001b, and Carreras et al., 2000, for example) have also used Simulink® in the investigation of AUV control and dynamics. Further details regarding the development of the simulator is discussed in the following sections with emphasis on the simulation procedure, simulator layout, and specialized m-file® programming.

6.2.1 Simulation Procedure

There were three main stages to the overall simulation procedure: initialization, execution, and post processing. The simulation steps are shown in greater detail in Figure 6-1. In the figure, specialized m-file® routines are shown in an alternate font (such as `SiminitX`, for example) where 'X' is used to designate the controller (such as PD or LQG/LTR). The simulations were run over a predetermined interval, until the stop time, T , was reached. The time step size was 0.02 seconds (corresponding to 50 Hz) and the results were refined at two intermediate points during each time-step. (In other words, the simulations were run as if the time-step was equivalent to 0.00667 seconds (150 Hz) but with data only recorded for every third point or 0.02 seconds). In cases where a tuner was included in the control architecture, it was operated at a frequency less than that of the overall simulation. Unless noted otherwise, computations by the tuner and the resulting tuning actions were performed once every 0.1 seconds (10 Hz, denoted by T_{tune} in Figure 6-1).

A fourth-order Runge-Kutta continuous solver with variable step size (`ode45` in MATLAB®) was used in all simulations (further information regarding Runge-Kutta can be found in a standard numerical methods text such as Hoffman, 1992, or Boyce and DiPrima, 1992). During simulation, the allowed relative error tolerance for each state was 0.1% of the state value and the maximum allowed absolute error was 1×10^{-6} . The maximum error in simulation at each time step for each state was the maximum of the relative and absolute error tolerance. The real-time duration required to run a 70 second simulation (3500 time-steps) on a 1.6 GHz *Athlon* processor with 1 GB of RAM was approximately 20 minutes.

6.2.2 Simulator Layout

The overall simulator layout in Simulink® (see Figure 6-2) closely matched that of the control system block diagram. The *navigation module*, *controller*, *plant*, and *sensors* sub-systems were constructed using nested block diagrams. In Field's simulator, the *navigation module* computed reference states based on interpolation from a set of user supplied waypoints. For this thesis, the commanded trajectories in depth and heading were assigned step input changes and all of the states were held constant—speed had a constant non-zero reference while all other states were held at zero. The exact layout of the *controller* block depended on the control strategy used; specific

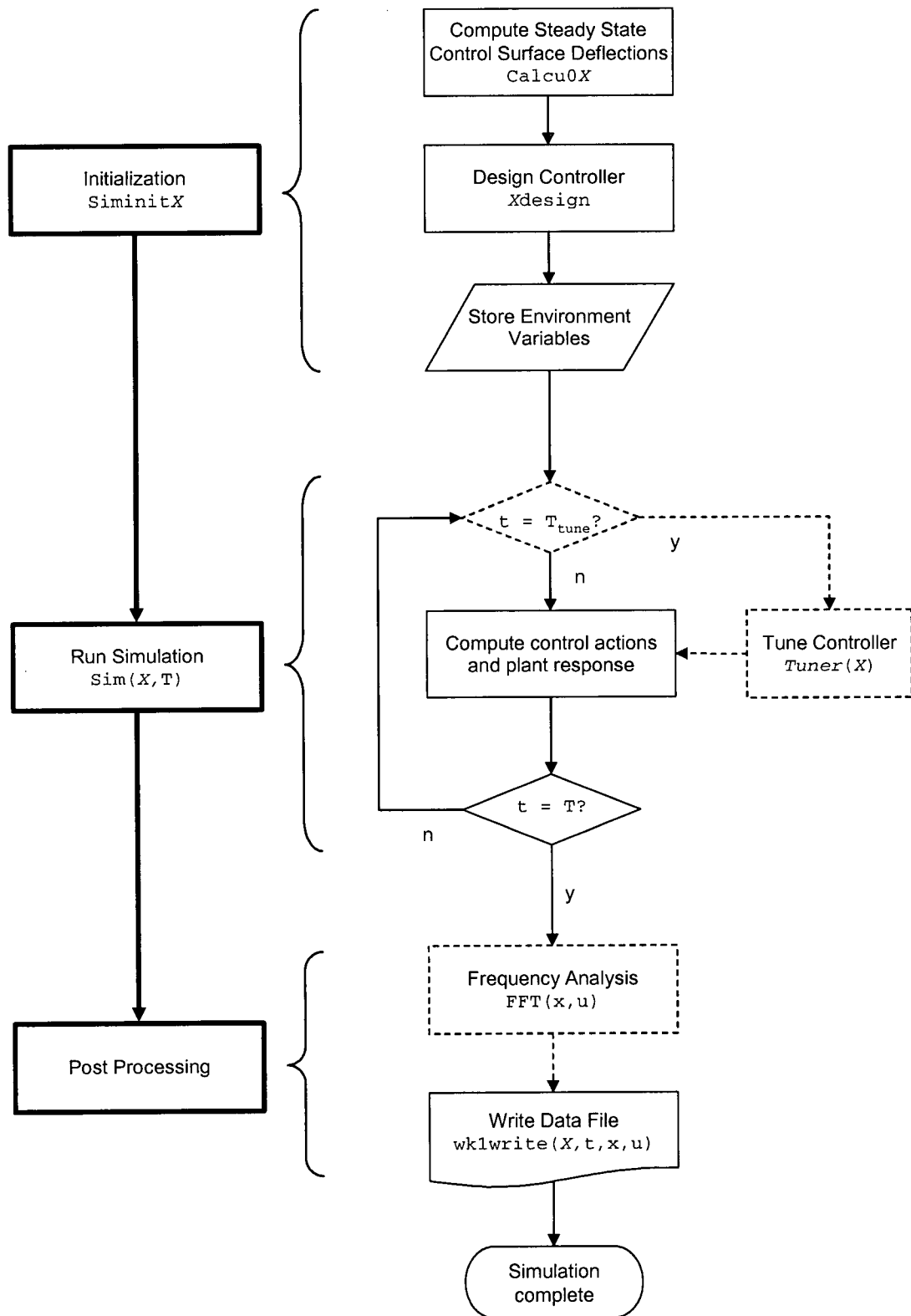


Figure 6-1 Simulation process schematic

information for each controller can be found in Chapter 5. The same design for the *plant* block was used in all cases and is shown in Figure 6-3.

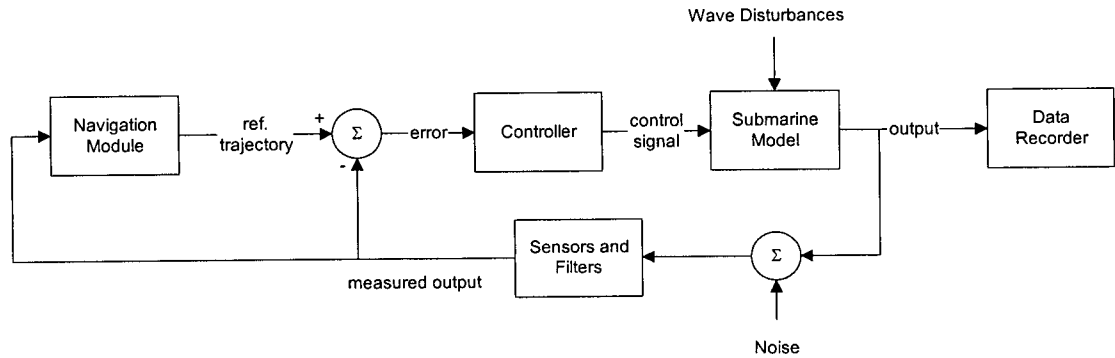


Figure 6-2 Simulator block diagram

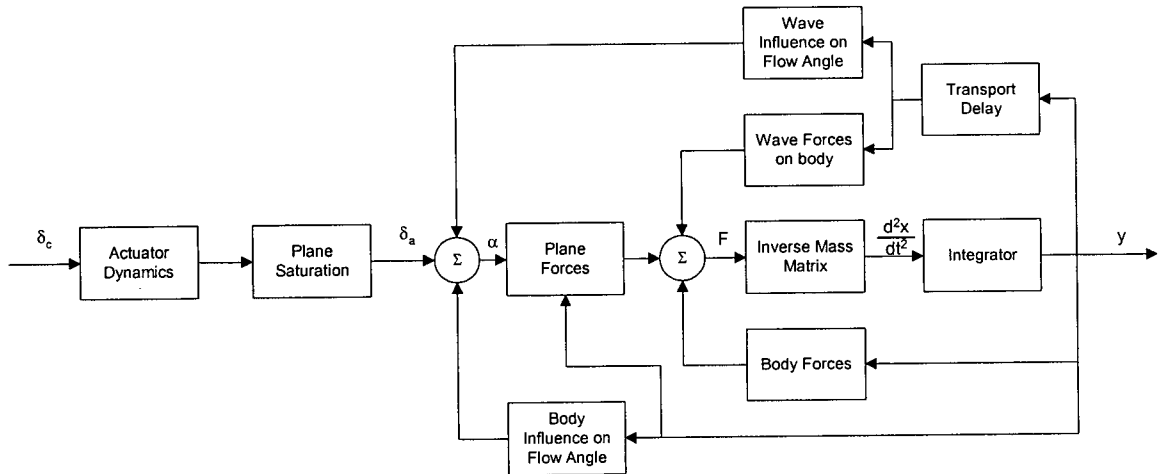


Figure 6-3 Simulator plant block diagram

In the *plant* block, the commanded plane deflections, δ_c , were adjusted to account for the dynamics of the vehicle actuation system (the rate at which planes could change deflections) as well as the physical saturation limits (the maximum obtainable deflections). The resulting actual deflections, δ_a , were combined with the change in incidence angle due to the vehicle orientation and motion—including wave effects where applicable—in order to determine the net incidence angle on the planes, α . The plane forces were computed according to Section 4.8 and were combined with the hydrodynamic, hydrostatic, gravitational, and wave induced body forces to determine the net force on the vehicle. By multiplying the net body force by the inverse mass matrix, the vehicle acceleration was determined which in turn was integrated to give the vehicle state.

Finally, the *sensor and filter* block (in Figure 6-2) added measurement noise independently to each state and then processed signals with an anti-aliasing filter and an analog-digital converter (as shown in Figure 6-4). The noise was represented as stochastic and stationary with a gaussian nor-

mal distribution characterized by the variance as shown in Table 6-1. The analog to digital conversion was modelled using a zero-order hold system with the quantization also shown in the table.

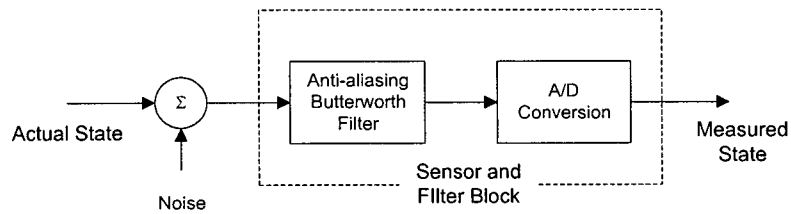


Figure 6-4 Simulator sensor and filter block diagram

Table 6-1 Sensor noise characteristics

State	Variance	Quantization
u	0.0038 m^2/s^2	0.1 m/s
p	0.43 deg^2/s^2	0.2 deg/s
q	0.25 deg^2/s^2	0.2 deg/s
r	0.02 deg^2/s^2	0.2 deg/s
x	2.9 m^2	1 m
y	2.9 m^2	1 m
z	0.0007 m^2	0.1 m
ϕ	0.11 deg^2	0.1 deg
θ	0.015 deg^2	0.1 deg
	0.54 deg^2	0.1 deg

Further information regarding simulator development (including complete details of the system design and operation, the plant model, and noise and disturbance characteristics) can be found in (Field, 2000). Simulink® block diagrams for all systems are provided in Appendix E.2.

6.2.3 Simulation Programming

Specialized MATLAB® code was required to design and operate the Simulink® system. Where possible, built-in MATLAB® commands were used but the majority of code was custom written. For both the PD and LQG/LTR control methodologies, gains were determined and assigned using MATLAB® routines called during the initialization phase of the simulations (see Figure 6-1). In cases where a tuner was used with the controller, function calls were made from Simulink® blocks during simulation; simulation processing was paused while MATLAB® routines recomputed and reassigned controller parameters. To determine the body forces, plane forces, and wave effects in the *plant* block, similar function calls from Simulink® were made to m-file® programs during the simulations. The code used in the simulations is provided in Appendix E.1.

6.3 SIMULATION TEST CASES AND EVALUATION

6.3.1 Evaluation Manoeuvres

AUVs can be designed to perform a wide variety of tasks but are typically employed as platforms for instrumentation. In such applications, improved disturbance rejection and manoeuvrability are in general highly beneficial. In a mapping operation for example, excessive motion of the platform may result in smearing or distortion of the sonar image. Likewise, in cases where a towfish containing instrumentation is pulled by an AUV, there is significant interaction between the vehicles (Seto and Watt, 1998); for acceptable performance, a high degree of towfish stability is required so, again, the AUV must remain stable.

To examine the manoeuvrability and disturbance rejection of the DOLPHIN in simulation, a representative manoeuvre was selected. This manoeuvre, shown in Figure 6-5, is characterized by a 180 metre segment of straight and level flight with a depth change of 0.5 metre at the 60 metre mark. A 180 degree turn to starboard is then initiated and the simulation is run out through a final segment of straight and level flight. Simulations were conducted with a constant commanded forward speed of 6.0 m/s for a duration of 70 seconds. The length of the run-out at the end of the simulation was approximately 145 metres but depended on how well the vehicle could maintain the commanded speed throughout the manoeuvre as well as how quickly it could perform the turn.

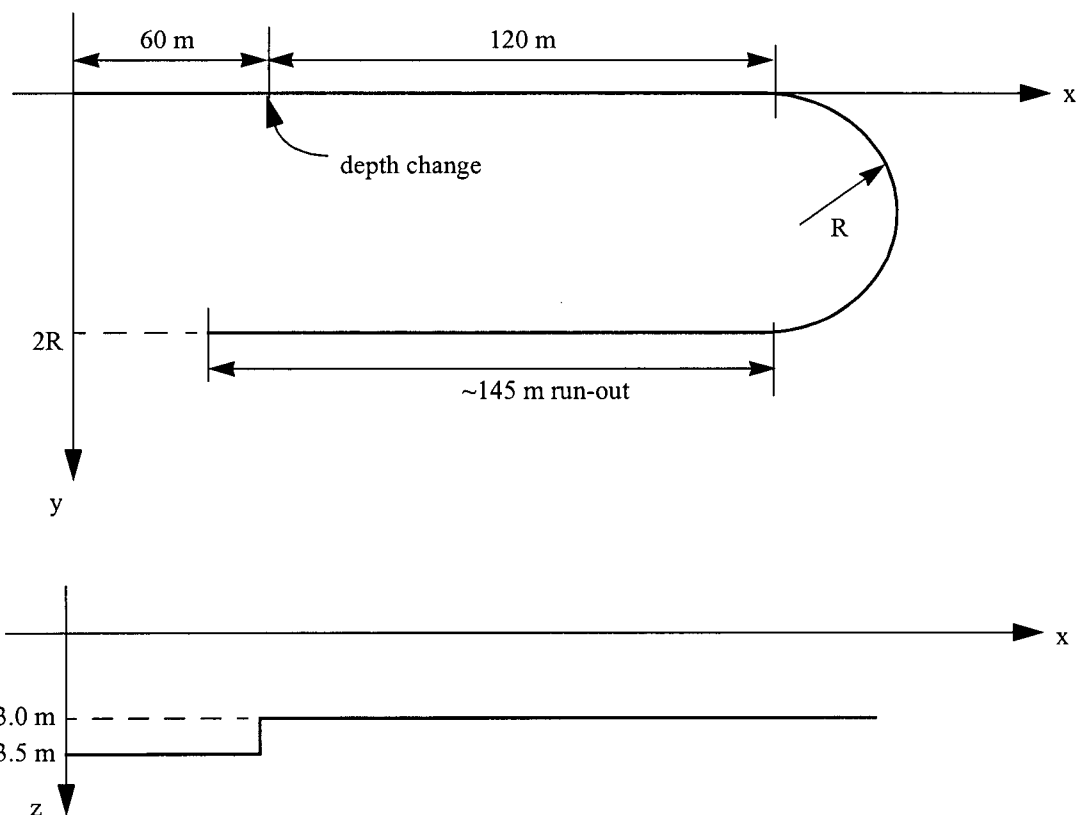


Figure 6-5 Manoeuvre used for performance evaluation

In addition, for frequency analysis of the vehicle response, a second manoeuvre consisting of straight and level flight at 3.5 m depth and 6.0 m/s commanded forward speed was used. This simulation was conducted for 81.92 seconds such that the total number of steps was equal to a power of two (81.92 seconds with 0.02 second step size is equivalent to $4096 \text{ steps} = 2^{12}$).

6.3.2 Evaluation Criteria

The criteria for performance evaluation of the vehicle and controller were threefold. First and foremost, the stability of the vehicle was considered; configurations in which unstable behavior was observed were deemed to be unusable. Secondly, cases were identified that violated operational constraints; specifically, these cases included complete submersion of the snorkel—the snorkel is required for communication as well as to provide air to the diesel engine—and hull breach of the free surface. Considering the 3.5 metre operating depth, the independent limits on depth, roll, and pitch were +1.06/-3.0 metres, ± 39.8 degrees, and ± 39.8 degrees respectively (for combinations of these motions, the limits were even more stringent). Finally, three performance indices were developed to analyze behavior of different configurations in a fictitious seafloor mapping exercise.

The performance indices were defined in terms of the percentage of data lost during a hypothetical seafloor scanning operation using the trajectories above. The vehicle was assumed to be operating in water of 100 metre mean depth with a downward facing sonar beam of 50 metre transverse width (see Figure 6-6). In this idealized environment, the sonar beam width was divided into 1000 segments (pixels) and the sonar resolution (pixel size) was assumed to be 0.05 metres in all directions. With reference to the commanded trajectory, error in vehicle position and pose resulted in inaccuracy in sonar beam placement on the sea floor. In Table 6-2, the sensitivity of sonar beam inaccuracy to errors in body position and orientation is shown.

All three performance indices quantify the error in the sonar beam position, in pixels, relative to the total number of pixels scanned. One index, J_{ct} , is used for the complete trajectory of Figure 6-5, J_{sl} , is used for the straight and level portions of Figure 6-5 only; and the final index, J_{sa} , is the significant amplitude from the response spectra (explained in detail below) in straight and level flight. All three indices are strictly positive quantities with an improvement in performance associated with a decrease in the performance index; for each index, a value of zero indicates error-free performance.

During the turn of Figure 6-5, the lateral position, y , and the yaw angle, ψ , were not included in the performance indices—there were no reference values for these quantities during the turn—but depth, z , roll, ϕ , and pitch, θ were included in the J_{ct} index. The turn was considered to begin at $x=180$ metres and to last for 16 seconds; this period was sufficient for a vehicle travelling at the commanded speed of 6 m/s to complete a 180 degree turn with a 30.5 metre radius. In this approach, configurations which were less effective in turning or could not maintain speed during a turn were penalized.

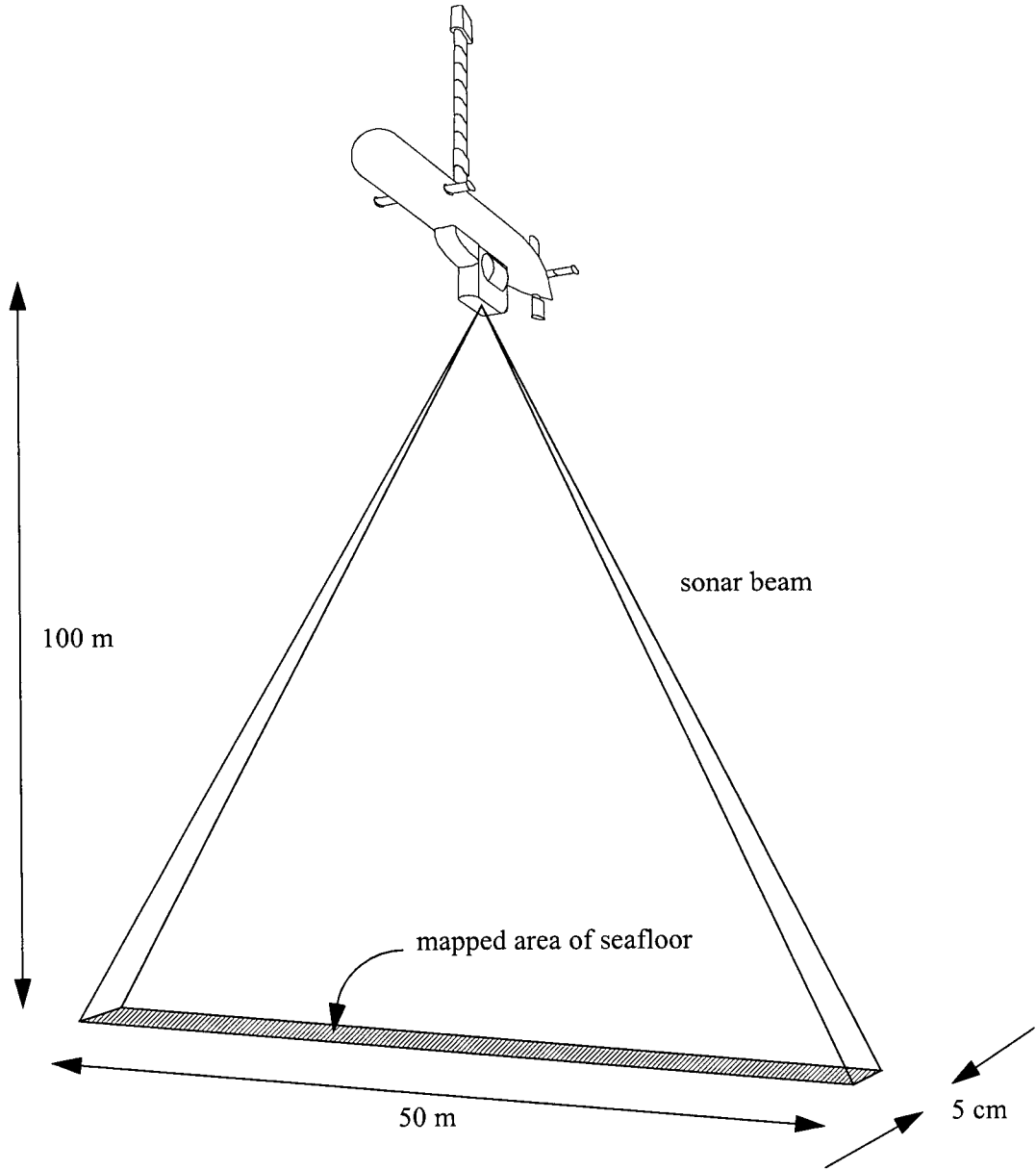


Figure 6-6 Fictitious scanning operation used in performance evaluation

Table 6-2 Body position and orientation corresponding to one sonar segment error

Description	Parameter	Error Sensitivity
lateral position	y	$s_y = 0.05$ m/pixel
vertical position	z	$s_z = 0.05$ m/pixel
roll angle	ϕ	$s_\phi = 0.028$ deg/pixel
trim angle	θ	$s_\theta = 0.028$ deg/pixel
yaw angle	ψ	$s_\psi = 0.229$ deg/pixel

J_{ct} Performance Index

The J_{ct} performance index is a measure of the ability of a vehicle to track a complicated trajectory and it is applied both in calm water and in waves. The exact definition of the performance index, J_{ct} , is:

$$J_{ct} = \frac{1}{N \cdot P} \sum_{n=0}^N \begin{cases} \left| \frac{y_n - y_r}{s_y} \right| + \left| \frac{z_n - z_r}{s_z} \right| + \left| \frac{\phi_n - \phi_r}{s_\phi} \right| + \left| \frac{\theta_n - \theta_r}{s_\theta} \right| + \left| \frac{\psi_n - \psi_r}{s_\psi} \right| & \begin{cases} n < 1500 \\ n > 2300 \end{cases} \\ \left| \frac{z_n - z_r}{s_z} \right| + \left| \frac{\phi_n - \phi_r}{s_\phi} \right| + \left| \frac{\theta_n - \theta_r}{s_\theta} \right| & \text{otherwise} \end{cases} \quad (131)$$

The total number of pixels scanned is the product of the sonar beam width, P , in pixels, and the number of time-steps, N . As the time-step size used in the simulations was 0.02 seconds, the beginning of the turn ($x=180$ m) for a vessel travelling at 6 m/s corresponded to time-step $n = 1500$. The end of the turn, 16 seconds after the initiation, corresponded to $n = 2300$. At each time-step, the difference between the actual and reference value for each state (y , z , ϕ , θ and ψ) was computed and scaled by the sensitivity factor from Table 6-2. In equation (131), the reference values generated by the *Navigation Module* are denoted with subscript r and the actual values at each time-step are denoted with n .

J_{sl} Performance Index

The J_{sl} index is a more reasonable measure of performance for a vehicle intended for track-line survey operations where the primary function is to maintain a straight and level course and quickly

recover from changes in direction or depth. As with J_{ct} , the J_{sl} performance index was applied in both calm water and waves. The definition of this second performance index is

$$J_{sl} = \frac{1}{(N - N_t)P} \sum_{n=0}^N \begin{cases} \left| \frac{y_n - y_r}{s_y} \right| + \left| \frac{z_n - z_r}{s_z} \right| + \left| \frac{\phi_n - \phi_r}{s_\phi} \right| + \left| \frac{\theta_n - \theta_r}{s_\theta} \right| + \left| \frac{\psi_n - \psi_r}{s_\psi} \right| & \begin{cases} n < 1500 \\ n > 2300 \end{cases} \\ 0 & \text{otherwise} \end{cases} \quad (132)$$

In this case, only the number of time-steps during the commanded straight and level flight was used in the computation of the total number of pixels. In other words, the number of time-steps during the turn, $N_t = 800$, was removed from the total number of steps, N , in computing the total number of pixels.

J_{sa} Performance Index

The third performance index, J_{sa} was the significant amplitude from the scanning error spectrum. It is a measure of the wave disturbance rejection qualities of a particular configuration of vehicle and controller and is applied only in waves. To determine J_{sa} , simulations were conducted for 4096 time-steps (81.92 seconds) in straight and level flight in head seas of sea state three. At each time-step, n , the scanning error, j , was defined as

$$j_n = \left| \frac{y_n - y_r}{s_y} \right| + \left| \frac{z_n - z_r}{s_z} \right| + \left| \frac{\phi_n - \phi_r}{s_\phi} \right| + \left| \frac{\theta_n - \theta_r}{s_\theta} \right| + \left| \frac{\psi_n - \psi_r}{s_\psi} \right| \quad (133)$$

A fast Fourier transform (FFT) analysis was performed in order to obtain the response spectrum the scanning error, $S_j(n)$. (The reader is referred to a numerical analysis text such as Burden and Faires, 1997, for further information on the FFT procedure.) In keeping with convention, the spectrum S_j was expressed in terms of the square of the response amplitudes (see, for example, Journée, 2001).

The performance index, J_{sa} , was the significant amplitude which represents the mean value of the highest one-third portion of the amplitudes; as given by Journée (2001), this is mathematically defined as

$$2 \sqrt{\int_0^\infty S(\omega) d\omega} \quad (134)$$

As such, J_{sa} is given by

$$J_{sa} = 2 \sqrt{\sum_{n=0}^{4096} S_j(\omega) \Delta\omega} = 2 \sqrt{\sum_{n=0}^{4096} S_j(\Delta\omega \cdot n) \Delta\omega} \quad (135)$$

Where, $\Delta\omega$ is the size of the frequency bands in the computed spectra and is given by

$$\Delta\omega = \frac{1}{81.92s} = 0.0122Hz \quad (136)$$

Control Effort

As a final note, control effort was not included in the performance indices as the main impact of large control effort was only a slight increase in the overall body drag. Appendages (including the planes, rudder, and rear stabilizer) represent only 10% of the total drag on a lone DOLPHIN (Watt et al., 1997). The contribution to total drag drops to approximately 5% under typical towing conditions (Seto and Watt, 1998). Therefore, even significant changes in plane control effort (and hence drag) would have a very limited impact on the overall vehicle energy consumption.

6.3.3 Simulated Cases

The cases examined by simulation were grouped into three main areas: the effect of accurate and complete hydrodynamic modelling of control surfaces; the effect of control surface configuration; and the effect of the control system design. The hydrodynamic modelling examined the effect of improving the plant model in simulation while using the existing (conventional) model in controller design; likewise, the effect of using the improved model in both plant and controller was analyzed. The study of control surface configuration used both the control surface geometries and layouts that showed the most promise based on experimental data of Chapter 3. Finally, the investigation of the control system design was based on the three PD and three LQG/LTR controller augmentations summarized in Chapter 5.

The simulations were conducted in straight and level flight and using the manoeuvre of Figure 6-5. Likewise, both calm water and sea state three based on a Bretschneider spectrum were used. The simulations are summarized in brief in Table 6-3; a comprehensive summary of the simulations is given in Appendix F.1.

Table 6-3 Cases considered in simulation

Parameter changed	Vehicle	Model	Controller	Path	Sea
Plant model	Standard	Varied	LQG/LTR	Figure 6-5	Calm
Model for controller design	Standard	Varied	LQG/LTR	Figure 6-5	Calm
Plane geometry	Varied	New	LQG/LTR	Figure 6-5	Calm
	Varied	New	LQG/LTR	Figure 6-5	Sea State 3
	Varied	New	LQG/LTR	Straight	Sea State 3
Plane mounting location	Varied	New	LQG/LTR	Figure 6-5	Calm
	Varied	New	LQG/LTR	Figure 6-5	Sea State 3
	Varied	New	LQG/LTR	Straight	Sea State 3
Controller	Standard	New	Varied	Figure 6-5	Calm
	Standard	New	Varied	Figure 6-5	Sea State 3
	Standard	New	Varied	Straight	Sea State 3

6.4 RESULTS: INFLUENCE OF MODELLING IMPROVEMENTS

The influence of the various improvements to control surface modelling from Chapter 3 and Chapter 4 were studied through the simulation. In addition to improvements in the estimates of the control surface hydrodynamic derivatives, the effect of trim (Sections 3.3.2 and 4.4) and yaw (Sections 3.2.4 and 4.5), plane stall (Sections 4.2.1 and 4.5.1), and bowplane-sternplane interaction (Sections 3.3 and 4.6) were included. All modelling improvement simulations were conducted using the *standard* plane configuration with the LQG/LTR control system. LQG/LTR control weightings of $\mu = 5.0 \times 10^{-6}$ and $\rho = 0.005$ were used in this series of tests. Although these weightings did not produce an ideal controller for any one case, they did produce a working controller for every case. The control weightings of $\mu = 0.0005$ and $\rho = 0.05$ determined in Chapter 5 generally resulted in better performance but could not be used for the examination of modelling improvements since in some situations the changes to the plant resulted in non-minimal modes in the Kalman filter design.

6.4.1 Changes to the Plant Model

Simulations were conducted to examine the effect of control surface modelling errors on system performance. The simulations were based on a controller designed for the conventional plant model but acting upon improved plant models that more accurately represented the true control surface hydrodynamic behavior. In short, the simulations quantified the influence of neglecting plant hydrodynamic information in the controller development and instead treating it unmodelled disturbances. Five cases were considered using the standard vehicle configuration and basic LQG/LTR controller. In addition to the conventional model, originally developed by Field (2000), the features modelled were the bowplane-sternplane interaction effects, the effect of yaw on the bowplanes, the effect of trim on the bowplanes, and the effect of Reynolds number and yaw on the stall angle.

The simulation results for the commanded trajectory of Figure 6-5 in calm water are summarized in Table 6-4 in terms of the performance indices. A complete summary of tabulated simulation data is provided in Appendix F.2.1. There is very little difference between the J_{ct} performance indices of the various models—from highest to lowest, the difference is 3.1%. Interestingly, the performance actually improves when plane interaction and trim influence are included in the plant model but neglected in the control strategy. In terms of the controller, these effects are essentially unmodelled disturbances that happen to have a beneficial influence. Absolute differences between the J_{sl} performance indices are even less than those with the J_{ct} index.

Table 6-4 Effect of model improvements on performance in calm water with LQG/LTR control

Effects Modelled in Plant	Performance Index	
	J_{ct}	J_{sl}
None (original plant)	0.1105	0.0026
Plane interaction only	0.1070	0.0022
Yaw influence only	0.1106	0.0025
Trim influence only	0.1073	0.0024
Plane stall influence only	0.1093	0.0025
All effects	0.1078	0.0023

Only a minor difference in roll was observed for the four cases—RMS roll error ranged from 6.9 degrees to 7.1 degrees—and there was no observed difference in the RMS error of depth, pitch, and yaw (see Appendix F.2.1 for complete data). Although these findings appear to suggest that the simulation outcome does not strongly depend on whether the hydrodynamic effects are included in the plant, with a less robust controller there were differences noted in the simulation output.

Using a simple PD controller, simulations were conducted both with the original plant model and with all the control surface hydrodynamic improvements added. Unlike with the LQG/LTR controller, there was a large decrease in performance effectiveness when the complete plant model was used (see Table 6-5). Specifically, the unmodelled bowplane-sternplane interaction resulted in a steady state pitch error as shown in Figure 6-7; a similar steady state error in depth was also observed. Without integral action, the PD controller was unable to account for steady state error. (The influence of controller methodology and design on vehicle performance is considered in detail in Section 6.6.)

Table 6-5 Effect of model improvements on performance in calm water with PD control

Effects Modelled in Plant	Performance Index	
	J_{ct}	J_{sl}
None (original plant)	0.0124	0.0096
All effects	0.0184	0.0167

6.4.2 Changes to the Controller Model

Simulations were also conducted with the new hydrodynamic information incorporated in the controller as well as the plant; these tests complement those above in which the new hydrodynamics were included in the plant only. In this case, only the most complete plant model (with the trim, yaw, stall, and plane interaction effects) was used. In the models used for controller design, the different effects were included both individually and as a group. The performance is summarized in Table 6-6 and the complete data is provided in Appendix F.2.2.

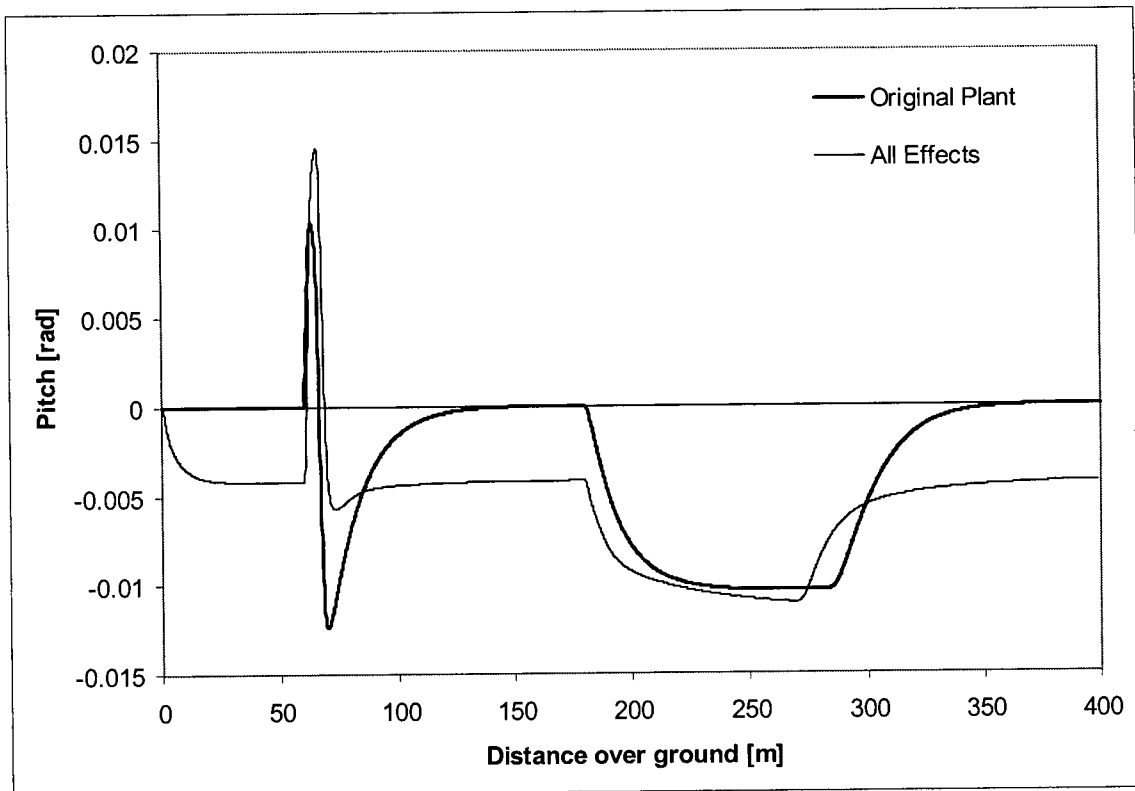


Figure 6-7 Influence of the plant model on PD controller performance in pitch

Table 6-6 Effect of controller model on performance in calm water with LQG/LTR control

Effects Modelled in Controller	Performance Index	
	J_{ct}	J_{sl}
None (original controller)	0.1078	0.0023
Plane interaction only	0.1120	0.0024
Yaw influence only	0.1078	0.0023
Trim influence only	0.1078	0.0023
Plane stall influence only	0.1078	0.0023
All effects	0.1120	0.0024

The performance for the straight and level portions of the manoeuvre, characterized by J_{sl} , was virtually unaffected by the changes to the model used for the controller. For the entire manoeuvre, the inclusion of trim, yaw, and stall effects in the LQG/LTR controller had no significant effect (the values of J_{sl} and J_{ct} , as well as other simulation outputs, remained unchanged). This is because the LQG/LTR controller was designed based on linearization about an operating point with trim and yaw equal to zero (for which there are no trim or yaw effects on the planes). This linearized controller was then used for all conditions; specifically, the controller remained unchanged for non-zero trim and yaw angles.

Bowplane-sternplane interaction—which is almost at maximum for straight and level flight—does have an effect on performance when incorporated in the controller. When the new hydrodynamic effects are included in both controller and plant, the controller compensates for them and the system operates very similarly to the original model (that is, the case where interaction effects are not included in either the controller or plant). Parallel to what was observed in Section 6.4.1, the interaction effects appear to have a somewhat beneficial influence as the vehicle performance is better when they are not included in the controller. Although neglecting the interaction effects may appear to have some benefits in this case, the effects are unmodelled disturbances that change the forces on control surfaces from those commanded by the controller.

In general, with a robust controller the difference in simulation with and without the control surface hydrodynamic model improvements were small but this is not to suggest that these effects should be omitted. A limited number of trials were conducted for this thesis and there may be cases in which simulation output may more strongly depend on the control surface model used. In particular, if the controller is unable to adequately compensate for the added hydrodynamic effects in some situation—due to limitations in control surface response rate or saturation limits, for example—the simulation outcome could change significantly.

6.5 RESULTS: EVALUATION OF PLANE CONFIGURATION

Simulations were conducted to investigate the effect of control surface configuration on performance. The modelled experimental data of Chapter 3 and Chapter 4 for plane geometry and position were used. All simulations were conducted with the LQG/LTR control system with control weightings $\mu = 1.21 \times 10^{-5}$ and $\rho = 0.05$. The control weightings of $\mu = 0.0005$ and $\rho = 0.05$ from Chapter 5 could not be used for the examination of the plane configuration since the changes to the plant resulted in non-minimal modes in the Kalman filter design in some instances.

6.5.1 Plane Geometry

Four different combinations of plane geometry were examined through simulation. In addition to the *standard* configuration, the *long* and *short* bowplanes were used as were the *long* sternplanes (see Table 3-2 on page 45 for physical specifications). The changes in geometry were limited to the plane span as forces on the planes were found to be primarily a function of planform area (for the range of geometries studied, as noted in Chapter 3).

Calm Water

For the test manoeuvre of Figure 6-5 in calm water, the resulting performance indices are summarized for each of the plane combinations in Table 6-7. For the entire manoeuvre (characterized by the J_{ct} index) the *short* bowplane configuration showed the best performance while *long* bowplanes were least effective. In contrast, for the performance over the straight and level positions of the commanded trajectory, the *long* bowplanes were by far the most effective and the *short* bowplanes were the least effective. Complete performance information, including maximum and RMS errors, turn radii, and plane saturation statistics can be found in Appendix F.3.1.

Table 6-7 Effect of plane geometry on performance in calm water

Plane Geometry (Bowplane - Sternplane)	Performance Index	
	J_{ct}	J_{sl}
Standard - Standard	0.0957	0.0057
Long - Standard	0.0999	0.0028
Short - Standard	0.0886	0.0062
Standard - Long	0.0960	0.0074

For each of the position and pose states, the *long* bowplane configuration generally had smaller errors over the entire trajectory. For illustration, the depth as a function of horizontal distance travelled is shown in Figure 6-8 and is typical of most states in terms of how the various plane configurations ranked. In almost all respects, the *long* bowplanes performed better than the *standard* bowplanes which in turn performed better than the *short* bowplanes. The relatively poor J_{ct} performance index for the *long* bowplanes is predominantly due to an increased average roll angle during the turn (see Figure 6-9). The *long* sternplanes ranked poorly in terms of both J_{ct} and J_{sl} . As a further measure of performance, *short* bowplanes operated in saturation for 4.2% of the trajectory compared to 2.6% for the *long* sternplanes, 2.5% for the *standard* bowplanes, and only

1.6% for the *long* bowplanes. In other words, the *long* bowplanes achieved generally better performance and used less control effort in the process.

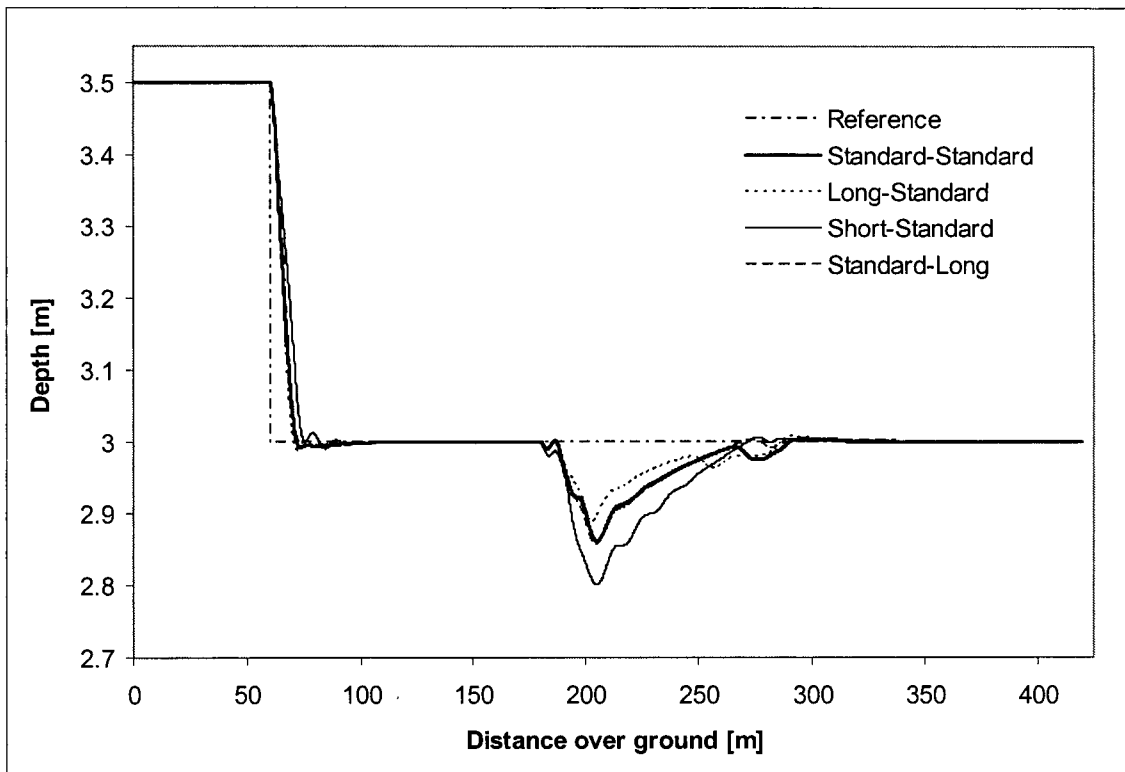


Figure 6-8 Depth history in calm water for various plane geometry combinations

Sea State Three

With the same simulations as above conducted in waves of sea state three and with sensor noise, the *short* bowplanes were the least effective in all regards (see Table 6-8). Over the entire trajectory, the *standard* configuration performed best (measured using J_{ct}) followed closely by the *long* bowplanes. In the straight and level portions of the manoeuvre with a turn, again the *long* bowplanes were most effective; considering only wave disturbance rejection (measured by J_{sa}) the *long* bowplanes were by far the most effective.

To further examine the frequency response, spectra and significant amplitudes were computed for sway, depth, roll, pitch, yaw, bowplane deflection and stemplane deflection (all are provided in Appendix F.3.1). The depth spectra are shown in Figure 6-10 (with the steady state component removed). As would be expected from J_{sa} , the *long* bowplane configuration had the best wave compensation as shown by the lowest response curve. The bowplane deflection spectra are shown in Figure 6-11; the *short* bowplanes show the most plane activity and the *long* bowplanes show the least. These findings are consistent with those above; overall, the *long* bowplanes best track the commanded trajectory while rejecting wave disturbances and using the least control effort.

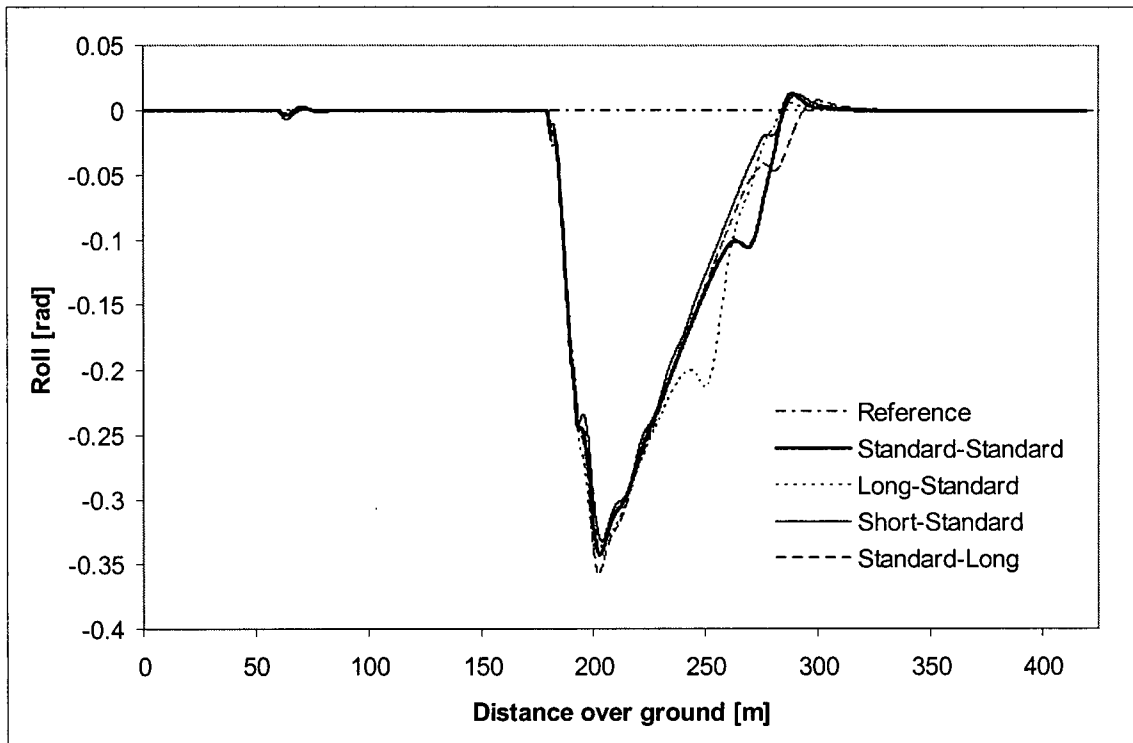


Figure 6-9 Roll history in calm water for various plane geometry combinations

Table 6-8 Effect of plane geometry on performance in sea state three

Plane Geometry (Bowplane - Sternplane)	Performance Index		
	J_{ct}	J_{sl}	J_{sa}
Standard - Standard	0.0970	0.0154	0.479
Long - Standard	0.0984	0.0126	0.222
Short - Standard	0.1030	0.0204	0.397
Standard - Long	0.0997	0.0141	0.308

6.5.2 Plane Location

In addition to plane geometry, four plane location configurations were considered in simulation. The configurations were those that showed potential for improved performance based on the experimental and modelling analysis (Chapter 3 and Chapter 4 respectively); they included the *standard* configuration, *anhedral* bowplanes, a *Y-tail* configuration, and *keel* planes. Specifications for each of these configurations were provided in Table 3-3 on page 46.

Calm Water

The performance indices for each of the configurations in calm water are given in Table 6-9 with complete data summarized in Appendix F.3.2. Similar to observations with plane geometry, the

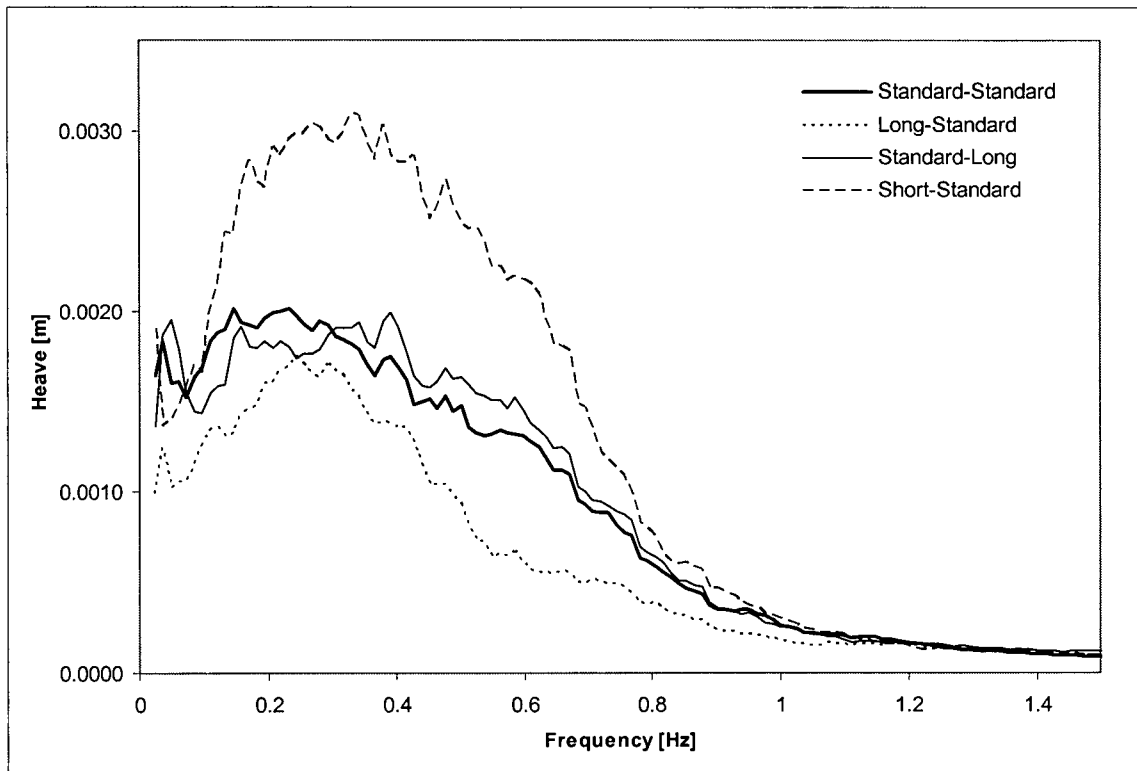


Figure 6-10 Heave response based on bowplane geometry for sea state three (head seas)

best performing configuration in straight and level conditions (*Y-tail*) was least effective over the entire trajectory; the *keel* planes were poor strictly in the straight and level portions but effective over the entire trajectory.

Significant differences were noted in the x - y path of the different configurations as shown in Figure 6-12. The average turn radius of the *Y-tail* was 26% less than that of the *standard* configuration (22.5 metres compared to 30.5 metres). In the *Y-tail* configuration, where sternplanes had dihedral, a component of the associated control force acts in the y -direction thus assisting the rudder in turning. The *anhedral* bowplanes, mounted ahead of the centre of gravity of the vehicle, appear to have an opposite effect in that the average radius of curvature of the turn increases to 31.2 metres. The criteria of the manoeuvre used in evaluation was to change heading by 180 degrees rather than follow a set of waypoints; it is expected—although it has not been verified—that the *anhedral* bowplanes would perform better in waypoint tracking as they allow control of sway directly without a change in heading. Finally, the *keel* planes had an average turn radius of 30.4 metres, similar to the *standard* configuration, but there was an offset in y -position introduced during the depth change. There was no corrective action taken in this case since the trajectory is based on heading not y -position.

The fast, tight turn of the *Y-tail* configuration is accompanied by large roll (see Figure 6-13) which was the primary source of error. The maximum roll angle of *Y-tail* configuration was approximately 28.7 degrees corresponding to an increase in submergence of the snorkel of 0.49 metres (in calm water at 3.5 metres depth). At this roll angle, 0.82 metres of snorkel remain above the water

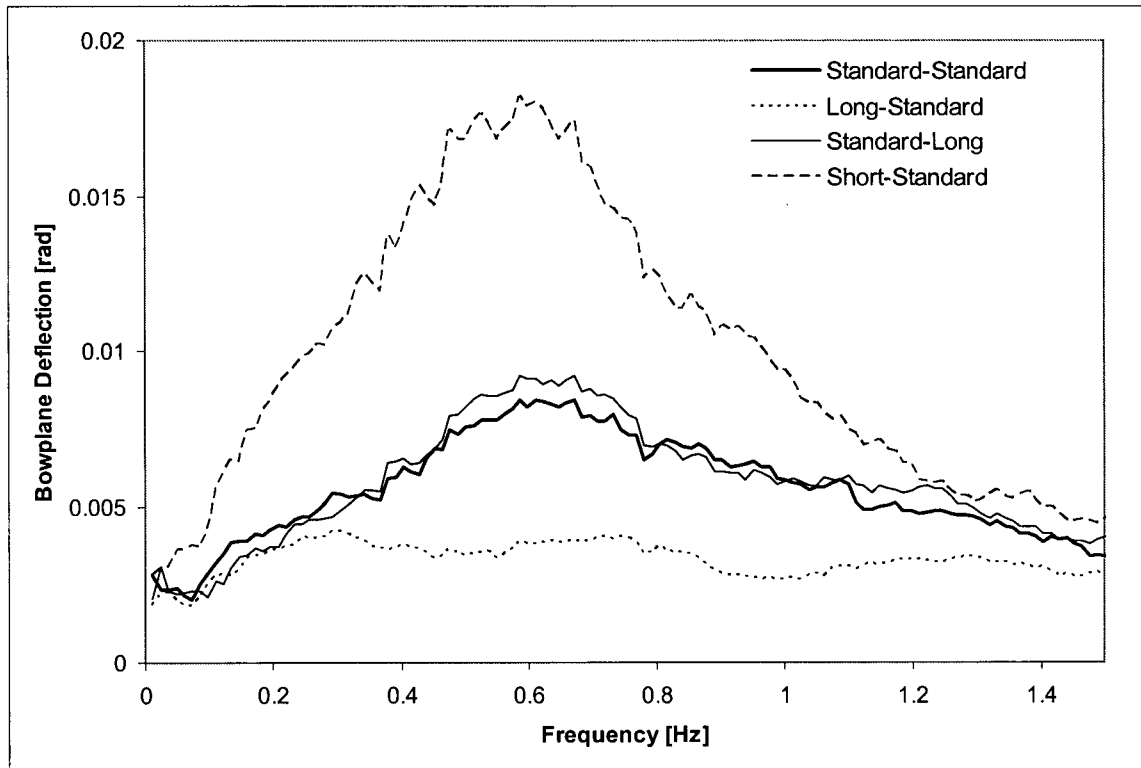


Figure 6-11 Bowplane deflection based on plane geometry for sea state three (head seas)

Table 6-9 Effect of plane location on performance in calm water

Plane Position	Performance Index	
	J_{ct}	J_{sl}
Standard	0.0957	0.0057
Anhedral Bowplanes	0.0900	0.0077
Y-tail	0.1015	0.0018
Keel Planes	0.0912	0.0154

line; for comparison, at minimum 1.1 metres of snorkel remain above the calm water line for the *standard* configuration during the turn. As an aside, by increasing the weighting to roll error in the controller, the turn was performed with reduced roll as shown in Figure 6-14. In this case, the roll error was artificially scaled by a factor of ten in the controller; not only was the physical roll error reduced substantially but the J_{ct} and J_{sl} performance indices improved to 0.0481 and 0.0016 respectively (both significantly lower than any other configuration).

Once again considering the original control error weighting, considerable differences were noted with respect to control effort over the course of the manoeuvre. The *standard* and *anhedral* bowplanes operated in saturation for 2.5% and 2.4% of the time, respectively, over the trajectory. With the *Y-tail*, the bowplanes were in saturation 8.7% of the time, predominantly in trying to cor-

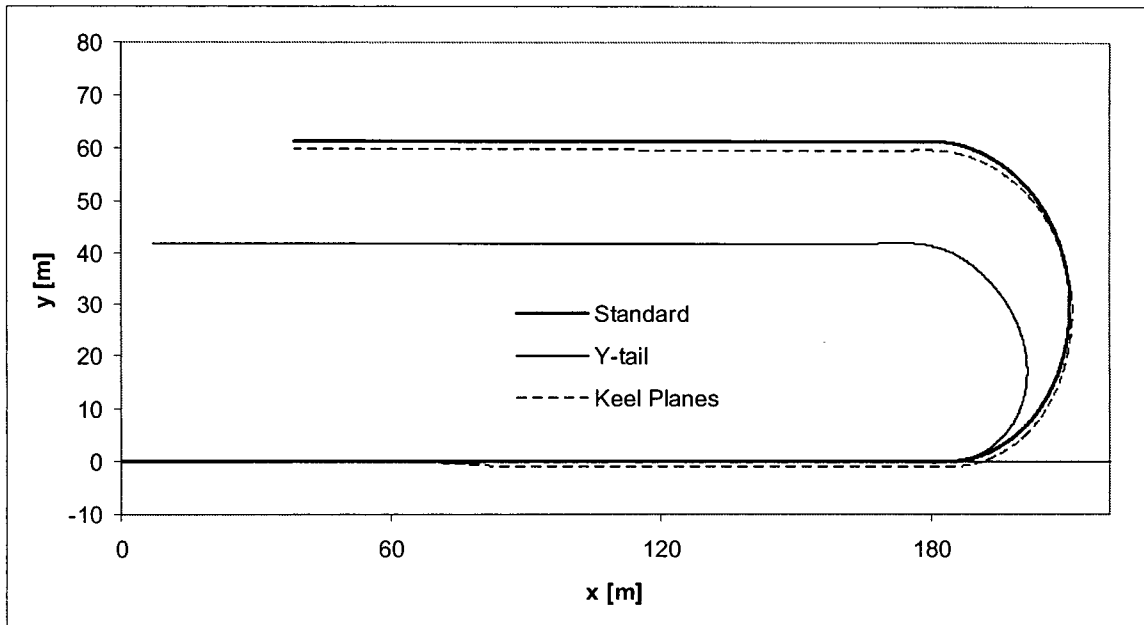


Figure 6-12 Trajectory in x - y plane for alternate plane locations

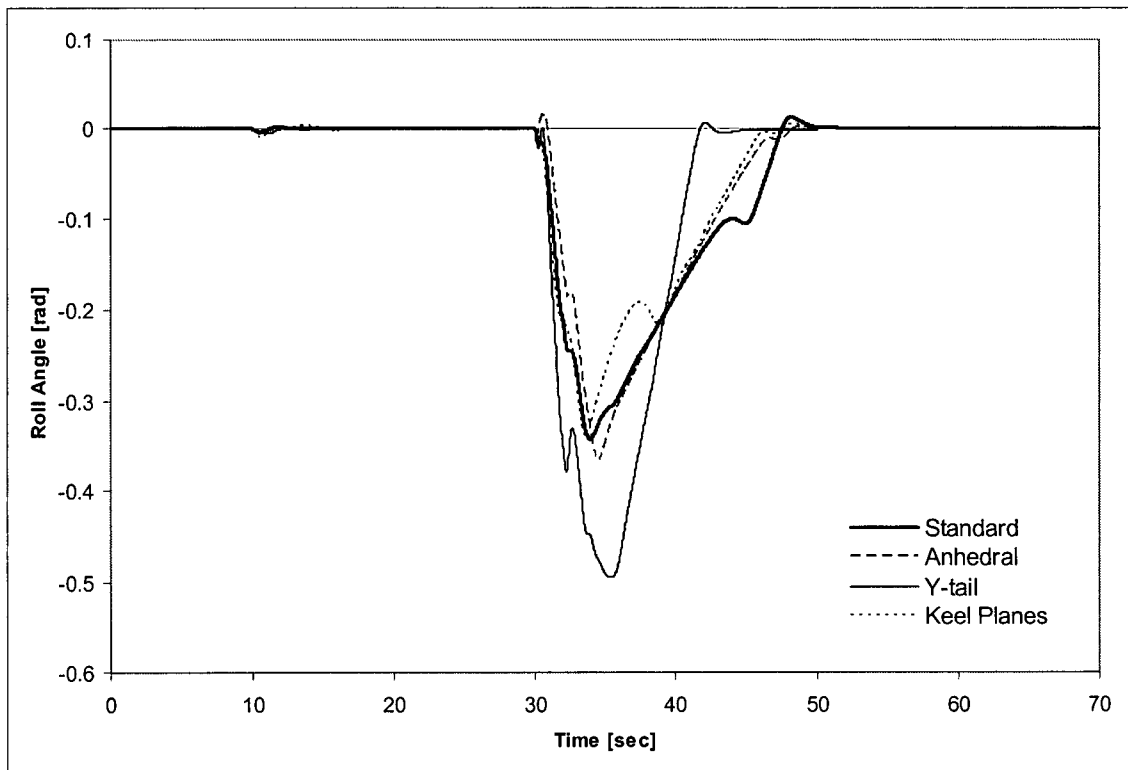


Figure 6-13 Roll history in calm water for alternate plane locations

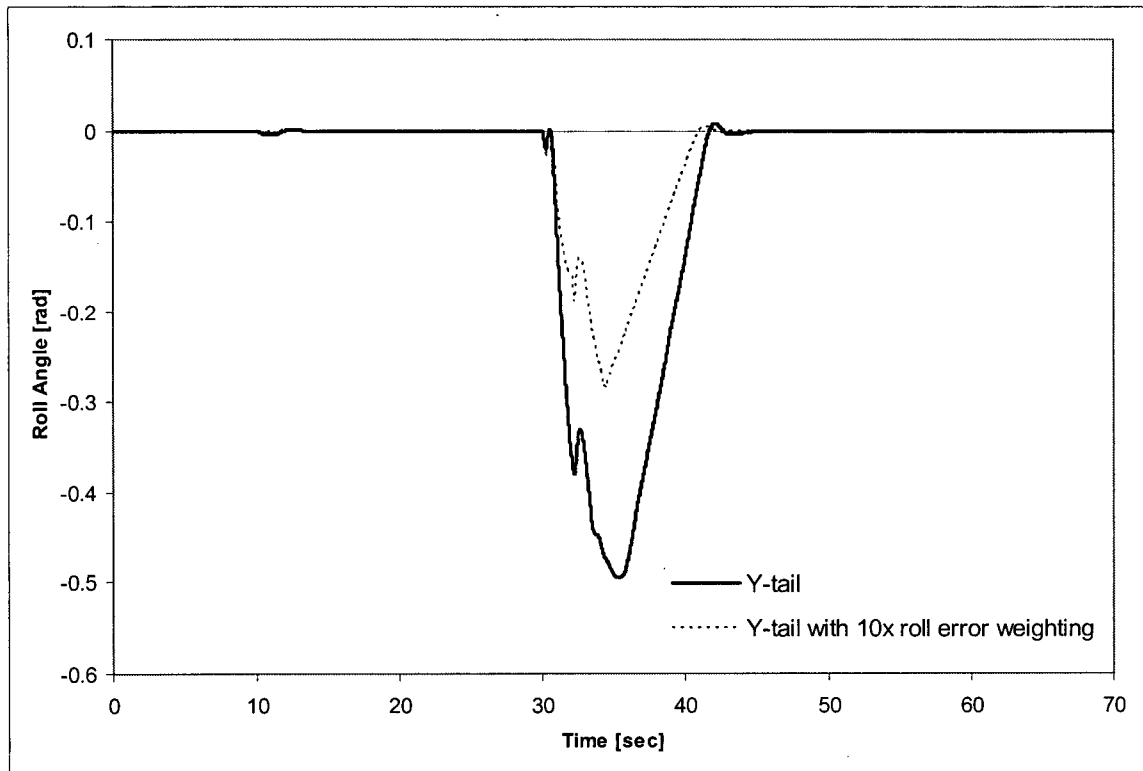


Figure 6-14 Roll history in calm water for Y-tail with increased roll error sensitivity

rect for the large roll during the turn. The *keel* planes operated in saturation 12.5% of the time both as a result of pitch error during the depth change and roll error during the turn.

Sea State Three

The performance summary for the alternate plane locations in sea state three is given in Table 6-10. The *Y-tail* performs best over the straight sections of the turning manoeuvre while the *anhedral* bowplanes are best over the complete trajectory and show the best wave disturbance rejection characteristics. The *keel* planes are effective at rejecting wave disturbances but rank poorly compared to other configurations through all portions of the path following manoeuvre.

Table 6-10 Effect of plane location on performance in sea state three

Plane Position	Performance Index		
	J_{ct}	J_{sl}	J_{sa}
Standard	0.0970	0.0154	0.479
Anhedral Bowplanes	0.0839	0.0160	0.231
Y-tail	0.1046	0.0136	0.430
Keel Planes	0.1049	0.0338	0.338

The differences in bowplane usage were even more dramatic in waves as compared to calm water; the proportion of the trajectory with bowplane saturation for the *standard*, *anhedral*, *Y-tail*, and *keel* planes was 2.1%, 4.2%, 5.3%, and 23.4% respectively. The bowplane deflection spectra are shown in Figure 6-15. In addition to operating in saturation most often, the *keel* planes were also the most active as shown by the pronounced peak at frequencies near 0.5 Hz. The *Y-tail* and *standard* configuration showed similar frequency response spectrum, significantly lower in magnitude than both the *keel* and *anhedral* planes.

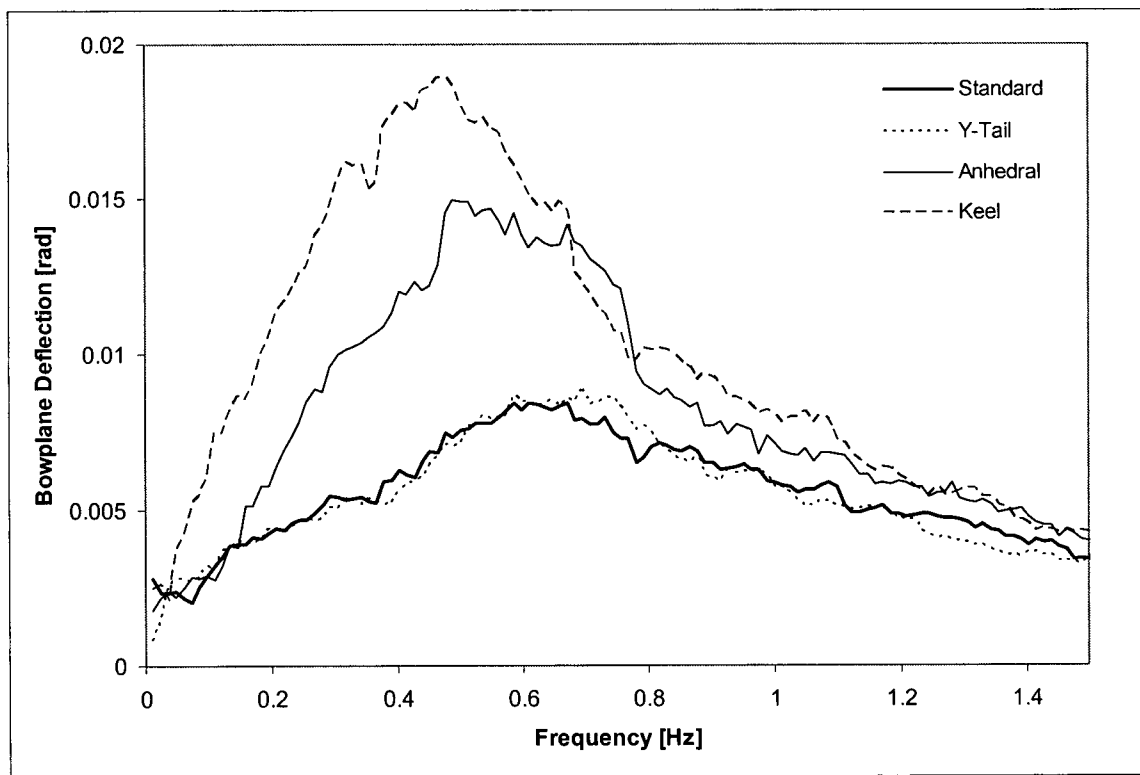


Figure 6-15 Bowplane deflection spectra based on plane location for sea state three head seas

Finally, when considering the sway and yaw significant amplitudes of each configuration, the *anhedral* planes showed improvements in wave disturbance rejection in those states of 74% and 23% compared to the *standard* planes. As was alluded earlier, the downward inclination of the *anhedral* planes is expected to provide improved performance in sway and yaw due to the redundancy in the control those states. The improvements in sway and yaw were with the *anhedral* planes were offset by increases in the significant amplitudes in heave and pitch by 32% and 17% respectively. Complete results, including all tables and spectra, are provided in Appendix F.3.2.

6.6 RESULTS: EVALUATION OF CONTROL SYSTEM

In addition to the effect of the control surface configuration on vehicle performance, the influence of the controller and controller improvements were examined. The majority of work was based on the LQG/LTR controller developed by Field (2000) but a simple PD controller modelled after one reported by Shupe and McGeer (1987) was also considered. The main objective was to determine if it was possible to improve performance by accounting for the new control surface hydrodynamic information in the controller design. For both the PD and LQG/LTR controllers, the basic control strategy was augmented in an attempt to account for the new control surface hydrodynamic effects added to the plant. All simulations were conducted using the *standard* plane configuration.

6.6.1 PD Controller Performance

Three augmentations of a PD controller were considered: a basic PD controller, a PD controller with gain scheduling, and a PD controller with a series compensator tuned using fuzzy logic. Details regarding the development of each of the controllers were provided in Section 5.3. For each controller, simulations were conducted with the trajectory of Figure 6-5 in both calm water and in sea state three with waves moving in the $-x$ direction (that is, in head seas for the start of the manoeuvre). Various response spectra were also computed by considering straight and level flight in sea state three head seas for 3.5 metres depth.

Calm Water

For the three PD controller augmentations, the performance indices for the evaluation manoeuvre in calm water are summarized in Table 6-11. In general, there are only minor differences between the controllers. For the complete trajectory, the PD controller with gain scheduling has a performance equivalent to the basic PD controller; the PD controller with a fuzzy-tuned series compensator has a slightly poorer performance index (roughly 3.5% higher). Over the straight and level portions of the trajectory, both the gain scheduled PD controller and the PD controller with series compensation showed an improvement in the J_{sl} performance index of over 5%.

Table 6-11 Effect of PD control structure on performance in calm water

Control Structure	Performance Index	
	J_{ct}	J_{sl}
PD	0.0114	0.0098
PD with Gain Scheduling	0.0114	0.0093
PD with Fuzzy Compensation	0.0118	0.0093

The improved straight and level performance of the controllers with gain scheduling and fuzzy compensation is largely due to reduced pitch error. The maximum pitch errors for these controllers were 0.7 and 0.6 degrees, respectively, compared to 1.0 degrees for the basic PD controller. However, the two PD controller augmentations also had slightly larger RMS depth errors and larger average bowplane deviations compared to the basic PD controller. Complete details regarding the performance of the PD controllers are provided in Appendix F.4.1.

As an aside, for the PD controller with series compensation, simulations of Section 6.4.1 on page 184 were repeated where the improved control surface hydrodynamic model was used for the plant but the conventional model was used in controller development. The resulting pitch history is shown in Figure 6-16; the steady state error previously observed is greatly reduced as is the maximum pitch error during the turn. The steady state error that remains is due to the slight discrepancy between the plant and the compensator in the representation of the bowplane-sternplane interaction. The pitch error during the turn with the compensator and improved plant is even smaller than the basic controller and original plant. A similar improvement in steady state depth error was also noted.

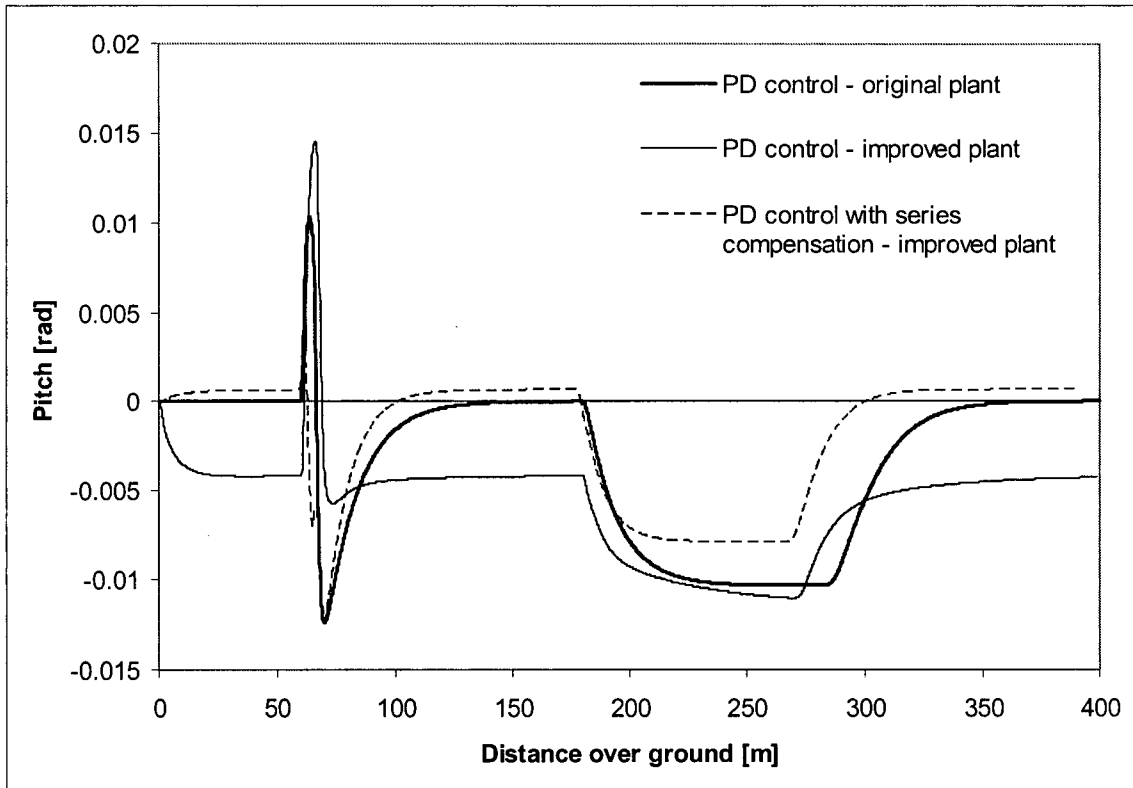


Figure 6-16 Pitch history comparison for PD controller with and without fuzzy compensator

Sea State Three

In sea state three, the basic PD controller showed comparable performance to the gain scheduling and series compensation augmentations (see Table 6-12). With the wave disturbances, both the gain scheduling controller and the controller with fuzzy tuned series compensation had 8% lower maximum pitch error compared to the basic controller; however, the maximum depth errors were 1% and 6% higher respectively. Complete details for all three controller augmentations are summarized in Appendix F.4.1.

The response spectra for depth are shown in Figure 6-17 below. The PD controller with series compensation had a lower response than the basic PD controller while the gain scheduling implementation had higher response. Similar results were observed for other motions and in terms of

Table 6-12 Effect of PD control structure on performance in sea state three

Control Structure	Performance Index		
	J_{ct}	J_{sl}	J_{sa}
PD	0.0233	0.0222	0.125
PD with Gain Scheduling	0.0235	0.0223	0.135
PD with Fuzzy Compensation	0.0236	0.0222	0.124

plane deflection, both augmentations to the PD controller showed less plane activity than the basic controller. Complete frequency response spectra plots are provided in Appendix F.4.1.

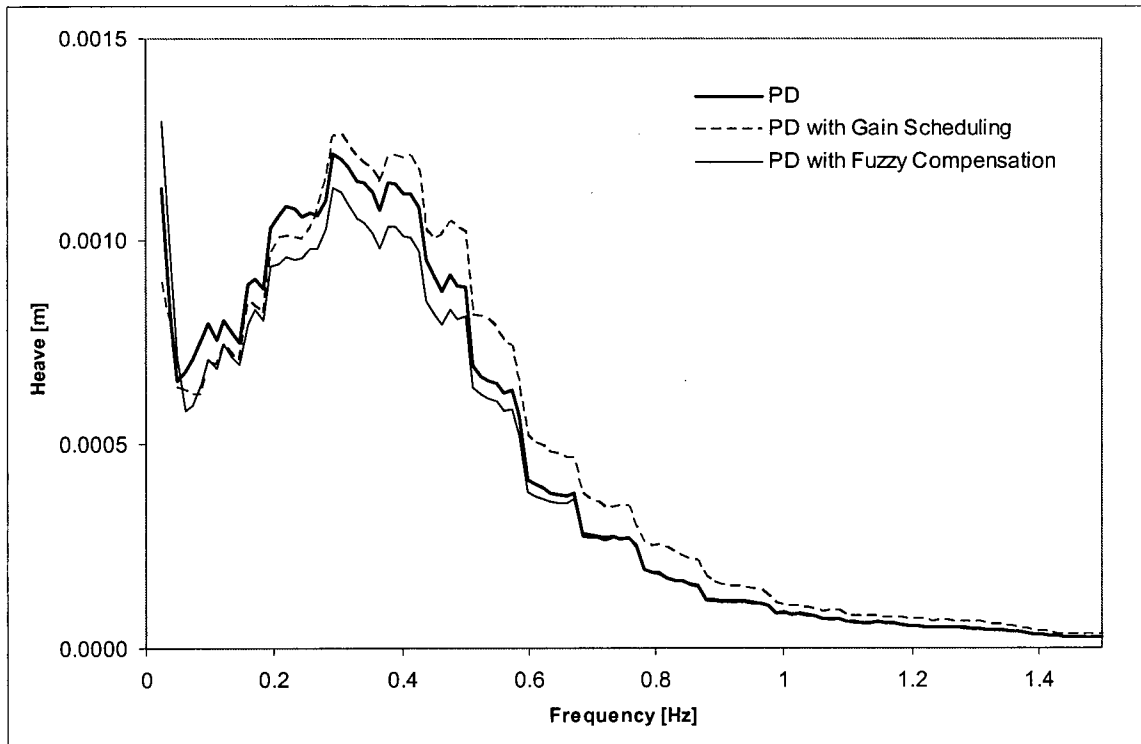


Figure 6-17 Depth response spectra for PD controller augmentations in sea state three head seas

6.6.2 LQG/LTR Controller Performance

Three augmentations of the LQG/LTR controller were considered: a basic LQG/LTR controller developed by Field (2000), a sliding mode LQG/LTR controller, and an LQG/LTR controller with fuzzy-tuned series compensation. Details regarding the development of each of the controllers were provided in Section 5.4. Similar to with the PD controllers, simulations were conducted with the trajectory of Figure 6-5 in both calm water and in sea state three, as well as for straight and level flight in sea state three head seas. The *standard* vehicle configuration was used for all tests and control weightings of $\mu = 0.0005$ and $\rho = 0.05$ were used in LQG/LTR controller.

Calm Water

For the three LQG/LTR controllers considered, the performance indices for the evaluation manoeuvre in calm water are summarized in Table 6-13. For both the complete trajectory and the straight and level portions of the trajectory, the sliding mode LQG/LTR controller had the best performance. The J_{ct} and J_{sl} performance indices were approximately 12% and 60% better respectively than the basic LQG/LTR controller. The basic LQG/LTR controller and the LQG/LTR controller with series compensation showed similar performance.

Table 6-13 Effect of LQG/LTR control structure on performance in calm water

Control Structure	Performance Index	
	J_{ct}	J_{sl}
Basic LQG/LTR	0.1014	0.0058
Sliding Mode LQG/LTR	0.0891	0.0023
LQG/LTR with fuzzy tuned series compensation	0.1018	0.0059

The improved performance of the sliding mode controller was primarily due to reduced error in roll, pitch and depth. Although it does not influence the performance index, the sliding mode augmentation also showed significantly reduced average plane deviation and fewer occurrences of plane bowplane saturation than the other two controllers. Compared to the basic LQG/LTR controller, average bowplane deviation was reduced by 39%, sternplane deviation was reduced by 54%, and the incidences of bowplane saturation were reduced by 64%. Complete details regarding the performance of the three LQG/LTR controllers are provided in Appendix F.4.2.

Sea State Three

In sea state three, the basic and series compensated LQG/LTR controllers again showed similar performance and in this case the sliding mode LQG/LTR controller ranked just slightly lower in the path following (as shown in Table 6-14). Errors in roll, pitch, and yaw were responsible for the poorer performance with the sliding mode controller; the J_{ct} and J_{sl} indices were 1% and 7% larger respectively. In terms of wave disturbance rejection, the sliding mode augmentation was the most effective and showed a 6% improvement in the J_{sa} index in comparison to the basic LQG/LTR controller. Compared to the other controllers in sea state three, the bowplanes with the sliding mode controller exhibited lower average deviation and fewer instances of saturation while the sternplanes had higher deviation and increased saturation. Complete performance details are provided in Appendix F.4.2.

Table 6-14 Effect of LQG/LTR control structure on performance in sea state three

Control Structure	Performance Index		
	J_{ct}	J_{sl}	J_{sa}
Basic LQG/LTR	0.0954	0.0103	0.191
Sliding Mode LQG/LTR	0.0963	0.0110	0.179
LQG/LTR with fuzzy tuned series compensation	0.0954	0.0106	0.192

The response curves for depth are shown in Figure 6-18 below. The sliding mode LQG/LTR controller showed significantly improved depth response in waves (over the dominant frequencies) in comparison to the other two controllers. Similar improvements were also noted for other states (see Appendix F.4.2). Consistent with the above discussion of control effort, the sliding mode controller had lower deflection spectrum for the bowplanes and higher spectrum for the sternplanes when compared to the other controllers. Of the other two controllers, the series compensation augmentation showed a slight improvement in disturbance rejection and control effort based on a comparison of the response spectra to the basic controller.

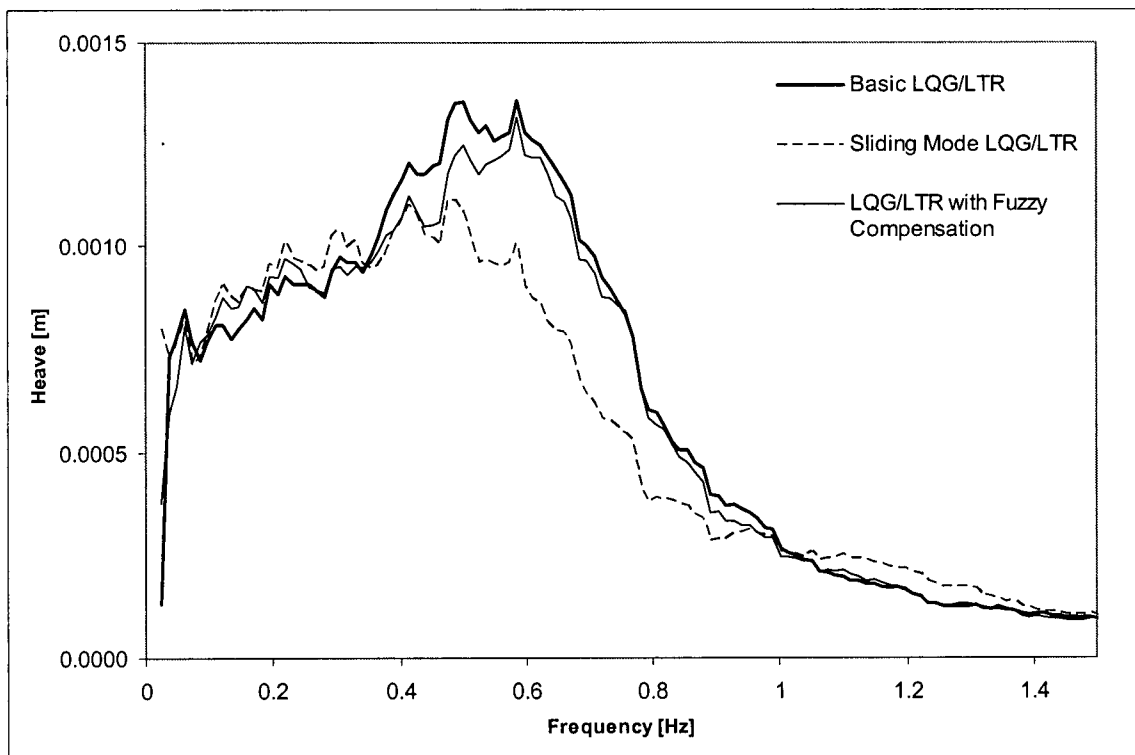


Figure 6-18 Heave response for LQG/LTR augmentations in sea state three, head seas

6.6.3 Comparison of PD and LQG/LTR Control Strategies

The primary focus of the above analysis was to examine controller enhancements to account for newly identified control surface hydrodynamic behavior. For completeness, the best augmenta-

tions of the two main control methodologies (PD with gain scheduling and sliding mode LQG/LTR) are briefly compared below for calm water and sea state three.

Calm Water

In calm water, dramatically better performance was noted with the sliding mode LQG/LTR controller for straight and level portions of the evaluation trajectory while the gain scheduled PD controller performed much better when considering the entire trajectory (see Table 6-15). In general, the LQG/LTR controller had larger maximum errors in depth and pitch but also recovered more quickly (see for example Figure 6-19 and Figure 6-20). The cause of the lower ranked J_{ct} performance index of the LQG/LTR controller was the large roll angles experienced during the turn as shown in Figure 6-21.

Table 6-15 Gain scheduled PD to Sliding Mode LQG/LTR comparison for calm water

Performance Index		
Control Structure	J_{ct}	J_{sl}
Sliding mode LQG/LTR	0.0891	0.0023
PD with gain scheduling	0.0114	0.0093

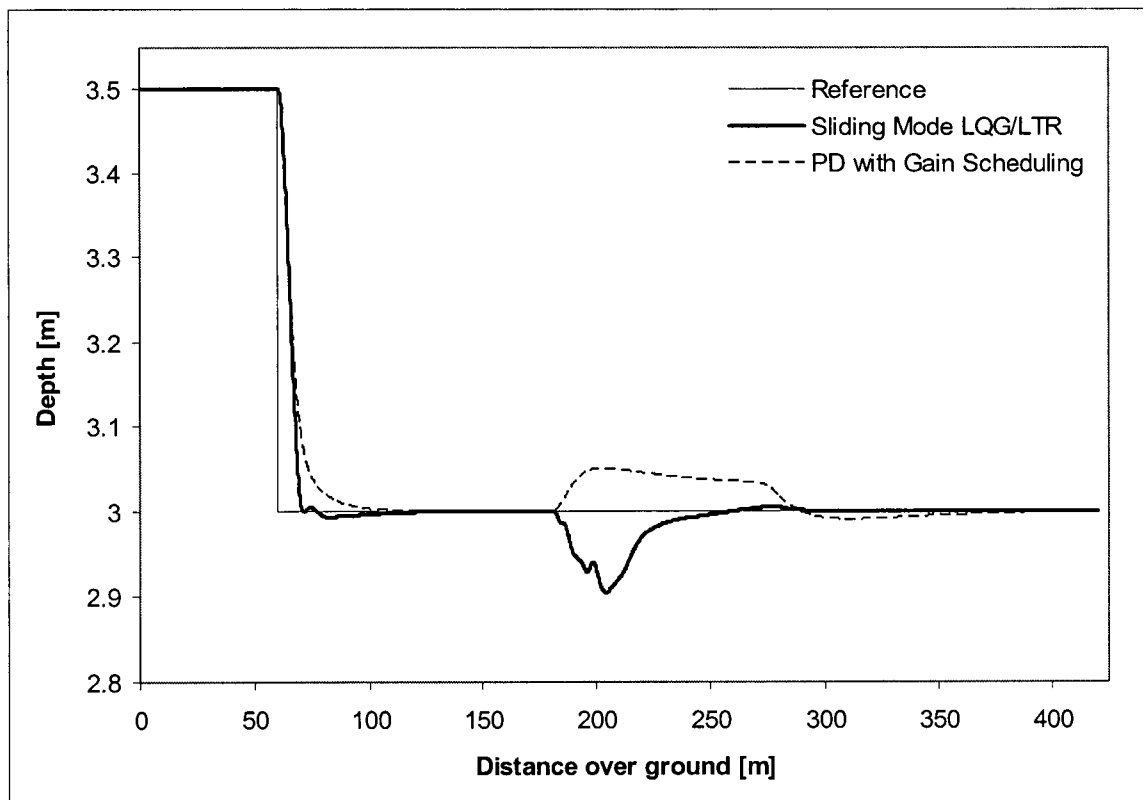


Figure 6-19 Depth history for Gain Scheduled PD and Sliding Mode LQG/LTR in calm water

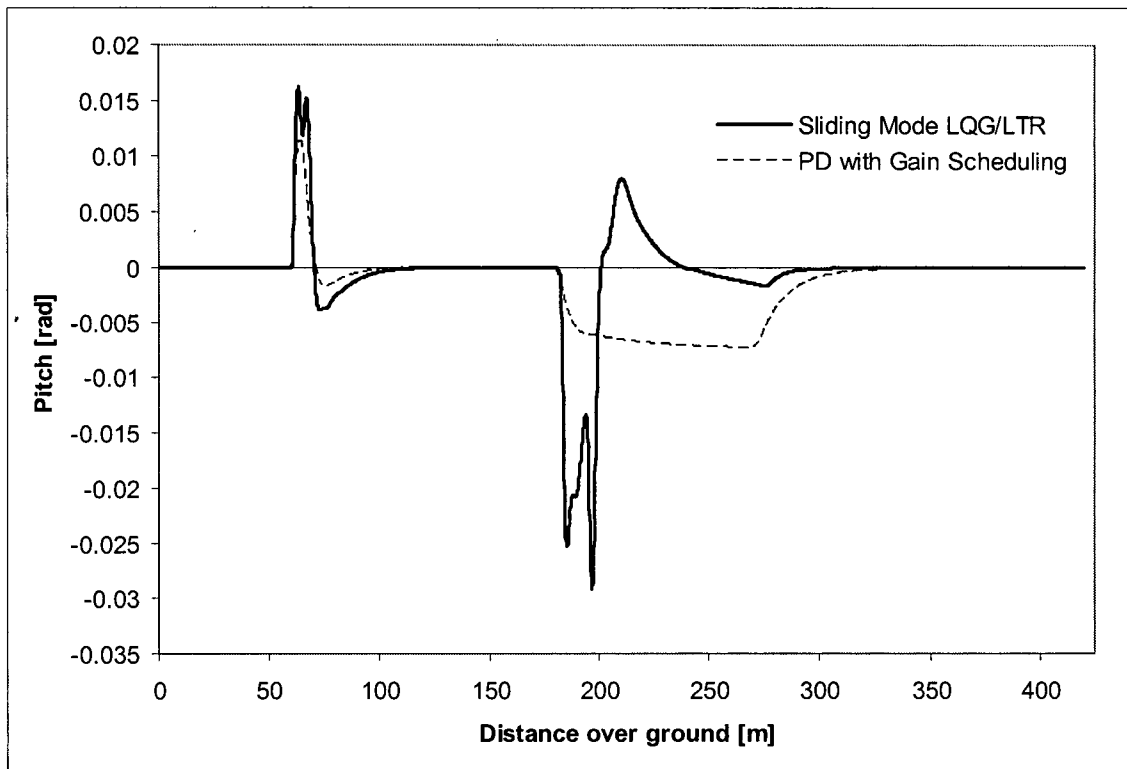


Figure 6-20 Pitch history for Gain Scheduled PD and Sliding Mode LQG/LTR in calm water

With the planes mounted in the *keel* position, considerable differences in performance were noted with the PD and LQG/LTR controllers. Specifically, the vehicle response became unstable under the PD controller while remaining bounded with the LQG/LTR controller (see Figure 6-23).

The instability with the PD controller is believed to result from the generation of an unfavorable pitch moment due to the keel plane position aft of the centre of gravity of the vehicle. As with other configurations with the PD controller, the front (keel) planes were used solely for depth control and pitch and roll control was assigned to the sternplanes. As shown in Figure 6-22, in trying to move the vehicle downward in the z -direction, the keel planes cause a pitching moment that tends to rotate the vehicle nose up. If the pitch moment is not negated by the sternplanes, the keel planes must work not only against the sternplanes (which generate an upward force in trying to counter the pitch moment) but also the propeller (which pushes the inclined vehicle even farther from the target depth). As an aside, for cases where the bowplanes were mounted forward of the centre of gravity, the resulting pitching moment caused by the bowplanes tends to pitch the vehicle in a favorable direction that assists in the depth change through the vehicle flight.

The performance of the LQG/LTR controller in this case was not impressive compared to other plane configurations but, most importantly, the vehicle stability was not threatened. The influence of pitch due to the keel planes is apparent; the error depth initially decreases but then begins to increase as the vehicle pitches (in this case nose down). Due to the coupled nature of the LQG/LTR control strategy, the control is able to recover. The ability to account for changes in the vehicle, both modelled and otherwise, is a strong endorsement for the LQG/LTR methodology.

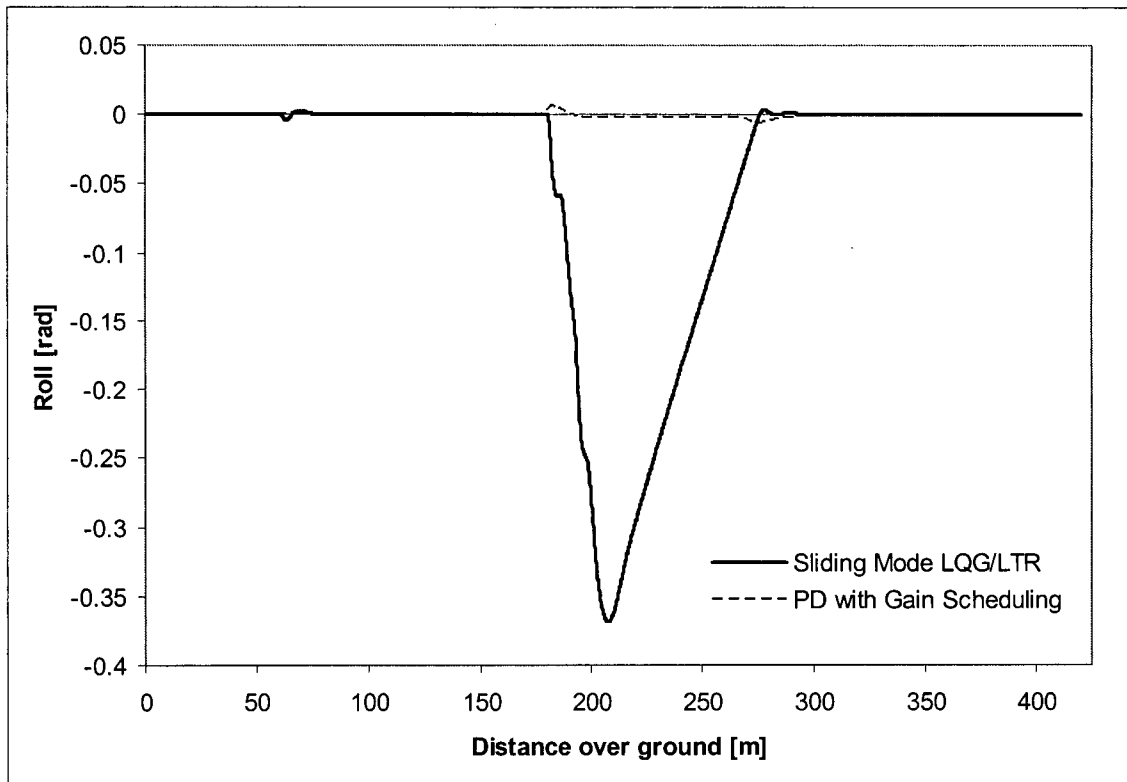


Figure 6-21 Roll history for Gain Scheduled PD and Sliding Mode LQG/LTR in calm water

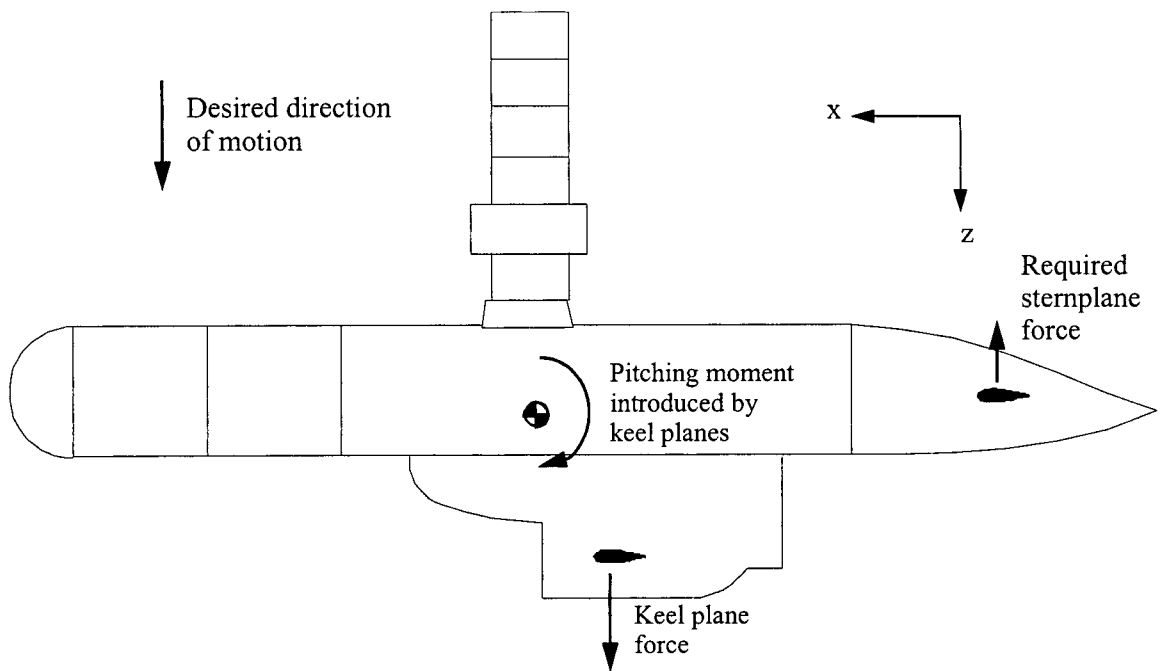


Figure 6-22 Keel planes correcting for depth error

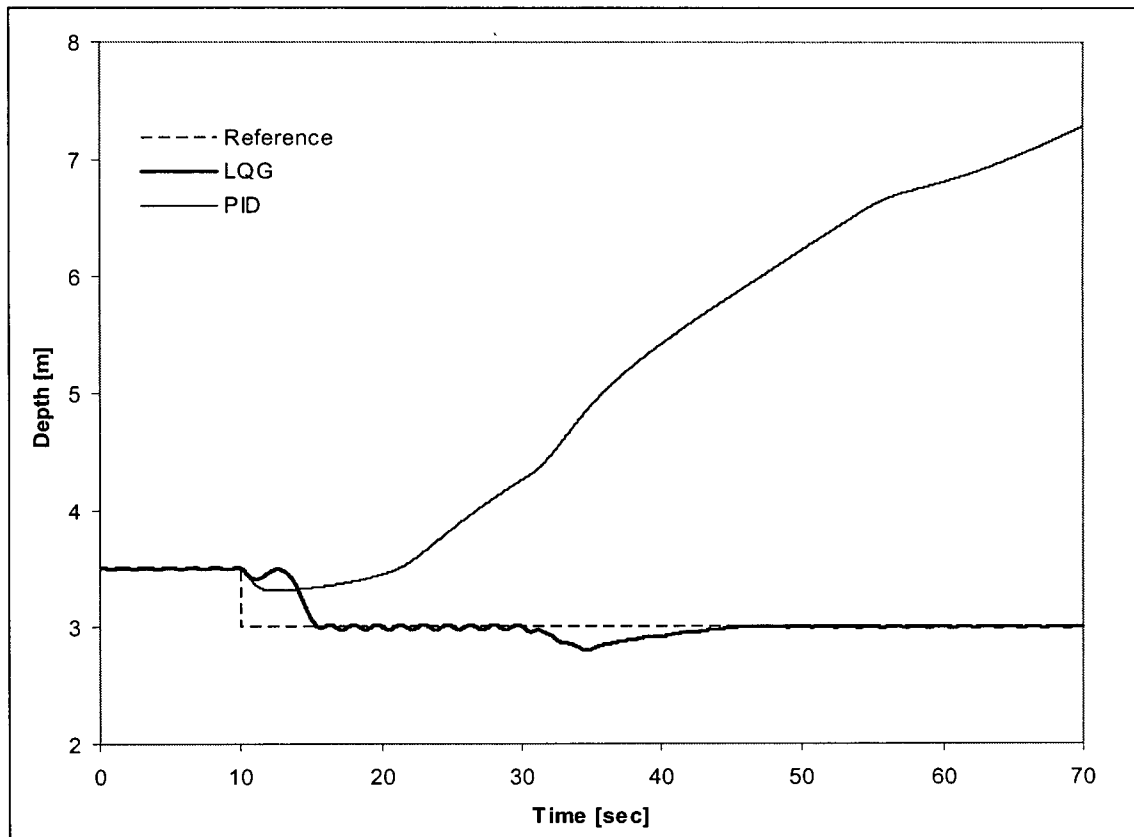


Figure 6-23 Stability in depth for PID and LQG/LTR controllers with keel planes

Sea State Three

At sea state three, the differences in performance indices between controllers was less pronounced (see Table 6-16). Again, the sliding mode LQG/LTR controller was better over the straight and level portions of the trajectory and the PD controller with gain scheduling was better over the complete trajectory. The depth and deflection spectra for head seas are compared for the two controllers in Figure 6-24 and Figure 6-25 respectively. In general, the PD controller appears to show better performance in waves as both the depth response and bowplane deflection spectra remain lower than those for the LQG/LTR controller over most frequencies. Spectra for other motions as well as the sternplane deflection also favoured the PD controller.

Table 6-16 Gain scheduled PD to Sliding Mode LQG/LTR comparison for sea state three

Control Structure	Performance Index		
	J_{ct}	J_{sl}	J_{sa}
Sliding Mode LQG/LTR	0.0963	0.0110	0.179
PD with Gain Scheduling	0.0235	0.0223	0.135

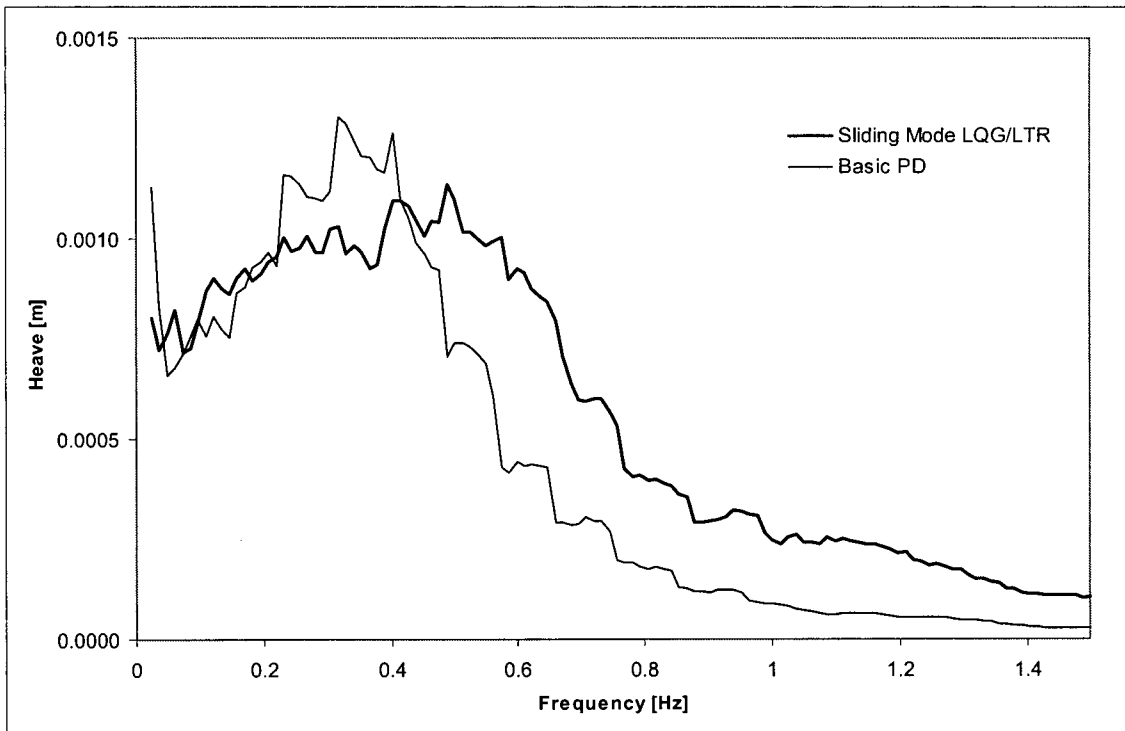


Figure 6-24 Heave response for Sliding Mode LQG/LTR and PD (sea state 3 head seas)

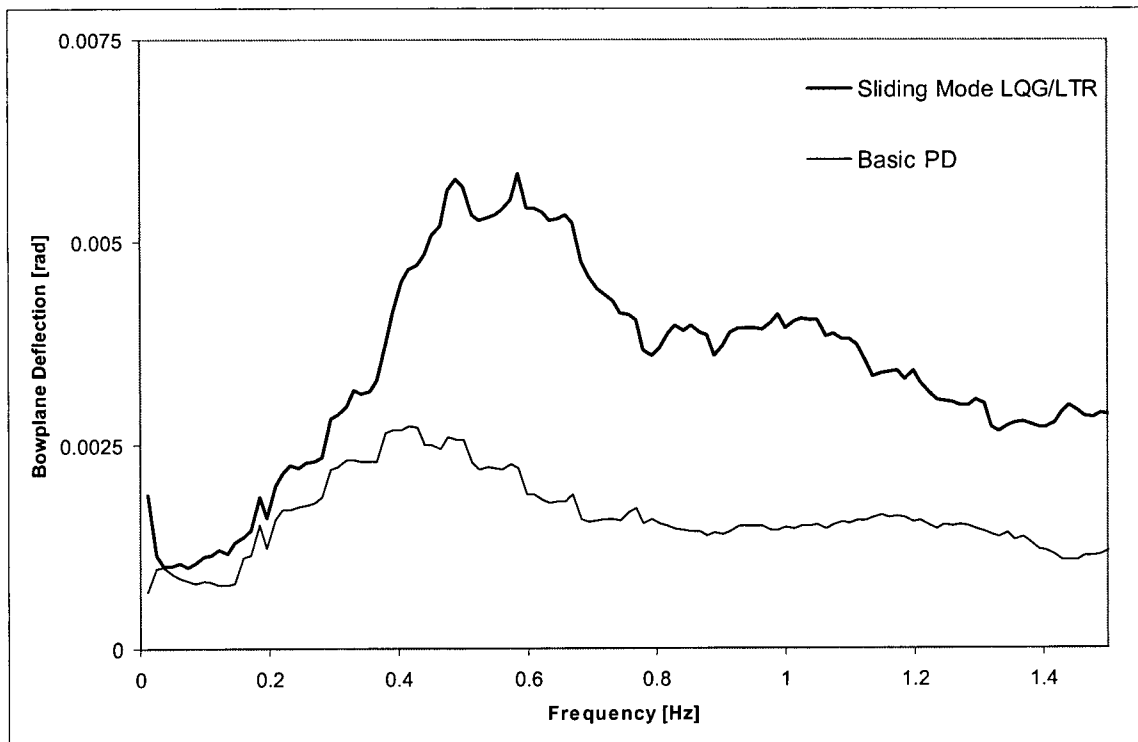


Figure 6-25 Deflection spectra for Sliding Mode LQG/LTR and PD (sea state 3 head seas)

6.7 SUMMARY

The development of an AUV control and dynamics simulation package in MATLAB® and Simulink® was presented in this chapter. The procedures and evaluation criteria used in the simulations were also discussed. Simulation results were presented for three main categories: the influence of control surface modelling improvements, the influence of control surface configuration, and the influence of controller methodology.

Control Surface Modelling Improvement, Simulation Results

- Control surface hydrodynamic effects described in Chapter 3 and Chapter 4 (including trim, yaw, and bowplane-sternplane interaction) were included in both the simulation plant model and controller development.
- Addition of the various effects to the plant but leaving them unmodelled in the controller had a small but measurable influence on performance. When a PD controller was used, a steady state error was introduced to the plant output unless compensation was added to the controller.
- Including the control surface hydrodynamic effects in the plant as well as the controller resulted in simulation output similar to when the effects were not included in either the plant or controller. That is, for the simulated manoeuvre, the controller appears to be able to effectively compensate for the new hydrodynamic effects.

Control Surface Configuration, Simulation Results

- Various control surface geometries were examined with bowplanes and sternplanes located in the standard position. The best overall performance was found with *long* bowplanes and *standard* sternplanes; they showed the best tracking in straight and level flight, the best disturbance rejection, and required the least control effort.
- Of the different control surface positions considered, the *Y-tail* configuration had the best performance in straight and level flight and greatly reduced the minimum turn radius. This configuration suffered from increased roll during a turn but it was shown that this could be effectively compensated by increasing roll error weighting in the LQG/LTR controller.
- When the bowplanes were replaced by keel planes (slightly aft of the vehicle centre of gravity) unstable behavior was noted when using a PD controller.

Controller Design, Simulation Results

- Both PD and LQG/LTR control strategies were examined for use in AUV control. Both controllers were found to have merit although in one instance, the PD controller exhibited unstable behavior; under none of the circumstances tested did the LQG/LTR controller become unstable.
- For the PD controller, two further augmentations were considered in an attempt to improve performance based on the new data for control surface hydrodynamics. The first augmentation used gain scheduling to adjust controller gains (based on vehicle orientation) and the second used a fuzzy-tuned series compensator to adjust control surface deflections directly. Considering all aspects of vehicle performance, each of the three PD controllers had particular strengths but overall the best performance was found with the PD controller with gain scheduling.

-
- With the LQG/LTR controller, two enhancements were also investigated: sliding mode control and a fuzzy-tuned series compensator. Again, each controller augmentation had specific merits but the sliding mode LQG/LTR controller showed the best performance overall.

7

CONCLUSION

In this chapter, the findings regarding the hydrodynamics, modelling, and control of planes on a near-surface underwater vehicle are discussed. The results are summarized and recommendations are presented for future work.

7.1 SUMMARY

The main objective of this research was to improve the understanding and effectiveness of control surfaces on an AUV. This goal was approached from two different avenues: through a physical perspective in terms of hydrodynamics and from a management perspective in terms of control. The interrelationship of these two aspects was implicitly addressed in mathematical modelling of control surface performance.

7.1.1 Overview

As presented in Chapter 3, control surface hydrodynamic behavior was examined through experimentation using a specially designed 1/4-scale model. Tests were conducted in both wind tunnel and towing tank facilities and forces generated by the bowplanes and sternplanes were measured by custom-built load cells. In addition to the vehicle operating conditions (including speed, trim, yaw, and sea state) the geometry and placement of the planes on the model was studied. The performance was evaluated based on the force to deflection relationship of the planes with particular emphasis on differences observed due to operating condition and configuration. Trim was found to influence the bowplane performance and have the same effect as increasing the plane deflection by an amount equal to 1.5 times the trim angle. In yaw, the performance of the leeward bowplane was found to improve and two counter rotating vortices shed by the hull were noted; the performance of the windward bowplane deteriorated. In all conditions, the bowplanes were found to affect the sternplane performance; the bowplane-sternplane interaction was strongly dependent on plane configuration and vehicle orientation. Finally, waves produced an oscillating force on the planes that decreased with depth and became less significant with forward speed.

The mathematical modelling detailed in Chapter 4 used various analytical and numerical techniques to validate, predict, and mathematically describe the experimental findings from Chapter 3. Semi-empirical predictions of control surface performance in straight and level flight agreed well with experimentally measured values. Bowplane performance in trim was accurately predicted by empirical relations describing the flow angle about an inclined cylinder. In yaw, the two counter-rotating vortices shed by the hull were found to explain the increase in the effectiveness of the leeward side plane; the improved performance of the leeward plane and the corresponding decrease in performance of the windward plane were described using empirical relationships derived from the experiments. A simple line vortex model of the flow aft of the bowplanes accurately predicted the interaction between bowplanes and sternplanes. The use of linear wave theory to describe the effects of free surface waves on the control surfaces gave results that closely matched experimental values.

Several different control strategies were developed to make use of the improved knowledge and modelling of control surface hydrodynamic behavior. In Chapter 6, the vehicle and controller performance was evaluated using a submarine simulation package developed previously by Field (2000) and enhanced with the improved models of control surface performance developed in this work. An LQG/LTR controller designed by Field for his simulator was used along with sliding mode and series compensation augmentations devised in Chapter 5. Additionally, a PD controller (including gain scheduling and series compensation augmentations) was designed.

7.1.2 Influence of Control Surface Performance Model

The mathematical models of control surface performance developed through this work were considerably different from previously available models. The greatest differences were in the bowplane performance in trim and yaw and in the interaction between bowplanes and sternplanes. For example, a 10% difference in bowplane force was predicted between the improved and the conventional control surface performance models for a ± 5 degree trim angle. Similarly, for a ± 10 degree yaw angle, the forces on the port and starboard bowplanes changed by $\pm 6\%$; of particular concern was the fact that the port and starboard planes reacted differently to yaw—one increased in force and one decreased in force for the same deflections—and as a result generated a rolling moment that was not predicted in the conventional model. Finally, the bowplane-sternplane interaction resulted in changes in the sternplane force of 25% or more in straight and level flight. Additionally, the actions of the bowplanes resulted in pitching moments on the vehicle not considered in a controller designed based on a conventional model of control surface performance.

Even given these substantial differences between the control surface models, only modest differences were noted in vehicle performance in simulation. For a fictitious scanning manoeuvre used for the evaluation of vehicle behavior, there was only a 3% change in the path following performance index when the conventional control surface model in the plant was replaced by the improved model (working with an LQG/LTR controller). The differences were mainly attributed to the bowplane-sternplane interaction effect. With a PD controller, a difference in performance of approximately 48% was noted between the conventional and improved control surface hydrodynamic models; however, the absolute difference was similar in magnitude to that with the LQG/LTR controller. The main cause of the difference with the PD controller was again the bowplane-sternplane interaction and a significant steady state error was noted in pitch and depth. Neither controller showed unstable behavior with the standard control surface configuration when the plant models were changed. Similar differences in performance were also noted when changes were made to the models used in controller design (that is, when the improved models were used in both the plant and the controller design).

Overall, these results tend to suggest that simple, conventional control surface performance models can be adequate for preliminary simulation and development of underwater vehicles provided that a robust controller (such as LQG/LTR) is used. Although the differences in performance of the control surfaces between the conventional and improved models were significant, the overall effect on vehicle performance and control effort with the LQG/LTR controller was small. Such a treatment of control surface modelling must be approached with caution though as only a limited number of operating conditions and manoeuvres were examined; there may be situations that were not studied in which performance changes significantly or stability is threatened. When a less robust controller such as PD is used, significant differences (such as steady state error) can be expected between the conventional and improved control surface models and therefore the most accurate (the improved) control surface hydrodynamics model should be used.

7.1.3 Influence of Control Surface Configuration

The plane performance was primarily a function of the planform area and did not change significantly based on mounting location on the hull; however, the interaction between the bowplanes and sternplanes was strongly dependent on both plane geometry and location. A simple potential

flow model was able to accurately predict the bowplane-sternplane interaction for different plane configurations, trim angles, and Reynolds number. In general, this model can be used in underwater vehicle design to predict control surface interaction.

Unlike the effect of modelling discussed above, the overall vehicle performance in simulation was strongly dependent on the control surface configuration. For example, when the exposed span of the bowplanes was increased by roughly 30% over the *standard* configuration, the disturbance rejection performance improved by 54% (as measured through the significant amplitude of scanning error in a hypothetical sea-floor mapping exercise). When bowplanes were mounted with anhedral, the average bowplane-sternplane interaction was reduced by over 50% and when the sternplanes were mounted in a *Y-tail* configuration, the interaction dropped by almost 70%. In simulation, wave disturbance rejection performance of the *anhedral* and *Y-tail* configurations improved by 52% and 12% respectively; with the *Y-tail*, there was also a 26% reduction in the vehicle turning radius.

Beyond the vehicle-specific findings, the study of control surface configuration demonstrated that control surfaces must be selected with care on an AUV. System performance can be significantly changed by small modifications to control surface location and geometry. Furthermore, in controlling depth, the forward control surfaces generate a pitching moment that appears to assist the depth change through inclining the vehicle in a favorable trim orientation; in cases where the forward planes are positioned even slightly aft of vehicle centre of gravity, the opposite effect is observed and poor depth-keeping performance and possible loss of stability result.

7.1.4 Influence of Controller Design

Six different control strategies were developed and examined through simulation. Three controllers were based on the PD architecture previously used with the DOLPHIN (Shupe and McGeer, 1987) and included gain scheduling and series compensation augmentations. The remaining three controllers were based on the LQG/LTR architecture as developed by Field (2000) and included sliding mode and series compensation implementations.

The three PD controllers all behaved similarly in terms of path following and response in waves; only minor differences in the responses in the various states were noted and all performance indices were comparable. Unmodelled plant characteristics had an adverse effect on the PD controller performance and resulted in steady state errors in the vehicle position and pose. Likewise, the PD control strategy was not able to operate the vehicle when significant changes were made to the control surface layout (specifically, when bowplanes were replaced by the *keel* planes).

The LQG/LTR controller was relatively insensitive to modelling errors and changes in the plant. Steady state errors were not observed and the vehicle response remained stable for all of the cases considered. Of the LQG/LTR controllers, the sliding mode augmentation performed best overall while similar performance was noted between the basic design and the series compensated implementation. In general, the LQG/LTR controllers performed well in waves but exhibited large pitch, roll, and depth excursions during turns. It was shown that by artificially increasing error weighting in the controller (such as for roll), the overall system performance in turning could be dramatically improved. There is great potential for further improving the performance of the LQG/LTR controller although this may involve a potentially lengthy tuning procedure.

In comparing the PD and LQG/LTR control schemes, each had specific strengths and weaknesses. The performance with the PD controller tended to be better on average, particularly in trajectory following; the LQG/LTR tended to have larger maximum errors during a manoeuvre but it also recovered more quickly after a manoeuvre. The dramatically different behavior in roll suggests that the dissimilarity in controller performance is likely not simply a result of differences in controller tuning. More likely, the differences in performance are due to the decoupled sub-system approach with PD versus the fully coupled approach with LQG/LTR. The key difference between the two control methodologies was the ability of the LQG/LTR controller to continue to operate effectively in the presence of changes to the plant (both in terms physical changes and modelling errors).

7.2 RECOMMENDATIONS

7.2.1 Hydrodynamics and Modelling

Control surface performance was modelled based on experiments conducted under static conditions up to the limitations of the respective test facilities. Control surface performance is known to strongly depend on Reynolds number yet it was not possible to match Reynolds number to full-scale values. In this regard, it would be beneficial to verify that the scaling procedures used provide reasonable estimates of full-scale control surface performance. Similarly, the body influence in yaw significantly changed bowplane performance through a vortex structure that developed on the leeward side of the hull. The vortex structure and the resulting influence on the bowplanes may also be influenced by Reynolds number; tests approaching full-scale Reynolds number should be conducted to validate the results from the wind tunnel tests.

The force to deflection behavior and fore-aft interaction of the control surfaces were determined experimentally under static conditions. Plane deflections were held constant throughout measurements; in active operation (more typical of control surfaces in practice) performance may be different and should be measured. Likewise, the bowplane-sternplane interaction was measured in uniform flow and should also be measured in more realistic conditions with waves and body motion.

Finally, the influence of trim, yaw, and waves were investigated independently and then combined in models. There may be coupling effects between these parameters and the test matrix should be expanded to include combinations of the various effects and thereby validate the models used.

7.2.2 Control and Evaluation

In some cases, considerable improvements in performance were realized through slight changes in controller parameters. A more detailed analysis of controller tuning and optimization should be conducted.

The stability of the various control strategies was not explicitly examined. An analysis of stability, including the influence of the fuzzy tuned compensators and sliding mode LQG/LTR controller, should be performed.

As a long-term goal, an actively controlled free-swimming or partially captive model should be considered to test and validate controllers. Such a system would be the most realistic tool for modelling autonomous underwater vehicle performance next to sea trials on an actual AUV. The errors introduced in the mathematical modelling of performance would be eliminated and all hydrodynamic characteristics would be fully represented (including any effects not measured during the experiments).

7.3 CONCLUSIONS

The three main objectives in this study of AUV control surface hydrodynamics were: to improve the accuracy and completeness of control surface hydrodynamic models; to determine if existing control surface hydrodynamic models are adequate for AUV control system design and simulation; and to identify potential improvements in control surface design and usage for DOLPHIN-like AUVs. Relating to these objectives, the following key conclusions were identified:

- existing models of control surface performance prediction are very good for simple cases (such as for isolated planes or straight and level flight)
- substantial differences in control surface performance were noted during manoeuvring (non-zero trim or yaw) as well as due to bowplane-sternplane flow interactions
- with a robust controller (such as LQG/LTR) only minor differences in vehicle performance were noted when more complete and realistic control surface performance models were used; changes to control surface models introduced steady state error when used with a simple controller without integral action (such as PD)
- substantial changes to vehicle performance were noted when the control surface geometry and arrangement of control surfaces on the vehicle was modified; in particular, improvements were noted with both longer planes and anhedral/dihedral planes
- PD and LQG/LTR control schemes showed different performance; LQG/LTR tended to recover from errors more quickly and also showed increased robustness to changes in the vehicle
- in general, the various augmentations to the control system designed to account for changes in control surface behaviour showed only limited benefit; a sliding mode LQG/LTR controller demonstrated a significant improvement in performance

APPENDICES

APPENDIX A - SUPPLEMENTARY CALCULATIONS

A.1 Bowplane Upwash Calculations

The bowplane is replaced by the bound and trailing vortices shown in Figure A-1 where Γ is the circulation. As noted by Pauchet (1997), the three dimensionality associated with the formation of the trailing vortices is restricted to a distance of about one chord length behind the plane. The reader is referred to Talay (1975), Jacob (1995), von Mises (1959) for further discussion regarding modelling lifting surfaces using vortices.

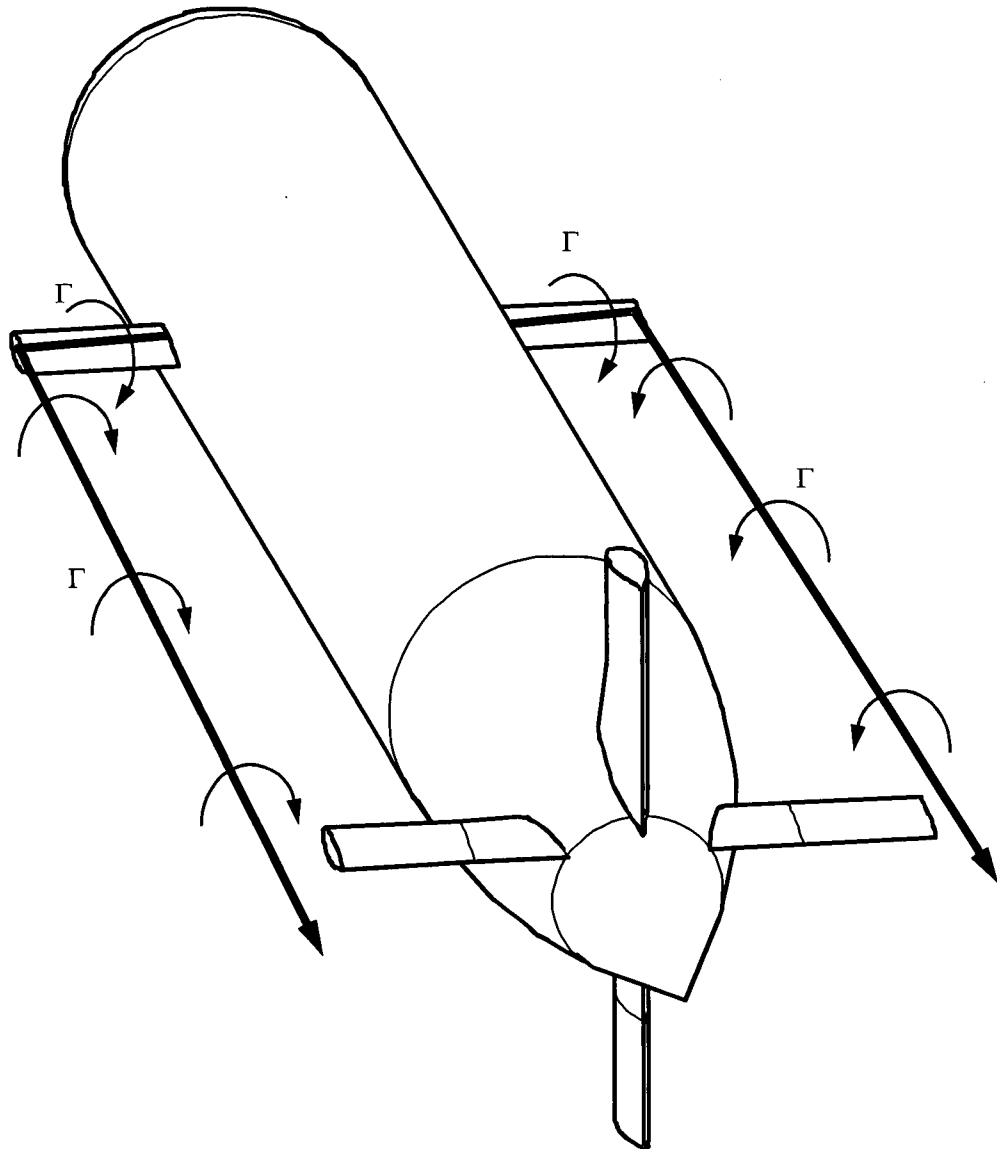


Figure A-1 Vortex system used in upwash calculations

Based on the Kutta-Joukowski lift theorem, the force generated by a plane of exposed span b_{exp} is

$$L = \Gamma U_{\infty} \rho b_{\text{exp}} \quad (137)$$

where L is the lift, Γ is the circulation, U_∞ is the freestream flow velocity, and ρ is the fluid density. Replacing the lift by non-dimensional coefficient of lift,

$$C_L = \frac{L a_e}{\rho U_\infty^2 b_{\text{exp}}^2} \quad (138)$$

where $a_e = \frac{2b_{\text{exp}}}{C}$ is the aspect ratio, the circulation is given by

$$\Gamma = \frac{C_L U_\infty b_{\text{exp}}}{a_e} \quad (139)$$

The hull can be replaced by using a system of image vortices as shown in Figure A-2.

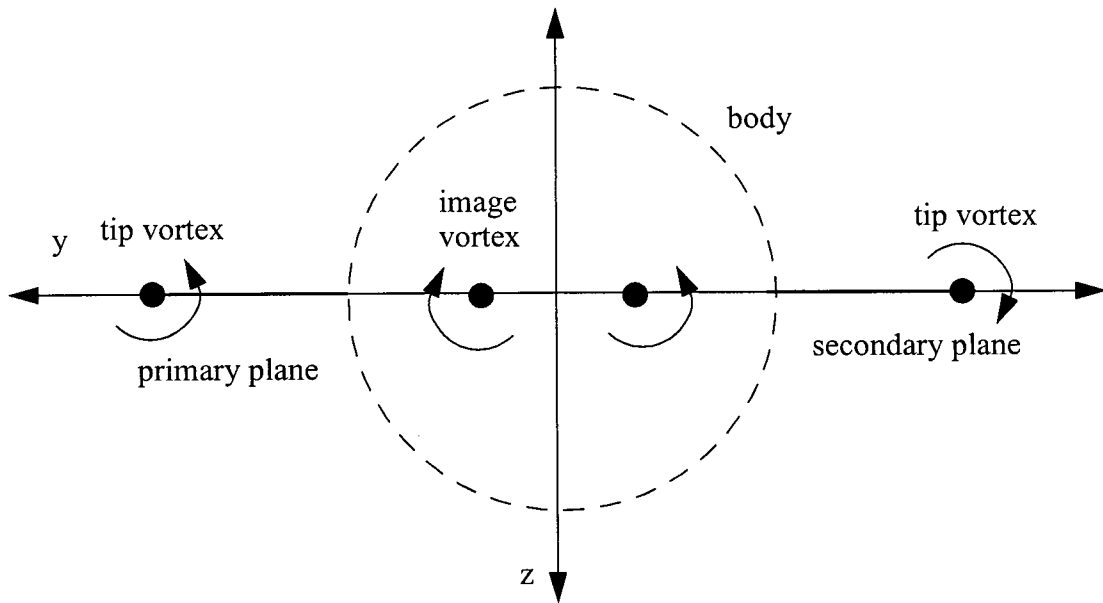


Figure A-2 Vortex system for forward planes (freestream flow into page)

The radial distance, r_{vi} , of the image vortices from the hull centreline is

$$r_{vi} = \frac{R^2}{|r_v|^2} r_v \quad (140)$$

where r_v is the radial position of the primary tip vortex and R is the hull radius. The strength of the image vortices, Γ , is the same as that of the tip vortices although the direction of rotation is opposite. For an isolated appendage (mounted against a wall) the image vortex is simply mirrored about the root of the plane as (shown in Figure A-3).

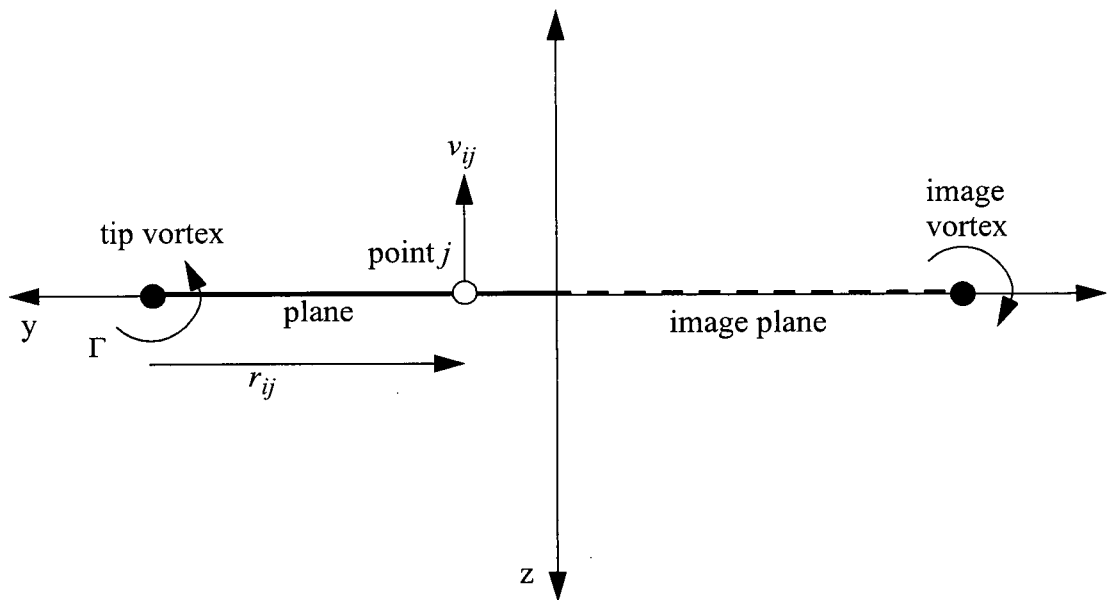


Figure A-3 Vortex system for forward planes (freestream flow into page)

The upwash in each case was computed for all points along the plane by vectorially combining the induced flow velocity from the vortices (real and image) with the free stream flow. The induced velocity computed at point j on the plane for vortex i according to

$$v_{ij} = \frac{\Gamma_j}{2\pi r_{ij}^2} \quad (141)$$

with the resulting induced velocity as shown in Figure A-3. The bound vortices on the control surfaces were not considered. From equation (139), Γ is the same for the body-mounted and isolated planes for a given force C_L . By the small angle approximation, the overall effect of the bound vortex on the upwash angle will be similar in each case; that is, the overall upwash angle is approximately a linear combination of the effects of the bound, trailing, and image vortices. When the difference in upwash between the isolated and body-mounted planes is computed, the bound vortex effects will cancel.

A comparison of the upwash for the body-mounted and isolated planes is shown in Figure A-4. The results are from the *short* bowplanes located on the hull centreline with a forward speed of 17 m/s (similar to the wind tunnel tests) and a C_L of 0.4 (corresponding roughly to a plane deflection of 14 degrees). The computed upwash angles are plotted against the non-dimensional position on the plane span measured from the root.

The outboard portions of the planes show the strongest upwash due to the presence of the tip vortices. Overall, the body-mounted plane has greater upwash due to the close proximity of the hull image vortex and due to the effect of the body on the incident flow. The 'trim effect' noted in

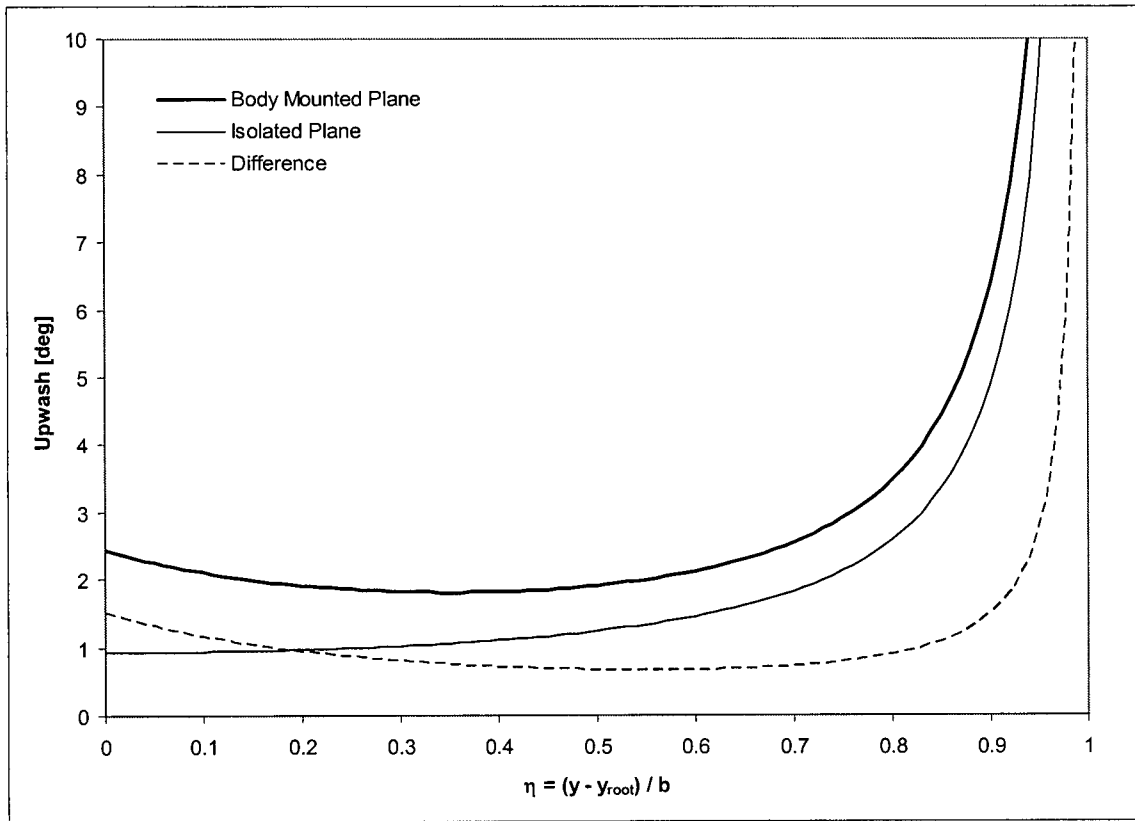


Figure A-4 Upwash comparison for isolated and body-mounted planes

equation (26) on page 30 was used in an attempt to account for the effect of the hull on the upwash. Specifically, the computed upwash for the body-mounted planes was scaled by

$$\left[1 + \left(\frac{R}{y} \right)^2 \right] \quad (142)$$

For the sample case considered above, the average computed upwash for the isolated plane was 1.3 degrees over the inboard portion of the plane. Specifically, the region from $\eta = 0$ to $\eta = 0.8$ was considered as the tip vortex locally induces unrealistically high velocities in the absence of viscous effects. In contrast, the body-mounted plane produces an upwash of 2.1 degrees on average over the span to $\eta = 0.8$ (the upwash was 1.4 degrees prior to the hull correction of equation (142)). The difference in upwash between the isolated and body mounted plane for the case studied was 0.85 degrees or 6% of the 14 degree plane deflection.

A.2 Change in Stall Angle With Aspect Ratio

Coefficient of lift versus angle of incidence data were reported by Zimmerman (1933) for Clark Y airfoils of differing aspect ratio. The stall angle measured from the various curves is shown in Figure A-5. An exponential best fit curve of the form

$$\alpha_{stall} = 16.735 + 45.484e^{-a_e} \quad (143)$$

closely describes the behavior of stall angle, α_{stall} , with aspect ratio, a_e (where the α_{stall} is measured in degrees).

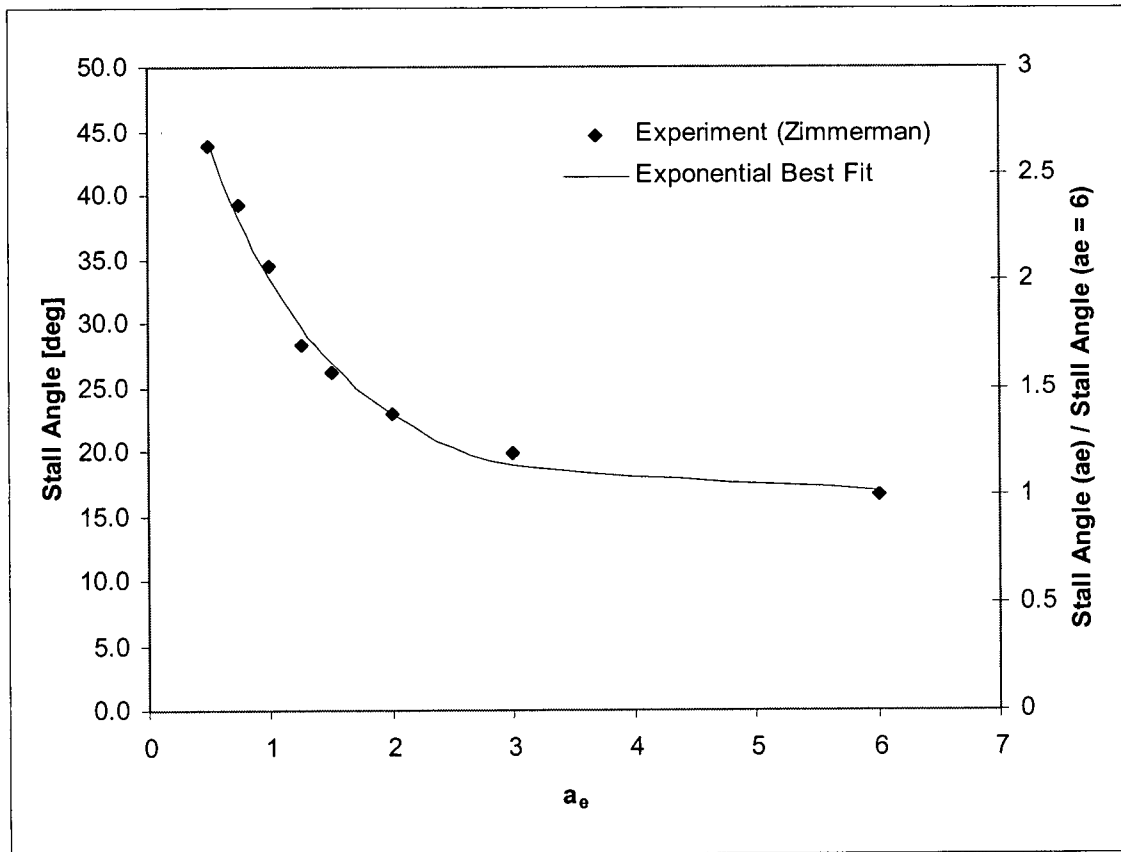


Figure A-5 Change in Stall Angle With Aspect Ratio for Clark Y Airfoil

The ratio of the stall angle for a given a_e to the stall angle for $a_e = 6$ is also shown in the figure. Assuming that a two-dimensional wing has the same stall angle as a wing with $a_e = 6$, the curve from the figure could be used to provide an estimate of the stall angle for wings with $0.5 < a_e < 6$. In reality, a two-dimensional wing would be expected to have a stall angle slightly less than that for a wing with $a_e = 6$ so the above procedure would produce a conservatively low estimate of stall angle.

A.3 Change in Maximum Lift Coefficient with Reynolds Number

Semi-empirical data provided by Barlow et al. (1999) were used to predict the change in maximum lift coefficient, $\Delta C_{L,max}$, with respect to Reynolds number. $\Delta C_{L,max}$ for a variety of airfoil series is presented in Figure A-6 using a reference chord-based Reynolds number of 8.3 million; the airfoil families are given in Table A-1.

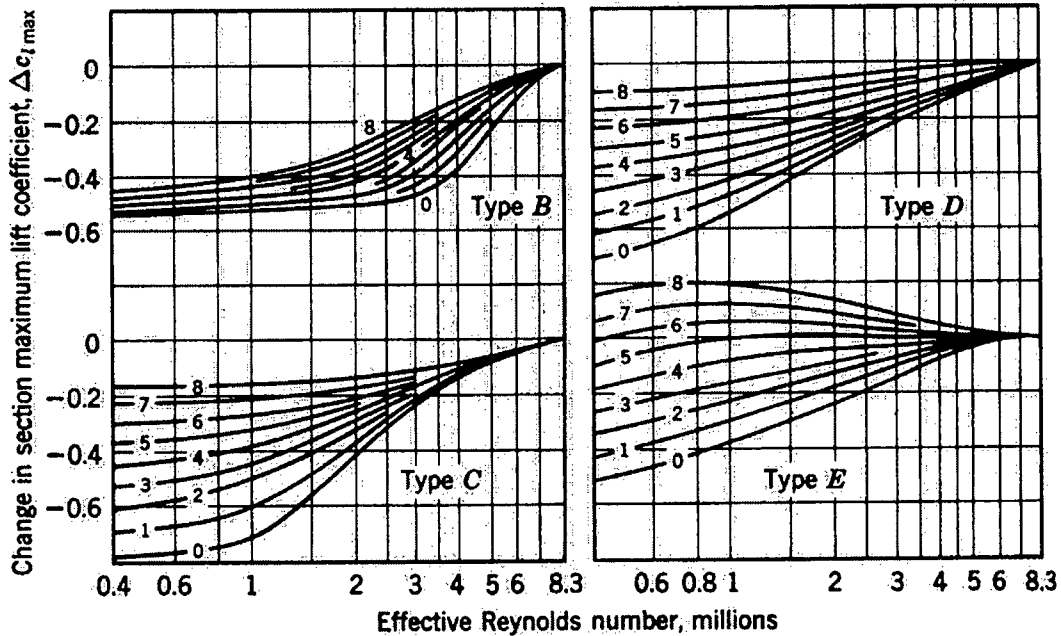


Figure A-6 Effect of Reynolds number on $C_{L,max}$ (Barlow et al., 1999)

Table A-1 Stall Types for Selected Airfoils

NACA Airfoil	Stall Type	NACA Airfoil	Stall Type
0006	A	4412	C4
0009	B0	4415	D4
0012	C0	4418	E4
0015	D0	4421	E5
0018	E0	23006	A
0021	E1	23009	C2
0025	E2	23012	D2
0030	-	23015	D2
2212	C3	23018	E2
2409	B2	23021	E2
2412	C2	43012	D4
2415	D2	43015	D4
2418	E2	43018	E4

Table A-1 Stall Types for Selected Airfoils (Continued)

NACA Airfoil	Stall Type	NACA Airfoil	Stall Type
4406	A6	63012	D6
4409	B4	63018	E7

For the NACA 0025 plane used on DOLPHIN, a best fit expression was added to curve *E2* in Figure A-6. The form of the best fit expression was

$$\Delta C_{L, max} \cong \begin{cases} 0 & \text{for } Re > 5.3 \text{ million} \\ -2.099 + 0.312 \log Re & \text{for } Re < 5.3 \text{ million} \end{cases} \quad (144)$$

and is shown compared to digitized data from Barlow et al. (1999) in Figure A-7.

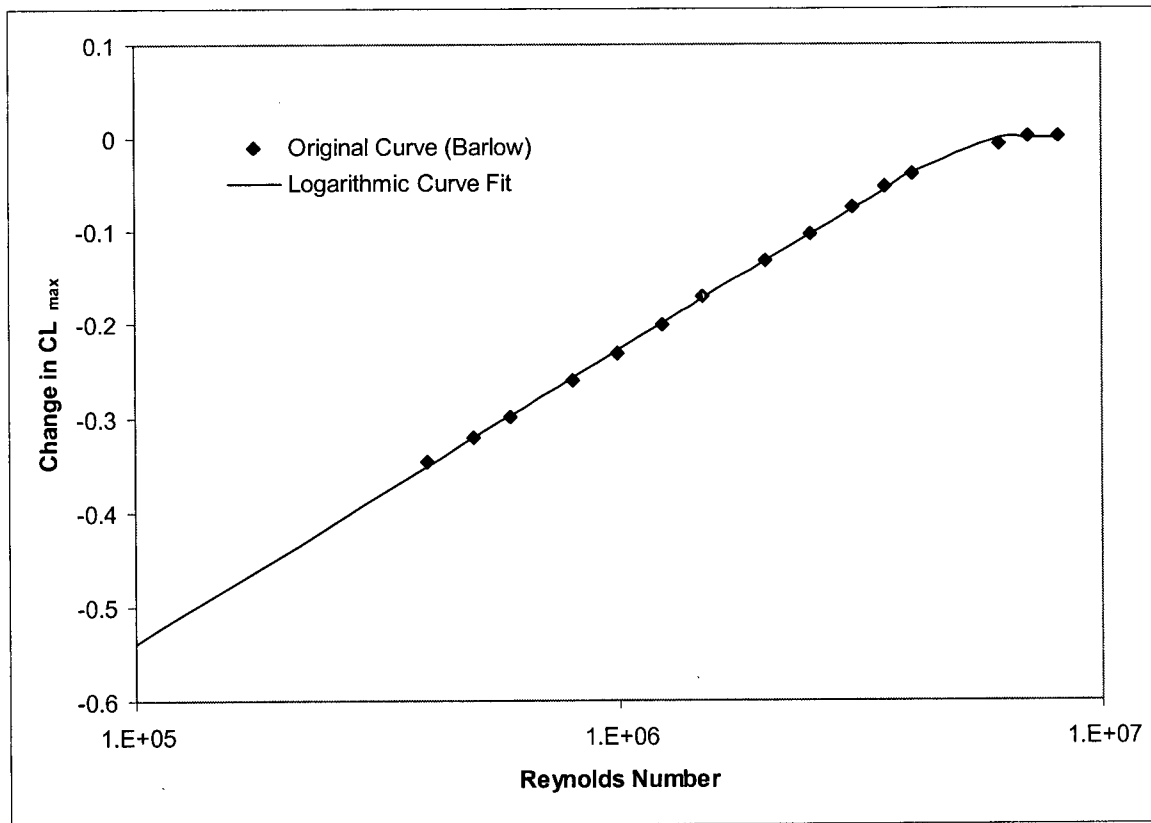


Figure A-7 Effect of Reynolds number on $\Delta C_{L, max}$ for NACA 0025 airfoil

A.4 Analytical Prediction of Yaw Influence on Bowplanes

An analytical analysis of the effect of the two hull vortices in yaw on the bowplanes was conducted. The objective was to determine if the increased lift curve slope and stall angle observed on the leeward planes could be attributed to the vortices. The vortex pattern observed in yaw was presented in Figure 2-12 on page 32 and is shown, in a slightly different form, in Figure A-8 below.

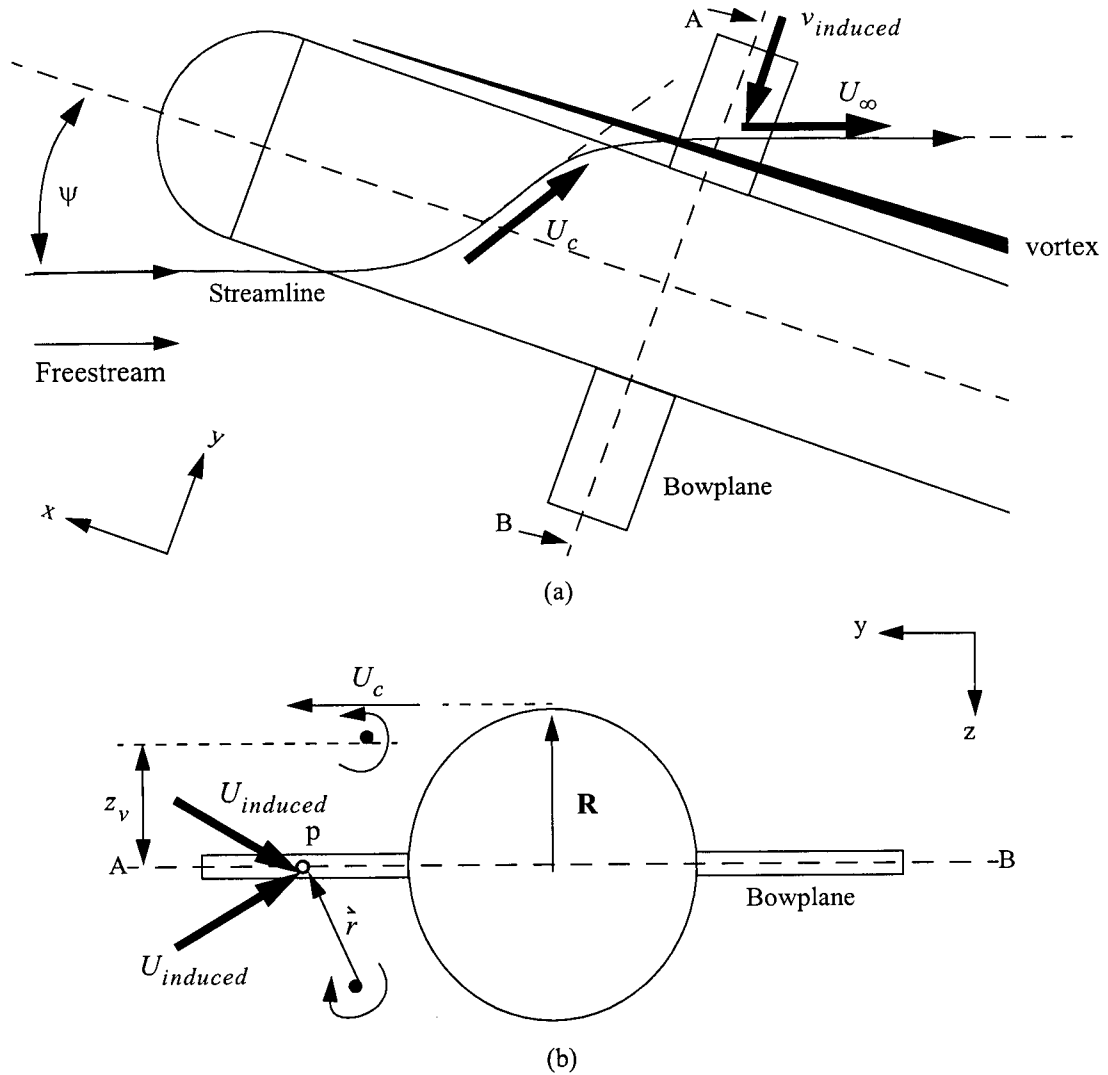


Figure A-8 Normalized bowplane lift curve slope dependence on yaw angle

In order to predict the effect of yaw on the bowplanes, the two hull vortices were idealized as line vortices as shown in part (b) of Figure A-8. For every point, p , along the bowplane span, each vortex induces a velocity of

$$v_{induced} = \frac{\Gamma}{2r} \tag{145}$$

where Γ is the vortex strength and the velocity is directed perpendicular to the vector, \vec{r} (that is, perpendicular to the line from the core of the vortex in question to point p). As the two hull vortices are symmetric about the x - y plane, the vertical components of the induced velocity cancel and the result is a net induced velocity along the plane span, as shown in Figure A-8 (a).

Using rough estimates of the strength and location of the hull vortices, the induced velocity across a leeward bowplane was predicted. The line vortices shown in Figure A-8 (b) were assumed to be located at the mean y and z positions as determined in Section 2.4.2. More specifically, these locations were $y/R = 0.99$ and $z/R = +/-0.38$ as measured with respect to the hull centreline axis.

As information was not otherwise available, a crude estimate of the strength of the vortices was made based on the cross-flow velocity over the cylindrical hull, U_c . From White (1991), the maximum velocity over a cylinder aligned normal to incoming flow is 1.6 times the freestream velocity. In an attempt to account for the hull yaw angle, the crossflow velocity was approximated as

$$U_c(\psi) \approx 1.6U_\infty \sin \psi \quad (146)$$

which correctly approaches $U_c/U_\infty = 1.6$ for $\psi = 90$ degrees and $U_c/U_\infty = 0$ for $\psi = 0$ degrees. A crude estimate of the vortex strength was then made assuming that the velocity in the vortex at an elevation equal to the top of the hull was equal to the crossflow velocity. That is, with reference to Figure A-8 (b),

$$\Gamma(\psi) \approx U_c(\psi)2\pi(R - z_v) = 1.6U_\infty \sin \psi 2\pi(R - z_v) \quad (147)$$

With the vortex locations and strength estimated, equation (145) was used to compute the induced velocity across the plane span. At each point, p , along the plane span, the net velocity, U_{plane} , and the flow angle with respect to the $-x$ -axis, ψ_{plane} , were computed (see Figure A-9). As noted by Hoerner (1939), lift force on a rectangular wing of low aspect ratio (that is, $a_e \approx 1$ to 5) are roughly proportional to the cosine of the yaw angle. Therefore, each element along the span was treated as an airfoil at a yaw angle of ψ_{plane} in a freestream flow with velocity U_{plane} . This is clearly an oversimplification as it ignores the effect of the hull on the flow over the plane.

For a given point, p , described by the vector, \vec{r} , the net induced velocity on the plane span is

$$v_{\text{induced}}(\psi) \approx 2 \frac{1.6U_\infty \sin \psi 2\pi(R - z_v) z_v}{2\pi \frac{|\vec{r}|}{|\vec{r}|}} = 3.2U_\infty \sin \psi (R - z_v) \frac{z_v}{|\vec{r}|^2} \quad (148)$$

This velocity is directed towards the body on the y -axis.

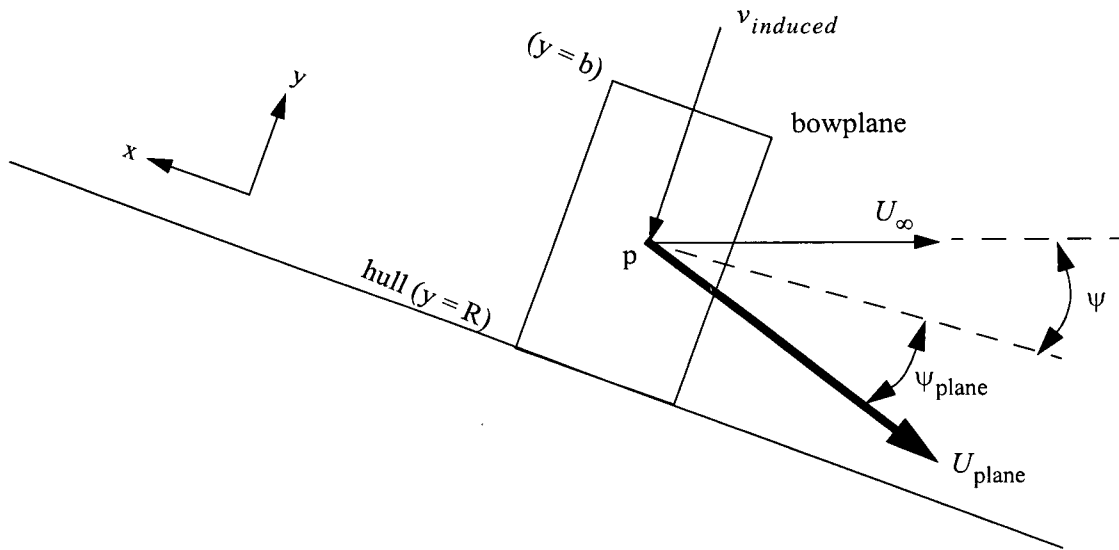


Figure A-9 Description of flow velocity components on the bowplane in yaw

A.5 Control Surface Interaction Potential Flow Model

A.5.1 Bowplane Tip Vortex Model

The vortex positions and orientations are shown schematically in Figure A-10 for the cross section at the forward plane location. The direction of flow is into the page and the vortex orientations are shown for positive z -force on the planes. By virtue of the symmetry about the z -axis, computations were only performed on the starboard plane (the left plane in Figure A-10). Further justification for the modelling of tip vortices is provided in Appendix A.1.

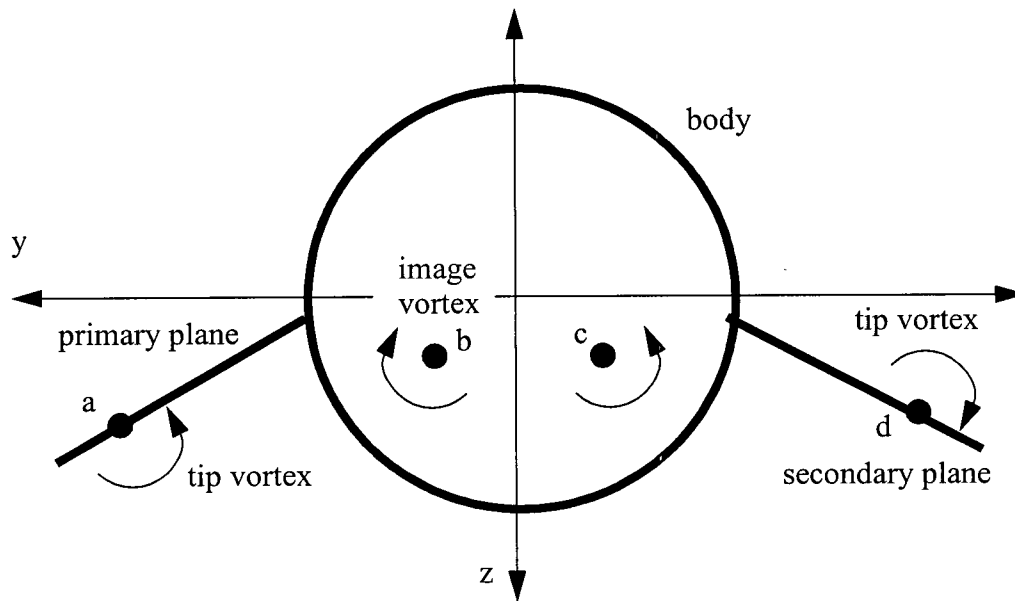


Figure A-10 Vortex system for forward planes (freestream flow into page)

Vortex Strength

Based on the Kutta-Joukowski lift theorem, the force generated by a plane of exposed span b_{exp} is

$$L = \Gamma U_{\infty} \rho b_{\text{exp}} \quad (149)$$

where L is the lift, Γ is the circulation, U_{∞} is the freestream flow velocity, and ρ is the fluid density. Replacing the lift by non-dimensional coefficient of lift,

$$C_L = \frac{L a_e}{\rho U_{\infty}^2 b_{\text{exp}}^2} \quad (150)$$

where $a_e = \frac{2b_{\text{exp}}}{C}$ is the aspect ratio, the circulation is given by

$$\Gamma = \frac{C_L U_\infty b_{\text{exp}}}{a_e} \quad (151)$$

After some initial transient behavior, tip vortices form and have the same strength as the circulation given in equation (151). As noted by Lloyd (1974), since the lifting surfaces are of low aspect ratio, the contributions of the bound vortices can be neglected. The strength of the image vortices is the same as the respective tip vortices but the direction of rotation is opposite. In the current work, measured fore plane coefficient of lift data was used. If not available, a suitable semi-empirical approximation for the lift curve slope was proposed by Whicker and Fehlner (1958):

$$\frac{dC_L}{d\varepsilon} = \frac{1.8\pi a}{1.8 + \cos\Omega \sqrt{4 + \frac{a^2}{\cos^4\Omega}}} \quad (152)$$

where Ω is the plane sweep angle.

Vortex Locations

The span-wise position of the forward plane tip vortices were determined from helium bubble path flow visualization experiments. After an initial transient, the vortex positions were typically inward from the tip by about 5% of the plane span. The position of the two image vortices was determined position of the tip vortices in conjunction with the wall boundary condition of the body. The position of each image vortex, \vec{r}_{vi} , in terms of the associated tip vortex, \vec{r}_v , is

$$\vec{r}_{vi} = \frac{R_h^2}{|\vec{r}_v|^2} \vec{r}_v \quad (153)$$

where R_h is the hull radius and positions in the y-z plane are measured from the centre of the hull to the vortex cores.

Tip Vortex Path

The tangential velocity component \vec{v}_{ij} introduced to point i by a vortex j is given by:

$$\vec{v}_{ij} = \frac{\vec{\Gamma}_j \times \vec{r}_{ji}}{2\pi |\vec{r}_{ji}|^2} \quad (154)$$

where \times represents the vector cross product, $\vec{\Gamma}_j$ is the circulation of vortex j along in the x-direction, and \vec{r}_{ji} is the position vector in the y-z plane from vortex j to the point i . Using

equation (154), it is possible to express the tangential velocity component in terms of the measured coefficient of lift from the planes:

$$\vec{v}_{ij} = \frac{C_L U_\infty s}{2\pi a} \cdot \frac{\hat{e}_1 \times \vec{r}_{ji}}{|\vec{r}_{ji}|^2} \quad (155)$$

The unit vector in the x-direction, \hat{e}_1 , has been included in this case to complete the vector cross product. Figure A-11 shows the vortex system and the resulting velocity components from vortices b , c , and d onto point a (corresponding to the starboard tip vortex core). The vortex core at point a has a resulting velocity component, \vec{v}_i in the y-z plane equal to the vector sum of the three velocities \vec{v}_{id} , \vec{v}_{ib} and \vec{v}_{ic} . The angle of the resulting y-z plane velocity vector, ϕ , is measured about point i starting from the positive y-direction as shown.

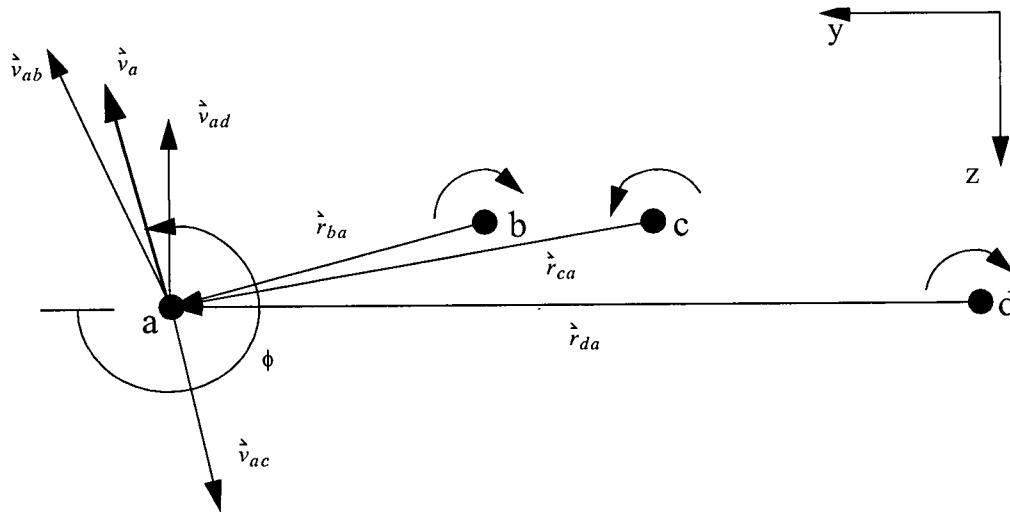


Figure A-11 Vortex system for forward planes (freestream flow into page)

Using the small angle approximation, the angle formed by the vortex to the direction of freestream flow is:

$$\gamma \cong \frac{|v_a|}{U_\infty} \quad (156)$$

which for the complete system becomes

$$\gamma \cong \left| \frac{b_{\text{exp}}}{2\pi a_e} \cdot \sum_{j=b}^u \frac{C_{Lj} \hat{e}_1 \times \vec{r}_{ja}}{|\vec{r}_{ja}|^2} \right| \quad (157)$$

A.5.2 Bowplane Vortex Interaction with Sternplanes

As a first order approximation, the position in the y - z plane of the starboard forward tip vortex at the longitudinal position of the aftward plane is given by

$$\vec{r}_{a(aft)} \cong \vec{r}_{a(fore)} + \gamma\chi[\cos\phi \cdot \hat{e}_2 + \sin\phi \cdot \hat{e}_3] \quad (158)$$

where χ is the distance along the x -axis from the forward to aft planes and \hat{e}_2 and \hat{e}_3 are unit vectors along the y - and z -axes respectively. In the general case, the downstream position of the port tip vortex is found in the same manner; however, port-starboard symmetry can be applied in most situations.

Flow Angle on Aft planes

Using the position of the forward plane tip vortices computed from the first order approximation above, the positions of the two image vortices for the aft portion of the body are computed. The same method is used as outlined above except in this case, the centre of the tail is allowed to deviate from the y - z plane origin by a displacement \vec{r}_t as shown in Figure A-12. The tail cross section is assumed circular with a radius of R_t and the image vortex locations are determined by:

$$\vec{r}_{vi} = \left(\frac{R_t}{|\vec{r}_v|} \right)^2 \vec{r}_v - \vec{r}_t \quad (159)$$

The induced tangential velocity components of the two tip and two image vortices were computed for a point p , at a relative span-wise position of ζ , on the aft plane. Figure A-12 shows the geometric conventions using the starboard side of the tail; although not shown in the figure, the tip and image vortices from the port side are also included in the computation. The resulting flow velocity in the y - z plane at point p is denoted by \vec{v}_p and computed by the vector sum of the velocities

\vec{v}_{pa} , \vec{v}_{pb} , \vec{v}_{pc} and \vec{v}_{pd} . To account for aft plane anhedral angles different from zero ($\alpha \neq 0$), dot product is applied between the net flow velocity and the aft plane normal vector, \hat{n} .

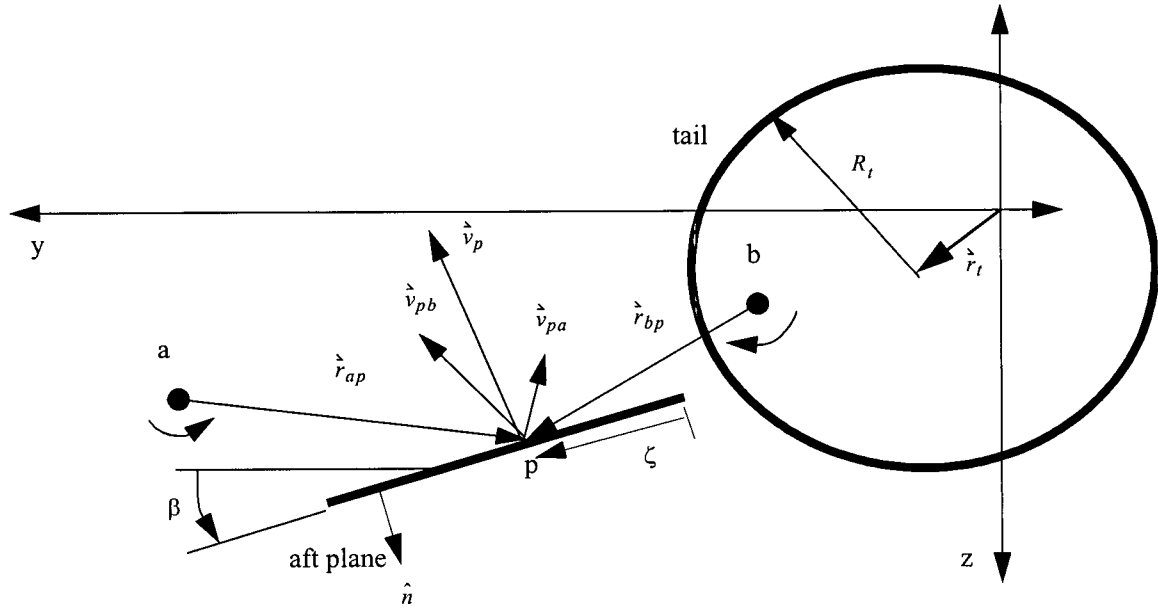


Figure A-12 Starboard side vortex system at aft plane (freestream flow into page)

The above calculations are applied along the entire aft plane span, for values of ζ from 0 to the span length. Note that the plane does not necessarily originate from the body, as shown in Figure A-12. The incident flow angle to each point along the span is approximated by

$$\gamma_p \cong \frac{\vec{v}_p \cdot \hat{n}}{U_\infty} \quad (160)$$

The force on the plane is computed using the known lift curve slope from previous experiments. Alternatively, the semi-empirical lift curve slope approximation by Whicker and Fehlner given in Section 2.4.1 on page 27 could be used. The normal force elements are integrated along the entire plane span to give the total force on the plane.

APPENDIX B - DOLPHIN SCALE MODEL DETAILS

B.1 Scale Model Engineering Drawings

Table B-1 Scale model component list

Number	Description (drawing name)
Figure B-1	Model assembly (ISE98-0011)
Figure B-2	Fore hull section (ISE98-0001)
Figure B-3	Hull nose (ISE98-0002)
Figure B-4	Mid-hull section (ISE98-0003 sheet 1 of 2)
Figure B-5	Mid-hull section (ISE98-0003 sheet 2 of 2)
Figure B-6	Aft hull section (ISE98-0007)
Figure B-7	Tail section (ISE98-0005)
Figure B-8	Mast connection (dorsal) (ISE98-0004)
Figure B-9	Mast tube (ISE98-0010)
Figure B-10	Mast assembly (ISE98-0012)
Figure B-11	Strain gauge assembly to mast (ISE98-0021)
Figure B-12	Mast fairing assembly (ISE98-0023)
Figure B-13	Keel assembly (ISE98-0026)
Figure B-14	Sternplane deflection control assembly (ISE98-0018)
Figure B-15	Sternplane deflection control lead screw nut (ISE98-0015)
Figure B-16	Sternplane deflection control arm components (ISE98-0013)
Figure B-17	Sternplane deflection control motor casing (ISE98-0019)
Figure B-18	Bowplane stepper motor connector (ISE98-0014)
Figure B-19	Bowplane load cell shaft (ISE98-LC-1)
Figure B-20	Sternplane load cell shaft (ISE98-LC-2)
Figure B-21	Load cell sleeve (ISE98-LC-3)
Figure B-22	Load cell sub-assembly (ISE98-LC-5)
Figure B-23	Bowplane load cell strain gauge installation (ISE98-LC-7)
Figure B-24	Sternplane load cell shaft (ISE98-LC-8)
Figure B-25	Bowplane load cell assembly (ISE98-LC-10)
Figure B-26	Sternplane hull insert (ISE98-LC-6)
Figure B-27	Force balance setup in wind tunnel (ISE98-B-1)
Figure B-28	Force balance assembly (ISE98-B-2)
Figure B-29	Force balance beam (ISE98-B-3)
Figure B-30	Balance pitch mechanism load bearing pin (ISE98-B-4)
Figure B-31	Balance pitch mechanism adjustment rod (ISE98-B-7)
Figure B-32	Main balance beam assembly (ISE98-B-12)

Table B-1 Scale model component list (Continued)

Number	Description (drawing name)
Figure B-33	Balance beam clamp for mast (ISE98-B-13)
Figure B-34	Force balance beam strain gauge installation (ISE98-B-14)
Figure B-35	Power and instrumentation wiring diagram (ISE98-E-1)

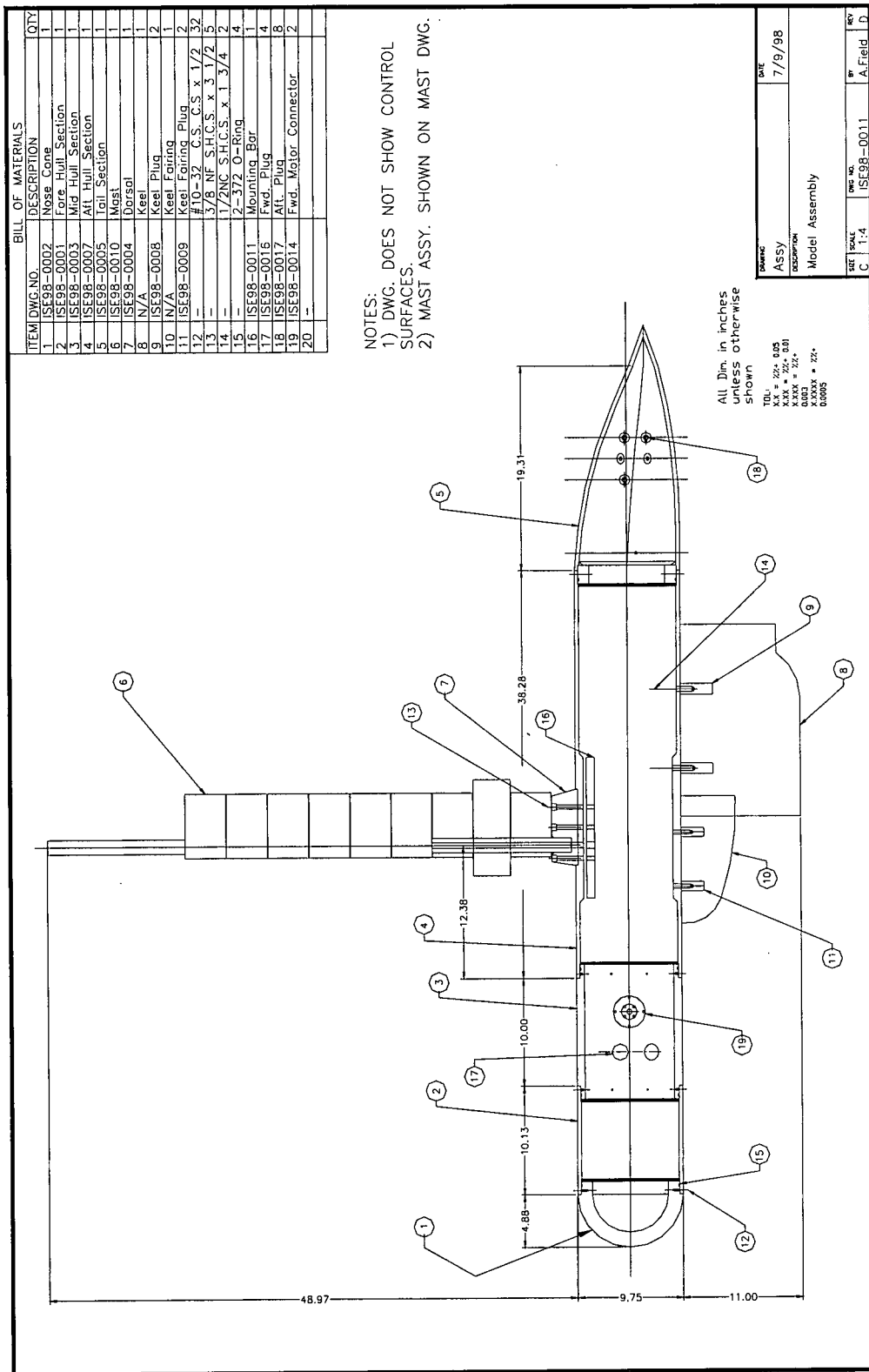


Figure B-1 Model assembly (ISE98-0011)

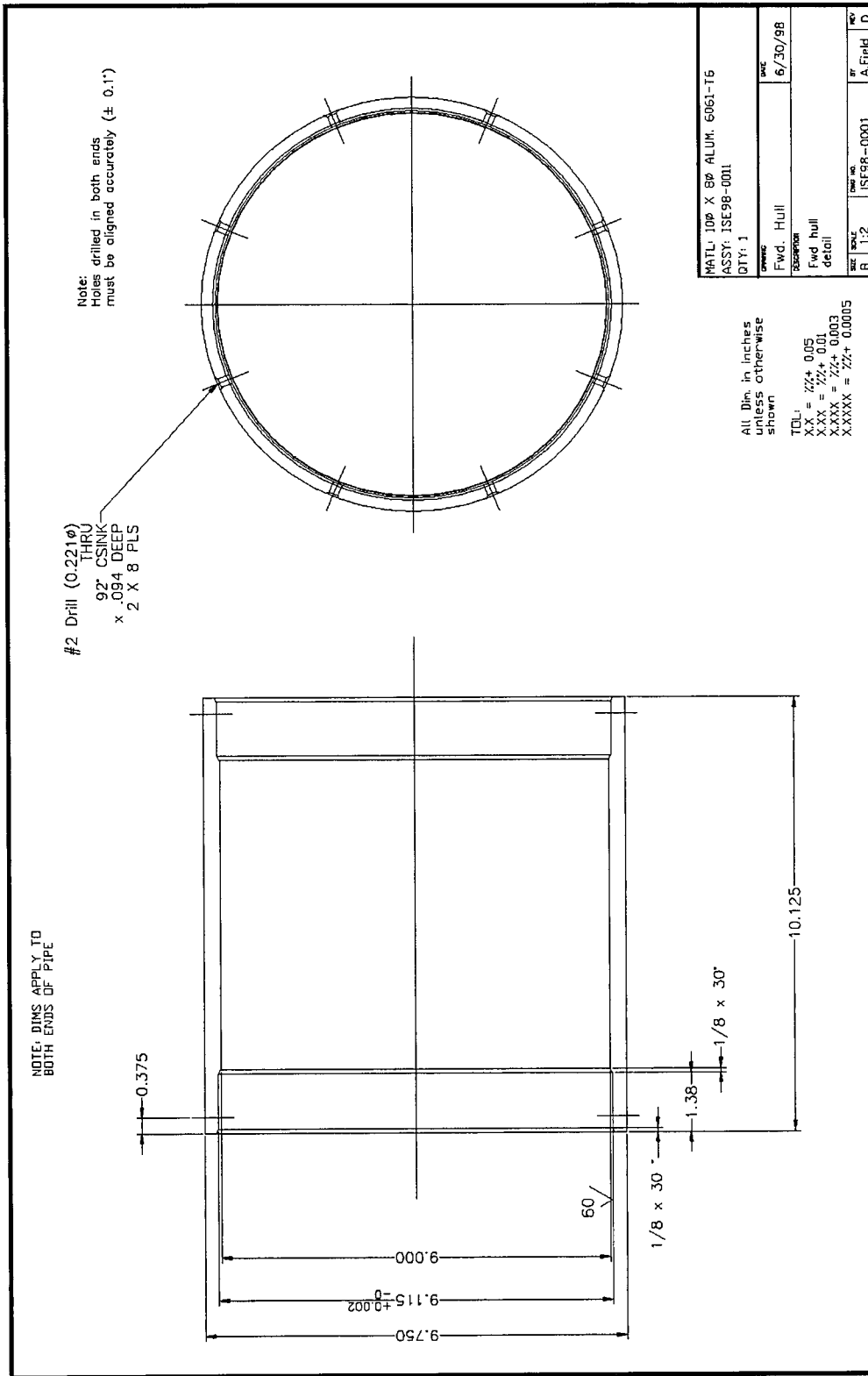


Figure B-2 Fore hull section (ISE98-0001)

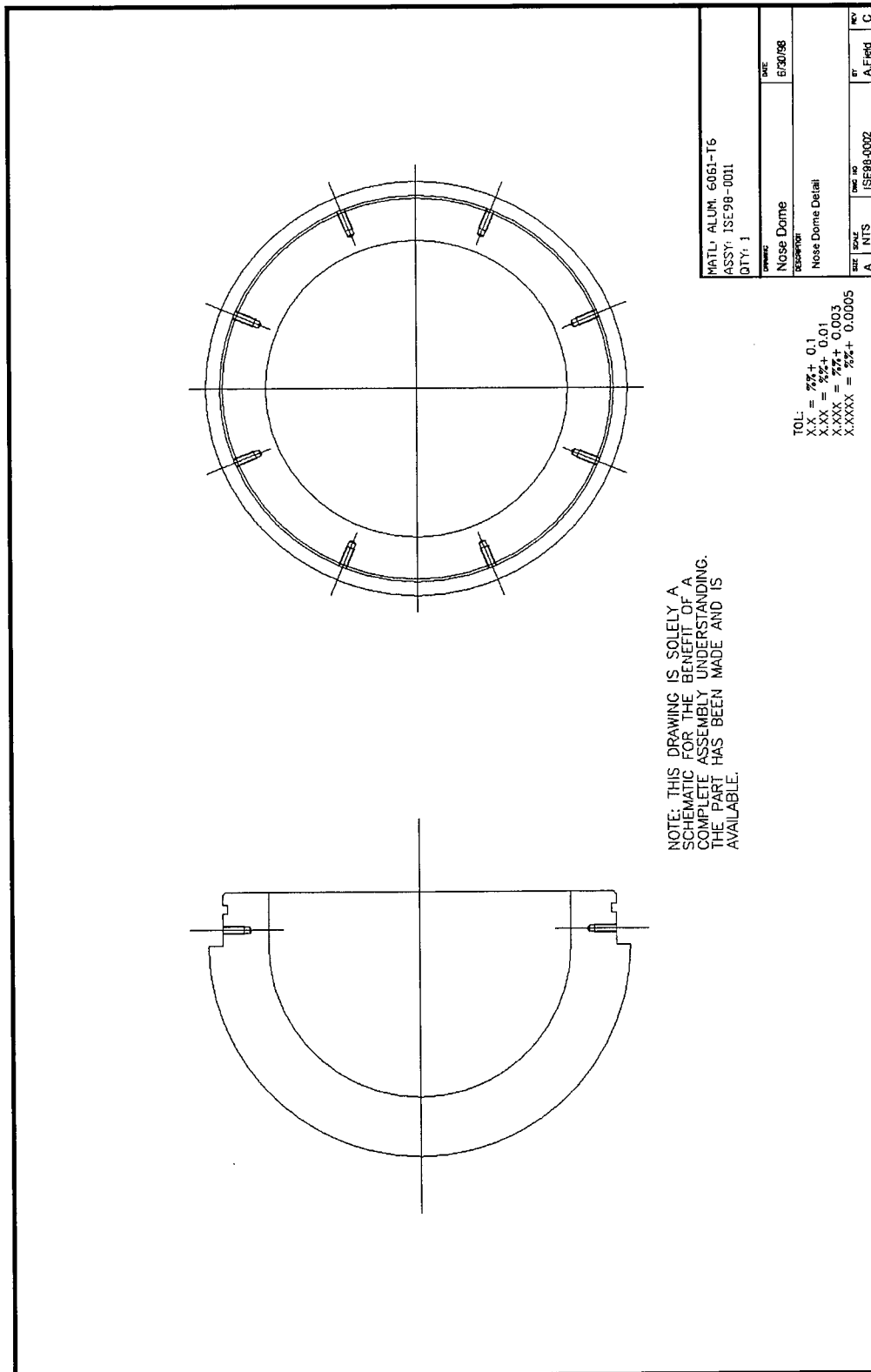


Figure B-3 Hull nose (ISE98-0002)

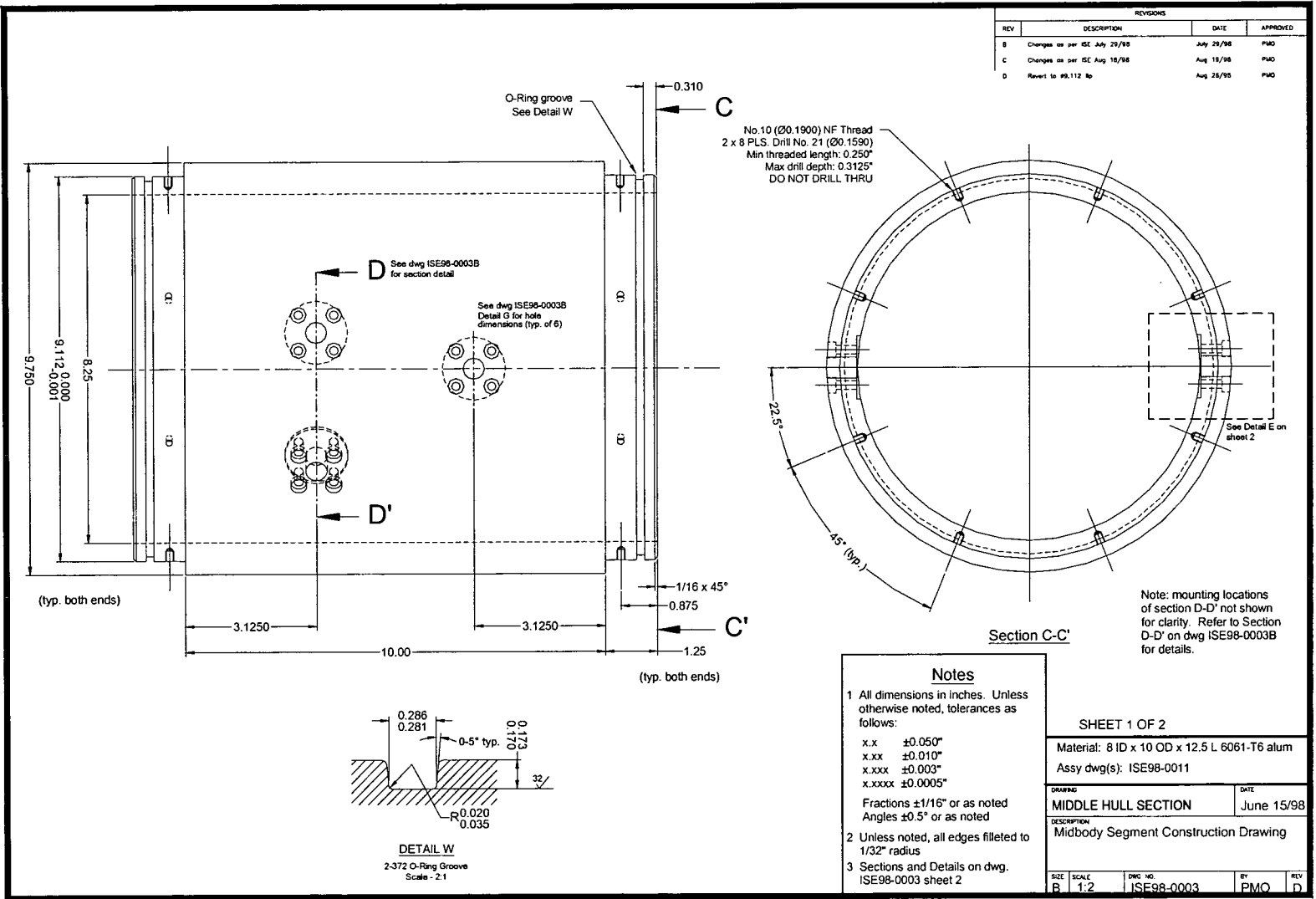


Figure B-4 Mid-hull section (ISE98-0003 sheet 1 of 2)

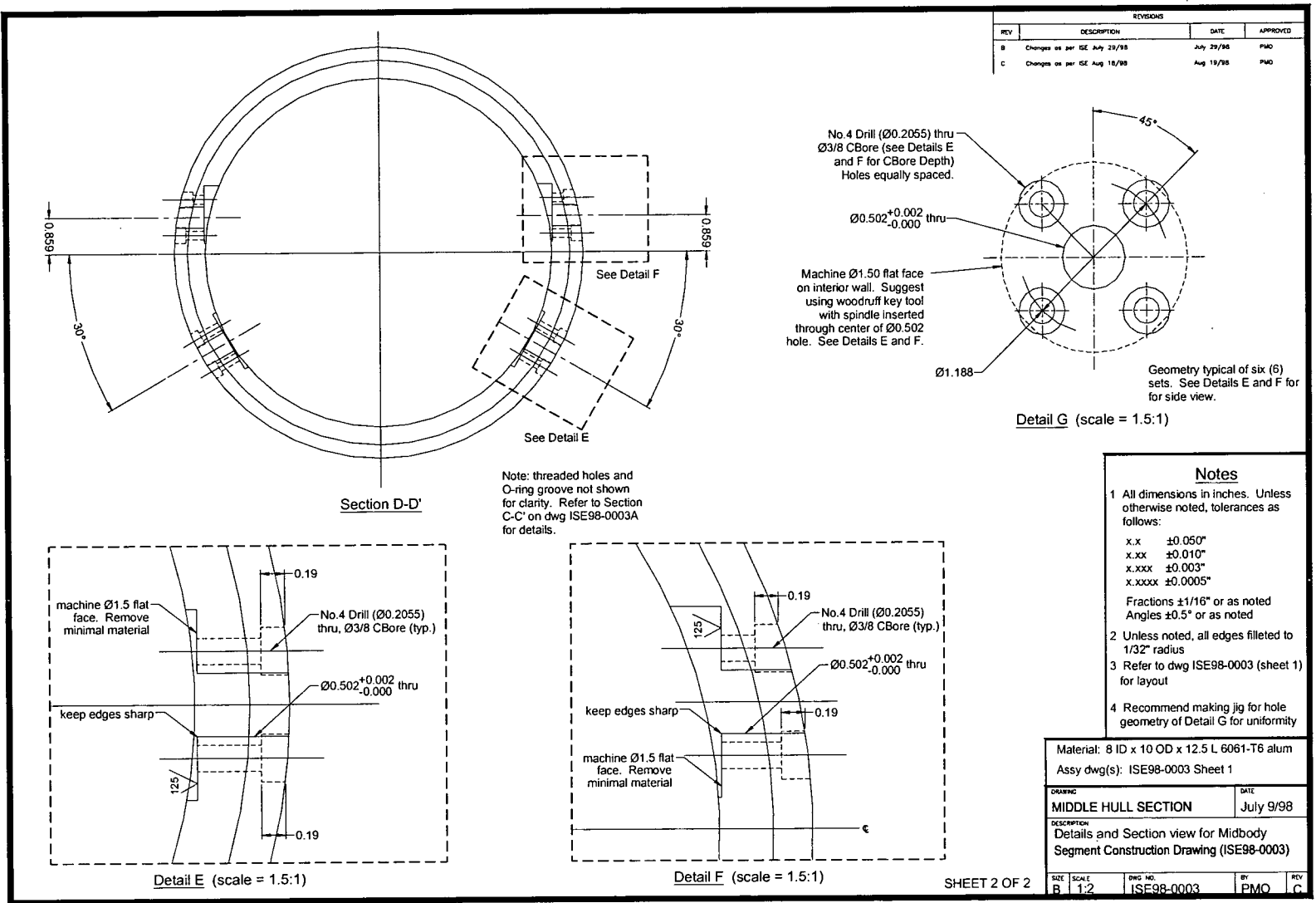


Figure B-5 Mid-hull section (ISE98-0003 sheet 2 of 2)

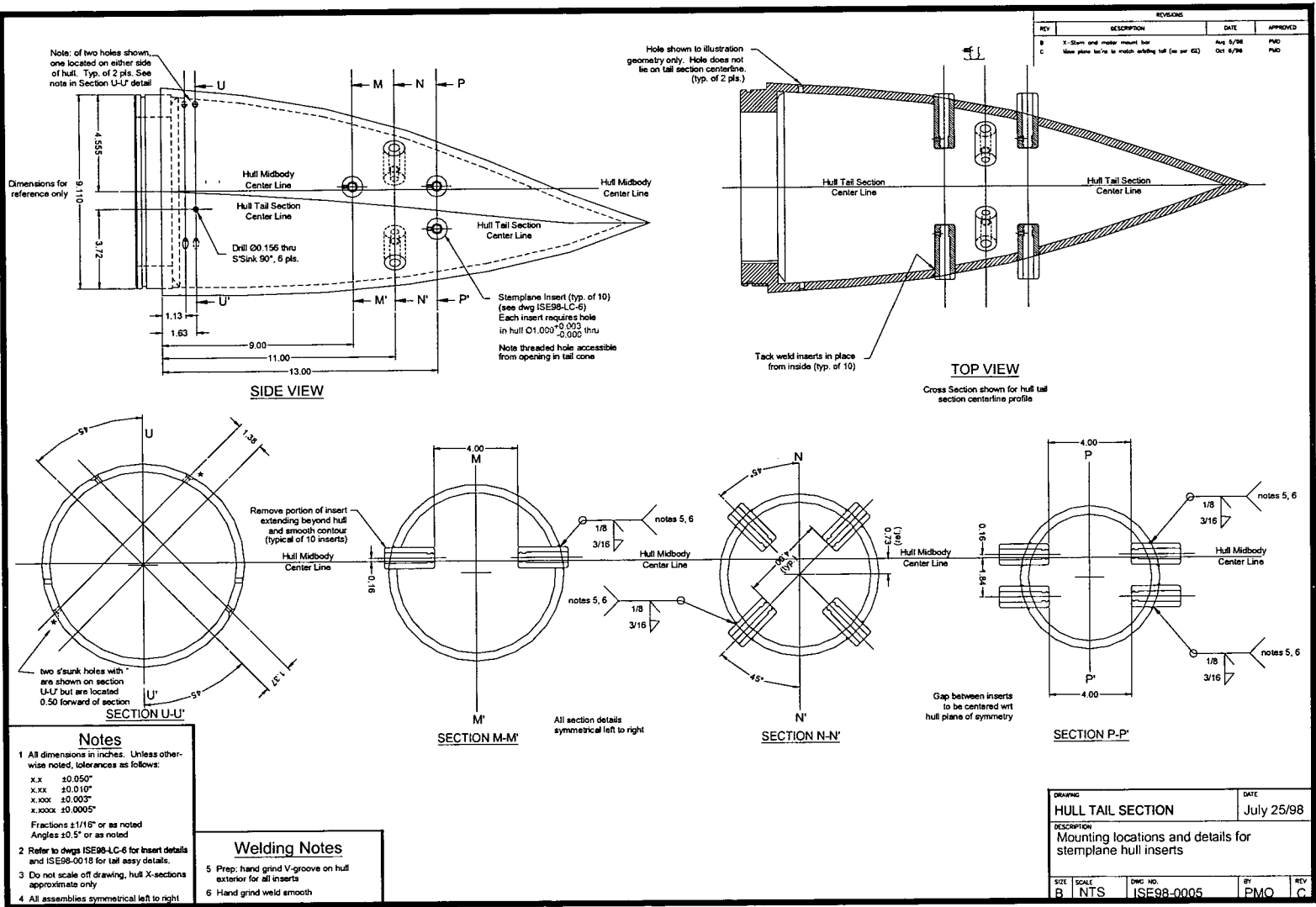


Figure B-7 Tail section (ISE98-0005)

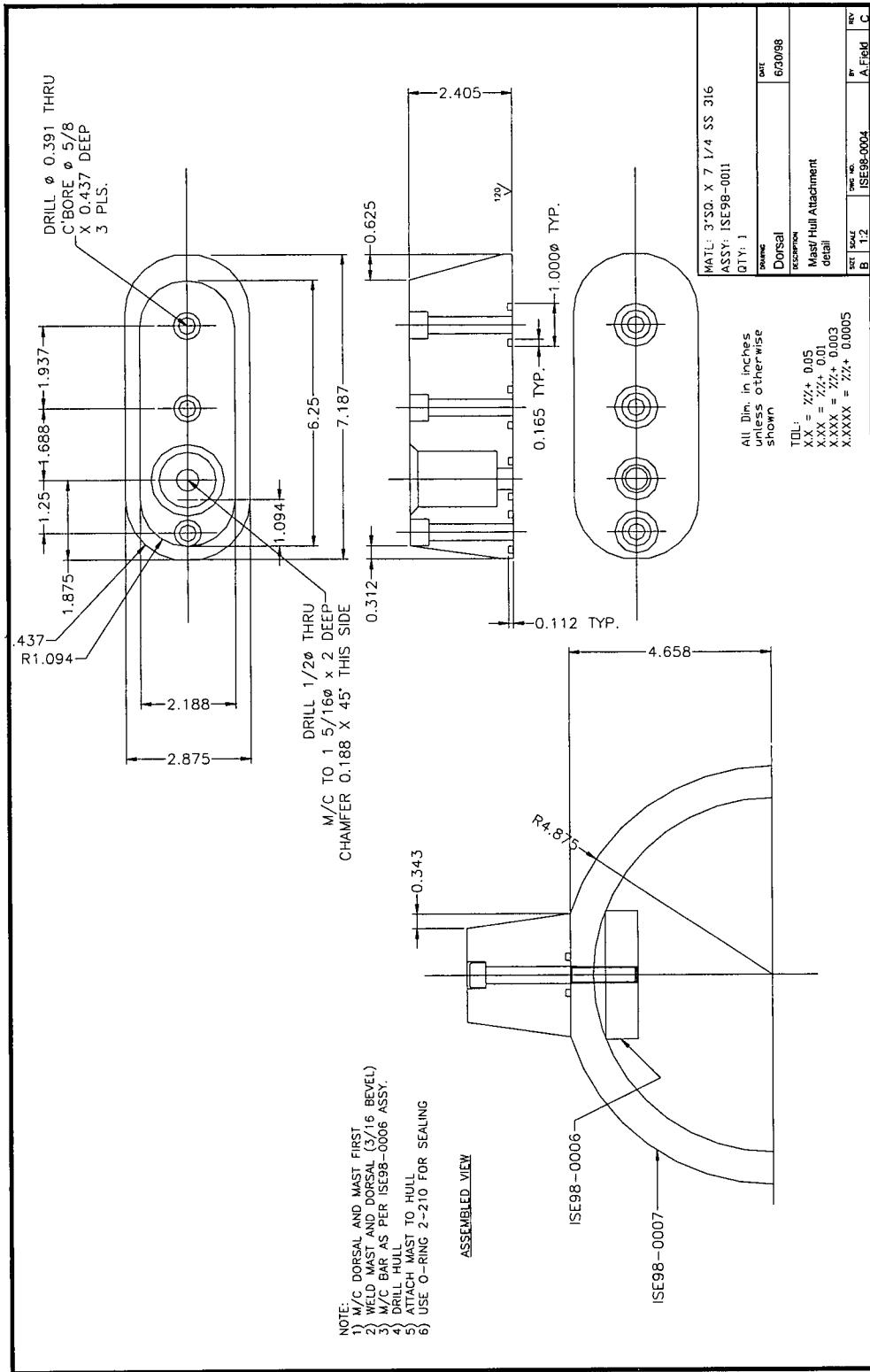


Figure B-8 Mast connection (dorsal) (ISE98-0004)

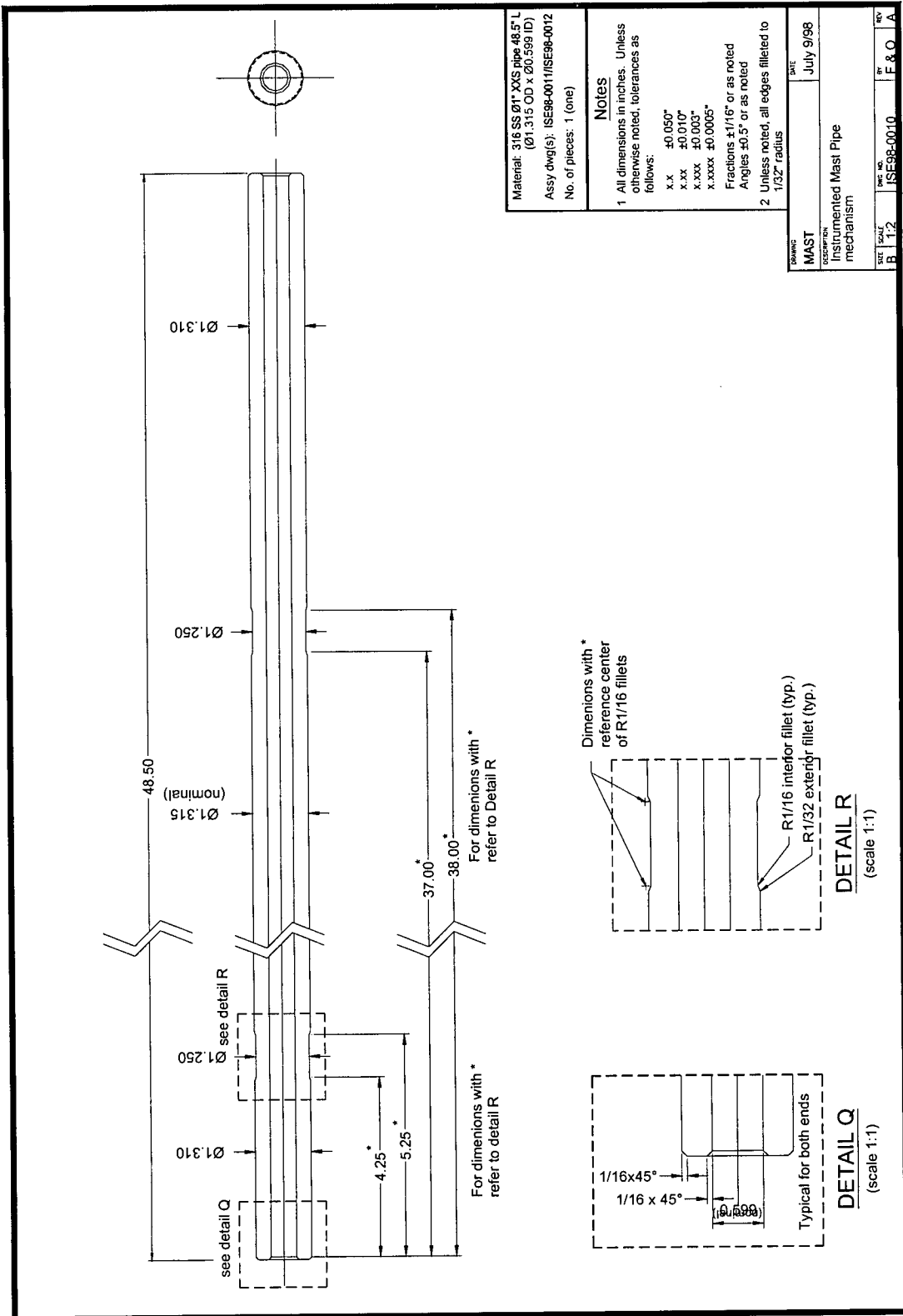


Figure B-9 Mast tube (ISE98-0010)

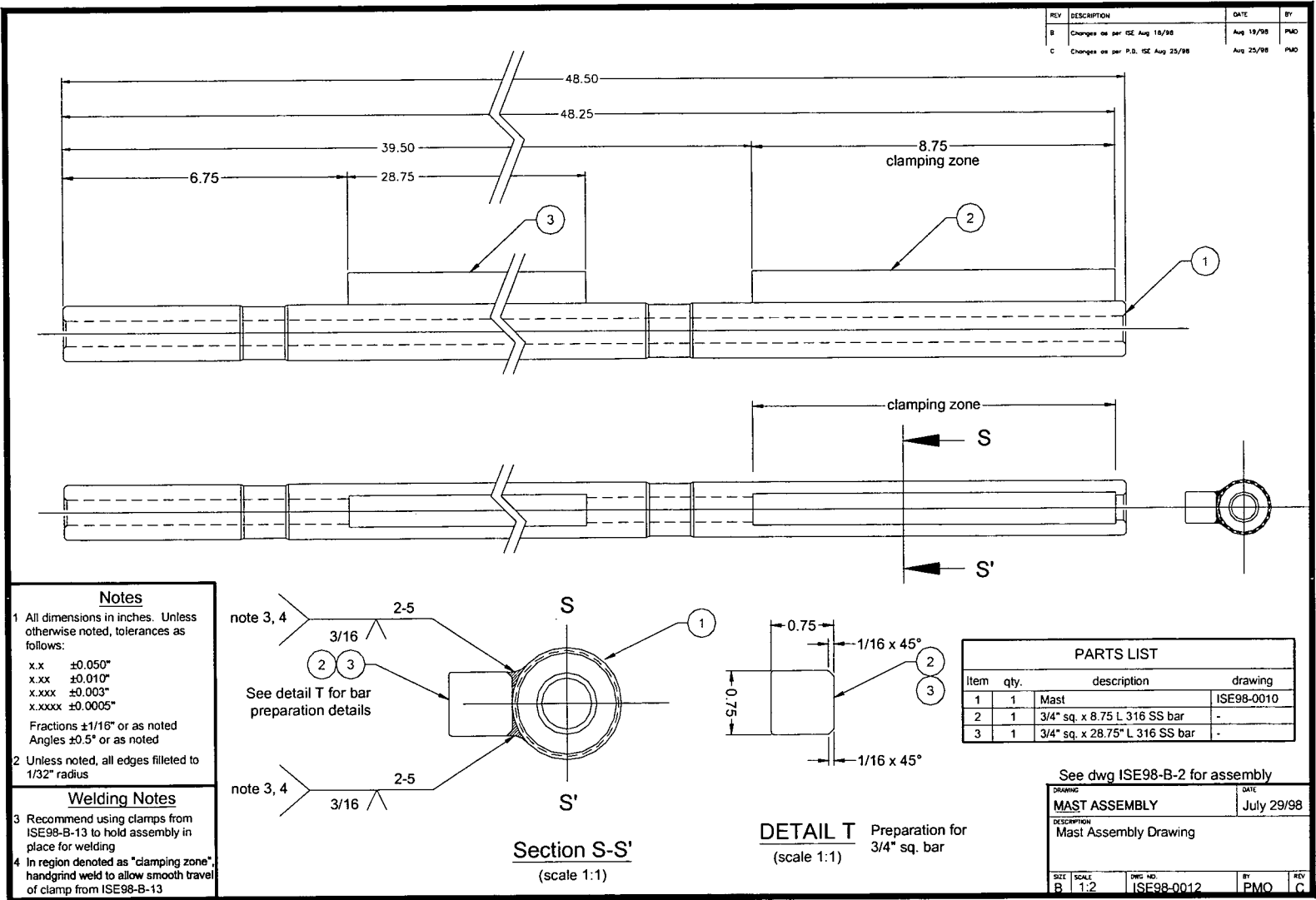


Figure B-10 Mast assembly (ISE98-0012)

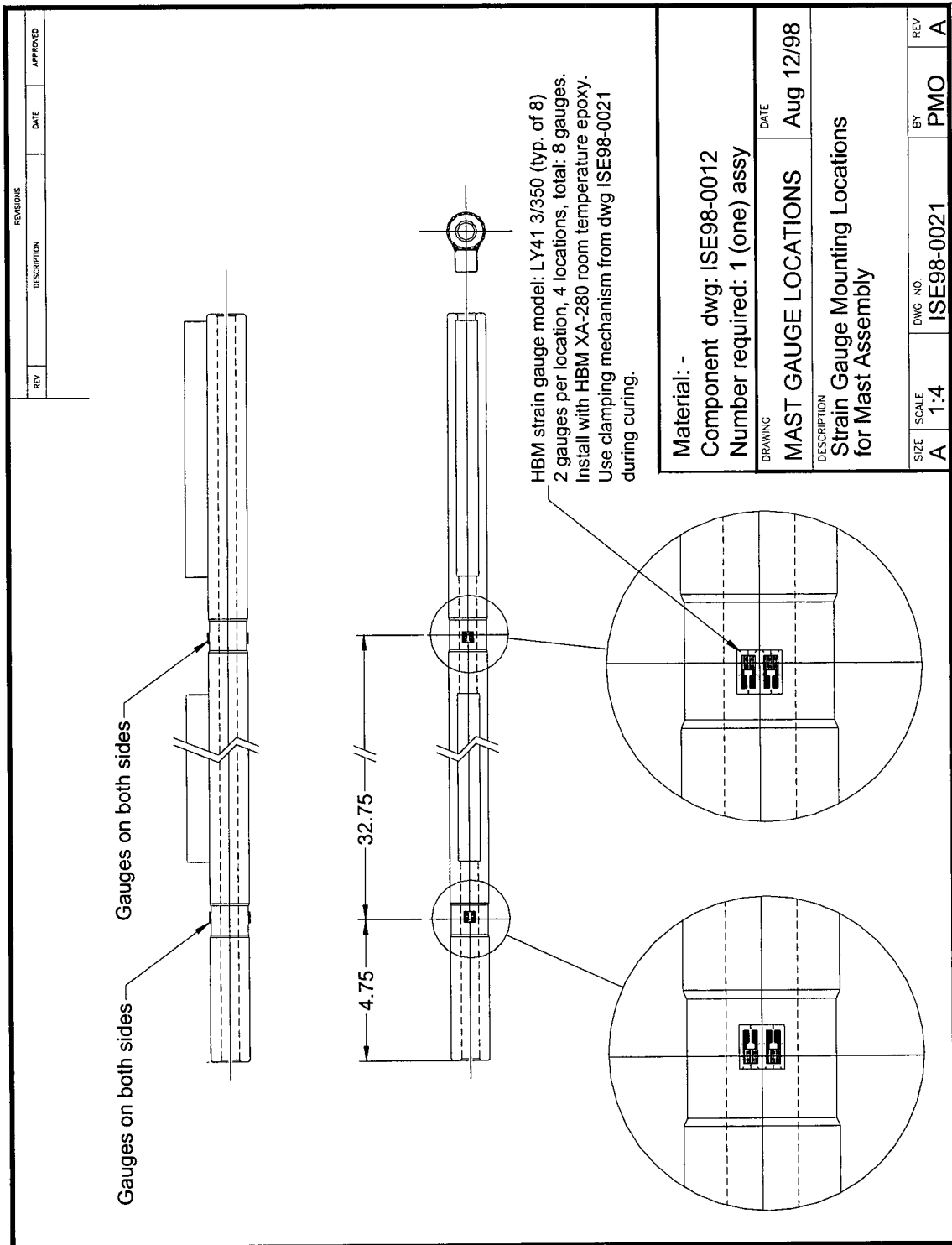


Figure B-11 Strain gauge assembly to mast (ISE98-0021)

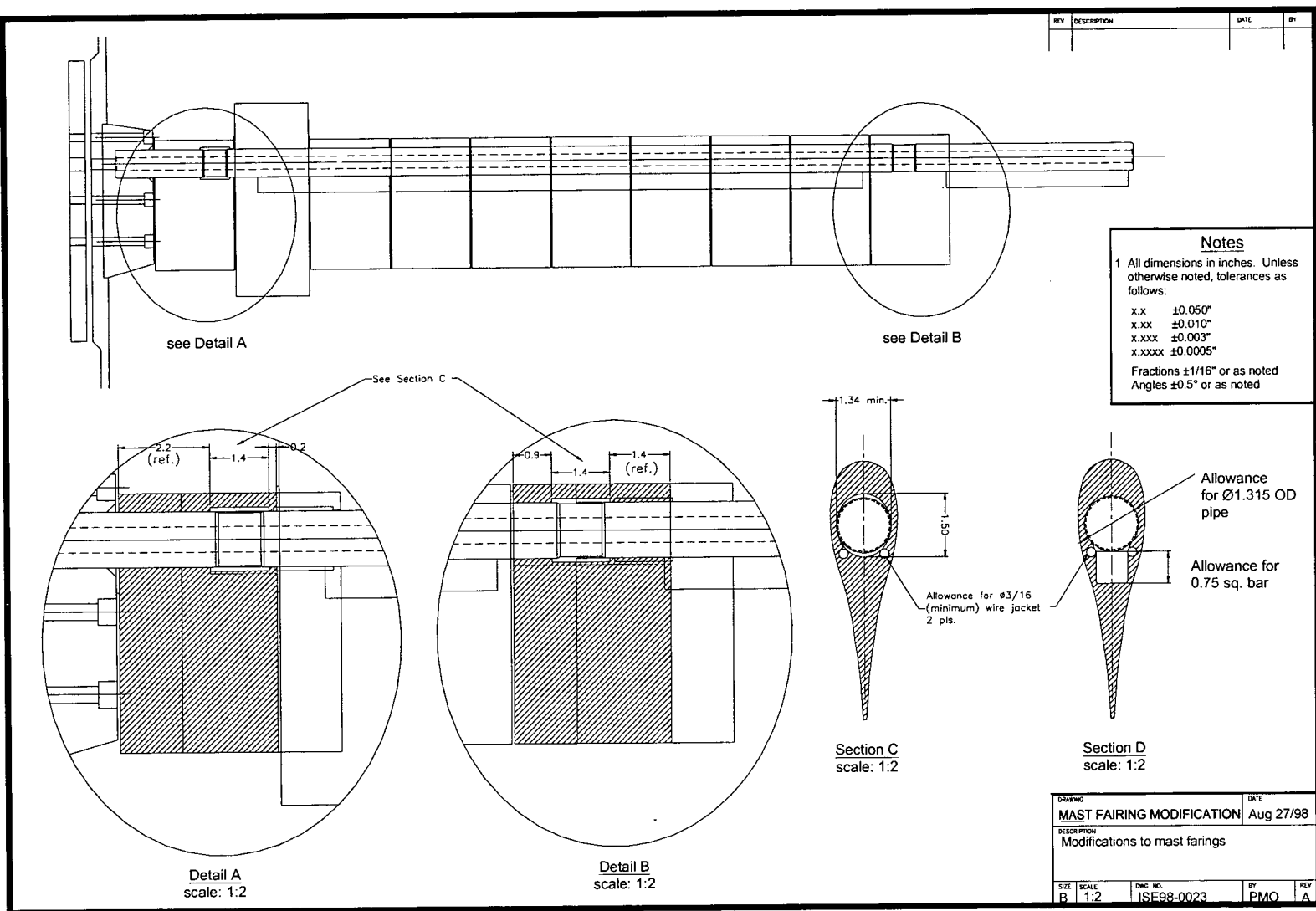


Figure B-12 Mast fairing assembly (ISE98-0023)

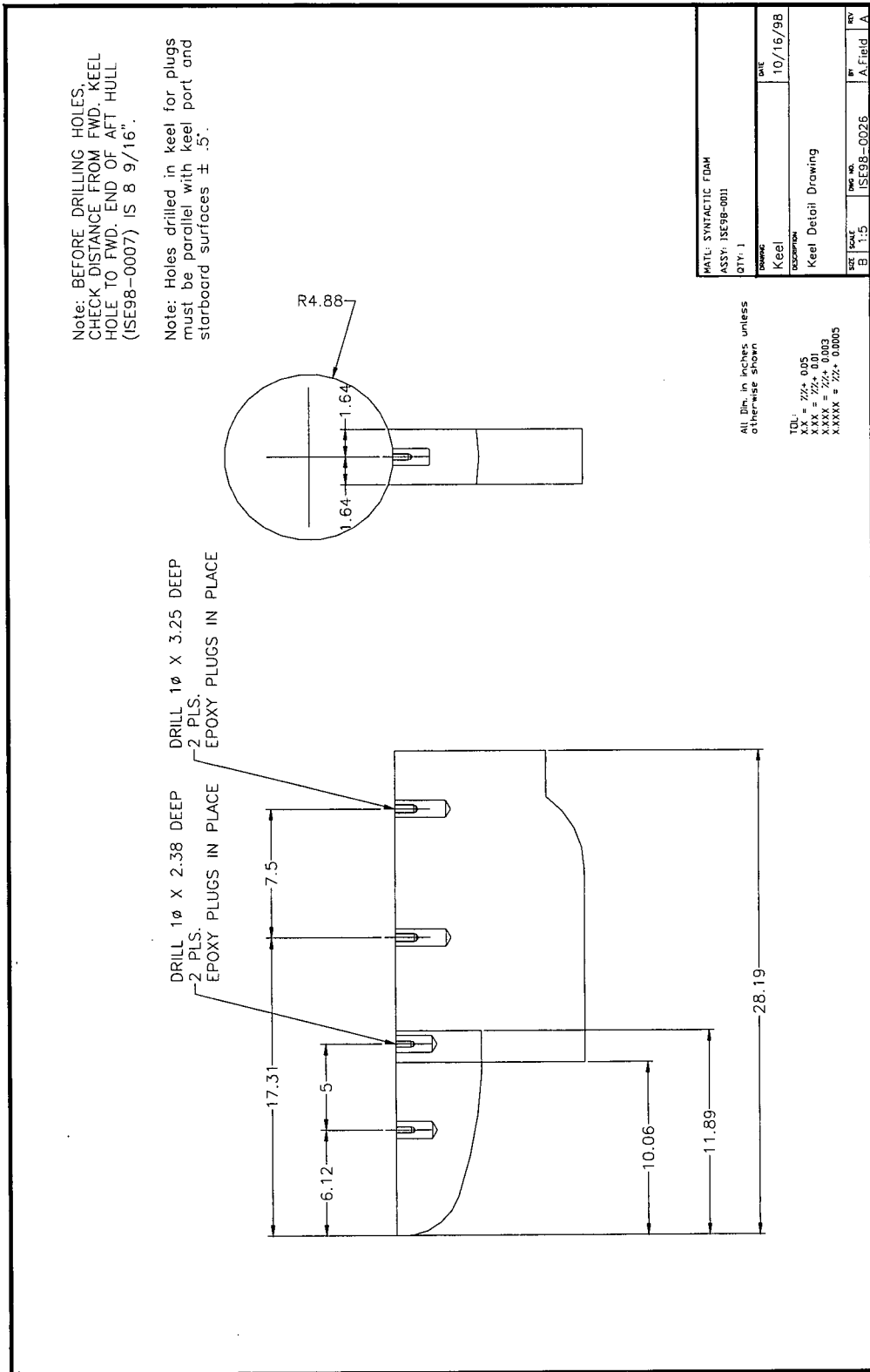


Figure B-13 Keel assembly (ISE98-0026)

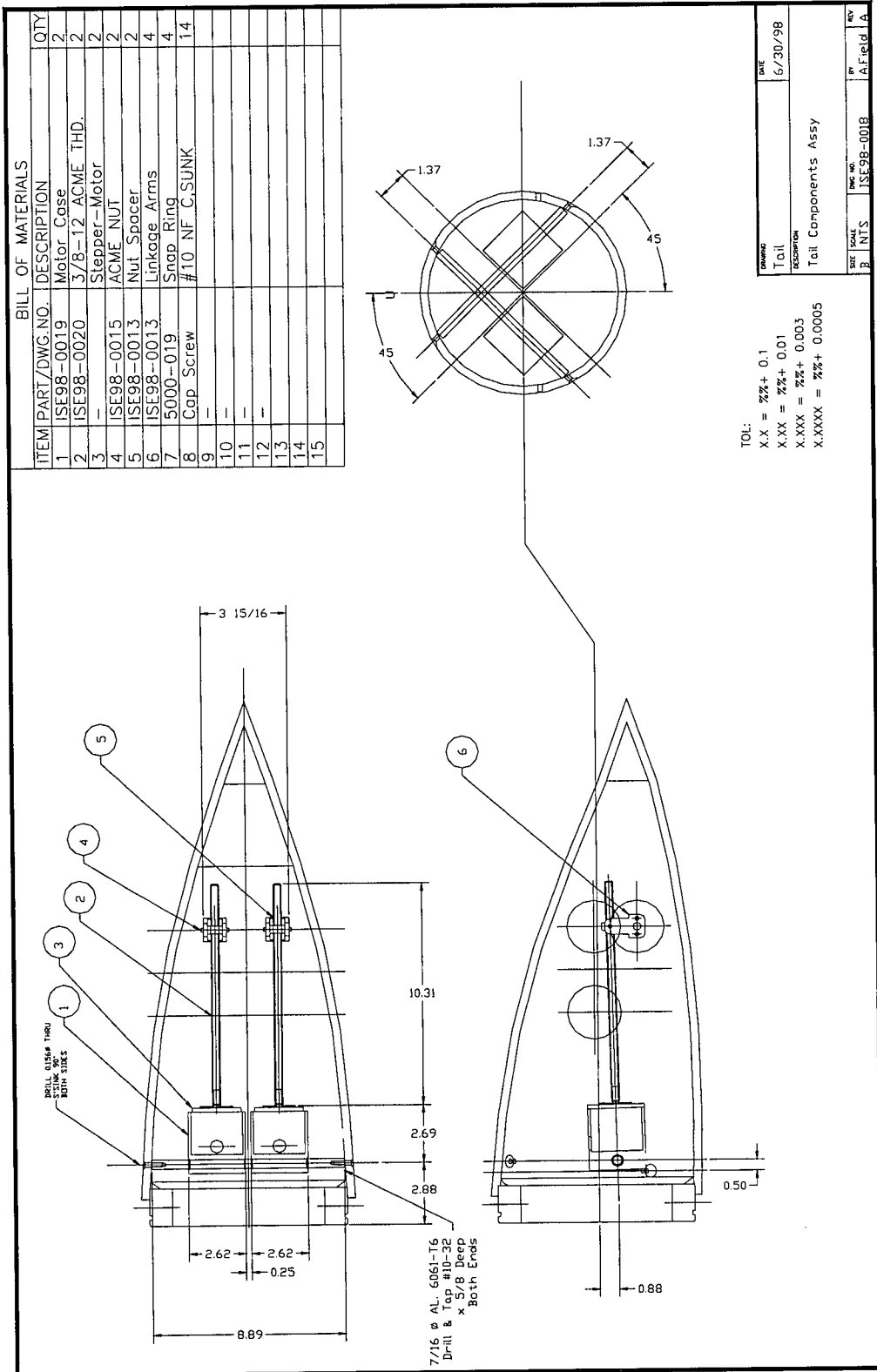


Figure B-14 Stemplane deflection control assembly (ISE98-0018)

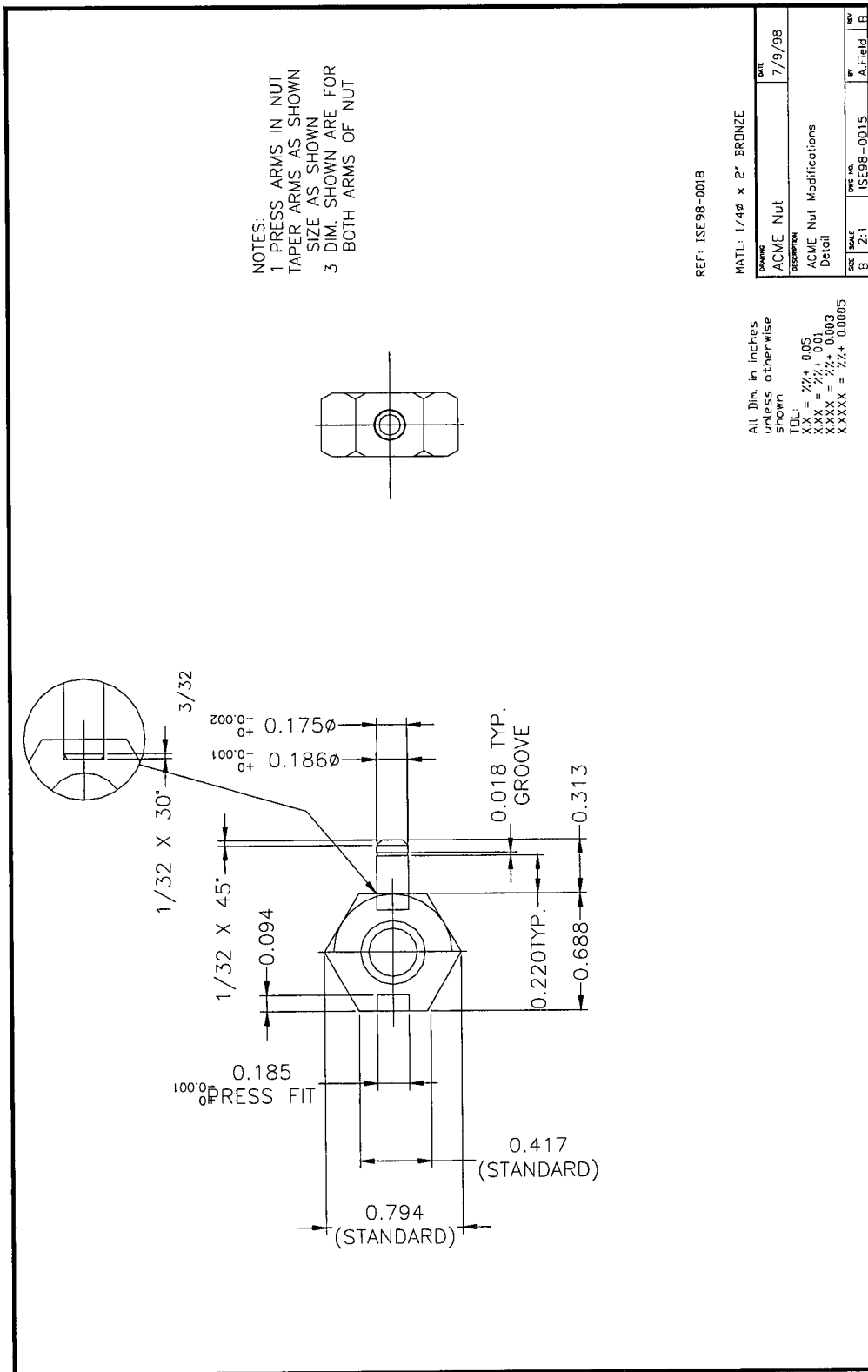


Figure B-15 Sternplane deflection control lead screw nut (ISE98-0015)

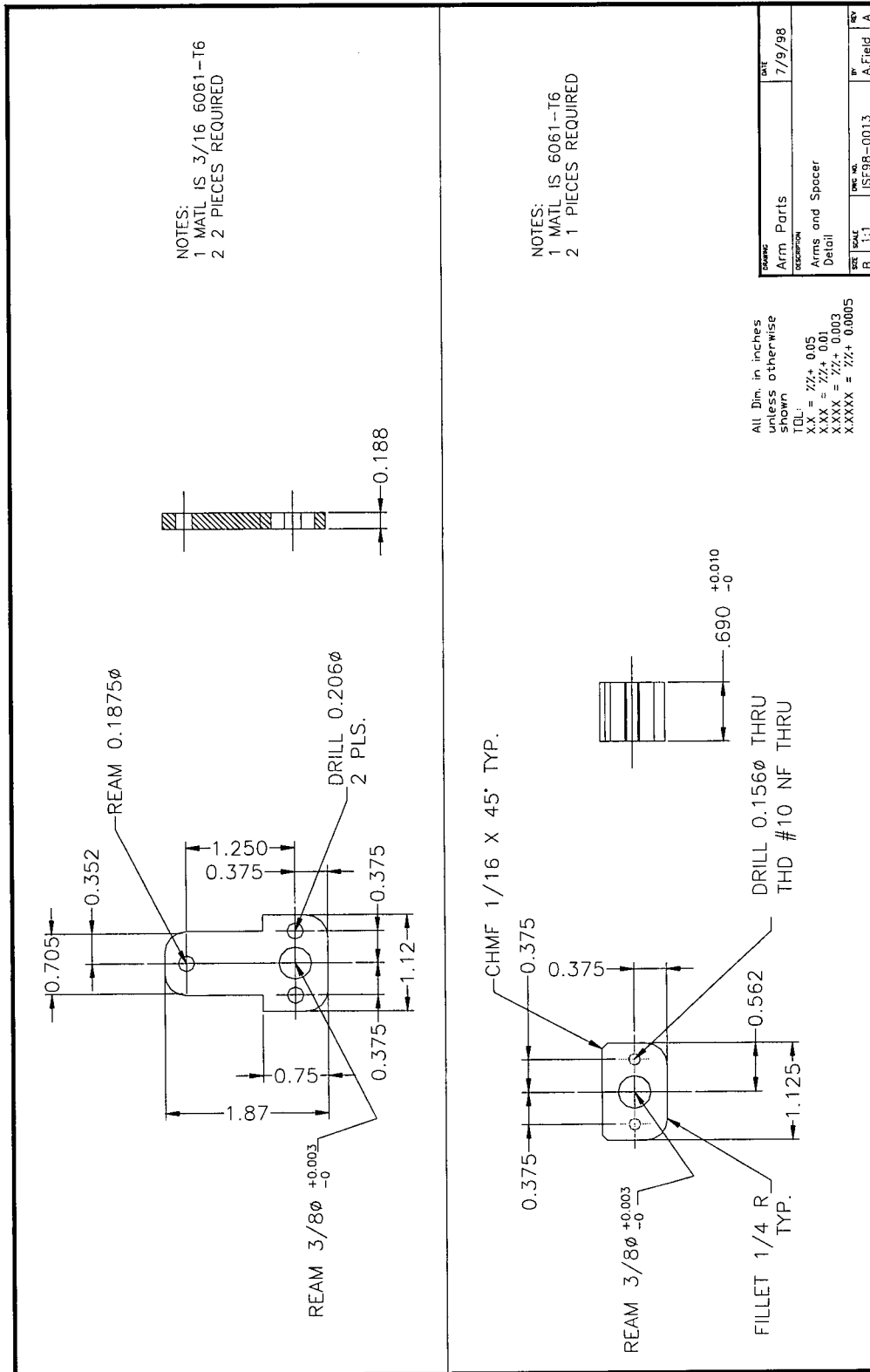


Figure B-16 Sternplane deflection control arm components (ISE98-0013)

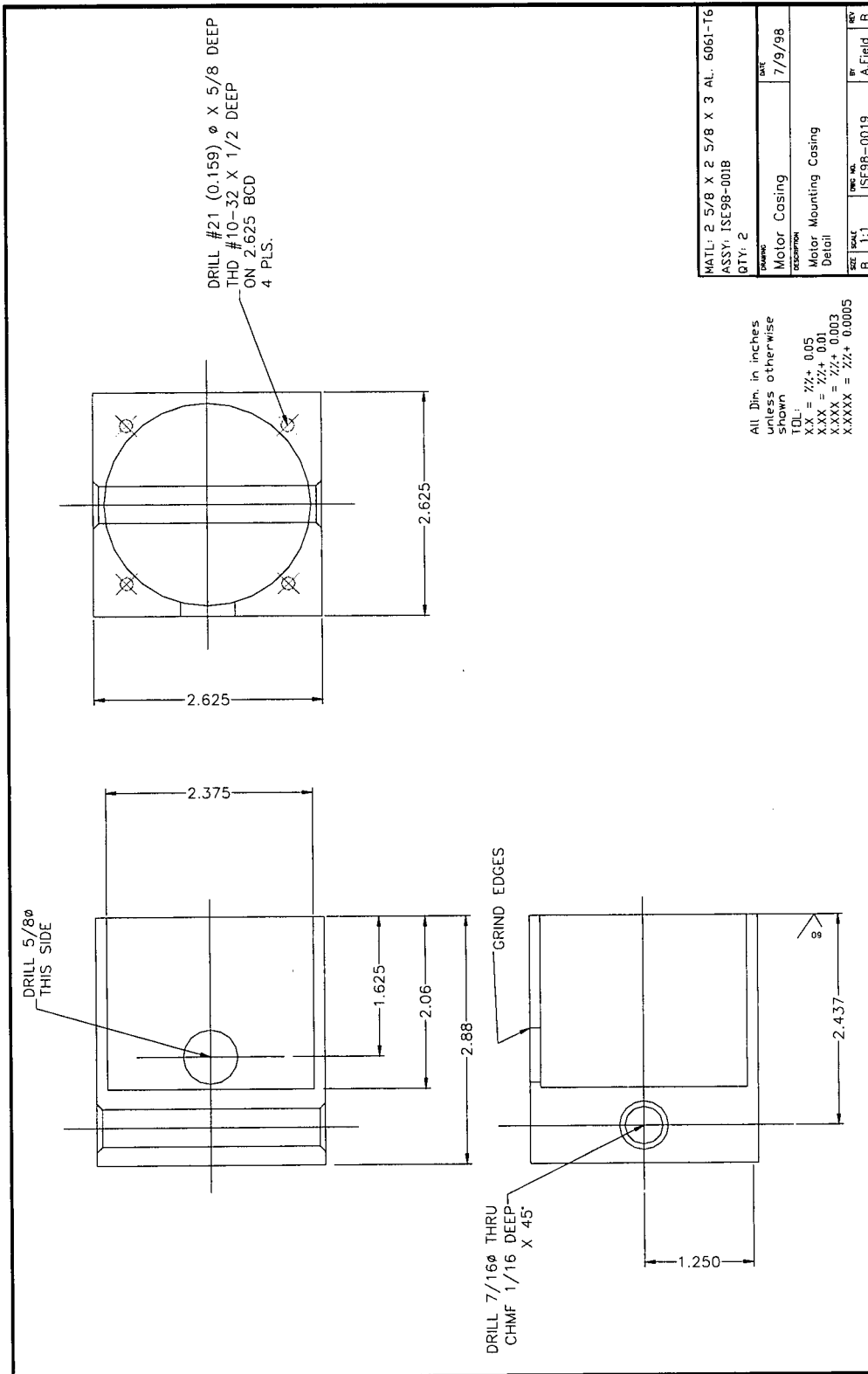


Figure B-17 Sternplane deflection control motor casing (ISE98-0019)

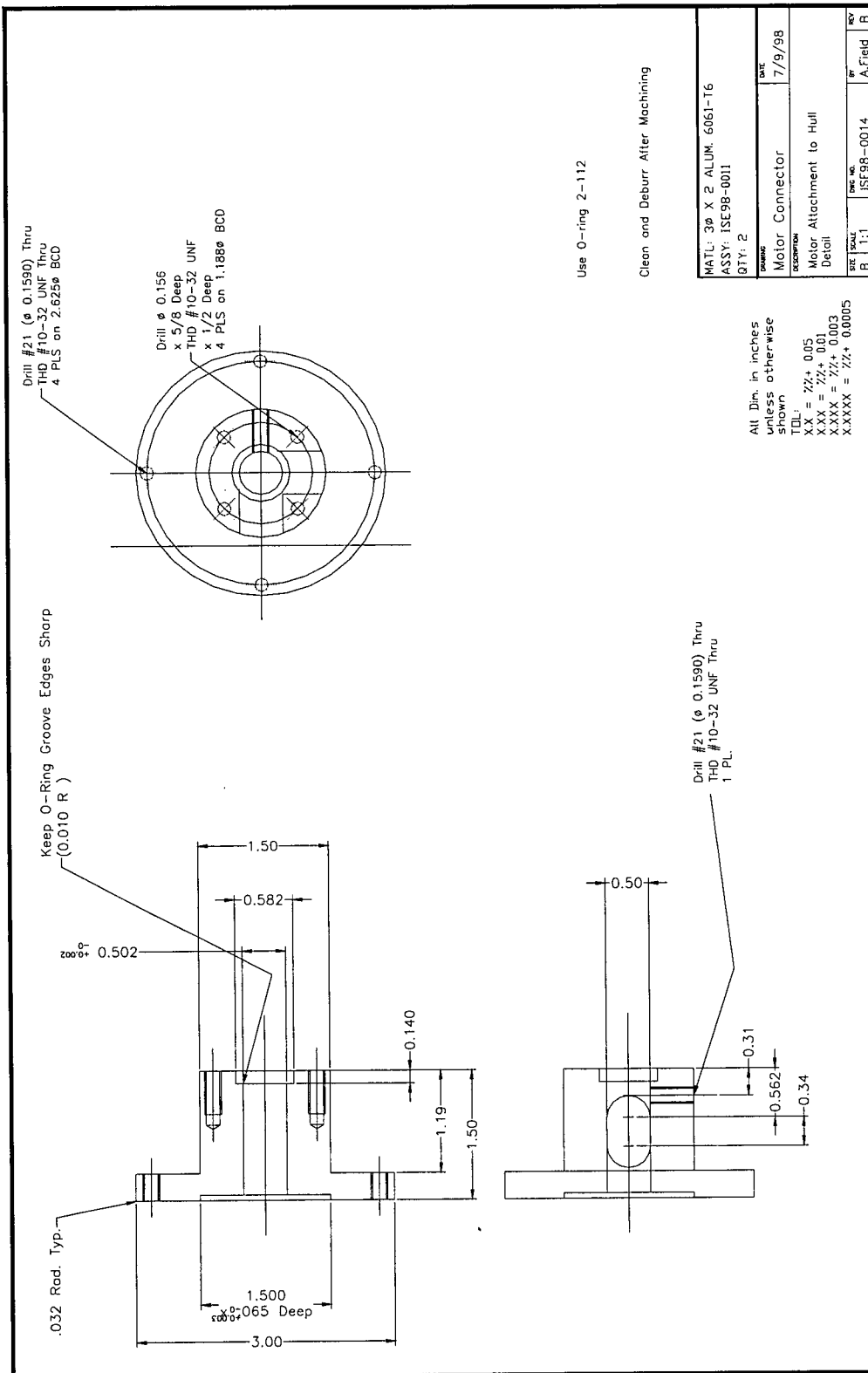


Figure B-18 Bowplane stepper motor connector (ISE98-0014)

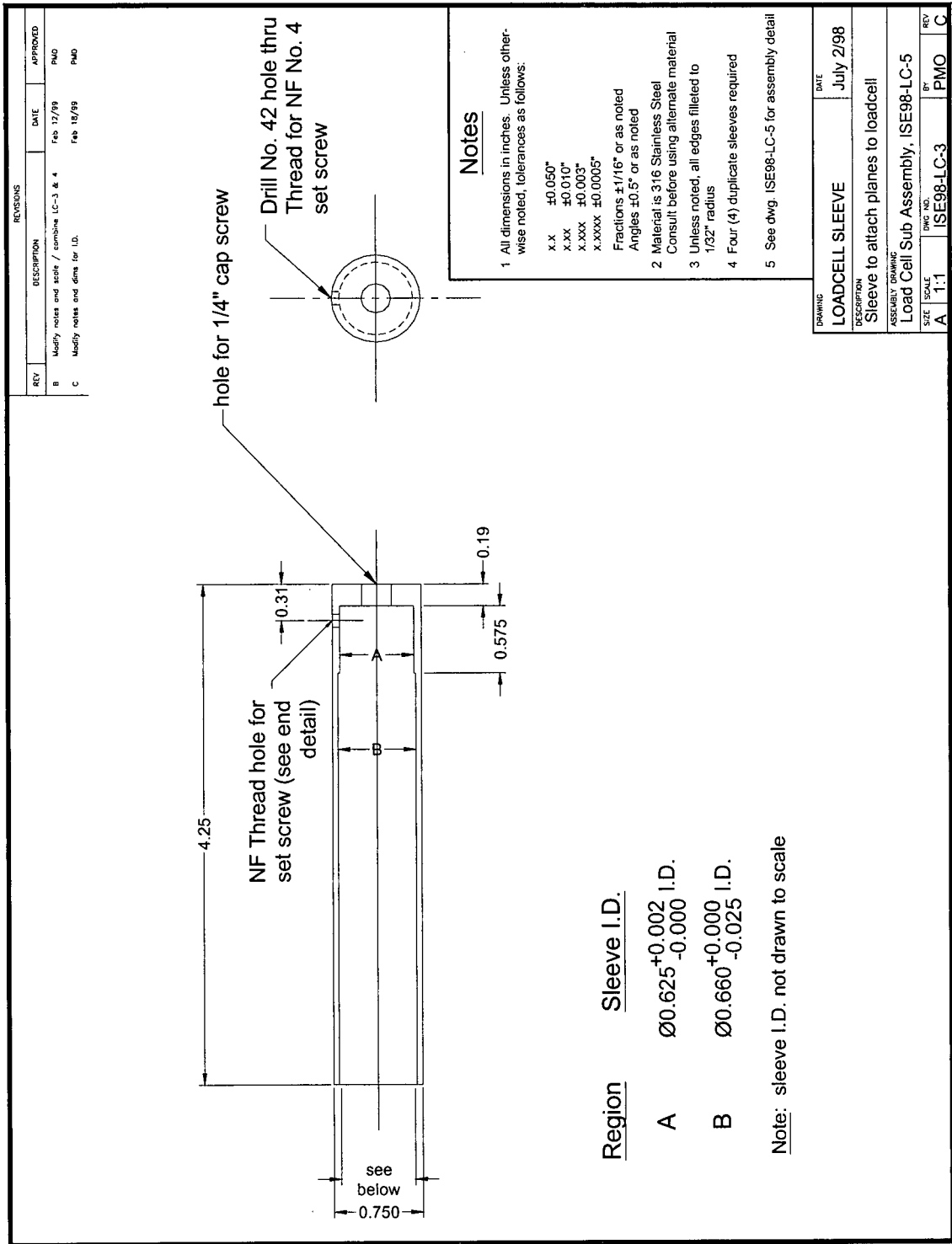


Figure B-21 Load cell sleeve (ISE98-LC-3)

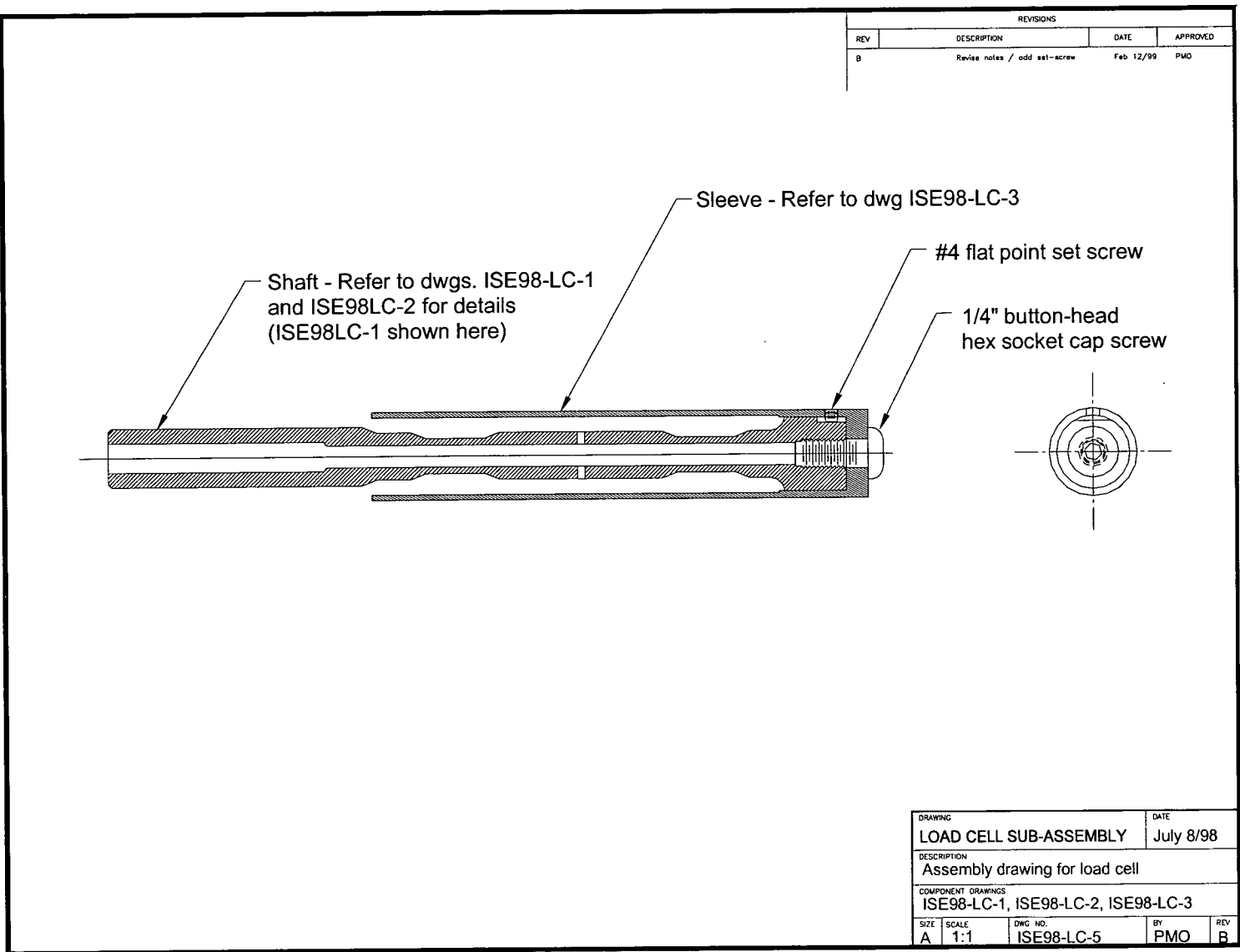


Figure B-22 Load cell sub-assembly (ISE98-LC-5)

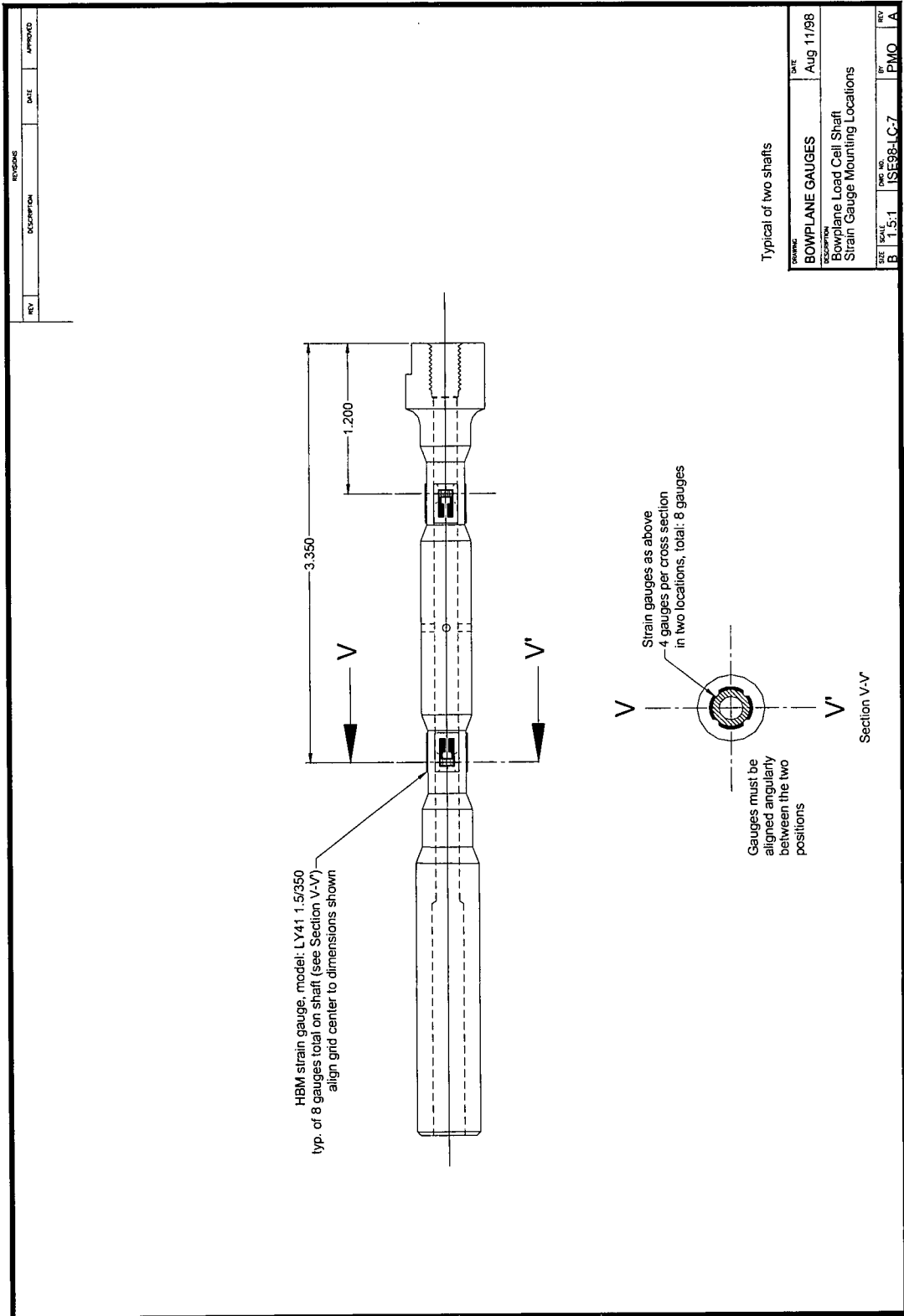


Figure B-23 Bowplane load cell strain gauge installation (ISE98-LC-7)

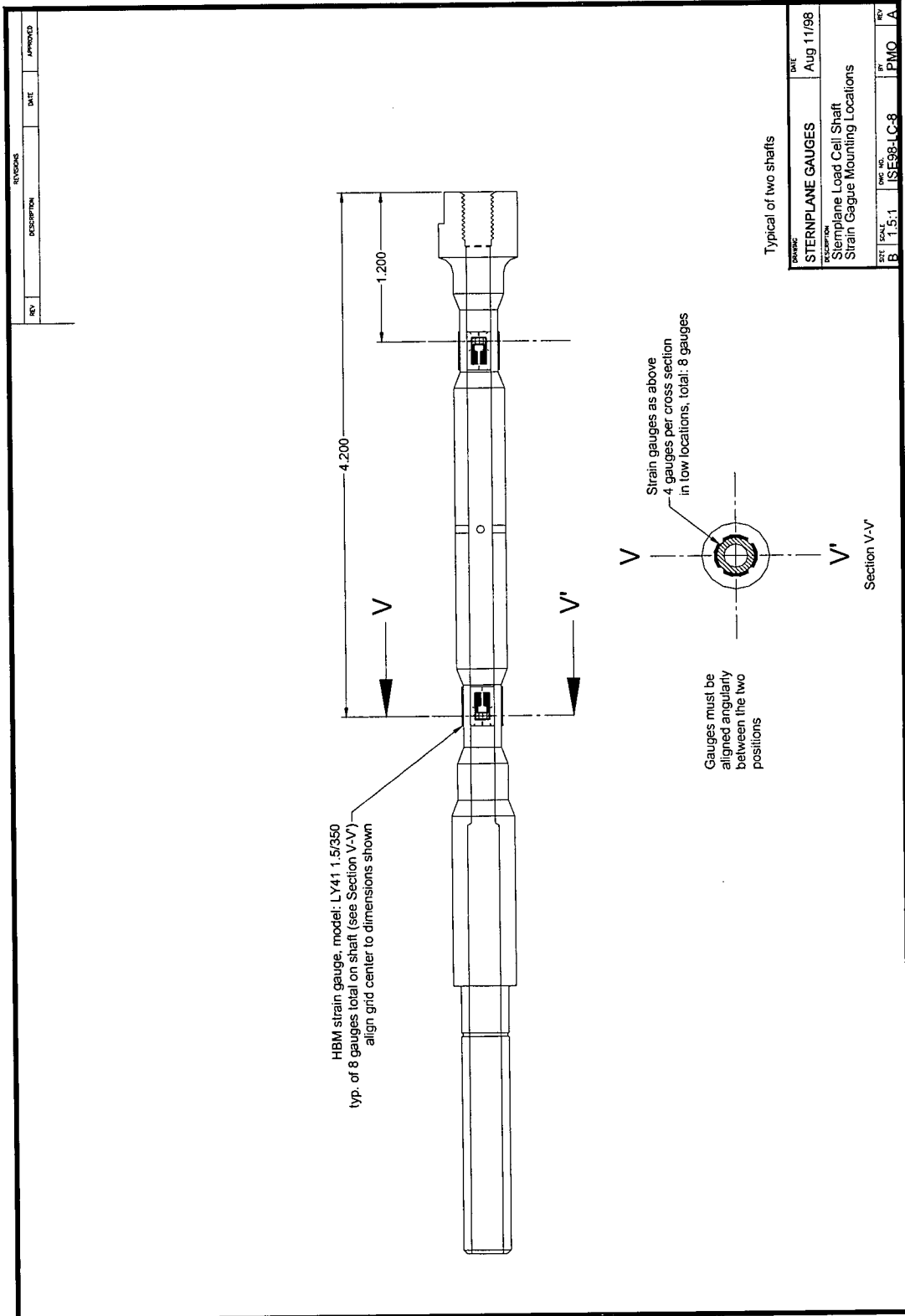


Figure B-24 Sternplane load cell shaft (ISE98-LC-8)

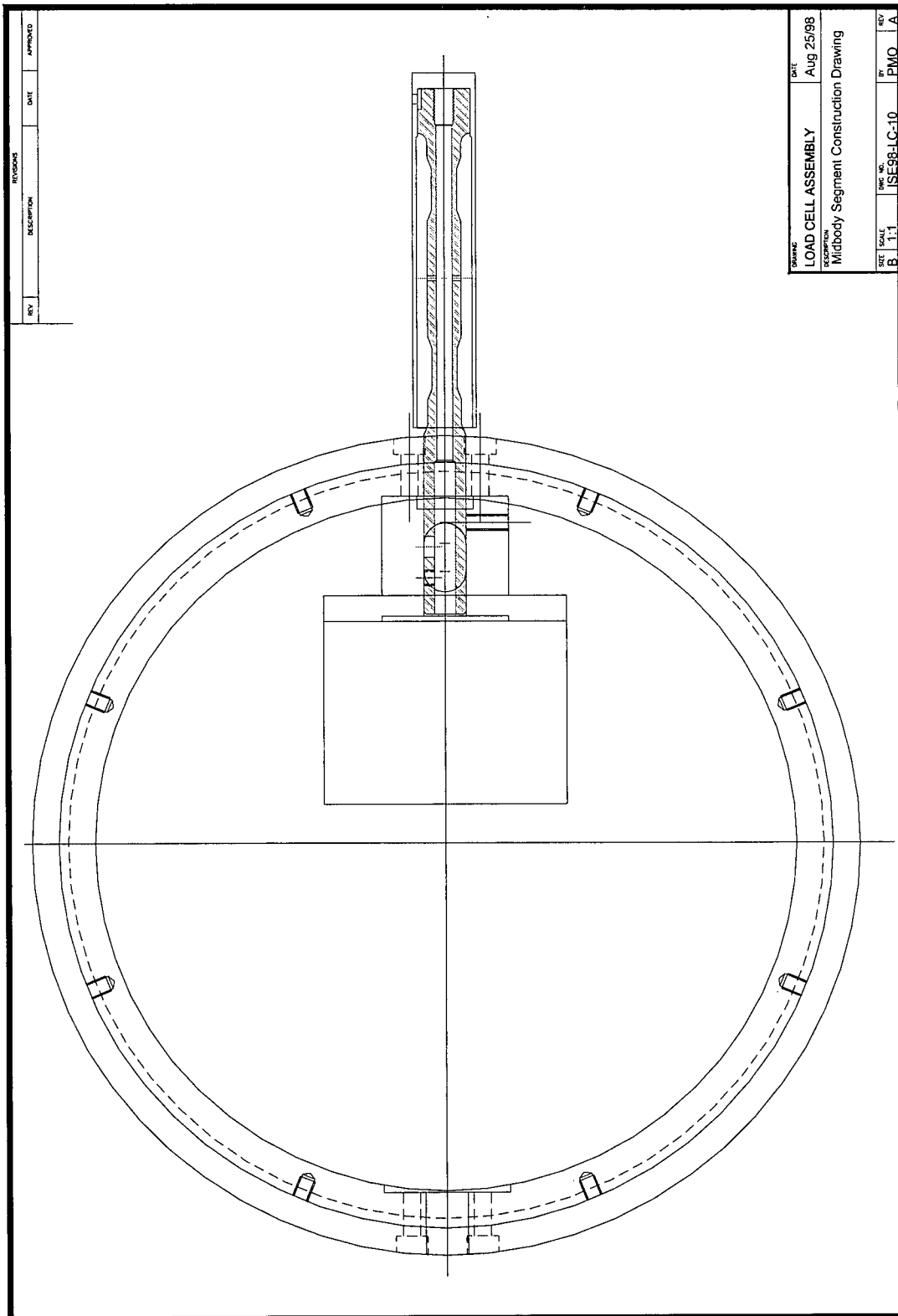
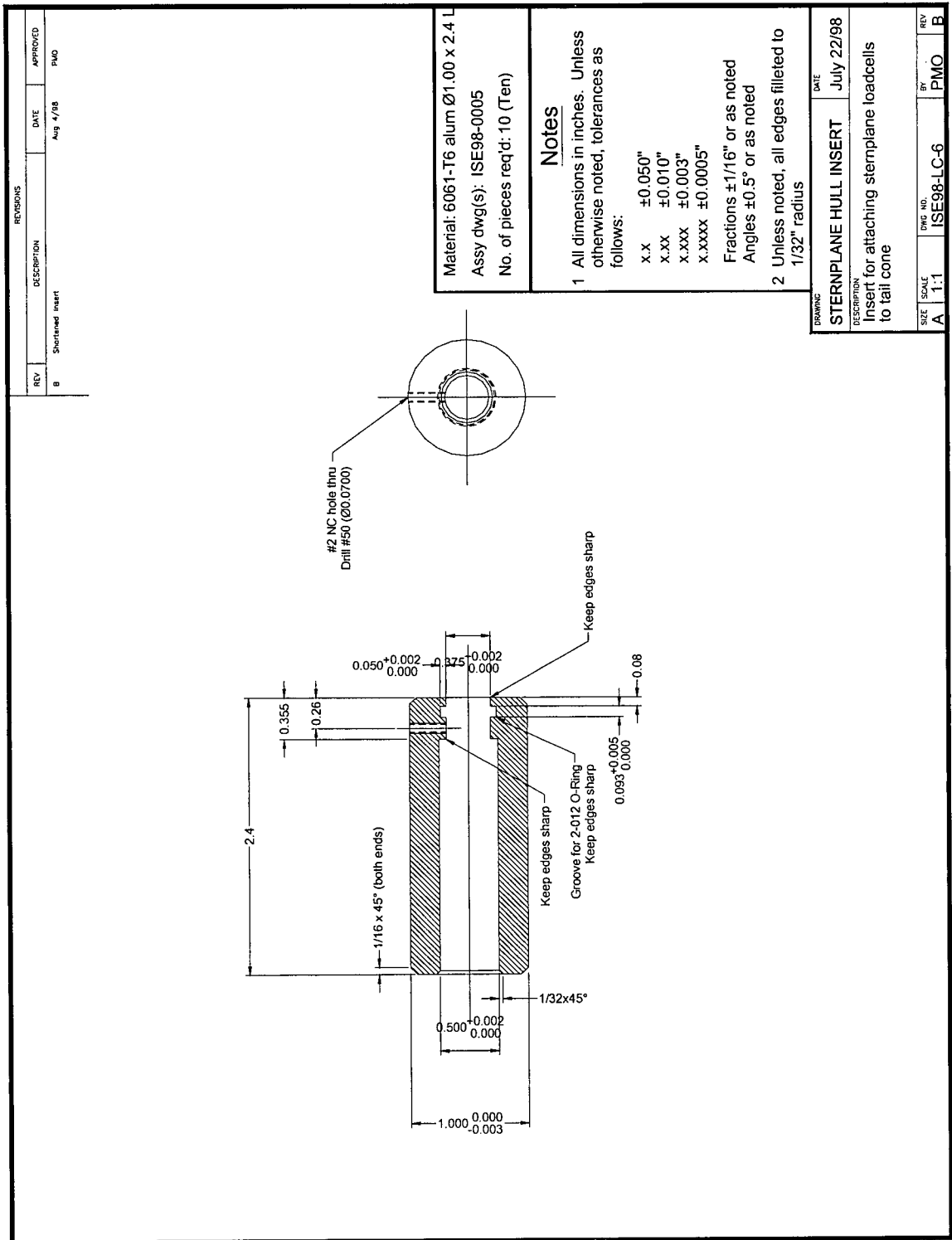


Figure B-25 Bowplane load cell assembly (ISE98-LC-10)



Material: 6061-T6 alum Ø1.00 x 2.4 L
Assy dwg(s): ISE98-0005
No. of pieces req'd: 10 (Ten)

- Notes**
- All dimensions in inches. Unless otherwise noted, tolerances as follows:
 x.x ±0.050"
 x.xx ±0.010"
 x.xxx ±0.003"
 x.xxxx ±0.0005"
 Fractions ±1/16" or as noted
 Angles ±0.5° or as noted
 - Unless noted, all edges filleted to 1/32" radius

DRAWING	DATE
STEREPLANE HULL INSERT	July 22/98

DESCRIPTION	SCALE	DWG. NO.	BY	REV
Insert for attaching sternplane loadcells to tail cone	A 1:1	ISE98-LC-6	PMO	B

Figure B-26 Sternplane hull insert (ISE98-LC-6)

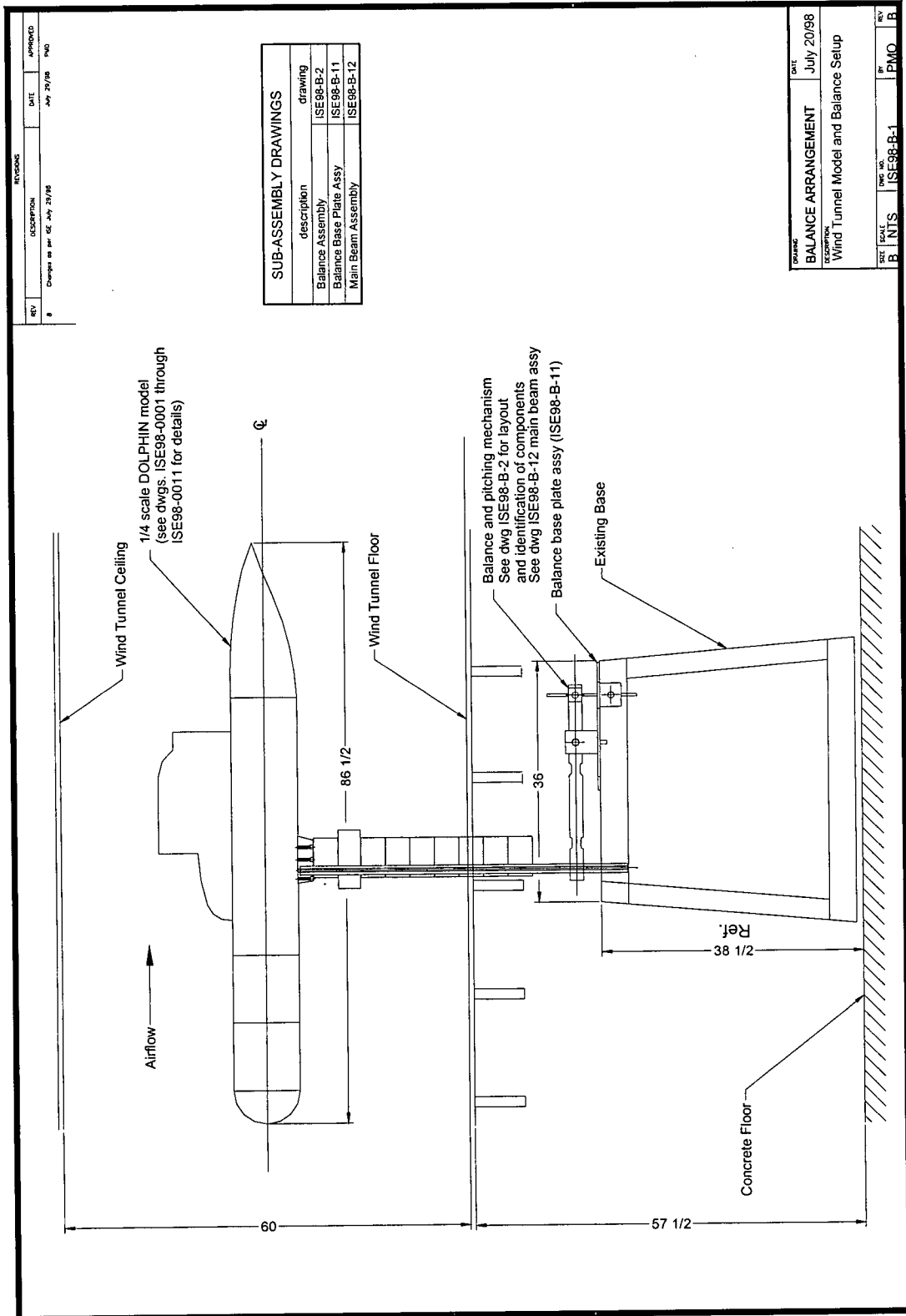


Figure B-27 Force balance setup in wind tunnel (ISE98-B-1)

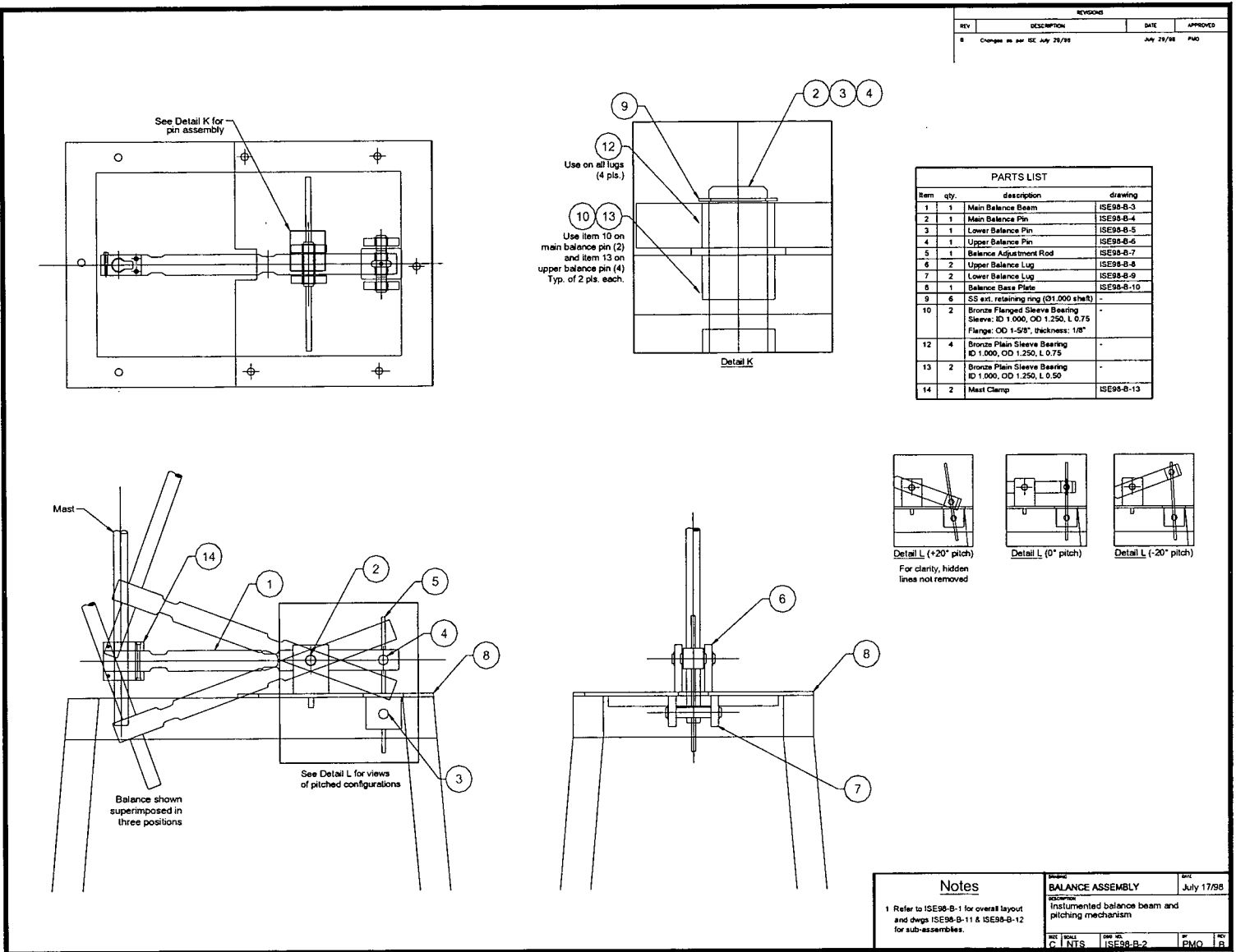


Figure B-28 Force balance assembly (ISE98-B-2)

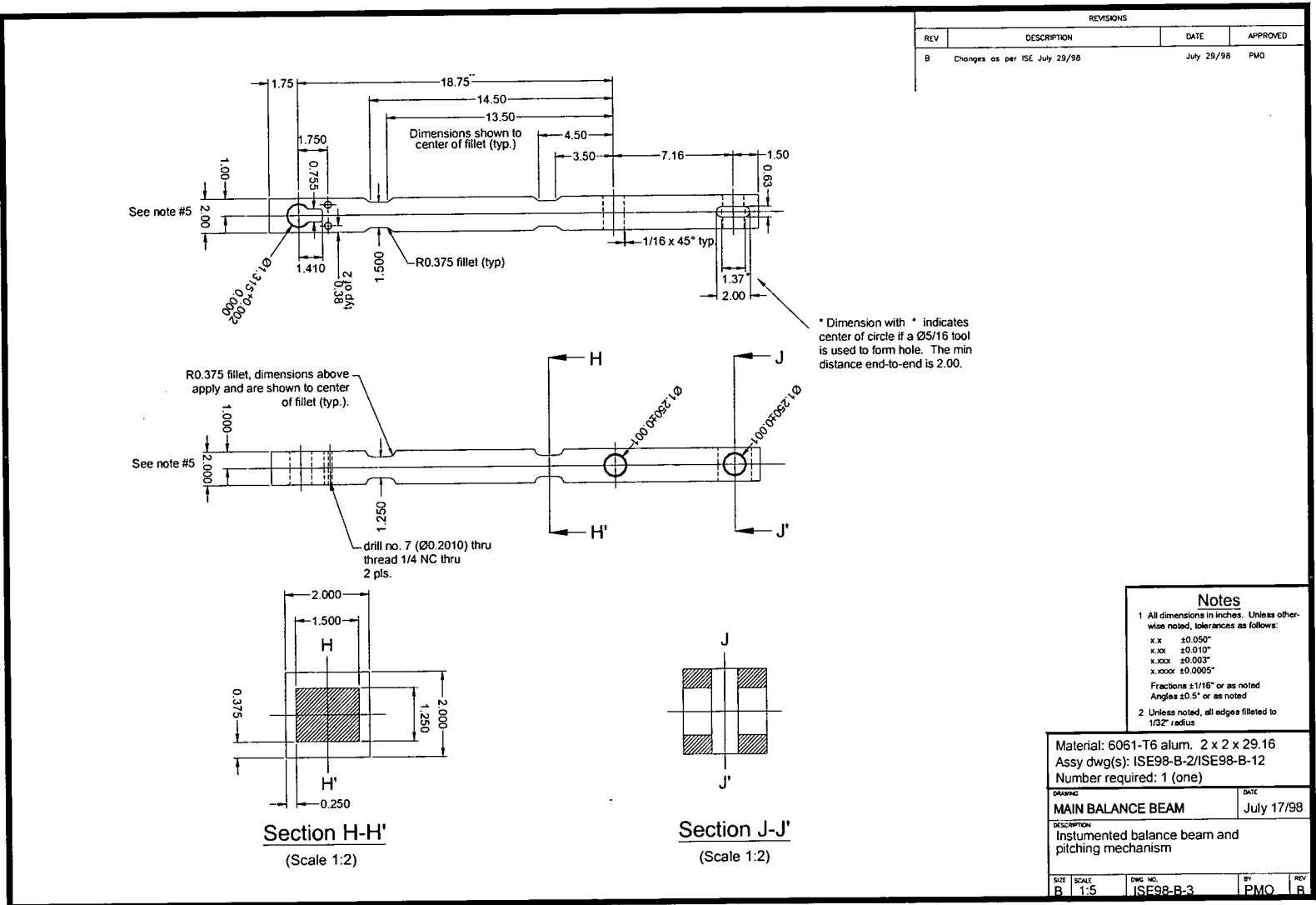


Figure B-29 Force balance beam (ISE98-B-3)

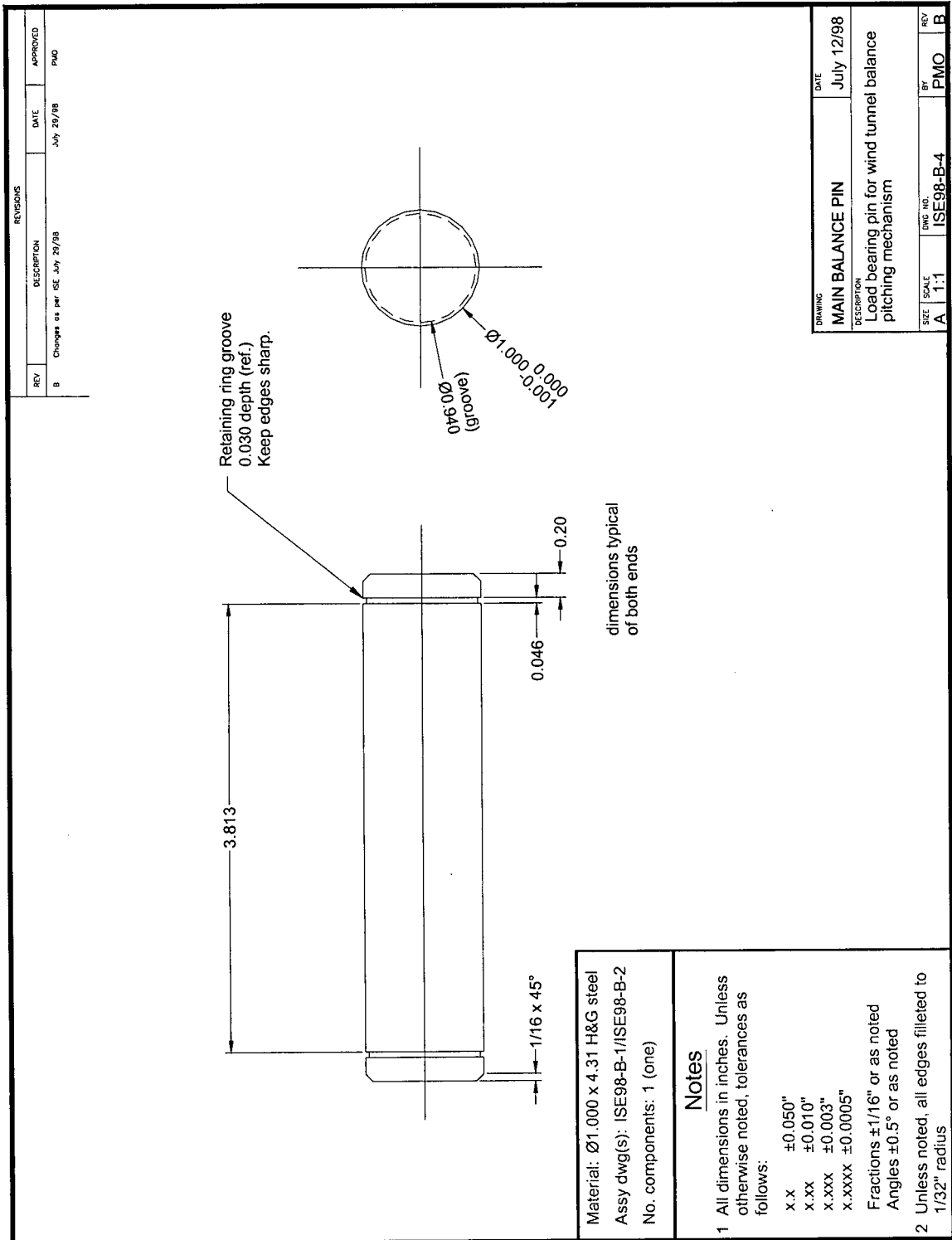


Figure B-30 Balance pitch mechanism load bearing pin (ISE98-B-4)

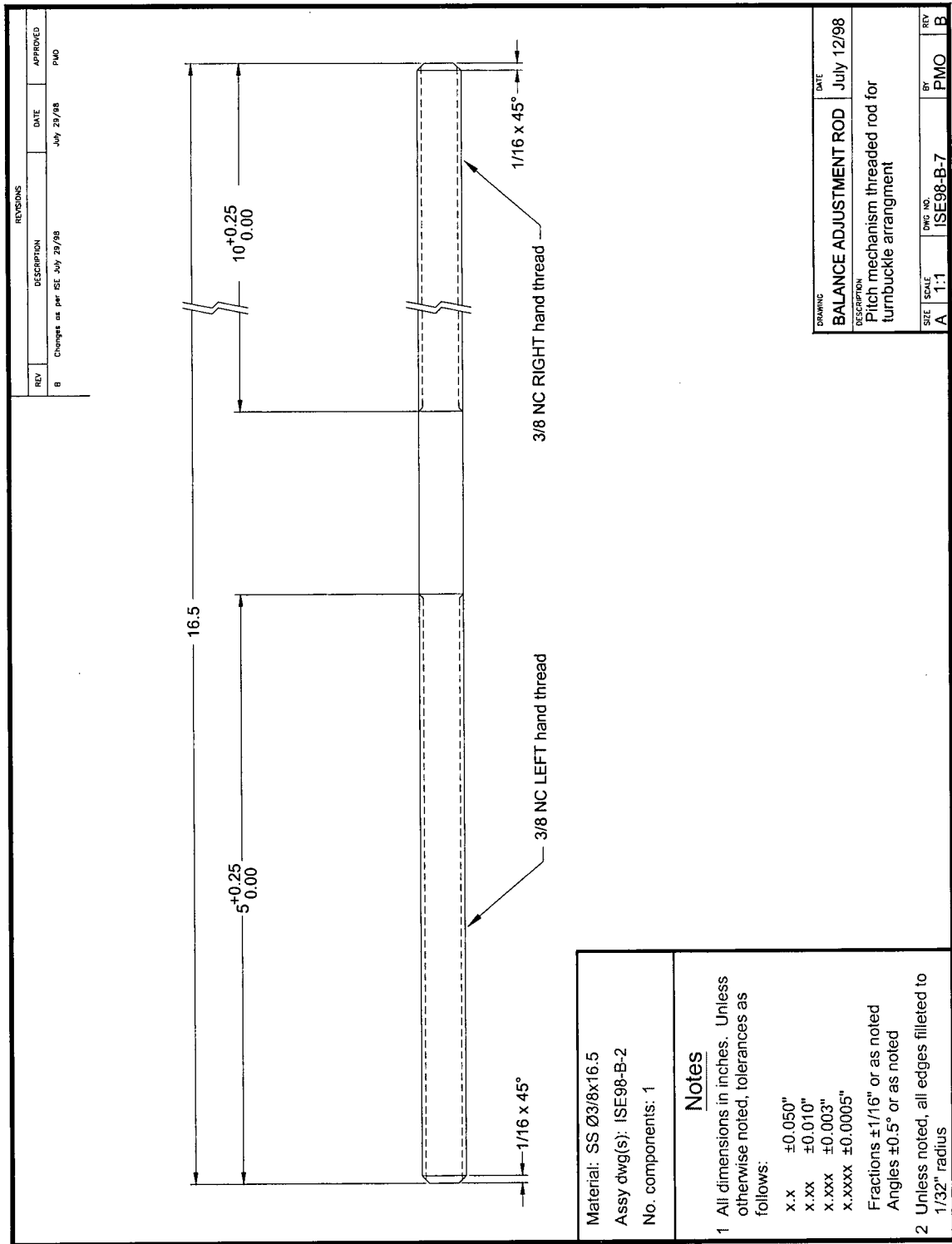


Figure B-31 Balance pitch mechanism adjustment rod (ISE98-B-7)

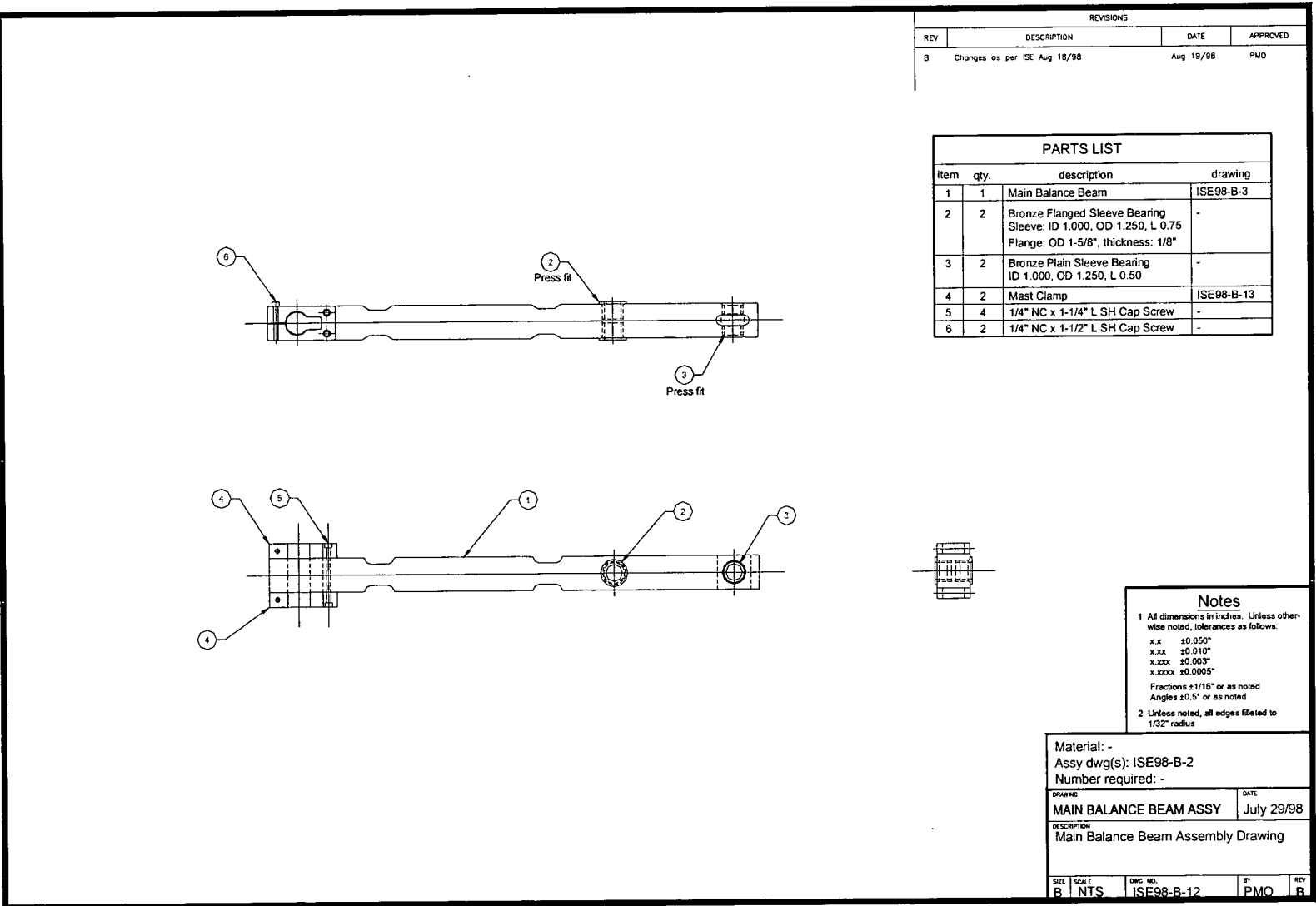


Figure B-32 Main balance beam assembly (ISE98-B-12)

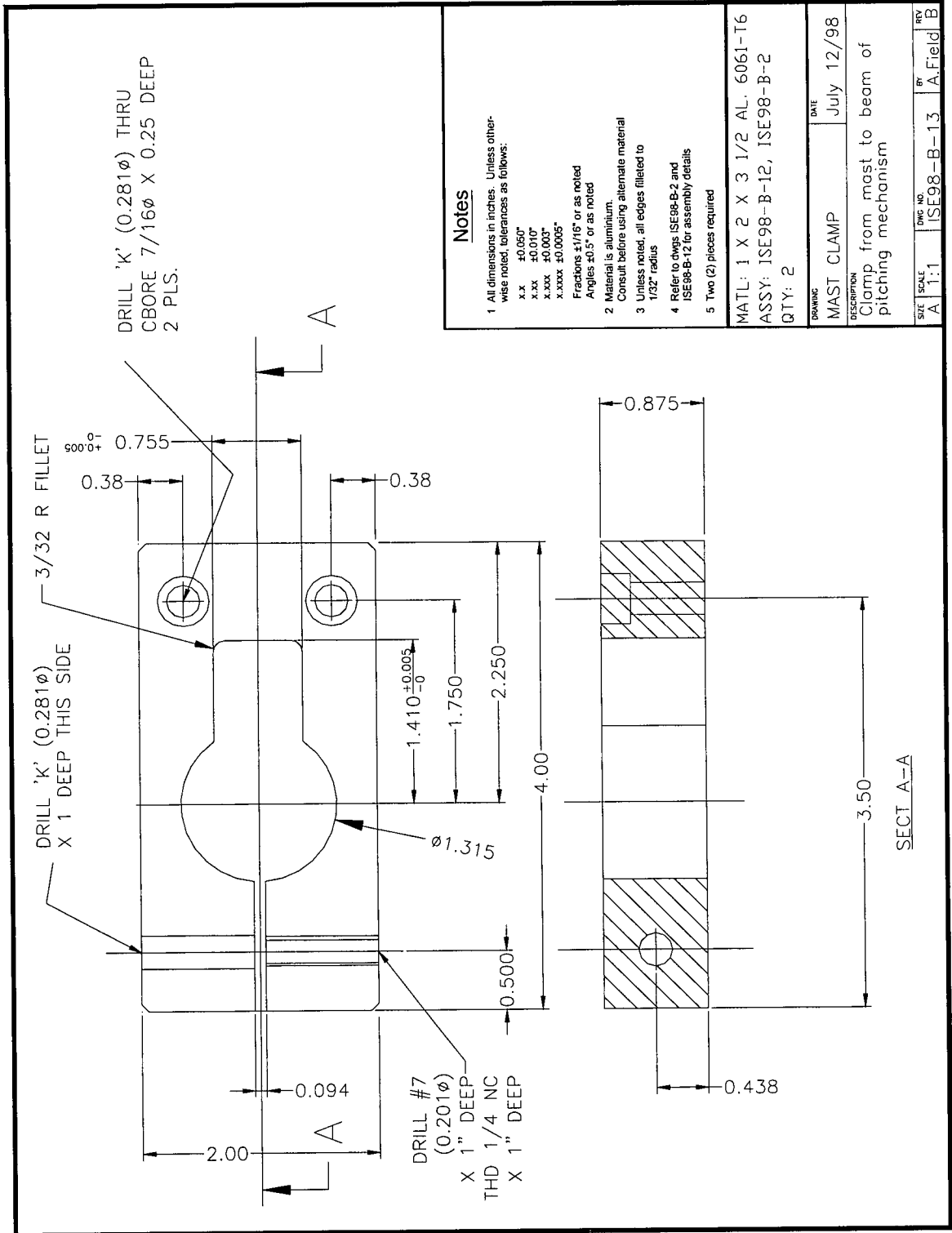


Figure B-33 Balance beam clamp for mast (ISE98-B-13)

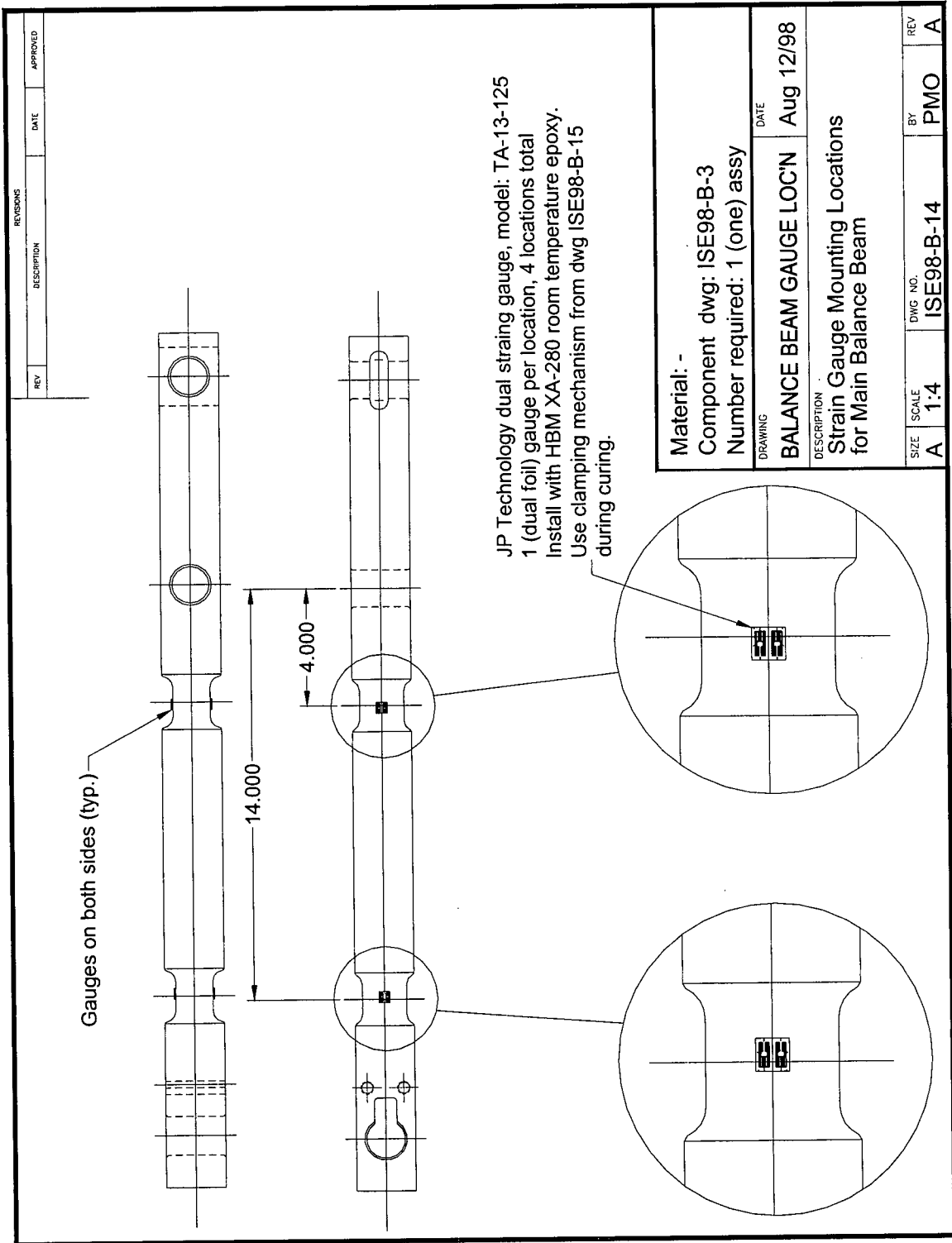


Figure B-34 Force balance beam strain gauge installation (ISE98-B-14)

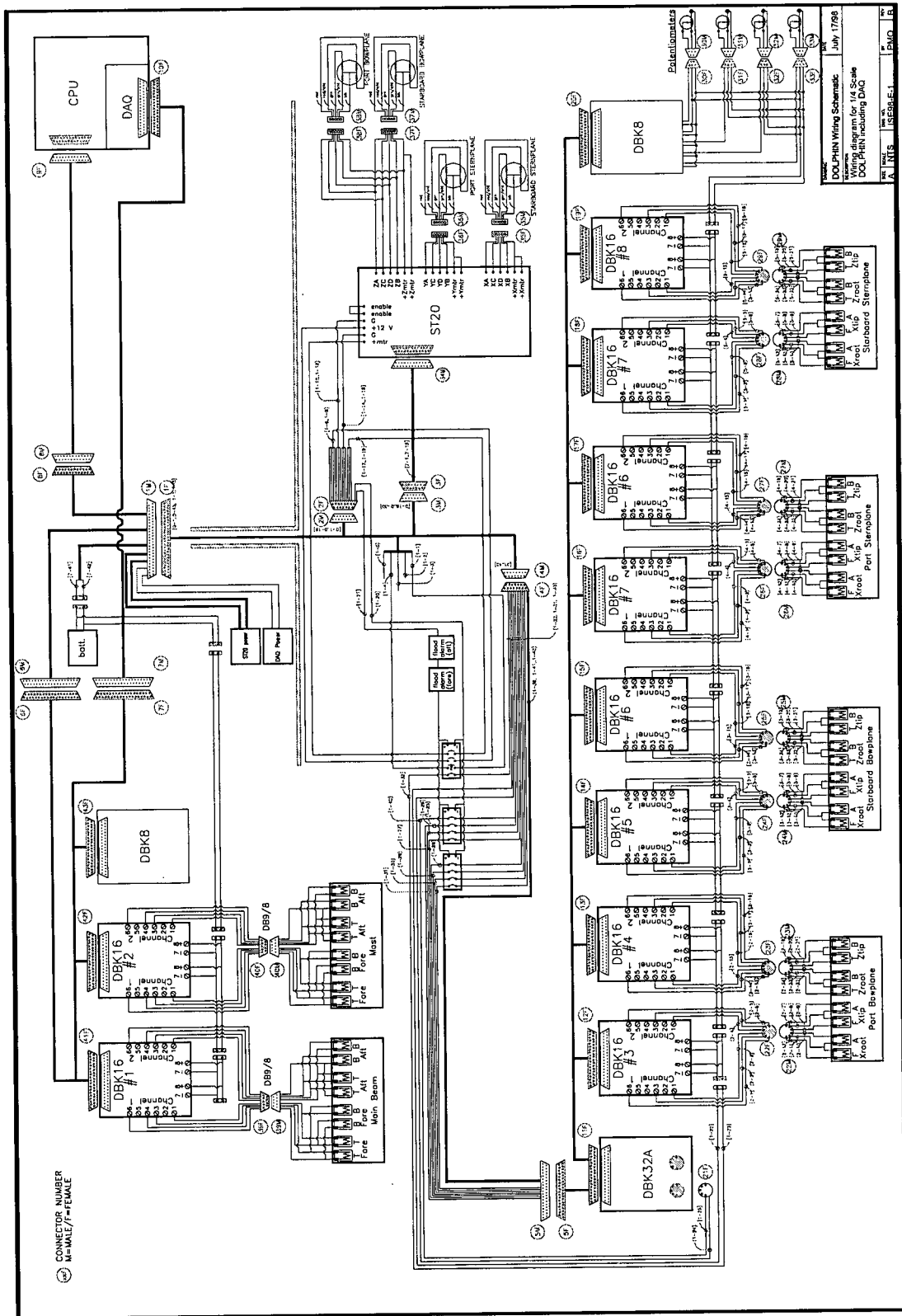


Figure B-35 Power and instrumentation wiring diagram (ISE98-E-1)

B.2 Load Cell Design

The load cells were custom designed and fabricated for the measurement of plane forces. The bowplane and sternplane load cells were constructed from 302 stainless steel to the specifications in Figure B-19 and Figure B-20 respectively. Although the 302 stainless steel had reduced yield strength compared to many other steels, it was selected for improved machinability characteristics (see, for example, Walsh, 1994). The diameter of the load cell was reduced in the regions where the strain gauges were applied in order to locally increase the strain without compromising the overall stiffness. Eight strain gauges were applied as shown in Figure B-23 and Figure B-24.

The design load was determined assuming a maximum non-dimensional Z' force of 0.0015 estimated using the methods of Chapter 2. For a maximum speed of 3.5 m/s in the tow tank, where $\rho = 998 \text{ kg/m}^3$, the maximum expected force is $Z = 28 \text{ N}$. This force was used in the load cell design and the resulting deflection and microstrain are shown in Figure B-36 and Figure B-37. The maximum deflection of 1 mm is suitable as is the maximum microstrain of 1200 (microstrain is the ratio of elongation to overall length multiplied by 10^6).

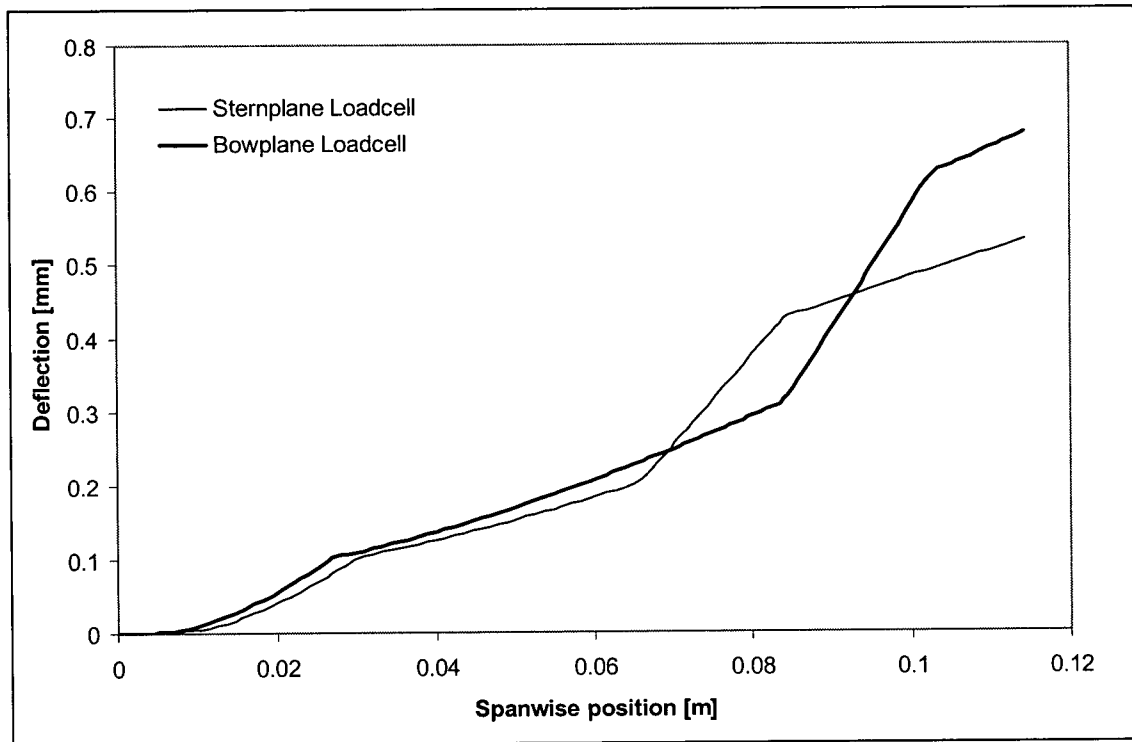


Figure B-36 Load cell deflection for maximum design load

Each half-bridge circuit measured bending moment—two corresponding to lift and two corresponding to drag—and in post-processing the moments were used to estimate lift and drag. Considering lift, the moments on the inboard and outboard gauges were K_i and K_o respectively, and

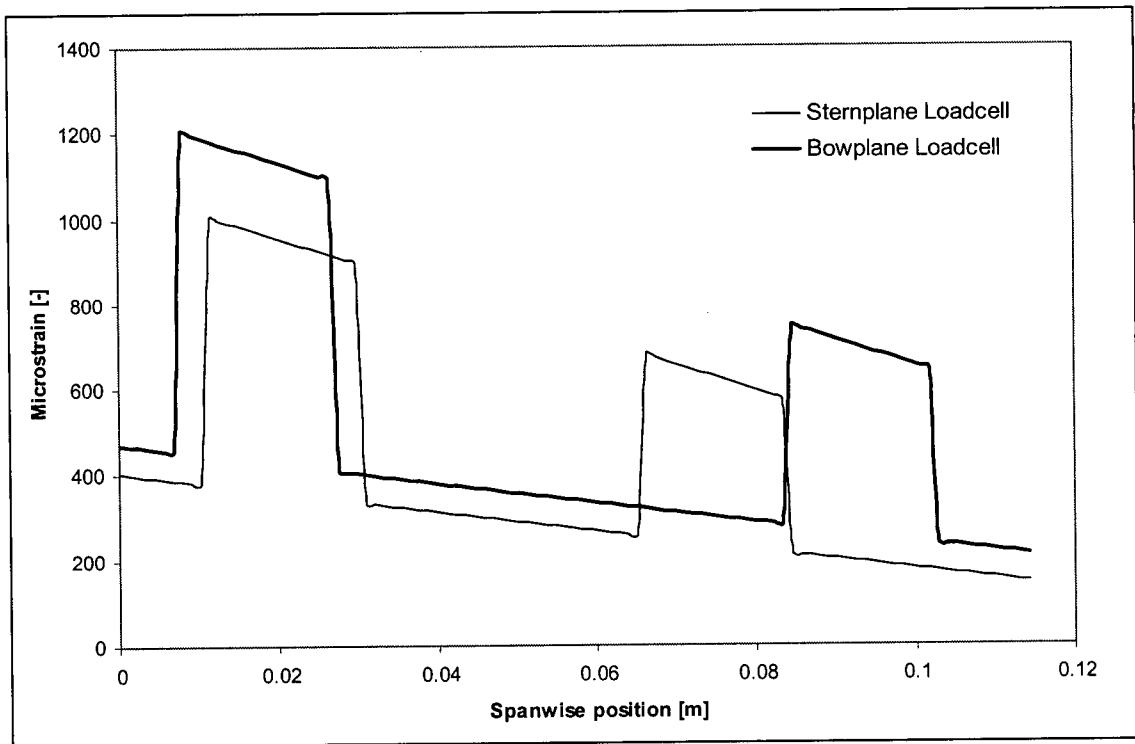


Figure B-37 Load cell microstrain for maximum design load

the longitudinal separation distance of the gauges was Δy . The corresponding force is measured according to

$$Z = \frac{K_i - K_o}{\Delta y} \quad (161)$$

This represents a shear-beam style arrangement and is insensitive to the point of force application. The span-wise center of pressure—that is, the location along the plane span at which the force, Z , could be assumed to act—was also computed from the moment measurements by

$$y_{cp} = y_i + \frac{K_i}{K_i - K_o} \Delta y \quad (162)$$

where y_i is the spanwise position of the inboard gauges.

Sample calibration data for the X and Z forces is shown in Figure B-38 for the measured voltage against applied load. The force is applied in the z direction; the measured X force is due to coupling in the load cell. Both measurements are linearly related to the applied load—given the correlation coefficients (R^2) close to unity—and the error in the measurements is low.

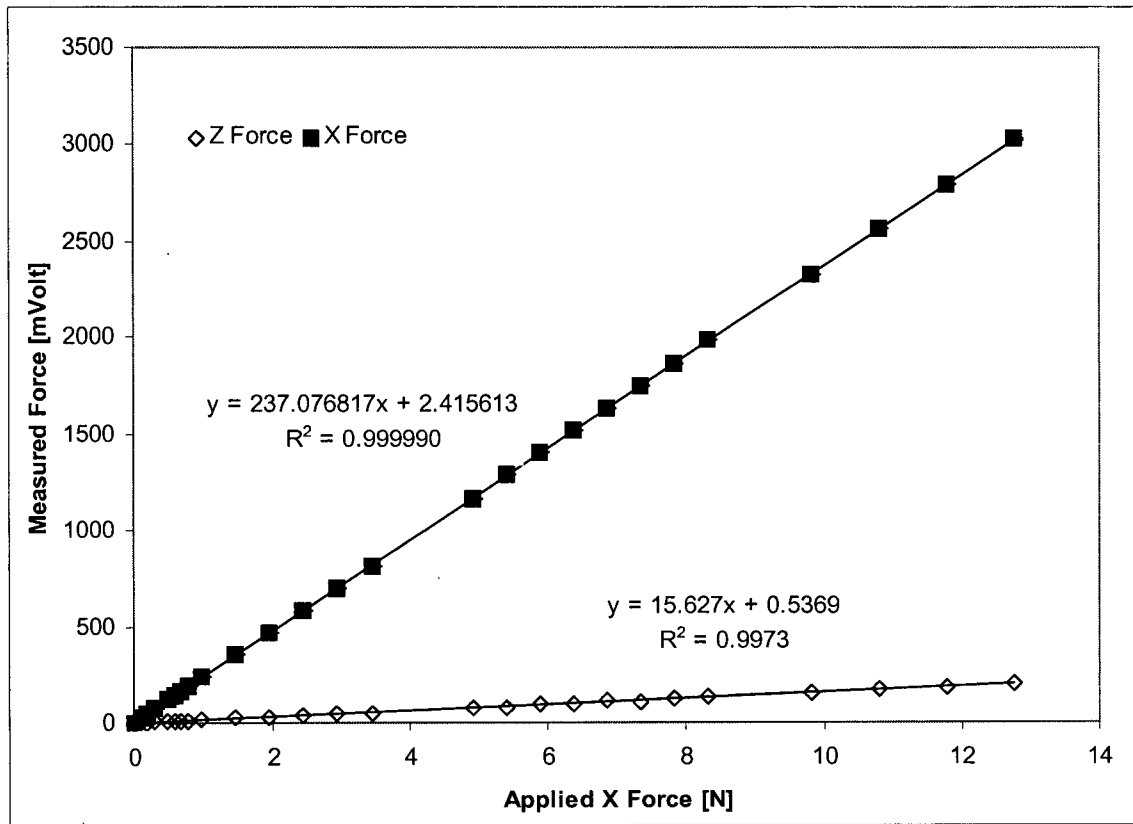


Figure B-38 Sample load cell calibration data

The slopes of the X and Z measurements are 15.6 mVolt/N and 237.1 mVolt/N respectively. These slopes are used, in conjunction with similar slopes from an applied load in the X direction, to form a decoupling calibration matrix, T^* , where

$$T^* = \begin{bmatrix} t_{xx} & t_{xz} \\ t_{zx} & t_{zz} \end{bmatrix} \quad (163)$$

The matrix element t_{ij} gives the measured voltage in the i direction as a result of an applied load in the j direction. Using the data above as an example, the value of t_{xz} is the 15.6 mVolt/N slope and t_{zz} is the 237.1 mVolt/N slope. The elements t_{xx} and t_{zx} are determined from the slopes for a load applied in the x -direction.

In general, for forces in the X and Z direction, the voltages v_x and v_z are measured. The quiescent readings (the voltages when no load is applied) are v_{x0} and v_{z0} . The voltages are related to the applied force through

$$\begin{bmatrix} v_x \\ v_z \end{bmatrix} - \begin{bmatrix} v_{x0} \\ v_{z0} \end{bmatrix} = \begin{bmatrix} t_{xx} & t_{xz} \\ t_{zx} & t_{zz} \end{bmatrix} \begin{bmatrix} X \\ Z \end{bmatrix} = \mathbf{T} \begin{bmatrix} X \\ Z \end{bmatrix} \quad (164)$$

In order to convert known voltage readings to the unknown forces and therefore be determined according to

$$\begin{bmatrix} X \\ Z \end{bmatrix} = \mathbf{T}^{*-1} \left(\begin{bmatrix} v_x \\ v_z \end{bmatrix} - \begin{bmatrix} v_{x0} \\ v_{z0} \end{bmatrix} \right) \quad (165)$$

or

$$\begin{bmatrix} X \\ Z \end{bmatrix} = \mathbf{T} \left(\begin{bmatrix} v_x \\ v_z \end{bmatrix} - \begin{bmatrix} v_{x0} \\ v_{z0} \end{bmatrix} \right) \quad (166)$$

where

$$\mathbf{T} = \frac{1}{t_{xx}t_{zz} - t_{xz}t_{zx}} \begin{bmatrix} t_{zz} & -t_{xz} \\ -t_{zx} & t_{xx} \end{bmatrix} \quad (167)$$

with t_{ij} defined as above.

B.3 Boundary Layer Tripping

In order to minimize the effects of delayed boundary layer transition, boundary layer trips were installed on all regions of the model in which transition was naturally expect to occur for the full size vehicle. The function of the trips was to cause a transition from laminar to turbulent flow in the boundary layer by placing an obstruction in the flow.

The regions in which boundary layer trips were located are identified in Figure B-39 by the dark, jagged lines. In particular, the trips were positioned on the nose, mast fairings, keel (two positions), rudder, stabilizer, and on all of the control surfaces.

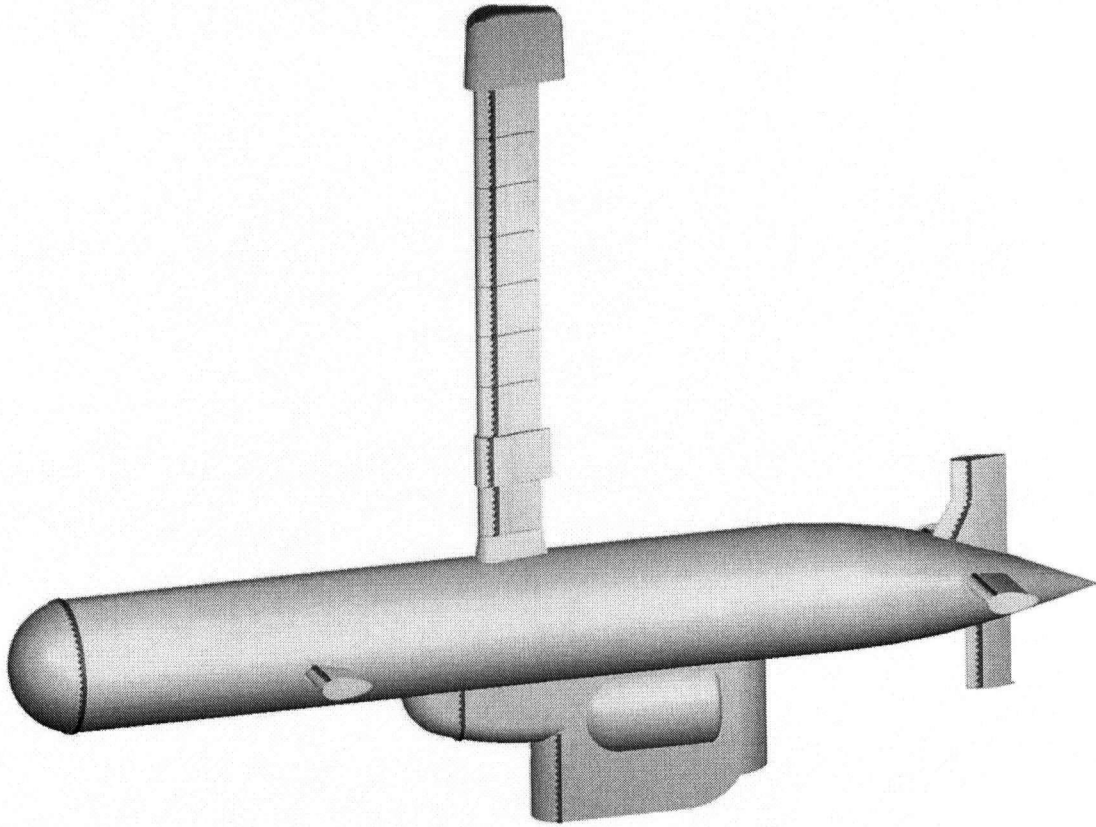


Figure B-39 Boundary Layer Trip Mounting Locations

The style of trip that was used featured a zig-zag cut leading edge and a straight trailing edge. More information on the effectiveness of this style of trip can be found in (Torres, 1999) along with a comparison to other boundary layer trip geometries. The trip was constructed from multiple layers of clear, packing-type tape and the leading edge was formed using fabric pinking shears.

The thickness and mounting location for the boundary layer trips was computed using Thwaites method as outlined by White (1991). The correlation method of Thwaites uses the integral momentum method and is described in the following equations. In the following discussion, the

thickness of the trips, t_{trip} , and the location at which they were positioned, s , is identified in general for the nose in Figure B-40.

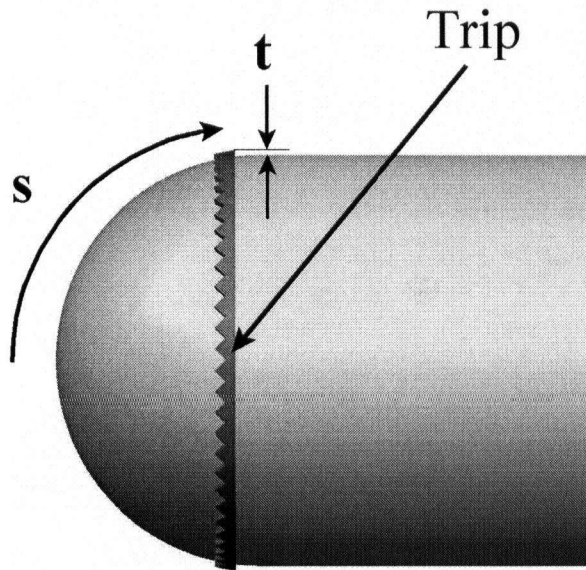


Figure B-40 Boundary Layer Trip Terminology

First, the integral momentum equation is written in terms of a parameter, λ_t

$$\lambda_t = \frac{\delta_2^2 U'}{\nu} = \left(\frac{\delta_2}{\delta_0} \right)^2 \Lambda \quad (168)$$

where U' is the convective acceleration locally outside the boundary layer, δ_2 is the momentum thickness, ν is the kinematic viscosity, δ_0 is the boundary layer thickness, and Λ is the Karman-Pohlhausen parameter. Two further parameters are defined: the shear correlation

$$\frac{\tau_w \delta_2}{\mu U} \approx S(\lambda_t) \quad (169)$$

and the shape-factor correlation

$$H = \frac{\delta_1}{\delta_2} \approx H(\lambda_t) \quad (170)$$

White gives an approximation of $H(\lambda)$ using the parameter $z_t = (0.25 - \lambda_t)$

$$H(\lambda_t) \approx 2.0 + 4.14z_t - 83.5z_t^2 + 854z_t^3 - 3337z_t^4 + 4576z_t^5 \quad (171)$$

Thwaites was able to show that for all types of laminar boundary layers $\theta(x)$ is predicted to within 3% by

$$\delta_2^2 \approx \frac{0.45\nu}{U^6} \int_0^s U^5 ds \quad (172)$$

From this result, λ_t is computed through equation (168) and $H(\lambda_t)$ through equation (171). It follows that the displacement thickness δ_1 is computed through equation (170).

At this point, the one-step method of Wazzan is used to predict the transition Reynolds number. The results of Wazzan are also presented in (1991). In particular, the Reynolds number for transition is given by

$$\log(Re_{s, tr}) \approx -40.4557 + 64.8066H - 26.7538H^2 + 3.3819H^3 \quad (173)$$

Using the Reynold number based on the local position on the body Re_s and the values of the parameter, H , from above, it is possible to predict the point of transition. The point at which Re_s is equal to the value of $Re_{s, tr}$ gives the value of the parameter, H , at the transition point. Working backwards it is possible to solve for λ_t , s , δ_1 , or δ_2 for example.

In other words, given the body geometry and an estimate of the velocity at different stations on that body, it is possible to predict where transition will occur as well as the displacement and boundary layer thicknesses.

In the case of this research, the transition point was computed for the full scale vehicle using the techniques above. Using the same relative location on the model, the computations were repeated to give the boundary layer displacement thickness at this point. A boundary layer trip was sized so as to be roughly the same size as the displacement thickness; that is, $t_{trip} = \delta_1$.

In practice, trips were made slightly larger than calculations suggested. Multiple layers of packing tape were used to form the trip thickness. Using the method of Thwaites it was also possible to check for separation. In the case of the model nose, premature laminar separation was predicted just slightly upstream of the suggested trip location. In this case, the trip was moved forward to inhibit the laminar separation.

Given that the control surfaces were constantly deflected at non-zero angles, the computations for the boundary layer trips on the planes were not entirely accurate. In the end, the trips were positioned at just slightly forward of the computed position at roughly the 3% chord line to maintain trip effectiveness at higher deflections.

APPENDIX C - NUMERICAL CALCULATIONS

C.1 Slope Error Estimation

The estimated error in the resulting slope from a linear regression was computed based on the standard error. Considering a series of n datum points with independent variable $x_1 \dots x_n$ and dependent variable $y_1 \dots y_n$, the standard error in slope is given by

$$\text{Slope Error} = \frac{S_{y,x}}{\sigma(x)\sqrt{n}} \quad (174)$$

where $S_{y,x}$ is the standard error of the predicted y values for each x value in the regression and $\sigma(x)$ is the standard deviation of the independent variables. The definition of $S_{y,x}$ is

$$S_{y,x} = \sqrt{\frac{1}{n(n-2)} \left[n\Sigma y^2 - (\Sigma y)^2 - \frac{[n\Sigma xy - \Sigma x\Sigma y]^2}{n\Sigma x^2 - (\Sigma x)^2} \right]} \quad (175)$$

C.2 Radius of Curvature Calculation

The radius of curvature expresses the rate of turning of a line tangent to a curvilinear path. A small radius of curvature describes a “tight” curve while a very large radius of curvature (approaching infinity) describes a straight line.

Mathematically, the radius of curvature at some point, s , along a path is defined as:

$$\rho(s) = \frac{1}{\left| \frac{d\hat{T}}{ds} \right|} \quad (176)$$

where \hat{T} is the unit tangent vector at the point, s , on the curve:

$$\hat{T} = \frac{d\vec{r}}{ds} \quad (177)$$

It is important to note the distinction that \vec{r} is a vector describing the coordinates of a point

$$\vec{r} = x\hat{i} + y\hat{j} + z\hat{k} \quad (178)$$

while s is simply the path length to that point

$$s = s(t) = \int_{t_0}^t \frac{d\vec{r}}{d\tau}(\tau) d\tau \quad (179)$$

For this work, the value of s was computed using a first-order marching scheme

$$s_t \cong s_{t-1} + \sqrt{(x_t - x_{t-1})^2 + (y_t - y_{t-1})^2 + (z_t - z_{t-1})^2} \quad (180)$$

where the subscript represents the time step index

A second-order finite difference method was the used to compute the derivative in equation (177). Considering the three-dimensional case at time, t , the values of x , y , and z were used at times $t + 1$ and $t - 1$:

$$\hat{T} = \frac{x_{t+1} - x_{t-1}}{s_{t+1} - s_{t-1}}\hat{i} + \frac{y_{t+1} - y_{t-1}}{s_{t+1} - s_{t-1}}\hat{j} + \frac{z_{t+1} - z_{t-1}}{s_{t+1} - s_{t-1}}\hat{k} \quad (181)$$

The derivative in equation (176) is then computed using the result of equation (181):

$$\frac{d\hat{T}}{ds} = \frac{\hat{T}_{t+1} - \hat{T}_{t-1}}{s_{t+1} - s_{t-1}} \quad (182)$$

or in terms of x , y , z , and s this gives

$$\begin{aligned} \frac{d\hat{T}}{ds} = & \frac{x_{t+2}(s_{t-2}-s_t) + x_t(s_{t+2}-s_{t-2}) + x_{t-2}(s_t-s_{t+2})}{(s_{t+2}-s_t)(s_{t-2}-s_t)(s_{t+1}-s_{t+1})} \hat{i} \\ & + \frac{y_{t+2}(s_{t-2}-s_t) + y_t(s_{t+2}-s_{t-2}) + y_{t-2}(s_t-s_{t+2})}{(s_{t+2}-s_t)(s_{t-2}-s_t)(s_{t+1}-s_{t+1})} \hat{j} \\ & + \frac{z_{t+2}(s_{t-2}-s_t) + z_t(s_{t+2}-s_{t-2}) + z_{t-2}(s_t-s_{t+2})}{(s_{t+2}-s_t)(s_{t-2}-s_t)(s_{t+1}-s_{t+1})} \hat{k} \end{aligned} \quad (183)$$

which in turn gives

$$\left| \frac{d\hat{T}}{ds} \right| = \frac{\sqrt{\left(\frac{x_{t+2}-x_t}{s_{t+2}-s_t} - \frac{x_t-x_{t-2}}{s_t-s_{t-2}} \right)^2 + \left(\frac{y_{t+2}-y_t}{s_{t+2}-s_t} - \frac{y_t-y_{t-2}}{s_t-s_{t-2}} \right)^2 + \left(\frac{z_{t+2}-z_t}{s_{t+2}-s_t} - \frac{z_t-z_{t-2}}{s_t-s_{t-2}} \right)^2}}{s_{t+1}-s_{t-1}} \quad (184)$$

The radius of curvature can then be calculated according to equation (176) to give

$$\rho(t) = \frac{s_{t+1}-s_{t-1}}{\sqrt{\left(\frac{x_{t+2}-x_t}{s_{t+2}-s_t} - \frac{x_t-x_{t-2}}{s_t-s_{t-2}} \right)^2 + \left(\frac{y_{t+2}-y_t}{s_{t+2}-s_t} - \frac{y_t-y_{t-2}}{s_t-s_{t-2}} \right)^2 + \left(\frac{z_{t+2}-z_t}{s_{t+2}-s_t} - \frac{z_t-z_{t-2}}{s_t-s_{t-2}} \right)^2}} \quad (185)$$

Considering the radius of curvature in the horizontal plane only, this becomes:

$$\rho(t) = \frac{\tilde{s}_{t+1}-\tilde{s}_{t-1}}{\sqrt{\left(\frac{x_{t+2}-x_t}{\tilde{s}_{t+2}-\tilde{s}_t} - \frac{x_t-x_{t-2}}{\tilde{s}_t-\tilde{s}_{t-2}} \right)^2 + \left(\frac{y_{t+2}-y_t}{\tilde{s}_{t+2}-\tilde{s}_t} - \frac{y_t-y_{t-2}}{\tilde{s}_t-\tilde{s}_{t-2}} \right)^2}} \quad (186)$$

where \tilde{s} is used to represent the path length in the horizontal plane

$$\tilde{s}_t \cong \tilde{s}_{t-1} + \sqrt{(x_t-x_{t-1})^2 + (y_t-y_{t-1})^2} \quad (187)$$

APPENDIX D - CONTROLLER DEVELOPMENT

D.1 State Space Equations

In state space, the submarine model is represented by the following equations

$$\dot{\mathbf{x}} = \mathbf{A}\mathbf{x} + \mathbf{B}\mathbf{u} + \mathbf{M}\mathbf{w} \quad (188)$$

$$\mathbf{y} = \mathbf{C}\mathbf{x} + \mathbf{D}\mathbf{u} + \mathbf{I}n \quad (189)$$

where \mathbf{x} is the vehicle state vector

$$\mathbf{x} = [u \ v \ w \ p \ q \ r \ x \ y \ z \ \phi \ \theta \ \psi]^T, \quad (190)$$

\mathbf{u} is the controller output vector given by the commanded plane deflections, rudder deflection, and propeller speed

$$\mathbf{u} = [\delta_{fp} \ \delta_{fs} \ \delta_{ap} \ \delta_{as} \ \delta_r \ n]^T \quad (191)$$

and \mathbf{y} is the vehicle output

$$\mathbf{y} = [u \ z \ \phi \ \theta \ \psi]^T \quad (192)$$

The construction of the plant matrix, \mathbf{A} , for a six degree-of-freedom submarine is complicated; it is easiest to visualize the 12×12 matrix as the union of four 6×6 sub-matrices as given by

$$\mathbf{A} = \begin{bmatrix} -(\mathbf{M}_{rb} + \mathbf{M}_A)^{-1}(\mathbf{C}_{rb} + \mathbf{C}_A + \mathbf{D}_d) & -(\mathbf{M}_{rb} + \mathbf{M}_A)^{-1}\mathbf{G} \\ \mathbf{Q} & \mathbf{0} \end{bmatrix} \quad (193)$$

where

\mathbf{M}_{rb} is the rigid body mass matrix

$$\mathbf{M}_{rb} = \begin{bmatrix} m & 0 & 0 & 0 & mz_g & -my_g \\ 0 & m & 0 & -mz_g & 0 & mx_g \\ 0 & 0 & m & my_g & -mx_g & 0 \\ 0 & -mz_g & my_g & I_{xx} & -I_{xy} & -I_{xz} \\ mz_g & 0 & -mx_g & -I_{yx} & I_{yy} & -I_{yz} \\ -my_g & mx_g & 0 & -I_{zx} & -I_{zy} & I_{zz} \end{bmatrix} \quad (194)$$

\mathbf{C}_{rb} is the coriolis matrix (195)

$$C_{rb} = \begin{bmatrix} 0 & 0 & 0 & m(y_g q + z_g r) & -m(x_g q - w) & -m(x_g r + v) \\ 0 & 0 & 0 & -m(z_g q + x_g p) & m(z_g r + x_g p) & -m(y_g r - u) \\ 0 & 0 & 0 & -m(z_g p - v) & m(z_g r + x_g p) & m(x_g p + y_g q) \\ -m(y_g q + z_g r) & m(y_g p + w) & m(z_g p - v) & 0 & -I_{yz}q - I_{xz}p + I_{zz}r & I_{yz}r + I_{xy}p - I_{yy}q \\ m(x_g q - w) & -m(z_g r + x_g p) & m(z_g q + x_g p) & I_{yz}q + I_{xz}p - I_{zz}r & 0 & -I_{xz}r - I_{xy}q + I_{xx}p \\ m(x_g r + v) & m(y_g r - u) & -m(x_g p + y_g q) & -I_{yz}r - I_{xy}p + I_{yy}q & I_{xz}r + I_{xy}q - I_{xx}p & 0 \end{bmatrix}$$

M_A is the added mass matrix

$$M_A = - \begin{bmatrix} X_u & X_v & X_w & X_p & X_q & X_r \\ Y_u & Y_v & Y_w & Y_p & Y_q & Y_r \\ Z_u & Z_v & Z_w & Z_p & Z_q & Z_r \\ K_u & K_v & K_w & K_p & K_q & K_r \\ M_u & M_v & M_w & M_p & M_q & M_r \\ N_u & N_v & N_w & N_p & N_q & N_r \end{bmatrix} \quad (196)$$

C_A is the coriolis contribution to the mass matrix

$$C_A = \begin{bmatrix} 0 & 0 & 0 & 0 & -a_3 & a_2 \\ 0 & 0 & 0 & a_3 & 0 & -a_1 \\ 0 & 0 & 0 & -a_2 & a_1 & 0 \\ 0 & -a_3 & a_2 & 0 & -b_3 & b_2 \\ a_3 & 0 & -a_1 & b_3 & 0 & -b_1 \\ -a_2 & a_1 & 0 & -b_2 & b_1 & 0 \end{bmatrix} \quad (197)$$

where

$$a_1 = X_u \cdot u + X_v \cdot v + X_w \cdot w + X_p \cdot p + X_q \cdot q + X_r \cdot r, \quad (198)$$

$$a_2 = X_v \cdot u + Y_v \cdot v + Y_w \cdot w + Y_p \cdot p + Y_q \cdot q + Y_r \cdot r, \quad (199)$$

$$a_3 = X_w \cdot u + Y_w \cdot v + Z_w \cdot w + Z_p \cdot p + Z_q \cdot q + Z_r \cdot r, \quad (200)$$

$$b_1 = X_p \cdot u + Y_p \cdot v + Z_p \cdot w + K_p \cdot p + K_q \cdot q + K_r \cdot r, \quad (201)$$

$$b_2 = X_u \cdot u + Y_q \cdot v + Z_q \cdot w + K_q \cdot p + M_q \cdot q + M_r \cdot r, \quad (202)$$

and

$$b_3 = X_u \cdot u + Y_v \cdot v + Z_w \cdot w + K_p \cdot p + M_q \cdot q + N_r \cdot r \quad (203)$$

The linear damping matrix, \mathbf{D} , is given by

$$\mathbf{D}_d = - \begin{bmatrix} X_u & X_v & X_w & X_p & X_q & X_r \\ Y_u & Y_v & Y_w & Y_p & Y_q & Y_r \\ Z_u & Z_v & Z_w & Z_p & Z_q & Z_r \\ K_u & K_v & K_w & K_p & K_q & K_r \\ M_u & M_v & M_w & M_p & M_q & M_r \\ N_u & N_v & N_w & N_p & N_q & N_r \end{bmatrix} \quad (204)$$

\mathbf{Q} is the rotation matrix with elements i and j defined by the dot product of unit normal vectors e_i and e_j .

D.2 LQG/LTR Controller Design

D.2.1 Determination of W_{in}

The method of determining the covariance matrix, W_{in} , of the disturbances for the LQG/LTR controller is reproduced below. The derivation is reproduced from Field (2000).

A common design requirement is to have the singular value curves together at crossover frequency. To accomplish this, singular value decomposition is used (see Strang, 1988, for example, for further information on singular value decomposition)

$$C(j\omega I - A)^{-1} M \left(\frac{1}{\mu} W \right)^{\frac{1}{2}} = U E V \quad (205)$$

This is solved for a frequency of 5.42 rad/sec. W_2 is defined according to

$$W_2^{1/2} = W^{1/2} (I + \alpha_1 \text{real}(v_1 v_1^T)) \cdot (I + \alpha_2 \text{real}(v_2 v_2^T)) \cdot \dots \cdot (I + \alpha_5 \text{real}(v_5 v_5^T)) \quad (206)$$

where α_i is a multiplier for scaling each particular singular value and v_i is a column vector of V .

To bring the values together, α_i is selected as

$$\alpha_i = \frac{1}{E_{ii}} - 1 \quad i = 1, 2, \dots, 5 \quad (207)$$

and the value of W_{in} used in determining the filter gains is

$$W_{in} = W_2^{1/2} (W_2^{1/2})^T \quad (208)$$

D.2.2 Tuning of LQG/LTR Parameters

Simulations of straight and level flight in sea state three head seas were used to obtain the optimal LQG/LTR tuning parameters (μ and ρ). The fast Fourier transform (FFT) was used to determine the frequency response of the vehicle in depth and pitch as well as the control effort in terms of bowplane deflection. The resulting spectra are shown in Figure D-1 through Figure D-3 for the combinations of μ and ρ given in Table D-1. The values in the table were based on ranges suggested by Field (2000).

Table D-1 LQG/LTR tuning parameter combinations

Case	μ	ρ
1	0.05	0.5
2	0.005	0.5
3	0.005	0.05
4	0.0005	0.05
5	0.0005	0.005

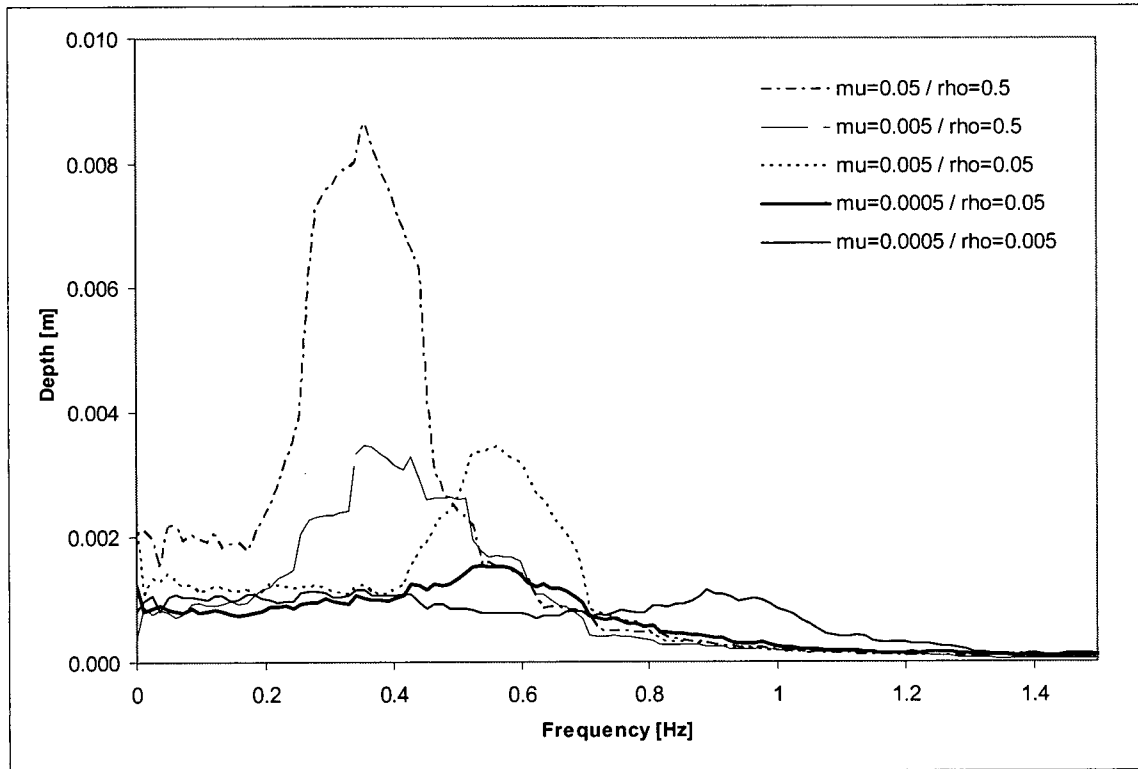


Figure D-1 Depth response spectra for various LQG/LTR parameters (sea state three head seas)

The best compromise between performance and control effort is obtained with $\mu = 0.0005$ and $\rho = 0.05$. Increasing ρ beyond 0.05 increased the plane activity (control effort) and also increased the system sensitivity to higher frequency disturbances. The combination of $\mu = 0.0005$ and $\rho = 0.05$ had the lowest significant amplitudes (proportional to the area under the spectra).

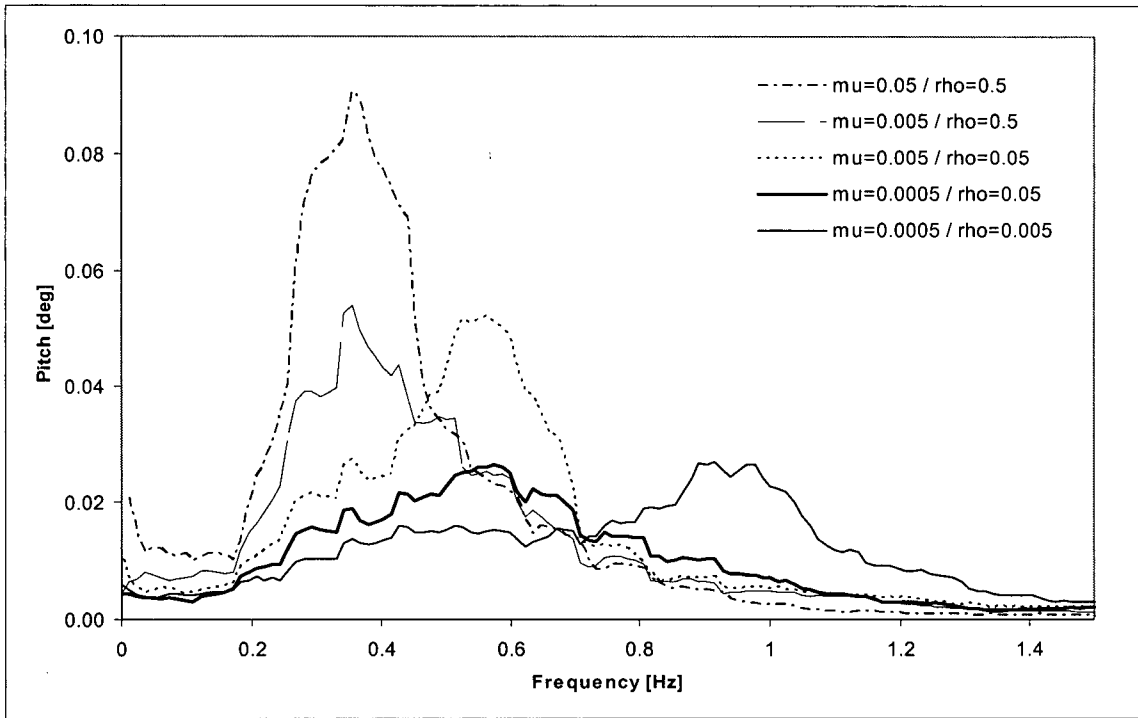


Figure D-2 Pitch response spectra for various LQG/LTR parameters (sea state three head seas)

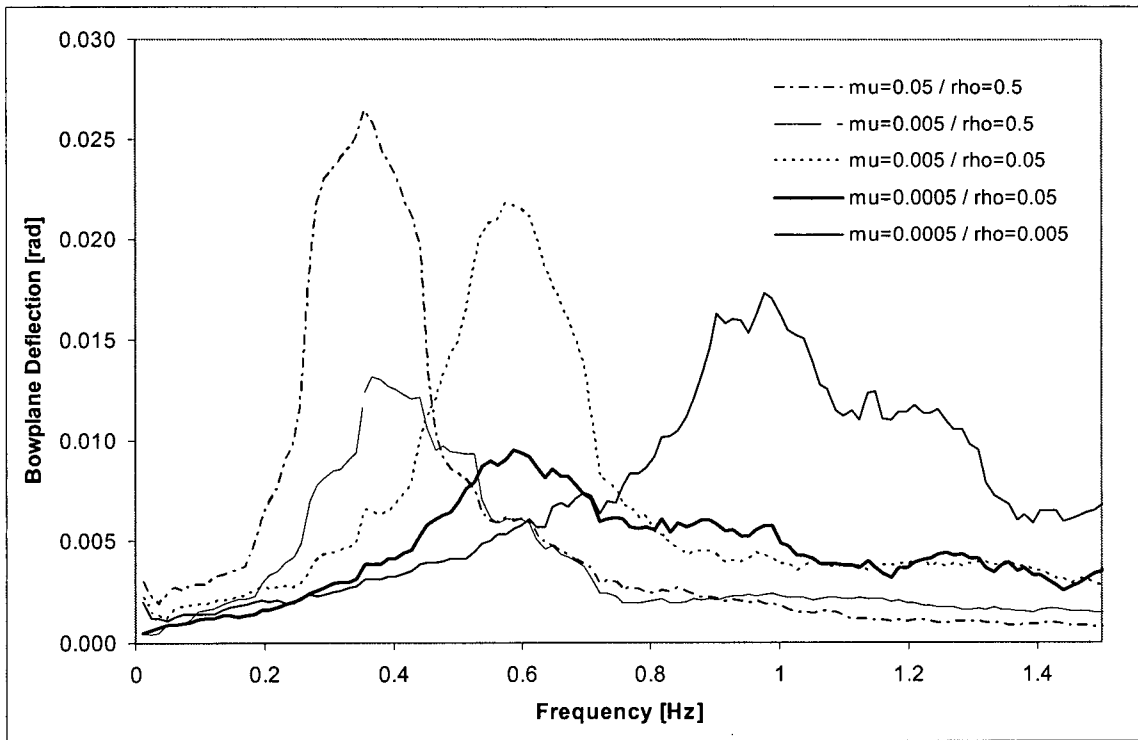


Figure D-3 Bowplane spectra for various LQG/LTR parameters (sea state three head seas)

APPENDIX E - MATLAB / SIMULINK PROGRAM

E.1 MATLAB Simulation m.file® Summary

E.1.1 Overview

The simulation m-files® are listed below in Table E-1 with a brief description. The complete code is provided in the following sections.

Table E-1 Summary of simulation m.file®

Filename ^a	Description
BatchfileX.m	initial file run in simulation; calls other files and stores data
Calcu0X.m	determines the feed forward control outputs for initial state
flqgdesign.m	computes the LQG/LTR controller and filter gains
fuzrepid.m	computes and reassigns the fuzzy-tuned PD series compensator gains
gsrepid.m	reassigns PD controller gains in gain scheduling implementation
Jmat.m	determines forces and moments on the vehicle given the state
LinearizeX.m	creates plant matrices A and B based on derivatives of system equations
Loadparam.m	loads all geometric, kinematic, and dynamic parameters
SiminitX.m	initializes the simulation environment
rid.m	removes row pos from matrix Ain to give matrix A
ridrow.m	removes row pos from matrix Ain to give matrix A
smlqgdesign.m	determines nine sliding mode controllers from LQG/LTR
smlqggainset.m	reassigns the sliding mode controller gains
SPMA.m	determines body forces and moments in the plant
SPMB.m	determines plane forces and moments in the plant
SPMB_S.m	determines plane forces and moments in the simulated plant
swnoise.m	produces wave forces on a circular hull shape

a. X indicates controller name (such as PD or LQG)

E.1.2 Batchfile.m

```

%%%%%%%%%%%%%%%%%%%%%%%%%%%%%%%%%%%%%%%%%%%%%%%%%%%%%%%%%%%%%%%%%%%%%%%%
%
% batchfilpid.m
%
% inputs:  none
% outputs: none
% initial file run in simulation; calls other files and stores data
% written by Peter Ostafichuk
% Nov 2003
%%%%%%%%%%%%%%%%%%%%%%%%%%%%%%%%%%%%%%%%%%%%%%%%%%%%%%%%%%%%%%%%%%%%%%%%

clear                % clears all variables
clear global         % clears all global variables

% added directories to the MATLAB path
addpath c:\subsim
addpath c:\subsim\data
addpath c:\subsim\variables
addpath c:\subsim\models
addpath c:\subsim\pid

% global variables
global Kpfac        % controller proportional gain factor
global Kdfac        % controller derivative gain factor
global Mfaint       % boolean for BP-SP interaction modelling in plant
global Msaton       % boolean for plane stall modelling in plant
global Meffdef      % boolean for BP trim effect modelling in plant
global Myaweff      % boolean for BP yaw effect modelling in plant
global Sfaint       % boolean for BP-SP interaction modelling in controller
global Ssaton       % boolean for plane stall modelling in controller
global Seffdef      % boolean for BP trim effect modelling in controller
global Syaweff      % boolean for BP yaw effect modelling in controller
global Bptype Sptype %strings indicating bowplane and sternplane types

% initialization
Kpfac=4;% controller proportional gain factor
Kdfac=2;% controller derivative gain factor

% turn on all modelling effects in controller and plant
Model=1;
Simulation=1;
Mfaint=Model;
Msaton=Model;
Meffdef=Model;
Myaweff=Model;
Sfaint=Simulation;
Ssaton=Simulation;
Seffdef=Simulation;
Syaweff=Simulation;

for loop = 1:7, % start loop; cycle between different types of planes
    switch(loop)
        case 1
            Bptype = 'std';
            Sptype = 'std';
        case 2
            Bptype = 'short';
            Sptype = 'std';
        case 3

```

```

        BPtrype = 'long';
        SPtype = 'std';
    case 4
        BPtrype = 'anh';
        SPtype = 'std';
    case 5
        BPtrype = 'std';
        SPtype = 'long';
    case 6
        BPtrype = 'std';
        SPtype = 'ytail';
    case 7
        BPtrype = 'keel';
        SPtype = 'std';
    end;

% call simulation initialization m.file
siminitpid;

%assign model name
model='pid';

% determine simulation filename
datafile=strcat('c:\subsim\data\Oct2003\',model, '-', BPtrype, '-', SPtype,...
    '-', num2str(Kpfac), '-', num2str(Kdfac), '.wkl');

% set simulation options
options=simset('Solver','ode45','RelTol',1e-3,'AbsTol',1e-6,'Refine',1);

%run simulation from time 0 to 70 seconds
sim(model, [0, 70], options);
%write the datafile to spreadsheet for use in excel
wklwrite(datafile,[T X U]);

% simulation routine for wave spectra
% currently disabled
%sim(model,[0 81.92],options);% run simulation for 4096 timesteps
%ffft=0:50/4096:50; fft=ffft;% assign frequencies used to vector fft
%Xfft=abs(fft(X(:,:))*2/4096);% conduct FFT of plant output vector X
%Ufft=abs(fft(U(:,:))*2/4096);% conduct FFT of controller output U
%zerorow=zeros(4097,1); % a row of zeros for separators

% write the FFT data file, separate data by rows of zeros
%wklwrite(datafile,[T X zerorow U zerorow fft Xfft zerorow Ufft]);

end; %end for loop
end; %end batchfile.m

```

E.1.3 Calcu0

```

%%%%%%%%%%%%%%%%%%%%%%%%%%%%%%%%%%%%%%%%%%%%%%%%%%%%%%%%%%%%%%%%%%%%%%%%
%
% calcu0pid.m
%
% inputs:  state vector for linearization
% outputs: feed forward controller outputs
% called by simint.m
% determines the feedforward control outputs for initial state
% written by Adrian Field
% revised by Peter Ostafichuk
% Nov 2003
%%%%%%%%%%%%%%%%%%%%%%%%%%%%%%%%%%%%%%%%%%%%%%%%%%%%%%%%%%%%%%%%%%%%%%%%
function[u0]=calcu0(xlin_1);

% global variables (mass matrix and feed forward control output)
global invMM MM u0

%initial guess for control surface deflections
u1=[0.1 0.1 -0.1 -0.1 0 10]';

%initialize u0
u0=[0 0 0 0 0 0]';

%initialize computed state
x0_=[inv(MM), zeros(6,6); zeros(6,6), eye(6,6)]*SPMA(xlin_1,2);

%loop until u0 ceases to change
while (abs(u0(1)-u1(1))+abs(u0(2)-u1(2))+abs(u0(3)-u1(3))+abs(u0(4)-u1(4))+...
      abs(u0(5)-u1(5))+abs(u0(6)-u1(6)))>0.000001
    u0=u1; %update u0
    x1_=[inv(MM), zeros(6,6); zeros(6,6), eye(6,6)]*SPMB_S(xlin_1,u0);%find new state
    [A,B]=linearizepid(xlin_1, u0);%linearize state
    delu=-pinv([inv(MM), zeros(6,6); zeros(6,6), eye(6,6)]*B)*(x0_+x1_);%compute delta u0
    delu(1:5)=delu(1:5)/10;%relax delta u0 value (slower but more stable convergence)
    u1=u0+delu;%assign new u1
end; %while loop (u0 isn't changing)

u0 = u1%update u0

%assign feedforward control to simulation
set_param('pid/Controller/SSFF','value','u0');

```

E.1.4 flqgdesign.m

```

%%%%%%%%%%%%%%%%%%%%%%%%%%%%%%%%%%%%%%%%%%%%%%%%%%%%%%%%%%%%%%%%%%%%%%%%
%
% flqgdesign.m
%
% inputs:  state and control output
% outputs: LQG/LTR controller
% siminit
% computes the LQG/LTR controller and filter gains
% written by Adrian Field 1999
% revised by Peter Ostafichuk Nov 2003
%%%%%%%%%%%%%%%%%%%%%%%%%%%%%%%%%%%%%%%%%%%%%%%%%%%%%%%%%%%%%%%%%%%%%%%%

function []=flqgdesign(xlin,ui);

%controller gains and parameters as global variables
global A10in B10in C10in L10in K10in Ko Ki
global mu ro

%evaluation frequency range (log values)
freq=logspace(-2,2);

%compute linearized plant
[A,B,Aspm,Bspm]=linearizeflqg(xlin,ui);

%removed uncontrolled states from plant matrices
A1=rid(Aspm,7);
A2=rid(A1,7);
B1=ridrow(Bspm,7);
B2=ridrow(B1,7);

%complete assignment of initial plant matrices
A=A2;
B=B2;
C=[
1 0 0 0 0 0 0 0 0 0;
0 0 0 0 0 0 1 0 0 0;
0 0 0 0 0 0 0 1 0 0;
0 0 0 0 0 0 0 0 1 0;
0 0 0 0 0 0 0 0 0 1;
0 0 0 0 0 0 0 0 0 1];
D=zeros(5,6);

%show open loop plant response
Gs=ss(A,B,C,D);
sigma(Gs,freq);
grid on
disp([' ']);
disp(['See system open loop response... (press any key when ready)']);
pause

% assign state space matrices for integrator augmentation
A10=A;
D10=D;
B10=B*Ki;
C10=Ko*C;
A10ind=[-0.000001*eye(6), zeros(6,10); B10, A10];
A10in=[zeros(6,6), zeros(6,10); B10, A10];
B10in=[eye(6); zeros(10,6)];
C10in=[zeros(5,6), C10];
D10in=[zeros(5,6)];

```

```

M10in=[0.5*Ki; B10];
W=eye(6);
N=eye(5);

%show open loop responses of plant with scaled inputs and outputs
G10ins=ss(A10in,B10in,C10in,zeros(5,6));
sigma(G10ins,freq);
grid on
disp([' ']);
disp(['See scaled system open loop response... (press any key when ready)']);
pause

%check controllability of system
Co=ctrb(A10in,B10in);
if (length(A10in)-rank(Co)>0)
    disp(['WARNING!!! There are uncontrollable states'])
end

%check observability of system
Ob=obsv(A10in,C10in);
if (length(C10in)-rank(Ob)>0)
    disp(['WARNING!!! There are unobservable states'])
end

if (length(C10in)-rank(Ob)==1)
    disp(['          The unobservable states are likely due to the integrator'])
end

%===== FILTER DESIGN =====

% get frequency response of system
H=freqresp(ss(A10in,M10in*sqrtm(W),C10in,zeros(5,6)),freq);

% use singular value decomposition to scale crossover frequencies
[U,E,V]=svd(H(:,:,28));%changed reference value for w=1.1 rad/sec
alpha=1./diag(E)-1;
W5=sqrtm(W)...
    *(eye(6)+alpha(1)*real(V(:,1)*V(:,1)'))...
    *(eye(6)+alpha(2)*real(V(:,2)*V(:,2)'))...
    *(eye(6)+alpha(3)*real(V(:,3)*V(:,3)'))...
    *(eye(6)+alpha(4)*real(V(:,4)*V(:,4)'))...
    *(eye(6)+alpha(5)*real(V(:,5)*V(:,5)'));
W5=W5*W5';

%determine filter (L10in) gains and show response
[L10in,P,E]=lqe(A10in,M10in,C10in,W5,mu*N);
L10ins=ss(A10in,L10in,C10in,zeros(5,5));
sigma(L10ins,freq);
grid on
disp([' ']);
disp(['See preliminary filter frequency response... (press any key when ready)']);
pause

%===== CONTROLLER DESIGN =====

% increase error weighting to pitch
Koweight=diag([1 1 1 100 1]); %error weighting for plane geometry

%determine controller (K10in) gains and show response
K10in=lqr(A10in,B10in,C10in'*Koweight*C10in,ro*eye(6));
K10ins=ss(A10in-B10in*K10in-L10in*C10in,L10in,-K10in,zeros(6,5));
KG10ins=series(K10ins,G10ins);

```

```

sigma1(KG10ins,freq);
grid on

%assign controller values to simulation
set_param('flgg/Controller/Ain','D','A10in');
set_param('flgg/Controller/Bin','D','B10in');
set_param('flgg/Controller/Cin','D','C10in');
set_param('flgg/Controller/Lin','D','L10in');
set_param('flgg/Controller/Kin','D','-K10in');
set_param('flgg/Controller/Ko','D','-Ko');
set_param('flgg/Controller/Ki','D','Ki');

```

E.1.5 fuzrepid

```

%%%%%%%%%%%%%%%%%%%%%%%%%%%%%%%%%%%%%%%%%%%%%%%%%%%%%%%%%%%%%%%%%%%%%%%%
%
% fuzrepid.m
%
% inputs:  bowplane yaw scaling factors and bp-sp interaction factor
% outputs: series compensator gains Kc and Kr
% computes and reassigns the fuzzy-tuned PD series compensator gains
% written by Peter Ostafichuk 2003
%%%%%%%%%%%%%%%%%%%%%%%%%%%%%%%%%%%%%%%%%%%%%%%%%%%%%%%%%%%%%%%%%%%%%%%%
function [] = fuzrepid(fpVfac,fsVfac,faint);

%compensator matrix gains
global Kc Kr

Kc(1,1) = 1/fpVfac;      %reduce Port BP deflection due to increased force in yaw
Kc(2,2) = 1/fsVfac;      %reduce Starboard BP deflection due to increased force in yaw
Kc(3,1) = -faint*0.596;  %subtract Port BP interaction force from Port SP
Kc(4,2) = -faint*0.596;  %subtract Starboard BP interaction force from Starboard SP

Kr(3,1) = -faint*0.596;  %subtract Port BP interaction force due to u0 from Port SP
Kr(4,2) = -faint*0.596;  %subtract Port BP interaction force due to u0 from Port SP

%reassign gains to simulation
set_param('fuzpid/Compensator','D','Kc');
set_param('fuzpid/Remu0','D','Kr');

```

E.1.6 gsrepid

```

%%%%%%%%%%%%%%%%%%%%%%%%%%%%%%%%%%%%%%%%%%%%%%%%%%%%%%%%%%%%%%%%%%%%%%%%
%
% gsrepid.m
%
% inputs:  bowplane yaw scaling factors, interaction factor
% outputs: redesigned PD controller (Kpd)
% reassigns PD controller gains in gain scheduling implementation
% written by Peter Ostafichuk 2003
%%%%%%%%%%%%%%%%%%%%%%%%%%%%%%%%%%%%%%%%%%%%%%%%%%%%%%%%%%%%%%%%%%%%%%%%
function [] = fuzgsrepid(fpVfac_, fsVfac_, faint_, ui);

%reference the global controller gains
global Kdfac Kpfac Krfac Kpd

%scale the proportional/derivative controller
Kpd(1,3)=1*Kdfac/fpVfac_; %dfp vs w
Kpd(1,9)=2*Kpfac/fpVfac_; %dfp vs z
Kpd(2,3)=1*Kdfac/fsVfac_; %dfs vs w
Kpd(2,9)=2*Kpfac/fsVfac_; %dfs vs z

Kpd(3,3)=-1*Kdfac*faint_*fpVfac_*0.596; %dap from q
Kpd(3,9)=-2*Kpfac*faint_*fpVfac_*0.596; %dap from theta
Kpd(4,3)=-1*Kdfac*faint_*fsVfac_*0.596; %das from q
Kpd(4,9)=-2*Kpfac*faint_*fsVfac_*0.596; %das from theta

%reassign the controller gains to the simulation
set_param('fuzgsrepid/Controller/K','D','-Kpd');

```

E.1.7 Jmat

```

%%%%%%%%%%%%%%%%%%%%%%%%%%%%%%%%%%%%%%%%%%%%%%%%%%%%%%%%%%%%%%%%%%%%%%%%
%
% Jmat.m
%
% inputs:   state vector
% outputs:  transformation matrix
% various
% determines forces and moments on the vehicle given the state
% written by Adrian Field 1999
%%%%%%%%%%%%%%%%%%%%%%%%%%%%%%%%%%%%%%%%%%%%%%%%%%%%%%%%%%%%%%%%%%%%%%%%

function [J] = Jmat(x);
% transformation matrix
phi=x(1);
theta=x(2);
psi=x(3);

T1=[1 0 0
    0 cos(phi) sin(phi)
    0 -sin(phi) cos(phi)];
T2=[cos(theta) 0 -sin(theta)
    0 1 0
    sin(theta) 0 cos(theta)];
T3=[cos(psi) sin(psi) 0
    -sin(psi) cos(psi) 0
    0 0 1];
J1=T3'*T2'*T1';
J2=[ 1 sin(phi)*tan(theta) cos(phi)*tan(theta)
    0 cos(phi) -sin(phi)
    0 sin(phi)/cos(theta) cos(phi)/cos(theta)];

J=[J1 zeros(3,3); zeros(3,3) J2];

```

E.1.8 Linearize

```

%%%%%%%%%%%%%%%%%%%%%%%%%%%%%%%%%%%%%%%%%%%%%%%%%%%%%%%%%%%%%%%%%%%%%%%%
%
% linearizepid.m
%
% inputs:  state xi and control output ui
% outputs: plant matrices A and B
% called by calcu0.m SPMB.m SPMB_S.m
% creates plant matrices A and B based on derivatives of system equations
% written by Adrian Field
% revised by Peter Ostafichuk
% Nov 2003
%%%%%%%%%%%%%%%%%%%%%%%%%%%%%%%%%%%%%%%%%%%%%%%%%%%%%%%%%%%%%%%%%%%%%%%%
function [A,B,Aspm,Bspm]=linearize_pid(xi,ui);

% register global variables
global Sfaint Ssaton Seffdef Syaweff Ki Kp u0
global USat LSat
global fpsat apsat assat rsat psat maxdef
global MM invMM

%load geometric, kinematic, and dynamic quantities
loadparam;

%set maximum permissible plane and propeller outputs
maxdef = 0.44;
psat = 1200;

%rename input variables by standard names
u=xi(1); v=xi(2); w=xi(3); p=xi(4); q=xi(5); r=xi(6);
x=xi(7); y=xi(8); z=xi(9); phi=xi(10); theta=xi(11); psi=xi(12);

dfp=ui(1); dfs=ui(2); dap=ui(3); das=ui(4);
dr=ui(5); dn=ui(6);

%compute the local yaw at the bowplanes and sternplanes
yawfp = -atan2((v+xfp*r),u); %port bowplane
yawfs = -yawfp; %starboard bowplane
yawap = -atan2(v,u); %port sternplane
yawas = -yawap; %starboard sternplane

%compute the local trim at the bowplanes and sternplanes
trimfp = atan2((w-xfp*q),u); %port bowplane
trimfs = trimfp; %starboard bowplane
trimap = atan2(w,u); %port sternplane
trimas = trimap; %starboard sternplane

%determine the effective deflection at planes based on local trim
dfpeff=dfp + 1.5*trimfp*Seffdef;
dfseff=dfs + 1.5*trimfs*Seffdef; %Seffdef is set in siminit,
dapeff=dap + 1.0*trimap*Seffdef; %values = 0 (no effective plane angle effects)
daseff=das + 1.0*trimas*Seffdef; % 1 (compute effective plane angle)
dreff = dr + 1.0*yawap*Seffdef;

%determine the yaw scaling factor; sternplanes set to 1 (i.e. no scaling)
%Syaweff defined in siminit, 0 = no yaw effects, 1 = yaw effects
%Foreplane Port Vertical Force Scaling Factor
fpVfac = 1 + Syaweff*(-4.2935*yawfp^3-0.2203*yawfp);
%Foreplane Starboard Vertical Force Scaling Factor
fsVfac = 1 + Syaweff*(-4.2935*yawfs^3-0.2203*yawfs);
apVfac = 1;%Aftplane Port Vertical Force Scaling Factor

```

```

asVfac = 1;%Aftplane Starboard Vertical Force Scaling Factor

%Sfaint = bowplane sternplane interaction, initialized in siminit
%port side
fapint = -1*Sfaint*(1-231.9*yawap^2+681.1*abs(yawap)^2.5-515.4*abs(yawap)^3)*... %yaw
        (0.280-15.64*abs(trimap-0.0271))^1.5+28.61*(trimap-0.0271)^2)*faintscale; %trim
%starboard side
fasint = -1*Sfaint*(1-231.9*yawas^2+681.1*abs(yawas)^2.5-515.4*abs(yawas)^3)*...%yaw
        (0.280-15.64*abs(trimas-0.0271))^1.5+28.61*(trimas-0.0271)^2)*faintscale;%trim

Re = u*L*1000000; %Reynolds number

if Ssaton == 1 %set the saturation levels (stall angles) on the planes
    %***** compute the theoretical plane saturation levels
    fpsat=min(maxdef,max(0.05,0.109*log(Re/1000000)+0.135))-1.5*trimfp;
    fssat=min(maxdef,max(0.05,0.109*log(Re/1000000)+0.135))-1.5*trimfs;
    apsatsat=min(maxdef,max(0.05,0.109*log(Re/1000000)+0.135))-1.0*trimap;
    assatsat=min(maxdef,max(0.05,0.109*log(Re/1000000)+0.135))-1.0*trimas;
    rsat = maxdef-1.0*yawap;
    %adjust the bowplane stall for yaw angle
    fpsat=min(maxdef, fpsat*(1-0.125*yawfp-7.60*yawfp^3));
    fssat=min(maxdef, fssat*(1-0.125*yawfs-7.60*yawfs^3));
else %set planes to operate at full range of deflections
    fpsat = maxdef;
    fssat = maxdef;
    apsatsat = maxdef;
    assatsat = maxdef;
    rsat = maxdef;
end;

%update the values of the saturation blocks in the simulation
USat=[fpsat fssat apsatsat assatsat rsat psat]'-u0;
LSat=-[fpsat fssat apsatsat assatsat rsat 0]'-u0;
set_param('pid/Controller/Integrator','Uppersaturationlimit','USat');
set_param('pid/Controller/Integrator','Lowersaturationlimit','LSat');

%***** Assign elements of A matrix *****
A=zeros(12,12);

A(1,1)= D3*(Xw_) *q - D3*(Xv_) *r+...
        D2*(2*Xuu*u+Xuv*v+Xuw*w) +D3*(Xup*p+Xuq*q+Xur*r)+...
        2*D2*u*(Xdfpdp*dfpeff^2+Xdfsd*dfseff^2+Xdapdap*dapeff^2 +...
        Xdasdas*daseff^2+Xdrdr*dreff^2)+ rho*D04*(Xdn/D00*dn);
A(1,2) = m*r + D3*(Yw_) *q -D3*(Yv_) *r + D2*(Xuv) *u;
A(1,3) = m*(-1) *q+ D3*(Zw_) *q-D3*(Yw_) *r+D2*(Xuw) *u;
A(1,4) = -m*(my*q+mz*r) ++D4*(Zp_) *q-D4*(Yp_) *r+D3*(Xup) *u;
A(1,5) = -m*(my) *p+m*(2*mx) + D3*(Xw_*u+Yw_*v+Zw_*w)+...
        D4*(Zp_*p+Zq_*2*q+Zr_*r)-D4*(Yq_) *r+D3*(Xuq) *u;
A(1,6) = -m*(mz) *p+m*(mx*2*r+v)+D4*(Zr_) *q-...
        D3*(Xv_*u+Yv_*v+Yw_*w)-D4*(Yp_*p+Yq_*q+Yr_*2*r)+...
        D3*(Xur) *u;
A(1,11)=- (W-B) *cos(theta);

A(2,1) = m*(-1) *r-D3*(Xw_) *p+D3*(Xu_) *r+...
        D2*(Yuu*2*u+Yuv*v+Yuw*w)+D3*(Yup*p+Yuq*q+Yur*r)+2*D2*u*...
        ((Ydfp*dfpeff+Ydfpdp*dfpeff*abs(dfpeff)) *fpVfac+...
        (Ydfs*dfseff+Ydfsdfs*dfseff*abs(dfseff)) *fsVfac+...
        (Ydap*dapeff+Ydapdap*dapeff*abs(dapeff)) *apVfac+...
        (Ydas*daseff+Ydasdas*daseff*abs(daseff)) *asVfac+...
        sqrt((Zdfp*dfpeff+Zdfpdp*dfpeff*abs(dfpeff))^2+...
        (Ydfp*dfpeff+Ydfpdp*dfpeff*abs(dfpeff))^2)*sign(Zdfp*dfpeff)*...
        fpVfac*fapint*sin(-SPdihedral)+...

```

```

sqrt((Zdfs*dfseff+Zdfsdfs*dfseff*abs(dfseff))^2+...
(Ydfs*dfseff+Ydfsdfs*dfseff*abs(dfseff))^2)*sign(Zdfs*dfseff)*...
fsVfac*fasint*sin(SPdihedral));
A(2,2) = D3*(Yw_)*p+D3*(Xv_)*r+D2*(Yuv)*u;
A(2,3) = m*p - D3*(Zw_)*p + D3*(Xw_)*r+D2*(Yuw)*u;
A(2,4) = m*(my*2*p+w)-m*(mx)*q-D3*(Xw_*u+Yw_*v+Zw_*w)-...
D4*(Zp_*2*p+Zq_*q+Zr_*r)+D4*(Xp_)*r+D3*(Yup)*u;
A(2,5) = -m*(mz*r+mx*p)-D4*(Zq_)*p+D4*(Xq_)*r+D3*(Yuq)*u;
A(2,6) = -m*(mz)*q+m*(my*2*r-u)-D4*(Zr_)*p+...
D3*(Xu_*u+Xv_*v+Xw_*w)+D4*(Xp_*p-Xq_*q-Xr_*2*r)+...
D3*(Yur)*u;
A(2,10)=(W-B)*cos(theta)*cos(phi);
A(2,11)=- (W-B)*sin(theta)*sin(phi);

A(3,1) = m*q+D3*(Xv_)*p-D3*(Xu_)*q+D2*(Zuu*2*u+Zuv*v+Zuw*w)+...
D3*(Zup*p+Zuq*q+Zur*r)+2*D2*u*...
((Zdfp*dfpeff+Zdfpdp*dfpeff*abs(dfpeff))*fpVfac+...
(Zdfs*dfseff+Zdfsdfs*dfseff*abs(dfseff))*fsVfac+...
(Zdap*dapeff+Zdapdap*dapeff*abs(dapeff))*apVfac+...
(Zdas*daseff+Zdasdas*daseff*abs(daseff))*asVfac+...
sqrt((Zdfp*dfpeff+Zdfpdp*dfpeff*abs(dfpeff))^2+...
(Ydfp*dfpeff+Ydfpdp*dfpeff*abs(dfpeff))^2)*sign(Zdfp*dfpeff)*...
fpVfac*fapint*cos(SPdihedral))+...
sqrt((Zdfs*dfseff+Zdfsdfs*dfseff*abs(dfseff))^2+...
(Ydfs*dfseff+Ydfsdfs*dfseff*abs(dfseff))^2)*sign(Zdfs*dfseff)*...
fsVfac*fasint*cos(SPdihedral));
A(3,2) = -m*p+D3*(Yv_)*p-D3*(Xv_)*q+D2*(Zuv)*u;
A(3,3) = D3*(Yw_)*p-D3*(Xw_)*q+D2*(Zuw)*u;
A(3,4) = m*(mz*2*p-v)-m*(mx)*r+...
D3*(Xv_*u+Yv_*v+Yw_*w)+D4*(Yp_*2*p+Yq_*q+Yr_*r)-...
D4*(Xp_)*q+D3*(Zup)*u;
A(3,5) = m*(mz*2*q+u)-m*(my)*r+...
D4*(Yq_)*p-D3*(Xu_*u+Xv_*v+Xw_*w)-...
D4*(Xp_*p+Xq_*2*q+Xr_*r)+D3*(Zuq)*u;
A(3,6) = -m*(mx*p+my*q)+D4*(Yr_)*p-D4*(Xr_)*q+...
+D3*(Zur)*u;
A(3,10) = -(W-B)*cos(theta)*sin(phi);
A(3,11) = -(W-B)*sin(theta)*cos(phi);

A(4,1) = m*(my*q+mz*r)+D3*(Xw_)*v-D3*(Xv_)*w+...
D4*(Xr_)*q-D4*(Xq_)*r+D3*(Kuu*2*u+Kuv*v+Kuw*w)+...
D4*(Kup*p+Kuq*q+Kur*r)+2*D2*u*...
((Zdfp*dfpeff+Zdfpdp*dfpeff*abs(dfpeff))*fpVfac*yfp-...
(Ydfp*dfpeff+Ydfpdp*dfpeff*abs(dfpeff))*fpVfac*zfp+...
(Zdfs*dfseff+Zdfsdfs*dfseff*abs(dfseff))*fsVfac*yfs-...
(Ydfs*dfseff+Ydfsdfs*dfseff*abs(dfseff))*fsVfac*zfs+...
(Zdap*dapeff+Zdapdap*dapeff*abs(dapeff))*apVfac*yap-...
(Ydap*dapeff+Ydapdap*dapeff*abs(dapeff))*apVfac*zap+...
(Zdas*daseff+Zdasdas*daseff*abs(daseff))*asVfac*yas-...
(Ydas*daseff+Ydasdas*daseff*abs(daseff))*asVfac*zas-...
sqrt((Zdfp*dfpeff+Zdfpdp*dfpeff*abs(dfpeff))^2+...
(Ydfp*dfpeff+Ydfpdp*dfpeff*abs(dfpeff))^2)*sign(Zdfp*dfpeff)*...
fpVfac*fapint*sqrt(yap^2+zap^2)+...
sqrt((Zdfs*dfseff+Zdfsdfs*dfseff*abs(dfseff))^2+...
(Ydfs*dfseff+Ydfsdfs*dfseff*abs(dfseff))^2)*sign(Zdfs*dfseff)*...
fsVfac*fasint*sqrt(yas^2+zas^2)+...
Kdr*dreff+Kdrdr*dreff*abs(dreff));
A(4,2) = -m*(my*p+w)-m*(-1)*w+...
D3*(Xw_*u+Yw_*2*v+Zw_*w)+D4*(Zp_*p+Zq_*q+Zr_*r)-...
D3*(Yv_)*w+D4*(Yr_)*q-D4*(Yq_)*r+D3*(Kuv)*u;
A(4,3) = -m*v-m*(mz*p-v)+...
D3*(Zw_)*v-D3*(Xv_*u+Yv_*v+Yw_*2*w)-D4*(Yp_*p+Yq_*q+Yr_*r)+...

```

```

D4*(Zr_)*q-D4*(Zq_)*r+D3*(Kuw)*u;
A(4,4) = -m*(my)*v-m*(mz)*w+...
(Jxz)*q-(Jxy)*r+D4*(Zp_)*v-D4*(Yp_)*w+...
D5*(Kr_)*q-D5*(Kq_)*r+D4*(Kup)*u;
A(4,5) = m*(my)*u+(Jyz*2*q+Jxz*p-Jzz*r)-(-Jyy)*r+...
+D4*(Zq_)*v-D4*(Yq_)*w+...
D4*(Xr_*u+Yr_*v+Zr_*w)+D5*(Kr_*p+Mr_*2*q+Nr_*r)+...
D5*(Mq_)*r+D4*(Kuq)*u;
A(4,6) = m*(mz)*u+(-Jzz)*q-(Jyz*2*r+Jxy*p-Jyy*q)+...
D4*(Zr_)*v-D4*(Yr_)*w+D5*(Nr_)*q+...
D4*(Xq_*u+Yq_*v+Zq_*w)+D5*(Kq_*p+Mq_*q+Mr_*2*r)+...
D4*(Kur)*u;
A(4,10)=- (my*W-by*B)*cos(theta)*sin(phi)-(mz*W-bz*B)*cos(theta)*cos(phi);
A(4,11)=- (my*W-by*B)*sin(theta)*cos(phi)+(mz*W-bz*B)*sin(theta)*sin(phi);

A(5,1) = -m*(mx*q-w)+-m*w-...
D3*(Xw_*2*u+Yw_*v+Zw_*w)-D4*(Zp_*p+Zq_*q+Zr_*r)+...
D3*(Xu_)*w+D4*(Xr_)*p+D4*(Xu_)*r+...
D3*(Muu*2*u+Muv*v+Muw*w)+D4*(Mup*p+Muq*q+Mur*r)+2*D2*u*...
((Zdfp*dfpeff+Zdfpdp*dfpeff*abs(dfpeff))*fpVfac*(-xfp)+...
(Zdfs*dfseff+Zdfsdfs*dfseff*abs(dfseff))*fsVfac*(-xfs)+...
(Zdap*dapeff+Zdapdap*dapeff*abs(dapeff))*apVfac*(-xap)+...
(Zdas*daseff+Zdasdas*daseff*abs(daseff))*asVfac*(-xas)+...
sqrt((Zdfp*dfpeff+Zdfpdp*dfpeff*abs(dfpeff))^2+...
(Ydfp*dfpeff+Ydfpdp*dfpeff*abs(dfpeff))^2)*sign(Zdfp*dfpeff)*...
fpVfac*fapint*cos(SPdihedral)*(-xap)+...
sqrt((Zdfs*dfseff+Zdfsdfs*dfseff*abs(dfseff))^2+...
(Ydfs*dfseff+Ydfsdfs*dfseff*abs(dfseff))^2)*sign(Zdfs*dfseff)*...
fsVfac*fasint*cos(SPdihedral)*(-xas)+...
Mdrdr*dreff^2);
A(5,2) = +m*(mz*r+mx*p)-D3*(Yw_)*u+D3*(Xv_)*w-...
D4*(Yr_)*p+D4*(Xv_)*r+D3*(Muv)*u;
A(5,3) = -m*(-1)*u-m*(mz*q+u)-D3*(Zw_)*u+...
D3*(Xu_*u+Xv_*v+Xw_*2*w)+D4*(Xp_*p+Xq_*q+Xr_*r)-...
D4*(Zr_)*p+D4*(Xw_)*r+D3*(Muv)*u;
A(5,4) = m*(mx)*v-(Jyz*q+Jxz*2*p-Jzz*r)+(-Jxx)*r-...
D4*(Zp_)*u+D4*(Xp_)*w-D4*(Xr_*u+Yr_*v+Zr_*w)-...
D5*(Kr_*2*p+Mr_*q+Nr_*r)+D5*(Xp_)*r+...
D4*(Mup)*u;
A(5,5) = -m*(mx)*u-m*(mz)*w-(Jyz)*p+(Jxy)*r-...
D4*(Zq_)*u+D4*(Xq_)*w-D5*(Mr_)*p+...
D5*(Xq_)*r+D4*(Muq)*u;
A(5,6) = +m*(mz)*v-(-Jzz)*p+(Jxz*2*r+Jxy*q-Jxx*p)-...
D4*(Zr_)*u+D4*(Xr_)*w-D5*(Nr_)*p+...
D4*(Xu_*u+Xv_*v+Xw_*w)+D5*(Xp_*p+Xq_*q+Xr_*2*r)+...
D4*(Mur)*u;
A(5,10)=(mx*W-bx*B)*cos(theta)*sin(phi);
A(5,11)=- (mz*W-bz*B)*cos(theta)+(mx*W-bx*B)*sin(theta)*cos(phi);

A(6,1) = -m*(mx*r+v)-m*(-1)*v+...
D3*(Xv_*2*u+Yv_*v+Yw_*w)+D4*(Yp_*p+Yq_*q+Yr_*r)-...
D3*(Xu_)*v+D4*(Xq_)*p-D4*(Xp_)*q+...
D3*(Nuu*2*u+Nuv*v+Nuw*w)+D4*(Nup*p+Nuq*q+Nur*r)+...
+2*D2*u*(Ndr*dreff+Ndrdr*dreff*abs(dreff))+...
(Ydfp*dfpeff+Ydfpdp*dfpeff*abs(dfpeff))*fpVfac*xfp+...
(Ydfs*dfseff+Ydfsdfs*dfseff*abs(dfseff))*fsVfac*xfs+...
(Ydap*dapeff+Ydapdap*dapeff*abs(dapeff))*apVfac*xap+...
(Ydas*daseff+Ydasdas*daseff*abs(daseff))*asVfac*xas+...
sqrt((Zdfp*dfpeff+Zdfpdp*dfpeff*abs(dfpeff))^2+...
(Ydfp*dfpeff+Ydfpdp*dfpeff*abs(dfpeff))^2)*sign(Zdfp*dfpeff)*...
fpVfac*fapint*sin(-SPdihedral)*(xap)+...
sqrt((Zdfs*dfseff+Zdfsdfs*dfseff*abs(dfseff))^2+...

```

```

(Ydfs*dfseff+Ydfsdfs*dfseff*abs(dfseff))^2)*sign(Zdfs*dfseff)*...
fsVfac*fasint*sin(SPdihedral)*(xas));
A(6,2) = -m*u-m*(my*r-u)+...
D3*(Yv_) *u-D3*(Xu_*u+Xv_*2*v+Xw_*w)-D4*(Xp_*p+Xq_*q+Xr_*r)+...
D4*(Yq_) *p-D4*(Yp_) *q+D3*(Nuv)*u;
A(6,3) = +m*(mx*p+my*q)+D3*(Yw_) *u-D3*(Xw_) *v+...
D4*(Zq_) *p-D4*(Zp_) *q+D3*(Nuw)*u;
A(6,4) = m*(mx)*w+(Jyz*r+Jxy*2*p-Jyy*q)-(-Jxx)*q+...
D4*(Yp_) *u-D4*(Xp_) *v+...
D4*(Xq_*u+Yq_*v+Zq_*w)+D5*(Kq_*2*p+Mq_*q+Mr_*r)-...
D5*(Kp_) *q+D4*(Nup)*u;
A(6,5) = m*(my)*w+(-Jyy)*p-(Jxz*r+Jxy*2*q-Jxx*p)+...
D4*(Yq_) *u-D4*(Xq_) *v+D5*(Mq_) *p-...
D4*(Xp_*u+Yp_*v+Zp_*w)-D5*(Kp_*p+Kq_*2*q+Kr_*r)+...
D4*(Nup)*u;
A(6,6) = -m*(mx)*u-m*(my)*v+...
(Jyz)*p-(Jxz)*q+D4*(Yr_) *u-...
D4*(Xr_) *v+D5*(Mr_) *p-D5*(Kr_) *q+...
D4*(Nur)*u;
A(6,10)=(mx*W-bx*B)*cos(theta)*cos(phi);
A(6,11)=- (mx*W-bx*B)*sin(theta)*sin(phi)+(my*W-by*B)*cos(theta);

A(7:12,1:6)=Jmat([phi,theta,psi]);

%%%%%%%%%%%%%%%%%%%%%%%%%%%%%%%%%%%%%%%%%%%%%%%%%%%%%%%%%%%%%%%%%%%%%%%% B matrix elements %%%%%%%%%
B=zeros(12,6);

B(1,1)= D2*u^2*(2*Xdfpdpf*abs(dfp));
B(1,2)= D2*u^2*(2*Xdfsdfs*abs(dfs));
B(1,3)= D2*u^2*(2*Xdapdap*abs(dap));
B(1,4)= D2*u^2*(2*Xdasdas*abs(das));
B(1,5)= D2*u^2*(2*Xdrdr*abs(dr));
B(1,6)= rho*D04*(Xdn*u/D00+2*Xdndn*dn);

B(2,1)= D2*u^2*((Ydfp+2*Ydfpdpf*dfp)*fpVfac+...
sqrt((Zdfp + 2*Zdfpdpf*dfp)^2+...
(Ydfp + 2*Ydfpdpf*dfp)^2)*sign(Zdfp)*...
fpVfac*fapint*sin(-SPdihedral));
B(2,2)= D2*u^2*((Ydfs+2*Ydfsdfs*dfs)*fsVfac+...
sqrt((Zdfs + 2*Zdfsdfs*dfs)^2+...
(Ydfs + 2*Ydfsdfs*dfs)^2)*sign(Zdfs)*...
fsVfac*fasint*sin(SPdihedral));
B(2,3)= D2*u^2*(Ydap+2*Ydapdap*dap)*apVfac;
B(2,4)= D2*u^2*(Ydas+2*Ydasdas*das)*asVfac;
B(2,5)= D2*u^2*(Ydr+2*Ydrdr*dr);

B(3,1)= D2*u^2*((Zdfp+2*Zdfpdpf*dfp)*fpVfac+...
sqrt((Zdfp + 2*Zdfpdpf*dfp)^2+...
(Ydfp + 2*Ydfpdpf*dfp)^2)*fpVfac*sign(Zdfp)*...
fapint*cos(SPdihedral));
B(3,2)= D2*u^2*((Zdfs+2*Zdfsdfs*dfs)*fsVfac+...
sqrt((Zdfs + 2*Zdfsdfs*dfs)^2+...
(Ydfs + 2*Ydfsdfs*dfs)^2)*fsVfac*sign(Zdfs)*...
fasint*cos(SPdihedral));
B(3,3)= D2*u^2*(Zdap+2*Zdapdap*dap)*apVfac;
B(3,4)= D2*u^2*(Zdas+2*Zdasdas*das)*asVfac;

B(4,1)= D2*u^2*((Zdfp+2*Zdfpdpf*dfp)*fpVfac*yfp-...
sqrt((Zdfp + 2*Zdfpdpf*dfp)^2+...
(Ydfp + 2*Ydfpdpf*dfp)^2)*fpVfac*sign(Zdfp)*...
fapint*sqrt(yap^2+zap^2));

```

```

B(4,2)= D2*u^2*((Zdfs+2*Zdfsdfs*dfs)*fsVfac*yfs+...
sqrt((Zdfs + 2*Zdfsdfs*dfs)^2+...
(Ydfs + 2*Ydfsdfs*dfs)^2)*fsVfac*sign(Zdfs)*...
fasint*sqrt(yas^2+zas^2));
B(4,3)= D2*u^2*(Zdap+2*Zdapdap*dap)*apVfac*yap;
B(4,4)= D2*u^2*(Zdas+2*Zdasdas*das)*asVfac*yas;
B(4,5)= D2*u^2*(Kdr+2*Kdrdr*dr);

B(5,1)= D2*u^2*((Zdfp+2*Zdfpdpf*dfp)*fpVfac*(-xfp)+...
sqrt((Zdfp + 2*Zdfpdpf*dfp)^2+...
(Ydfp + 2*Ydfpdpf*dfp)^2)*fpVfac*sign(Zdfp)*...
fapint*cos(SPdihedral)*(-xap));
B(5,2)= D2*u^2*((Zdfs+2*Zdfsdfs*dfs)*fsVfac*(-xfs)+...
sqrt((Zdfs + 2*Zdfsdfs*dfs)^2+...
(Ydfs + 2*Ydfsdfs*dfs)^2)*sign(Zdfs)*...
fsVfac*fasint*cos(SPdihedral)*(-xas));
B(5,3)= D2*u^2*(Zdap+2*Zdapdap*dap)*apVfac*(-xap);
B(5,4)= D2*u^2*(Zdas+2*Zdasdas*das)*asVfac*(-xas);
B(5,5)= D2*u^2*(2*Mdrdr*abs(dr));

B(6,1)= D2*u^2*((2*Xdfpdpf*abs(dfp))*(-yfp)+...
sqrt((Zdfp + 2*Zdfpdpf*dfp)^2+...
(Ydfp + 2*Ydfpdpf*dfp)^2)*fpVfac*sign(Zdfp)*...
fapint*sin(-SPdihedral)*(xap));
B(6,2)= D2*u^2*((2*Xdfsdfs*abs(dfs))*(-yfs)+...
sqrt((Zdfs + 2*Zdfsdfs*dfs)^2+...
(Ydfs + 2*Ydfsdfs*dfs)^2)*fsVfac*sign(Zdfs)*...
fasint*sin(SPdihedral)*(xas));
B(6,3)= D2*u^2*(2*Xdapdap*abs(dap))*(-yap);
B(6,4)= D2*u^2*(2*Xdasdas*abs(das))*(-yas);
B(6,5)= D2*u^2*(Ydr+2*Ydrdr*dr)*xr;

Aspm=[inv(MM), zeros(6,6); zeros(6,6), eye(6,6)]*A;
Bspm=[inv(MM), zeros(6,6); zeros(6,6), eye(6,6)]*B;

```

E.1.9 Loadparam

```

%%%%%%%%%%%%%%%%%%%%%%%%%%%%%%%%%%%%%%%%%%%%%%%%%%%%%%%%%%%%%%%%%%%%%%%%
%
% loadparam.m
%
% inputs:  none
% outputs: none
% called by: multiple
% loads all geometric, kinematic, and dynamic parameters
% written by Adrian Field
% revised by Peter Ostafichuk
% Nov 2003
%%%%%%%%%%%%%%%%%%%%%%%%%%%%%%%%%%%%%%%%%%%%%%%%%%%%%%%%%%%%%%%%%%%%%%%%

%global variables
global MM invMM
global Bptype Sptype

L=8.534;           %length (m)
m=4390; b=4605;   %mass; bouyancy (kg)
rho=1025;         %density of water (kg/m^3)
g=9.81;          %gravity m/s^2

mx=0;   my=0;   mz=0;           %position of center of mass
bx=0.086; by=0;   bz=-0.137;   %position of center of Bouyancy
                                %position of cent mass from nose (-4.173,0,0.188)
                                %position of CB from nose (-4.084,0,0.051)

Jxx=1315; Jyy=5900; Jzz=5057; %moment of inertia kg/m^2
Jxy=0; Jxz=0; Jyz=0; Jzx=0; Jzy=0; Jyx=0;
W=m*g;
B=b*g;

D0=0.5*rho; D1=D0*L; D2=D1*L; D3=D2*L; D4=D3*L; D5=D4*L;
D00=0.7159;                                     %prop dia
D04=D00^4;
A=3.141592654*0.5^2;                             %x-sectional area

%----- HULL ADDED MASS COEFFICIENTS
Xu_=-0.000949; Xv_=0; Xw_=0; Xp_=0; Xq_=0; Xr_=0;
Yu_=0; Yv_=-0.0408; Yw_=0; Yp_=0.000547; Yq_=0; Yr_=0.00139;
Zu_=0; Zv_=0; Zw_=-0.0226; Zp_=0; Zq_=-0.0000510; Zr_=0;
Ku_=0; Kv_=0.000547; Kw_=0; Kp_=-0.000105; Kq_=0; Kr_=-0.00000370;
Mu_=0; Mv_=0; Mw_=-0.0000510; Mp_=0; Mq_=-0.00175; Mr_=0;
Nu_=0; Nv_=0.00139; Nw_=0; Np_=-0.00000370; Nq_=0; Nr_=-0.00183;

%----- HULL DAMPING COEFFICIENTS
Xuu=-0.00315; Xuv=0; Xuw=0; Xup=0; Xuq=0; Xur=0;
Yuu=0; Yuv=-0.099; Yuw=0; Yup=0.00677; Yuq=0; Yur=0.0250;
Zuu=0; Zuv=0; Zuw=-0.0670; Zup=0; Zuq=-0.00658; Zur=0;
Kuu=0; Kuv=0.00406; Kuw=0; Kup=-0.00145; Kuq=0; Kur=-0.000578;
Muu=0; Muv=0; Muw=0.00120; Mup=0; Muq=-0.00687; Mur=0;
Nuu=0; Nuv=-0.005; Nuw=0; Nup=0.000086; Nuq=0; Nur=-0.00747;

%----- CONTROL SURFACE GEOMETRIC PARAMETERS -----
switch lower(Sptype)
case 'std'
    SPdihedral = 0;
    Fdap=-0.00856; Fdas=Fdap; Fdapdap=0.011; Fdasdas=Fdapdap; %standard SP
    faintscale = 1;
case 'long'

```

```

        SPdihedral = 0;
        %Fdap=-0.00889; Fdas=Fdap; Fdapdap=0.0114; Fdasdas=Fdapdap;    %long SP
        Fdap=-0.0112; Fdas=Fdap; Fdapdap=0.0144; Fdasdas=Fdapdap;    %long SP
        faintscale = 0.735;
    case 'ytail'
        SPdihedral = 3.14159265/4;
        %Fdap=-0.00889; Fdas=Fdap; Fdapdap=0.0114; Fdasdas=Fdapdap;    %long SP
        Fdap=-0.0112; Fdas=Fdap; Fdapdap=0.0144; Fdasdas=Fdapdap;    %long SP
        faintscale = 0.035;
    otherwise
        disp ('Cannot find the Sternplane type: ', SPTYPE);
    end;

switch lower(BPtype)
    case 'std'
        BPdihedral = 0;
        Fdfs=-0.00510; Fdfp=Fdfs; Fdfsdfs=-0.00191; Fdfpdpf=Fdfsdfs;    %standard BP
    case 'anh'
        BPdihedral = -3.14159265/6;
        Fdfs=-0.00510; Fdfp=Fdfs; Fdfsdfs=-0.00191; Fdfpdpf=Fdfsdfs;    %standard BP
        faintscale = 0.250;
    case 'anhl'
        BPdihedral = -3.14159265/6;
        Fdfs=-0.00668; Fdfp=Fdfs; Fdfsdfs=-0.00191; Fdfpdpf=Fdfsdfs;    %standard BP
        faintscale = 0.250;
    case 'long'
        BPdihedral = 0;
        Fdfs=-0.00668; Fdfp=Fdfs; Fdfsdfs=-0.00252; Fdfpdpf=Fdfsdfs;    %long BP
        faintscale = 0.705;
    case 'short'
        BPdihedral = 0;
        Fdfs=-0.00352; Fdfp=Fdfs; Fdfsdfs=-0.00132; Fdfpdpf=Fdfsdfs;    %short BP
        faintscale = 0.700;
    case 'keel'
        BPdihedral = 0;
        Fdfs=-0.00510; Fdfp=Fdfs; Fdfsdfs=-0.00191; Fdfpdpf=Fdfsdfs;    %standard BP
        faintscale = 0;
    otherwise
        disp ('Cannot find the Bowplane type: ', BPtype);
    end;

switch lower(BPtype)
    case 'keel'
        xfp = -0.537;    xfs = xfp;    %correct position
        %xfp = 0;    xfs = xfp;    %alternate test position
        yfp = -0.407;    yfs = -yfp;
        zfp = -0.188+0.0873+1.745;    zfs=zfp;
    otherwise
        xfp=1.865; xfs=xfp;%longitudinal position of planes and rudder
        yfp=-0.699*cos(BPdihedral);yfs=-yfp;
        zfp=-0.188+0.0873-0.699*sin(BPdihedral);zfs=zfp;    %vertical position of bowplanes
    end;

xap=-3.369;xas=xap;    xr=xap ;    %longitudinal position of planes and rudder
yap=-0.621*cos(SPdihedral);yas=-yap;yr=0;    %lateral position of planes and rudder
zap=-0.188-.0016-.621*sin(SPdihedral);zas=zap;%vertical position of sternplanes
zr=-0.188+0.528+.103;    %vertical position of rudder

%----- CONTROL SURFACE FORCE COEFFICIENTS
Xdfpdpf=-0.00362; Xdfsdfs=-0.00362;
Xdapdap=-0.00337; Xdasdas=-0.00337;
Xdrdr=-0.00342; Xdn=0.0000733; Xndn=0.1351;

```

```

Ydr=0.00917; Ydrdr=-0.00215;

Ydfs=Fdfs*sin(BPdihedral); Ydfp=-Ydfs; Ydfsdfs=Fdfsdfs*sin(BPdihedral); Ydfpdp=-Ydfsdfs;
Zdfs=Fdfs*cos(BPdihedral); Zdfp=Zdfs; Zdfsdfs=Fdfsdfs*cos(BPdihedral); Zdfpdp=Zdfsdfs;
Ydas=Fdas*sin(SPdihedral); Ydap=-Ydas; Ydasdas=Fdasdas*sin(SPdihedral); Ydapdap=-Ydasdas;
Zdas=Fdas*cos(SPdihedral); Zdap=Zdas; Zdasdas=Fdasdas*cos(SPdihedral); Zdapdap=Zdasdas;
Kdr=-zr*Ydr; Kdrdr=-zr*Ydrdr;
Mdrdr=zr*Xdrdr;
Ndr= xr*Ydr;Ndrdr= xr*Ydrdr;

%----- Mass Matrix

% inertial terms
mi=[ m 0 0 0 m*mz -m*my;
      0 0 m 0 -m*mz 0 m*mx;
      0 0 m m*my -m*mx 0;
      0 -m*mz m*my Jxx -Jxy -Jxz;
      m*mz 0 -m*mx -Jxy Jyy -Jyz;
      -m*my m*mx 0 -Jxz -Jyz Jzz];

% added mass terms
ma=-[ Xu_ Xv_ Xw_ Xp_ Xq_ Xr_;
      Yu_ Yv_ Yw_ Yp_ Yq_ Yr_;
      Zu_ Zv_ Zw_ Zp_ Zq_ Zr_;
      Ku_ Kv_ Kw_ Kp_ Kq_ Kr_;
      Mu_ Mv_ Mw_ Mp_ Mq_ Mr_;
      Nu_ Nv_ Nw_ Np_ Nq_ Nr_];

ma(1:3,1:3)=ma(1:3,1:3)*D3;
ma(1:3,4:6)=ma(1:3,4:6)*D4;
ma(4:6,1:3)=ma(4:6,1:3)*D4;
ma(4:6,4:6)=ma(4:6,4:6)*D5;

%sum of both mass matrices
MM=mi+ma;

invMM = inv(MM);

```

E.1.10 Siminit (PID)

```

%%%%%%%%%%%%%%%%%%%%%%%%%%%%%%%%%%%%%%%%%%%%%%%%%%%%%%%%%%%%%%%%%%%%%%%%
%
% siminitpid.m
%
% inputs:   none
% outputs:  none
% called by batchfile.m
% initializes the simulation environment
% written by Peter Ostafichuk
% Nov 2003
%%%%%%%%%%%%%%%%%%%%%%%%%%%%%%%%%%%%%%%%%%%%%%%%%%%%%%%%%%%%%%%%%%%%%%%%

%----- global variables for plane saturation
global fpsat fssat apsat assat rsat psat maxdef USat LSat
%----- gobal variables for modelling hydrodynamic effects in plant
global Waveon Mfaint Msaton Meffdef Myaweff
%----- global variables for modelling hydrodynamic effects in controller
global Sfaint Ssaton Seffdef Syaweff
%----- controller gain matrix
global K
%----- mass matrices and initial states
global invMM MM u0 xinit

loadparam;          %loads all geometric values

Waveon = 0;%logical value for determining if waves are used
set_param('pid/plant/Waveon1','gain','Waveon');
set_param('pid/plant/Waveon2','gain','Waveon');

% Initial states: speed = 6 m/s forward, depth = 3.5 m, all others 0
xinit=[6. 0. 0 0 0 0 0 0 3.5 0 0 0];

%compute initial control action (feed forward control)
u0=calcu0pid(xinit);

%design the pd controller
piddesign(xinit,u0);

%call the fuzzy control surfaces (if fuzzy tuning used)
%YBpfismat=readfis('YBP.fis');
%TBPfismat=readfis('TBP.fis');
%YTSPfismat=readfis('YTSP.fis');

% call the wave file
filen='wnoise3';% sea state 3

% set wave parameters
phiwd=180;          %wave direction (180 = head seas)
clear a w2
load(filen,'w2','a');
wspec=[a;w2]';
Cd=0.65;
Cm=1.95;
wseed=0;

% filtering information:
aliascutoff=25;
aliaswn=aliascutoff*2*pi;
ap=roots([1 2*0.707*aliaswn aliaswn^2]);
ap1=ap(1);

```

```
ap2=ap(2);
ag1 = ap1*ap2;
```

```
%initial values
Xhat=0;
Xhatin=0;
Fwave=0;
wavedplanes=0;
h=0;
ten_angles=0;
```

E.1.11 rid.m

```
%%%%%%%%%%%%%%%%%%%%%%%%%%%%%%%%%%%%%%%%%%%%%%%%%%%%%%%%%%%%%%%%%%%%%%%%
%
% rid.m
%
% inputs:  matrix Ain and row pos index
% outputs: matrix A
% various
% removes row pos from matrix Ain to give matrix A
% written by Adrian Field 1999
%%%%%%%%%%%%%%%%%%%%%%%%%%%%%%%%%%%%%%%%%%%%%%%%%%%%%%%%%%%%%%%%%%%%%%%%

function [A]=rid(Ain,pos);

A=[Ain(1:pos-1,1:pos-1),Ain(1:pos-1,pos+1:size(Ain,2));
   Ain(pos+1:size(Ain,1),1:pos-1),Ain(pos+1:size(Ain,1),pos+1:size(Ain,2))];
```

E.1.12 ridrow.m

```
%%%%%%%%%%%%%%%%%%%%%%%%%%%%%%%%%%%%%%%%%%%%%%%%%%%%%%%%%%%%%%%%%%%%%%%%
%
% ridrow.m
%
% inputs:  matrix Ain and row pos index
% outputs: matrix A
% various
% removes row pos from matrix Ain to give matrix A
% written by Adrian Field 1999
%%%%%%%%%%%%%%%%%%%%%%%%%%%%%%%%%%%%%%%%%%%%%%%%%%%%%%%%%%%%%%%%%%%%%%%%

function [A]=ridrow(Ain,pos);

A=[Ain(1:pos-1,:);Ain(pos+1:size(Ain,1),:)];
```

E.1.13 smlqgdesign

```

%%%%%%%%%%%%%%%%%%%%%%%%%%%%%%%%%%%%%%%%%%%%%%%%%%%%%%%%%%%%%%%%%%%%%%%%
%
% smlqgdesign.m
%
% inputs:   state and control output
% outputs:  none
% determines nine sliding mode controllers from LQG/LTR
% original LQG/LTR design procedure written by Adrian Field
% revised by Peter Ostafichuk
% Nov 2003
%%%%%%%%%%%%%%%%%%%%%%%%%%%%%%%%%%%%%%%%%%%%%%%%%%%%%%%%%%%%%%%%%%%%%%%%
function[]=smlqgdesign(xlin,ui);

%global variables defined for current controller
global A10in B10in C10in L10in K10in Ko Ki
%global variables defined for nine sliding mode controllers
global A1 A2 A3 A4 A5 A6 A7 A8 A9
global B1 B2 B3 B4 B5 B6 B7 B8 B9
global L1 L2 L3 L4 L5 L6 L7 L8 L9
global K1 K2 K3 K4 K5 K6 K7 K8 K9
global mu ro
global loop

%frequency range of interest in log units
freq=logspace(-2,2);

%determined linearized plant matrices
[A,B,Aspm,Bspm]=linearizegslqg(xlin,ui);
A11=rid(Aspm,7);
A22=rid(A11,7);
B11=ridrow(Bspm,7);
B22=ridrow(B11,7);
A=A22;
B=B22;
C=[
1 0 0 0 0 0 0 0 0 0;
0 0 0 0 0 0 1 0 0 0;
0 0 0 0 0 0 0 1 0 0;
0 0 0 0 0 0 0 0 1 0;
0 0 0 0 0 0 0 0 0 1];
D=zeros(5,6);

%examine plant open loop response
Gs=ss(A,B,C,D);
sigma(Gs,freq);
grid on
disp([' ']);
disp(['See system open loop response... (press any key when ready)']);
pause

%scaled plant and convert to integrator implementation
A10=A;
D10=D;
B10=B*Ki;
C10=Ko*C;
A10ind=[-0.000001*eye(6), zeros(6,10); B10, A10];
A10in=[zeros(6,6), zeros(6,10); B10, A10];
B10in=[eye(6); zeros(10,6)];
C10in=[zeros(5,6), C10];
D10in=[zeros(5,6)];

```

```

M10in=[0.5*Ki; B10];
W=eye(6);
N=eye(5);

%examine scaled plant open loop response
G10ins=ss(A10in,B10in,C10in,zeros(5,6));
sigma(G10ins,freq);
grid on
disp([' ']);
disp(['See scaled system open loop response... (press any key when ready)']);
pause

%check for controllability
Co=ctrb(A10in,B10in);
if (length(A10in)-rank(Co)>0)
    disp(['WARNING!!! There are uncontrollable states'])
end

%check for observability
Ob=obsv(A10in,C10in);
if (length(C10in)-rank(Ob)>0)
    disp(['WARNING!!! There are unobservable states'])
end
if (length(C10in)-rank(Ob)==1)
    disp(['          The unobservable states are likely due to the integrator'])
end

%===== filter design =====
%obtain system frequency response
H=freqresp(ss(A10in,M10in*sqrtm(W),C10in,zeros(5,6)),freq);

%use singular value decomposition to match state crossover frequencies
[U,E,V]=svd(H(:,:,26)); %changed reference value for w=1.1 rad/sec
alpha=1./diag(E)-1;
W5=sqrtm(W)...
    *(eye(6)+alpha(1)*real(V(:,1)*V(:,1)'))...
    *(eye(6)+alpha(2)*real(V(:,2)*V(:,2)'))...
    *(eye(6)+alpha(3)*real(V(:,3)*V(:,3)'))...
    *(eye(6)+alpha(4)*real(V(:,4)*V(:,4)'))...
    *(eye(6)+alpha(5)*real(V(:,5)*V(:,5)'));
W5=W5*W5';

%determine filter gains (L10in) and show response
[L10in,P,E]=lqe(A10in,M10in,C10in,W5,mu*N);
L10ins=ss(A10in,L10in,C10in,zeros(5,5));
sigma(L10ins,freq);
grid on
disp([' ']);
disp(['See preliminary filter frequency response... (press any key when ready)']);
%pause

%===== controller design=====
% weight pitch error
Koweight=diag([1 1 1 100 1]); %error weighting for plane geometry

%determine controller gains (K10in) and show response
K10in=lqr(A10in,B10in,C10in'*Koweight*C10in,ro*eye(6));
K10ins=ss(A10in-B10in*K10in-L10in*C10in,L10in,-K10in,zeros(6,5));
KG10ins=series(K10ins,G10ins);
sigma1(KG10ins,freq);
grid on

```

```
disp(strcat('Currently working on loop: ', num2str(loop)));

switch(loop)
    case 1 %default case 0 trim 0 yaw
        A1 = A10in;
        B1 = B10in;
        L1 = L10in;
        K1 = K10in;

        %assign controller parameters to simulation
        set_param('gslqg/Controller/Cin','D','C10in');
        set_param('gslqg/Controller/Ko','D','-Ko');
        set_param('gslqg/Controller/Ki','D','Ki');
        set_param('gslqg/Controller/Ain','D','A10in');
        set_param('gslqg/Controller/Bin','D','B10in');
        set_param('gslqg/Controller/Lin','D','L10in');
        set_param('gslqg/Controller/Kin','D','-K10in');

    case 2 %+trim 0 yaw
        A2 = A10in;
        B2 = B10in;
        L2 = L10in;
        K2 = K10in;

    case 3 %-trim 0 yaw
        A3 = A10in;
        B3 = B10in;
        L3 = L10in;
        K3 = K10in;

    case 4 %0trim +yaw
        A4 = A10in;
        B4 = B10in;
        L4 = L10in;
        K4 = K10in;

    case 5 %0 trim - yaw
        A5 = A10in;
        B5 = B10in;
        L5 = L10in;
        K5 = K10in;

    case 6 %+trim +yaw
        A6 = A10in;
        B6 = B10in;
        L6 = L10in;
        K6 = K10in;

    case 7 %+trim -yaw
        A7 = A10in;
        B7 = B10in;
        L7 = L10in;
        K7 = K10in;

    case 8 %-trim +yaw
        A8 = A10in;
        B8 = B10in;
        L8 = L10in;
        K8 = K10in;

    case 9 %-trim -yaw
        A9 = A10in;
        B9 = B10in;
        L9 = L10in;
        K9 = K10in;

end;
```

E.1.14 smlqggainset

```

%%%%%%%%%%%%%%%%%%%%%%%%%%%%%%%%%%%%%%%%%%%%%%%%%%%%%%%%%%%%%%%%%%%%%%%%
%
% smlqggainset.m
%
% inputs:   state and control output
% outputs:  none
% called by simulation
% reassigns the sliding mode controller gains
% written by Peter Ostafichuk
% Nov 2003
%%%%%%%%%%%%%%%%%%%%%%%%%%%%%%%%%%%%%%%%%%%%%%%%%%%%%%%%%%%%%%%%%%%%%%%%
function [] = gslqggainset(xi,ui);

%defines global variables including parameters of 9 controllers
global xinit u0 count
global A10in B10in L10in K10in Ki Ko
global A1 A2 A3 A4 A5 A6 A7 A8 A9
global B1 B2 B3 B4 B5 B6 B7 B8 B9
global L1 L2 L3 L4 L5 L6 L7 L8 L9
global K1 K2 K3 K4 K5 K6 K7 K8 K9
global maxtrim maxyaw
global count

%load geometric, kinematic, and dynamic variables
loadparam

%convert inputs to standard names
u=xi(1); v=xi(2); w=xi(3); p=xi(4);   q=xi(5);   r=xi(6);
x=xi(7); y=xi(8); z=xi(9); phi=xi(10); theta=xi(11); psi=xi(12);

dfp=ui(1); dfs=ui(2); dap=ui(3);
das=ui(4); dr=ui(5); dn=ui(6);

%compute the loacal trim and yaw at the port foreplanes
yaw = -atan2((v+xfp*r),u);
trim = atan2((w-xfp*q),u);

%determine sliding mode controller using bumpless switching
%find the four nearest-neighbor controllers;
%use switching to remove yaw effect and give high and low controller
%high and low controllers to be switched (later)
if (yaw >= 0)
    if(trim >= 0)   %CASE I - positive trim positive yaw
        Ahigh = A2 + yaw/maxyaw*(A7-A2);
        Alow = A1 + yaw/maxyaw*(A4-A1);

        Bhigh = B2 + yaw/maxyaw*(B7-B2);
        Blow = B1 + yaw/maxyaw*(B4-B1);

        Lhigh = L2 + yaw/maxyaw*(L7-L2);
        Llow = L1 + yaw/maxyaw*(L4-L1);

        Khigh = K2 + yaw/maxyaw*(K7-K2);
        Klow = K1 + yaw/maxyaw*(K4-K1);
    else           %CASE II - negative trim positive yaw
        Ahigh = A1 + yaw/maxyaw*(A4-A1);
        Alow = A3 + yaw/maxyaw*(A8-A3);

        Bhigh = B1 + yaw/maxyaw*(B4-B1);
        Blow = B3 + yaw/maxyaw*(B8-B3);
    end
end

```

```

    Lhigh = L1 + yaw/maxyaw*(L4-L1);
    Llow = L3 + yaw/maxyaw*(L8-L3);

    Khigh = K1 + yaw/maxyaw*(K4-K1);
    Klow = K3 + yaw/maxyaw*(K8-K3);
end;
%compute controller gains for CASE I and CASE II
A10in = Alow + trim/maxtrim*(Ahigh-Alow);
B10in = Blow + trim/maxtrim*(Bhigh-Blow);
L10in = Llow + trim/maxtrim*(Lhigh-Llow);
K10in = Klow + trim/maxtrim*(Khigh-Klow);

else
    if (theta >= 0)        %CASE III - positive trim negative yaw
        Ahigh = A2 + yaw/maxyaw*(A2-A6);
        Alow = A1 + yaw/maxyaw*(A1-A5);

        Bhigh = B2 + yaw/maxyaw*(B2-B6);
        Blow = B1 + yaw/maxyaw*(B1-B5);

        Lhigh = L2 + yaw/maxyaw*(L2-L6);
        Llow = L1 + yaw/maxyaw*(L1-L5);

        Khigh = K2 + yaw/maxyaw*(K2-K6);
        Klow = K1 + yaw/maxyaw*(K1-K5);

    else                    %CASE IV - negative trim negative yaw
        Ahigh = A1 + yaw/maxyaw*(A1-A5);
        Alow = A3 + yaw/maxyaw*(A3-A9);

        Bhigh = B1 + yaw/maxyaw*(B1-B5);
        Blow = B3 + yaw/maxyaw*(B3-B9);

        Lhigh = L1 + yaw/maxyaw*(L1-L5);
        Llow = L3 + yaw/maxyaw*(L3-L9);

        Khigh = K1 + yaw/maxyaw*(K1-K5);
        Klow = K3 + yaw/maxyaw*(K3-K9);

    end;

    %compute controller gains for CASE III and CASE IV
    A10in = Ahigh + trim/maxtrim*(Ahigh-Alow);
    B10in = Bhigh + trim/maxtrim*(Bhigh-Blow);
    L10in = Lhigh + trim/maxtrim*(Lhigh-Llow);
    K10in = Khigh + trim/maxtrim*(Khigh-Klow);
end;

%assign controller gains to simulation
set_param('gslqg/Controller/Ain','D','A10in');
set_param('gslqg/Controller/Bin','D','B10in');
set_param('gslqg/Controller/Lin','D','L10in');
set_param('gslqg/Controller/Kin','D','-K10in');

```

E.1.15 SPMA

```

%%%%%%%%%%%%%%%%%%%%%%%%%%%%%%%%%%%%%%%%%%%%%%%%%%%%%%%%%%%%%%%%%%%%%%%%
%
% SPMA.m
%
% inputs:   state vector
% outputs:  forces and moments on vehicle (in sys)
% called by simulations and calcu0
% determines body forces and moments in the plant
% written by Adrian Field 1999
% revised by Peter Ostafichuk
% Nov 2003
%%%%%%%%%%%%%%%%%%%%%%%%%%%%%%%%%%%%%%%%%%%%%%%%%%%%%%%%%%%%%%%%%%%%%%%%
function [sys] = SPMA(xi,flag);

%mass matrix as global variable
global MM

%reassign names of input matrix to standard names
u=xi(1); v=xi(2); w=xi(3); p=xi(4);   q=xi(5);   r=xi(6);
x=xi(7); y=xi(8); z=xi(9); phi=xi(10); theta=xi(11); psi=xi(12);

%load geoemtric, kinematic, and dynamic variables
loadparam

% transformation matrix
J=Jmat(xi(10:12));
J1=J(1:3,1:3);
J2=J(4:6,4:6);

%determine forces on submarine
if or((flag==2),(flag==3)), %flag 2 = forces; flag 3 = acceleration
    X = -m*(my*q+mz*r)*p+m*(mx*q-w)*q+m*(mx*r+v)*r+...
        D3*(Xw_*u+Yw_*v+Zw_*w)*q +D4*(Zp_*p+Zq_*q+Zr_*r)*q-...
        D3*(Xv_*u+Yv_*v+Yw_*w)*r -D4*(Yp_*p+Yq_*q+Yr_*r)*r+...
        D2*(Xuu*u+Xuv*v+Xuw*w)*u +D3*(Xup*p+Xuq*q+Xur*r)*u-...
        (W-B)*sin(theta);

    X1 = m*(v*r-w*q+mx*(q^2+r^2)-my*(p*q)+mz*(p*r))+...
        D4*(Yp_*r*p-Yr_*r^2+Zq_*q^2)+D3*(-Yv_*v*r+Zw_*w*q)+...
        D2*(Xuu*u^2)-(W-B)*sin(theta);

    Y = m*(my*p+w)*p-m*(mz*r+mx*p)*q+m*(my*r-u)*r-...
        D3*(Xw_*u+Yw_*v+Zw_*w)*p-D4*(Zp_*p+Zq_*q+Zr_*r)*p+...
        D3*(Xu_*u+Xv_*v+Xw_*w)*r+D4*(Xp_*p+Xq_*q+Xr_*r)*r+...
        D2*(Yuu*u+Yuv*v+Yuw*w)*u+D3*(Yup*p+Yuq*q+Yur*r)*u+...
        (W-B)*cos(theta)*sin(phi);

    Y1 = m*(w*p-u*r-mx*(q*p)+my*(p^2+r^2)-mz*(q*r))+...
        D4*(-Zq_*p*q)+D3*(Xu_*u*r+Yup*u*p+Yur*u*r-Zw_*w*p)+...
        D2*(Yuv*v)+(W-B)*cos(theta)*sin(phi);

    Z = m*(mz*p-v)*p+m*(mz*q+u)*q-m*(mx*p+my*q)*r+...
        D3*(Xv_*u+Yv_*v+Yw_*w)*p+D4*(Yp_*p+Yq_*q+Yr_*r)*p-...
        D3*(Xu_*u+Xv_*v+Xw_*w)*q-D4*(Xp_*p+Xq_*q+Xr_*r)*q+...
        D2*(Zuu*u+Zuv*v+Zuw*w)*u+D3*(Zup*p+Zuq*q+Zur*r)*u+...
        (W-B)*cos(theta)*cos(phi);

    Z1 = m*(u*q-v*p+mx*(r*p)-my*(r*q)+mz*(p^2+q^2))+...
        D3*(Xu_*u*q+Yv_*v*p+Yp_*p^2+Yr_*r*p+Zuq*u*q)+...
        D2*(Zuw*u*w)+(W-B)*cos(theta)*cos(phi);
end

```

```

K = m*(my*q+mz*r)*u-m*(my*p+w)*v-m*(mz*p-v)*w+...
    (Jyz*q+Jxz*p-Jzz*r)*q-(Jyz*r+Jxy*p-Jyy*q)*r+...
D3*(Xw_*u+Yw_*v+Zw_*w)*v+D4*(Zp_*p+Zq_*q+Zr_*r)*v-...
D3*(Xv_*u+Yv_*v+Yw_*w)*w-D4*(Yp_*p+Yq_*q+Yr_*r)*w+...
D4*(Xr_*u+Yr_*v+Zr_*w)*q+D5*(Kr_*p+Mr_*q+Nr_*r)*q-...
D4*(Xq_*u+Yq_*v+Zq_*w)*r-D5*(Kq_*p+Mq_*q+Mr_*r)*r+...
D3*(Kuu*u+Kuv*v+Kuw*w)*u+D4*(Kup*p+Kuq*q+Kur*r)*u+...
    (my*W-by*B)*cos(theta)*cos(phi)-(mz*W-bz*B)*cos(theta)*sin(phi);
K1 = (Jyy-Jzz)*q*r+(p*q)*Jxz-(r^2-q^2)*Jyz-(p*r)*Jxy+...
    D5*(Kr_*p*q-Mq_*q*r+Nr_*q*r)+D4*(Yr_*v*q-Zq_*w*r-Yp_*(-w*p)+Kup*u*p+Kur*u*r)+...
    D3*(Zw_*v*w-Yv_*v*w+Kuw*u*w)+(my*W-by*B)*cos(theta)*cos(phi)-(mz*W-
bz*B)*cos(theta)*sin(phi);

M = -m*(mx*q-w)*u+m*(mz*r+mx*p)*v-m*(mz*q+u)*w-...
    (Jyz*q+Jxz*p-Jzz*r)*p+(Jxz*r+Jxy*q-Jxx*p)*r-...
D3*(Xw_*u+Yw_*v+Zw_*w)*u-D4*(Zp_*p+Zq_*q+Zr_*r)*u+...
D3*(Xu_*u+Xv_*v+Xw_*w)*w+D4*(Xp_*p+Xq_*q+Xr_*r)*w-...
D4*(Xr_*u+Yr_*v+Zr_*w)*p-D5*(Kr_*p+Mr_*q+Nr_*r)*p+...
D4*(Xu_*u+Xv_*v+Xw_*w)*r+D5*(Xp_*p+Xq_*q+Xr_*r)*r+...
D3*(Muu*u+Muv*v+Muw*w)*u+D4*(Mup*p+Muq*q+Mur*r)*u-...
    (mz*W-bz*B)*sin(theta)-(mx*W-bx*B)*cos(theta)*cos(phi);

M1 = -(Jxx-Jzz)*r*p+q*r*Jxy-(q^2-r^2)*Jxy-q*p*Jyz+...
    D5*(Kp_*p*r-Kr_*q^2-r^2)-Nr_*p*r)+D4*(Yp_*v*r-Yr_*v*p-Zq_*u*q+Muq*u*q)+...
    D3*(Xu_*u*w-Zw_*u*w+Muw*u*w)-(mz*W-bz*B)*sin(theta)-(mx*W-bx*B)*cos(theta)*cos(phi);

N = -m*(mx*r+v)*u-m*(my*r-u)*v+m*(mx*p+my*q)*w+...
    (Jyz*r+Jxy*p-Jyy*q)*p-(Jxz*r+Jxy*q-Jxx*p)*q+...
D3*(Xv_*u+Yv_*v+Yw_*w)*u+D4*(Yp_*p+Yq_*q+Yr_*r)*u-...
D3*(Xu_*u+Xv_*v+Xw_*w)*v-D4*(Xp_*p+Xq_*q+Xr_*r)*v+...
D4*(Xq_*u+Yq_*v+Zq_*w)*p+D5*(Kq_*p+Mq_*q+Mr_*r)*p-...
D4*(Xp_*u+Yp_*v+Zp_*w)*q-D5*(Kp_*p+Kq_*q+Kr_*r)*q+...
D3*(Nuu*u+Nuv*v+Nuw*w)*u+D4*(Nup*p+Nuq*q+Nur*r)*u+...
    (mx*W-bx*B)*cos(theta)*sin(phi)+(my*W-by*B)*sin(theta);

N1 = -(Jyy-Jxx)*p*q+(r*p)*Jyz-(q^2-p^2)*Jxy-r*q*Jzx+...
    D5*(-Kp_*p*q+Mq_*p*q-Kr_*q*r)+D4*(Yr_*u*r+Yp_*u*p-v*q)+Zq_*w*p)+...
    D4*(Nup*u*p+Nur*u*r)+D3*(-Xu_*u*v+Yv_*u*v+Nuv*u*v)+...
    (mx*W-bx*B)*cos(theta)*sin(phi)+(my*W-by*B)*sin(theta);

x_ = J1(1,1:3)*[u v w]';
y_ = J1(2,1:3)*[u v w]';
z_ = J1(3,1:3)*[u v w]';
phi_ = J2(1,1:3)*[p q r]';
theta_ = J2(2,1:3)*[p q r]';
psi_ = J2(3,1:3)*[p q r]';

F=[X Y Z K M N x_ y_ z_ phi_ theta_ psi_]';

end;

if flag==2, sys=F; end; %for flag 2, return the forces

if flag==3, %for flag 3, return the accelerations

    xi_=[inv(MM), zeros(6,6); zeros(6,6), eye(6,6)]*F;
    sys=xi_;
end;

```

E.1.16 SPMB

```

%%%%%%%%%%%%%%%%%%%%%%%%%%%%%%%%%%%%%%%%%%%%%%%%%%%%%%%%%%%%%%%%%%%%%%%%
%
% SPMB.m
%
% inputs:  state vector and controller outputs
% outputs: forces and moments due to planes (in sys)
% called by simulations and calcu0
% determines plane forces and moments in the plant
% written by Adrian Field 1999
% revised by Peter Ostafichuk
% Nov 2003
%%%%%%%%%%%%%%%%%%%%%%%%%%%%%%%%%%%%%%%%%%%%%%%%%%%%%%%%%%%%%%%%%%%%%%%%

function [sys] = SPMB(xi,ui);

%global variables determine if hydrodynamic effects are modelled
global Mfaint Meffdef Myaweff Msaton maxdef

%rename inputs to standard variable names
u=xi(1); v=xi(2); w=xi(3); p=xi(4);   q=xi(5);   r=xi(6);
x=xi(7); y=xi(8); z=xi(9); phi=xi(10); theta=xi(11); psi=xi(12);

dfp=ui(1); dfs=ui(2); dap=ui(3);
das=ui(4); dr=ui(5); dn=ui(6);

%load geometric, kinematic, and dynamic variables
loadparam

%compute the local yaw at the bowplanes and sternplanes
yawfp = -atan2((v+xfp*r),u);   %port bowplane
yawfs = -yawfp;               %starboard bowplane
yawap = -atan2(v,u);          %port sternplane
yawas = -yawap;               %starboard sternplane

%compute the local trim at the bowplanes and sternplanes
trimfp = atan2((w-xfp*q),u);   %port bowplane
trimfs = trimfp;               %starboard bowplane
trimap = atan2(w,u);           %port sternplane
trimas = trimap;               %starboard sternplane

%determine the effective deflection at planes based on local trim
dfpeff=dfp + 1.5*trimfp*Meffdef;
dfseff=dfs + 1.5*trimfs*Meffdef;   %Meffdef is set in siminit,
dapeff=dap + 1.0*trimap*Meffdef;   %values = 0 (no effective plane angle effects)
daseff=das + 1.0*trimas*Meffdef;   %           1 (compute effective plane angle)
dreff = dr + 1.0*yawap*Meffdef;

%determine the yaw scaling factor; sternplanes set to 1 (i.e. no scaling)
%Myaweff defined in siminit, 0 = no yaw effects, 1 = yaw effects
fpVfac = 1 + Myaweff*(-4.2935*yawfp^3-0.2203*yawfp);%Foreplane Port Vertical Scaling
fsVfac = 1 + Myaweff*(-4.2935*yawfs^3-0.2203*yawfs);%Foreplane Starboard Scaling
apVfac = 1;%Aftplane Port Vertical Force Scaling Factor
asVfac = 1;%Aftplane Starboard Vertical Force Scaling Factor

%Sfaint = bowplane sternplane interaction, initialized in siminit
%port side
fapint = -1*Sfaint*(1-231.9*yawap^2+681.1*abs(yawap)^2.5-515.4*abs(yawap)^3)*...%yaw
        (0.280-15.64*abs(trimap-0.0271)^1.5+28.61*(trimap-0.0271)^2)*faintscale;%trim

%starboard side

```

```

fasint = -1*Sfaint*(1-231.9*yawas^2+681.1*abs(yawas)^2.5-515.4*abs(yawas)^3)*...%yaw
(0.280-15.64*abs(trimas-0.0271)^1.5+28.61*(trimas-0.0271)^2)*faintscale;%trim influence

Re = u*L*1000000;%Reynolds number

if Msaton == 1 %set the saturation levels (stall angles) on the planes
    %***** compute the theoretical plane saturation levels
    fpsat=min(maxdef,max(0.05,0.109*log(Re/1000000)+0.135))-1.5*trimfp;
    fssat=min(maxdef,max(0.05,0.109*log(Re/1000000)+0.135))-1.5*trimfs;
    apsatsat=min(maxdef,max(0.05,0.109*log(Re/1000000)+0.135))-1.0*trimap;
    assatsat=min(maxdef,max(0.05,0.109*log(Re/1000000)+0.135))-1.0*trimas;
    rsat = maxdef-1.0*yawap;
    %adjust the bowplane stall for yaw angle
    fpsat=min(maxdef,fpsat*(1-0.125*yawfp-7.60*yawfp^3));
    fssat=min(maxdef,fssat*(1-0.125*yawfs-7.60*yawfs^3));
else
    %set planes to operate at full range of deflections
    fpsat = maxdef;
    fssat = maxdef;
    apsatsat = maxdef;
    assatsat = maxdef;
    rsat = maxdef;
end;

%output forces based on at most the deflection at stall
dfpeff = min(dfpeff, fpsat);
dfpeff = max(dfpeff, -fpsat);
dfseff = min(dfseff, fssat);
dfseff = max(dfseff, -fssat);
dapeff = min(dapeff, apsatsat);
dapeff = max(dapeff, -apsatsat);
daseff = min(daseff, assatsat);
daseff = max(daseff, -assatsat);

%***** compute the hydrodynamic plane forces
%Drag Force
X= D2*u^2*(Xdfpdftp*dfpeff^2+Xdfsdfs*dfseff^2+Xdapdap*dapeff^2 +...
Xdasdas*daseff^2+Xdrdr*dreff^2)+ rho*D04*(Xdn*u/D00*dn+Xndn*dn*abs(dn));

%BOWPLNAES
%Side Force
Yr= D2*u^2*(Ydr*dreff+Ydrdr*dreff*abs(dreff));

Yfp = D2*u^2*... %Foreplane Port
(Ydfp*dfpeff+... %Lift coefficient slope
Ydfpdftp*dfpeff*abs(dfpeff))*...%2nd order lift coefficient
fpVfac;

Yfs = D2*u^2*... %Foreplane Starboard
(Ydfs*dfseff+... %Lift coefficient slope
Ydfsdfs*dfseff*abs(dfseff))*...%2nd order lift coefficient
fsVfac;

%Control Force
Zfp = D2*u^2*... %Foreplane Port
(Zdfp*dfpeff+... %Lift coefficient slope
Zdfpdftp*dfpeff*abs(dfpeff))*...%2nd order lift coefficient
fpVfac;%yaw angle bowplane force correction

Zfs = D2*u^2*... %Foreplane Starboard
(Zdfs*dfseff+... %Lift coefficient slope
Zdfsdfs*dfseff*abs(dfseff))*...%2nd order lift coefficient
fsVfac;%yaw angle bowplane force correction

```

```

%STERNPLANES
%Side Force
Yap = D2*u^2*... %Aftplane Port
      (Ydap*dapeff+... %Lift coefficient slope
      Ydapdap*dapeff*abs(dapeff))*...%2nd order lift coefficient
      apVfac+...
      sqrt(Yfp^2+Zfp^2)*sign(Zfp)*fapint*sin(-SPdihedral);

Yas = D2*u^2*... %Aftplane Port
      (Ydas*daseff+... %Lift coefficient slope
      Ydasdas*daseff*abs(daseff))*...%2nd order lift coefficient
      asVfac+...
      sqrt(Yfs^2+Zfs^2)*sign(Zfs)*fasint*sin(SPdihedral);

Zap = D2*u^2*... %Aftplane Port
      (Zdap*dapeff+... %Lift coefficient slope
      Zdapdap*dapeff*abs(dapeff))*...%2nd order lift coefficient
      apVfac+...
      sqrt(Yfp^2+Zfp^2)*sign(Zfp)*fapint*cos(SPdihedral); %port bowplane interaction

Zas = D2*u^2*... %Aftplane Port
      (Zdas*daseff+... %Lift coefficient slope
      Zdasdas*daseff*abs(daseff))*...%2nd order lift coefficient
      asVfac+...
      sqrt(Yfs^2+Zfs^2)*sign(Zfs)*fasint*cos(SPdihedral); %starboard bowplane interaction

Y = Yfp + Yfs + Yap + Yas + Yr;
Z = Zfp + Zfs + Zap + Zas; %combined control force due to all planes

K = yfp*Zfp-zfp*Yfp + yfs*Zfs-zfs*Yfs +...
      yap*Zap-zap*Yap + yas*Zas-zas*Yas +...
      D2*u^2*(Kdr*dreff + Kdrdr*dreff*abs(dreff));

M = -(Zfp*xfp+Zfs*xfs+Zap*xap+Zas*xas)+...%pitching moment due to plane lift
      D2*u^2*(zfp*Xdfpdpf*dfpeff^2+... %pitch M due to port foreplane drag
      zfs*Xdfsdfs*dfseff^2+... %pitch M due to starboard foreplane drag
      zap*Xdapdap*dapeff^2+... %pitch M due to port aftplane drag
      zas*Xdasdas*daseff^2+... %pitch M due to starboard aftplane drag
      Mdrdr*dr^2); %pitching moment due to rudder

N= D2*u^2*(Ndr*dreff+Ndrdr*dreff*abs(dreff)-...%yaw moment due to rudder
      yfp*Xdfpdpf*dfpeff^2-... %yaw moment due to port foreplane drag
      yfs*Xdfsdfs*dfseff^2-... %yaw moment due to starboard foreplane drag
      yap*Xdapdap*dapeff^2-... %yaw moment due to port aftplane drag
      yas*Xdasdas*daseff^2)+... %yaw mement due to starboard aftplane drag
      xfp*Yfp + xfs*Yfs + xap*Yap + xas*Yas;

x_ = 0;
y_ = 0;
z_ = 0;
phi_ = 0;
theta_ = 0;
psi_ = 0;

F=[X Y Z K M N x_ y_ z_ phi_ theta_ psi_]'; %combine forces into vector
sys= F; %function output is the force vector

```

E.1.17 SPMB_S

```

%%%%%%%%%%%%%%%%%%%%%%%%%%%%%%%%%%%%%%%%%%%%%%%%%%%%%%%%%%%%%%%%%%%%%%%%
%
% SPMB_S.m
%
% inputs:  state vector and controller outputs
% outputs: forces and moments due to planes (in sys)
% called by simulations and calcu0
% determines plane forces and moments in the simulated plant
% based on SPMB written by Adrian Field 1999
% revised by Peter Ostafichuk
% Nov 2003
%%%%%%%%%%%%%%%%%%%%%%%%%%%%%%%%%%%%%%%%%%%%%%%%%%%%%%%%%%%%%%%%%%%%%%%%

function [sys] = SPMB_S(xi,ui);

%global variables determine if hydrodynamic effects are modelled
global Sfaint Seffdef Syaweff Ssaton maxdef

%rename inputs to standard variable names
u=xi(1); v=xi(2); w=xi(3); p=xi(4);   q=xi(5);   r=xi(6);
x=xi(7); y=xi(8); z=xi(9); phi=xi(10); theta=xi(11); psi=xi(12);

dfp=ui(1); dfs=ui(2); dap=ui(3);
das=ui(4); dr=ui(5); dn=ui(6);

%load geometric, kinematic, and dynamic variables
loadparam

%compute the local yaw at the bowplanes and sternplanes
yawfp = -atan2((v+xfp*r),u);   %port bowplane
yawfs = -yawfp;               %starboard bowplane
yawap = -atan2(v,u);          %port sternplane
yawas = -yawap;               %starboard sternplane

%compute the local trim at the bowplanes and sternplanes
trimfp = atan2((w-xfp*q),u);   %port bowplane
trimfs = trimfp;              %starboard bowplane
trimap = atan2(w,u);           %port sternplane
trimas = trimap;              %starboard sternplane

%determine the effective deflection at planes based on local trim
dfpeff=dfp + 1.5*trimfp*Seffdef;
dfseff=dfs + 1.5*trimfs*Seffdef;   %Seffdef is set in siminit,
dapeff=dap + 1.0*trimap*Seffdef;   %values = 0 (no effective plane angle effects)
daseff=das + 1.0*trimas*Seffdef;   %           1 (compute effective plane angle)
dreff = dr + 1.0*yawap*Seffdef;

%determine the yaw scaling factor; sternplanes set to 1 (i.e. no scaling)
%Syaweff defined in siminit, 0 = no yaw effects, 1 = yaw effects
fpVfac = 1 + Syaweff*(-4.2935*yawfp^3-0.2203*yawfp);%Foreplane Port Vertical Force Scaling
Factor
fsVfac = 1 + Syaweff*(-4.2935*yawfs^3-0.2203*yawfs);%Foreplane Starboard Vertical Force
Scaling Factor
apVfac = 1;   %Aftplane Port Vertical Force Scaling Factor
asVfac = 1;   %Aftplane Starboard Vertical Force Scaling Factor

%Sfaint = bowplane sternplane interaction, initialized in siminit
%port side
fapint = -1*Sfaint*(1-231.9*yawap^2+681.1*abs(yawap)^2.5-515.4*abs(yawap)^3)*...%yaw
(0.280-15.64*abs(trimap-0.0271)^1.5+28.61*(trimap-0.0271)^2)*faintscale;%trim influence

```

```

%starboard side
fasint = -1*Sfaint*(1-231.9*yawas^2+681.1*abs(yawas)^2.5-515.4*abs(yawas)^3)*...%yaw
        (0.280-15.64*abs(trimas-0.0271)^1.5+28.61*(trimas-0.0271)^2)*faintscale;%trim influence

Re = u*L*1000000;%Reynolds number

if Ssat == 1 %set the saturation levels (stall angles) on the planes
    %***** compute the theoretical plane saturation levels
    fpsat=min(maxdef,max(0.05,0.109*log(Re/1000000)+0.135))-1.5*trimfp;
    fssat=min(maxdef,max(0.05,0.109*log(Re/1000000)+0.135))-1.5*trimfs;
    apsat=min(maxdef,max(0.05,0.109*log(Re/1000000)+0.135))-1.0*trimap;
    assat=min(maxdef,max(0.05,0.109*log(Re/1000000)+0.135))-1.0*trimas;
    rsat = maxdef-1.0*yawap;
    %adjust the bowplane stall for yaw angle
    fpsat=min(maxdef,fpsat*(1-0.125*yawfp-7.60*yawfp^3));
    fssat=min(maxdef,fssat*(1-0.125*yawfs-7.60*yawfs^3));
else
    %set planes to operate at full range of deflections
    fpsat = maxdef;
    fssat = maxdef;
    apsat = maxdef;
    assat = maxdef;
    rsat = maxdef;
end;

%output forces based on at most the deflection at stall
dfpeff = min(dfpeff, fpsat);
dfpeff = max(dfpeff, -fpsat);
dfseff = min(dfseff, fssat);
dfseff = max(dfseff, -fssat);
dapeff = min(dapeff, apsat);
dapeff = max(dapeff, -apsat);
daseff = min(daseff, assat);
daseff = max(daseff, -assat);

%***** compute the hydrodynamic plane forces
%Drag Force
X= D2*u^2*(Xdfpdp*dfpeff^2+Xdfsdfs*dfseff^2+Xdapdap*dapeff^2 +...
    Xdasdas*daseff^2+Xdrdr*dreff^2)+ rho*D04*(Xdn*u/D00*dn+Xdndn*dn*abs(dn));

%BOWPLNAES
%Side Force
Yr= D2*u^2*(Ydr*dreff+Ydrdr*dreff*abs(dreff));

Yfp = D2*u^2*... %Foreplane Port
    (Ydfp*dfpeff+... %Lift coefficient slope
    Ydfpdp*dfpeff*abs(dfpeff))*... %2nd order lift coefficient
    fpVfac;

Yfs = D2*u^2*... %Foreplane Starboard
    (Ydfs*dfseff+... %Lift coefficient slope
    Ydfsdfs*dfseff*abs(dfseff))*... %2nd order lift coefficient
    fsVfac;

%Control Force
Zfp = D2*u^2*... %Foreplane Port
    (Zdfp*dfpeff+... %Lift coefficient slope
    Zdfpdp*dfpeff*abs(dfpeff))*... %2nd order lift coefficient
    fpVfac; %yaw angle bowplane force correction

Zfs = D2*u^2*... %Foreplane Starboard
    (Zdfs*dfseff+... %Lift coefficient slope

```

```

Zdfsdfs*dfseff*abs(dfseff))*...      %2nd order lift coefficient
fsVfac;                               %yaw angle bowplane force correction

%STERNPLANES
%Side Force
Yap = D2*u^2*...                       %Aftplane Port
      (Ydap*dapeff+...                 %Lift coefficient slope
      Ydapdap*dapeff*abs(dapeff))*... %2nd order lift coefficient
apVfac+...
      sqrt(Yfp^2+Zfp^2)*sign(Zfp)*fapint*sin(-SPdihedral);

Yas = D2*u^2*...                       %Aftplane Port
      (Ydas*daseff+...                 %Lift coefficient slope
      Ydasdas*daseff*abs(daseff))*... %2nd order lift coefficient
asVfac+...
      sqrt(Yfs^2+Zfs^2)*sign(Zfs)*fasint*sin(SPdihedral);

Zap = D2*u^2*...                       %Aftplane Port
      (Zdap*dapeff+...                 %Lift coefficient slope
      Zdapdap*dapeff*abs(dapeff))*... %2nd order lift coefficient
      apVfac+...
      sqrt(Yfp^2+Zfp^2)*sign(Zfp)*fapint*cos(SPdihedral); %port bowplane interaction

Zas = D2*u^2*...                       %Aftplane Port
      (Zdas*daseff+...                 %Lift coefficient slope
      Zdasdas*daseff*abs(daseff))*... %2nd order lift coefficient
asVfac+...
      sqrt(Yfs^2+Zfs^2)*sign(Zfs)*fasint*cos(SPdihedral); %starboard bowplane interaction

Y = Yfp + Yfs + Yap + Yas + Yr;
Z = Zfp + Zfs + Zap + Zas;             %combined control force due to all planes

K = yfp*Zfp-zfp*Yfp + yfs*Zfs-zfs*Yfs +...
      yap*Zap-zap*Yap + yas*Zas-zas*Yas +...
      D2*u^2*(Kdr*dreff + Kdrdr*dreff*abs(dreff));

M = -(Zfp*xfp+Zfs*xfs+Zap*xap+Zas*xas)+... %pitching moment due to plane lift
      D2*u^2*(zfp*Xdfpdpf*dfpeff^2+... %pitch M due to port forplane drag
      zfs*Xdfsdfs*dfseff^2+...       %pitch M due to starboard foreplane drag
      zap*Xdapdap*dapeff^2+...       %pitch M due to port aftplane drag
      zas*Xdasdas*daseff^2+...       %pitch M due to starboard aftplane drag
      Mdrdr*dr^2);                   %pitching moment due to rudder

N= D2*u^2*(Ndr*dreff+Ndrdr*dreff*abs(dreff)-... %yaw moment due to rudder
      yfp*Xdfpdpf*dfpeff^2-...       %yaw moment due to port foreplane drag
      yfs*Xdfsdfs*dfseff^2-...       %yaw moment due to starboard foreplane drag
      yap*Xdapdap*dapeff^2-...       %yaw moment due to port aftplane drag
      yas*Xdasdas*daseff^2)+...       %yaw mement due to starboard aftplane drag
      xfp*Yfp + xfs*Yfs + xap*Yap + xas*Yas;

x_ = 0;
y_ = 0;
z_ = 0;
phi_ = 0;
theta_ = 0;
psi_ = 0;

F=[X Y Z K M N x_ y_ z_ phi_ theta_ psi_]'; %combine forces into vector
sys= F; %function output is the force vector

```

E.1.18 swnoise.m

```

%%%%%%%%%%%%%%%%%%%%%%%%%%%%%%%%%%%%%%%%%%%%%%%%%%%%%%%%%%%%%%%%%%%%%%%%
%
% swnoise.m
%
% inputs:   time state control wave direction wavespectrum Cd Cm wseed
% outputs: forces and moments on body
% various
% produces wave forces on a circular hull shape
% from wave amplitudes and frequencies found by brett.m
% calculates additive vel, acc, height for each x location
% along the hull length and adds them
% can change wave direction
% forces based on encounter frequency
% input u = d/dt(u,v,w,p,q,r),d/dt(x,y,z,phi,theta,psi),u,v,w,p,q,r,
% (x,y,z,phi,theta,psi)
% outputs d/dt(u,v,w,p,q,r) disturbance in body frame
% states are Forces and Moments in Body frame
% written by Adrian Field 1999
%%%%%%%%%%%%%%%%%%%%%%%%%%%%%%%%%%%%%%%%%%%%%%%%%%%%%%%%%%%%%%%%%%%%%%%%

function [sys,x0,str,ts]=swnoise(t,x,u,flag,phiwd,wspec,Cd,Cm,wseed);

switch flag,

    %%%%%%%%%%%%%%%
    % Initialization %
    %%%%%%%%%%%%%%%
    case 0,
        [sys,x0,str,ts]=mdlInitializeSizes;

    %%%%%%%%%%%%%%%
    % Update %
    %%%%%%%%%%%%%%%
    case 2,
        sys=mdlUpdate(t,x,u);

    %%%%%%%%%%%%%%%
    % Outputs %
    %%%%%%%%%%%%%%%
    case 3,
        sys=mdlOutputs(t,x,u);

    %%%%%%%%%%%%%%%
    % Unhandled flags %
    %%%%%%%%%%%%%%%
    case {1, 2, 3, 4, 9 },
        sys = [];

    %%%%%%%%%%%%%%%
    % Unexpected flags %
    %%%%%%%%%%%%%%%
    otherwise
        error(['Unhandled flag = ',num2str(flag)]);

end
% end csfunc

%
%=====

```

```

% mdlInitializeSizes
% Return the sizes, initial conditions, and sample times for the S-function.
%=====
%
function [sys,x0,str,ts]=mdlInitializeSizes;

sizes = simsizes;
sizes.NumContStates = 0;
sizes.NumDiscStates = 7;
sizes.NumOutputs = 13;
sizes.NumInputs = 24;
sizes.DirFeedthrough = 7;
sizes.NumSampleTimes = 1;

sys = simsizes(sizes);
x0 = [0 0 0 0 0 0 0];
str = [];
ts = [-1 0];

% end mdlInitializeSizes
%%%%%%%%%%%%%%%%%%%%%%%%%%%%%%%%%%%%%%%%%%%%%%%%%%%%%%%%%%%%%%%%%%%%%%%%

function sys=mdlUpdate(t,x,u,phiwd,wspec,Cd,Cm,wseed);

pi=3.14159;
g=9.81;
rho=1025;          % density of water

xp=u(1:12);
xi=u(13:24);

load wspec a w2

phiwr=phiwd/180*pi;          % direction of wave travel 0 to 2*pi rad. (z down)
xcg=4.173;          % location of cg
xL=8.534;          % length of hull
D=0.5;          % diameter of hull
nx=16;          % number of hull points for integration
rand('state',wseed);          % sets the seed of the random generator
offset=rand(length(w2),1)*2*pi;
unit=[cos(phiwr) sin(phiwr) 0]; % unit vector in dir. of phiw in inertial frame
T=1./(w2/(2*pi)); % period of waves
L=(g*T.^2)/(2*pi); % wavelength (based on deep water)

% Find position relative to waves
% Find phase angle
% Find wave height

for n=1:nx;
    x(n)=-xL/(nx-1)*n+xcg; % body location of hull point (nose to stern)
    xn(n)=x(n)*cos(xi(12))+xi(7); %inertial x loc. of hull point
    yn(n)=x(n)*sin(xi(12))+xi(8); %inertial y loc. of hull point
    zn(n)=-xi(9)+x(n)*sin(xi(11)); %inertial z loc. of hull point
    xw(n)=dot([xn(n) yn(n) 0],unit); % (dot) wave loc of hull point
    theta=(2*pi*xw(n)./L-w2*t+offset'); % phase angle
    h(n)=sum(a.*cos(theta)); % wave height at point neg. as submarine is pos.
    down.

    % wave vel and acc in inertial frame
    ww(n)=-sum(pi*2*a./T.*exp(2*pi*(zn(n)./L)).*sin(theta));
    vw(n)=sum(pi*2*a./T.*exp(2*pi*(zn(n)./L)).*cos(theta))*sin(phiwr-xi(12));
    uw(n)=sum(pi*2*a./T.*exp(2*pi*(zn(n)./L)).*cos(theta))*cos(phiwr-xi(12));

```

```

az(n)=-sum(-4*a.*(pi./T).^2.*exp(2*pi*(-xi(9)./L)).*cos(theta));
ay(n)=sum(4*a.*(pi./T).^2.*exp(2*pi*(-xi(9)./L)).*sin(theta))*sin(phiwr-xi(12));
ax(n)=sum(4*a.*(pi./T).^2.*exp(2*pi*(-xi(9)./L)).*sin(theta))*cos(phiwr-xi(12));

% wave vel and acc in body frame
J=Jmat(xi(10:12));
bodyvel=inv(J(1:3,1:3))*[uw(n) vw(n) ww(n)]';
bodyacc=inv(J(1:3,1:3))*[ax(n) ay(n) az(n)]';

% hull vel and acc in body frame
wh(n)=xi(3)-x(n)*xi(5);
vh(n)=xi(2)-x(n)*xi(6);
azh(n)=xp(3)-xi(1)*xi(5)+xi(2)*xi(4)+x(n)*(-xp(5));
ayh(n)=xp(2)-xi(3)*xi(4)+xi(1)*xi(6)+x(n)*(-xp(4));

% forces in body frame
Z(n)=Cd/2*rho*D*(bodyvel(3)-wh(n))*abs(bodyvel(3)-wh(n))+Cm*(pi*D^2/4)*rho*(bodyacc(3)-
azh(n));
Y(n)=Cd/2*rho*D*(bodyvel(2)-vh(n))*abs(bodyvel(2)-vh(n))+Cm*(pi*D^2/4)*rho*(bodyacc(2)-
ayh(n));

M(n)=-Z(n).*x(n);
N(n)=-Y(n).*x(n);
end;

Z=sum(Z)*xL/nx;
Y=sum(Y)*xL/nx;
M=sum(M)*xL/nx;
N=sum(N)*xL/nx;

X=0; K=0;

sys=[X Y Z K M N h(5)];

% end update

%=====  

% mdlOutputs  

% Return the block outputs.  

%=====  

%  

function sys=mdlOutputs(t,x,u);

sys=[x(1:6); zeros(6,1);x(7)];

% end mdlOutputs

```

E.2 Simulink® Block Diagrams

Table E-2 Simulink® Block Diagrams

Figure	Name	Description
Figure E-1	Generic controller layout	Basic block diagram
Figure E-2	Navigation Module	Reference signal generator
Figure E-3	Heading correction	Corrects 0 to 2π into $-\pi$ to π
Figure E-4	Compass Correction	Converts radians to degrees
Figure E-5	Write data	Stores data to workspace and displays
Figure E-6	Noise	Adds noise to measured signals
Figure E-7	Anti-aliasing filter	Butterworth filter for measurements
Figure E-8	Gain scheduling PD controller	Gain scheduling implementation layout
Figure E-9	Controller tuner	Tuner layout
Figure E-10	Controller with series compensation	Series compensation layout

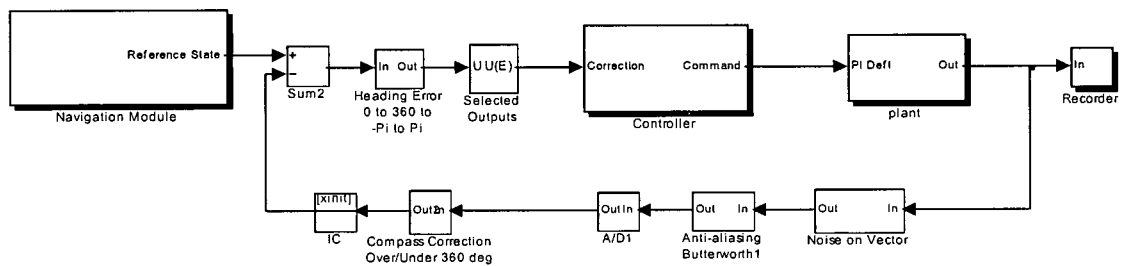


Figure E-1 Generic controller layout

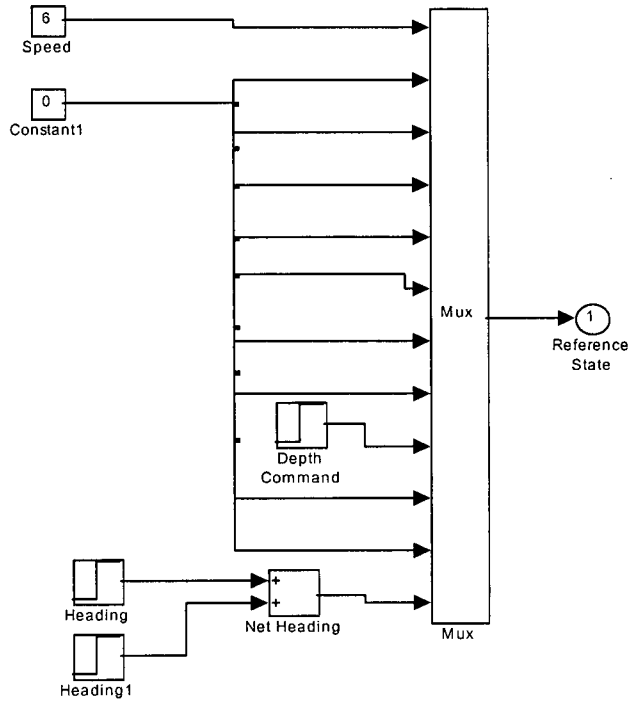


Figure E-2 Navigation Module

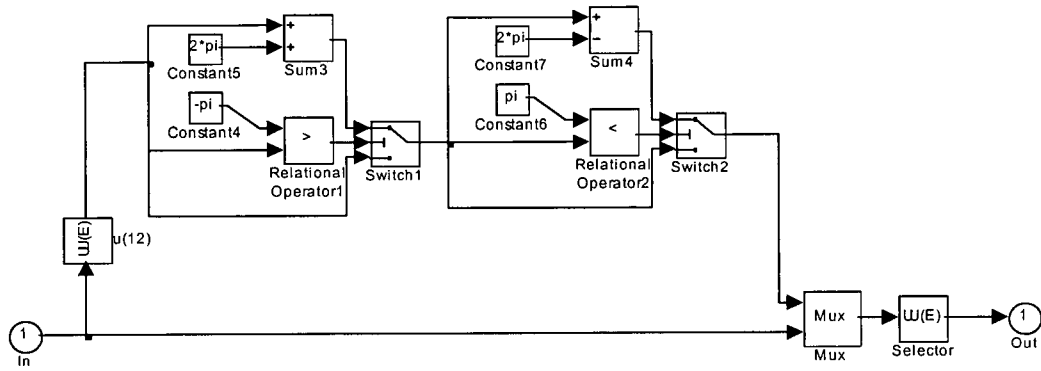


Figure E-3 Heading correction

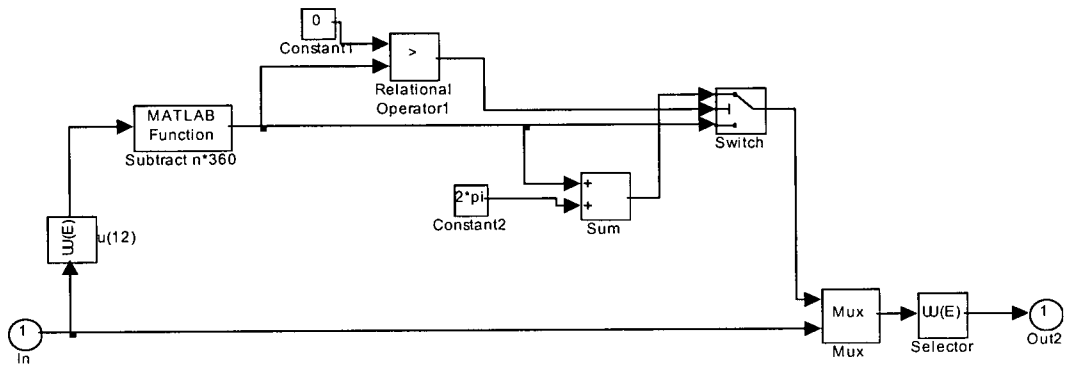


Figure E-4 Compass Correction

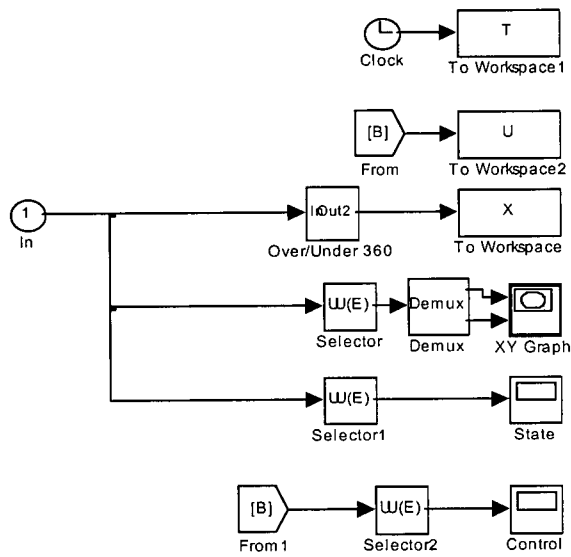


Figure E-5 Write data

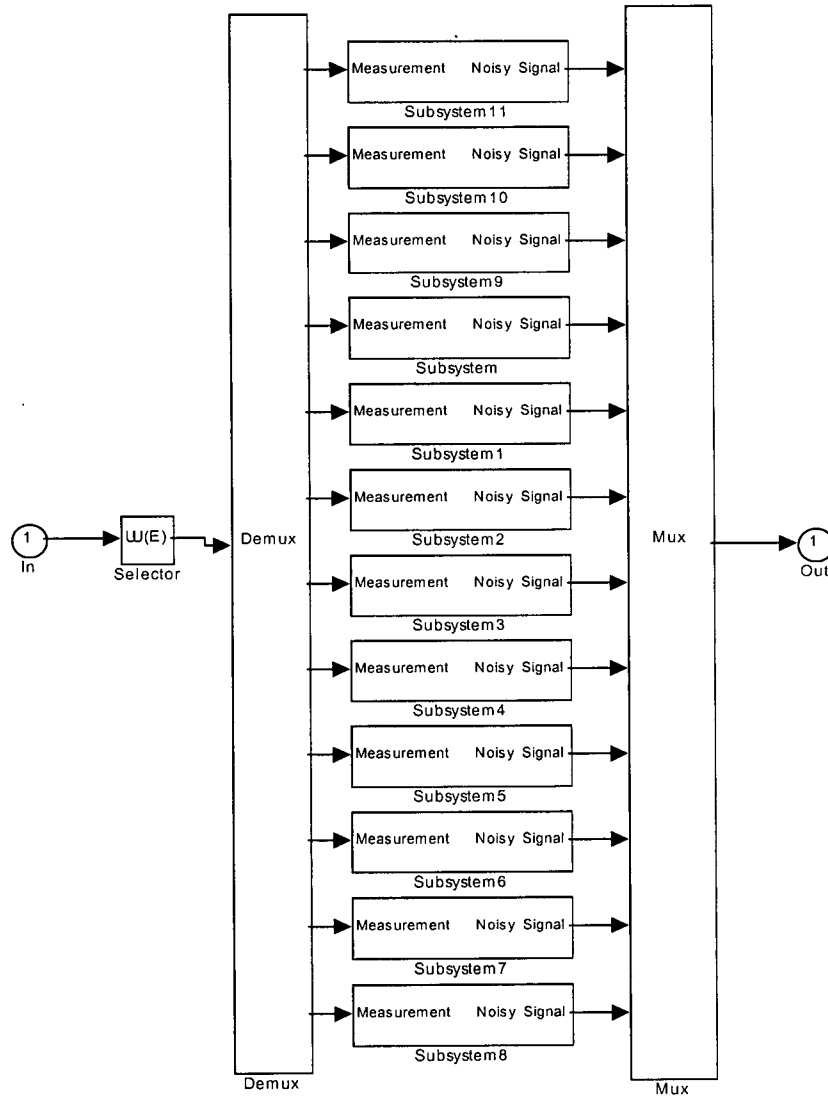


Figure E-6 Noise

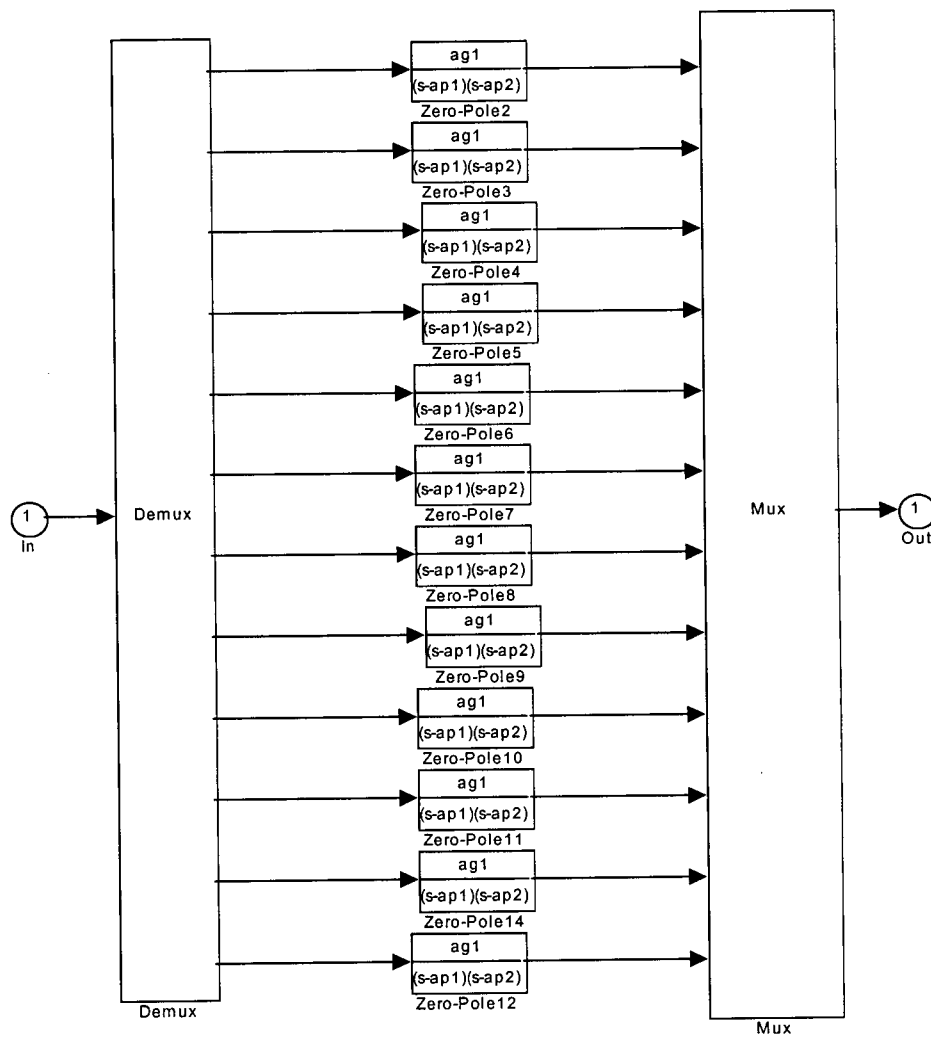


Figure E-7 Anti-aliasing filter

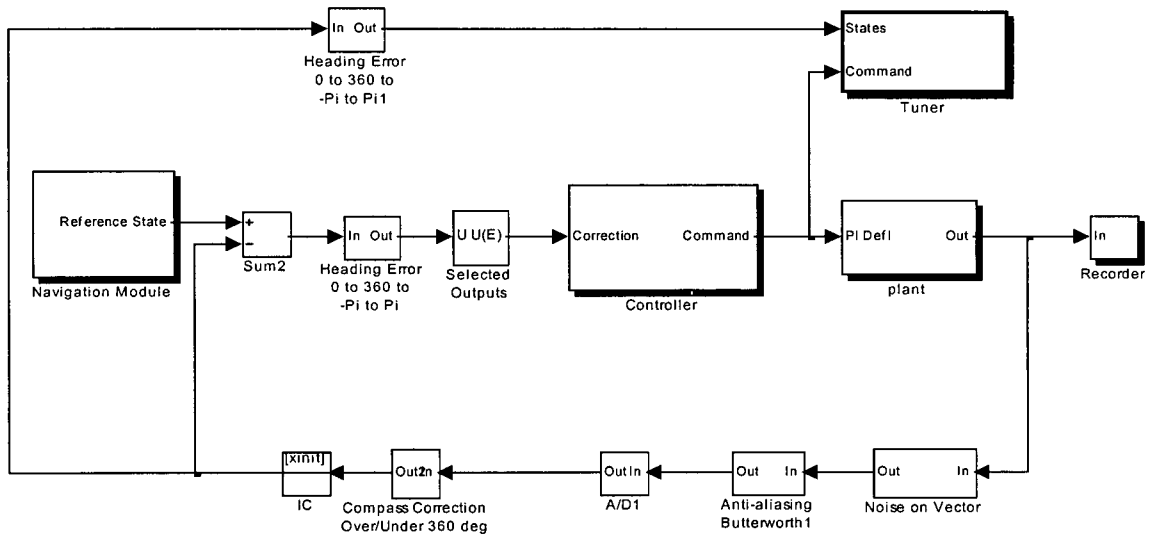


Figure E-8 Gain scheduling PD controller

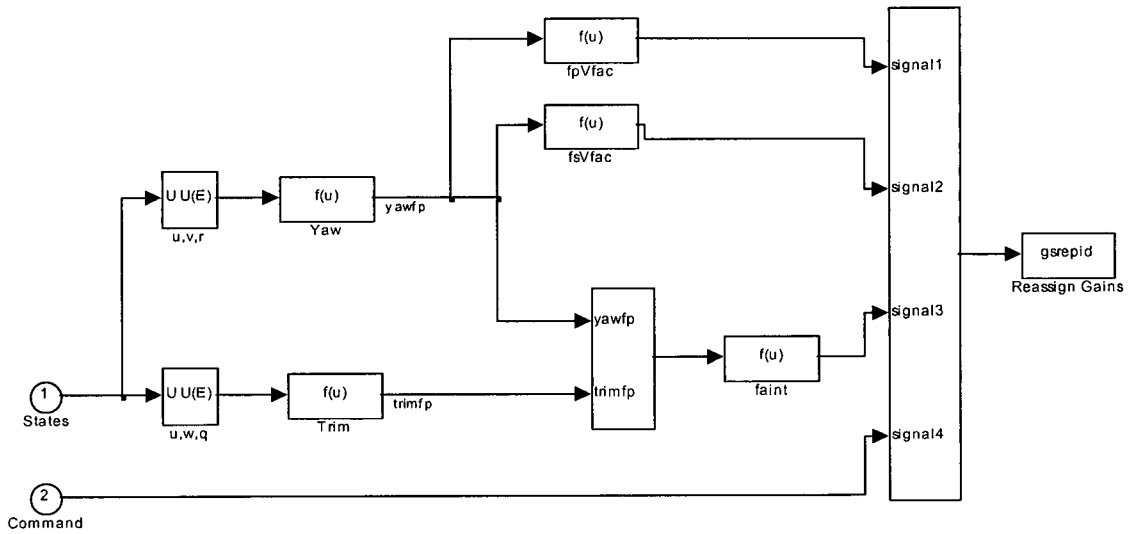


Figure E-9 Controller tuner

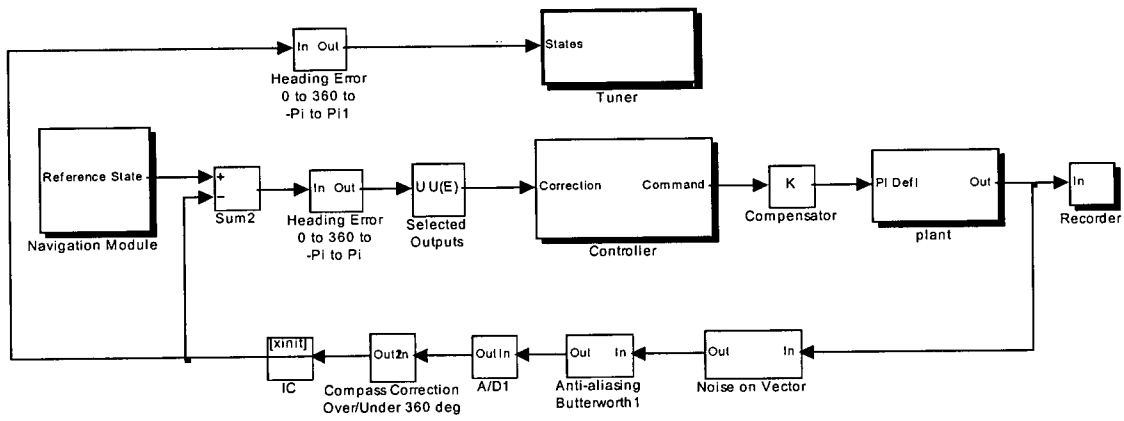


Figure E-10 Controller with series compensation

APPENDIX F - SIMULATION RESULTS

F.1 Simulations Conducted

The cases examined by simulation were grouped into three main areas: the effect of accurate and complete hydrodynamic modelling of control surfaces; the effect of control surface configuration; and the effect of the control system design. The hydrodynamic modelling included the effect of improving the plant model in simulation while using the existing (conventional) model in controller design as well as using the improved model in both plant and controller. The study of control surface configuration used the control surface geometries and layouts that showed the most promise based on experimental data. Finally, the investigation of the control system design was based on the three PD and three LQG/LTR controller augmentations summarized in Chapter 5.

The complete range of cases considered in the simulations is summarized in Table F-1. A legend at the foot of the table defines the symbols used for the hydrodynamic models and controllers. Calm water tests are identified by sea state 0. Some simulations are repeated in the table to illustrate the relationship with other simulations; repeat entries have the same simulation number in the first column.

Table F-1 Cases considered in simulation

No.	Plant Model ^a	Model for Controller ^a	Bowplane	Sternplane	Controller ^b	Manoeuvre	Sea State
Changes to model in plant only							
1	Old	Old	<i>Standard</i>	<i>Standard</i>	LQG/LTR	Figure 6-5	0
2	Int	Old	<i>Standard</i>	<i>Standard</i>	LQG/LTR	Figure 6-5	0
3	Stall	Old	<i>Standard</i>	<i>Standard</i>	LQG/LTR	Figure 6-5	0
4	Trim	Old	<i>Standard</i>	<i>Standard</i>	LQG/LTR	Figure 6-5	0
5	Yaw	Old	<i>Standard</i>	<i>Standard</i>	LQG/LTR	Figure 6-5	0
6	New	Old	<i>Standard</i>	<i>Standard</i>	LQG/LTR	Figure 6-5	0
7	New	Old	<i>Standard</i>	<i>Standard</i>	PD	Figure 6-5	0
Changes to model in controller only							
6	New	Old	<i>Standard</i>	<i>Standard</i>	LQG/LTR	Figure 6-5	0
8	New	Int	<i>Standard</i>	<i>Standard</i>	LQG/LTR	Figure 6-5	0
9	New	Stall	<i>Standard</i>	<i>Standard</i>	LQG/LTR	Figure 6-5	0
10	New	Trim	<i>Standard</i>	<i>Standard</i>	LQG/LTR	Figure 6-5	0
11	New	Yaw	<i>Standard</i>	<i>Standard</i>	LQG/LTR	Figure 6-5	0
12	New	New	<i>Standard</i>	<i>Standard</i>	LQG/LTR	Figure 6-5	0
Changes to control surface geometry							
12	New	New	<i>Standard</i>	<i>Standard</i>	LQG/LTR	Figure 6-5	0
13	New	New	<i>Short</i>	<i>Standard</i>	LQG/LTR	Figure 6-5	0
14	New	New	<i>Long</i>	<i>Standard</i>	LQG/LTR	Figure 6-5	0
15	New	New	<i>Standard</i>	<i>Long</i>	LQG/LTR	Figure 6-5	0
16	New	New	<i>Standard</i>	<i>Standard</i>	LQG/LTR	Figure 6-5	3
17	New	New	<i>Short</i>	<i>Standard</i>	LQG/LTR	Figure 6-5	3
18	New	New	<i>Long</i>	<i>Standard</i>	LQG/LTR	Figure 6-5	3
19	New	New	<i>Standard</i>	<i>Long</i>	LQG/LTR	Figure 6-5	3
20	New	New	<i>Standard</i>	<i>Standard</i>	LQG/LTR	Straight	3
21	New	New	<i>Short</i>	<i>Standard</i>	LQG/LTR	Straight	3
22	New	New	<i>Long</i>	<i>Standard</i>	LQG/LTR	Straight	3
23	New	New	<i>Standard</i>	<i>Long</i>	LQG/LTR	Straight	3
Changes to control surface layout							
12	New	New	<i>Standard</i>	<i>Standard</i>	LQG/LTR	Figure 6-5	0
24	New	New	<i>Anhedral</i>	<i>Standard</i>	LQG/LTR	Figure 6-5	0
25	New	New	<i>Keel</i>	<i>Standard</i>	LQG/LTR	Figure 6-5	0
26	New	New	<i>Standard</i>	<i>Y-Tail</i>	LQG/LTR	Figure 6-5	0
16	New	New	<i>Standard</i>	<i>Standard</i>	LQG/LTR	Figure 6-5	3

Table F-1 Cases considered in simulation (Continued)

No.	Plant Model ^a	Model for Controller ^a	Bowplane	Sternplane	Controller ^b	Manoeuvre	Sea State
27	New	New	<i>Anhedral</i>	<i>Standard</i>	LQG/LTR	Figure 6-5	3
28	New	New	<i>Keel</i>	<i>Standard</i>	LQG/LTR	Figure 6-5	3
29	New	New	<i>Standard</i>	<i>Y-Tail</i>	LQG/LTR	Figure 6-5	3
20	New	New	<i>Standard</i>	<i>Standard</i>	LQG/LTR	Straight	3
30	New	New	<i>Anhedral</i>	<i>Standard</i>	LQG/LTR	Straight	3
31	New	New	<i>Keel</i>	<i>Standard</i>	LQG/LTR	Straight	3
32	New	New	<i>Standard</i>	<i>Y-Tail</i>	LQG/LTR	Straight	3
Changes to control strategy							
12	New	New	<i>Standard</i>	<i>Standard</i>	LQG/LTR	Figure 6-5	0
33	New	New	<i>Standard</i>	<i>Standard</i>	LQG-SC	Figure 6-5	0
34	New	New	<i>Standard</i>	<i>Standard</i>	SM-LQG	Figure 6-5	0
35	New	New	<i>Standard</i>	<i>Standard</i>	PD	Figure 6-5	0
36	New	New	<i>Standard</i>	<i>Standard</i>	GS-PD	Figure 6-5	0
37	New	New	<i>Standard</i>	<i>Standard</i>	PD-SC	Figure 6-5	0
38	New	Old	<i>Standard</i>	<i>Standard</i>	PD-SC	Figure 6-5	0
39	New	New	<i>Standard</i>	<i>Standard</i>	LQG/LTR	Figure 6-5	3
40	New	New	<i>Standard</i>	<i>Standard</i>	LQG-SC	Figure 6-5	3
41	New	New	<i>Standard</i>	<i>Standard</i>	SM-LQG	Figure 6-5	3
42	New	New	<i>Standard</i>	<i>Standard</i>	PD	Figure 6-5	3
43	New	New	<i>Standard</i>	<i>Standard</i>	GS-PD	Figure 6-5	3
44	New	New	<i>Standard</i>	<i>Standard</i>	PD-SC	Figure 6-5	3
45	New	New	<i>Standard</i>	<i>Standard</i>	LQG/LTR	Straight	3
46	New	New	<i>Standard</i>	<i>Standard</i>	LQG-SC	Straight	3
47	New	New	<i>Standard</i>	<i>Standard</i>	SM-LQG	Straight	3
48	New	New	<i>Standard</i>	<i>Standard</i>	PD	Straight	3
49	New	New	<i>Standard</i>	<i>Standard</i>	GS-PD	Straight	3
50	New	New	<i>Standard</i>	<i>Standard</i>	PD-SC	Straight	3

a. Model legend - Int: bowplane-sternplane interaction; New: all control surface hydrodynamic effects modelled including Int, Stall, Trim, and Yaw; Old: previous (conventional) control surface hydrodynamic model; Stall: change in plane stall angle with Reynolds number and yaw angle; Trim: change in bowplane effective deflection in trim; Yaw: change in bowplane force with yaw

b. Controller legend - GS-PD: gain scheduling PD controller; LQG/LTR: Linear quadratic gaussian with loop transfer recovery; SM-LQG: Sliding mode LQG/LTR; LQG-SC: LQG/LTR controller with series compensation; PD: proportional-derivative; PD-SC: PD controller with series compensation

F.2 Evaluation of Modelling Influence

F.2.1 Influence of Plant Model Improvements

Table F-2 Effect of hydrodynamic effects modelled in plant on performance in calm water

Parameter	Effects Modelled in Plant					
	old plant	inter-action	yaw	trim	stall	new plant
Performance Index, J_{ct}	0.1105	0.1070	0.1106	0.1073	0.1093	0.1078
Performance Index, J_{sl}	0.0026	0.0022	0.0025	0.0024	0.0025	0.0023
RMS Roll Error [deg]	7.1	6.9	7.1	6.9	7.0	6.9
RMS Pitch Error [deg]	0.1	0.1	0.1	0.1	0.1	0.1
RMS Yaw Error [deg]	0.6	0.6	0.6	0.6	0.6	0.8
RMS Depth Error [m]	0.03	0.03	0.03	0.03	0.03	0.03
Maximum Roll Error [deg]	25.3	24.3	25.4	24.3	24.8	24.1
Maximum Pitch Error [deg]	0.9	0.6	0.9	0.7	0.9	0.6
Maximum Yaw Error [deg]	9.0	9.1	8.8	8.9	8.3	14.7
Maximum Depth Error ^a [m]	0.12	0.12	0.12	0.12	0.12	0.12
Average Turn Radius [m]	30.1	30.1	30.1	30.1	30.1	30.3
Bowplane Deviation ^b [deg]	3.9	3.9	3.8	4.0	4.1	3.9
Sternplane Deviation [deg]	6.5	4.8	6.3	4.8	6.8	4.6
Bowplane Saturation [%]	3.3	3.3	3.3	3.1	3.3	3.4
Sternplane Saturation [%]	0.3	0.5	0.3	0.0	0.3	0.5

a. the maximum error in depth was considered for $x > 120$ m, 60 m after the step change in depth

b. plane deviations are measured as the average absolute deflection from the mean deflection

F.2.2 Influence of Controller Model Improvements

Table F-3 Effect of hydrodynamic effects included in controller on performance in calm water

Parameter	Effects Modelled in Controller					
	none	inter- action	yaw	trim	stall	all
Performance Index, J_{ct}	0.1078	0.1119	0.1078	0.1078	0.1078	0.1122
Performance Index, J_{sl}	0.0023	0.0024	0.0023	0.0023	0.0023	0.0024
RMS Roll Error [deg]	6.9	7.1	6.9	6.9	6.9	7.2
RMS Pitch Error [deg]	0.1	0.1	0.1	0.1	0.1	0.1
RMS Yaw Error [deg]	0.8	0.7	0.8	0.8	0.8	0.7
RMS Depth Error [m]	0.03	0.03	0.03	0.03	0.03	0.03
Maximum Roll Error [deg]	24.1	24.5	24.1	24.1	24.1	24.6
Maximum Pitch Error [deg]	0.6	0.9	0.6	0.6	0.6	0.7
Maximum Yaw Error [deg]	14.7	12.8	14.7	14.7	14.7	12.6
Maximum Depth Error ^a [m]	0.13	0.12	0.13	0.13	0.13	0.12
Average Turn Radius [m]	30.3	30.3	30.3	30.3	30.3	30.3
Bowplane Deviation ^b [deg]	3.9	3.8	3.9	3.9	3.9	3.8
Sternplane Deviation [deg]	4.6	3.6	4.6	4.6	4.6	3.6
Bowplane Saturation [%]	3.4	3.6	3.4	3.4	3.4	3.7
Sternplane Saturation [%]	0.5	0.5	0.5	0.5	0.5	0.5

a. the maximum error in depth was considered for $x > 120$ m, 60 m after the step change in depth

b. plane deviations are measured as the average absolute deflection from the mean deflection

F.3 Evaluation of Vehicle Geometry

F.3.1 Plane Geometry

Table F-4 Effect of plane geometry on performance in calm water

Parameter	Configuration (bowplane - sternplane)			
	std-std	long-std	short-std	std-long
Performance Index, J_{ct}	0.0957	0.0999	0.0886	0.0960
Performance Index, J_{sa}	0.0057	0.0028	0.0062	0.0074
RMS Roll Error [deg]	5.8	6.1	5.5	5.9
RMS Pitch Error [deg]	0.2	0.3	0.2	0.2
RMS Yaw Error [deg]	1.1	0.8	1.6	1.4
RMS Depth Error [m]	0.04	0.03	0.06	0.04
Maximum Roll Error [deg]	19.6	19.5	19.1	20.5
Maximum Pitch Error [deg]	1.4	1.5	1.3	1.5
Maximum Yaw Error [deg]	15.6	13.8	20.6	20.0
Maximum Depth Error ^a [m]	0.14	0.11	0.20	0.14
Average Turn Radius [m]	30.5	30.3	30.7	30.7
Bowplane Deviation ^b [deg]	3.7	3.9	3.3	5.3
Sternplane Deviation [deg]	4.0	5.9	3.5	5.6
Bowplane Saturation [%]	2.5	1.6	4.2	2.6
Sternplane Saturation [%]	0.1	0.1	0.2	0.1

a. the maximum error in depth was considered for $x > 120$ m, 60 m after the step change in depth

b. plane deviations are measured as the average absolute deflection from the mean deflection

Table F-5 Effect of plane geometry on performance in sea state 3

Configuration (bowplane - sternplane)				
Parameter	std-std	long-std	short-std	std-long
Performance Index, J_{ct}	0.0970	0.0984	0.1030	0.0997
Performance Index, J_{sl}	0.0154	0.0126	0.0204	0.0141
RMS Roll Error [deg]	5.6	5.8	5.6	5.9
RMS Pitch Error [deg]	0.3	0.2	0.4	0.3
RMS Yaw Error [deg]	1.4	1.2	2.0	1.4
RMS Depth Error [m]	0.05	0.03	0.08	0.05
Maximum Roll Error [deg]	20.0	21.9	17.8	21.9
Maximum Pitch Error [deg]	1.4	1.3	1.8	1.5
Maximum Yaw Error [deg]	14.5	13.9	22.5	14.7
Maximum Depth Error ^a [m]	0.16	0.10	0.20	0.17
Average Turn Radius [m]	30.6	30.5	30.6	30.6
Bowplane Deviation ^b [deg]	5.1	4.5	5.9	5.2
Sternplane Deviation [deg]	4.7	4.8	4.6	4.2
Bowplane Saturation [%]	2.1	0.9	13.1	2.4
Sternplane Saturation [%]	0.3	0.3	0.7	0.3

a. the maximum error in depth was considered for $x > 120$ m, 60 m after the step change in depth

b. plane deviations are measured as the average absolute deflection from the mean deflection

Table F-6 Spectral analysis for plane geometry effect on performance in sea state 3

Configuration (bowplane - sternplane)				
Significant Amplitude	std-std	long-std	short-std	std-long
Sway [m]	0.0099	0.0045	0.0073	0.0061
Heave [m]	0.0028	0.0021	0.0028	0.0042
Roll [deg]	0.0227	0.0241	0.0192	0.0206
Pitch [deg]	0.0319	0.0247	0.0309	0.0495
Yaw [deg]	0.0274	0.0246	0.0286	0.0271
Bowplane deflection [deg]	1.143	0.869	1.218	1.755
Sternplane deflection [deg]	1.192	1.133	1.106	1.250
J_{sa} [-]	0.479	0.222	0.397	0.308

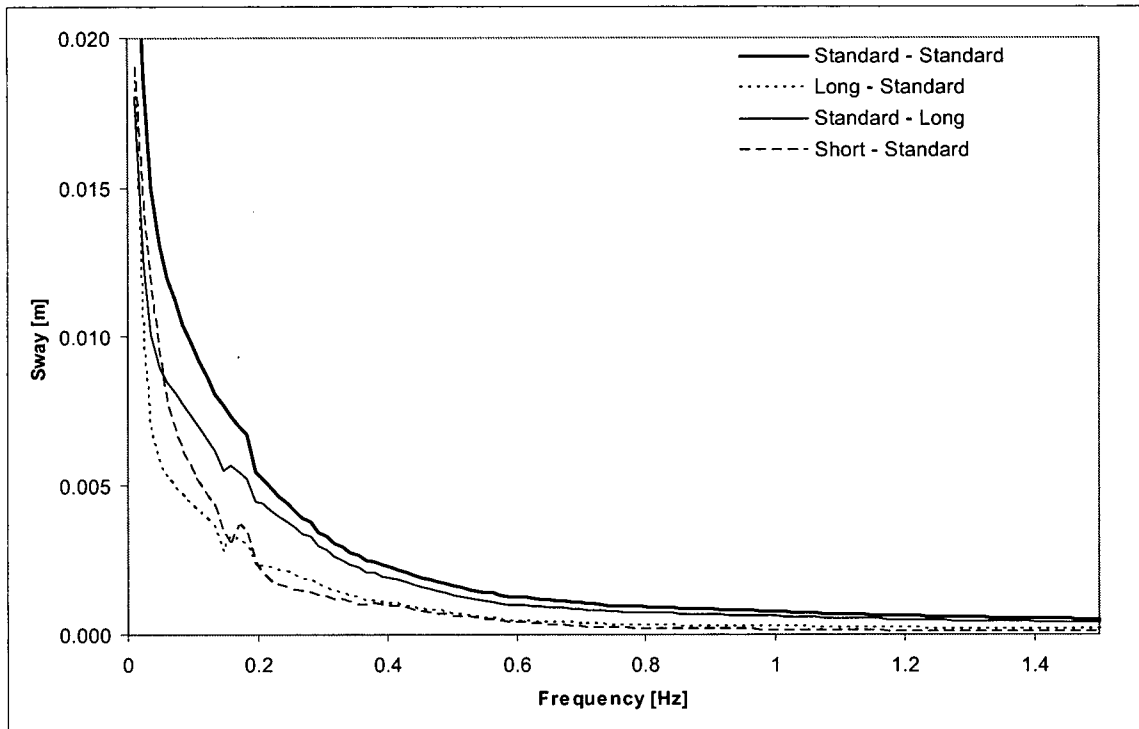


Figure F-1 Sway response based on control surface geometry in sea state three head seas

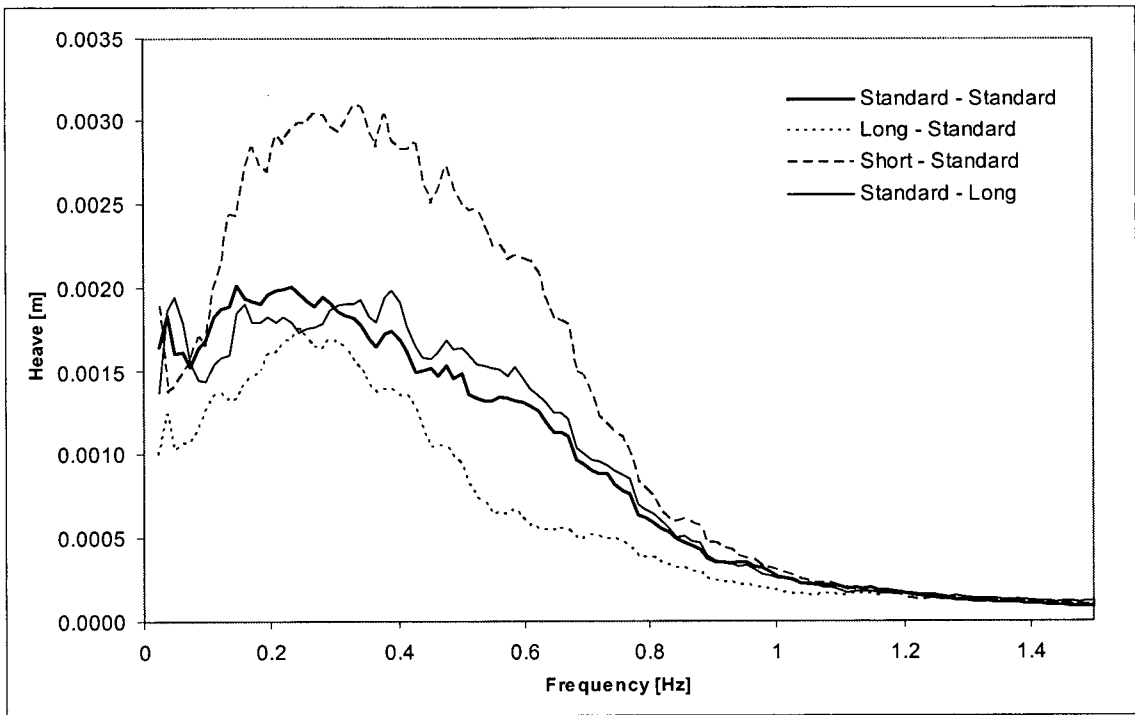


Figure F-2 Heave response based on control surface geometry in sea state three head seas

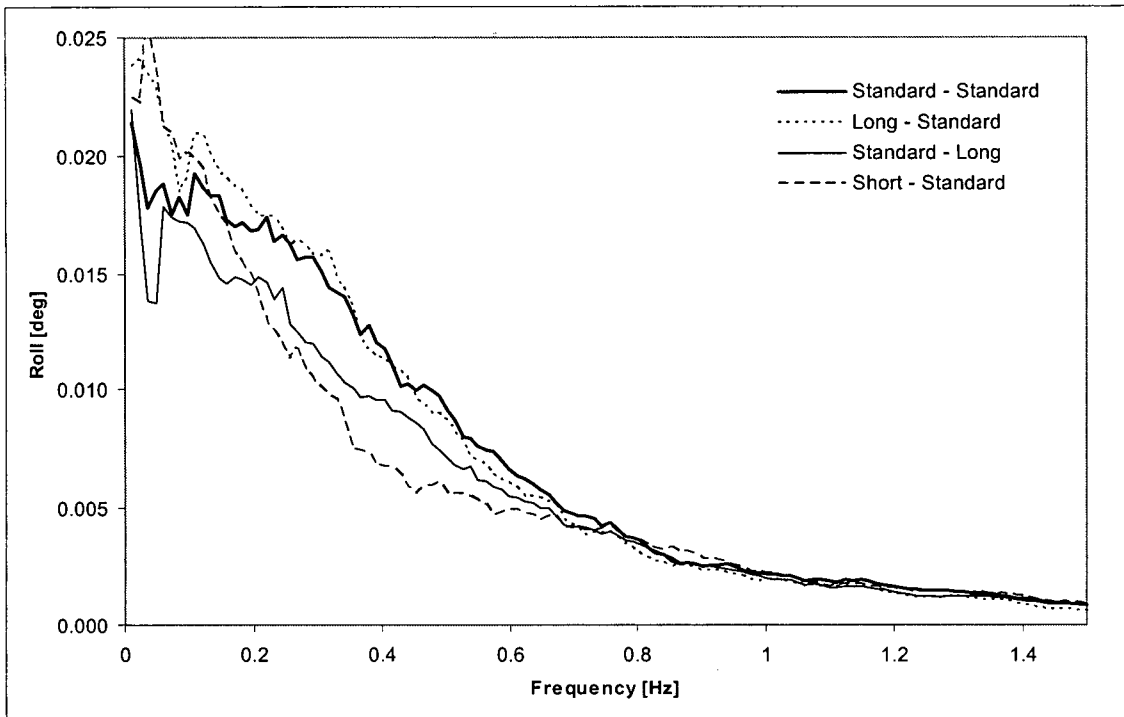


Figure F-3 Roll response based on control surface geometry in sea state three head seas

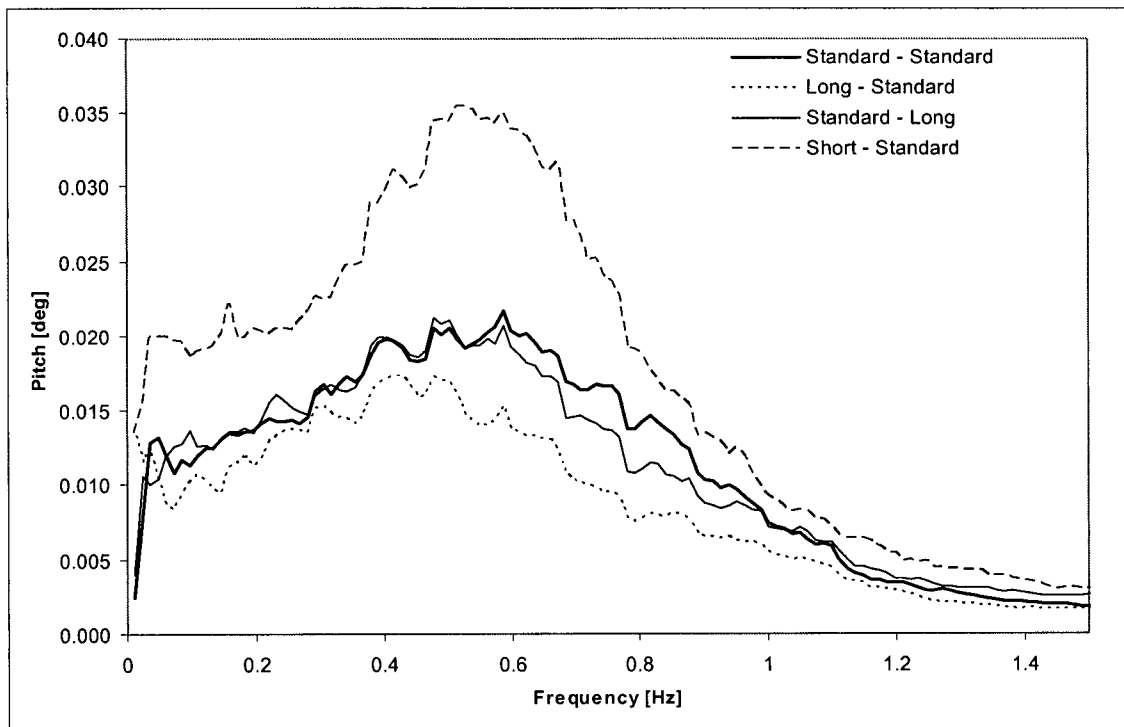


Figure F-4 Pitch response based on control surface geometry in sea state three head seas

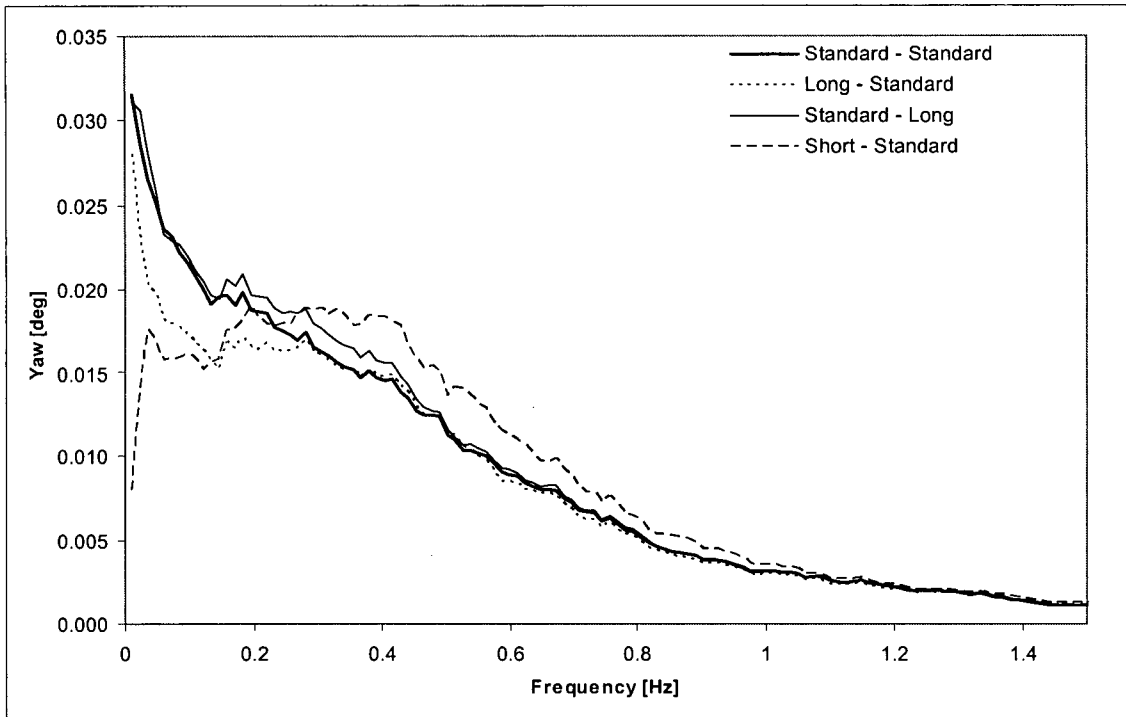


Figure F-5 Yaw response based on control surface geometry in sea state three head seas

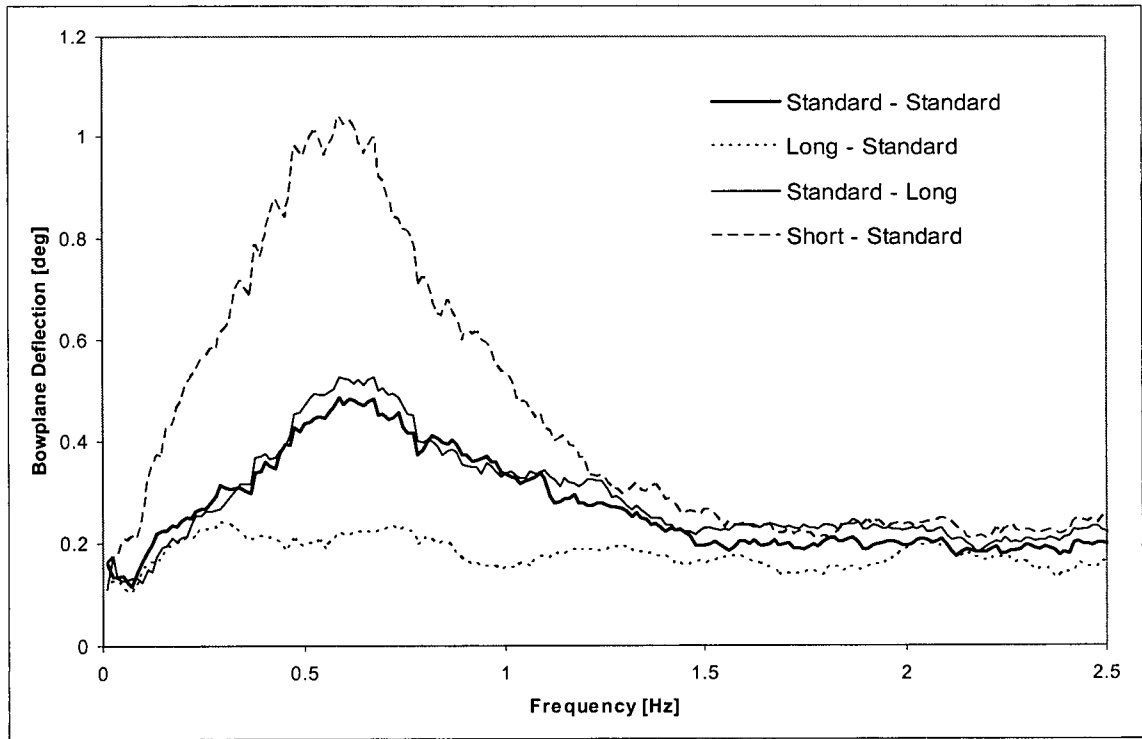


Figure F-6 Bowplane deflection based on control surface geometry in sea state three head seas

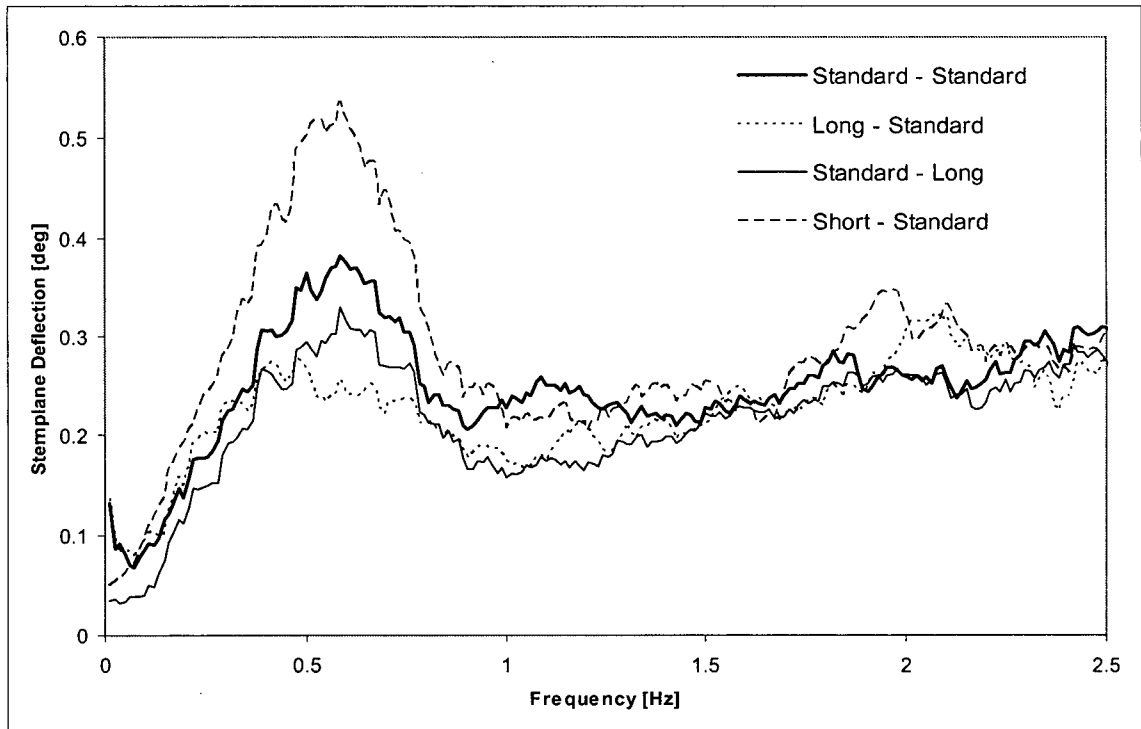


Figure F-7 Sternplane deflection based on control surface geometry in sea state three head seas

F.3.2 Plane Location

Table F-7 Effect of plane location on performance in calm water

Parameter	Configuration			
	standard	anhedral bowplanes	Y-tail	keel planes
Performance Index, J_{ct}	0.0957	0.0900	0.1015	0.0912
Performance Index, J_{sl}	0.0057	0.0077	0.0018	0.0154
RMS Roll Error [deg]	5.8	5.6	7.7	5.2
RMS Pitch Error [deg]	0.2	0.2	0.2	0.5
RMS Yaw Error [deg]	1.1	2.6	0.5	3.2
RMS Depth Error [m]	0.04	0.04	0.08	0.07
Maximum Roll Error [deg]	19.6	21.0	28.4	19.5
Maximum Pitch Error [deg]	1.4	1.3	1.0	2.9
Maximum Yaw Error [deg]	15.6	34.6	3.7	17.2
Maximum Depth Error ^a [m]	0.14	0.13	0.28	0.23
Average Turn Radius [m]	30.5	31.2	22.5	30.4
Bowplane Deviation ^b [deg]	3.7	3.3	3.5	2.9
Sternplane Deviation [deg]	4.0	3.7	2.7	3.9
Bowplane Saturation [%]	2.5	2.4	8.7	12.5
Sternplane Saturation [%]	0.1	0.2	1.2	4.6

a. the maximum error in depth was considered for $x > 120$ m, 60 m after the step change in depth

b. plane deviations are measured as the average absolute deflection from the mean deflection

Table F-8 Effect of plane location on performance in sea state 3

Parameter	Configuration			
	standard	anhedral bowplanes	Y-tail	keel planes
Performance Index, J_{ct}	0.0970	0.0839	0.1046	0.1049
Performance Index, J_{sl}	0.0154	0.0160	0.0136	0.0338
RMS Roll Error [deg]	5.6	4.8	6.9	5.0
RMS Pitch Error [deg]	0.3	0.3	0.2	0.7
RMS Yaw Error [deg]	1.4	1.4	1.0	5.2
RMS Depth Error [m]	0.05	0.04	0.09	0.08
Maximum Roll Error [deg]	20.0	16.6	26.2	18.4
Maximum Pitch Error [deg]	1.4	1.5	1.0	3.8
Maximum Yaw Error [deg]	14.5	15.7	4.5	35.8
Maximum Depth Error ^a [m]	0.16	0.12	0.27	0.21
Average Turn Radius [m]	30.6	30.6	24.9	30.4
Bowplane Deviation ^b [deg]	5.1	5.9	6.1	6.1
Sternplane Deviation [deg]	4.7	4.8	5.9	6.0
Bowplane Saturation [%]	2.1	4.2	5.3	23.4
Sternplane Saturation [%]	0.3	0.3	0.6	5.8

a. the maximum error in depth was considered for $x > 120$ m, 60 m after the step change in depth

b. plane deviations are measured as the average absolute deflection from the mean deflection

Table F-9 Spectral analysis for plane location effect on performance in sea state 3

Significant Amplitude	Configuration			
	Standard	Y-Tail	Anhedral	Keel
Sway [m]	0.0099	0.0087	0.0026	0.0054
Heave [m]	0.0028	0.0025	0.0037	0.0039
Roll [deg]	0.0227	0.0330	0.0251	0.0168
Pitch [deg]	0.0319	0.0293	0.0373	0.0386
Yaw [deg]	0.0274	0.0246	0.0211	0.0334
Bowplane deflection [deg]	1.143	1.190	1.528	1.770
Sternplane deflection [deg]	1.192	1.268	1.219	0.988
J_{sa} [-]	0.479	0.430	0.231	0.338

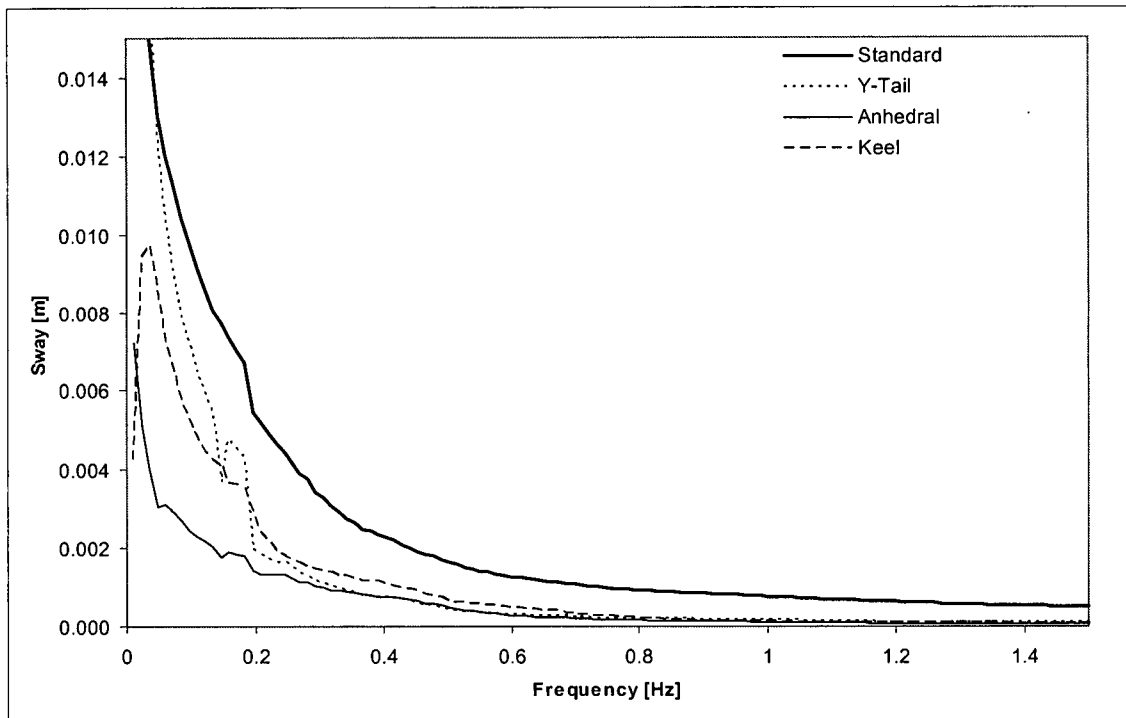


Figure F-8 Sway response based on control surface position in sea state three head seas

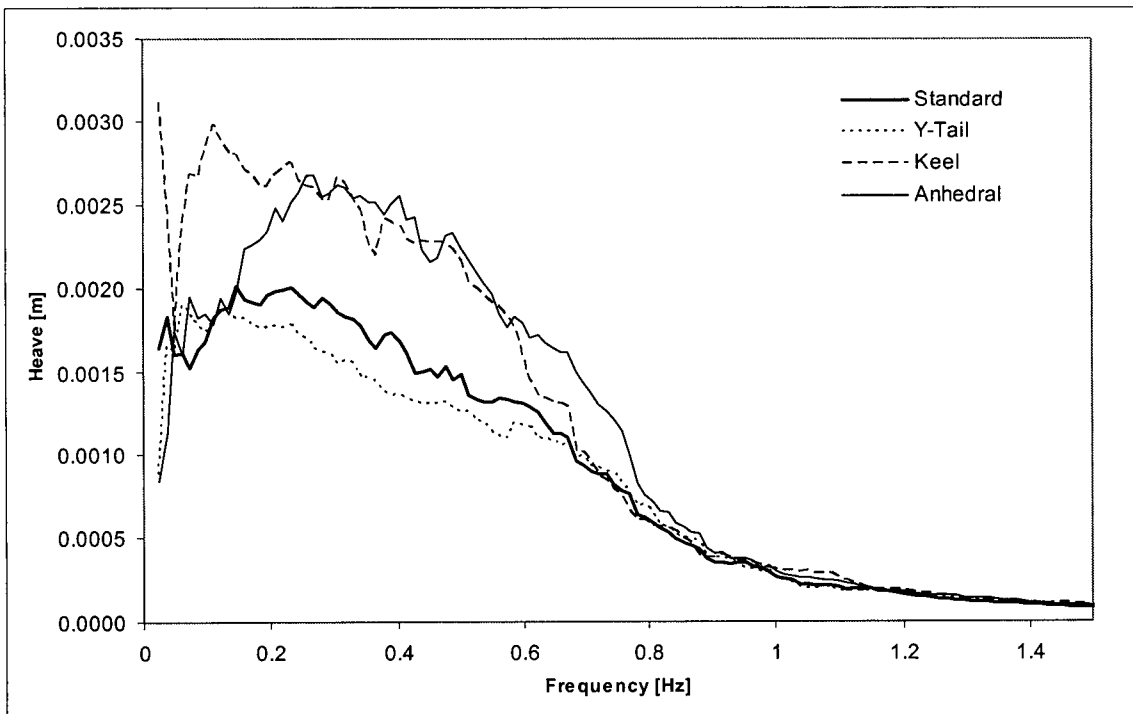


Figure F-9 Heave response based on control surface position in sea state three head seas

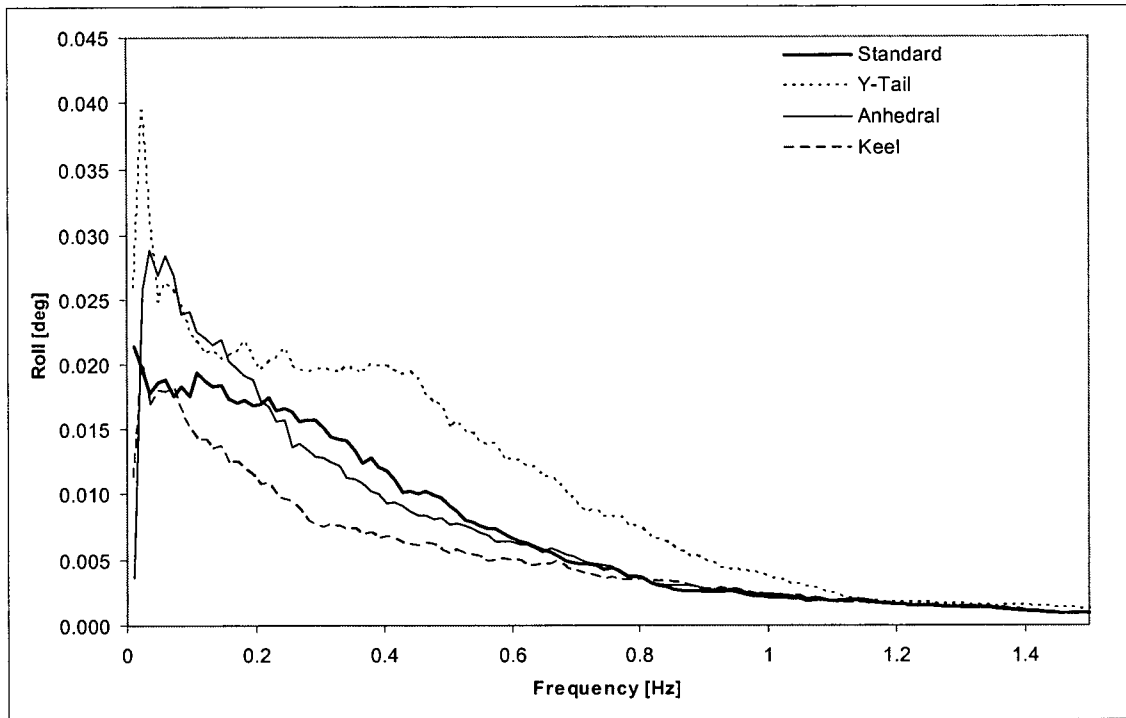


Figure F-10 Roll response based on control surface position in sea state three head seas

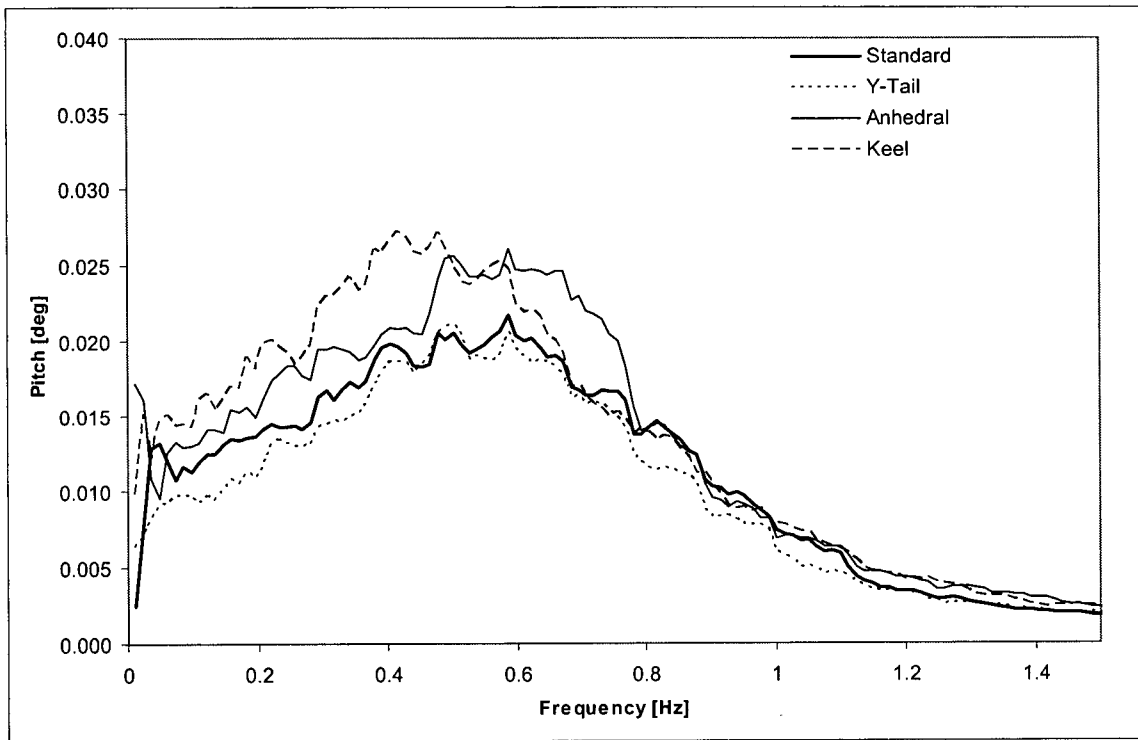


Figure F-11 Pitch response based on control surface position in sea state three head seas

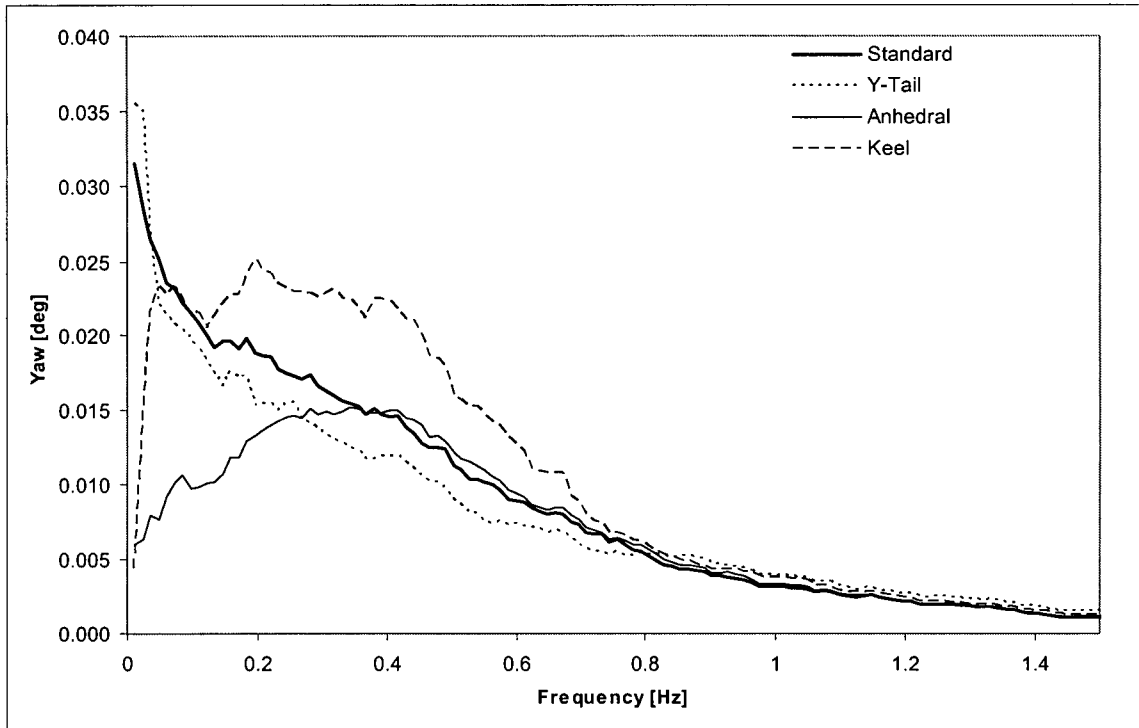


Figure F-12 Yaw response based on control surface position in sea state three head seas

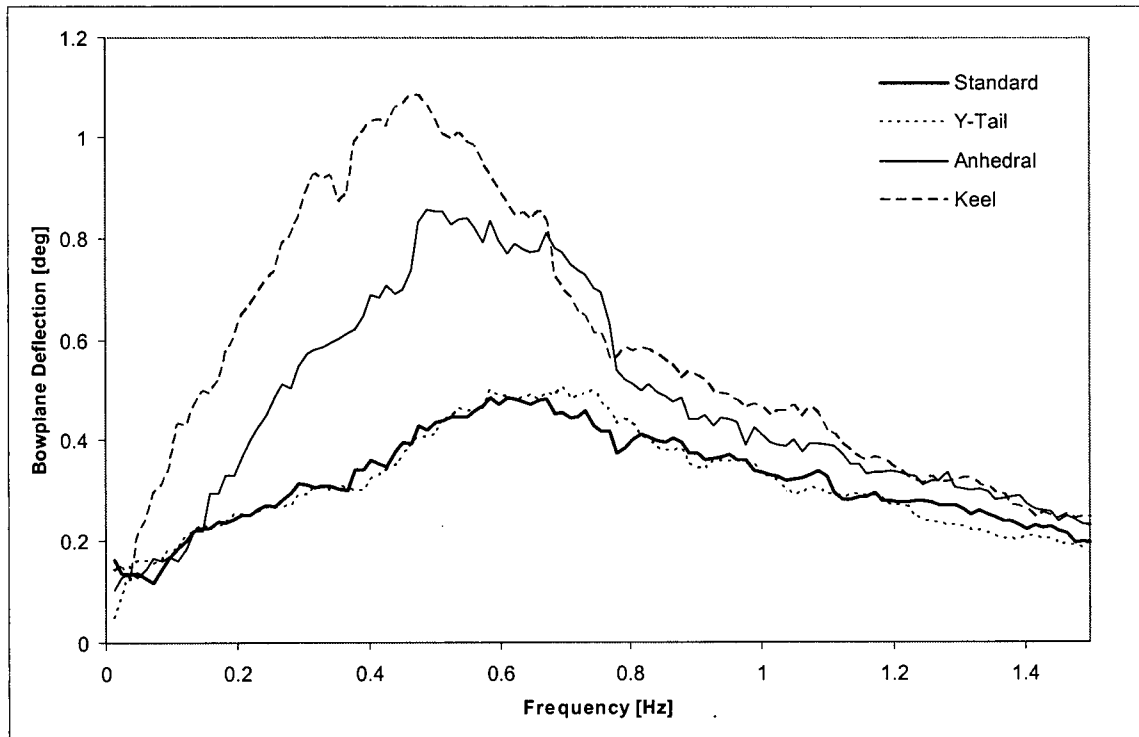


Figure F-13 Bowplane deflection based on control surface position in sea state three head seas

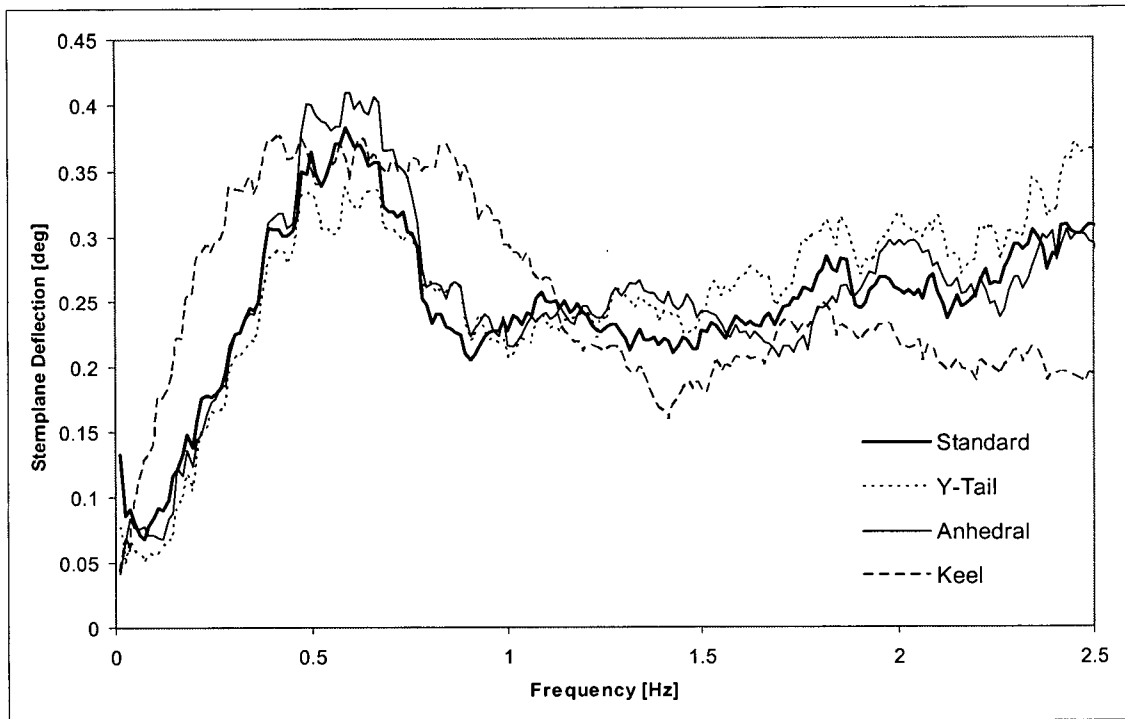


Figure F-14 Sternplane deflection based on control surface position in sea state three head seas

F.4 Evaluation of Control System

F.4.1 PD Controller Augmentations

Table F-10 Effect of PD controller augmentation on performance in calm water

Parameter	Controller		
	PD	PD with Gain Scheduling	PD with Fuzzy Compensator
Performance Index, J_{ct}	0.0114	0.0114	0.0118
Performance Index, J_{sl}	0.0098	0.0093	0.0093
RMS Roll Error [deg]	0.1	0.1	0.1
RMS Pitch Error [deg]	0.2	0.2	0.2
RMS Yaw Error [deg]	16.4	16.2	16.1
RMS Depth Error [m]	0.02	0.03	0.03
Maximum Roll Error [deg]	0.4	0.4	0.4
Maximum Pitch Error [deg]	1.0	0.7	0.6
Maximum Yaw Error [deg]	117.6	116.7	116.1
Maximum Depth Error ^a [m]	0.04	0.05	0.06
Average Turn Radius [m]	30.4	30.4	30.4
Bowplane Deviation [deg] ^b	1.1	1.3	1.5
Sternplane Deviation [deg]	0.6	0.6	0.6
Bowplane Saturation [%]	0.7	0.7	0.7
Sternplane Saturation [%]	0.0	0.0	0.0

a. the maximum error in depth was considered for $x > 120$ m, 60 m after the step change in depth

b. plane deviations are measured as the average absolute deflection from the mean deflection

Table F-11 Effect of PD controller augmentation on performance in sea state 3

Parameter	Controller		
	PD	PD with Gain Scheduling	PD with Fuzzy Compensator
Performance Index, J_{ct}	0.0233	0.0235	0.0236
Performance Index, J_{sl}	0.0222	0.0223	0.0222
RMS Roll Error [deg]	0.2	0.2	0.2
RMS Pitch Error [deg]	0.5	0.5	0.5
RMS Yaw Error [deg]	19.8	19.7	19.6
RMS Depth Error [m]	0.04	0.04	0.05
Maximum Roll Error [deg]	0.8	0.8	0.8
Maximum Pitch Error [deg]	1.4	1.3	1.3
Maximum Yaw Error [deg]	129.5	129.4	128.8
Maximum Depth Error ^a [m]	0.09	0.09	0.10
Average Turn Radius [m]	30.7	30.7	30.7
Bowplane Deviation [deg] ^b	3.6	3.8	3.8
Sternplane Deviation [deg]	1.8	2.0	2.0
Bowplane Saturation [%]	0.7	0.7	0.7
Sternplane Saturation [%]	0.0	0.0	0.0

a. the maximum error in depth was considered for $x > 120$ m, 60 m after the step change in depth

b. plane deviations are measured as the average absolute deflection from the mean deflection

Table F-12 Spectral analysis for PD controller performance in sea state 3

Significant Amplitude	Controller		
	PD	PD with Gain Scheduling	PD with Fuzzy Compensator
Sway [m]	0.0040	0.0039	0.0042
Heave [m]	0.0015	0.0015	0.0014
Roll [deg]	0.0102	0.0101	0.0101
Pitch [deg]	0.0167	0.0185	0.0152
Yaw [deg]	0.0088	0.0088	0.0088
Bowplane deflection [deg]	0.0108	0.0141	0.0105
Sternplane deflection [deg]	0.0054	0.0060	0.0048
J_{sa} [-]	0.125	0.135	0.124

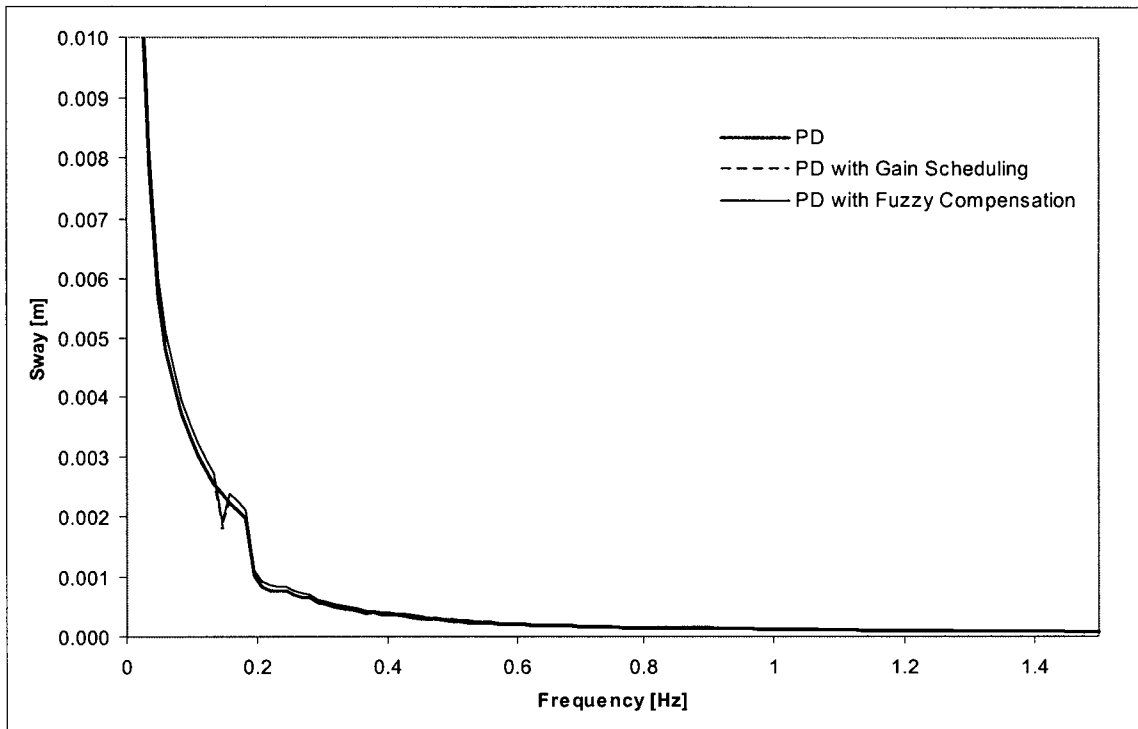


Figure F-15 Sway response for PD augmentations in sea state three head seas

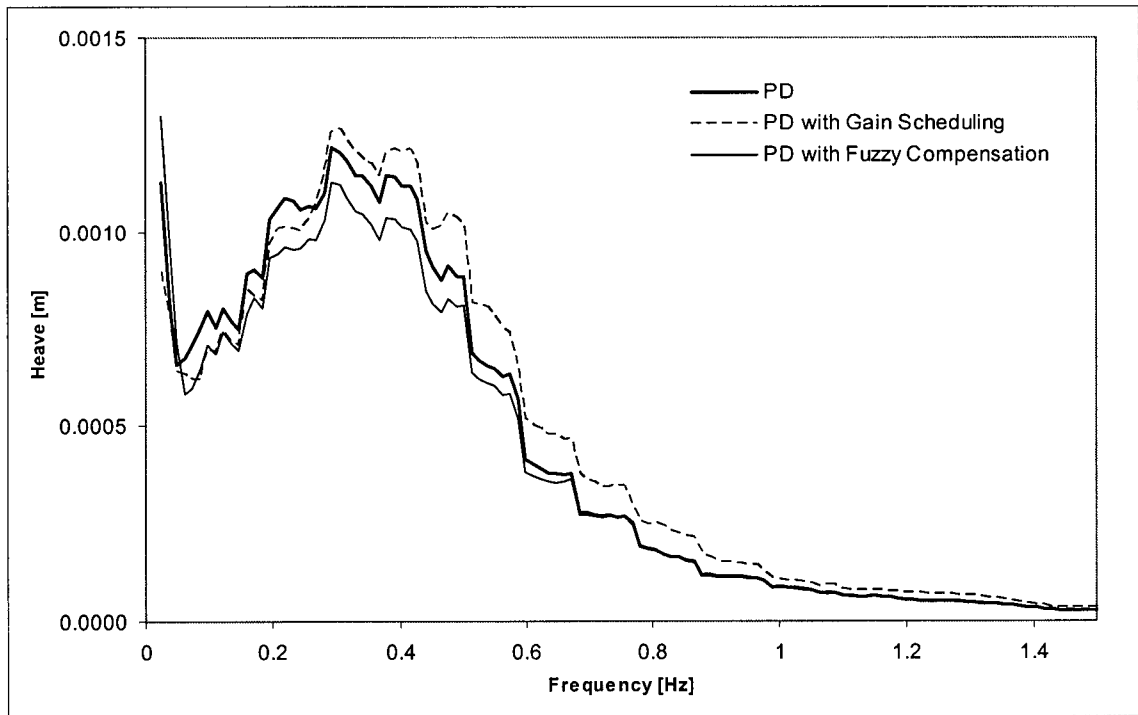


Figure F-16 Depth response spectra for PD augmentations in sea state three head seas

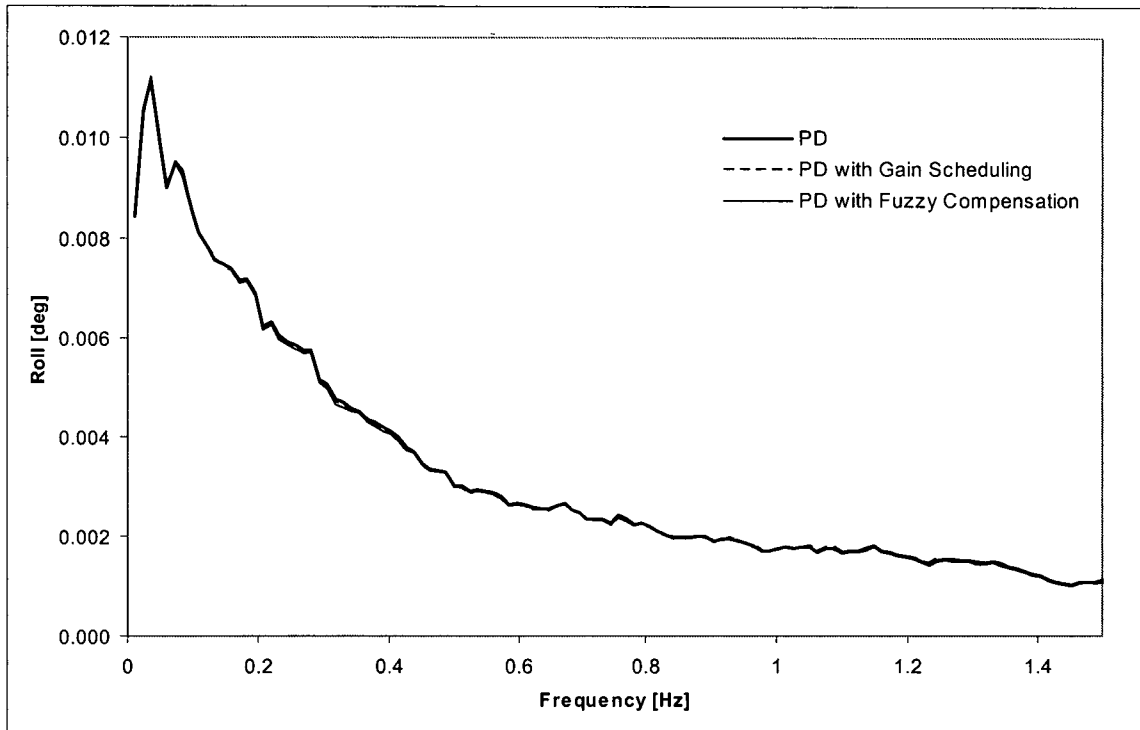


Figure F-17 Roll response spectra for PD augmentations in sea state three head seas

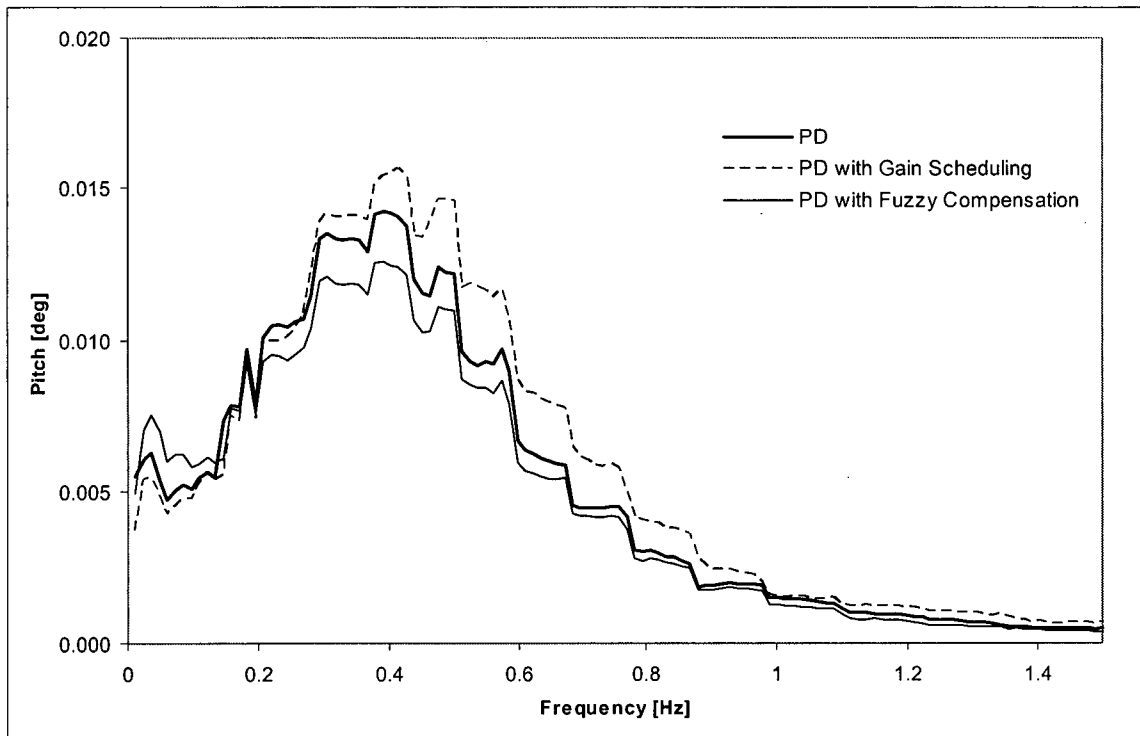


Figure F-18 Pitch response spectra for PD augmentations in sea state three head seas

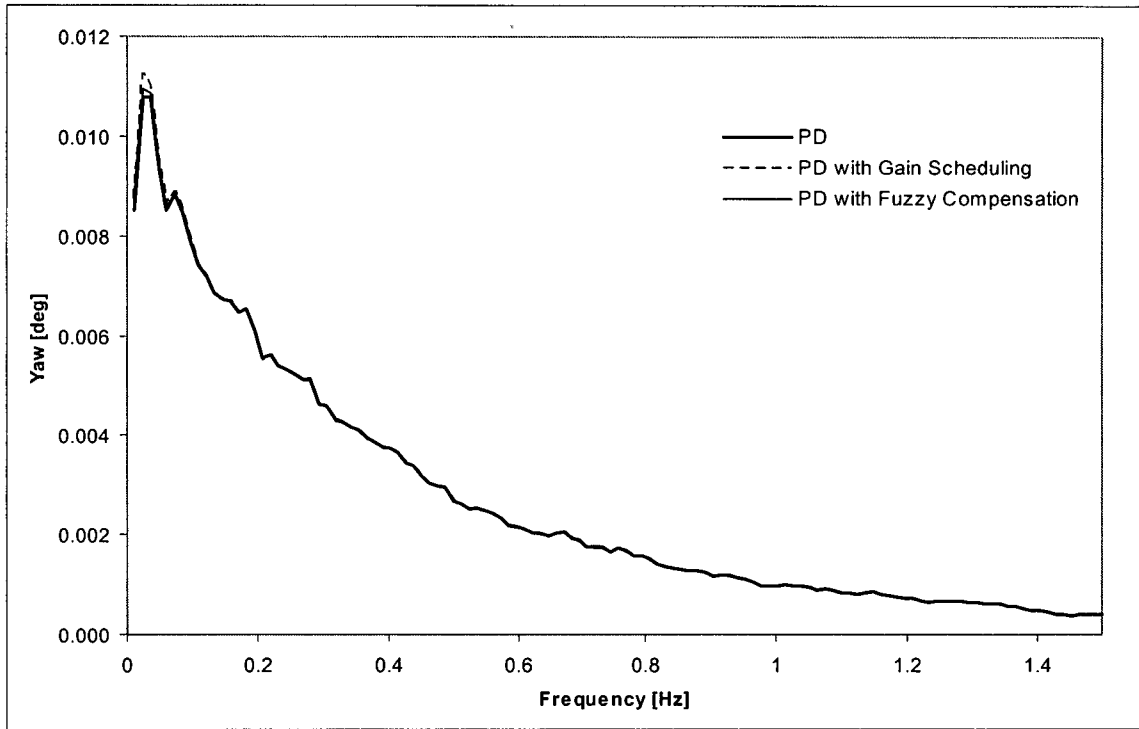


Figure F-19 Yaw deflection spectra for PD augmentations in sea state three head seas

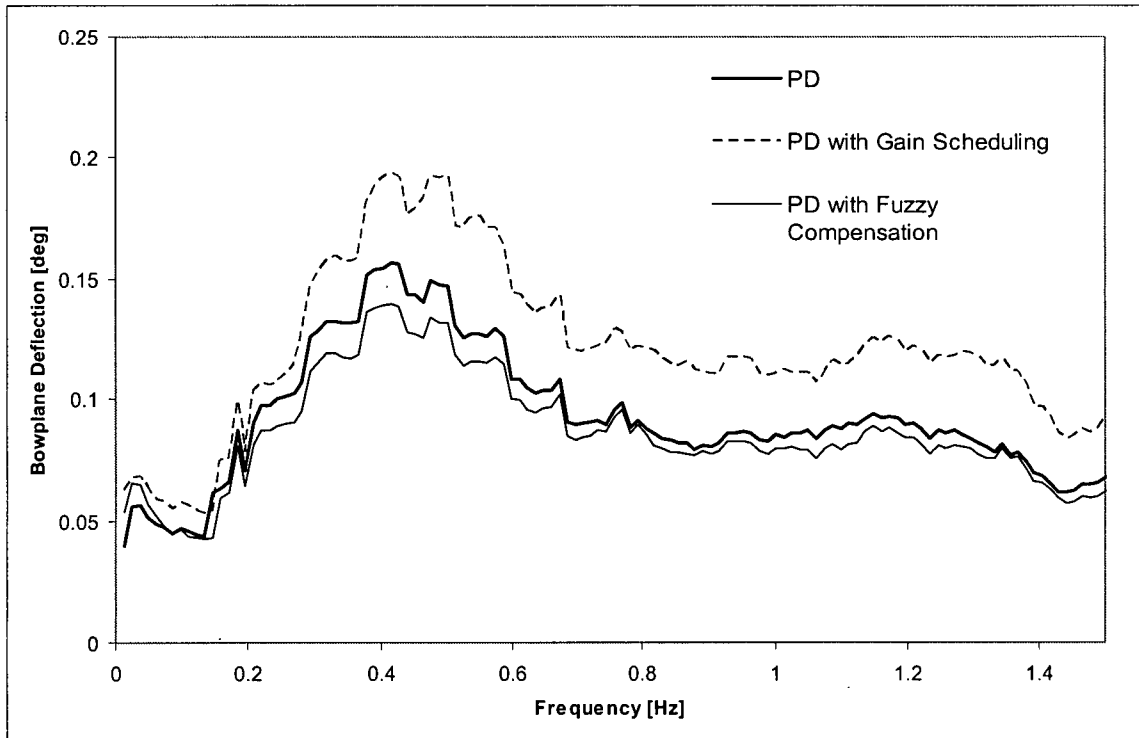


Figure F-20 Bowplane deflection spectra for PD augmentations in sea state three head seas

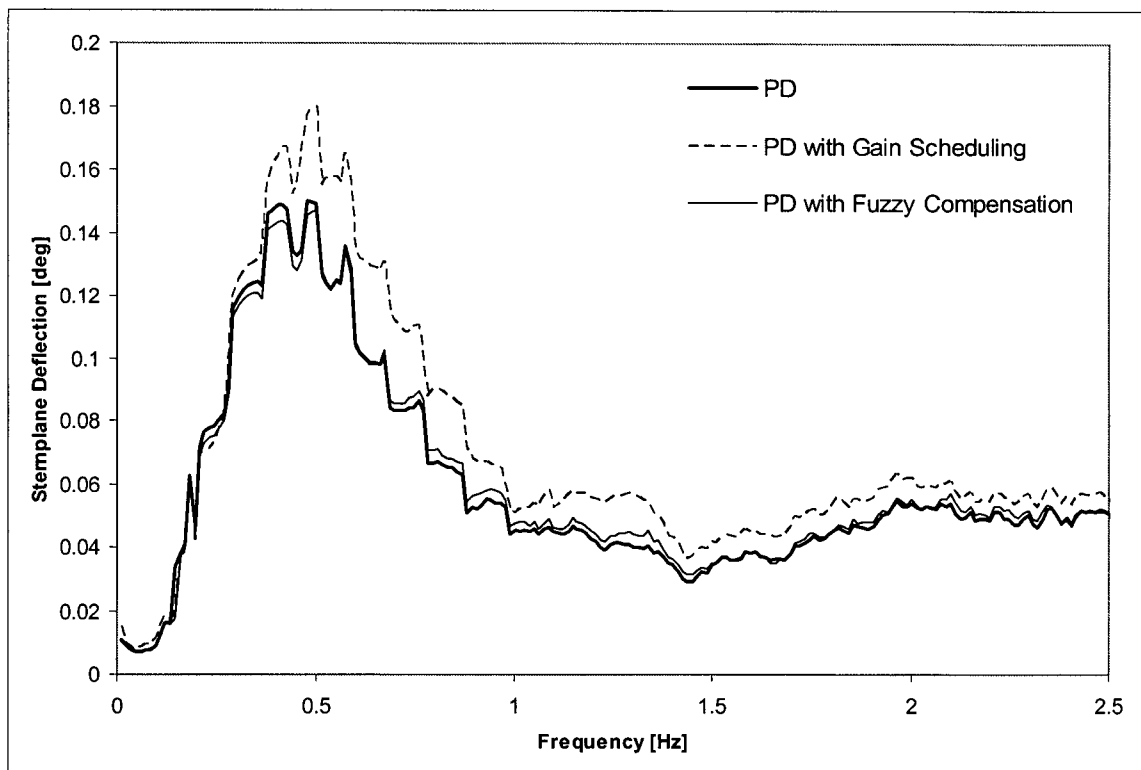


Figure F-21 Sternplane deflection spectra for PD augmentations in sea state three head seas

F.4.2 LQG/LTR Controller Augmentations

Table F-13 Effect of LQG/LTR augmentation on performance in calm water

Parameter	Controller		
	LQG/LTR	Sliding Mode LQG/LTR	LQG/LTR with Fuzzy Compensator
Performance Index, J_{ct}	0.1014	0.0891	0.1018
Performance Index, J_{sl}	0.0058	0.0023	0.0059
RMS Roll Error [deg]	6.1	5.8	6.1
RMS Pitch Error [deg]	0.4	0.3	0.4
RMS Yaw Error [deg]	1.0	1.1	1.0
RMS Depth Error [m]	0.04	0.02	0.04
Maximum Roll Error [deg]	21.1	21.1	21.1
Maximum Pitch Error [deg]	1.8	1.7	1.8
Maximum Yaw Error [deg]	12.5	17.8	12.4
Maximum Depth Error ^a [m]	0.17	0.10	0.17
Average Turn Radius [m]	30.4	30.5	30.4
Bowplane Deviation [deg] ^b	3.9	2.4	3.9
Sternplane Deviation [deg]	4.1	1.9	4.0
Bowplane Saturation [%]	3.6	1.3	3.8
Sternplane Saturation [%]	0.7	0.9	0.6

a. the maximum error in depth was considered for $x > 120$ m, 60 m after the step change in depth

b. plane deviations are measured as the average absolute deflection from the mean deflection

Table F-14 Effect of LQG/LTR augmentation on performance in sea state 3

Parameter	Controller		
	LQG/LTR	Sliding Mode LQG/LTR	LQG/LTR with Fuzzy Compensator
Performance Index, J_{ct}	0.0954	0.0963	0.0954
Performance Index, J_{sl}	0.0103	0.0110	0.0106
RMS Roll Error [deg]	5.7	5.7	5.7
RMS Pitch Error [deg]	0.3	0.3	0.3
RMS Yaw Error [deg]	1.1	1.1	1.1
RMS Depth Error [m]	0.04	0.03	0.04
Maximum Roll Error [deg]	21.0	20.8	20.7
Maximum Pitch Error [deg]	1.5	1.5	1.4
Maximum Yaw Error [deg]	14.5	12.0	14.9
Maximum Depth Error ^a [m]	0.15	0.07	0.15
Average Turn Radius [m]	30.5	30.4	30.5
Bowplane Deviation [deg] ^b	4.9	4.4	4.7
Sternplane Deviation [deg]	3.4	4.1	3.4
Bowplane Saturation [%]	3.1	2.1	2.9
Sternplane Saturation [%]	1.1	1.5	1.0

a. the maximum error in depth was considered for $x > 120$ m, 60 m after the step change in depth

b. plane deviations are measured as the average absolute deflection from the mean deflection

Table F-15 Spectral analysis for LQG/LTR controller performance in sea state 3

Significant Amplitude	Controller		
	LQG/LTR	Sliding Mode LQG/LTR	LQG/LTR with Fuzzy Compensator
Sway [m]	0.0034	0.0036	0.0036
Heave [m]	0.0019	0.0016	0.0018
Roll [deg]	0.0070	0.0071	0.0070
Pitch [deg]	0.0306	0.0294	0.0297
Yaw [deg]	0.0211	0.0219	0.0210
Bowplane deflection [deg]	0.0143	0.0113	0.0138
Sternplane deflection [deg]	0.0128	0.0126	0.0130
J_{sa} [-]	0.191	0.179	0.192

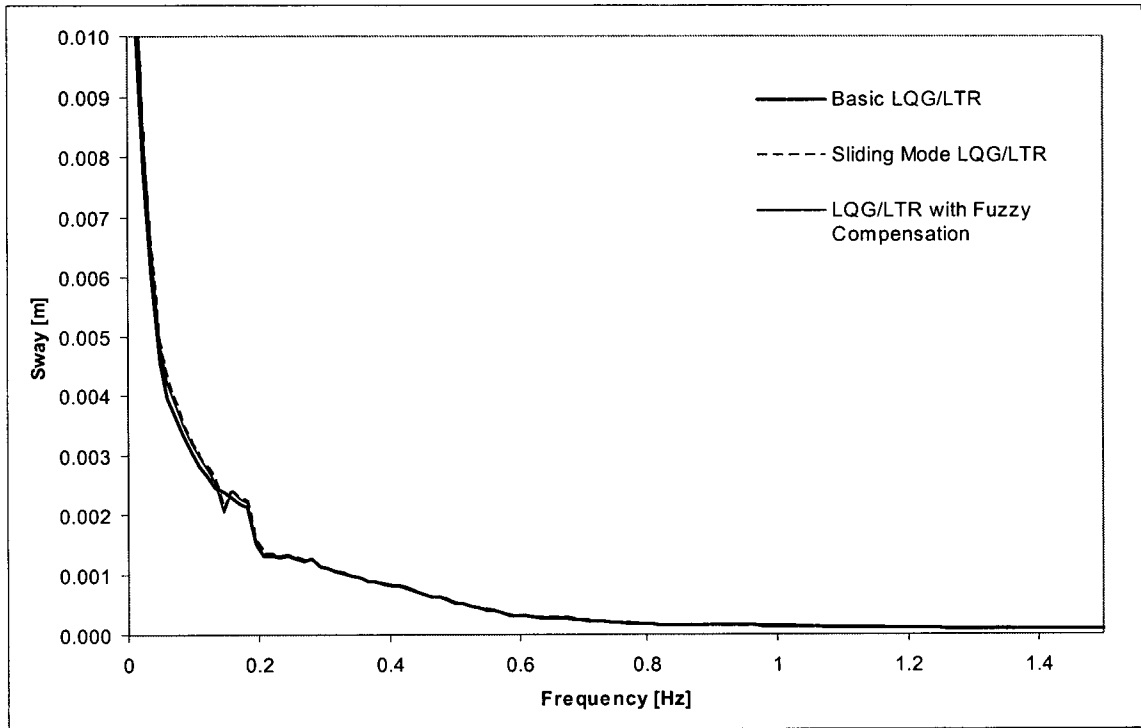


Figure F-22 Sway response spectra for LQG augmentations in sea state three head seas

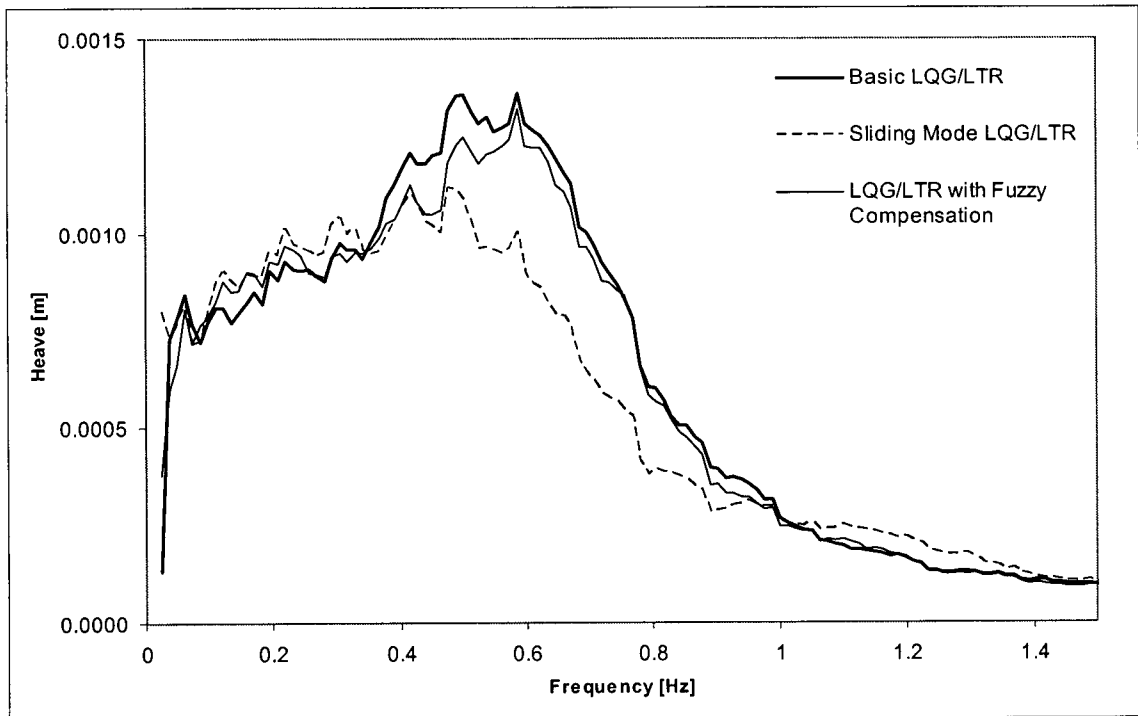


Figure F-23 Depth response spectra for LQG augmentations in sea state three head seas

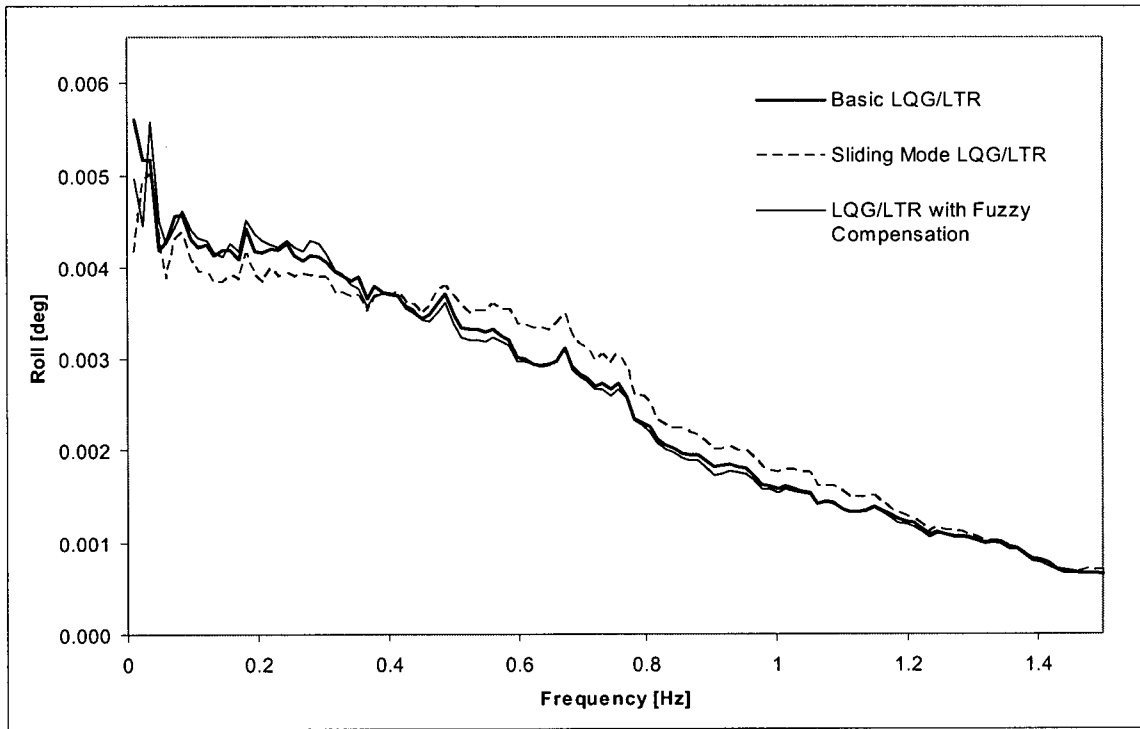


Figure F-24 Roll response spectra for LQG augmentations in sea state three head seas

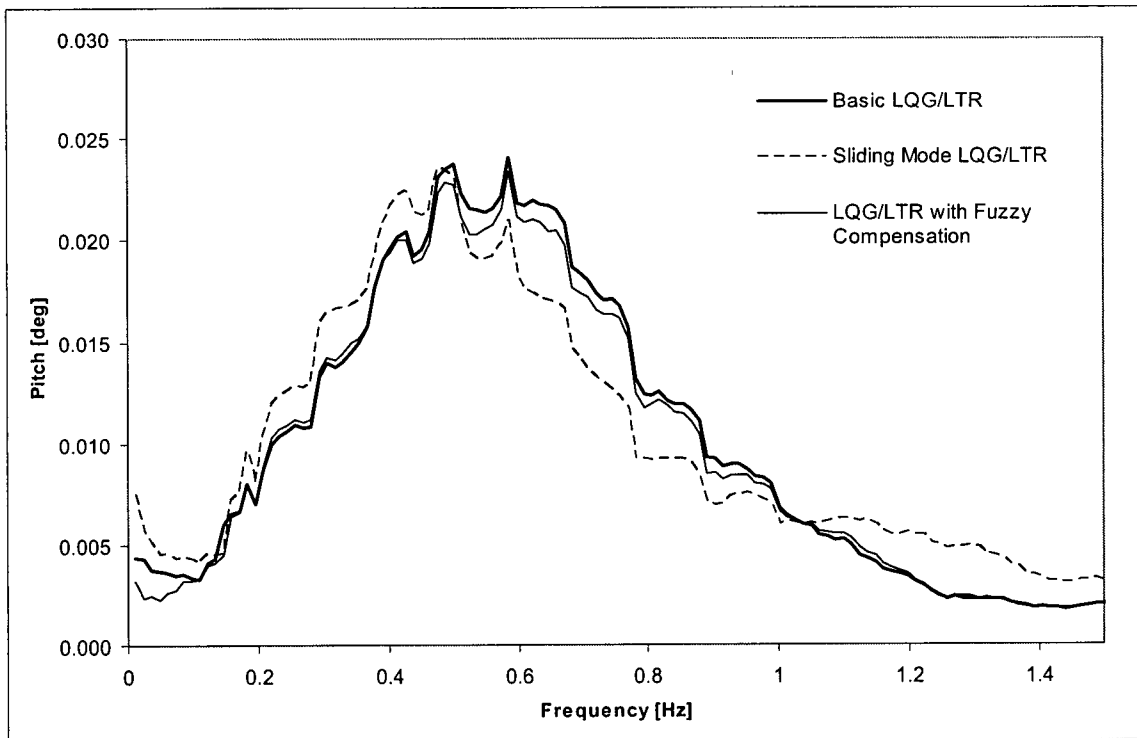


Figure F-25 Pitch response spectra for LQG augmentations in sea state three head seas

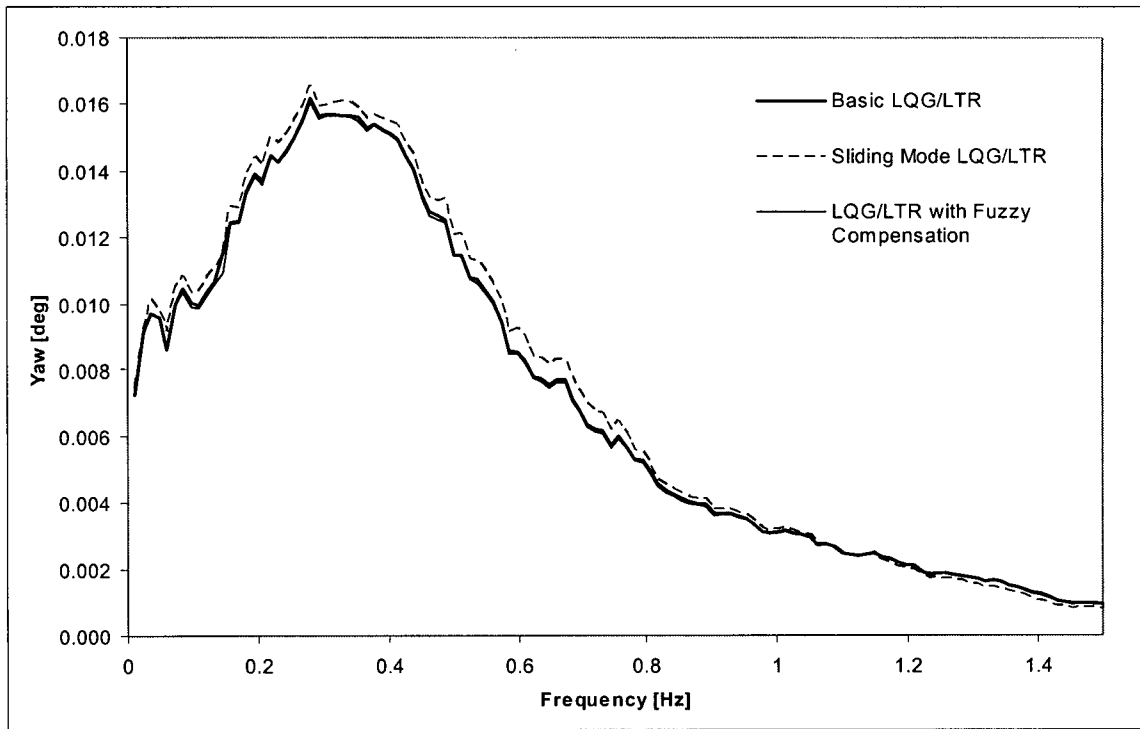


Figure F-26 Yaw response spectra for LQG augmentations in sea state three head seas

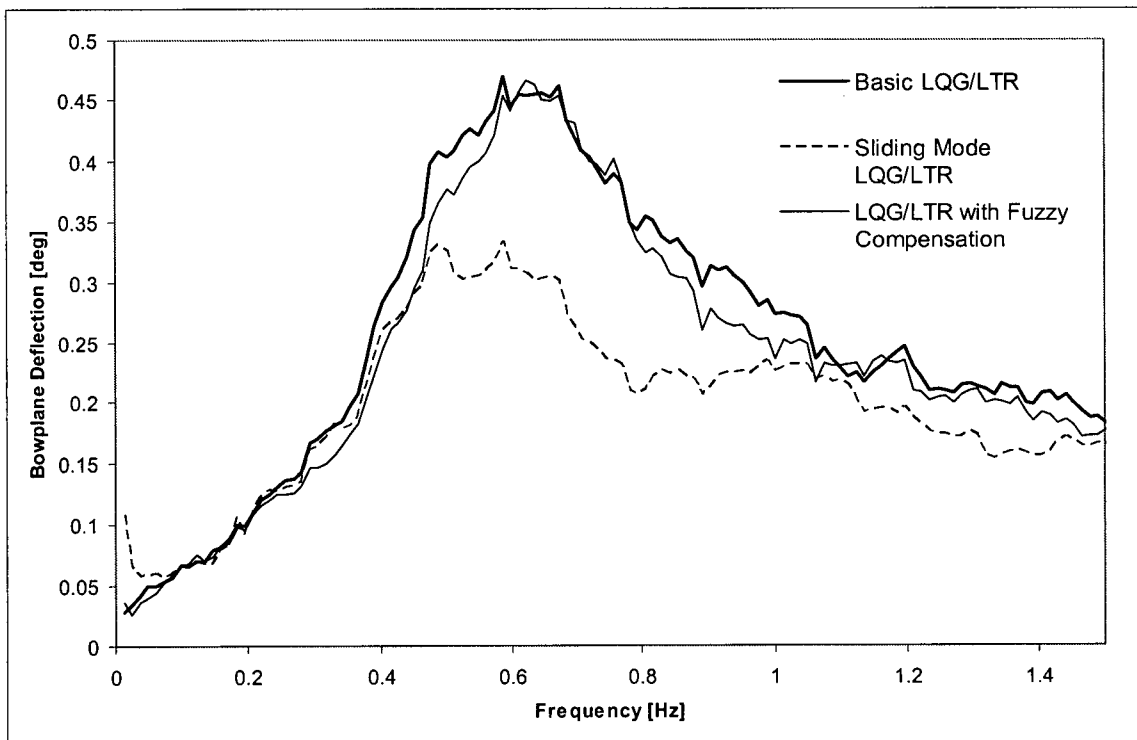


Figure F-27 Bowplane deflection spectra for LQG augmentations in sea state three head seas

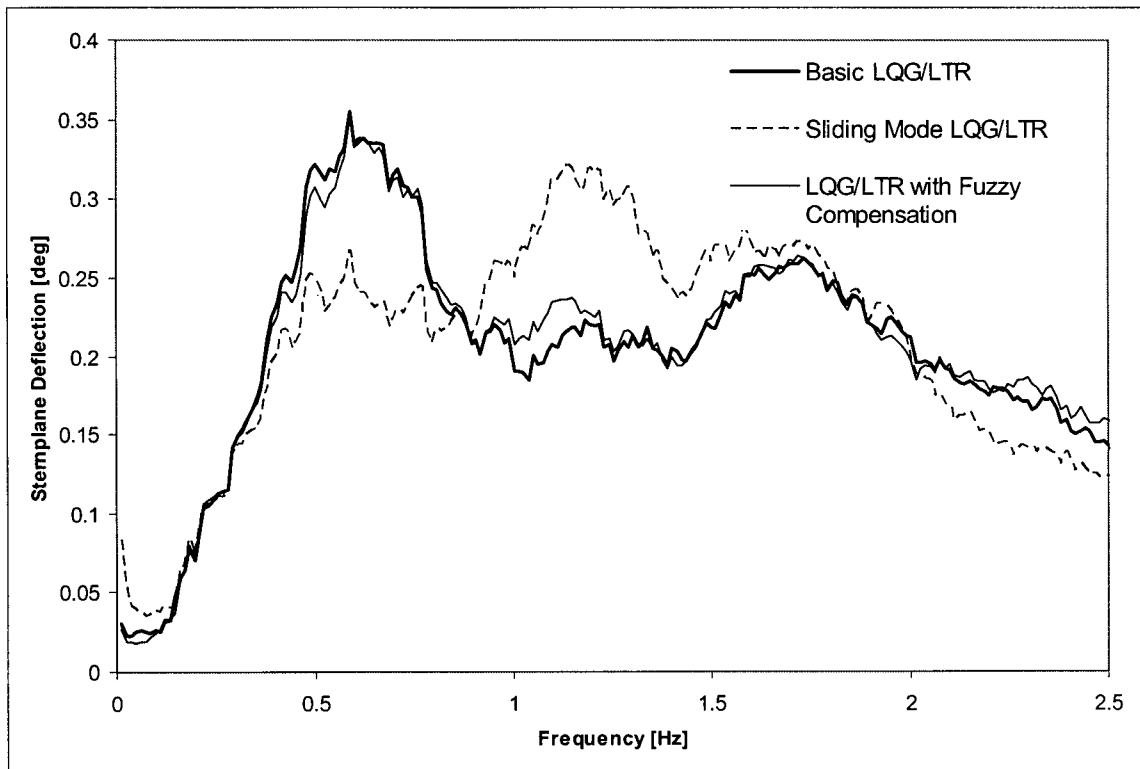


Figure F-28 Sternplane deflection spectra for LQG augmentations in sea state three head seas

REFERENCES

A

- Akiyama, H., et al. "Mission to Europa's Sub-Surface Ocean and Search for Possible Biological Traces." *Advances in Space Research*, Vol. 23, No. 2, pp. 367-370, 1999.
- Allen, H. Julian and Edward W. Perkins. "Characteristics of Flow Over Inclined Bodies of Revolution." NACA Report RM A50L07, March 5, 1951.
- An, Edgar and Samuel M. Smith. "An Experimental Self-Motion Study of the Ocean Explorer AUV in Controlled Sea States." *IEEE Journal of Oceanic Engineering*, Vol. 23, No. 3, July 1998.
- An, Edgar, et al. "Coastal Oceanography Using a Small AUV." *Journal of Atmospheric and Oceanic Technology*, Vol. 18, No. 2, pp. 215-234, February 2001.
- Ananthakrishnan, P., and K-Q. Zhang. "AUV Motion in a Wave Field." *Proc. of the Oceans '98 Conference, IEEE*, Vol. 2, 28 Sept - 1 Oct, pp. 1059-63, 1998.
- Aronson, Dag, and Per Lekander. "Experimental and Computational Analysis of the Flow on a Swept Wing with Small Aspect Ratio at Low Reynolds Numbers." Report FFA TN 1985-52, Flygtekniska Försöksanstalten, Sweden, 1986.
- Asakawa, Kenichi, et al. "Design Concept and Experimental Results of the Autonomous Underwater Vehicle AQUA EXPLORER 2 for the Inspection of Underwater Cables." *Advanced Robotics*, Vol. 16, No. 1, pp 27-42, 2002.
- Ashley, Holt and Marten Landahl. *Aerodynamics of Wings and Bodies* Dover Publications, New York, 1965.
- Åström, Karl J. and Björn. Wittenmark. *Computer Controlled Systems*. Third Ed., Prentice Hall, 1997.
- Aucher, M. "Dynamique des Sous-Marins." Imprimerie Nationale, Paris, Tran. Doug Lawrence, Dept. of Secretary of State, Halifax, 1981.
- Avallone, Eugene A., and Theodore Baumeister III. *Marks' Standard Handbook for Mechanical Engineers*. 10th Ed., McGraw-Hill, Toronto, 1996.

B

- Banerjee, J.S., K.O. Jones, and D. Williams. "Design considerations for a Model Reference Fuzzy Adaptive Controller." *Transactions of the Institute of Measurement and Control*, Vol. 23, No. 3, pp. 141-62, 2001.
- Barlow, Jewel B., William H Rae, Jr. and Alan Pope. *Low-Speed Wind Tunnel Testing*. Third Ed., John Wiley and Sons, Toronto, 1999.
- Barlow, Jewel, Daniel Harris, and Robert Ranzenbach. "Time Domain Simulation of Underwater Vehicles." *International Symposium and Workshop on Force Acting on a Manoeuvring Vessel*, Val de Reuil, France, September 1998.
- Bossley, K.M., M. Brown, and C.J. Harris. "Neurofuzzy Identification of an Autonomous Underwater Vehicle." *International Journal of Systems Science*, Vol. 30, No. 9, pp 901-913, 1999.

- Boyce, William, and Richard DiPrima. *Elementary Differential Equations and Boundary Value Problems*. 5th Ed., John Wiley and Sons, Toronto, 1992.
- Bullivant, W.K. "Tests of the NACA 0025 and 0035 Airfoils in the Full-Scale Wind Tunnel." NACA Report No. 708. 1941.
- Burden, Richard, and J. Douglas Faires. *Numerical Analysis*. 6th Ed., Brooks Cole Publishing, Toronto, 1997.
- Butler, Bruce. "Positioning and navigation for the DOLPHIN vehicle using LORAN-C." Proc. of Intervention '90, Marine Technology Society, Vancouver, pp. 233-8, 1990.
- Bystrom, L. "Adaptive Control of a Submarine in a Snorting Condition in Waves." Proc. of Warship 88, the International Symposium on Conventional Naval Submarines, 3-5 May, 1988.

C

- Caccia, Massimo, and Gianmarco Veruggio. "Modeling, Identification, Control and Guidance of Unmanned Underwater Vehicles." *Underwater Vehicle Technology*, Vol. 12, Eds. Choi, S.K. and J. Yuh, TSI Press, 2001.
- Cancelliere, Frederick M. "Unmanned Undersea Vehicle Technology 'A U.S. Naval Sea Systems Command Undersea Warfare Center Perspective'." *Underwater Vehicle Technology*, Eds. Song K. Choi, Junku Yuh, TSI Press, Albuquerque, pp. 1-9, 2001.
- Carder, Kendall L., et al. "Ocean-Science Mission Needs - Real-Time AUV Data for Command, Control, and Model Inputs." *IEEE Journal of Oceanic Engineering*, Vol. 26, No. 4, October 2001.
- Carreras, M., J. Battle, P. Ridao, and G.N. Roberts. "An overview on Behaviour-Based Methods for AUV Control." Proc. of the 5th IFAC Conference on Manoeuvring and Control of Marine Crafts, Aalborg, Denmark, 23-5, August, 2000.
- Cellier, Francois E., Hilding Elmqvist, Martin Otter, and William S. Levine. "Determining Models." *The Control Handbook*. Ed. William S. Levine, CRC Press, 1996.
- Clancy, Tom. *Submarine*. Berkley Books, New York, 1993.
- Conway, John, and M. Mackay. "Prediction of the Effects of Body Separation Vortices on Submarine Configurations Using the CANAERO Panel Method." AIAA Paper 90-0302, 28th Aerospace Sciences Meeting, 8-11 January, Reno, Nevada, 1990.
- Craven, Paul J., Robert Sutton, Roland S. Burns, and Yong-Ming Dai. "Multivariable Intelligent Control Strategies for an Autonomous Underwater Vehicle." *International Journal of Systems Science*, Vol. 30, No. 9, pp 965-80, 1999.
- Cristi, Roberto, Fotis A. Papoulias, and Anthony J. Healy. "Adaptive Sliding Mode Control of Autonomous Underwater Vehicles in the Dive Plane." *IEEE Journal of Oceanic Engineering*, Vol. 15, No. 3, July, pp. 152-60, 1990.

D

- de Silva, Clarence. *Intelligent Control - Fuzzy Logic Applications*. CRC Press, New York, 1995.

- Dempsey, Elizabeth M. "Static Stability Characteristics of a Systematic Series of Stern Control Surfaces on a Body of Revolution." Report 77-0085, David Taylor Model Basin, Bethesda, Maryland, 1977.
- den Hertog, Vincent, Vinod J. Modi. "Trailing Edge Moving Surface Boundary Layer Control - Manoeuvring Performance of an AUV." Proc. of the Sixth Canadian Marine Hydromechanics and Structures Conference, Vancouver, 23-26 May, 2001.
- den Hertog, Vincent. Private communication. November 1997.
- DiBitetto, P.A., "Fuzzy Logic for Depth Control of Unmanned Undersea Vehicles." IEEE Journal of Oceanic Engineering, Vol. 20, pp. 242-248, 1995.
- Dominguez, Rodolfo R. "Effects of Yaw on Bowplane Performance on DOLPHIN." Mech 597 M. Eng. Report, University of British Columbia, Vancouver, Canada. September, 2000.
- Doucy, Olivier, Dandal Brutzman and Anthony Healey. "Near Surface Manoeuvring and Station-Keeping for an Autonomous Underwater Vehicle." Proc. of the NATO Symposium on Applied Vehicle Technology, Ankara, Turkey, October, 2000.
- Dougherty, F., and G. Woolweaver. "At-Sea Testing of an Unmanned Underwater Vehicle Flight Control System." Proc. of the 1990 Symposium on Autonomous Underwater Vehicle Technology, pp. 65-73, 1990.

E

- Edwards, Joseph R., Henrik Schmidt, and Kevin D. LePage. "Bistatic Synthetic Aperture Target Detection and Imaging With an AUV." IEEE Journal of Oceanic Engineering, Vol. 26, No. 4, October 2001.
- Eppler, Richard. "An Empirical Criterion for Laminar-to-Turbulent Boundary Layer Transition." Technical Soaring, Vol. 23, No. 2, April, pp. 34-42, 1999.
- Eppler, Richard. *Airfoil Design and Data*. Springer-Verlag, New York, 1990.

F

- Feldman, J. "DETNSRDC Revised Standard Submarine Equations of Motion." David Taylor Naval Ship Research and Development Center report DTNSRDC/SPD-0393/09, June, 1979.
- Feldman, Jerome P. "Method of Performing Captive-Model Experiments to Predict the Stability and Control Characteristics of Submarines." Report CRDKNSWC-HD-0393-25, Carderock Division, Naval Surface Warfare Center, Bethesda, Maryland, 1995.
- Ferguson, James, Allan Pope, Bruce Butler, and Ronald Verrall. "Theseus AUV - Two Record Breaking Missions." Sea Technology, pp. 65-70, Feb 1999.
- Ferguson, James, and Allan Pope. "Theseus - Multipurpose Canadian AUV", Sea Technology, pp. 19-26, April 1995.
- Field, A., D. Cherchas, S. Calisal, and P. Ostafichuk. "Adaptive Control of an Autonomous Vehicle Using Robust LQG/LTR Designs." Proc. of the 6th Canadian Marine Hydromechanics and Structures Conference, Vancouver, 23-26 May, pp. 289-300, 2001..

Field, Adrian, Dale Cherchas, and Sander Calisal. "Optimal Control of an Autonomous Underwater Vehicle." *Underwater Vehicle Technology*, Vol. 12. Eds. Song K. Choi, Junku Yuh, TSI Press, Albuquerque, pp 67-82, 2000.

Field, Adrian. "Simulation, Modelling and Control of a Near-Surface Underwater Vehicle." Diss. University of British Columbia, 2000.

Fryxell, D. P. Oliveira, A. Pascoal, and C. Silvestre. "Integrated Design of Navigation, Guidance and Control Systems for Unmanned Underwater Vehicles." *Proc. Oceans '94*, Vol. 3, pp. 105-110, 1993.

G

Ghaliya, Mounir Ben. "Modelling and robust Control of Uncertain Dynamical Systems Using Fuzzy Set Theory." *Int. Journal of Control*, Vol. 68, No. 6, pp. 1367-95, 1997.

Gilbert, R. "The Mine-Hunting DOLPHIN." *Proc. of Intervention '90*, Vancouver, BC, 25-27 June, 1990.

H

Hale, R.W., P. Tan, R.C. Stowell, and D.E. Ordway. "Development of an Integrated System for Flow Visualization in Air Using Neutrally-Buoyant Bubbles." Sage Action Inc. report SAI-RR 7107, 1971.

Han, Simon, Elaine Oum, and Quinton Talbot. "Investigation of the Effects of Downwash on Control Surface Performance." Project Report 9761, Department of Engineering Physics, University of British Columbia, 1998.

Hayes, Daniel R., James and H. Morrison. "Determining Turbulent Vertical Velocity, and Fluxes of Heat and Salt with an Autonomous Underwater Vehicle." *Journal of Atmospheric and Oceanic Technology*, Vol. 19, No. 5, pp. 759-779, May 2002.

Healey, Anthony J., and D. Marco. "Slow speed flight control of autonomous underwater vehicles - experimental results with NPS AUV II." *Proc. ISOPE*, pp. 523-532, 1992.

Healey, Anthony J., and David Lienard. "Multivariable Sliding-Mode Control for Autonomous Diving and Steering of Unmanned Underwater Vehicles." *IEEE Journal of Oceanic Engineering*, Vol. 18, No. 3, July 1993.

Hills, J.J., and D.R. Yoerger. "A Nonlinear Sliding Mode Autopilot for Unmanned Undersea Vehicles." *Proc. Oceans '94*, Vol. 3, pp. 93-98, 1994.

Hoerner, Sighard F., and Henry V. Borst. *Fluid-Dynamic Lift*, Hoerner Fluid Dynamics, Brick Town, N.J., 1975.

Hoerner, Sighard. "Forces and Moments on a Yawed Airfoil." NACA Report TM 906, Washington, August, 1939.

Hoffman, Joe. *Numerical Methods for Engineers and Scientists*. McGraw-Hill, Toronto, 1992.

Hogg, Robert V., and Johannes Ledolter. *Applied Statistics for Engineers and Physical Scientists*. 2nd Ed., Maxwell Macmillan Publishers, Toronto, 1992.

-
- Hopkin, David, Michael Davies, and Ian Gartshore. "The Aerodynamics and Control of a Remotely-Piloted Underwater Towed Vehicle." *Canadian Aeronautics and Space Journal*, Vol. 36, No. 3, September, pp. 122-9, 1990.
- Hopkin, David, Vince den Hertog. "The Hydrodynamic Testing and Simulation of an AUV." *Proc. of the Second Candian Marine Dynamics Conference, University of British Columbia, Vancouver, BC, August 9-11, 1993.*
- Huggins, A., and A.R. Packwood. "Wind Tunnel Experiments on a Fully Appended Laminar Flow Submersible for Oceanographic Survey." *Ocean Engineering*, Vol. 22, No. 2, pp. 207-221, 1995.
- Huyer, S. "Simulation of UUV Recovery Hydrodynamics." *Twenty-Third Symposium on Naval Hydrodynamics, the National Academy of Sciences, 2001.*

J

- Jacob, Jamey. "Experimental Investigation of the Trailing Vortex Wake of Rectangular Airfoils." *Diss. University of California at Berkley, 1995.*
- Jacobs, Eastman N., and Albert Sherman. "Airfoil Section Characteristics as Affected by Variations of the Reynolds Number." *NACA Report 586, 1937.*
- Jalving, Bjorn. "The NDRE-AUV Flight Control System." *IEEE Journal of Oceanic Engineering*, Vol. 19, No. 4, October 1994.
- Journée, J.M.J. "Theoretical Manual of SEAWAY." *Report 1216a, Delft University of Technology, Netherlands, pp. 247-52, 2001.*
- Juul, D. L., M. McDermott, E. L. Nelson, D. M. Barnett and G. N. Williams. "Submersible Control Using the Linear Quadratic Gaussian with Loop Transfer Recovery Method." *Symposium on Autonomous Underwater Technology, Cambridge, July, pp. 417-25, 1994,*

K

- Kim, Joonyoung, Kihun Kim, Hang S. Choi, Woojae Seong, and Kyu-Yeul Lee. "Estimation of Hydrodynamic Coefficients for an AUV Using Nonlinear Observers." *IEEE Journal of Oceanic Engineering*, Vol. 27, No. 4, October 2002.
- Kosko, Bart. *Fuzzy Thinking*. Hyperion, New York, 1993.
- Kubota, H., M.Y. Jia, T. Watanuki, and K. Susuki. "Fluid Dynamics of High Angle of Attack." *Proc. of the IUTAM Symposium, Tokyo, Japan, Sept, pp. 277-88, 1992.*
- Kulcsár, Balázs. "LQG/LTR Controller Design for an Aircraft Model." *Periodica Polytechnica Ser. Trasp. Eng. , Vol. 28, No. 1-2, pp. 131-142, 2000.*
- Kumagai, Michio, et al. "A New Autonomous Underwater Vehicle Designed for Lake Environment Monitoring." *Advanced Robotics*, Vol. 16, No.1, pp. 17-26, 2002.

L

- Lamb, Sir Horace. *Hydrodynamics*. 6th Ed. Cambridge University Press, 1997.

- Laval, Bernard, John S. Bird, Peter and D. Helland. "An Autonomous Underwater Vehicle for the Study of Small Lakes." *Journal of Atmospheric and Oceanic Technology*, Vol. 17, No. 1, pp. 69-76, January 2000.
- Lawrence, H.R., and A.H. Flax. "Wing-Body Interference at Subsonic and Supersonic Speeds - Survey and New Developments." *Journal of Aeronautical Sciences*, Vol. 21, No. 5, May 1954.
- Lea, R.K. "Control of a Tethered Underwater Flight Vehicle in the Horizontal Plane." *Proc. of the 10th International Symposium on Unmanned Untethered Submersible Technology*, pp. 261-271, 1997.
- Lea, R.K., R. Allen, and S.L. Merry. "A Comparative Study of Control Techniques for an Underwater Flight Vehicle." *International Journal of Systems Science*, Vol. 30, No. 9, pp. 947-64, 1999.
- Lea, R.K., R. Allen, S.L. Merry. "Surge Speed Control Methods for a Laminar-Flow Autonomous Underwater Vehicle." *Oceanic Engineering International*, Vol. 1, pp. 10-15, 1997.
- Lee, C.S. George, Jeen-Shing Wang, and Junku Yuh. "Self-Adaptive Neuro-Fuzzy Systems for Autonomous Underwater Vehicle Control." *Advanced Robotics*, Vol. 15, No. 5, pp. 589-608, 2001.
- Leith, D.J. "Survey of Gain-Scheduling Analysis and Design." *International Journal of Control*, Vol. 73, No. 11, July 10, pp. 1001-1025, 2000.
- Leith, D.J. and W.E. Leithead. "Appropriate Realisation of MIMO Gain-Scheduled Controllers." *International Journal of Control*, Vol. , No. 1, pp. 13-50, 1998.
- LePage, Kevin D., and Henrik Schmidt. "Bistatic Synthetic Aperture Imaging of Proud and Buried Targets From an AUV." *IEEE Journal of Oceanic Engineering*, Vol. 27, No. 3, July 2002.
- Levine, Edward R., Donald N. Connors, Richard R. Shell, and Robert C. Hanson. "Autonomous Underwater Vehicle-Based Hydrographic Sampling." *Journal of Atmospheric and Oceanic Technology*. Vol. 14, No. 6, pp. 1444-1454, 1997.
- Liceaga-Castro, and E. G. van der Molen. "A Submarine Depth Control System Design." *International Journal of Control*, Vol. 61, pp. 279-308, 1995.
- Liceaga-Castro, and E. G. van der Molen. "Submarine H-infinity Depth Control Under Wave Disturbances." *IEEE Journal of Oceanic Engineering*, Vol. 3, pp. 338-346, 1995.
- Lin Chih-Min and Chun-Fei Hsu. "Guidance Law Design by Adaptive Fuzzy Sliding-Mode Control." *Journal of Guidance, Control, and Dynamics*, Vol. 25, No. 2, pp. 248-56, 2000.
- Lloyd, A.R.J.M. "Roll Stabilizer Fins - A Design Procedure." *Royal Institution of Naval Architects*, Volume 117, pp. 233-254, 1974.
- Lorentz, Jorgen, and J. Yuh. "A Survey and Experimental Study of Neural Network AUV Control." *Proc. tAUV'96, IEEE, Monterey*, 1996.
- Lyons, D.J., and P.L. Bisgood. "An Analysis of the Lift Slope of Aerofoils of Small Aspect Ratio including Fins with Design Charts for Aerofoils and Control Surfaces." *Reports and Memoranda No. 2308, Ministry of Supply, London*, 1950.

M

- Mackay, Michael. "Semiempirical methods for predicting appendage forces." Private communication. April 1998,
- Mackay, Michael. "Submarine Hydrodynamics Research at Defence Research Establishment Atlantic." Proc. of the Second Canadian Marine Dynamics Conference, University of British Columbia, Vancouver, BC, Aug 9-11, 1993.
- Maltby, R.L., and R.F.A. Keating. "The Surface Oil Flow Technique for use in Low Speed Wind Tunnels." Flow Visualization in Wind Tunnels Using Indicators, NATA Advisory Group for Aeronautical Research and Development Fluid Dynamics Panel, 1962.
- McDonald, H., and D. Whitfield. "Self-Propelled Maneuvering Underwater Vehicles." Proc. of the Twenty-First Symposium on Naval Hydrodynamics, National Academy of Sciences, 1997.
- McFarlane, James R., Vincent den Hertog, and Ben Triplett. "Rover and Gofer - an AUV/ROV Hybrid." Proc. of the Sixth Canadian Marine Hydromechanics and Structures Conference, Vancouver, 23-26 May, pp. 281-8 2001.
- McTaggart, K.A., G.W. Johnston, W. Campbell, and S.P. Foster. "A Strip Theory Program for Submarine Motion in Waves." Proc. of the Second Canadian Marine Dynamics Conference, University of British Columbia, Vancouver, BC, Aug 9-11, 1993.
- McTaggart, K.A.. "SHIPMO7 - An Updated Strip Theory Computer Program for Predicting Ship Motions and Sea Loads in Waves." DREA Technical Memorandum 96/243, 1996.
- Merzkirch, Wolfgang. *Flow Visualization*. Second Ed. Academic Press, Inc., Toronto, 1987.
- Munk, M.M. "Downwash of Airplane Wings." NACA Technical Note 124, Langley Memorial Aeronautical Library, 1923.

N

- Naeem, W., R. Sutton, and S.M. Ahmad. "LQG/LTR Control of an Autonomous Underwater Vehicle Using a Hybrid Guidance Law." Proc. of GCUV'03, Newport, UK, April, pp. 35-40, 2003.
- Nahon, Meyer. "A Simplified Dynamics Model for Autonomous Underwater Vehicles." Proc. of the 1996 IEEE Symposium on Autonomous Underwater Vehicle Technology, June 1996.
- Nahon, Meyer. "Determination of Undersea Hydrodynamic Derivatives Using the USAF Datcom." Proc. of Oceans '93 Conference, Vol. 2, IEEE, 1993.
- Newman, J.N. *Marine Hydrodynamics*. MIT Press, 1977.

O

- Oh, Kyu-Hyun, Jung-Yup Kim, Ill-Woo Park, Jungho Lee and Jun-Ho Oh. "A Study on the Control of AUV's Homing and Docking." Proc. of the 9th IEEE Conference on Mechatronics and Machine Vision in Practice, Chiang Mai, Thailand, 2002.

Ostafichuk, Peter, Adrian Field, Sander Calisal, Dale Cherchas. "Low Speed Wind Tunnel Flow Visualization for the Study of Submarine Control Effectiveness." Proc. 5th Candian Marine Hydromechanics and Structures Conference, St. Johns, July 8-9, 1999.

P

Palm, William. *Control Systems Engineering*. John Wiley and Sons, Toronto, 1986.

Pauchet, A. "Velocity and Turbulence in the Near-Field Region of Tip Vortices from Elliptical Wings - Its Impact on Cavitation." Proc. of the Twenty-First Symposium on Naval Hydrodynamics, pp. 865-79, 1997.

Perrier, M., and Canudas-de-Wit, C. "Experimental Comparison of PID vs. PID Plus Nonlinear Controller for Subsea Robots." *Autonomous Robots*, Vol. 3, No. 2, pp. 195-212, 1996.

Perron, C., M. Mackay, and C. D. Williams. "Marine Dynamic Test Facility - The System." Proc. of the Workshop on Control and Simulation Systems for Underwater Vehicles, NRC Institute for Marine Dynamics, St. John's, Newfoundland, 19-20 October 1998

Peterson, Ronald S., Thai C. Nguyen, and Rafael R. Rodriguez. "Motion Minimization of AUVs for Improved Imaging Sensor Performance Beneath a Seaway." Proc. of the 1994 Symposium on Autonomous Underwater Vehicle Technology, 19-20 July, 1994.

Pope, Alan, and J.J. Harper. *Low-Speed Wind Tunnel Testing*. John Wiley and Sons, New York, 1966.

Potter, Merle C., and David C. Wiggert. *Mechanics of Fluids*. 2nd Ed., Prentice Hall, Toronto, 1997.

Prestero, Timothy. "Development of a Six-Degree of Freedom Simulation Model for the REMUS Autonomous Underwater Vehicle." Proc. of Unmanned Untethered Submersible Technology, New Hampshire, August, 2001b.

Prestero, Timothy. "Verification of a Six-Degree of Freedom Simulation Model for the REMUS AUtonomous Underwater Vehicle." Diss. MIT, September, 2001a.

R

Riedel, Jeffery S., and Anthony J. Healey. "Shallow Water Station Keeping of AUVs Using Multi-Sensor Fusion for Wave Disturbance Prediction and Compensation." Proc. of the Oceans '98 Conference, Vol. 2, IEEE, 28 Sept - 1 Oct, 1998.

Rodriguez, R.R., and G.J. Dobeck. "Guidance and Control System of the Large Scale Vehicle." Proc. of the 6th International Symposium on Unmanned Untethered Submersible Technology, pp. 434-51, 1989.

RWDI (Rowan Williams Davies & Irwin Inc.) "Flow Visualization Test of DREA Standard Submarine Model October - November 1988." Contractor Report CR/89/435 prepared for DREA, Canada, 1989.

S

- Schlichting, H. "Monograph on the Aerodynamics of the Mutual Interference Between the Components of an Aeroplane." (translation), NRC TT-92, July 1949.
- Seto, Mae and George D. Watt. "The Interaction Dynamics of a Semi-Submersible Towing a Large Towfish." Proc. of the International Offshore and Polar Engineering Conference and Exhibition, Vol. 2, pp. 263-270, 1998.
- Seto, Mae. Private communication. June 17 1998.
- Shupe, Landy, Ted McGeer. "A Fundamental Mathematical Model for the Longitudinal and Lateral/Directional Dynamics of the DOLPHIN Type Unmanned Semi-Submersible." DREP/RRMC Military Robotic Applications Workshop, Victoria, Aug 11-14, pp. 171-81, 1987.
- Silvestre, C., A. Pascoal, and A.J. Healey. "AUV Control Under Wave Disturbances." Proc. of the 10th International Symposium on Unmanned Untethered Submersible Technology, pp. 228-239, 1997.
- Smith, S.M., G.J.S. Rae, D.T. Anderson, A.M. Shein. "Fuzzy Logic Control of an Autonomous Underwater Vehicle." Control Engineering Practice, Vol. 2, pp. 321-331, 1994.
- Solberg, Paal Aer Hagtbedt. "Submarine Dynamics and Modelling." Report ICC-REP-5, University of Strathclyde Industrial Control Centre, 1992.
- Song, F., E. An, and S.M. Smith. "Design Robust Nonlinear Controllers for Autonomous Underwater Vehicles with Comparison of Simulated and At-sea Test Data." Journal of Vibration and Control, Vol. 8, No. 2, pp. 189-217, 2002.
- Song, Feijun and Samuel M. Smith. "Automatic Design and Optimization of Fuzzy Logic Controllers for an Autonomous Underwater Vehicle." Proc. of Oceans 2000, MTS/IEEE, pp. 829-34, 2000a.
- Song, Feijun and Samuel M. Smith. "Design of Sliding Mode Fuzzy Controllers for an Autonomous Underwater Vehicle with System Model." Proc. of Oceans 2000, MTS/IEEE,, pp. 835-40, 2000b.
- Spiegel, Murray. *Theory and Problems of Probability and Statistics*. McGraw-Hill, Toronto, 1992.
- Stack, John. "Tests in the Variable Density Wind Tunnel to Investigate the Effects of Scale and Turbulence on Airfoil Characteristics." NACA Technical Note 364, 1931.
- Stein, Gunter, and Michael Athans. "The LQG/LTR Procedure for Multivariable Feedback Control Design." IEEE Trans. on Automatic Control. Vol. AC-32, No. 2, pp. 105-14, 1987.
- Strang, Gilbert. *Linear Algebra and Its Applications*. 3rd Ed., Saunders College Publishing, Toronto, 1988.
- Suto, T., and T. Ura. "Development of a Small Cruising-Type AUV 'Manta-Ceresia' and Guidance System Constructed with Neural Network." Proc. of the 10th International Symposium on Unmanned Untethered Submersible Technology, pp. 69-74, 1997.

T

- Talay, Theodore A. "Introduction to the Aerodynamics of Flight." NASA Report SP-367, Langley Research Center, 1975.
- Tay, T.T., and J.B. Moore. "Adaptive LQG Controller with Loop Transfer Recovery." *International Journal of Adaptive Control and Signal Processing*. Vol. 5, pp. 135-149, 1991.
- Tipler, Paul. *Physics - For Scientists and Engineers*. 3rd. Ed., Worth, New York, pp. 412-3, 1991.
- Torres, M., D.J. Cappelleri, D.S. Anes, M.P. Reiter, and A.P. DeGuilio. "Turbulator Geometry Influence on Tripping Effectiveness Based on Low-Speed Wind Tunnel Data." *Technical Soaring*, Vol. 23, No. 1, Jan., 1999.
- Triantafyllou, Michael S., and Franz S. Hover. "Maneuvering and Control of Marine Vehicles." *Lecture Notes*, 13.49, Massachusetts Institute of Technology, Cambridge, 2002.
- Triantafyllou, Michael S., and Mark. A. Grosenbaugh. "Robust Control for Underwater Vehicle Systems with Time Delays." *IEEE Journal of Oceanic Engineering*, Vol. 16, No. 1, January, 1991.
- Tzafestas, S.G. and G.G. Rigatos. "A Simple Robust Sliding-Mode Fuzzy-Logic Controller of the Diagonal Type." *Journal of Intelligent and Robotic Systems*, Vol. 26, pp. 353-88, 1999.
- Tzafestas, S.G., G.G. Rigatos, and G.A. Vagelatos. "Design of Fuzzy Gain-Scheduled Robust Controllers Using Kharitonov's External Gain Margin Theory." *Journal of Intelligent & Fuzzy Systems*, Vol. 10, pp. 39-56, 2001.

U

- Underwater Magazine, "Making the Oilfield ROV Autonomous - What Will It Take?" November/December 2000.

V

- van den Berg, B., W.J. Piers, and E. de Boer. "Calculation of the Flow Around a Swept Wing Taking into Account the Effect of the Three Dimensional Boundary Layer." Report NLR TR 77066 U, National Aerospace Laboratory, Netherlands, 1977.
- Venugopal, K.P., R. Sudhakar, and A.S. Pandya. "On-Line Learning Control of Autonomous Underwater Vehicles Using Feed-Forward Neural Networks." *IEEE Journal of Oceanic Engineering*, Vol. 17, pp. 308-319, 1992.
- von Mises, Richard. *Theory of Flight*. Dover Publications, 1959.

W

- Wadlin, Kenneth L., John A. Ramsen, and Victor L. Vaughan, Jr. "The Hydrodynamic Characteristics of Modified Rectangular Flat Plates Having Aspect Ratios of 1.00, 0.025, and 0.125 and Operating Near a Free Water Surface." NACA Report 1246, 1955.

-
- Walsh, Ronald. *McGraw-Hill Machining and Metalworking Handbook*. McGraw-Hill, Toronto, 1994.
- Watt, George D. "On the Necessity for Modelling Submarine Propeller Transverse Forces During Simulations of High Speed Maneuvers." Proc. of the Second Canadian Marine Dynamics Conference, University of British Columbia, Vancouver, BC, Aug 9-11, 1993.
- Watt, George D., Mae Seto, and Terry Brockett. "Hydrodynamic Considerations for Semi-Submersible Minehunting Vehicles." Proc. of the Fourth Canadian Marine Hydromechanics and Structures Conference, Ottawa, 25-27 June 1997.
- Watt, George D., Vinh D. Nguyen, Keven R. Cooper, and Bernard Tanguay. "Wind Tunnel Investigations of Submarine Hydrodynamics.", Canadian Aeronautics and Space Journal, Vol. 39, No. 3, September, pp. 119-26, 1993.
- Watt, George, and Eric Y. Fournier. "Submarine Propulsion Testing in the IAR 9m Wind Tunnel." Proc. of the Third Canadian Marine Hydrodynamics and Structures Conference, Halifax, 1995.
- Whicker, L Folger, Leo F. Fehlner, "Free-Stream Characteristics of a Family of Low-Aspect-Ratio All-Movable Control Surfaces for Application to Ship Design." Report 933, Revised Edition. David Taylor Model Basin, Bethesda, Maryland, 1958.
- White, Frank M. *Fluid Mechanics*. 2nd Ed., McGraw-Hill, Toronto, 1986.
- White, Frank M. *Viscous Fluid Flow*. 2nd Ed. McGraw-Hill, New York, 1991.
- Willcox, J. Scott, James G. Bellingham, Yanwu Zhang, and Arthur B. Baggeroer. "Performance Metrics for Oceanographic Surveys With Autonomous Underwater Vehicles." IEEE Journal of Oceanic Engineering, Vol. 26, No. 4, October 2001.
- Williams, Christopher D., Neil Bose, Mark-Andrew Butt, and Mae L. Seto. "Mast/Snorkel Performance of the DOLPHIN AUV." Transactions Society of Naval Architects and Marine Engineers, 108, 2000.

X

- Xu, M., and S.M. Smith. "Adaptive Fuzzy Logic Depth Controller for Variable Buoyancy System of Autonomous Underwater Vehicles." Proc. of the 3rd IEEE Conference on Fuzzy Systems, pp. 1191-6, 1994.

Z

- Zhang, Yanwu et al. "Acoustic Doppler Velocimeter Flow Measurement from an Autonomous Underwater Vehicle with Applications to Deep Ocean Convection." Journal of Atmospheric and Oceanic Technology, Vol. 18, No. 12, pp. 2038-51, 2001b.
- Zhang, Yanwu, Arthur B. Baggeroer, and James G. Bellingham. "Spectral-Feature Classification of Oceanographic Processes Using an Autonomous Underwater Vehicle." IEEE Journal of Oceanic Engineering, Vol. 26, No. 4, October 2001a.
- Ziegler, J.G., and N.B. Nichols. "Optimal Settings for Automatic Controllers." Trans. ASME, Vol. 64, No. 11, pg. 759, 1942.

Zimmerman, C.H. "Characteristics of Clark Y Airfoils of Small Aspect Ratio." NACA Report 431, 1933.

INDEX OF AUTHORS

A

Aihara, Y. 31, 68
 Akiyama, H. 3
 Allen, H. Julian 31, 68
 Allen, R. 8, 101
 An, Edgar 2, 9, 39
 Ananthakrishnan, P. 39
 Anderson, D.T. 8
 Aronson, Dag 20
 Asakawa, Kenichi 2
 Ashley, Holt 108
 Åström, Karl 100, 139, 147, 172
 Athans, Michael 140
 Aucher, M. 20–21, 28–30, 63, 107–108
 Avallone, Eugene A. 42

B

Banerjee, J.S. 142
 Barlow, Jewel 9, 13, 41–43, 55, 62, 73, 101,
 103–104, 222–223
 Baumeister III, Theodore 42
 Bisgood, P.L. 31, 172
 Borst, Henry 21, 30
 Bossley, K.M. 101
 Boyce, William 173
 Brockett, Terry 7, 37
 Bullivant, W. Kenneth 56, 102
 Burden, Richard 181
 Butler, Bruce 139
 Bystrom, L. 8

C

Caccia, Massimo 101
 Calisal, Sander 9, 100
 Cancelliere, Fredrick 3, 141
 Canudas-de-Wit, C. 8, 139
 Carder, Kendall L. 2–3
 Carreras M. 173
 Cellier, Francois E. 101
 Cherchas, Dale 9, 100
 Clancy, Tom 1
 Conway, John 101
 Craven, Paul J. 2, 142
 Cristi, Roberto 8, 141

D

Davies, Michael 36
 de Silva, Clarence 141–142
 Dempsey, Elizabeth M. 31, 33, 172
 den Hertog, Vincent 7, 14, 41, 147
 DiBiterro, P.A. 8
 DiPrima, Richard 173
 Dobeck, G.J. 8
 Dominguez, Rodolfo 68, 87, 128
 Doucy, Olivier 7
 Dougherty, F. 8
 Dutton, Ken 139–141, 147, 172

E

Edwards, Joseph R. 2
 Elmqvist, Hilding 101
 Eppler, Richard 48

F

Faires, J. Douglas 181
 Fehlner, Leo 20, 27, 107–108, 172
 Feldman, J. 14
 Feldman, Jerome P. 41–42, 101
 Ferguson, James 2
 Field, Adrian 7, 9–10, 27, 38, 40, 89, 100,
 137, 140–141, 143, 159–162, 164, 170,
 172–173, 176, 184, 196, 198, 209, 211,
 285
 Fournier, Eric 43
 Fryxell, D.P. 8

G

Gartshore, Ian 36
 Ghalia, Mounir Ben 140
 Gilbert, R. 2

H

Hale, R.W. 73
 Han, Simon 7
 Harper, J.J. 62
 Harris, Daniel 9
 Hayes, Daniel R. 2
 Healey, Anthony 3, 8–9, 40, 101
 Hills, J.J. 8
 Hoerner, Sighard 21, 30, 116, 118, 225

Hoffman, Joe 173
Hogg, Robert V. 92
Hopkin, David 36, 41, 101
Hover, Franz 7
Hsu, Chun-Fei 142
Huggins, A. 2, 41
Huyer, S. 101

J

Jacob, Jamey 119, 217
Jacobs, Eastman 102, 105
Jalving, Bjorn 8, 101
Journée, J.M.J. 39, 89
Juil, D.L. 140

K

Kawamura, R. 31
Keating, R.F.A. 55
Kim, Joonyoung 41, 101
Kosko, Bart 141
Kulcsár, Balázs 140
Kumagai, Michio 3
Kuwamura, R. 68

L

Lamb, Sir Horace 38, 129
Landahl, Marten 108
Laval, Bernard 2
Lea, R.K. 8, 101, 142
Ledolter, Johannes 92
Lee, C.S. George 141
Leinard, David 8
Leith, D.J. 141
Leithead, W.E. 141
Lekander, Per 20
LePage, Kevin D. 2
Levine, Edward R. 2
Levine, William S. 101
Liceaga-Castro, E. 8
Lienard, David 101
Lin, Chih-Min 142
Lloyd, A.R. 35–36
Lorentz, Jorgen 2, 8
Lyons, D.J. 31, 172

M

Mackay, Michael 21, 29–30, 33, 101

Maltby, R.L. 55
Marco, D. 8
McDonald, H. 101
McFarlane, James R. 3
McGeer, Ted 2–3, 137, 139, 146, 170, 196,
211
McTaggart, K.A. 101, 172
Merry, S.L. 8, 101
Merzkirch, Wolfgang 55, 62, 73
Modi, Vinod J. 14
Moore, J.B. 140
Morison, James H. 2
Munk, M.M. 35

N

Naeem, W. 140, 173
Nahon, Meyer 101, 171–172
Newman, J.N. 38
Nguyen, Thai C. 8
Nichols, N.B. 147

O

Oh, Kyu-Hyun 7
Ostafichuk, Peter 73, 100
Otter, Martin 101

P

Packwood, A.R. 2, 41
Palm, William 100, 139, 145, 147, 172
Pandya, A.S. 8
Papoulias, F.A. 8
Pascoal, A. 9
Pauchet, A. 217
Perkins, Edward W. 31, 68
Perrier, M. 8
Perron, C. 41
Peterson, Ronald S. 3, 8, 39
Pierre, M. 139
Pope, Alan 62
Pope, Allan 2
Potter, Merle C. 42
Prestero, Timothy 7, 173

R

Rae, G.J.M. 8
Ranzenbach, Robert 9
Riedel, Jeffery S. 3, 9, 40

- Rigatos, G.G. 142
Rodriguez, Rafael 8
RWDI (Rowan Williams Davies & Irwin Inc.)
55
- S**
Schmidt, Henrik 2
Seto, Mae 5-7, 37, 43, 177, 182
Seto, Mae. Private communication. August 13,
1997. 7
Shein, A.M. 8
Sherman, Albert 102
Shupe, Landy 2-3, 137, 139, 146, 170, 196,
211
Silvestre, C. 9
Smith, Samuel 8-9, 39, 142
Solberg, Paal Are Hagtbedt 101
Song, Feijun 9, 137, 142, 172
Spiegel, Murray 92
Stack, John 102
Stein, Gunter 140
Sudhakar, R. 8
Suto, T. 9
- T**
Talay, Theodore 21, 57, 80, 119, 217
Tay, T.T. 140
Tipler, Paul 89, 129
Torres, M. 47, 274
Triantafyllou, Michael 7
Tzfestas, S.G. 142
- U**
Underwater Magazine 3
Ura, T. 9
- V**
van den Berg, B. 20
van der Molen, G. 8
Venugopal, K.P. 8
Veruggio, Gianmarco 101
von Mises, Richard 108, 119, 217
- W**
Wadlin, Kenneth 38, 94
Walsh, Ronald 270
Watt, George 2-3, 5-7, 11, 23, 37, 41, 43,
100, 177, 182
Whicker, L. Folger 20, 27, 107-108, 172
White, Frank 21, 31, 42, 102, 129, 225, 274,
276
Whitfield, D. 101
Wiggert, David C. 42
Willcox, J. Scott 2
Williams, Christopher D. 5, 24
Wittenmark, Björn 100, 139, 147, 172
Woolweaver, G. 8
- X**
Xu, M. 8
- Y**
Yoerger, D.R. 8
Yuh, J. 2, 8
- Z**
Zhang, K-Q. 39
Zhang, Yanwu 2
Ziegler, J.G. 147
Zimmerman, C.H. 21, 221

SUBJECT INDEX

A

Adaptive control. See Control, Adaptive
 Aft plane
 see Sternplane
 Aircraft elevators, 35
 Airfoil, 19
 NACA, 19
 Angle of attack. See Angle of incidence
 Angle of incidence, 27, 30, 40
 Equation, 27
 In trim, 30, 64
 See also Hull, Flow angle in trim
 Anhedral, 23
 Illustration, 23
 Applications
 Cable Inspection, 2
 Space exploration, 3
 Articulated mast, 24
 Aspect ratio, 20
 Equation, 20
 Autonomous underwater vehicle, 2-3, 7
 Application, 2-3
 Applications, 6
 ARPA UUV, 8
 Autosub, 8
 Control
 Fuzzy logic, 8-9
 Gain scheduling, 8
 H-infinity, 8
 Linear quadratic, 8
 Linear Quadratic Regulator, 8
 LQG/LTR, 9
 LQG/LTR, Adaptive, 9
 Neural network, 8
 Non-linear PID, 8
 PID, 8-9
 Sliding mode, 8-9
 CSS, 8
 Degrees of freedom, 4
 DOLPHIN, 5, 9
 LDUUV, 8
 LSV, 8
 Manta-Ceresia, 9
 MARIUS, 8
 MUST, 8
 NDRE-AUV, 8
 NPS AUV II, 8
 NPS PHOENIX, 9
 Ocean Explorer, 9

Ocean Voyager, 8
 ODIN, 8
 Previous work, 8
 Range, 2
 Subzero II, 8
 VORTEX, 8

AUV

see Autonomous underwater vehicle

B

Boundary layer, 47
 Dependence on Reynolds number, 47
 Transition, 275
 Tripping, 47, 274-275
 Bowplane, 14, 105, 107, 109
 Depth control, 3
 Differentially deflected, 37
 Effect of trim on, 30, 64-67, 69, 111
 Effect of yaw on, 68, 71-72, 113-117, 224
 Hull influence on, 29, 32, 70, 72
 Illustration, 4, 14
 Interaction with sternplane, 73, 75-76, 79-80, 82, 227, 230
 Layout
 Illustration, 23
 Performance prediction, 29-30, 32
 Position, 3, 45-46

C

Chord, 18-19
 Equation, 18
 Illustration, 19
 Circulation, 228
 Coefficient
 Drag, 28
 Force, 28, 42
 Lift, 27, 42, 103, 222-223
 Equation, 16
 Control
 Adaptive, 140-142
 Autonomous underwater vehicle, 8
 Previous work, 8
 Feedback, 138
 Fuzzy logic, 142, 151-156, 158, 169
 Gain scheduling, 141, 147, 149-150
 Integral action, 139

- LQG/LTR, 139–140, 159–169
 Design, 164–165, 285
 Filter design, 161–163
Illustration, 159
 Performance, 198, 200
 Sliding mode, 164, 166–168
 Tuning, 285–287
- PD, 146–147
Illustration, 147
 Instability, 202–203
 Performance, 196, 200
 Steady state error, 186, 197
- PID, 138–139
 Research summary, 8
 Sliding mode, 141, 164, 166–168
- Control effort, 182
 Control output, 282
 Control surface, 15, 44
 Actuation, 45, 47
 Anhedral, 23
 Apect ratio, 21
 Articulated mast, 24
 Aspect ratio, 20, 45
Equation, 20
 Chord, 18, 45
 Construction
Illustration, 45
 Definitions, 16
 Dihedral, 23
 Endplate *see* Endplate
 Foil, 19
 Free surface influence, 39
 Geometry, 18, 57–59, 188
 Chord, 18
 Hull influence, 29
Illustration, 18–19
 Interaction, 35
 Inverted Y-tail, 24
 Isolated, 27–28
 Performance, 54, 56, 58
 Keel planes, 24
Illustration, 26
 Instability, 202–203
 Layout, 23, 45–46, 60–61, 190
Illustration, 23, 25, 46
 Low aspect ratio, 21
 Minimum drag, 28
 Performance prediction, 27–31, 33–34
 performance prediction, 29
 Planform
 Rectangular, 20
 Planform area, 20
Equation, 20
 Rudder, 3
 Scale model, 44
 Span, 19, 45
 Sweep, 20, 45
 Tail configuration, 24
 Taper, 27, 45
 Taper ratio, 20
 Thickness, 19
 Thickness ratio, 29
 Tip geometry effect, 27
 Vertical position, 23, 30
 X-tail, 24
 Y-tail, 24
- Control, LTR, 140
 Controller model, 185
 Coupling effects, 101
 Crossflow drag, 27
- D**
- Data collection, 53
 Decoupling, 101
 Depth, 93
 Control of, 3, 39
 Effect on control surface, 38
 Influence on control surface, 93–95, 129–130
 Influence on wave orbital velocity, 90
- Dihedral, 23
Illustration, 23
- Dimensinal analysis, 42
 Dimensionless variables, 42
- Disturbances
 Compensation, 39
 due to Coupling, 101
 Wave, 40
 Wave induced, 40
- DOLPHIN, 5–7, 10, 37, 40, 172
 Applications, 6
 Drawings, 233
Illustration, 5
 Initial development, 7
 Operating depth, 5
 Operation, 5
 Semi-submersible design, 5
 Snorkel, 6
 Specifications, 6
- Dorado, 5
 Downwash, 35, 37
 Drag

- Coefficient, 28
 Crossflow, 27
 Dynamic pressure, 16
- E**
- Endplate, 21–22, 59
 Illustration, 22
 Performance, 59–60, 80
 Performance prediction, 21
 Engineering drawings, 233
 Europa, 3
 Evaluation
 Control effort, 182
 Manoeuvre, 177
 Illustration, 177
 Performance index, 178–180, 182
 Evaluation criteria, 178
- F**
- Feed forward compensation, 144–145
 Illustration, 145
 Fence *see* Endplate, 21
 Filter, 175–176
 Flight vehicle, 3
 Flow angle to planes
 Illustration, 28
 Flow visualization
 Bubble path, 73–75, 81, 84–85
 Oil film, 55–57, 64–65
 Yarn Tuft, 63
 Yarn tuft, 62–63, 68, 71
 Foil, 44
 NACA, 19
 Foil Section, 19
 Foil section, 19
 Force
 Coefficient, 28
 Non-dimensional, 16–17, 55
 Fore plane
 see Bowplane
 Free surface, 89
 Froude number, 42
 Fuzzy logic, 141, 151–156, 158
 Membership function, 154, 156–157
 Rulebase, 153, 155–156
- G**
- Gain scheduling. *See* Control, Gain scheduling
- H**
- Heave, 15
 Control of, 3
 Illustration, 4
 Hull
 Boundary layer, 33
 Effect of curvature, 29
 Flow angle in trim, 30
 Equation, 30
 Flow angle in trim *Illustration*, 30
 Flow separation, 47
 Influence on bowplane, 224
 Influence on control surface, 29
 Vortex, 224
 Vortices, 31–32, 71
 Illustration, 32
 Location, 32
 Hydrodynamic derivative, 17, 107–108, 133
 Equation, 17
- I**
- Identification, 101
 Image vortex, 218, 228
 Incident flow angle
 Illustration, 28
 Incident flow angle. *see* Angle of Incidence
 Inclined cylinder, 30–31
 International Submarine Engineering, 2, 5, 7, 10
 Inverted Y-tail, 24
 ISE
 see International Submarine Engineering
 Isolated control surface, 27
 see Control surface, Isolated
- K**
- Kalman Filter, 140
 Keel planes, 24
 Illustration, 26
 Kutta-Joukowski lift theorem, 217, 227
- L**
- Lakes, AUV use in, 2
 Leading edge, 19
 Lift coefficient, 27
 Lift coefficient *see* Coefficient, Lift, 16
 Lift-curve slope, 27
 Equation, 27
 Linear quadratic gaussian
 see Control, LQG
 Load cell, 44, 48–49

Assembly, 52
 Illustration, 52
 Calibration, 52, 272–273
 Design, 270–271
 Illustration, 45, 253–254, 256–259
 Principle of operation, 49
 Loop transfer recovery. *See* Control, LTR
 Low aspect ratio
 Definition, 28
 LTR. *See* Control, LTR

M

Manoeuvre
 see Evaluation, Manoeuvre, 177
 Manoeuvring, 3
 Matlab, 172
 Mine countermeasures, 2
 Modelling
 for Simulation, 7
 Moments
 Non-dimensionalized, 16
 Motion
 Decoupling, 3

N

NACA, 19, 28, 102
 0015, 28
 0025, 44
 Foil, 19
 Minimum drag, 28
 Non-dimensional variables, 42

P

Performance index, 139, 164
 PID. *See* Control, PID
 Pitch, 15
 Control of, 3
 Illustration, 4
 Pitch control, 3
 Plane, 14
 see also Bowplane or Sternplane
 see Control surface
 Plant, 175, 184–185
 Plant matrix, 282
 Potential flow, 227

Q

Quantization, 176

R

Radius of curvature
 Calculation, 279
 rectangular, 20
 Remotely operated vehicle, 2–3
 Reynolds number, 42, 47
 Effect on stall, 55, 102–103, 133, 222–223
 Scaling, 103
 Riccati equation, 140
 Roll, 15
 Control of, 3
 Due to rudder, 3
 Illustration, 4
 Roll control, 7
 Roll stabilizer fins, 35
 ROV
 see Remotely operated vehicle
 Rudder, 3
 Illustration, 4
 Roll moment, 3
 Yaw control, 3

S

Scale model
 Assembly, 43
 Development, 43
 Illustration, 44
 Mounting, 48
 Illustration, 50–51
 Trim adjustment, 48
 Use of propulsion with, 43
 Yaw adjustment, 48
 Scaling, 42
 In tow tank, 43
 In wind tunnel, 43
 Reynolds number, 47
 Semi-span, 19
 see also Span, 19
 Sensor, 175–176
 Imaging, 39
 Performance, 39
 Sensor noise, 176
 Series compensation, 145, 151–156, 158, 169
 Illustration, 145
 Sign conventions, 15
 Signal conditioning, 48–49
 Significant amplitude, 181
 Similarity, 42
 In tow tank, 42
 In wind tunnel, 42

- Simulation, 172
 Autonomous underwater vehicle, 8
 Error, 173
 Layout, 173, 175
 of DOLPHIN, 171
 Plant layout, 175
 Process *Illustration*, 174
 Programming, 176
 Speed, 173
- Simulink, 172
- Sliding mode control. See Control, Sliding mode
- Slope error estimate, 278
- Space exploration, 3
- Span, 19
Illustration, 19
- Stall, 102–103, 222–223
- Stall angle, 55
- State space, 143–144, 282
- Steady state error, 186
- Sternplane, 3, 14
 Effect of trim on, 70
 Hull influence on, 31, 33–34
Illustration, 4, 14
 Layout, 24
 Performance prediction, 31, 33–34
 Pitch control, 3
 Position, 45–47
 Roll control, 3
 Tail efficiency factor, 31
- Surge, 15
Illustration, 4
- Surge control, 3
- Sway, 15
Illustration, 4
- Sweep, 20
- Swept wing
 see Sweep, 20
- System identification. See Identification
- T**
- Tail Efficiency, 31
- Taper, 27
- Taper ratio, 20, 27
- Testing facilities, 53
- Theseus, 2
- Thickness
 see Control Surface, Thickness
- Three-term controller. See Control, PID
- Tip vortex, 217, 227–228
- Tip vortex. See also trailing vortex., 37
- Tow tank, 53
- Trailing edge, 19
- Trailing vortex, 35–36
- trailing vortex, 37
- Trailing vortex, see Tip vortex
- Trim, 30
 See also Bowplane, Effect of trim on
- U**
- Underwater vehicle
 Origns, 1
- Upwash, 217–220
- V**
- Vortices
 Hull, 31
 Hull *Illustration*, 32
 In yaw, 71
 in Yaw, 31
- W**
- Wave
 Orbital velocity, 40, 90
- Wave disturbance. See Disturbances, Wave
- Wind tunnel, 53
- X**
- X-tail, 24
- Y**
- Yaw, 15
 Hull vortices, 31
Illustration, 4
- Y-tail, 24
 Roll error, 194
 Turning radius, 193
- Y-tail, Inverted, 24